

Self-Assembled Nanostructures in Organic Electronics

Rachel Catherine Kilbride

The University of Sheffield

Faculty of Science

Department of Physics and Astronomy

December 2021

A thesis submitted in partial fulfilment of the requirements for the degree of
Doctor of Philosophy

Acknowledgements

When deciding to take on the difficult task of a PhD in experimental physics, I could never have predicted that I would be part of the select few doing a PhD in the middle of global pandemic. The Covid-19 pandemic has changed the world we live in and trust in science is more important than ever. It is for this reason that I would first like to offer a heartfelt thank you to all frontline and essential workers, volunteers and all of those responsible for the successful development and roll out of the vaccine. All of your hard work has made it possible for me to submit this thesis during a pandemic.

A sincere thank you goes to my supervisor Andy Parnell for his constant support and enthusiasm about science. You go above and beyond to help your students and there is no better example of that than the support you provided during the pandemic and all your hard work getting the labs back open. Thank you for making research fun, for always striving to do good science and for always having time for your students. I am also immensely grateful to Richard Jones for his supervision, for introducing me to the wonderful world of X-ray and neutron scattering and for being a calming influence in stressful situations. I am grateful to both of you for your wonderful supervision, expertise and support.

I thank all of my group members in the Soft Matter and Biophysics group at Sheffield. When I began my PhD, we were a group of 6 but have since more than doubled in size, growing to become an inter-departmental research group, covering a diverse range of extremely exciting research. Thanks to all of you for your extraordinary science and for making Sheffield a great place to work. Special thanks to Stephanie Burg, Tom Sexton, Tom Catley and honorary group member Mike Weir for all your support and friendship over the past few years.

I thank David Lidzey for persuading me to do a PhD, for all of his advice on publishing and for welcoming me into the Electronic and Photonic Molecular Materials (EPMM) group at Sheffield. I thank all of the current EPMM members and alumni. In particular, I thank Emma Spooner for all of the sleep-deprived hours spent assisting with beamtime experiments, for her device expertise and for all of the helpful discussions. I also thank Joel Smith, Mary O’Kane, Kirsty McGhee, Claire Greenland, Tom Routledge, Onkar Game, James Bishop, Rahul Jayaprakash, Kyriakos Georgiou and more recently Tim Thornber and Peter Claronino for being great colleagues and for all of the Friday evenings at Uni Arms.

I thank all of the wonderful researchers outside of Sheffield that I have been fortunate to collaborate with at Imperial College London, The University of Surrey, Trinity College Dublin, Porto University, Wuhan University, Minnesota University and Oxford University. In particular, I thank Matt Bidwell for his expertise in synthesising so many, exciting deuterated materials to characterise. I am also hugely grateful to Jess Wade for introducing me to the fascinating world of chiral materials and for her support of early career researchers.

Next, I must acknowledge all of the beamline scientists at ISIS and ILL who I have had the pleasure to work with. These are Rob Dalglish, Steve King, Jos Cooper, Adam Washington, Nina Juliane-Steinke, Philipp Gutfreund and Thomas Saerbeck. Being a beamline scientist is often a thankless task but I am extremely grateful for your invaluable help on beamline experiments, particularly those that were adapted and performed remotely because of the pandemic. I also thank all of the friends I made on the ISIS neutron training course and for making the neutron scattering community such an enjoyable community to be a part of.

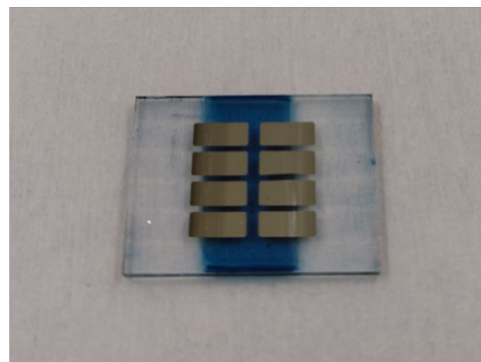
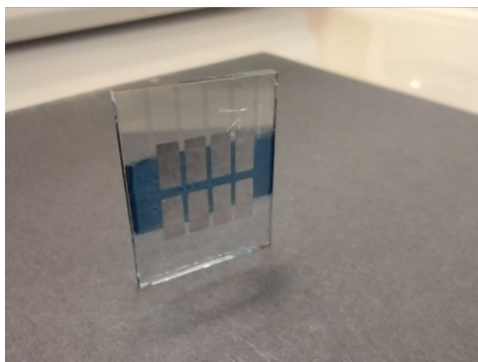
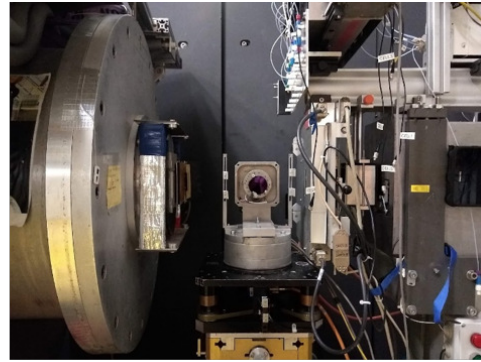
A huge thank you goes to my housemates JP and Michael for putting up with me during thesis writing and for making our home a welcoming place to relax after a tough day. A special thank you goes to Michael for making so many delicious meals and for all of his \LaTeX wizardry.

Finally, I thank all of my friends and wonderful family back home in Liverpool. To my parents Lorraine and Kevin, Sister Sarah and Brother Paul, I am not sure if you will ever read this but know that I am indebted to all of the support you have provided, particularly after what has been a truly difficult few years. Thank you for all the video calls, trips back home, “survival treat boxes” and visits to Sheffield. You have always supported my curiosity and love of science, and this work would not have been possible without it.

Abstract

Conjugated organic materials have the remarkable ability to absorb and emit light and transport electrical charge. Over the past century, this phenomenon has fascinated physicists, chemists, materials scientists and more as it allows the semiconducting properties of *inorganic* materials like silicon to be combined with the material properties of *organic* materials like polymers. By controlling the chemical properties of these organic materials, we can tune the wavelengths or *colour* of light that they emit and absorb, and we can use scalable printing technologies to fabricate ultra-thin, organic semiconducting films at low-cost and high throughput. These concepts have led to developments in a broad range of optoelectronic applications such as the organic light emitting diodes (OLEDs) we use in display technologies to the organic solar cells (OSCs) we use to power electrical devices. A common theme underpinning the performance of each of these technologies is the morphological optimisation of soft-matter systems, which self-assemble into complex, intricate structures at length scales intermediate between atomic and macroscopic scales. This leads to a rich hierarchical phase behaviour that strongly influences the performance and stability of the device.

In this thesis, I investigate the relationships between organic thin film nanostructure, optoelectronic performance and stability with the aim of developing a better understanding of the characteristics required to fabricate highly efficient, stable technologies. The majority of the research focuses on understanding these relationships in high performing OSC systems, which rely on the fabrication of a photoactive blend film of conjugated polymer semiconductors and small molecule electron acceptors. Over the past decade the power conversion efficiency (PCE) of OSCs has more than doubled with PCEs > 20% now in reach. Such a rapid rise in efficiency is largely due to the development of a new class of electron acceptor material; non-fullerene electron acceptors (NFAs). In this work, I explore how factors such as the choice of casting solvent, solvent additive processing and NFA molecular design influence the structure-performance-stability relationships of polymer : NFA based systems. To do this, I use a broad range of structural characterisation techniques such as grazing incidence X-ray scattering, small angle neutron scattering and neutron reflectivity to probe the entire three-dimensional morphology of the film. In the final chapter, I expand these techniques to characterise the molecular self-assembly of novel chiral small molecules in thin films for chiro-optoelectronic applications.



Front Matter

Declaration of Originality

I, the author, confirm that the work described in this thesis was undertaken at The University of Sheffield between September 2017 and December 2021 under the supervision of Dr Andrew J. Parnell, Professor Richard A. L. Jones and Professor David G. Lidzey. I confirm that the thesis is my own work, except where work that has formed part of jointly authored publications has been included. My own contribution and the contribution of the other authors to this work has been explicitly indicated below. I confirm that appropriate credit has been given within the thesis where reference has been made to the work of others. This work has not been submitted in whole or in part for any other degree at this or any other institution.

Rachel Catherine Kilbride (December 2021)

0.1 Thesis Format

For Chapters 4-6, the experimental work, data analysis, interpretation and writing was primarily completed by myself. In the case of Chapter 7, the work was prepared in collaboration with Imperial College London and has been submitted as a journal article for publication. In this thesis, the manuscript has been reformatted from the most recent version into the style of the thesis for continuity. Each results chapter is preceded by a foreword summarising the work and its relation to the thesis and wider field. For ease of readability, numeration of content aside from page numbers is specific to each chapter. References for all chapters are provided at the end of the thesis.

0.2 Collaborators

All collaborators who have contributed to work in this thesis are listed below followed by their affiliations. Specific contributions are outlined in the Author Contributions for each chapter.

- Andrew J. Parnell¹
- Ana Charas²
- David G. Lidzey¹
- Derick K. L. Liew¹
- Dong Kuk Kim^{3,4}
- Emma L. K. Spooner¹
- Erin Johnson⁵
- Francesco Salerno^{4,6}
- Gabriel Bernardo²

- Iain McCulloch^{4,6}
- Janet A. Christenson⁷
- Jenny Nelson^{4,6}
- Jessica Wade^{3,4}
- Joel A. Smith^{1,8}
- Julia A. Schmidt^{4,6}
- Kaicheng Shi⁷
- Khalid I. A. Doudin⁹
- Kim Jelfs^{4,6}
- Luc LeBlanc⁵
- Mary E. O’Kane¹
- Matthew Bidwell^{4,6}
- Matthew J. Fuchter^{4,6}
- Philipp Gufreund¹⁰
- Richard A. L. Jones^{1,11}
- Robert M. Dalgliesh¹²
- Ronald L. Christenson⁷
- Russell J. Holmes⁷
- Sandrine Heutz^{3,4}
- Stephanie L. Burg¹
- Tao Wang^{13,14}

0.2.1 Affiliations

1. Department of Physics and Astronomy, The University of Sheffield, Hicks Building, Hounsfield Road, Sheffield, S3 7RH, United Kingdom
2. LEPABE – Laboratory for Process Engineering, Environment, Biotechnology and Energy, Faculty of Engineering, University of Porto, Porto 4200-465, Portugal
3. Department of Materials and London Centre of Nanotechnology, Imperial College London, Exhibition Road, London SW7 2AZ, United Kingdom
4. Centre of Processable Electronics, Imperial College London, Exhibition Road, London SW7 2AZ, United Kingdom
5. Department of Chemistry, Dalhousie University, 6274 Coburg Road, Halifax, Nova Scotia, Canada B3H 4R2
6. Department of Chemistry and Molecular Sciences Research Hub, Imperial College London, White City Campus, 82 Wood Lane, London W12 0BZ, United Kingdom
7. Department of Chemical Engineering and Materials Science, The University of Minnesota, Minneapolis, MN 55455, USA
8. Department of Physics, Clarendon Laboratory, University of Oxford, Oxford, OX1 3PU, United Kingdom
9. Department of Chemistry, The University of Sheffield, Dainton Building, Brook Hill, Sheffield, S3 7HF, United Kingdom
10. Institute Laue-Langevin, 71 avenue des Martyrs, 38042 Grenoble, France

11. Department of Materials, The University of Manchester, Sackville Street Building, Manchester, M1 3BB, United Kingdom
12. ISIS Neutron and Muon Spallation Source, Rutherford Appleton Laboratories, Oxfordshire, United Kingdom
13. School of Materials Science and Engineering, Wuhan University of Technology, Wuhan 430070, China
14. State Key Laboratory of Silicate Materials for Architectures, Wuhan University of Technology, Wuhan 430070, China

Publications

0.3 Published Work

Benjamin G. Freestone[†], Joel A. Smith[†], Giacomo Piana, **Rachel C. Kilbride**, Andrew J. Parnell, Luca Sortino, David M. Coles, Orianna B. Ball, Natalia Martsinovich, Courtney J. Thompson, Tarek I. Alanazi, Onkar S. Game, Alexander I. Tartakovskii, Pavlos Lagoudakis, and David G. Lidzey*. Low-dimensional emissive states in non-stoichiometric methylammonium lead halide perovskites. *Journal of Materials Chemistry A*, 7(18):11104–11116, 2019

Mengxue Chen, Zhuohan Zhang, Wei Li, Jinlong Cai, Jiangsheng Yu, Emma L. K. Spooner, **Rachel C. Kilbride**, Donghui Li, Baocai Du, Robert S. Gurney, Dan Lui, Weihua Tang, David G. Lidzey, and Tao Wang*. Regulating the morphology of fluorinated non-fullerene acceptor and polymer donor via binary solvent mixture for high efficiency polymer solar cells. *Science China Chemistry*, may 2019

Wei Li, Zuo Xiao, Jinlong Cai, Joel A. Smith, Emma L. K. Spooner, **Rachel C. Kilbride**, Onkar S. Game, Xianyi Meng, Donghui Li, Huijun Zhang, Mengxue Chen, Robert S. Gurney, Dan Liu, Richard A. L. Jones, David G. Lidzey, Liming Ding, and Tao Wang*. Correlating the electron-donating core structure with morphology and performance of carbon-oxygen-bridged ladder-type non-fullerene acceptor based organic solar cells. *Nano Energy*, jul 2019

Mengxue Chen, Dan Liu, Wei Li, Robert S. Gurney, Donghui Li, Jinlong Cai, Emma L. K. Spooner, **Rachel C. Kilbride**, James D. McGettrick, Trystan M. Watson, Zhe Li, Richard A. L. Jones, David G. Lidzey, and Tao Wang*. Influences of Non-fullerene Acceptor Fluorination on Three-Dimensional Morphology and Photovoltaic Properties of Organic Solar Cells. *ACS Applied Materials & Interfaces*, 11(29):26194–26203, jul 2019

Michael P. Weir*, Daniel T. W. Toolan*, **Rachel C. Kilbride**, Nicholas J. W. Penfold, Adam L. Washington, Stephen M. King, James Xiao, Zhilong Zhang, Victor Gray, Simon Dowland, Jurjen Winkel, Neil C. Greenham, Richard H. Friend, Akshay Rao, Anthony J. Ryan, and Richard A. L. Jones. Ligand Shell Structure in Lead Sulfide–Oleic Acid Colloidal Quantum Dots Revealed by Small Angle Scattering. *The Journal of Physical Chemistry Letters*, 10(16):4713–4719, aug 2019

Baocai Du, Renyong Geng, Wei Li, Donghui Li, Yuchao Mao, Mengxue Chen, Xue Zhang, Joel A. Smith, **Rachel C. Kilbride**, Mary E. O’Kane, Dan Liu, David G. Lidzey, Weihua Tang, and Tao Wang*. 13.9% Efficiency Ternary Nonfullerene Organic Solar Cells Featuring Low-Structural Order. *ACS Energy Letters*, 4(10):2378–2385, jul 2019

Wei Li, Zuo Xiao, Joel A. Smith, Jinlong Cai, Donghui Li, **Rachel C. Kilbride**, Emma L.K. Spooner, Onkar S. Game, Xianyi Meng, Dan Liu, Richard A.L. Jones, David G. Lidzey, Liming Ding, and Tao Wang*. Enhancing the efficiency of PTB7-Th:COi8DFIC-based ternary solar cells with versatile third components. *Applied Physics Reviews*, 6(4):041405, dec 2019

Donghui Li, Xiaolong Chen, Jinlong Cai, Wei Li, Mengxue Chen, Yuchao Mao, Baocai Du, Joel A. Smith, **Rachel C. Kilbride**, Mary E. O’Kane, Xue Zhang, Yuan Zhuang, Pang Wang, Hui Wang, Dan Liu, Richard A.L. Jones, David G. Lidzey, and Tao Wang*. Non-fullerene acceptor fibrils enable efficient ternary organic solar cells with 16.6% efficiency. *Science China Chemistry*, 63(10):1461–1468, oct 2020

Jinlong Cai, Hui Wang, Xue Zhang, Wei Li, Donghui Li, Yuchao Mao, Baocai Du, Mengxue Chen, Yuan Zhuang, Dan Liu, Hua Li Qin, Yan Zhao, Joel A. Smith, **Rachel C. Kilbride**, Andrew J. Parnell, Richard A.L. Jones, David G. Lidzey, and Tao Wang*. Fluorinated solid additives enable high efficiency non-fullerene organic solar cells. *Journal of Materials Chemistry A*, 8(8):4230–4238, feb 2020

Joel A. Smith, Onkar S. Game, James E. Bishop, Emma L.K. Spooner, **Rachel C. Kilbride**, Claire Greenland, Rahul Jayaprakash, Tarek I. Alanazi, Elena J. Cassella, Alvaro Tejada, Ganna Chistiakova, Michael Wong-Stringer, Thomas J. Routledge, Andrew J. Parnell, Deborah B. Hammond, and David G. Lidzey*. Rapid Scalable Processing of Tin Oxide Transport Layers for Perovskite Solar Cells. *ACS Applied Energy Materials*, 3(6):5552–5562, jun 2020

Daniel T.W. Toolan*, Michael P. Weir*, **Rachel C. Kilbride**, Jon R. Willmott, Stephen M. King, James Xiao, Neil C. Greenham, Richard H. Friend, Akshay Rao, Richard A.L. Jones, and Anthony J. Ryan. Controlling the structures of organic semiconductor quantum dot nanocomposites through ligand shell chemistry. *Soft Matter*, 16(34):7970–7981, sep 2020

Tarek I. Alanazi, Onkar S. Game, Joel A. Smith, **Rachel C. Kilbride**, Claire Greenland, Rahul Jayaprakash, Kyriacos Georgiou, Nicholas J. Terrill, and David G. Lidzey*. Potassium iodide reduces the stability of triple-cation perovskite solar cells. *RSC Advances*, 10(66):40341–40350, nov 2020

M. Prabodhi A. Nanayakkara, Lidija Matjačić, Sebastian Wood, Filipe Richheimer, Fernando A. Castro, Sandra Jenatsch, Simon Züfle, **Rachel C. Kilbride**, Andrew J. Parnell, Mateus G. Masteghin, Hashini M. Thirimanne, Andrew Nisbet, K. D. G. Imalka Jayawardena, and S. Ravi P. Silva*. Ultra-Low Dark Current Organic–Inorganic Hybrid X-Ray Detectors. *Advanced Functional Materials*, page 2008482, nov 2020

David G. Bossanyi, Maik Matthiesen, Shuangqing Wang, Joel A. Smith, **Rachel C. Kilbride**, James D. Shipp, Dimitri Chekulaev, Emma Holland, John E. Anthony, Jana Zaumseil, Andrew J. Musser, and Jenny Clark*. Emissive spin-0 triplet-pairs are a direct product of triplet–triplet annihilation in pentacene single crystals and anthradithiophene films. *Nature Chemistry*, pages1–9, dec 2020

Andrew Selkirk, Nadezda Prochukhan, Ross Lundy, Cian Cummins, Riley Gatensby, **Rachel C. Kilbride**, Andrew Parnell, Jhonattan Baez Vasquez, Michael Morris, and Parvaneh Mokarian-Tabari*. Optimization and Control of Large Block Copolymer Self-Assembly via Precision Solvent Vapor Annealing. *Macromolecules*, page 2543, jan 2021

Kirsty E. McGhee, Anton Putintsev, Rahul Jayaprakash, Kyriacos Georgiou, Mary E. O’Kane, **Rachel C. Kilbride**, Elena J. Cassella, Marco Cavazzini, Denis A. Sannikov, Pavlos G. Lagoudakis, and David G. Lidzey. Polariton condensation in an organic microcavity utilising a hybrid metal-DBR mirror. *Scientific Reports*, 11:1, 11(1):1–12, oct 2021

M Prabodhi, A Nanayakkara, Mateus G Masteghin, Laura Basiricò, Ilaria Fratelli, Andrea Ciavatti, **Rachel C. Kilbride**, Sandra Jenatsch, Thomas Webb, Filipe Richheimer, Sebastian Wood, Fernando A Castro, Andrew J Parnell, Beatrice Fraboni, K D G Imalka Jayawardena, S Ravi, and P Silva. Molecular Weight Tuning of Organic Semiconductors for Curved Organic–Inorganic Hybrid X-Ray Detectors. *Advanced Science*, page 2101746, nov 2021

Xueping Liu, Thomas Webb, Linjie Dai, Kangyu Ji, Joel A. Smith, **Rachel C. Kilbride**, Yuanyuan Huang, Jinxin Bi, Aobo Ren, Mozghan Yavari, Zhuo Wang, Yonglong Shen, Stephen J. Sweeney, Steven Hinder, Hui Li, David G. Lidzey, Samuel D. Stranks, Neil C. Greenham, S. Ravi P. Silva, Wei Zhang*. Interfacial engineering of dimensionally graded heterojunctions for efficient carrier transport in halide perovskite solar cells. *Energy & Environmental Materials*, dec 2021

0.4 Submitted

The following manuscripts have been submitted to journals and are currently undergoing review.

Harrison K. H. Lee, Katherine Stewart, Declan Hughes, Jeremy Barbe, Adam Pockett, **Rachel C. Kilbride**, Keith C. Heasman, Zhengfei Wei, Trystan M. Watson, Matthew J. Carnie, Ji-Seon Kim, Wing C. Tsoi*. Proton Radiation Hardness of Organic Photovoltaics: An In-depth Study

Kezia Sasistharan, **Rachel C. Kilbride**, Emma L. K. Spooner, Jenny Clark, Ahmed Iraqi, David G. Lidzey and Jonathan A. Foster*. Metal-organic framework nanosheets as templates to enhance performance in semi-crystalline organic photovoltaic cells

Chapter 7 as:

Jessica Wade^{†*}, Francesco Salerno[†], **Rachel C. Kilbride**[†], Dong Kuk Kim, Julia A. Schmidt, Joel A. Smith, Luc LeBlanc, Erin Johnson, Jenny Nelson, Tadashi Mori, Kim Jelfs, Sandrine Heutz and Matthew J Fuchter*. Controlling anisotropic properties through manipulation of chiral small molecule orientation in the bulk.

0.5 Manuscript in Preparation

The following manuscripts are in preparation and involve work presented in this thesis. The full author lists and publication titles will be confirmed prior to publishing.

Chapter 5 as:

Rachel C. Kilbride, Emma L. K. Spooner, Stephanie L. Burg, Derick K. L Liew, Robert Dalglish, Philipp Gutfreund, Ana Charas, Gabriel Bernardo, Tao Wang, David G. Lidzey, Richard A. L. Jones and Andrew J. Parnell*. The Impact of 1,8-diiodooctane on the Morphology, Performance and Stability of Organic Photovoltaics.

Chapter 6 as:

Rachel C. Kilbride, Matthew Bidwell, Emma L. K. Spooner, Robert Dalglish, Philip Gutfreund, David G. Lidzey, Iain McCulloch, Richard A. L. Jones and Andrew J. Parnell*. The Effect of Chemical Design on the Morphology, Performance and Stability of Non-fullerene Acceptor Organic Photovoltaics.

[†]These authors contributed equally. *Corresponding author(s)

Publicly Presented Work

ISIS Neutron Training Course
February 2018, Oxfordshire (U.K.)
(Poster Presentation)

UK Semiconductors IOP Competition
July 2018, Sheffield (U.K.)
(Oral Presentation)

ILL and ESS European User Meeting
October 2018, Grenoble (France)
(Poster Presentation)

Faculty of Science Graduate Showcase
March 2019, Sheffield (U.K.)
(Poster Presentation)

UK Neutron and Muon Science and User Meeting
April 2019, Coventry (U.K.)
(Poster Presentation)

European Conference on Neutron Scattering
July 2019, St Petersburg (Russia)
(Poster Presentation)

Next Generation Materials for Solar Photovoltaics
January 2020, London (U.K.)
(Poster Presentation)

3rd Year Research Talk
May 2020
(Virtual Oral Presentation)

Invited Research Talk to CBEPMM Group at Sheffield
August 2021
(Virtual Oral Presentation)

Nomenclature

Fundamental Physics Constants

c	Speed of light in a vacuum	$299\,792\,458\text{ m s}^{-1}$
\hbar	Reduced Planck constant	$1.054572 \times 10^{-34}\text{ J s}$
h	Planck constant	$6.626070 \times 10^{-34}\text{ J s}$
k_b	Boltzmann constant	$1.380649 \times 10^{-23}\text{ J K}^{-1}$
e	Elementary electron charge	$1.602176 \times 10^{-19}\text{ C}$
m_e	Electron mass	$9.109\,384\text{ kg}$
m_n	Neutron mass	$1.674\,927\text{ kg}$

Symbols used in the text

2θ	Scattering angle
β	Scattering length density
β_n	Neutron scattering length density
β_x	X-ray scattering length density
δ	Chemical shift
δ_D	Dispersive HSP
δ_{HSP}	Hildebrand solubility parameter
δ_H	Hydrogen-bonding HSP
δ_P	Dipolar HSP
$\frac{d\sigma}{d\Omega}$	Differential cross-section
λ	Wavelength
\mathcal{V}	Volume
\mathcal{V}_m	Molecular volume
ν	velocity

Ω	Solid angle
Φ	Incident flux
ϕ	In-plane scattering angle
ϕ_A	Acceptor volume fraction
ϕ_D	Donor volume fraction
ψ	Wavefunction
ρ	Mass density
σ	Cross-section
σ_R	Roughness
σ_{RMS}	RMS roughness
\mathbf{k}	Wavevector
\mathbf{k}_f	Scattered Wavevector
\mathbf{k}_i	Incident wavevector
\mathbf{Q}	Scattering vector
θ	Angle
θ_c	Critical angle
θ_f	Final angle
θ_i	Incident angle
θ_{CA}	Contact angle
ζ	Correlation length
A	Area
B	Background Intensity
b	Scattering length
b_p	Boiling point

DM_T	Deviation Metric
E	Energy
f	Frequency
I	Intensity
J	Current density
J_0	Dark current density
J_{SC}	Short-circuit current density
L	Thickness
l	Azimuthal quantum number
l_d	Exciton diffusion length
L_p	Long-period
m_l	Magnetic quantum number
m_s	Spin quantum number
n	Refractive index
n_p	Principal quantum number
P_v	Vapour pressure
$R(2\theta, \phi)$	Scattering rate
$R(Q)$	Reflectivity
R_S	Series Resistance
R_{SH}	Shunt Resistance
T	Temperature
t	Time
T_c	Crystallisation temperature
T_g	Glass transition temperature

T_m Melt temperature
 V Voltage
 V_m Mass density
 V_p Potential Energy
 V_{OC} Open-circuit voltage

Abbreviations

AFM Atomic force microscopy
AM Air mass
BHJ Bulk heterojunction
CD Circular dichroism
CIF Crystallographic information file
CTL Charge transport layer
DSC Differential scanning calorimetry
EQE External Quantum Efficiency
ETL Electron Transport Layer
FF Fill factor
GISAXS Grazing Incidence Small Angle X-ray Scattering
GIWAXS Grazing Incidence Wide Angle X-ray Scattering
HOMO Highest occupied molecular orbital
HSP Hansen solubility parameter
HTL Hole transport layer
IQE Internal Quantum Efficiency
LED Light emitting diode
LHCP Left-handed circularly polarised light

LUMO Lowest occupied molecular orbital
NFA Non-fullerene acceptor
NMR Nuclear magnetic resonance spectroscopy
NR Neutron Reflectivity
NREL National renewable energy laboratory
OLED Organic light emitting diode(s)
OPV Organic Photovoltaic(s)
PCE Power conversion efficiency
PL Photoluminescence
PV Photovoltaic
PXRD Powder X-ray Diffraction
RED Relative energy difference
RHCP Right-handed circularly polarised light
SANS Small Angle Neutron Scattering
SE Spectroscopic ellipsometry
SLD Scattering length density
SMA Small molecule acceptor
TCO Transparent Conductive Oxide
TGA Thermogravimetric analysis
UV Ultraviolet
XRD X-ray diffraction

Contents

Acknowledgements	i
Abstract	iii
Front Matter	v
0.1 Thesis Format	v
0.2 Collaborators	v
Publications	viii
0.3 Published Work	viii
0.4 Submitted	xi
0.5 Manuscript in Preparation	xi
Publicly Presented Work	xii
1 Introduction	1
1.1 A Changing Climate	1
1.2 The Commercialisation of Solar Photovoltaics	2
1.3 Organic Photovoltaics	3
1.4 Thesis Motivation	6
1.5 Thesis Overview	7
2 Background Theory of Organic Semiconductors	10
2.1 Introduction	10
2.2 Organic Semiconducting Materials	10
2.3 Organic Photovoltaics: An Overview	17
2.4 The Thermodynamics of Phase Separation	33
2.5 Correlating Self-Assembled Nanostructures with Optoelectronic Performance and Stability	40
3 Experimental Methods, Techniques and Theory	49
3.1 Introduction	49
3.2 Materials	49
3.3 OPV Solution Preparation and Thin Film Deposition	57
3.4 Organic Photovoltaic Devices	60
3.5 Film Wetting Behaviour and Surface Energy Characterisation	65
3.6 Surface Profilometry and Microscopy	69
3.7 Spectroscopy	71

3.8	Thermal Characterisation of Bulk Samples	78
3.9	Neutron and X-ray Scattering	79
4	Correlating Nanostructure with Optoelectronic Functionality in PBDB-T : ITIC Organic Photovoltaics with Non-Halogenated Solvents	116
4.1	Foreword	116
4.2	Author Contributions	116
4.3	Introduction	117
4.4	Experimental	121
4.5	Thermal Characterisation of PBDB-T and ITIC	123
4.6	Optoelectronic Properties	127
4.7	Large Scale Structures	137
4.8	Discussion	144
4.9	Summary	146
4.10	Supplementary Data	147
5	The Impact of 1,8-diiodooctane on the Morphology, Performance and Stability of Organic Photovoltaics	151
5.1	Foreword	151
5.2	Author Contributions	151
5.3	Introduction	152
5.4	Experimental	155
5.5	Optoelectronic Properties and Structural Characterisation of Fresh Films .	156
5.6	Tracking the Removal of DIO	190
5.7	Stability in Ambient Conditions	194
5.8	Stability in Inert Conditions	205
5.9	Discussion and Summary	212
5.10	Supplementary Data	215
6	The Effect of Chemical Design on the Morphology, Performance and Stability of Non-fullerene Acceptor Organic Photovoltaics	236
6.1	Foreword	236
6.2	Author Contributions	236
6.3	Introduction	237
6.4	Experimental	238
6.5	Characterising the Thermal Behaviour of Non-fullerene Acceptors	239
6.6	Initial Optoelectronic Properties and Morphology	245
6.7	Device Stability	270
6.8	Summary	273
6.9	Supplementary Data	274

7	Controlling Anisotropic Properties Through Manipulation of Chiral Small Molecule Orientation in the Bulk	277
7.1	Foreword	277
7.2	Author Contributions	277
7.3	Introduction	278
7.4	Experimental	280
7.5	Results and Discussion	281
7.6	Summary	300
8	Conclusion	302
8.1	Summary of the Thesis and its Contributions	302
8.2	Concluding Remarks	305
	References	306
	Appendix A Neutron Scattering Data Modelling	338
A.1	Chapter 5: Small Angle Neutron Scattering	338
A.2	Chapter 5: Neutron Reflectivity	339
A.3	Chapter 6: Small Angle Neutron Scattering	350
A.4	Chapter 6: Neutron Reflectivity	351
	Appendix B UV-Vis Photostability Studies	363

Introduction

1.1 A Changing Climate

Anthropogenic global warming, primarily from the burning of fossil fuels, is unequivocally the greatest challenge of our time and indeed all human history. The latest Intergovernmental Panel on Climate Change (IPCC) report published earlier this year paints an ominous picture of record atmospheric CO₂ emissions, the highest global temperature in at least the past 2000 years and average annual Arctic sea ice area at its lowest since at least 1850 [1]. The scale of recent changes in the climate are unprecedented and are destabilising both the natural environment and all aspects of human society in a myriad of ways through habitat and agricultural loss, pollution and increased frequency of extreme weather events [1, 2]. The IPCC report sends a clear message that global warming past the 2°C limit set by the Paris Agreement [3] will be exceeded by the end of the century leading to an irreversible domino effect of catastrophic climate events, *unless* there is a drastic reduction in anthropogenic emissions over the coming decades [1, 2]. Given that global energy consumption is expected to increase 60% by 2050 [4], and the international commitment to net-zero emissions by the same year [3], there is an urgent societal demand to radically reduce CO₂ emissions and develop new low carbon, sustainable energy technologies.

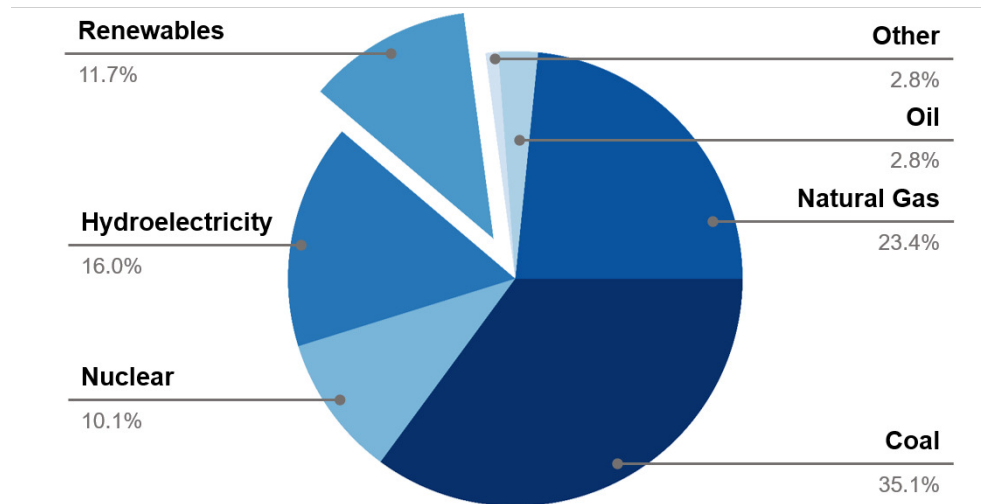


Figure 1.1: Global electricity generation contributions in 2020 [5].

Currently, renewable energy sources are primarily used for electricity generation. However, their contribution still falls behind that of fossil fuels (oil, coal and natural gas) which contributed 61.3% to the total global electricity generation share in 2020 (Figure 1.1) (and 83.1% to primary global energy consumption)[5]. Although the contribution of renewables will need to be increased significantly to achieve net-zero emissions, there are signs that the energy landscape is moving in the right direction. For example, annual global solar photovoltaic (PV) generating capacity increased by a record 21.5% in 2020, making solar PV the fastest growing renewable energy source worldwide [5]. Solar energy is estimated to deliver a yearly potential planetary resource of 23,000 TWy, far eclipsing the reserves of both finite non-renewable sources and the yearly potential of all other renewable sources [6, 7]. Despite obvious limitations such as changes in solar irradiance, cloud coverage, seasonal variances etc., harnessing just a fraction of the available solar resource could provide energy vastly exceeding annual global energy consumption (18.5 TWy in 2019) [7]. A combined effort, to increase renewable energy generating capacity whilst drastically reducing the global consumption of finite fossil fuels is critical to achieving the targets set out by the Paris Agreement [3]. Whilst solar PV currently only contributes a small fraction to global energy demands, it is clear that there is an enormous potential yet to be fully exploited for a diverse range of PV device applications.

1.2 The Commercialisation of Solar Photovoltaics

Solar PV devices were first made commercially in the 1970s [8]. Since then the cost of solar PV has plummeted roughly according to the historical experience curve; a log-log plot of cost versus cumulative volume, which predicts a 20% reduction in module cost for every doubling of cumulative volume [8]. This *learning rate* (LR) was estimated to be 23.8% in 2020 for utility scale solar PV [9] and in the last decade (between 2010 and 2020) the levelized cost of electricity (LCOE) has fallen by 85%, with current estimates predicting costs will be significantly lower than all other fossil-fuel alternatives in the next few years [10].

PV devices based on crystalline silicon (c-Si) currently dominate the solar energy market due to their impressively high power conversion efficiencies (PCEs) (>25% [11]) and exceptional operational lifetimes (>30 years [12, 13, 14]). Furthermore, they are durable in harsh weather conditions and only require a relatively small area for efficient power conversion. The combination of each of these factors along with the plummeting PV LCOE make it increasingly more difficult for other PV technologies to compete with c-Si. Despite this, there are several significant disadvantages to c-Si PV currently driving research focused on alternative PV materials. For example, c-Si is an indirect bandgap semiconductor suffering from weak absorption of the solar spectrum. Consequently, they perform poorly in low

light conditions and thick layers of material ($\sim 100 - 200\mu m$) are required for sufficient absorption. What's more, the low bandgap energy (1.1eV) results in a large proportion of the absorbed energy being lost through thermalisation mechanisms. Lastly and perhaps the most critical drawback, is the high temperature, energy-intensive fabrication required to produce large c-Si ingots through the Czochralski process [15, 16]. This process is commonly used to fabricate a number of different crystalline inorganic semiconductors but it requires the raw materials to be melted at high temperatures (1400 - 1500°C for Si) which increases the cost, speed and complexity of manufacturing. It is also important to consider the energy payback time (EPBT)- the estimated time for a PV system to produce an electrical energy equivalent to its input energy used in production. For c-Si, although production costs have fallen recently its EPBT is still estimated to be in the range of 1-2 years [17].

A number of alternative thin-film technologies have emerged with the aim of improving upon several of the pitfalls of c-Si. The current record cell efficiencies of various PV technologies is updated regularly by NREL and can be viewed elsewhere [11]. The primary motivation of thin-film technologies is to reduce the complexity and cost of manufacturing through low material consumption and more simplified processing methods. The first of these thin film technologies to emerge were based upon inorganic materials such as copper indium gallium diselenide (CIGS), cadmium telluride (CdTe) and amorphous silicon (a-Si) [18]. Over the past few decades, an increasing amount of research interest has shifted to focus on *third-generation* PV technologies such as dye-sensitized solar cells, perovskite solar cells, quantum dot solar cells and organic solar cells. These technologies have the potential to surpass the efficiency limit of a single-junction cell but current device efficiencies and stability remain inferior to c-Si PV technologies. Nevertheless, the rapid rise in efficiencies over the past two decades, particularly for organic and perovskite-based solar cells [11], combined with their ease of processing and significantly lower manufacturing costs, highlights the potential of these technologies as cheap, low-carbon renewable energy sources.

1.3 Organic Photovoltaics

The ability of carbon-based π -conjugated (organic) materials to absorb and emit light and transport charge make them an attractive material for a range of thin film optoelectronic applications such as light-emitting diodes, photovoltaics, photodetectors and thin film transistors [19]. Despite their potential and continuous advancement, the commercialisation of organic materials in electronics is a story of both great success and failure [20]. On the side of commercial success, organic light-emitting diodes (OLEDs) are the stand out example with their outstanding optical properties having revolutionised the display industry par-

ticularly for high contrast television and smartphone devices. Unfortunately, despite the similarities with OLED technologies, other organic electronic applications such as organic photovoltaics (OPV) and organic thin film transistors (OFTS) have not shared the same success making their impact outside of academic research so far, minimal.

OPV technologies are of particular interest because of their potential to contribute to the solar energy landscape in a versatile number of ways. For example, their compatibility with light-weight, flexible substrates and semi-transparent optical properties opens up a diverse range of tailored for purpose applications such as those related to building installations, transport and wearable technologies [21, 22, 23, 24]. Additionally, OPV devices are based on abundant, non-toxic raw materials that are typically solution-processed as ultra-thin ($< 100nm$) films at low-temperatures $25 - 200^{\circ}C$ requiring only small amounts of material ($1g/m^2$ [25]). This means they can be fabricated much more easily and much faster compared to c-Si technologies and over large-areas through roll-to-roll processes [26, 27]. Currently, the commercialisation of OPV is limited by two primary factors: efficiency and stability.

The highest efficiency OPV devices are typically achieved through the fabrication of a bulk heterojunction (BHJ) (discussed later in Chapter 2) composed of a light-harvesting blend film of conjugated donor polymer and small molecule electron acceptor materials, deposited between two electrodes [28]. During fabrication, the component materials of the thin film *self-assemble* to form a three-dimensional, phase-separated network of polymer and acceptor domains with characteristic length scales ranging from a few angstroms to hundreds of nanometers. The size, shape, distribution and purity of these domains plays an important role in the light-harvesting process through the generation of strongly bound electron-hole pairs called excitons and their subsequent dissociation into free charge carriers. It is the formation of these strongly bound excitons which limits the efficiency of OPV devices as the exciton must diffuse to a heterointerface (e.g. the interface between donor and acceptor domains) in order to dissociate into free charge carriers which can then be transported to the electrodes. Typical exciton diffusion lengths are of the order $\sim 10 - 50nm$ for most OPV materials [29]. It is therefore critical that the blend film nanostructure is engineered in such a way that permits both efficient exciton dissociation and free charge carrier transport. The steps involved with these processes are generally inefficient for most OPV materials, leading to significant voltage and recombination losses [30].

Despite this, the past 20 years has witnessed a rapid rise in the PCE of single-junction OPV cells, increasing from 2.5% in 2001 [31] to as high as $\sim 19\%$ earlier this year [32, 33] (Figure 1.2). This boost in efficiency has been the result of a resilient research field developing processing techniques, device architectures, BHJ nanostructure optimisation routes

and most significantly, new materials with improved light absorption and reduced voltage losses [34, 35, 30]. In particular, a new class of electron acceptors called non-fullerene acceptors (NFAs) now outperform traditional fullerene acceptor materials such as [6,6]-phenyl-C61-butyric acid methyl ester (PC₆₁BM) and [6,6]-phenyl-C71-butyric acid methyl ester (PC₇₁BM), presenting a new era for OPV research. Performance optimisation routes of OPVs based on fullerene acceptors are restricted given their chemical modification limitations, resulting in a PCE enhancement bottleneck. NFAs on the other hand exhibit significantly greater chemical tunability as they are composed of conjugated chemical building blocks, which can be changed and altered with ease. This has resulted in an explosion of new material possibilities (>51,000 [36]), providing considerably greater control of optical, structural, thermal and charge transport properties which has in turn opened up a wealth of device performance optimisation routes. The material landscape is so vast that a new field of computational OPV research has emerged focused on creating machine-learning algorithms to estimate material properties and aid the design of new high-efficiency, stable NFA molecules [37, 38, 39, 40].

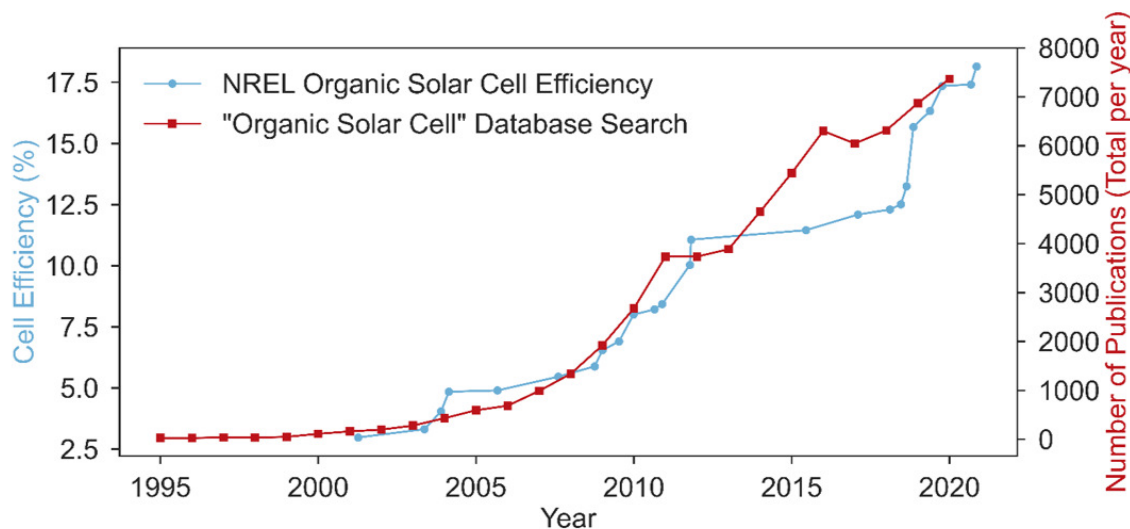


Figure 1.2: A historic summary of the best single-junction organic solar cell PCEs (data extracted from [11]) along with the annual total number of research article publications referring to "organic solar cell". Database searches were performed using Dimensions [41].

The recent developments in OPV device efficiency over the past couple of decades have coincided with a simultaneous surge in research interest with >7000 research articles referring to "Organic Solar Cell" published in 2020 compared to ~ 30 in 1995 (Figure 1.2). Despite such rapid advancements in the field, significant challenges remain. Most concerning is the considerably inferior long-term operational stability of OPV devices compared to c-Si technologies. The required operational lifetime of a PV device depends on the application but it is generally considered to be >5 years for flexible technologies and >25 years for building installations [20]. Whilst some accelerated ageing tests predict lifetimes >30 years for NFA based OPV systems [42], these studies are not representative of real-world conditions which involve seasonal and daily variances in temperature, humidity and light intensity. In general, OPV systems are vulnerable to a range of morphological, chemical, and photo instabilities [20] which can be accelerated by numerous extrinsic degradation factors.

At present, it is unclear if OPV technologies will offer a significant contribution to reducing anthropogenic CO₂ emissions. In 2018, only 13% of OPV studies which published PCE data also provided operational stability in 2018 [43]. The majority of academic OPV research is focused on efficiency rather than stability with only 13% of studies which published PCE data also providing operational stability in 2018 [43]. This is unsurprising given that most stability measurements require research efforts over a long time period and usually rely on specialist equipment to simulate solar irradiation in atmospheres with controlled temperature, humidity and oxygen levels. However, to avoid being consigned to history, further research into the underlying relationships between processing, film nanomorphology, device performance and stability is crucial.

1.4 Thesis Motivation

To improve the commercialisation of OPV, the PV scientific community must develop materials and fabrication processes capable of producing low-cost, scalable PV devices that exhibit both high efficiency *and* long-term operational stability. The key to this is to fabricate a bulk heterojunction with an optimised, stable morphology that is resistant to chemical and morphological degradation. It is therefore essential that the underlying factors determining device efficiency are well understood along with potential degradation mechanisms. This thesis has the following primary aims:

1. Characterise the self-assembly of nanostructures in conjugated organic thin films incorporating novel electron acceptors.
2. Understand how the findings from aim (1) link to film processing conditions and the resultant optoelectronic functionality of the organic thin films.

3. Correlate findings from aim (1) and (2) to the operational stability of films and devices.

Combined these aims will help develop the understanding that is critical to achieving stable, high-efficiency organic electronics.

1.5 Thesis Overview

This thesis is composed of the following chapters:

Chapter 2 provides the relevant background theory relating to the materials and concepts discussed in this thesis. An overview of organic semiconducting materials is first provided followed by a brief background of OPVs including a brief history, materials, device operation and bulk heterojunctions. The chapter continues with an introduction to the morphological characterisation of self-assembled nanostructures in organic thin films and concludes with an overview of the relationships between structure, optoelectronic properties and device stability, including a summary of the relevant literature and current knowledge gaps in the field.

Chapter 3 details the experimental methodology used throughout this thesis covering materials, film processing conditions, device fabrication and characterisation techniques. Each characterisation technique is introduced with relevant theory followed by more specific experimental details and its relation to the work presented in this thesis. Particular attention is paid to the use of neutron and X-ray scattering techniques to characterise organic thin films as they are used extensively throughout Chapters 4 - 7.

Chapter 4 is an investigation into the correlation between the choice of casting solvent and the morphology, optical properties and device performance of PBDB-T : ITIC based organic photovoltaics. Specifically, the research addresses the potential use of more industrial friendly non-halogenated solvents such as o-xylene and a carbon disulphide : acetone blend as alternatives to pernicious halogenated processing solvents such as chlorobenzene and chloroform which are typically used to fabricate high-efficiency devices. Processing thin films from non-halogenated solvents is more favourable for large-scale device fabrication, essential for the commercialisation of OPV, but such devices typically suffer from inferior performance. In this chapter, grazing incidence X-ray scattering measurements are combined with optical and PV characterisation to further understand the impact of processing solvent on structure-performance relationships.

Chapter 5 probes the impact of a high boiling point solvent additive (1,8-diiodooctane, DIO) on the morphology, performance and stability of PBDB-T : ITIC and PBDB-T :

PC₇₁BM organic photovoltaics using a range of structural and optoelectronic characterisation techniques. The inclusion of solvent additives in the casting solution is a common approach used to control the morphology of bulk heterojunction films. However, there is an increasing amount of research demonstrating the detrimental impact of DIO to the stability of devices through various degradation mechanisms such as photo-degradation and morphological instabilities. For the commercialisation of OPV it is essential that devices exhibit both high efficiency *and* long-term operational stability. It is therefore critical that the complex relationships between film processing conditions and the resulting film morphology, PV performance and stability are well understood. The work in this chapter aims to address one aspect of this, specifically the inclusion of small concentrations of DIO in the casting solution.

Chapter 6 focuses on exploring the effect of chemical design on the morphology, performance and stability of NFA-based organic photovoltaics using a range of structural and optoelectronic characterisation techniques. Since the breakthrough of NFA-based OPVs, a broad range of π conjugated core-groups, terminal groups and solubilising side-chain chemical moieties have been trialled as synthesis building blocks. Whereas fullerene-based blends typically require optimisation through film processing methods, NFAs can undergo significant device optimisation through chemical design alone as they possess a greater degree of chemical tunability. This study focuses specifically on characterising high-performing indacenothiophene (IDT) based NFAs (EH-IDTBR, O-IDTBR and O-IDTBCN) in binary blend films with the conjugated polymer PTB7-Th. Comparison is also made to a benchmark fullerene-based blend, PTB7-Th : PC₇₁BM. Given the diverse range of NFA chemical structures now available, it is essential that the choice of chemical moieties and the resulting structure-performance-stability relationships are well understood to inform the design of new, more efficient, more stable molecules suitable for commercialisation. The findings presented in this chapter aim to do this with particular focus on understanding the link between nanostructure self-assembly and stability.

Chapter 7 presents a novel approach to control the molecular orientation of organic chiral small molecules in thin films using both inorganic and organic structural templating layers. The properties of chiral π -conjugated molecules such as the absorption and emission of circularly polarised light are highly anisotropic and consequently their molecular orientation in the solid-state has a significant impact on the performance and efficiency of chiral optoelectronic devices. In this work, the impact of structural templating layers on the molecular packing of a chiral small molecule (2,2'-dicyano[6]helicene, CN6H) is characterised in detail using grazing incidence X-ray scattering measurements and 2D simulations. The observed changes in molecular self-assembly and orientation are then correlated to chiroptical functionality. Such templating methodologies offer a simple approach to engineering orientational control and consequently the anisotropic functional properties

of chiral molecular systems, essential for a range of emerging, next-generation technologies.

Chapter 8 concludes this thesis with summaries of the contributions of each experimental results chapter and their relation to the wider field of research. The limitations of key investigations are discussed concluding with future research directions to develop and progress the results presented in this work.

Appendix A includes additional neutron scattering modelling information related to the results presented in Chapter 5 and Chapter 6.

Appendix B includes the UV-Vis spectra from the photo-stability studies discussed in Chapter 5.

Background Theory of Organic Semiconductors

2.1 Introduction

In this chapter, a brief background of the overarching theory necessary to understand the experimental contributions presented in this thesis is provided. The topics discussed are adapted from more comprehensive discussions from Hook and Hall [44], Kittle [45], Nelson [46], Geoghegan and Hadziioannou [19], Jones and Richards [47] and Jones [48]. The chapter begins by introducing organic semiconducting materials from both an electronic and structural point of view. This is then expanded to an overview of the operating principles and theory of organic photovoltaic materials and devices. Here a brief summary of the history of the field, bulk heterojunctions and related materials is covered. The later sections focus on outlining the key morphological characteristics of organic thin films and their relation to the optoelectronic properties and stability of organic electronic devices.

2.2 Organic Semiconducting Materials

The characteristics that define metals, insulators and semiconductors is most easily visualised by considering the available energies for electrons in each material. In a solid, the available energy states form energy bands rather than the discrete energy levels in the case of free atoms. The two most important of these bands are those closest to the Fermi level; the conduction band and valence band. The valence band is the highest electron energy range and the conduction band is the lowest electron energy range. The conductivity of the solid is crucially determined by the susceptibility of electrons to be excited from the valence band to the conduction band which is defined by the energy gap between the them; the band gap energy (E_g). An illustration of the energy band gap in metals, semiconductors and insulators is displayed in Figure 2.1. In an insulator, all of the energy levels are either completely filled or empty and the band gap is sufficiently large that electrons are unable to be excited to the conduction band at ordinary temperatures. Electrons are immobilised in the solid and cannot conduct electric charge. In a metal, energy bands overlap and the concept of a band gap is meaningless as electrons are free to move without any applied electromotive force. In a semiconductor, the energy band gap is sufficiently small that thermal energy permits the promotion of a small fraction of electrons to the valence band at temperatures above absolute zero (0K). At 0K, thermal energy is nullified and electrons are confined to the valence band so the semiconductor behaves like an insulator. The population of electrons in the conduction band is governed by the Fermi-Dirac distribution:

$$f(E) = \frac{1}{e^{\frac{E-E_F}{k_B T}} + 1} \quad (2.1)$$

where k_B is the Boltzmann constant, T is temperature, E is the energy of a given electron state and E_F is the Fermi energy level. From Equation 2.1, at $E = E_F$, the exponential term reduces to 1 and $f(E) = 0.5$ so E_F can be considered as the electron energy level with a 50% probability of being occupied. For semiconductors, the Fermi level lies within the band gap and at ordinary temperatures most energy levels up to the Fermi level E_F are filled with a small population with energy $E > E_F$ in the conduction band. It is these electrons that determine the semiconducting properties of the material.

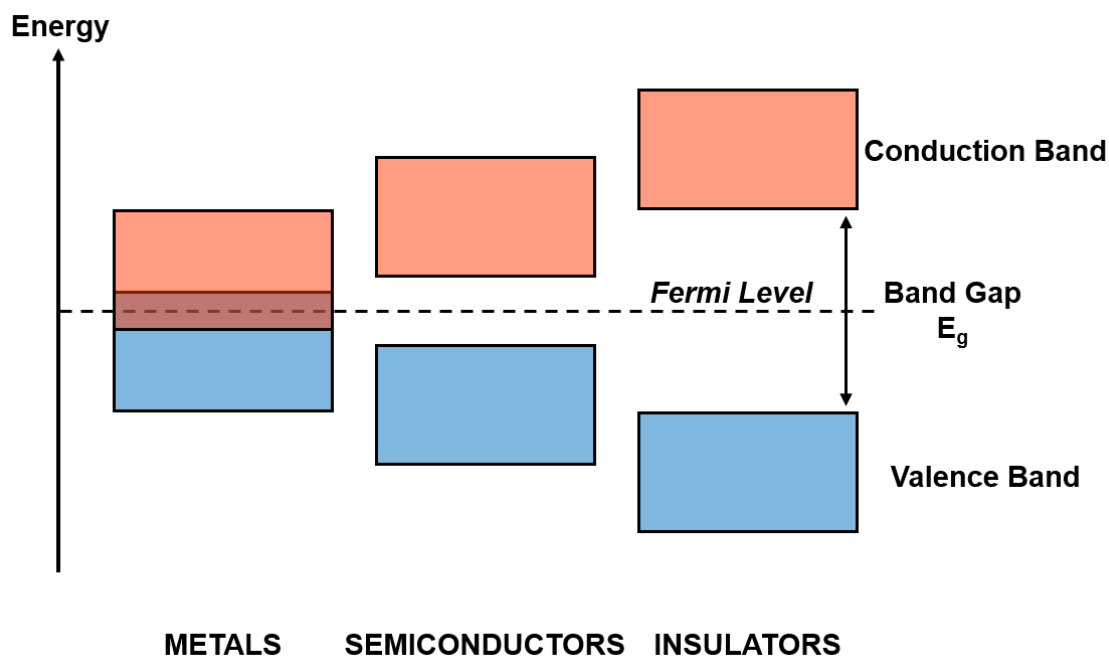


Figure 2.1: An illustration of the energy bands in metals, semiconductors and insulators that determine their electrical conductivity.

An *organic* semiconductor is a semiconductor made from carbon-based materials such as polymers and other carbon-based small molecules. At first, this may seem somewhat of an oxymoron given the prevalence of insulating plastics in our everyday lives. However, some organic materials have the remarkable ability to undergo a specific type of carbon bonding which gives rise to a band gap that permits the transport of charge. To understand

how band gaps are formed in organic semiconducting materials, it is first necessary to understand the properties of organic solids. In this section, the construction of an organic solid is built up starting with individual atoms to the formation of molecules, polymer chains and the larger phases they form in the bulk. For more detailed discussions concerning band theory of typical inorganic semiconducting materials, the reader is directed to more comprehensive overviews elsewhere [44, 45, 46].

2.2.1 Atomic Orbitals

The development of the quantum mechanical description of the atom in the early 20th century overturned J. J. Thompson's classical picture consisting of a positively charged nucleus surrounded by circular electron orbits. In 1913, Niels Bohr proposed the semi-classical theory which instead described electron orbitals as discrete energy levels surrounding the nucleus. The occupancy of these orbitals is determined by the Pauli Exclusion Principle, which states that two or more electrons cannot occupy the same quantum state, as defined by the quantum numbers n (principal quantum number), l (azimuthal quantum number), m_l (magnetic quantum number) and m_s (spin quantum number). Here, electrons can move instantaneously between energy levels through the absorption or emission of discretized energy. Later in the 20th century, Erwin Schrödinger took Bohr's model a step further and described the permitted energy levels of an atomic electron using probabilistic quantum mechanical wavefunctions. These wavefunctions describe the positions of electrons in permitted states as probability distributions that are typically solutions to the non-relativistic time-independent Schrödinger equation:

$$\left[\frac{-\hbar^2}{2m_e} \nabla^2 + V(\mathbf{r}) \right] \psi(\mathbf{r}) = E\psi(\mathbf{r}) \quad (2.2)$$

where \hbar is the reduced Planck constant ($\hbar = 2\pi/h$), m_e is the rest mass of an electron, ∇^2 is the Laplace operator ($\nabla^2 = \frac{\partial^2}{\partial x^2} + \frac{\partial^2}{\partial y^2} + \frac{\partial^2}{\partial z^2}$), V is the potential and E is energy. Using this description of an atom, the formation of electron orbitals can be rationalised by considering the allowed values of each quantum number. The principal quantum number n describes the size of the orbital and can be any positive integer ($n = 1, 2, 3, \dots$). The azimuthal quantum number l describes the orbital angular momentum of the electron $0 \leq l \leq n - 1$. The magnetic quantum number m_l describes the magnetic moment of the electron $-l \leq m_l \leq +l$ and the spin quantum number m_s describes the spin of the electron (spin up or spin down) ($m_s = \pm \frac{1}{2}$). Using these quantum numbers, electron orbitals are then divided into s , p and d orbitals according to their occupancy limits. As an example, the electron orbitals corresponding to the $n = 1$ and $n = 2$ states are summarised in Table 2.1

Quantum Number				Orbital Name	Number of Electrons
n	l	m_l	m_s		
0	0	0	+1/2	1s	2
			-1/2		
2	0	0	+1/2	2s	8
			-1/2		
	1	-1	+1/2	2p	
			-1/2		
		0	+1/2		
			-1/2		
		1	+1/2		
			-1/2		

Table 2.1: Quantum numbers n , l , m_l and m_s and corresponding orbital names that describe the permitted energy states of atomic electrons.

and the shape of the s , p and d orbitals surrounding a hydrogenic nucleus are displayed in Figure 2.2. The $n = 1$ energy level is referred to as the ground state and is made up of a single $1s$ orbital containing two electrons. The $n = 2$ energy level consists of $2s$ and $2p$ ($2p_x$, $2p_y$ and $2p_z$) orbitals with an occupancy of 2 and 6 electrons respectively. It is these $2p$ electron orbitals which contribute to the formation of hybridised carbon bonds (discussed below), central to the conductive properties of organic semiconductors. For larger atoms, electrons continue to fill energy states according to the Pauli Exclusion Principle. E.g. the $n = 3$ comprises $3s$, $3p$ and $3d$ electron orbitals with an occupancy of 2, 6 and 10 respectively. It should be noted that there are exceptions to the general order of orbital filling due to energy minimisation of the atom (e.g. the $4s$ orbital is at a lower energy than the $3d$ orbital and so is filled first). Electrons in the outermost energy level are termed the *valence electrons* and it is these electrons that are typically responsible for an element's chemical behaviour.

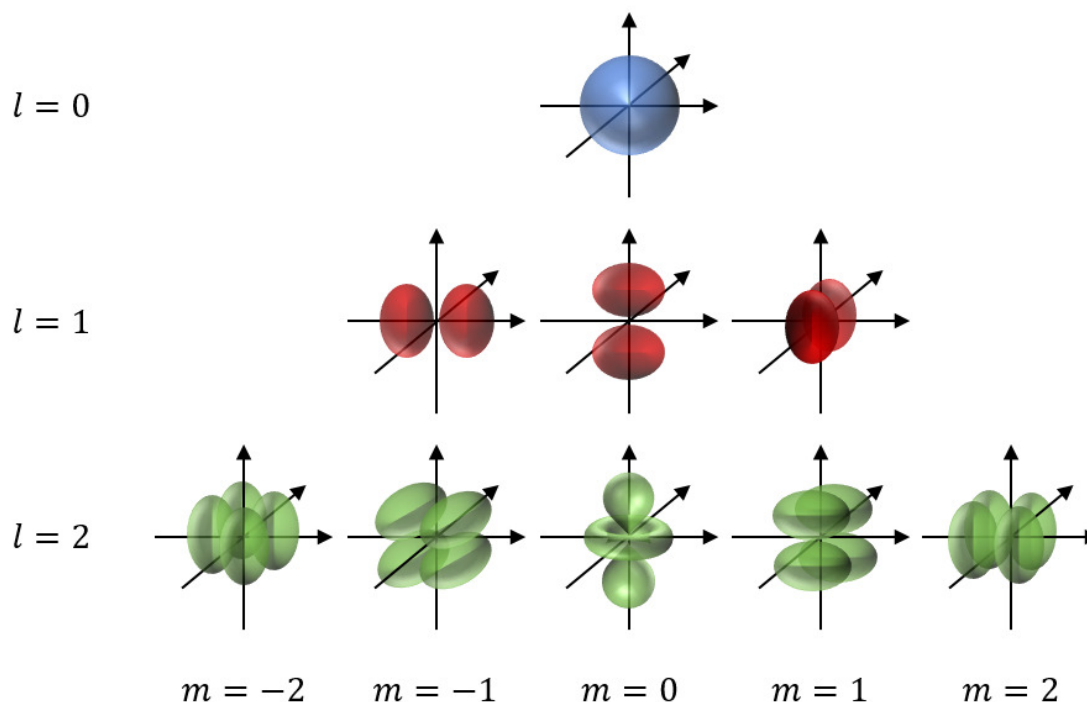


Figure 2.2: An illustration of the shape of the s , p and d atomic orbitals.

If the outer electron energy level of an atom is unfilled, it can bond together with another atom to form a molecule by either sharing, receiving or donating electrons such that the overall energy is minimised. In organic electronics, bonding between carbon atoms and the origin of a band gap can be understood by considering the principle of linear combination of atomic orbitals. For simplicity, first consider two hydrogen atoms each with a single electron with wavefunctions ϕ_A and ϕ_B respectively. When bonded together as a diatomic molecule (H_2), there are two possible energy states: a higher, unstable state (the anti-bonding orbital) which leads to molecular dissociation and a lower, stable state (the bonding orbital) corresponding to the most probable positions of the electrons (Figure 2.3a). These new energy states are formed from the linear combination of the two electron wavefunctions, $\psi = \phi_A + \phi_B$ for the stable molecule and $\psi = \phi_A - \phi_B$ for the unstable molecule, both of which are solutions to the Schrodinger equation (Equation 2.2). In the stable configuration, the two electrons are shared between the two atoms with the most probable position centred between the two nuclei. In the unstable configuration, the most probable position for the two electrons is on opposite sides of each nuclei.

Applying this principle to a diatomic helium molecule (He_2), each He atom contributes its first $1s$ electron to the lowest energy (bonding) orbital and the remaining two electrons fill

the anti-bonding orbital (Figure 2.3b). The anti-bonding orbitals have a larger influence on the overall stability of the molecule compared to the bonding orbitals and so in the case of a diatomic helium molecule, the filling of the anti-bonding orbital explains why it is less stable compared to the two individual He atoms. In the following section, these principles are applied to carbon atoms to understand the electrical conductivity capabilities of organic semiconductor materials.

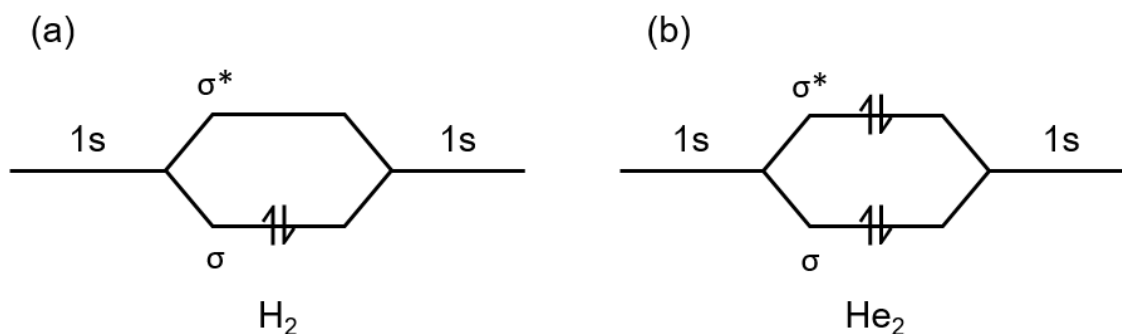


Figure 2.3: Energy states of (a) H_2 and (b) He_2 .

2.2.2 Hybridised Carbon Bonds

A neutral carbon atom has 6 electrons arranged in a $1s^2 2s^2 2p^2$ electronic structure (Figure 2.4a). This leads to three types of molecular carbon bonds through the phenomenon of orbital *hybridisation*. These are: sp^3 hybridisation, sp^2 hybridisation and sp hybridisation. In all cases, a $2s$ electron is promoted to the vacant $2p_z$ state (Figure 2.4b). For molecules that undergo sp^3 hybridisation, the remaining $2s$ and three $2p$ orbitals hybridise to form four hybrid sp^3 orbitals. This type of carbon bonding results in end-to-end bonds called sigma (σ)- bonds in a tetrahedral structure and occurs in alkanes such as methane. In the case of sp^2 hybridisation, the $2s$ orbital hybridises with two of the available $2p$ orbitals forming three sp^2 orbitals and leaving behind a single p_z orbital that does not undergo hybridisation. The three sp^2 hybridised orbitals form σ -bonds in a planar structure separated by an angle of 120° . When two sp^2 -hybridised carbon atoms bond together (e.g. ethylene, Figure 2.4c), an sp^2 orbital from each atom is used to form a covalent C=C bond and the four remaining sp^2 orbitals form σ bond with hydrogen atoms. The two leftover p_z electronic wavefunctions overlap to form delocalised π -bonds situated above and below the molecule (perpendicular to the plane of σ -bonds). π -bonds are much weaker compared to σ -bonds and are responsible for the semiconducting properties of many of the materials used in organic electronics. Finally, for completeness in the case of sp hybridisation (e.g. acetylene), the $2s$ orbital hybridises with one of the available $2p$ orbitals forming two sp orbitals and two p_z orbitals.

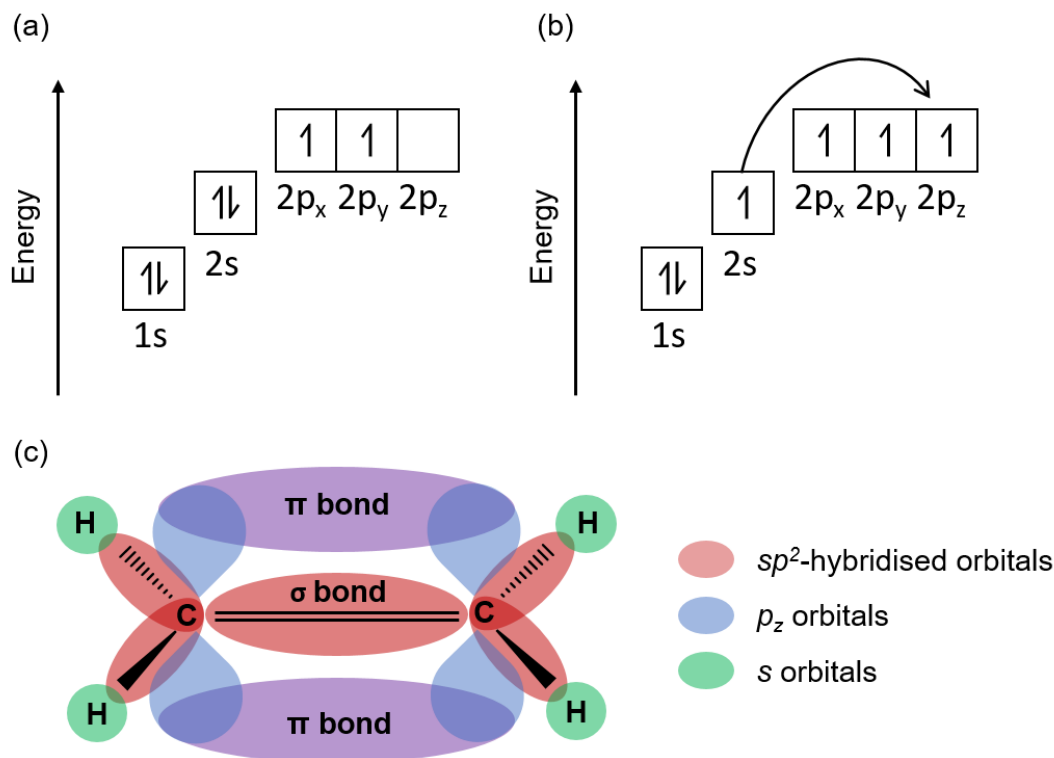


Figure 2.4: Electronic structure of (a) a neutral carbon atom and (b) a hybridised carbon atom where an electron from the 2s shell is promoted to the vacant 2p_z orbital. (c) A diagram of the π bond and σ bonds for ethylene.

2.2.3 Molecular Orbitals

As a consequence of the quantum mechanical nature of the atom, for every σ -bond and π -bond that forms when carbon atoms bond together, corresponding anti-bonding orbitals are also created (denoted as σ^* and π^*). The σ^* and π^* anti-bonding orbitals are at a higher energy level than the σ and π bonding orbitals and it is the difference between these frontier orbitals which gives rise to an energy gap (analogous to the band gap in inorganic semiconductors). The band gap in an organic semiconductor is equal to the difference in the lowest unoccupied (π -bond) molecular orbital (LUMO) and the highest occupied (π^* -bond) molecular orbital (HOMO). A HOMO-LUMO energy gap alone does not guarantee semiconducting properties (e.g. the energy gap of ethylene is 7.6eV which is too large to be considered a semiconductor). It is only when considering more complex molecules does the semiconducting capabilities of organic materials become apparent. For example, as the number of sp^2 -hybridised carbon bonds increases in a molecule, the increasing number of π -bonds and π^* -anti-bonds creates an additional energy level in the HOMO and LUMO

respectively. These additional bonds have the effect of gradually decreasing the HOMO-LUMO energy gap until it is sufficient for semiconducting properties.

Another important characteristic of organic semiconductors is *conjugation*. A conjugated molecule contains alternating single and double carbon bonds (-C=C-C=C-). This results in extended π orbitals of delocalised electrons along the carbon backbone of the molecule. Whilst σ - σ^* transitions are permitted in conjugated molecules, they lead to molecular instabilities. The extended π -system maintains structural integrity, permitting π - π^* transitions which are lower in energy compared to σ - σ^* transitions. The size of this extended π -system along the carbon backbone is often termed the *conjugation length*, which is the length over which charge transport is applicable. In reality, semiconducting behaviour in organic materials is much more complex than this given their generally disordered nature that leads to a poorly defined electronic band structure. Understanding the disordered morphology of organic semiconducting materials in the solid-state is therefore crucial to understanding their optoelectronic properties.

2.3 Organic Photovoltaics: An Overview

The concepts discussed in the previous section give rise to electrical conductivity in organic materials, forming the basis of a broad range of optoelectronic applications such as OLEDs, OFETS, OPV, organic photodetectors, organic lasers, biosensors and more [49, 50, 51]. In this section, focus is paid to organic photovoltaic applications to provide the necessary theory relating the majority of the experimental contributions in this thesis.

2.3.1 The Photovoltaic Effect

Light is made up of particle-like packets of energy called *photons*. The energy E of these photons is inversely proportional to the wavelength λ of the light:

$$E = \frac{hc}{\lambda} = hf = pc \quad (2.3)$$

where h is Planck's constant, c is the speed of light, f is the frequency of the light ($f = c/\lambda$) and p is the momentum of the photon ($p = h/\lambda$). When light with sufficient energy is incident on a solid, photons can be absorbed, exciting electrons to higher energy levels. In the extreme case of the photoelectric effect discovered by Einstein in 1905 [52], the electron absorbs an excessive amount of energy such that it is removed entirely from a metallic surface. The PV effect is closely related to the photoelectric effect but is much less extreme and considerably more useful for the generation of electrical energy. In a PV device, when an electron absorbs incident light, rather than being entirely removed, it is instead excited

to a higher energy level and drawn away by some intrinsic material asymmetry before it can relax back to the ground state. The extraction of charge associated with the excited state is fed into an external circuit, generating a voltage that drives electrons through a load in the circuit.

2.3.2 Absorbing Solar Radiation - The Shockley-Queisser Limit

The formation of an energy band gap in semiconductors between the valence and conduction bands is essential for the absorption of light. The optimum value of the band gap is related to the solar irradiance spectrum (Figure 2.5). The extra-terrestrial solar spectral irradiance is characteristic of a blackbody with a temperature of 5760K. This solar irradiance spectrum is termed air mass 0 (AM0). As solar irradiance passes through the Earth's atmosphere, it is attenuated and a portion is absorbed at certain wavelengths from atmospheric molecules such as water and CO₂ (Figure 2.5).

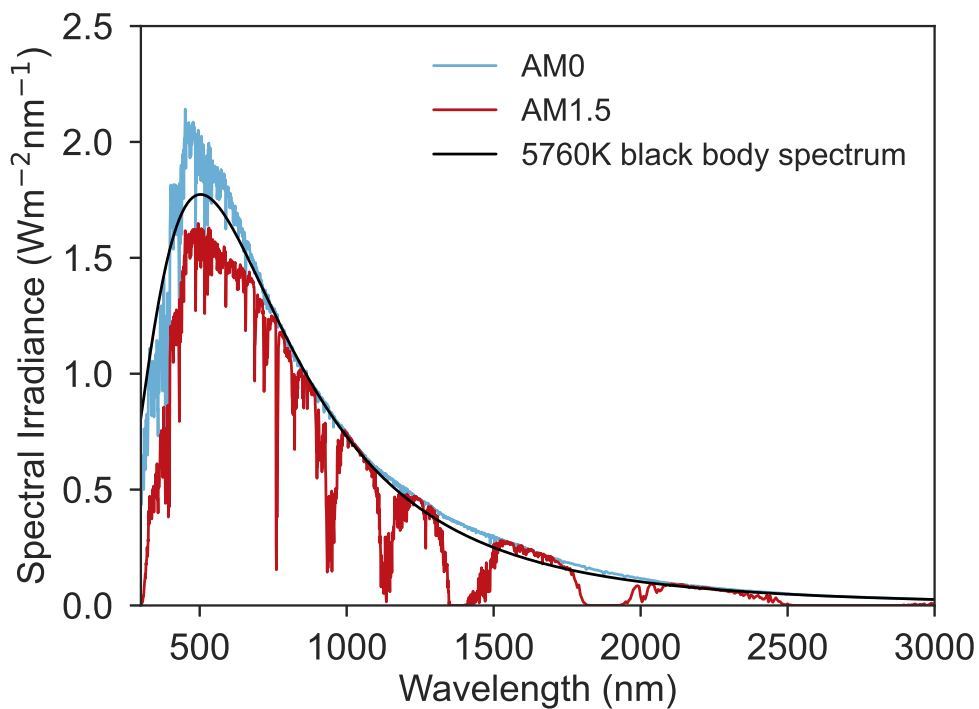


Figure 2.5: The standardised extra-terrestrial (AM0) and standard terrestrial (AM1.5) spectral irradiances measured by NREL [53] compared with the 5760K blackbody spectrum. (The blackbody spectrum is reduced in intensity for clarity)

To account for the attenuation in PV applications, a standardised solar spectral irradiance known as air mass 1.5 (AM1.5) is typically used to quantify the solar radiation available at mid-latitudes. The 1.5 factor corresponds to an incident angle of sunlight of 48° , which attenuates solar irradiance by a atmospheric thickness $\times 1.5$ the thickness of global atmosphere. It is typically normalised such that the integrated solar irradiance is equal to 1000 W m^{-2} . In reality, solar irradiance varies depending on location, season, cloud coverage etc. The ratio of generated power to the incident power on the solar cell is called the power conversion efficiency (*PCE*) and is the primary performance metric of a device (*PCE* will be described in further detail in the following sections).

In a semiconducting material, a photon with energy $hf > E_g$ is absorbed. If the band gap is small, a large portion of the AM1.5 spectrum in Figure 2.5 can be absorbed. If the band gap is too large, only a small portion of the AM1.5 spectrum can contribute to the photocurrent of a PV device. Naturally, the obvious choice of band gap might appear to be one that was sufficiently small to absorb the entire solar spectrum. Unfortunately, this is not the case as any photons absorbed with $hf > E_g$ release their excess energy as thermal energy in the device as excited electrons thermalise back to the edge of the conduction band. The competing goals to reduce this thermalisation process whilst absorbing as much solar irradiance as possible determines the optimal band gap of a PV device. This *detailed balance* combined with other loss mechanisms (discussed later) allow the theoretical maximum *PCE* of a single-junction solar cell to be calculated as a function of band gap energy [54, 55]. This is known as the Shockley-Queisser (S-Q) limit. From this, the optimum band gap to achieve the maximum theoretical *PCE* of $\sim 33\%$ is 1.34eV. For c-Si, the maximum theoretical *PCE* achievable for single-junction devices is around 29.4% [56].

The S-Q model is often applied to organic solar cells but the actual efficiency limit is predicted to be much lower due to further loss mechanisms such as the additional energy required for exciton dissociation (discussed later) which reduces the maximum achievable voltage of the solar cell and losses related to the photocurrent due to incomplete absorption [57]. Nevertheless, with the advent of NFAs some OSCs systems have demonstrated negligible voltage losses and the reduced band gap of NFA based systems (1.4 - 1.6 eV), increases the higher achievable theoretical *PCE* [55].

2.3.3 Characteristics of a Solar Cell

The operation of a solar cell is most easily described by the Shockley ideal diode equation (Equation 2.4) derived elsewhere [46]:

$$J(V) = J_{SC} - J_D = J_{SC} - J_0(e^{qV/k_B T} - 1) \quad (2.4)$$

Where J_{SC} is the short-circuit current density, J_D is the dark diode current density, J_0 is

the reverse diode current density and q is the elementary electron charge. As the applied bias V increases, the diode current increases exponentially. Equation 2.4 describes *ideal* diode behaviour. When non-ideal diode behaviour and parasitic losses are considered, Equation 2.4 is modified to:

$$J(V) = J_{SC} - J_0 \left(e^{\frac{q(V+J R_S)}{n k_B T}} - 1 \right) - \frac{V J R_S}{R_{SH}} \quad (2.5)$$

Where n is the ideality factor related to recombination in the solar cell [46], R_S is series resistance and R_{SH} is shunt resistance. R_S and R_{SH} are classed as parasitic resistances and will be discussed in further detail below. The performance of a solar cell is typically assessed by its current-voltage (J - V) characteristics (Figure 2.6).

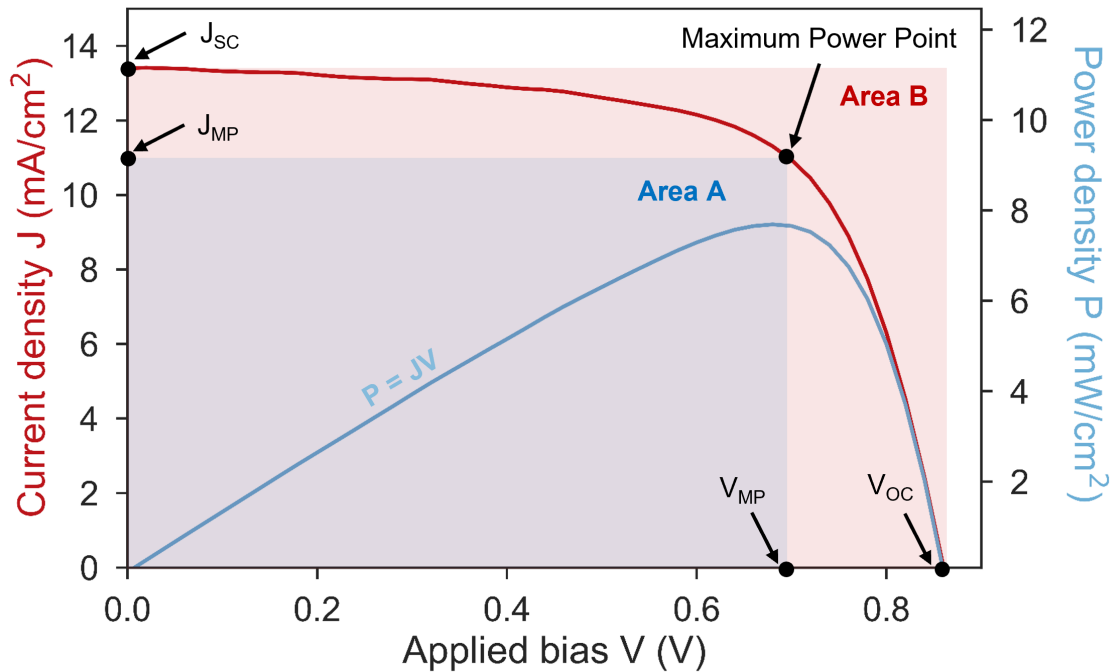


Figure 2.6: Current density - voltage (J - V) characteristics and power density output ($P = JV$) of a solar cell. Data is taken from a (J - V) sweep of a typical OPV device. The ratio of the red and blue shaded areas can be used to calculate the fill factor FF of the solar cell. The positions of the maximum power point, J_{SC} , V_{OC} , J_{MP} and V_{MP} are labelled.

By performing a J - V sweep, the characteristic performance metrics labelled in Figure 2.6 are extracted for the device. These are:

- **Short Circuit Current Density (J_{SC}):** is the photocurrent provided by the solar cell when the voltage is zero (i.e. short-circuit conditions). The current in a PV device is due to the built-in internal electric field established between the electrodes. J_{SC} is proportional to the number of incoming photons that are absorbed by the photoactive material. A short-circuit current *density* is used rather than just current I_{SC} as the photocurrent depends on the illuminated area A of the solar cell ($J_{SC} = I_{SC}/A$). It is typically given in units of mA/cm^2 .
- **Open Circuit Voltage (V_{OC}):** is the voltage across the device when the current is zero. It is effectively the voltage required to counteract the built-in field due to accumulation of electrons and holes at each contact (i.e. no charges are extracted). In a solar cell V_{OC} is given by [46]:

$$V_{OC} = \frac{nk_B}{q} \ln\left(\frac{J_{SC}}{J_0} + 1\right) \quad (2.6)$$

Generally in a PV device, the maximum voltage is dependent on the band gap of the light-harvesting photoactive layer (V_{OC} decreases with E_g).

- **Fill Factor (FF):** is the ratio of the red and blue areas shown in Figure 2.6 defined as:

$$FF = \frac{P_{max}}{V_{OC}J_{SC}} = \frac{J_{MP}V_{MP}}{J_{SC}V_{OC}} \quad (2.7)$$

The red area corresponds to the product of J_{SC} and V_{OC} , whereas the blue area corresponds to the maximum power point P_{max} (J_{MP} , V_{MP}) where the product of J and V is maximised. The FF of a solar cell is maximised by reducing R_S and increasing R_{SH} .

- **Power Conversion Efficiency (PCE):** is the ratio of power generated to the incident power on the solar cell. It is defined as:

$$PCE = \frac{P_{out}}{P_{in}} = \frac{J_{SC}V_{OC}FF}{P_{in}} \quad (2.8)$$

Where $P_{out} = J_{SC}V_{OC}FF$ is the generated power and P_{in} is the power of the incident light. As can be seen from Equation 2.8, the PCE of a solar cell is dependent on a number of PV metrics (J_{SC} , V_{OC} and FF).

In addition to the device metrics outline above, solar cells are also vulnerable to parasitic resistances (R_S and R_{SH}). The series resistance of a PV device concerns all processes that restrict charge extraction (i.e. current flow). To maximise R_S , the photon-absorbing layer and charge transport layers in the device should efficiently transport charge to the electrodes. They should therefore be free of defects, have good charge mobility and be an appropriate thickness. In a J - V sweep, a large series resistance primarily manifests as a reduction in V_{OC} and can be approximated by calculating the gradient of the curve at $V = V_{OC}$. Shunt resistance is related to leakage current in the device. A larger R_{SH} corresponds to less leakage current in the device and this value should therefore be maximised by ensuring good electrical contact between device layers and the electrodes. In a J - V sweep, shunt resistance can be approximated by calculating the inverse gradient of the curve at $V = 0$.

A solar cell is also limited by its quantum efficiencies. The internal quantum efficiency (IQE) of a solar cell is the fraction of photo-generated charges extracted from the solar cell compared to the total number of photons absorbed. IQE is therefore dependent on all processes related to charge generation, charge transport and charge extraction in a solar cell. The external quantum efficiency (EQE) of a solar cell is the fraction of extracted charges compared to the number of incident photons of a given energy. It is calculated via:

$$EQE(\lambda) = \frac{Jhc}{P(\lambda)\lambda q} \quad (2.9)$$

Where J is the photocurrent density and $P(\lambda)$ is the incident photon power at a given wavelength. The J_{SC} of a solar cell can be calculated from an EQE measurement by integrating the EQE spectra:

$$J_{SC} = q \int_{\lambda_1}^{\lambda_2} EQE(\lambda) \Phi_{ph}^{AM1.5} d\lambda \quad (2.10)$$

Where $\Phi_{ph}^{AM1.5}$ is the spectral photon flux.

2.3.4 Operation of an Organic Photovoltaic Device

Now that the basics of PV energy conversion and device metrics have been covered, the operation of organic-based PV devices are discussed next. For simplicity, the impact of film nanostructure is ignored here until following sections and the process of photocurrent generation is described purely from an optoelectronic point of view. The most effective way to describe the operation of an OPV device is with a simplified energy level diagram as illustrated in Figure 2.7. Here OPV device operation is divided into the following key steps:

1. Light absorption and photo-excitation

A photon with $E \geq E_g$ is absorbed by a molecule in the active layer (donor or acceptor) which excites an electron to a higher energy state leaving behind a positively charged vacancy or *hole*. In an organic molecule, this is typically a transition from the singlet ground state (S_0) in the HOMO to the first higher energy singlet state (S_1) in the LUMO. If the absorbed photon energy exceeds the energy difference between these two states, the electron can rapidly relax towards the lowest vibrational energy level in the LUMO. The excited electron and hole created through photo-excitation create a bound electron-hole pair called an *exciton*. Excitons are typically short-lived and will recombine on timescales of ~ 1 ns. The relaxation of the electron back to the ground state results in the emission of a photon with $E \neq E_g$ through the process of fluorescence.

2. Charge transfer state generation

To generate a photocurrent in the solar cell, the exciton must be dissociated into its constituent free charge carriers before the electron and hole recombine. For this to happen, the Coulomb interaction or *binding energy* E_B of the exciton must be overcome. For traditional organic semiconducting materials (e.g. fullerenes), E_B has been measured to be of the order ~ 0.3 eV [58]. This is much higher than the thermal energy $k_B T$ (~ 25 meV) of a PV device operating at ambient temperatures (300K). This means that the highly localised excitons in organic semiconductors cannot be dissociated by thermal energy alone and are typically termed *Frenkel excitons*. The origin of the high binding energies of Frenkel excitons are due to the strong coupling of the exciton to the atomic lattice and the relatively low dielectric constant of organic materials ($\epsilon_r \sim 3 - 4$ [59]). For OPV device operation, it is therefore crucial to have a method for dissociating the exciton so that free charge carriers can be transported to the electrical contacts. This is achieved at heterointerfaces in the device where the energy offset is sufficient to overcome the exciton binding energy. Heterointerfaces include the organic/metal interface at the electrical contacts or the donor/acceptor interfaces provided there is a sufficient HOMO-HOMO or LUMO-LUMO energy offset. In comparison to organic semiconducting materials, excitons in inorganic materials are highly delocalised, have considerably lower binding energies (a few meV [60]) and dielectric constants are much higher (~ 12 for silicon [61]). Excitons with these characteristics are termed *Wannier-Mott* excitons but the operation of inorganic PV devices is typically explained by treating the photo-excited states as free carriers with little attention paid to excitons [46].

If a Frenkel exciton in an organic semiconducting material is to dissociate it must undergo a process of diffusion to a heterointerface. For polymers, exciton diffusion occurs via a *hopping* mechanism either along the molecular chain (intrachain) or towards sites with lower energy (interchain). The two primary mechanisms of exciton diffusion in organic

semiconducting materials are Förster resonance energy transfer (FRET) and Dexter transfer. FRET is due to dipole-dipole interactions when the acceptor absorption spectrum overlaps the emission spectrum of the donor and typically occurs over a few nanometers [62]. Dexter transfer occurs over much smaller distances (<2nm) and is the result of direct carrier exchange between neighbouring moieties [62]. Further details of these processes are discussed in detail elsewhere [63] but are generally determined by the exciton diffusion length l_d . This is the average distance an exciton travels before it recombines. It is defined as:

$$l_d = \sqrt{nD\tau_e} \quad (2.11)$$

Where n is a dimension factor determining if diffusion is in 1, 2 or 3 dimensions, D is the diffusion constant and τ_e is the exciton lifetime (the average time that the exciton exists before recombining). Values of l_d are typically of the order \sim 5-10nm for most conjugated organic materials [64]. However, recently some studies have reported l_d values as high as 30-50nm for some NFAs [29, 65]. This length scale is critical in determining the optimum distance between donor and acceptor phases in the photoactive layer film, as will be discussed in further detail below.

If an exciton manages to successfully reach a heterointerface before recombination occurs, it can then undergo charge transfer provided the energy offset between the two materials is greater than the exciton binding energy. At donor/acceptor interfaces this corresponds to the LUMO-LUMO offset for electron transfer and the HOMO-HOMO offset for hole transfer. The minimum LUMO energy offset (ΔE_{LUMO}) (or HOMO energy offset ΔE_{HOMO}) is widely considered to be \sim 0.3V [58]. However, in some systems much smaller offsets as low as 0.1eV are sufficient [30, 66] suggesting it is largely dependent on the choice of material. The V_{OC} of device is determined by the energy difference between the HOMO of the donor and the LUMO of the acceptor $E_{HOMO-LUMO}$ as shown in Figure 2.7. To achieve optimum device performance it is therefore necessary to maximise $E_{HOMO-LUMO}$ whilst maintaining a sufficiently larger ΔE_{LUMO} (and ΔE_{HOMO}) to drive photo-induced charge transfer at the interface. The process of charge transfer leads to the formation of a charge-transfer (CT) state where the electron is situated on the LUMO level of the acceptor and the remaining hole is on the HOMO level of the donor. For charge carriers to be considered "free" and be available for charge transport to the electrical contacts, the electron and hole must escape their mutual Coulomb interaction. Unless the electron and hole are separated by a distance that overcomes this Coulomb interaction, they will undergo geminate recombination. Geminate recombination of charge carriers is recombination from the same initial state (i.e. the exciton). Non-geminate recombination can also occur when charge carriers from different initial states recombine.

3. Charge transport and extraction

After separation of the CT state, free carriers are transported to the electrical contacts and extracted into the external circuit of the device. The driving force of this process is an electric field, either built-in or applied externally. Here, charge transport is dependent on charge carrier mobility μ defined as:

$$\mu = \nu F \quad (2.12)$$

Where ν is the speed of the carrier and F is the applied electric field. In organic semiconducting materials, charge carrier mobility is also dependent on a number of other parameters such as temperature, molecular order and light intensity [67]. In general, charge mobilities of organic semiconducting materials are significantly lower than charge mobilities of inorganic materials.

For charge extraction, a free carrier must percolate through the bulk film to the electrical interface of the device. This requires donor and acceptor phases with high purity such that there is an appropriate extraction pathway for hole transport in the donor material and electron transport in the acceptor material. Another important factor is the free carrier drift length l_{drift} defined as:

$$l_{drift} = \mu\tau_c F \quad (2.13)$$

Where τ_c is the charge carrier lifetime (the average time that the carrier exists before recombining). l_{drift} along with the morphological composition of the film determine the efficiency of free carrier transport to the electrodes. l_{drift} additionally limits the thickness of the photoactive layer film for efficient device performance. If film thickness is much greater than l_{drift} , then the majority of carriers will recombine before reaching the electrical contacts for extraction. If a free charge carrier is successful in reaching an electrical contact, the charge can be extracted provided the provided the work function of the metal electrode or TCO is equal to or less than the donor HOMO and acceptor LUMO levels. If the difference between the work function of the cathode contact and the donor HOMO (or the anode contact and the acceptor LUMO) are large then this will result in additional voltage losses, affecting the maximum achievable V_{OC} of the device.

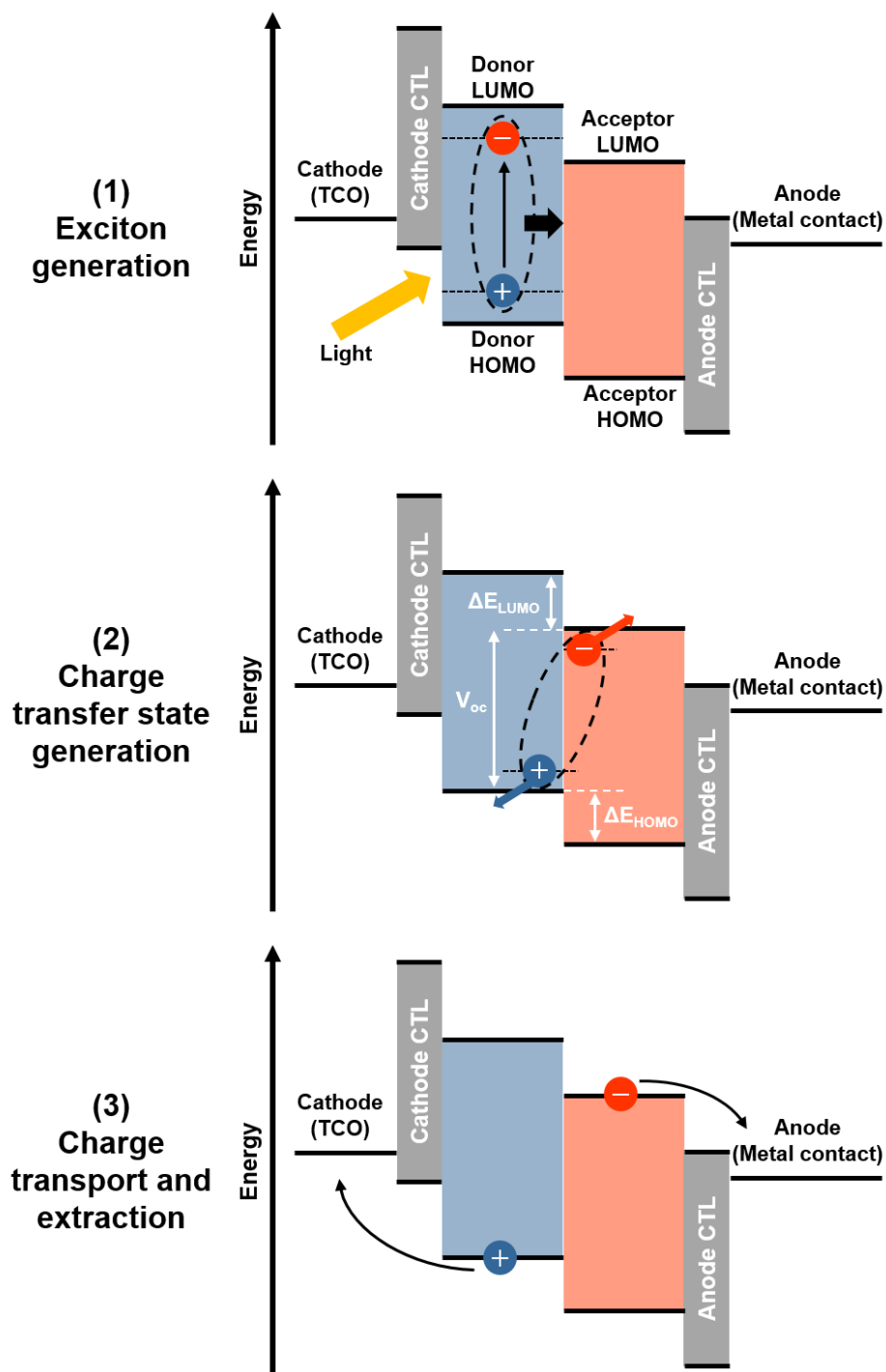


Figure 2.7: An energy diagram illustrating the key steps during the operation of an organic solar cell. In this example, an electron in the donor material is excited but the same concepts apply to photo-excitation in the acceptor material.

2.3.5 A Brief History of Organic Photovoltaics

Research into the PV effect in organic materials has a long history covered in more detailed reviews elsewhere [30, 68]. Much of the early development in the first half of the 20th Century focused on studying organic dyes and related materials [68]. The first organic compound to exhibit photoconductivity was anthracene [69, 70] followed by similar discoveries in a number of other organic materials such as methylene blue [71], chlorophylls [72, 73] and phthalocyanines [74, 75]. Many of these materials were also among the first organic compounds to demonstrate the PV effect by placing the organic material between two different metal contacts. However, the efficiency of these devices was significantly inferior to inorganic-based devices with *PCEs* remaining below 0.1% [73, 68].

Initial investigations into the photoconductivity of polymers focused on poly(vinyl carbazole) (PVK) [76] and later it was discovered that the conductivity of other polymers such as polyacetylene and poly(sulphur nitride) could be increased in the presence of particular dopants [77]. PV devices made from these polymers suffered from low open-circuit voltages that severely limited *PCE* values. In the early 1990s, attention shifted to the poly(p-phenylene vinylene) (PPV) and derivative polymers such as MEH-PPV and HO-PPV [78, 79]. These polymers demonstrated reduced voltage losses but power conversion efficiencies were still limited to around 0.1% [80, 81, 82]. An important observation was the sensitivity of PPV to atmospheric oxygen, which acts as a dopant due to its electron-accepting properties, analogous to a heterojunction in PV devices.

As mentioned previously, excitons require a heterointerface for dissociation (i.e. two different materials with different HOMO and LUMO levels). This concept was first realised by Tang in 1986 with the development of the *Tang Cell*; a bilayer PV device consisting of copper phthalocyanine and a perylene derivative [83]. The enhanced exciton dissociation efficiency at the donor-acceptor increased device *PCE* to around 1%. Following this breakthrough, numerous bilayer material systems were studied with the most successful devices based on polymer/ C_{60} architectures using polymers such as MEH-PPV [84] and PPV [85]. C_{60} is a member of the *fullerene* family of electron acceptors and will be discussed in further detail below.

One of the primary factors determining PV device efficiency is the abundance of heterointerfaces in the device for exciton dissociation. Due to the tightly bound, short-lived nature of excitons, the limited diffusion length provides an upper limit to the distance excitons should be formed from a donor-acceptor interface in the photoactive film. Although the bilayer architecture permits efficient exciton dissociation at the donor/acceptor interface, the thickness of these layers is restricted to the exciton diffusion length of each material as only the 10nm or so closest to the electrical contacts will contribute to the photocurrent.

This severely limits the optical depth of the photoactive layer, limiting the light-harvesting capabilities of the device. A successful solution to this was to use a distributed interface where the acceptor and donor materials are combined in a blend thin film creating a bulk heterojunction (BHJ) (Figure 2.8). In this configuration, interfacial area is significantly increased and films with considerably greater optical depth ($\sim 100nm$) can be fabricated. To prepare such architectures, the donor and acceptor materials are typically deposited from a blend solution or are co-evaporated to form a phase-separated film composed of an interpenetrating network of donor and acceptor domains.

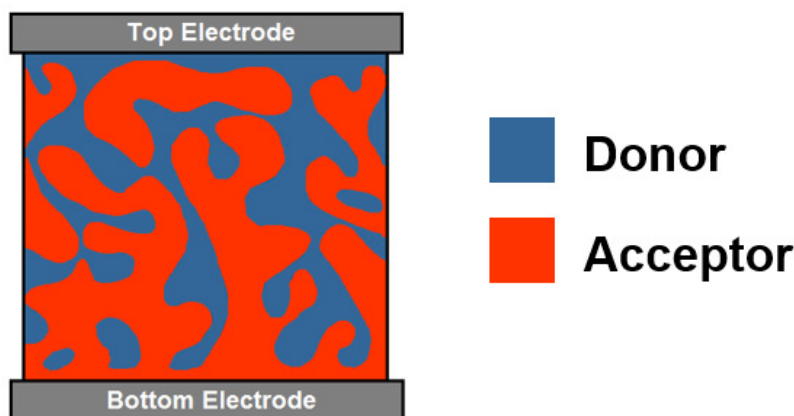


Figure 2.8: An illustration of a two-phase bulk heterojunction organic solar cell composed of donor and acceptor domains.

The first demonstration of a mixed donor and acceptor layer in an organic solar cell involved the addition of third mixed dye/dye blend layer, placed between the phthalocyanine and perylene layers of a Tang cell and resulted in a two-fold increase in device photocurrent [86]. This concept was then extended to polymer/ C_{60} systems [87, 88] but the poor solubility of C_{60} in most solvents limited the approach. To overcome this, a number of fullerene derivatives with solubilising side-chains were synthesised [89] allowing polymer/fullerene devices to reach *PCEs* as high as $\sim 2-3\%$ [31, 90].

After the initial demonstrations of bulk heterojunction organic solar cells, much of the research in the 2000s focused on developing materials, processing conditions and device architectures to increase device efficiency. The largest increases in *PCE* have been due to the synthesis of a new class of electron acceptor materials called non-fullerene acceptors (NFAs) which now greatly outperform fullerene-based acceptors. In the following section, an overview of electron acceptor materials and conjugated donor polymers used in organic photovoltaics is provided.

2.3.6 Electron Acceptors in Organic Photovoltaics

Traditionally, fullerene acceptors have been the electron acceptor of choice in organic photovoltaics because of their exceptional electronic properties [91]. Fullerenes are composed of a large conjugated carbon-cage in a ball-like structure. Although much of the early developments of OPV focused on C_{60} and C_{70} molecules, soluble fullerene derivatives such as $PC_{61}BM$ and $PC_{71}BM$, dominated the majority of research focus in the early 2000s due to their increased compatibility with solution-processing. Although this led to a steady rise in power conversion efficiencies during the early parts of the century [11], fullerenes have a number of limitations that resulted in a *PCE* enhancement bottleneck. The primary limitations of fullerenes include weak absorption of the solar spectrum, limited molecular tunability, expensive synthesis costs, poor miscibility with some conjugated polymers and poor stability [92].

In 2015, 3,9-bis(2-methylene-(3-(1,1-dicyanomethylene)-indanone))-5,5,11,11-tetrakis(4-hexylphenyl)-dithieno[2,3-d:2',3'-d']-s-indaceno[1,2-b:5,6-b']dithiophene (ITIC), an NFA based on an acceptor-donor-acceptor (A-D-A) structure was synthesised producing devices capable of *PCEs* as high as 6.80% in a blend with a common conjugated polymer (poly[4,8-bis(5-(2-ethylhexyl)thiophen-2-yl)benzo[1,2-b;4,5-b']dithiophene-2,6-diyl-alt-(4-(2-ethylhexyl)-3-fluorothieno[3,4-b]thiophene)-2-carboxylate-2,6-diyl)], PTB7-Th) [93]. Typically NFAs are composed of long conjugated backbones with solubilising side-chains and electron withdrawing end-groups. Shortly after the emergence of ITIC, optimisation processing conditions and blending with a new conjugated polymer (poly[(2,6-(4,8-bis(5-(2-ethylhexyl)thiophen-2-yl)-benzo[1,2-b:4,5-b']dithiophene))-alt-(5,5-(1',3'-di-2-thienyl-5',7'-bis(2-ethylhexyl)benzo[1',2'-c:4',5'-c']dithiophene-4,8-dione))], PBDB-T) pushed efficiencies beyond 11% [94]. NFAs offer a wealth of chemical tunability possibilities allowing the absorption window and energy levels of the molecule to be controlled. For example, since the synthesis of ITIC, a number of ITIC-based derivatives have been synthesised pushing efficiencies beyond 12% [95, 96]. Several NFAs such as those based on the IDTBR family of acceptors have also demonstrated impressive stabilities compared to fullerene-based systems [97, 98].

When work began on this thesis, ITIC-based systems were considered the state-of-the-art materials for OPV applications. However, over the past few years this has quickly been replaced by more efficient families of acceptors. Most notably the 2,2'-((2Z,2'Z)-((12,13-bis(2-ethylhexyl)-3,9-diundecyl-12,13-dihydro-[1,2,5]thiadiazolo[3,4-e]thieno[2'', 3':4',5']thieno[2', 3':4,5]pyrrolo[3,2-g]thieno[2',3':4,5]thieno[3,2-b]indole-2,10-diyl)bis(methanylylidene))bis(5,6-difluoro-3-oxo-2,3-dihydro-1H-indene-2,1-diylidene))dimalononitrile (Y6) family of NFAs has demonstrated *PCEs* as high as 19% [32, 33].

2.3.7 Polymers

A common group of materials used in organic electronics are *polymers*. Polymers are large molecules, composed of many repeat units called monomers which are covalently bonded together to form a long chain [48]. The number of monomers in the chain N is termed the *degree of polymerisation*. Generally, the synthesis of polymers results in a distribution of values for N characterised by a weight average (*molecular weight*, M_w) and a number average (*molecular number*, M_N). The ratio of M_w and M_N gives a measure of the distribution of N and is termed the *polydispersity index PDI*.

Ideal Random Walks

The overall dimensions of a polymer chain and their relation to the degree of polymerisation can be described in the framework of an ideal random walk for a freely jointed chain. In this simple model, it is assumed that a polymer is composed of N links of length a and that bonds between links are freely rotating with independent rotations. This means that the path of the polymer chain in space is a random walk where the end-to-end vector \mathbf{r} is the sum of N step vectors \mathbf{a}_i (i.e. the direction and size of each individual link in the polymer chain):

$$\mathbf{r} = \mathbf{a}_1 + \mathbf{a}_2 + \dots + \mathbf{a}_N = \sum_{i=1}^N \mathbf{a}_i \quad (2.14)$$

Which means the mean end-to-end distance of the polymer chain is:

$$\langle \mathbf{r} \cdot \mathbf{r} \rangle = \langle \mathbf{r}^2 \rangle = \left\langle \left(\sum_{i=1}^N \mathbf{a}_i \right) \cdot \left(\sum_{j=1}^N \mathbf{a}_j \right) \right\rangle = \left\langle \left(\sum_{i=1}^N \sum_{j=1}^N \mathbf{a}_i \cdot \mathbf{a}_j \right) \right\rangle \quad (2.15)$$

and for the N cases where $i = j$:

$$\langle \mathbf{r}^2 \rangle = Na^2 + \left\langle \left(\sum_{i \neq j} \mathbf{a}_i \cdot \mathbf{a}_j \right) \right\rangle \quad (2.16)$$

For a freely jointed polymer chain, there is no correlation between the directions of each step as they are random. As a result, the cross-terms in Equation 2.16 cancel when averaging giving the well-known relationship for a random walk:

$$\langle \mathbf{r}^2 \rangle = Na^2 \quad (2.17)$$

In terms of polymers, this means that the overall size of the polymer chain is proportional to the square root of the number of steps (i.e. monomers) in the chain. In reality, the bonds connecting monomers in a polymer chain have a bond angle associated with them

and cannot rotate freely. In this scenario, the cross-terms in Equation 2.16 do not cancel out and instead are equal to $a^2 \cos\theta$ where θ is the bond angle between successive links in the polymer chain. However, as $\cos\theta$ is always less than 1, this means that short-range correlations die away along the chain and the familiar random walk result in Equation 2.17 is recovered.

Polymer Crystallisation

Polymers used in OPV technologies are typically categorised as amorphous (glassy) or semi-crystalline [99]. Amorphous polymers are disordered in the solid-state, and tend to be glassy materials at room temperature. They are characterised by a glass transition temperature T_g , defined by a discontinuous change in thermodynamic quantities that are second derivatives of free energy [48]. At temperatures below T_g , the polymer is vitrified and chains are immobile. At temperatures above T_g , the amorphous polymer transitions from a glass to a liquid and polymer chains have a greater degree of mobility.

In contrast to elemental solids and small molecules, very few polymers can attain a fully crystalline state with full three-dimensional positional order. As a result, most polymers are *semi-crystalline* with very small crystals dispersed throughout an amorphous matrix. This behaviour is driven by the intrinsically slow kinetics associated with polymers because of their entangled state and built-in molecular disorder. The main driving forces determining polymer crystallisation are related to polymer architecture. Crystallisation is often hindered because of *quenched disorder* where the energy barrier for the polymer to reassemble into a more ordered arrangement is so large that the architecture is locked in place, even at absolute zero. Examples of factors, which can lead to quenched disorder in polymers include:

- **Tacticity:** the stereochemistry randomness or *tacticity* of a polymer with more than one type of chemical group attached to each carbon atom influences the resulting crystallisation behaviour of the polymer. As illustrated in (Figure 2.9), *Isotactic* polymers have the same side groups on the same side of the chain, *syndiotactic* polymers have an alternate arrangement and *atactic* polymers have a random arrangement. Atactic polymers exhibit *quenched disorder* as there is a large energy barrier to rotate the chemical groups into a more ordered isotactic or syndiotactic arrangement. For this reason, atactic polymers rarely crystallise and instead form amorphous glasses.
- **Branched side-chains:** the presence of branched side-chains hinder crystallisation as it is considerably harder for the polymer chains to pack into a regular crystal. In contrast, polymers that contain linear side-chains can pack much more easily into an ordered arrangement.

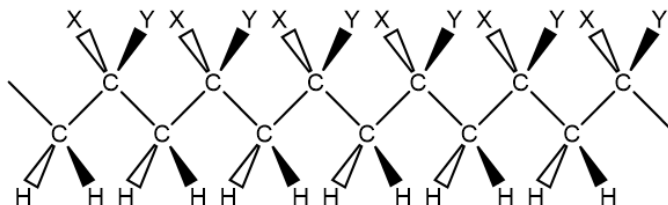
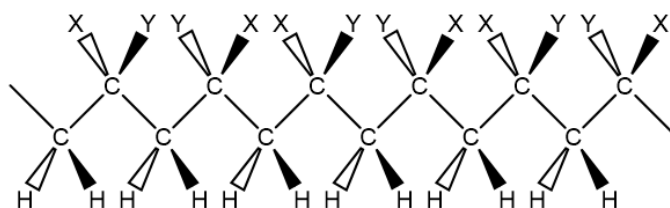
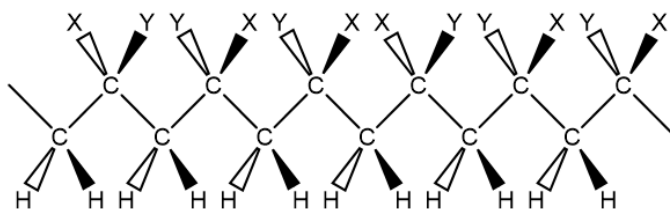
Isotactic**Syndiotactic****Atactic**

Figure 2.9: An illustration of three different polymer stereochemistries: isotactic, syndiotactic and atactic. X and Y are different chemical groups attached to each main chain carbon atoms.

- **Copolymers:** Copolymers are polymers composed of more than one type of repeat unit. Repeat units can organise in an alternate arrangement such as in the case of *block copolymers* or in a strictly prescribed but not periodic arrangement such as for *sequenced copolymers*. *Random copolymers*, composed of a random arrangement of repeat units can lead to quenched disorder, hindering crystallisation.
- **Regioregularity:** Polymer repeat units can also display isomerism. Regioregular polymers are composed of repeat units derived from the same isomer of the monomer. For example, regioregular poly(3-hexylthiophene) (P3HT) which has a regular end-to-end side-chain arrangement and is therefore semi-crystalline.

The basic unit of most polymer crystals is the chain-folded lamellae where the lamellar thickness L is independent of molecular weight and is typically $\sim 10\text{nm}$ [?]Jones2002). Ordered, chain-folded lamellae are separated by amorphous regions and individual polymer chains can be involved in multiple lamella and amorphous regions. At larger length scales, chain-folded lamellae crystallites can self-assemble into spherulites [100]. Here, sheaves of lamellar crystallites connected to amorphous segments, grow radially from a central nucleus forming structures up to micrometres in size. Such semi-crystalline systems are characterised by both a glass transition and a melting temperature T_m .

Conjugated Polymers

Polymers that possess conjugation (alternating single and double carbon bonds) are beneficial to a range of optoelectronic applications because their extended π -systems can absorb and emit light, and transport electrical charge. In OPV BHJ devices, conjugated polymers are often used as the donor material with small-molecule electron acceptors (SMAs). The highest efficiency devices are typically fabricated from semi-crystalline polymers due to their enhanced molecular ordering which aids charge transport in the device. Common examples include P3HT [97], PffBT4T-2OD (PCE11) [101], PTB7-Th [93] and PBDB-T (PCE12) [94].

2.4 The Thermodynamics of Phase Separation

To understand phase-separation in OPV blend films it is necessary to consider the thermodynamics of mixing. Generally speaking, two species will mix together if the mixture is more energetically favourable than the two separate components. Mathematically, this is described in terms of the free energy change of the mixture F_{mix} . The free energy of the mixture is related to the change in entropy S_{mix} and change in interaction energy U_{mix} of the mixture through the well know thermodynamic relation $F_{mix} = U_{mix} - TS_{mix}$ where T is temperature.

For a two-phase mixture containing a species A with volume fraction ϕ_A and a species B with volume fraction ($\phi_B \phi_A + \phi_B = 1$), the change in entropy can be calculated by considering each molecule of A and B arranged on a lattice where each lattice site has z nearest neighbours. The entropy per site can then be calculated using the Boltzmann formula:

$$S = -k_B \sum_i p_i \ln p_i \quad (2.18)$$

Where entropy is the sum over all states in the system i , each with probability p_i . For the simple two-phase mixture of A and B, S_{mix} is therefore given as:

$$S_{mix} = -k_B(\phi_A \ln \phi_A + \phi_B \ln \phi_B) \quad (2.19)$$

Here it is assumed neighbouring sites are independent of each other (mean field assumption). To find the energy of mixing U_{mix} it is assumed that molecules interact only with their nearest neighbours in a way that it is pairwise additive. The energy of interaction between two neighbouring A molecule sites is ϵ_{AA} , between two neighbouring B molecule sites is ϵ_{BB} and neighbouring A and B sites is ϵ_{AB} . Assuming each lattice site has $z\phi_A$ A neighbours and $z\phi_B$ B neighbours, the interaction energy per site is then $(z/2)(\phi_A^2\epsilon_{AA} + \phi_B^2\epsilon_{BB} + 2\phi_A\phi_B\epsilon_{AB})$. Subtracting this from the energy of the unmixed state $((z/2)(\phi_A\epsilon_{AA} + \phi_B\epsilon_{BB}))$ gives the energy of mixing as

$$U_{mix} = \frac{z}{2}[(\phi_A^2 - \phi_A)\epsilon_{AA} + (\phi_B^2 - \phi_B)\epsilon_{BB} + 2\phi_A\phi_B\epsilon_{AB}] \quad (2.20)$$

The strength of the energetic interaction between molecules A and B can be characterised by a single dimensional parameter - the interaction parameter χ defined as:

$$\chi = \frac{z}{k_B T} (2\epsilon_{AB} - \epsilon_{AA} - \epsilon_{BB}) \quad (2.21)$$

Assuming $\phi_A + \phi_B = 1$, Equation 2.20 can be written as:

$$U_{mix} = \chi\phi_A\phi_B \quad (2.22)$$

Finally, using the thermodynamic relation $F_{mix} = U_{mix} - TS_{mix}$, the free energy of mixing can be written as:

$$\frac{F_{mix}}{k_B T} = \phi_A \ln \phi_A + \phi_B \ln \phi_B + \chi\phi_A\phi_B \quad (2.23)$$

Equation 2.23 is a relatively simple equation but allows the phase behaviour of a mixture to be explored as a function of composition, depending only on temperature and the value of a single dimensionless parameter χ . In Figure 2.10, the free energy of mixing is plotted as a function of the volume fraction of polymer A, ϕ_A for different values of χ . At χ values > 2 the free energy curve has two minima and a maximum at $\phi_A = \phi_B = 0.5$. Here, it is energetically unfavourable for the polymers to mix and at $\phi_A = 0.5$ the mixture is unstable because the free energy can be minimised if the mixture phase separates into two components with concentrations depending on the position of the two minima. These compositions are termed the *coexisting compositions* and share a common tangent line (i.e. their derivatives are the same). The locus of these two points as temperature and the interaction parameter are changed gives the coexistence curve or *binodal*. For χ values < 2 the free energy curve has a single minimum at $\phi_A = \phi_B = 0.5$. Here, the minimum free energy of the system occurs when the polymers are mixed in a 50:50 mixture. A critical value of the interaction parameter can therefore be defined as:

$\chi > \chi_c = 2$ for phase separation
 $\chi < \chi_c = 2$ single phase at all compositions

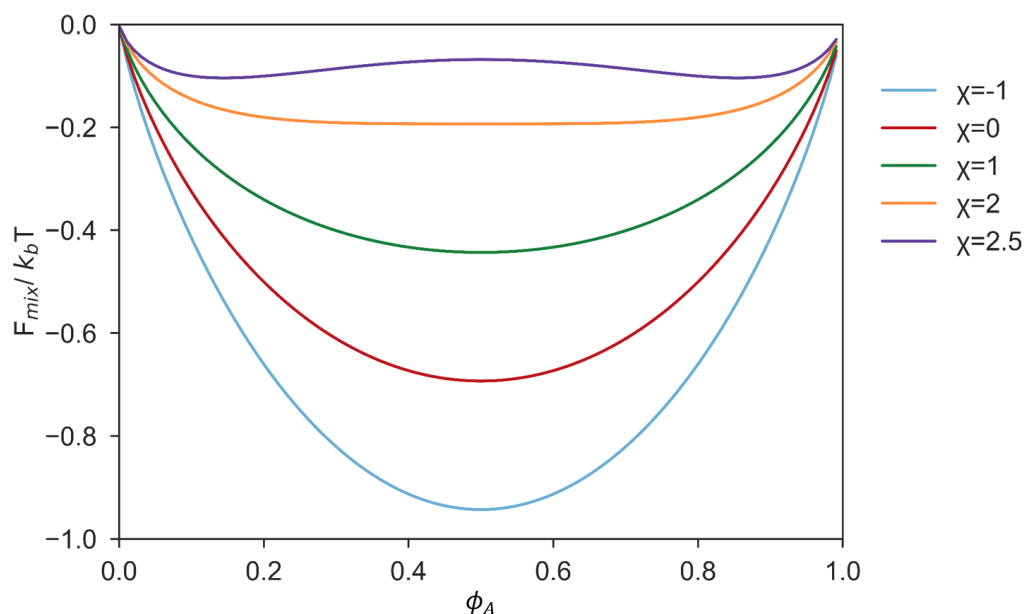


Figure 2.10: Free energy of mixing F_{mix} for a system of two species A and B for different values of the interaction parameter χ .

Another interesting characteristic of the free energy curves shown in Figure 2.10 is that their curvature ($d^2F/d\phi^2$) may be positive or negative. A change in curvature from negative to positive defines a change from an unstable mixture to a stable one. The boundary between these two conditions therefore occurs when $d^2F/d\phi^2 = 0$. The values of temperature and the interaction values for which this condition is satisfied is termed the *spinodal*. In Figure 2.11, the phase diagram for a mixture of two species A and B is plotted showing the binodal and spinodal curves. At conditions below the binodal curve, the mixture is stable and will exist as a single phase. At conditions above the spinodal, the mixture is unstable and will spontaneously phase separate. The intersection of the binodal and spinodal curves is known as the critical point. At conditions in-between the spinodal and binodal curves, the mixture is metastable. In the metastable region, the mixture is phase-separated but the two compositions are not coexisting compositions and are stable with respect to small fluctuations in composition. The system is locally stable but globally unstable with respect to separation into two coexisting phases and there is therefore an energy barrier required to reach the global free energy minimum.

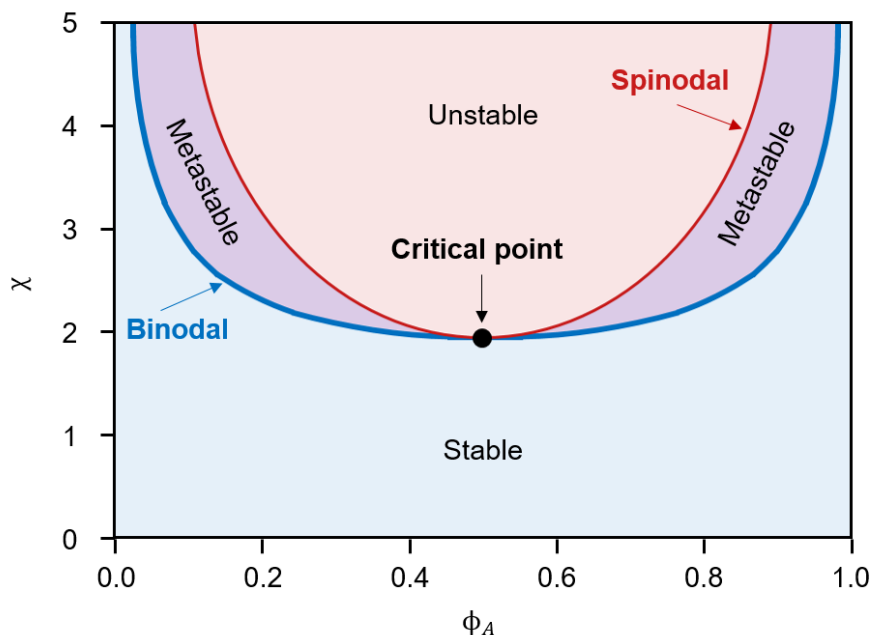


Figure 2.11: A phase diagram of a system of two species A and B showing the stable, metastable and unstable regions separated by the binodal and spinodal, as well as the critical point.

There are two primary phase-separation mechanisms: *spinodal decomposition* and *nucleation*. Spinodal decomposition occurs in the unstable part of the phase diagram and results in a continuous change in composition. The process occurs spontaneously as it is sensitive to the small concentration fluctuations present in any mixture at thermal equilibrium. Nucleation can occur in the metastable part of the phase diagram. As there is an energy barrier to reach the global free energy minimum, the system cannot phase separate via a continuous change in composition. Instead, a large composition fluctuation must take place forming a nucleus that can then grow in size (homogenous nucleation). Phase separation via nucleation can also occur as a result of impurities in the system, which lower the activation energy (heterogeneous nucleation).

2.4.1 Polymer : Polymer Interfaces

For two-phase polymer : polymer mixtures, the entropy of mixing is now also dependent on the degree of polymerisation N . This is because if the number of monomer units of a molecule increases from 1 to N , the entropy of mixing per molecule stays the same but the energy of mixing increases by a factor of N . Equation 2.23 can therefore be rewritten as:

$$\frac{F_{mix}}{k_B T} = \frac{\phi_A}{N} \ln \phi_A + \frac{\phi_B}{N} \ln \phi_B + \chi \phi_A \phi_B \quad (2.24)$$

Where F_{mix} represents the free energy of mixing per monomer unit and the interaction parameter χ is the energy of interaction per monomer which is independent of N . This approximation is the well-known Flory-Huggins free energy. The phase diagrams discussed earlier can be recalculated by substituting χ for χN . This means the critical value of the interaction parameter for polymer mixtures becomes:

$$\begin{aligned} \chi > \chi_c &= \frac{2}{N} \text{ for phase separation} \\ \chi < \chi_c &= \frac{2}{N} \text{ single phase at all compositions} \end{aligned}$$

As N is often a very large number for polymers, the unfavourable enthalpic interaction that can be tolerated before phase separation occurs is usually much smaller for polymers compared to small molecules. As a result, polymer mixtures tend to phase separate if they have a sufficiently large degree of polymerisation (i.e. large M_w). In these mixtures, the two polymer phases are essentially pure but the interfaces between them are not atomically sharp. For an atomically sharp interface would minimise unfavourable contacts between the two different polymers but would restrict the number of possible polymer configurations and therefore have a very large entropy cost. Instead, the interface must be diffuse and permit the protrusion of polymer chains into the opposite phase. There is therefore an associated equilibrium interfacial width w that balances the entropy cost of unfavourable interactions at the interface.

The interfacial width of a polymer : polymer interface can be approximated by again considering a polymer chain as a random walk. For a polymer mixture containing a polymer A and a polymer B, loops of polymer A will protrude into the polymer B phase as illustrated in Figure 2.12. Using the random walk result described above (Equation 2.17), the degree of polymerisation of protruding loops N_{loops} is given as:

$$w \sim a \sqrt{N_{loop}} \quad (2.25)$$

Where a is the size of the monomer. The loop has an associated unfavourable energy U_{int} due to the unfavourable contacts between segments of polymer A and segments of polymer B. There are N_{loops} contacts so U_{int} can be expressed as:

$$U_{int} \sim \chi N_{loop} k_B T \quad (2.26)$$

At equilibrium, U_{int} is of the order $k_B T$ so $1 \sim \chi N_{loop}$. Using Equation 2.25, the interfacial width w can therefore be expressed as:

$$w \sim \frac{a}{\sqrt{\chi}} \quad (2.27)$$

Values of w are typically of the order 1-3nm [48].

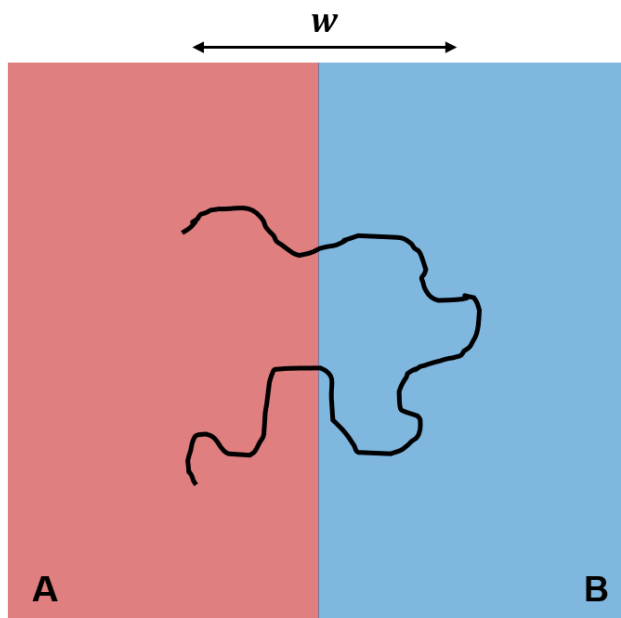


Figure 2.12: An illustration of the interface between two polymer phases (A and B). At the interface there is a mixed region characterised by an interfacial width w where loops of polymer A protrude into polymer B and vice versa.

2.4.2 Donor : Acceptor : Solvent Systems

The above treatment of two-phase polymer : polymer systems provides insight into the relationships between the degree of polymerisation, the interfacial width and the interaction parameter. For many OPV systems, active-layer films are solution-processed and so the system is in fact a three-phase system composed of donor, acceptor and solvent components. For such donor : acceptor : solvent mixtures, the Flory-Huggins free energy described previously (Equation 2.24) is given by:

$$\frac{F_{mix}}{k_B T} = \phi_S \ln \phi_S + \frac{\phi_D}{N_D} \ln \phi_D + \frac{\phi_A}{N_A} \ln \phi_A + \chi_{SD} \phi_S \phi_D + \chi_{SA} \phi_S \phi_A + \chi_{DA} \phi_D \phi_A \quad (2.28)$$

Where ϕ_S , ϕ_D and ϕ_A are the volume fractions of the solvent, donor and acceptor components respectively. χ_{SD} , χ_{SA} and χ_{DA} are the Flory-Huggins interaction parameters

between the solvent:donor, solvent:acceptor and donor:acceptor respectively. N_D and N_A are the degree of polymerisation for the donor and acceptor components respectively.

During thin film fabrication, donor and acceptor components dissolved in a mutual solvent are deposited onto a substrate via methods such as spin-coating (discussed in further detail in Chapter 3). The driving forces behind blend film formation and the resulting structural characteristics are governed by kinetic and thermodynamic parameters. Kinetic factors include the processing conditions that determine the film drying kinetics (e.g. solvent vapour pressure, film deposition technique). Thermodynamic factors concern the properties of the material such as the solubilities and interactions of the blend components in the casting solvents and their crystallisation behaviour [102]. In terms of phase separation, there are two competing processes during solvent evaporation. These are liquid-liquid (L-L) and solid-liquid (S-L) phase separation. L-L phase separation occurs via spinodal decomposition. S-L phase separation occurs when either the donor or the acceptor material reaches its solubility limit in the solvent. These processes can happen simultaneously or sequentially depending on the system. If neither happens, the dry film will consist of a finely mixed blend morphology.

In Figure 2.13, a schematic representation of a ternary phase diagram is shown for a solvent:donor:acceptor system. The binodal and spinodal curves are shown for different values of the donor:acceptor Flory-Huggins interaction parameter and the dashed black line represents the change in composition during solvent evaporation. Initially, the system consists of a single homogenous phase but during solvent evaporation the system crosses to the one-phase region to the two-phase region via L-L phase separation. The onset of this change is strongly linked to χ_{DA} , (i.e. low compatibility donor and acceptor with high χ_{DA} leads to a large two-phase region, Figure 2.13). For high χ_{DA} cases (blue curves in Figure 2.13), L-L phase separation leads to domain over-coarsening as a result of the unfavourable interactions between the donor and acceptor components and high solvent content during the early stages of evaporation.

In addition to χ_{DA} , the depth to which the blend enters the two-phase region (the *quench depth*) also influences the extent of L-L phase separation. Large-scale phase-separation typically occurs for fast solvent evaporation rates with a deep quench depth whilst slow evaporation rates reduce the extent of L-L phase separation. For systems with small χ_{DA} values, the one-phase region is large and the system reaches the unstable region during a later stage of solvent evaporation (red curves in Figure 2.13). L-L phase separation is therefore limited due to the more favourable interactions between the donor and acceptor components and low solvent content. At this stage, the donor and acceptor components may have also reached their solubility limits in favour of S-L phase separation instead of L-L phase separation, resulting in aggregation. S-L phase separation is driven by the

thermodynamic and kinetic factors discussed previously which determine the nucleation and growth processes. Materials which tend to crystallise easily (e.g. small molecules), are more likely to undergo S-L at this stage due to the low activation barrier. These processes can be controlled by changing the solvent drying dynamics and optimising the compatibility of the solutes.

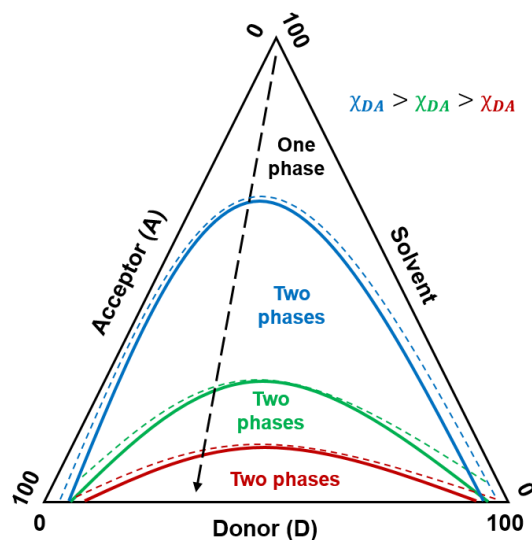


Figure 2.13: An illustration of a ternary phase diagram for a system composed of solvent (S), donor (D) and acceptor (A) components showing the binodal (dashed) and spinodal (solid) compositions for different donor:acceptor Flory-Huggins interaction parameters (χ_{DA}). The dashed black line represents the evolution of a blend film composition during solvent evaporation.

2.5 Correlating Self-Assembled Nanostructures with Optoelectronic Performance and Stability

The self-assembly of donor and acceptor domains in a BHJ organic solar cell plays an important role in the light-harvesting process through the generation and dissociation of excitons and proceeding transport and extraction of free charge carriers at the electrodes. In this section, the characterisation of self-assembled nanostructures is discussed and correlated with OPV performance and stability metrics.

There are a number of factors such as chemical design, film morphology and processing conditions that contribute to the fabrication of a stable, high efficiency OPV device. A

number of these are illustrated in Figure 2.14. A primary aim of this thesis concerns the characterisation of self-assembled structures in organic electronics. This covers a broad range of structural properties and requires a diverse range of characterisation techniques. In this section, an overview of the key structural properties of organic thin films is provided followed by their relation to OPV device performance and stability.

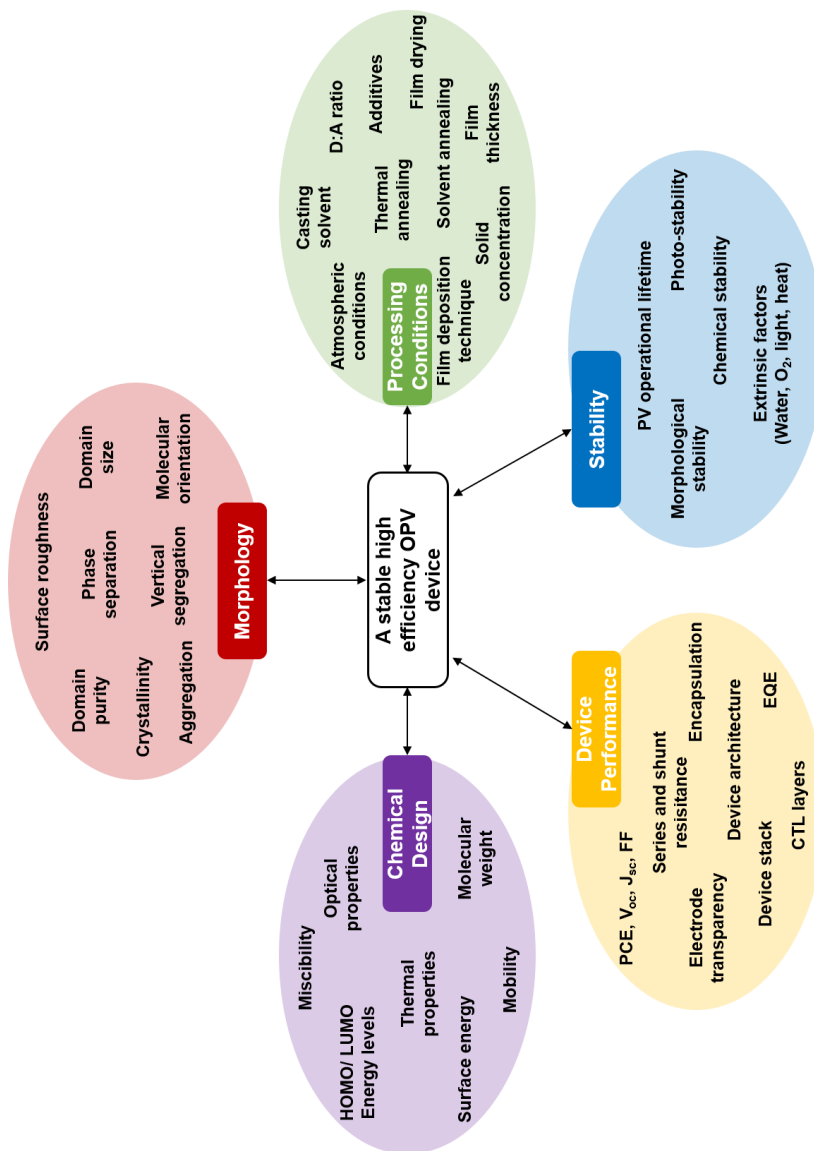


Figure 2.14: A diagram illustrating the key factors that contribute to a stable, high-efficiency OPV device. Factors are split into five categories: Chemical design, processing conditions, device performance, morphology and stability.

2.5.1 Characterising Self-Assembled Nanostructures in Organic Thin Films

To fully characterise the three-dimensional, hierarchical structure prevalent in many organic semiconducting thin films, a combination of structural characterisation techniques are typically required to probe a broad range of length scales. In Figure 2.15, the typical length scales probed by common scattering and microscopy based techniques is displayed, along with the structural properties they can probe in organic thin films. A common theme throughout this thesis is to divide structural characterisation up into three categories: small-scale structures, large-scale structures and vertical chemical composition.

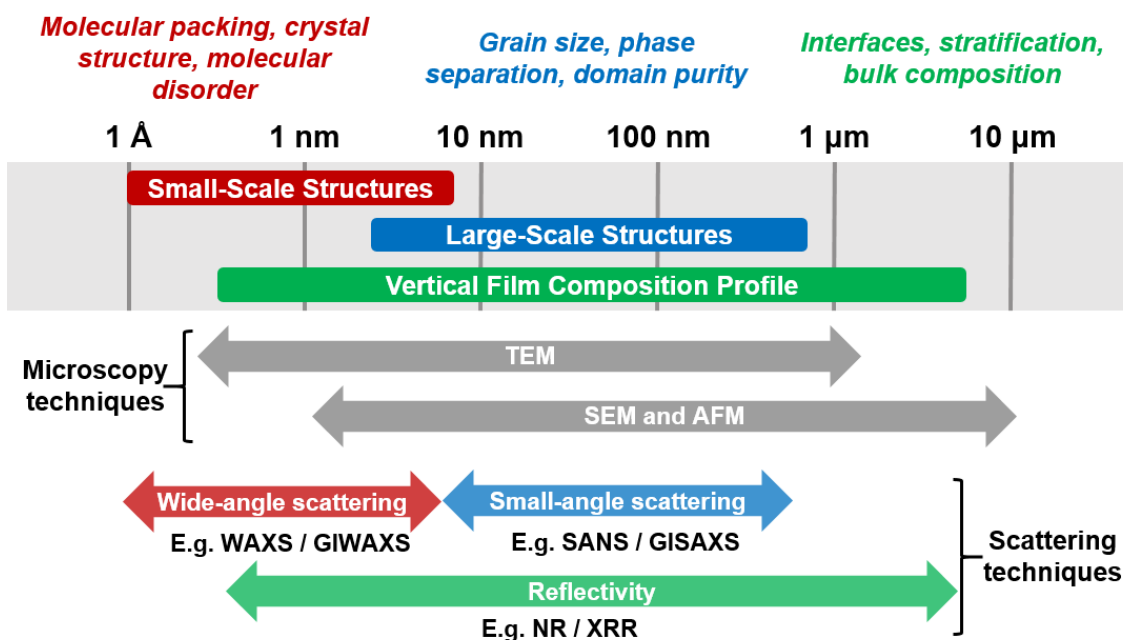


Figure 2.15: An illustration of some of the characteristic length scales present in organic thin films and examples of suitable scattering and microscopy characterisation techniques to probe them.

Small-scale structures concern those $\sim 0.1 - 1$ nm in size such as the molecular self-assembly and orientation of donor and acceptor components in the film. These types of structures can be characterised using transmission electron microscopy (TEM) [103] and wide angle scattering methods such as wide angle X-ray scattering (WAXS) and grazing incidence wide angle X-ray scattering (GIWAXS) [104]. On the larger scale (~ 10 nm - $1 \mu\text{m}$), structural properties of interest include the size and purity of phase-separated domains and crystallites. These structures can be characterised using scanning electron microscopy (SEM),

atomic force microscopy (AFM) and small angle scattering techniques such as small angle neutron scattering (SANS) [105] and grazing incidence small angle X-ray scattering (GISAXS) [106]. The vertical chemical composition of the film concerns the distribution of donor and acceptor domains in the plane perpendicular to the substrate and the composition of interfaces at the electrodes. It can be characterised using depth-profiling techniques such as neutron reflectivity (NR) and X-ray reflectivity (XRR) [101, 107, 108]. Key structural properties relating to each of the three categories are described below. Descriptions of all structural characterisation techniques used in this thesis are provided in Chapter 3.

Small Scale Structures

The molecular arrangement and orientation of the constituent organic molecules in a thin film can significantly affect the direction and efficiency of charge transport. In an OPV device, efficient charge transport is required in the direction perpendicular to the substrate. Typically, conjugated organic molecules either adopt a face-on or edge-on molecular orientation with respect to the substrate. This is illustrated in Figure 2.16 for a prototypical NFA (ITIC) [109]. Here, NFA molecular structure has been simplified to represent planar sheets. In reality, NFAs typically have planar backbones but the end-group and side-chain moieties can exhibit rotation away from the backbone plane. In Figure 2.16, three characteristic scattering length scales are labelled: the π - π stacking distance, the lamellar stacking distance and the alkyl stacking distance. For conjugated materials, charge transport occurs along the π - π stacking distance [110] due to the extended π -electron system. A face-on molecular orientation with aromatic groups aligned parallel to the substrate is therefore ideal for OPV systems.

The π - π stacking distance corresponds to the distance between neighbouring aromatic groups ($\sim 3 - 5\text{\AA}$ for most organic materials). For NFAs such as ITIC, molecular packing is dominated by π - π stacking of the terminal end-groups leading to a variety of larger chain-like and cluster-like aggregated structures [111]. The bulky phenyl-hexyl side-chains inhibit π - π of the aromatic backbone to avoid the formation of large aggregates. More generally, conjugated organic molecules can undergo J- and H- type aggregation through various slipped and columnar π - π stacking motifs respectively [110]. The lamellar stacking distance corresponds to the backbone-backbone distance or width of the molecule and the alkyl stacking distance corresponds to the distance between neighbouring side-chains.

In reality, the molecular packing of organic materials in a thin film can be considerably more complex, particularly for materials that exhibit polymorphism [112]. In such cases, the thin film structure is often different to the bulk crystal structure of the material due to the formation of non-equilibrium phases from rapid film deposition techniques such as spin-coating. Whilst this increases the difficulty of structural characterisation, it is these

intermediate states of order and the rich phase behaviour of organic molecules which offer novel processing routes to optimise device performance.

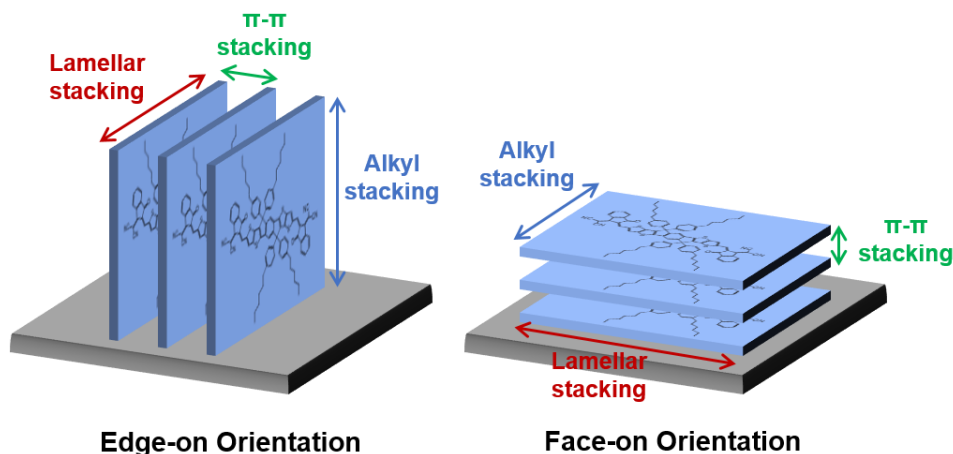


Figure 2.16: An illustration of typical edge-on and face-on molecular orientations of ITIC, a non-fullerene acceptor. Characteristic stacking directions are labelled for each orientation.

Large Scale Structures

In Section 2.4 the thermodynamics of phase separation was discussed above with respect to polymer:polymer blends. During fabrication of a polymer: SMA BHJ blend film, the constituent components typically phase-separate by the same means to form an interpenetrating network of acceptor and donor domains. The exciton diffusion length l_d of each material provides an upper limit of the characteristic phase separation length scale L_p of the system. If $L_p \ll l_d$, excitons will reach a heterointerface and dissociate but the percolation pathway will be insufficient for efficient charge transport and extraction. If $L_p \gg l_d$, most excitons will recombine before they diffuse to a heterointerface for dissociation to occur. If $L_p \sim l_d$, excitons will diffuse to a heterointerface for dissociation and there will be a sufficient extraction pathway for free charges to be extracted from the device.

Historically the optimum morphology of a device was considered to be a two-phase system of donor and acceptor domains with sharp interfaces (i.e. small interfacial widths w). More recently, it has been shown that a third, mixed phase of donor and acceptor material is beneficial for device performance due to an increase in donor/acceptor interfacial area and a more favourable percolation pathway [105, 113]. The impact of intermixing on the donor/acceptor interfaces in a BHJ solar cell is demonstrated in Figure 2.17. For

systems which are too finely intermixed (large interfacial width), there is an insufficient percolation pathway to the electrodes and free charge carriers recombine. For systems with diffuse interfaces, the large donor/acceptor interfacial area enhances the efficiency of exciton dissociation. Systems with sharp interfaces (small interfacial width) have a significantly reduced interfacial area, limiting sites for exciton dissociation.

The optimal degree of this intermixing termed the *percolation threshold* has been extracted for some OPV systems by measuring the amorphous-amorphous phase diagram [113]. In these studies, device performance can be correlated to the purity of domains and the Flory-Huggins interaction parameter χ [113, 114, 115].

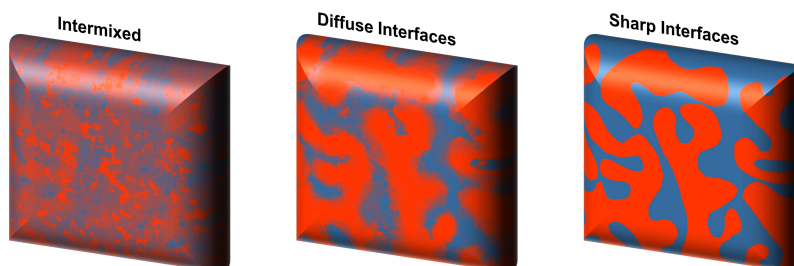


Figure 2.17: An illustration of different degrees of intermixing in a BHJ blend film for a finely intermixed system (left), a system with diffuse interfaces (centre) and a system with sharp interface (right).

Vertical Chemical Composition

In addition to molecular-scale packing and domain self-assembly, the distribution of acceptor and donor components in the plane perpendicular to the substrate also has a significant impact on the extraction of charges at the electrodes. For example, in a device which extracts holes at the bottom electrode and electrons at the top electrode, an accumulation of donor material at the film surface could act as a barrier, inhibiting electron extraction. This is illustrated in Figure 2.18. Here, an acceptor-rich layer has also formed at the bottom electrode restricting the extraction of holes. Interfacial segregation of this kind is often driven by differences in miscibility and surface energy of the donor and acceptor components [108, 116, 117].

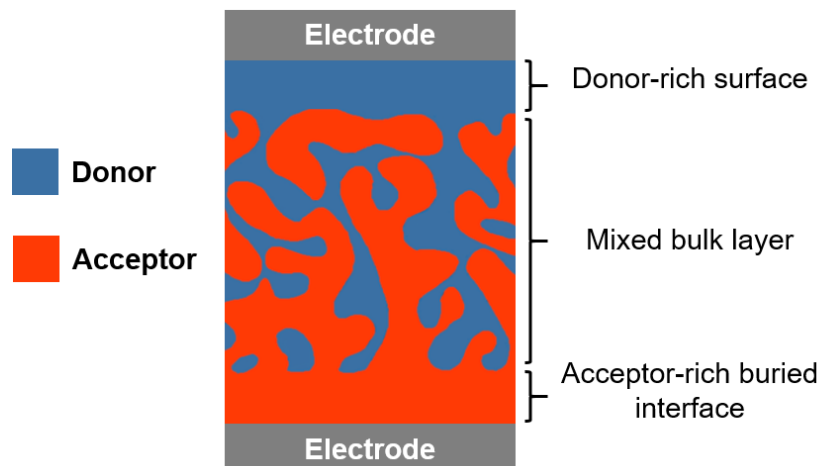


Figure 2.18: An illustration of a BHJ blend film where the top and bottom electrodes are enriched in donor and acceptor materials respectively.

2.5.2 Photovoltaic Performance

Earlier in this chapter, the characteristic PV device metrics (V_{OC} , J_{SC} , FF and PCE) of a solar cell were described. In a BHJ OPV device these metrics are related to the morphology of the photoactive blend film in the following ways [102]:

- **Short-circuit current density J_{SC} :** Is proportional to the number of incoming photons that are absorbed by the photoactive BHJ layer and the efficiency of processes determining exciton separation and charge transport through the device. It is therefore related to the absorption profiles and extinction coefficients of the component donor and acceptor materials and can be enhanced by increasing the molecular order of domains and percolation pathway through the device.
- **Open-circuit voltage V_{OC} :** The V_{OC} of a BHJ OPV device is related to the HOMO-LUMO energy offset between the donor and acceptor component materials and the efficiency of charge extraction in the device. Morphological optimisation can lead to a reduction in voltage losses through improved charge extraction but V_{OC} is ultimately limited by the HOMO-LUMO offset. A build of donor or acceptor material at an electrode interface in the device can affect charge extraction and consequently V_{OC} .
- **Fill-factor FF :** The FF of an organic solar cell is a measure of the efficiency of generated charge extraction in the device. In a similar way to J_{SC} , it therefore depends on the efficiency of processes relating to charge generation and transport in the device and is closely linked to the intermixing of domains and percolation pathway in the device.

- **Power Conversion Efficiency PCE :** The PCE of an OPV device combines the contributions from J_{SC} , V_{OC} and FF discussed above.
- **External Quantum Efficiency EQE :** The EQE of an organic solar cell is related to the generated photocurrent. It is therefore dependent on the absorption profiles of the donor and acceptor components. From a morphological point of view, it is impacted by the structural properties as J_{SC} .

2.5.3 Stability

In addition to high-efficiencies, OPV devices must also demonstrate long-term operational stability to be commercially viable. Whilst some OPV systems have demonstrated lifetimes as long as 30 years through accelerated ageing tests [42], these tests are not representative of real-world conditions where temperature, humidity and light intensity undergo daily, seasonal and annual variances. Some studies have investigated real-world conditions [118, 119]. However, these tests are usually restricted to durations of a year or less and it is difficult to extrapolate actual operational lifetimes. It is therefore important that the degradation routes of OPV systems are well understood to extend operational lifetimes for commercially viable products.

In general, an OPV device will exhibit a *burn-in* period during the initial stage of stability testing, corresponding to an exponential PCE loss. This is then followed by linear PCE loss. Whilst the origin of this burn-in period is not fully understood, numerous potential causes have been suggested, such as component demixing [120], fullerene dimerization [121] and trapped energy states [122]. In this section, key degradation factors of organic solar cells are discussed. Factors are divided into *extrinsic* factors and *intrinsic* factors [28].

Extrinsic Factors

Extrinsic stability factors are related to environmental factors such as oxygen, humidity, temperature and light. Oxygen and water diffusion into the photoactive film can result in chemical degradation through photo-oxidation of the active layer components [123] and oxidation of low work function metal contacts resulting in the formation of insulating metal oxide layers [28]. These processes reduce the efficiency of charge transport and extraction in the device. Additionally, degradation via light irradiation can occur due to UV-induced chemical instabilities and photo-oxidation when combined with oxygen [124, 125]. Extrinsic factors can largely be overcome by encapsulating devices to prevent the ingress of oxygen and moisture.

Intrinsic Factors

Intrinsic stability factors are related to the stability of the device materials and components. They include morphological and chemical instabilities. A primary cause of intrinsic degradation is the use of solvent additives during processing that can increase the rate of oxygen diffusion into the film and accelerate detrimental photo-chemical reactions [123, 126, 127]. Morphological instabilities are also linked to component demixing and formation of large crystallites due to poor thermal stability and large diffusion coefficients [128]. Whilst relationships between blend nanomorphology and stability are still emerging, a number of recent studies have aimed to quantify differences in miscibility, crystallisation behaviour and glass transition temperature with device performance metrics and stability [114, 128, 115].

Experimental Methods, Techniques and Theory

3.1 Introduction

This chapter details the experimental methodology used throughout this thesis with particular focus on neutron and X-ray scattering. The chapter begins with an introduction to the materials used in this thesis followed by thin film preparation and OPV device fabrication details. The remainder of the chapter is focused on describing the underlying physics and apparatus for all experimental characterisation techniques used throughout Chapters 4-7. Unless stated, all work was performed in the Department of Physics and Astronomy, Hicks Building Sheffield, United Kingdom.

3.2 Materials

The energy levels of all transparent conductive oxides (TCOs), hole transport layers (HTLs), donor polymers, electron acceptors, electron transport layers (ETLs) and metal contacts used in this thesis are displayed in Figure 3.1 along with the direction of holes and electrons during charge transfer. For conjugated donor polymers and small molecule electron acceptors, the highest occupied molecular orbital (HOMO) and lowest occupied molecular orbital (LUMO) energies are listed in Table 3.1. These values have been averaged from those found in literature as reported values often vary depending on processing conditions and measurement technique (e.g. cyclic voltammetry, ultraviolet photoelectron spectroscopy).

Material	HOMO (eV)	LUMO (eV)
PBDB-T	-5.30	-3.37
PTB7-Th	-5.18	-3.57
PC₇₁BM	-6.02	-4.16
ITIC	-5.51	-3.86
EH-IDTBR	-5.71	-3.90
O-IDTBR	-5.53	-3.82
O-IDTBCN	-5.75	-3.99

Table 3.1: Table of HOMO and LUMO energies of all OPV materials used in this thesis. Values averaged from aggregated literature results [129, 95, 130, 94, 131, 132, 133, 134, 93, 135, 136, 137, 97, 138, 139].

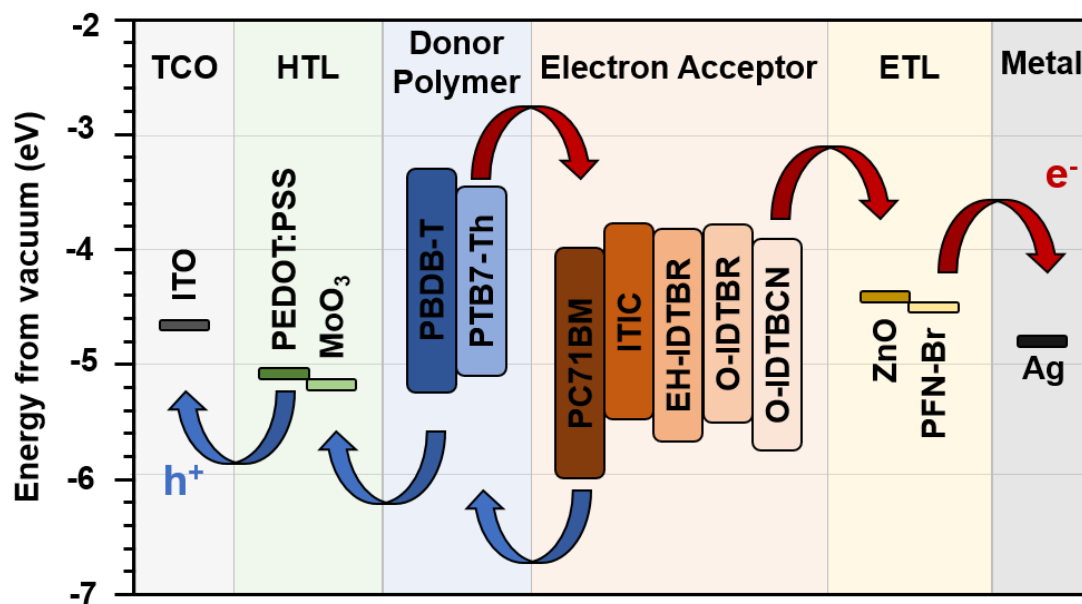


Figure 3.1: The conduction band (CB), valence band (VB), HOMO and LUMO energies from vacuum for all photovoltaic materials used in this thesis. Values are averaged from aggregated literature results [129, 95, 130, 94, 131, 132, 133, 134, 93, 135, 136, 137, 97, 138, 139]

All materials and solvents were used as received and stored in a nitrogen-filled glovebox. Oxygen and moisture levels were kept at <0.1 ppm inside gloveboxes for all sample preparation and measurements. Further information and chemical structures of all materials and solvents used in this thesis are provided below.

3.2.1 Conjugated Donor Polymers

The chemical structures of conjugated polymers used as donor materials in bulk heterojunction blends is shown in Figure 3.2. These include the medium bandgap polymer, PBDB-T and low bandgap polymer, PTB7-Th. PBDB-T is composed of 2-alkylthiophene-substituted benzo [1,2-b:4,5-b'] dithiophene (BDT) unit and 1,3-bis(thiophen-2-yl)-5,7-bis(2-ethylhexyl)benzo-[1,2-c:4,5-c']dithiophene-4,8-dione (BDD) unit with 2-ethylhexyl side chains. PTB7-Th is composed of the same BDT unit attached to a thieno[3,4-b]thiophene (TT) unit. PBDB-T was purchased from Ossila in (batches M1002 or M1001A2). PTB7-Th was purchased from Ossila (batch M0261A3). The molecular weight, molecular number and polydispersity index of each batch of polymer are provided in Table 3.2.

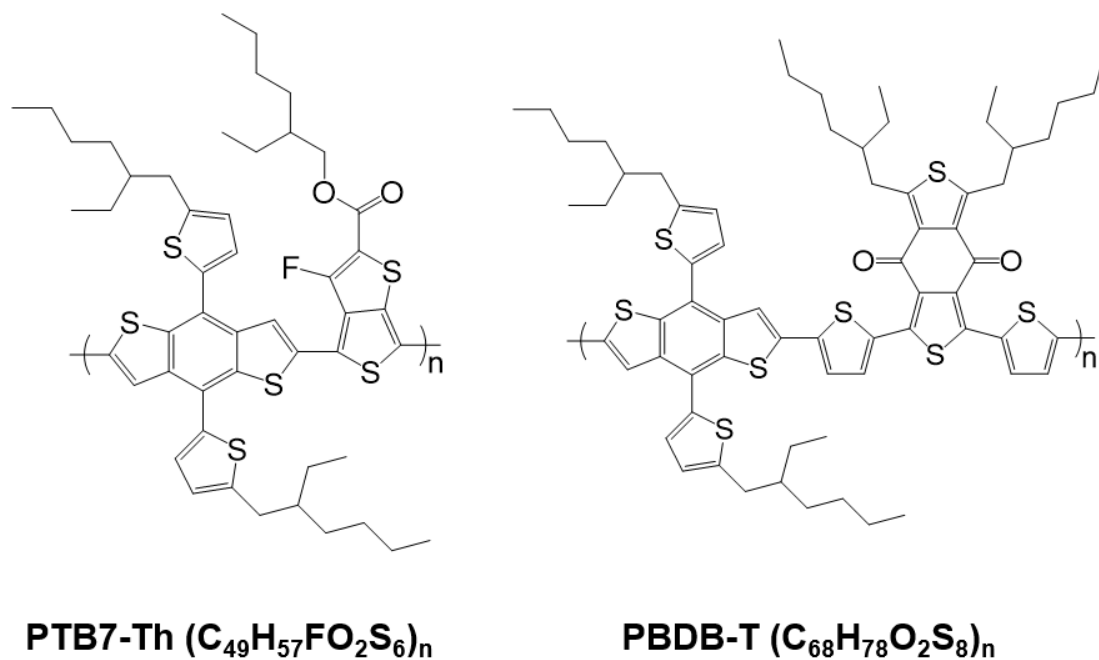


Figure 3.2: Chemical structures of conjugated donor polymers PTB7-Th and PBDB-T.

Polymer	Batch	M_W	M_N	PDI
PBDB-T	M1002	70,532	33,138	2.1
	M1001A2	142,718	60,189	2.37
PTB7-Th	M0261A3	57,183	29,285	1.95

Table 3.2: Batch details for PBDB-T and PTB7-Th polymers purchased from Ossila. (M_W = molecular weight, M_N = molecular number and PDI = polydispersity index).

3.2.2 Small Molecule Electron Acceptors

The chemical structures of all small molecules used as electron acceptors in BHJ blends are shown in Figure 3.3. These include PC₇₁BM, ITIC, 5,5'-[[4,9,9-tetrakis(2-ethylhexyl)-4,9-dihydro-s-indaceno[1,2-b:5,6-b']dithiophene-2,7-diyl]bis(2,1,3-benzothiadiazole-7,4-diylmethylidyne)]bis[3-ethyl-2-thioxo-4-thiazolidinone] (EH-IDTBR), 5,5'-[[4,4,9,9-Tetraoctyl-4,9-dihydro-s-indaceno[1,2-b:5,6-b']dithiophene-2,7-diyl]bis(2,1,3-benzothiadiazole-7,4-diylmethylidyne)]bis[3-ethyl-2-thioxo-4-thiazolidinone] (O-IDTBR), and 2,2'-(((4,4,9,9-tetraoctyl-4,9-dihydro-s-indaceno[1,2-b:5,6-b']dithiophene-2,7-diyl)bis(benzo[c][1,2,5]thiadiazole-7,4-diyl))bis(methaneylylidene))dimalononitrile (O-IDTBCN). ITIC, EH-IDTBR, O-IDTBR and O-IDTBCN are part of the acceptor-donor-acceptor (A-D-A) class of NFAs. In the case of ITIC, an indacenodithieno[3,2-b]thiophene (IT) central donor unit with phenylhexyl side-chains is flanked by 2-(3-oxo-2,3-dihydroinden-1-ylidene) malononitrile (IC) acceptor end groups. EH-IDTBR and O-IDTBR acceptors consist of an indacenodithiophene (IDT) core with either branched 2-ethylhexyl (EH-IDTBR) or linear n-octyl (O-IDTBR) side-chains flanked on either side by electron-deficient benzothiadiazole (BT) and 2-ethylrhodanine moieties. O-IDTBCN has an identical IDT core and n-octyl side-chains as O-IDTBR but the rhodanine terminal groups are substituted with a dicyanovinyl (DCV) electron withdrawing unit. ITIC (>99.0%) and PC₇₁BM (95%) were purchased from Ossila. EH-IDTBR, O-IDTBR and O-IDTBCN were purchased from 1-Material.

3.2.3 Deuterated Non-Fullerene Acceptors

For neutron scattering experiments, NFAs with deuterium-labelled end-groups or side-groups were synthesised by collaborators to increase the neutron scattering length density contrast between the acceptor and conjugated donor polymer (discussed later). The chemical structures of all deuterated NFAs are shown in Figure 3.4. These include end-group deuterated ITIC (d8-ITIC) and side-chain deuterated ITIC (d52-ITIC), O-IDTBR (d-O-IDTBR), EH-IDTBR (d-EH-IDTBR) and O-IDTBCN (d-O-IDTBCN).

3.2.4 Solvents and Solvent Additives

All solvents and solvent additives used in this thesis were purchased from Sigma Aldrich (99.8%, anhydrous). The chemical structures of casting solvents used to make solutions for OPV thin films are shown in Figure 3.5. These include chlorobenzene (CB), chloroform (CF), o-xylene, carbon disulphide (CS₂) and acetone. Additionally, the chemical structure of 1,8-diiodooctane (DIO), a high boiling point solvent additive is displayed as it was used for the preparation of samples throughout Chapter 5. The properties of all solvents and additives used in this thesis are summarised in Table 3.3.

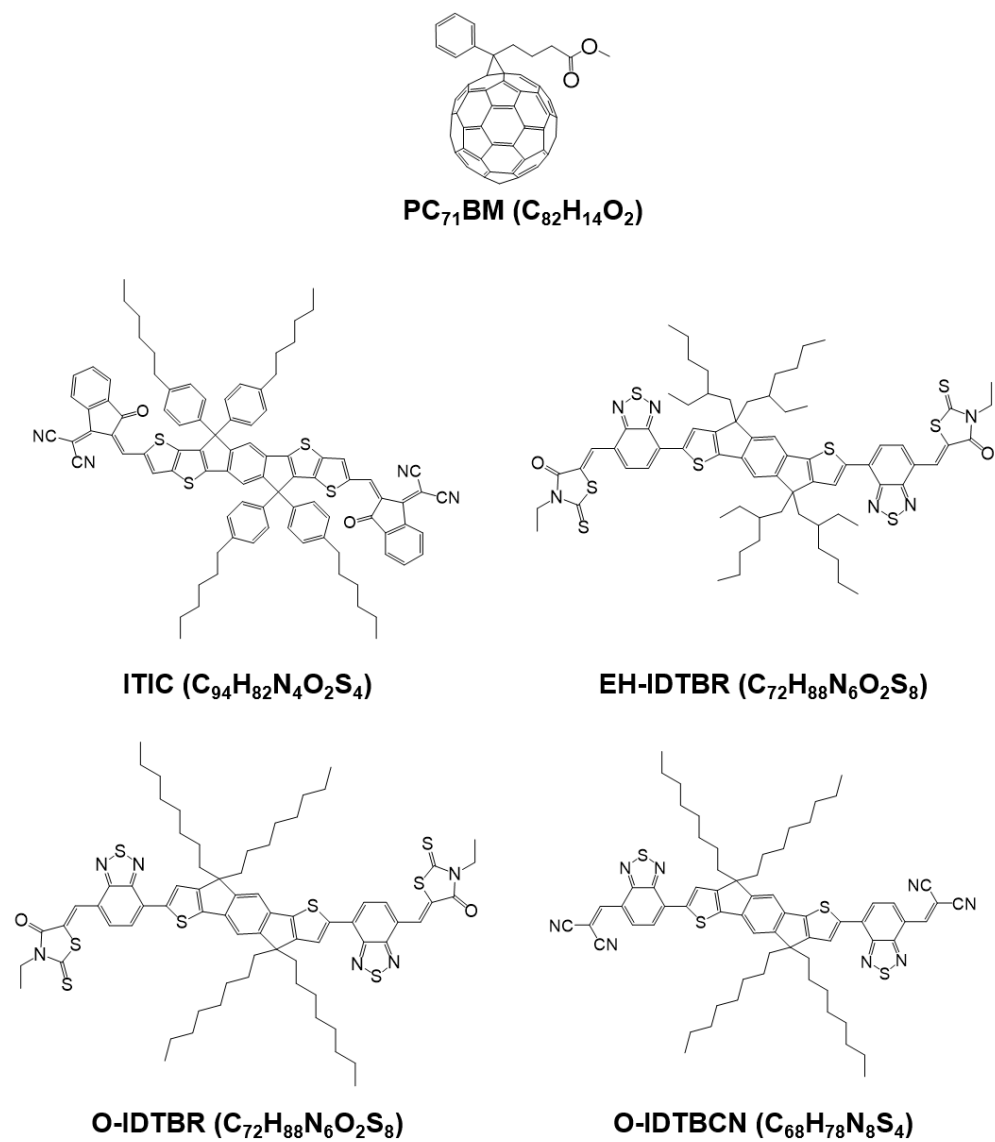


Figure 3.3: Chemical structures of fullerene acceptor PC₇₁BM and non-fullerene acceptors ITIC, EH-IDTBR, O-IDTBR and O-IDTBCN.

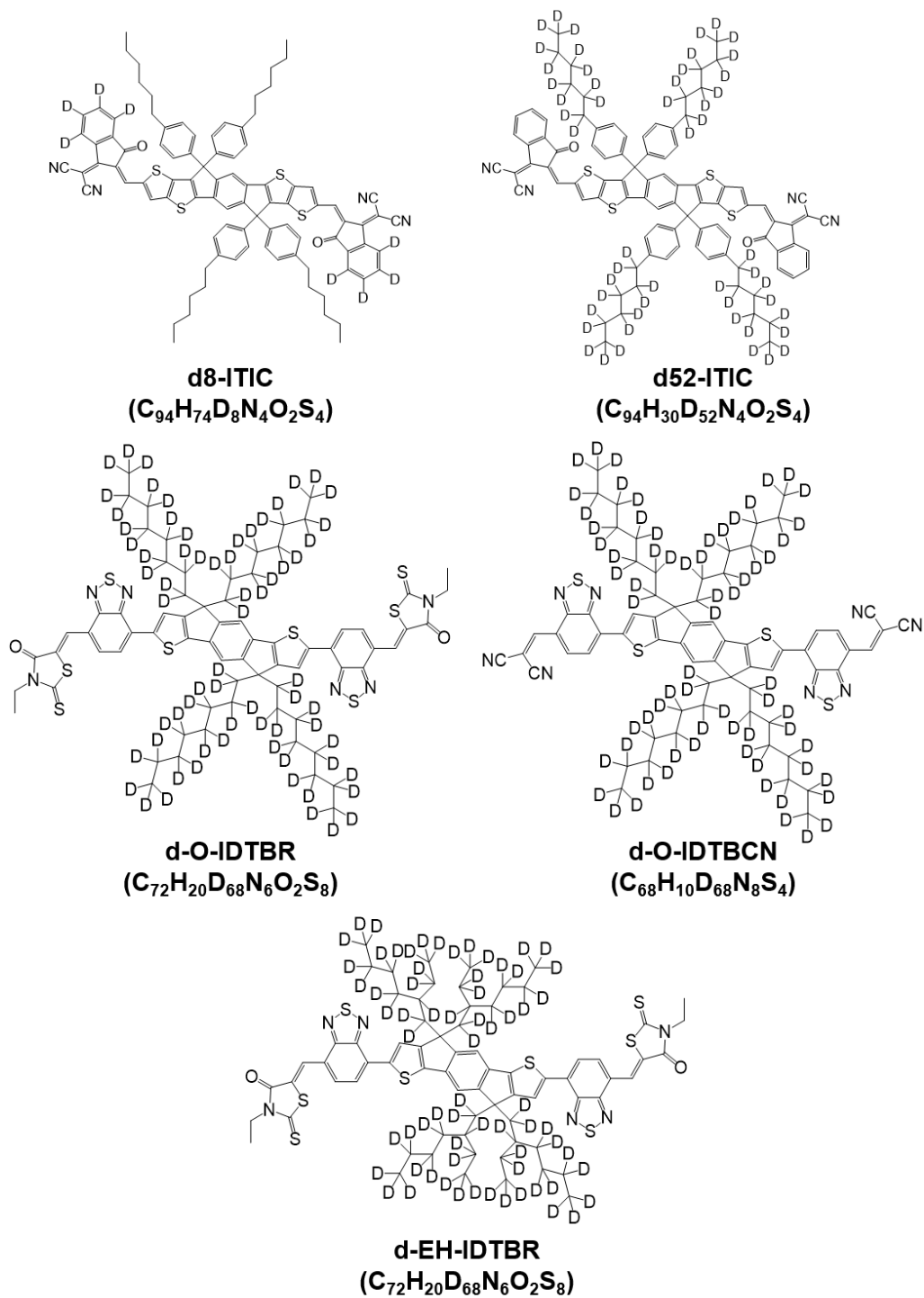


Figure 3.4: Chemical structures of deuterated NFAs d8-ITIC, d52-ITIC, d-O-IDTBR, d-O-IDTBCN and d-EH-IDTBR.

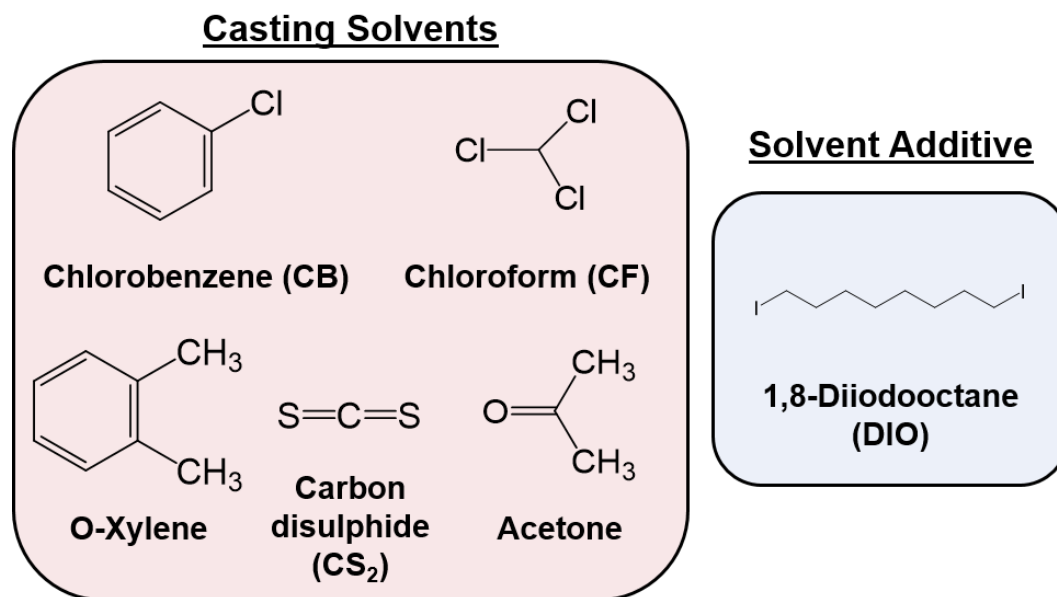


Figure 3.5: Chemical structures of casting solvents (chlorobenzene, chloroform, o-xylene, carbon disulphide and acetone) and solvent additives (1,8-diiodooctane and diphenyl ether).

Solvent	Formula	B_p (°C)	ρ (g/cm ³)	κ^a	v_p (mmHg) ^a	Polar/ Non-Polar
Chlorobenzene	C ₆ H ₅ Cl	132	1.11	6	12	Non-Polar
Chloroform	CHCl ₃	61	1.48	5	158	Non-Polar
O-Xylene	C ₈ H ₁₀	144	0.90	2.57	6	Non-Polar
Carbon disulfide	CS ₂	46	1.26	3	400	Non-Polar
Acetone	C ₃ H ₆ O	56	0.79	21	240	Polar
Methanol	CH ₄ O	65	0.79	33	128	Polar
Isopropyl alcohol	C ₃ H ₈ O	83	0.79	19	44	Polar
Dichloromethane	CH ₂ Cl ₂	40	1.33	9	475	Polar
1,8-diiodooctane	C ₈ H ₁₆ I ₂	168	1.84	—	0.003	Non-Polar
2-methoxyethanol	C ₃ H ₈ O ₂	124	0.97	16.93	6	Polar
Ethanolamine	C ₂ H ₇ NO	171	1.01	38	0.5	Polar

Table 3.3: Table of solvent properties for all solvents used in this thesis. B_p = boiling point, ρ = mass density, κ = dielectric constant and v_p = vapour pressure, — = unknown or not documented. Data was accumulated from various sources [140, 141, 142, 143].^aMeasured at $T = 20^\circ\text{C}$.

3.2.5 Charge Transport Layers

The choice of charge transport layers (CTLs) in OPV devices generally depends on the device architecture in use. Materials with high electron affinity such as zinc oxide (ZnO) and poly(9,9-bis(3'-(N,N-dimethyl)-N-ethylammonium-propyl-2,7-fluorene)-alt-2,7-(9,9-dioctyl fluorene))dibromide (PFN-Br) are used as electron transport layers (ETLs) and materials with low electron affinity such as poly(3,4-ethylenedioxythiophene):polystyrene sulfonate (PEDOT:PSS) and molybdenum oxide (MoO_3) are used as hole transport layers (HTLs). The chemical structures of PFN-Br and PEDOT:PSS are displayed in Figure 3.6. In addition to good charge transport abilities, there are several other properties that should be considered when selecting a CTL such as scalability, toxicity, chemical stability and transparency [144, 145]. For scalability, solution-processable CTLs such as ZnO and PEDOT:PSS are desirable for high throughput printing processes, however the materials must be soluble in an appropriate orthogonal solvent which does not dissolve other materials in the device (e.g. the photoactive layer). Additionally, materials which are toxic or harmful to human health such as carcinogenic NiOx and VOx should be avoided for better compatibility with large-scale manufacturing. In terms of stability, CTLs should be resistant to photodegradation and avoid unwanted chemical reactions with active layer materials. In this thesis, sol-gel-derived ZnO CTLs were prepared via a hydrolysis reaction using a precursor solution of 219.5mg zinc acetate dihydrate (Sigma Aldrich) in 2mL 2-ME with 60.4 μL ethanolamine acting as a stabilizer [146]. Precursor solutions were left stirring vigorously for 12h and filtered through a 0.45 μm PTFE microdisc filter before use. PFN-Br (Ossila batch M2230A1 or Lumtec) solutions were prepared in methanol at a concentration of 0.5mg/mL and left stirring overnight at room temperature. PEDOT:PSS in de-ionised (DI) water solution was purchased from Ossila (Al 4083). Before thin-film deposition, PEDOT:PSS solution was filtered through a 0.45 μm PVDF microdisc filter. MoO_3 was purchased from Sigma Aldrich and used as received.

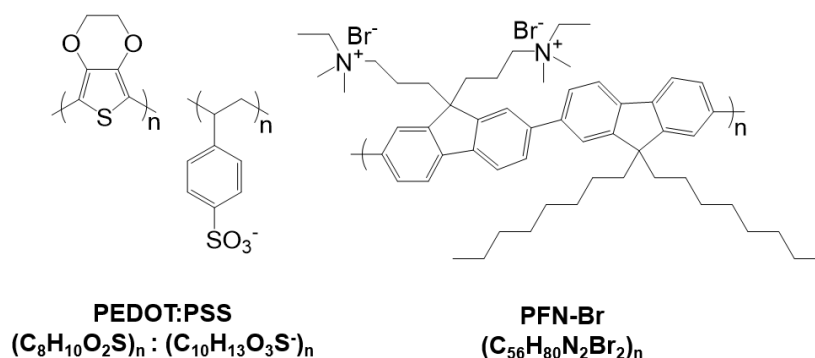


Figure 3.6: Chemical structures of hole charge transport layers PEDOT:PSS and electron charge transport layer PFN-Br.

3.3 OPV Solution Preparation and Thin Film Deposition

The majority of experiments in this thesis were performed on pure or blend thin films. Here a general overview of the solution preparation and thin film fabrication protocols are provided. These steps were used for all samples of interest in Chapter 4, Chapter 5 and Chapter 6 to ensure consistency and reproducibility.

3.3.1 Making OPV Solutions

The first step to prepare organic thin film samples or devices is to make the solution. In this thesis, all dry materials were weighed out in a fumehood in amber glass vials and solvents were added inside a nitrogen-filled glovebox. For blend solutions, the donor polymer was weighed out first followed by the acceptor material in the required weight ratio. After solvents were decanted, vials were wrapped in parafilm to prevent solvent evaporation and magnetic stirrer bars were added before leaving to stir overnight in the glovebox to dissolve. Solutions made from high boiling solvents (e.g. chlorobenzene and o-xylene) were left stirring at 60°C and those made from lower boiling point solvents (e.g. chloroform, carbon disulphide and acetone) were left stirring at room temperature.

3.3.2 Substrate Cleaning Procedure

All transparent substrates in this thesis were cleaned in the same way before thin film deposition using the following procedure:

1. **Sonication Step 1:** Substrates are first placed in a glass beaker and immersed in a mix of boiling DI water and Hellmanex (Z805939, 5 vol%) solution at a volume ratio of approximately 3:1 (DI water:Hellmanex) and then sonicated for 10 minutes in an ultrasonic water bath.
2. **Sonication Step 2:** Substrates are then rinsed with DI water and transferred to a separate glass beaker containing boiling DI water and again sonicated for 10 minutes to remove any residual Hellmanex.
3. **Sonication Step 3:** Substrates are transferred to a third glass beaker containing isopropyl alcohol (IPA) and sonicated for a final 10 minutes.
4. **UV-ozone Treatment:** Substrates are dried using a nitrogen gun and placed in an ultra-violet ozone (UVO) cleaner for 15 minutes.

Silicon substrates used were RCA cleaned following the reported procedure [147].

3.3.3 Spin-Coating

All thin films in this thesis were deposited via spin-coating. The desired material is dissolved in an appropriate solvents and a small amount is cast onto a spinning substrate. The combination of centrifugal forces and surface tension spread the solution across the substrate whilst the solvent evaporates to leave behind a uniform layer, a few nm to a few μm thick. Figure 3.7 displays this process which is typically divided into four main steps [148]:

1. **Deposition:** A substrate is secured onto a chuck either by vacuum or indentation and a small amount of solution, (typically $10\text{-}200\mu L$) is deposited via a pipette onto the substrate either before rotation (static deposition) or during rotation (dynamic deposition).
2. **Spin-Up:** The chuck is accelerated rapidly to reach the desired spin speed (typically $1000\text{-}6000$ rotations per minute (rpm)). The centrifugal motion of the rotating chuck spreads the solution across the substrate.
3. **Spin-Off:** The majority of the solution is spun off the substrate to the edges of the spin coater and the remaining solute concentrates into a thin film.
4. **Evaporation:** The thin film continues to thin as more solution is expelled and evaporated. The rate of solvent evaporation is dependent on a number of factors such as solvent volatility, vapour pressure and the spin-coating environment (in ambient or in a glovebox).

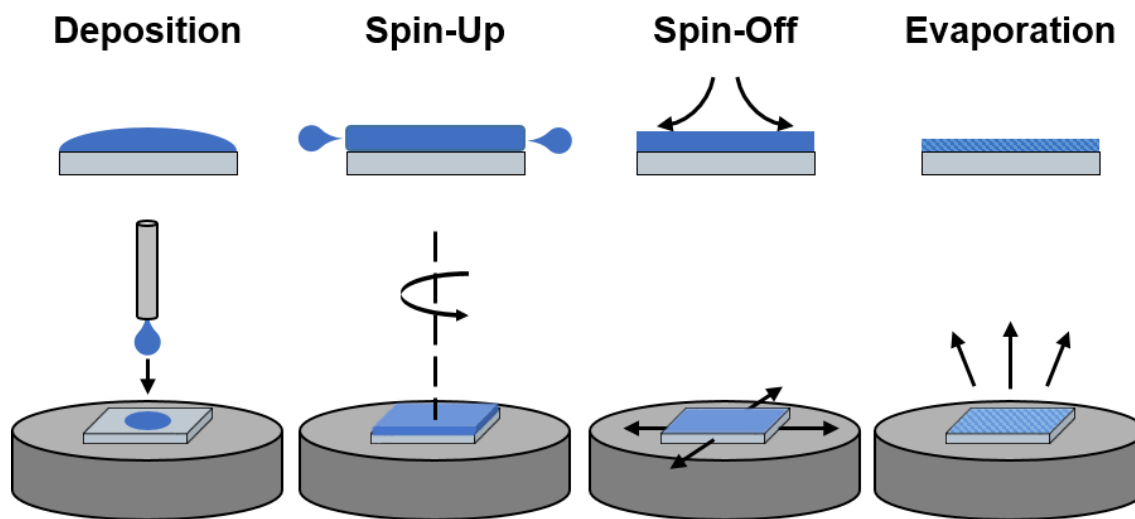


Figure 3.7: An illustration of the key steps in the spin-coating process.

Spin-coating is a low cost, relatively easy technique which outputs uniform, reproducible thin films with a high degree of thickness control. As such, its use is widespread both in research environments and across a diverse range of industrial sectors. For organic electronics, spin-coating is used extensively as it is capable of achieving the uniform thin films essential for high performing devices as well as the fast film drying times typically required for optimum nanostructure self-assembly [149, 150]. Despite such attributes, spin-coating is an inherently single-substrate process and it is therefore not capable of the high throughput achieved in roll-to-roll processes [27]. It is also only applicable to small substrates approximately a few centimetres wide and the majority of solution (95-98%) is wasted as it is expelled from the substrate [148]. This is not an issue for research environments but limits its applicability for large-scale manufacturing.

There are a number of theories that have been developed to describe the spin-coating process [148, 151, 152]. In general, the relationship between the spin-coated film thickness (L) and the rotational speed of the spin coater (ω) is approximated by the following relation:

$$L \propto \frac{1}{\sqrt{\omega}} \quad (3.1)$$

The exact film thickness is not only dependent on spin speed but also on a number of other parameters such as solid concentration, solvent boiling point, vapour pressure, solvent viscosity etc. Typically, the spin speed curve for a particular solution is calculated by measuring the thickness of one or more spin-coated films using techniques such as spectroscopic ellipsometry or Dektak profilometry. This allows a proportionality constant to be calculated from Equation 3.1 and a spin speed for a particular desired thickness can be determined.

3.3.4 Post-Deposition Treatments

After thin film deposition, it is common for the film to be treated by steps such as thermal annealing or solvent annealing to remove additional solvent and to optimise the nanomorphology of the blend film [153, 101, 154]. In this thesis, thermal annealing is used frequently to remove residual high boiling point solvents such as DIO and to control the crystallisation and phase separation of the component materials. All thermal annealing of organic layers in this thesis was performed in a nitrogen-filled glovebox at temperatures between 40-200°C for 10 minutes. Typically, thermal annealing was performed directly after film fabrication and samples were left to cool before further manipulation or characterisation.

3.4 Organic Photovoltaic Devices

The device performance metrics of a solar cell were described earlier in Subsection 2.3.3. Here the typical protocols for fabricating OPV devices are described along with the experimental setups used to characterise device performance and stability.

3.4.1 Device Architecture

The highest efficiency OPV devices are comprised of a series of sequentially deposited planar layers where the light-harvesting active layer is sandwiched between charge transport layers and electrodes. Typically, PV devices are described as having an *inverted* or *conventional* architecture (Figure 3.8). Here the difference is simply the direction of charge in the device, which in turn determines the choice of CTL and electrode materials.

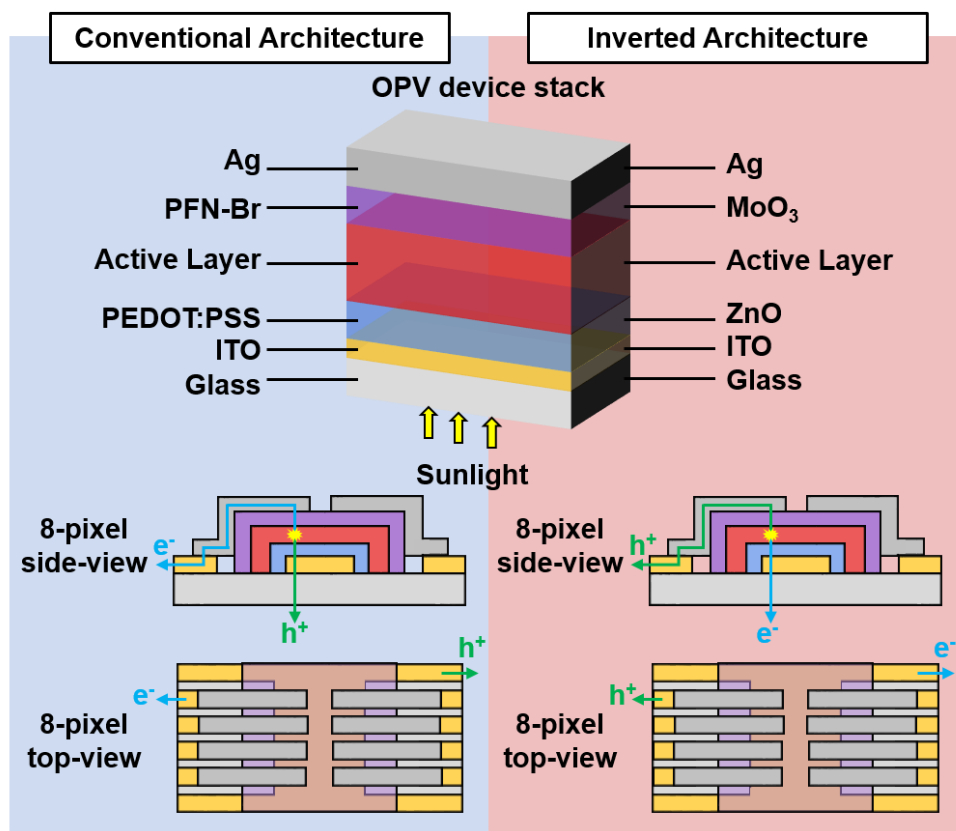


Figure 3.8: An illustration of the inverted and conventional device stacks used to fabricate the single junction organic solar cells described in this thesis. Below, the direction of holes and electrons during device operation in an 8-pixel device for each architecture are illustrated for side-view and top-view orientations.

For inverted architecture devices, electrons are collected at the bottom electrode (anode) and holes are collected at the top electrode (cathode). For conventional architecture devices, the opposite is true (holes collected at the bottom electrode, electrons collected at the top electrode). A combination of inverted and conventional device architectures were used throughout this thesis using 8-pixel indium tin oxide (ITO) substrates. In Chapter 4 and Chapter 5, devices were fabricated in a conventional architecture in a stack of glass/ITO/PEDOT:PSS/Active Layer/PFN-Br/Ag. In Chapter 6, devices were fabricated in an inverted architecture in a stack of glass/ITO/ZnO/Active Layer/MoO₃/Ag. In the 8-pixel configuration, devices are illuminated through bottom glass substrate and charges are directed to the contacts at the edge of the device as illustrated in Figure 3.8. Further information about device architectures and design can be found in more detailed reviews reported elsewhere [155, 156, 144].

3.4.2 Device Fabrication

The steps followed for OPV device fabrication are illustrated below in Figure 3.9.

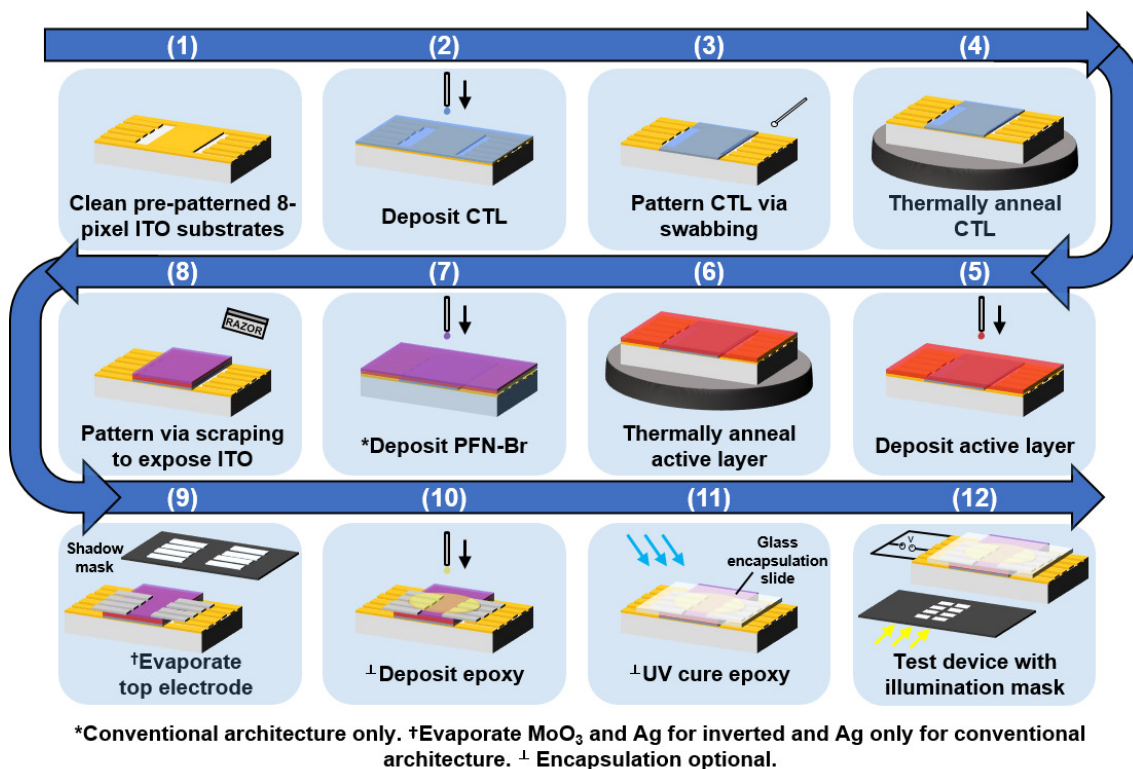


Figure 3.9: An illustration of the typical device fabrication protocol steps used to make OPV devices.

These are:

1. **Substrate Cleaning:** 8-pixel pre-patterned ITO substrates (Ossila - S211) were cleaned following the procedure outlined above in section 1.3.2.
2. **CTL deposition:** For conventional architecture devices, PVDF-filtered PEDOT:PSS solution was dynamically spin-coated at 6000rpm for 30s to form films approximately 30-40nm thick. For inverted devices, a ZnO precursor solution was statically spin-coated at 3000rpm for 30s.
3. **CTL patterning:** To expose the ITO pixels at the edge of the substrate, the CTL was patterned via swabbing with a cotton bud. PEDOT:PSS layers were swabbed with DI water and ZnO precursor layers were swabbed with methanol.
4. **CTL thermal annealing:** PEDOT:PSS layers were thermally annealed at 110°C for 15 minutes in air and then transferred to a nitrogen-filled glovebox and annealed for a further 15 minutes at 110°C to remove any excess water. ZnO precursor layers were thermally annealed at 150°C for 25 minutes in air forming ZnO via the sol-gel process described previously (section).
5. **Active layer deposition:** Active layer solutions consisting of a blend of donor conjugated polymer and small molecule electron acceptor materials were dynamically spin-coated to produce films approximately 80-100nm thick.
6. **Active layer thermal annealing:** If required, active layer films were thermally annealed in a nitrogen-filled glovebox at temperatures between 80-200°C for 10 minutes.
7. **PFN-Br deposition:** For conventional architecture devices, the electron transport layer PFN-Br was dynamically spin-coated at a spin speed of 3000rpm for 30s.
8. **Active layer patterning:** The active layer (and PFN-Br layer for conventional architecture devices) are patterned via gentle scraping with a razor blade to expose ITO pixels at the edge of the substrate.
9. **Top electrode evaporation:** For inverted devices, MoO₃ (10nm) and Ag (100nm) layers were thermally evaporated at a pressure of 2×10^{-6} mbar through a shadow mask with a pixel area of $4mm^2$. For conventional architecture devices, an Ag layer deposited via the same method.
10. **Epoxy deposition:** If required, devices are encapsulated using a UV curable epoxy (Ossila) which is dropped onto the centre of the substrate and covered with a glass encapsulation slide.

11. **Epoxy UV curing:** To cure the epoxy, devices are placed under a UV-lamp for 15 minutes.
12. **Test device:** Devices are illuminated through an aperture mask and J-V measurements are performed using a Newport 92251A-1000 solar simulator (see Subsection 3.4.3 for more details).

3.4.3 J-V Characterisation

The final step of the device fabrication protocol outline previously (Step 12 in Figure 3.9) is to test the device. Figure 3.10 shows the Newport 92251A-1000 solar simulator used to perform J-V sweeps of OPV devices. Before measurement, light intensity was calibrated to 100 mWcm^{-2} (1 SUN) using a NREL certified silicon reference cell. Devices were then illuminated through an aperture mask with a pixel area of 0.0256 cm^2 and the applied bias was typically swept from 0.0V to +1.2V (forward scan) and from +1.2V to 0V (reverse scan) at a scan speed of 0.4 Vs^{-1} using a Keithley 237 source measure unit. The J-V sweeps presented in this thesis were outputted by averaging forward and reverse scans for each pixel.

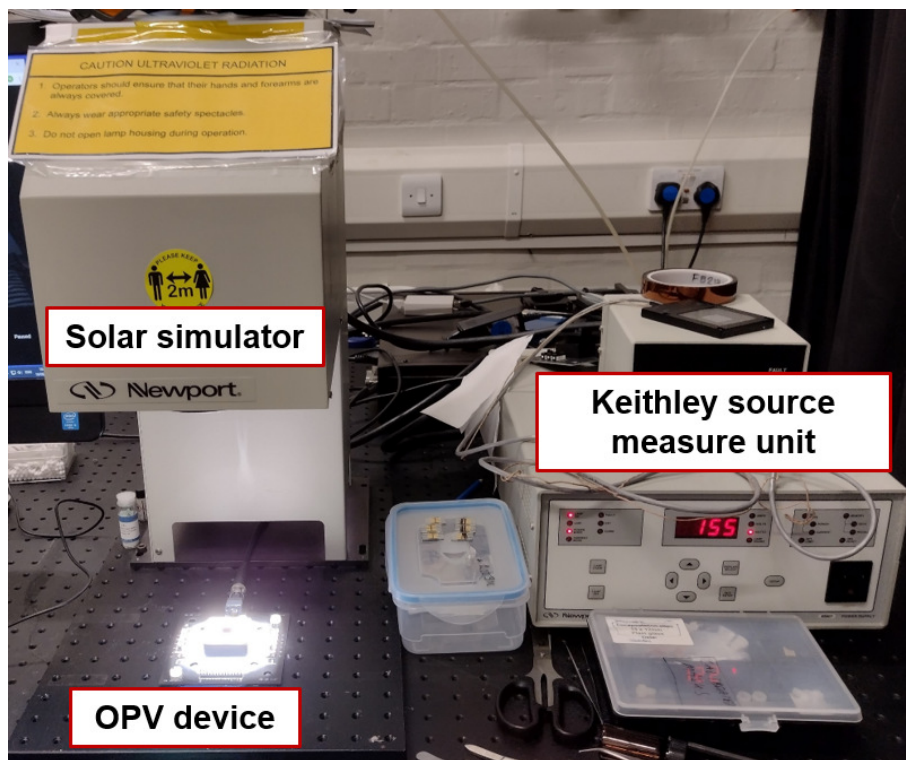


Figure 3.10: The experimental setup for J-V characterisation of OPV devices.

3.4.4 External Quantum Efficiency

The external quantum efficiency (EQE) of a solar cell was described previously in Chapter 2. In addition to J-V measurements described above, measuring the EQE of an OPV device provides a further method for comparing device performance. A white light source (L.O.T.-Oriel GmbH & Co, 10-150W halogen source) is directed towards a monochromator grating (Spectral Products, DK 240), producing a monochromatic light beam which is incident on the device. The generated photocurrent is measured using an Xtralien X100 source measure unit (Ossila). Prior to measurement, the monochromator is calibrated using a silicon photodiode (Newport 818-uv) which generates a known spectral response. Each EQE spectrum was measured across two wavelength ranges (390-700nm and 700-900nm) which were then collated into a single spectrum.

3.4.5 Stability Testing

In addition to device efficiency, device stability is also an important metric to consider for PV commercialisation. In this thesis, the stability of OPV devices was tested under the following conditions:

- **Dark/ ambient conditions:** Devices were wrapped in aluminium foil and stored in a laboratory drawer. Temperature and relative humidity in the laboratory were maintained at 17-22°C and 55-60% respectively.
- **Dark/ inert conditions:** Devices were wrapped in aluminium foil and stored in a nitrogen-filled glovebox at 21-23°C. Devices were periodically tested in ambient conditions and returned to the glovebox immediately after measurement.
- **Light/ ambient conditions:** Devices were irradiated in ambient conditions in an Atlas Suntest CPS+ tester (Figure 3.11) which outputs a spectrum close to AM1.5 at 1 SUN intensity ($100mWcm^{-2}$) as shown in Bovill et al. [157]. The system is equipped with a 1500W Xenon lamp with a Temperature and relative humidity maintained at 41-44°C and 23-27% respectively. Devices were mounted on an Ossila test board and pixels were tested sequentially under open-circuit conditions approximately every 20 minutes. Device metrics as a function of time were produced by tracking the three pixels on each device with the highest initial *PCE* and averaging.
- **Light/ inert conditions:** Devices were irradiated at 21-23°C in a nitrogen-filled glovebox by a class ABA LED-based solar simulator (Newport LSH-7320) (Figure 3.11). Although class ABA, this solar simulator has a lower UV component than the Atlas light source used to age samples under ambient conditions. Devices were tested periodically and the four pixels with the highest initial *PCE* for each device were tracked and averaged to output device metrics as a function of time.

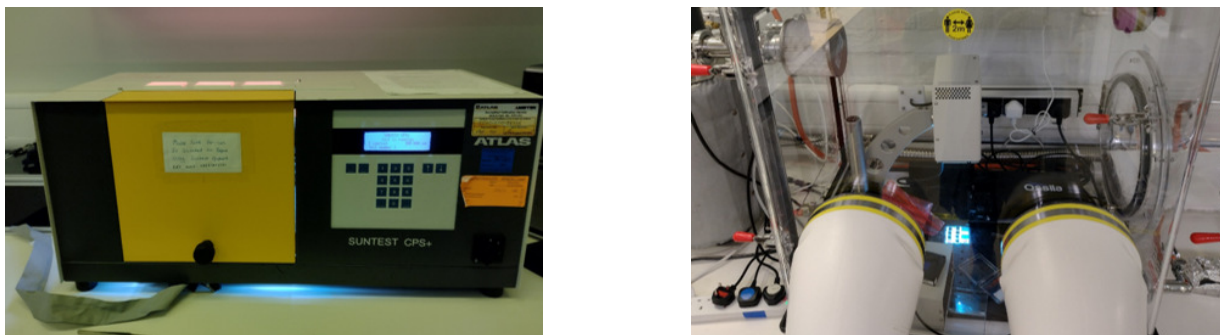


Figure 3.11: Atlas Suntest CPS+ tester (left) an LED-based solar simulator tester inside a glovebox for testing OPV devices (right).

3.5 Film Wetting Behaviour and Surface Energy Characterisation

The term *wetting* describes the contact between a liquid and solid surface (e.g. a droplet on a thin film surface) which results from intermolecular interactions. Measuring the contact angle (θ_{CA}), defined here as the angle at which the liquid droplet interface meets the solid film interface, can provide information about the wetting and physical properties of a material. In Figure 3.12, the change in contact angle of a water droplet on a surface is shown for different degrees of wettability. In the case of no wetting (e.g. water on a super hydrophobic surface), $\theta_{CA} = 180^\circ$. For total wetting (e.g. water on a super hydrophilic surface), $\theta_{CA} = 0^\circ$. Typically for most surfaces, a droplet partially wets and $0^\circ < \theta_{CA} < 180^\circ$.

3.5.1 Contact Angle Goniometry

Contact angle goniometry measurements are a quantitative way of measuring the ability of a liquid to coat a surface (i.e. its wettability) and are often used to estimate the surface energy of a material [117, 116]. In this thesis, all contact angle measurements were performed using a goniometer (Ossila) (Figure 3.13). The experimental setup consists of a monochromatic light source, a high-resolution camera and an adjustable sample stage. A liquid droplet is deposited onto a level thin film surface and an image or video is recorded. Contact angle values are extracted using the Ossila Contact Angle program that defines a baseline and traces the shape of the droplet via edge detection. The curve of the droplet is then modelled by a polynomial function and the gradient at the contact angle intercept is calculated using simple geometry where $\theta_{CA} = \tan^{-1}(\text{gradient})$.

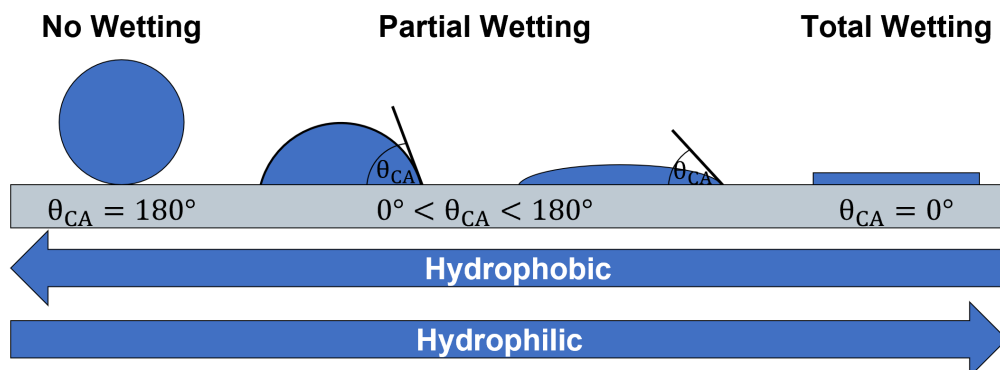


Figure 3.12: An illustration of the contact angle of a water droplet on a surface for different degrees of surface wettability; no wetting, partial wetting and total wetting.

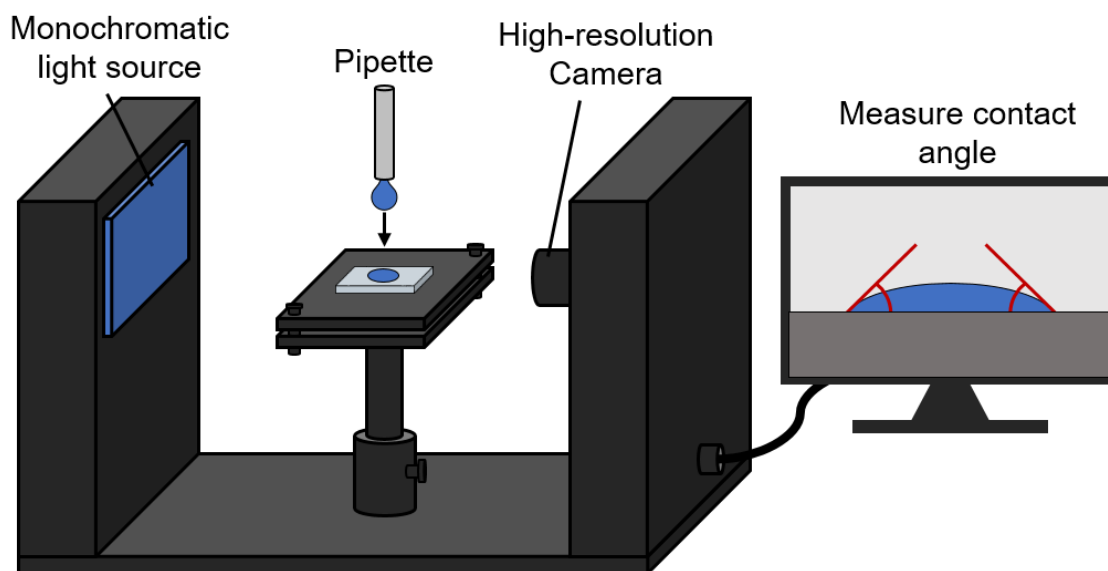


Figure 3.13: The experimental setup for contact angle goniometry measurements to measure the contact angle of a liquid droplet on a flat interface.

3.5.2 Surface Energy Estimations

In this thesis, surface energies of various materials were estimated using contact goniometry measurements. Surface energy is a measure of the incomplete bonding at the surface of a substrate. A large contact angle due to poor wetting is the result of a substrate with low surface energy. On the other hand, a small contact angle due to good surface wetting is the result of a material with high surface energy.

A number of models have been derived to describe surface energy including the Oss-Good model for polar surfaces [158], the Fowkes [159] and Owens-Wendt-Rabel and Kaelble [160, 161] models for moderately polar surfaces and the Zisman model for non-polar surfaces [162]. Each of these models is derived by balancing the forces at play when a liquid droplet meets a thin film surface as shown in Figure 3.14.

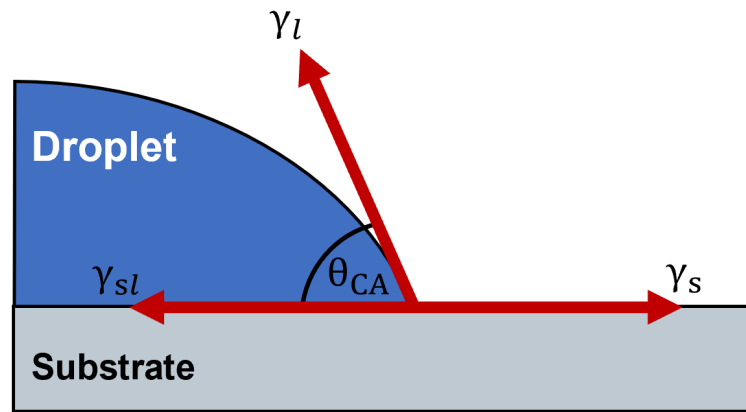


Figure 3.14: Illustration of the forces present at the interface between a liquid droplet on a solid substrate.

Forces arise from the surface tension due to the solid Interface γ_s , the solid-liquid interface γ_{sl} and the liquid interface γ_l . Equating these forces gives Young's equation [163]:

$$\gamma_s = \gamma_{sl} + \gamma_l \cos \theta_{CA} \quad (3.2)$$

Dupré's equation defines the work of adhesion W_{sl} (i.e. the work required to separate the droplet from the surface):

$$\gamma_{sl} = \gamma_l + \gamma_s - W_{sl} \quad (3.3)$$

Combining Equation 3.2 and Equation 3.3 gives the Young-Dupré equation:

$$W_{sl} = \gamma_l (1 + \cos \theta_{CA}) \quad (3.4)$$

The Young-Dupré equation is typically the starting point for each of the surface energy models mentioned above. In this thesis, all surface energy estimates were performed using the Fowkes model [159]. The Fowkes model is applicable for polar surfaces and assumes the surface tension of the solid is equal to the sum of dispersive (Van der Waals) (γ_{ds}) and polar (γ_{ps}) interactions between the solid film and liquid droplet:

$$\gamma_s = \gamma_{ds} + \gamma_{ps} \quad (3.5)$$

In the Fowkes model, the work of adhesion is given by:

$$W_{sl} = 2 \left(\sqrt{\gamma_{dl} \cdot \gamma_{ds}} + \sqrt{\gamma_{pl} \cdot \gamma_{ps}} \right) \quad (3.6)$$

where γ_{dl} and γ_{pl} are the dispersive and polar components of the liquid surface energy respectively. Equating Equation 3.6 to Equation 3.4 gives the primary Fowkes equation:

$$\sqrt{\gamma_{dl} \cdot \gamma_{ds}} + \sqrt{\gamma_{pl} \cdot \gamma_{ps}} = \frac{\gamma_l(1 + \cos\theta_{CA})}{2} \quad (3.7)$$

To estimate the surface energy of a solid thin film, the contact angle of a purely dispersive liquid (e.g. hexadecane) is measured so that $\gamma_{pl} = \gamma_{ps} = 0$ and $\gamma_{dl} = \gamma_l$. From this, Equation 3.7 reduces to:

$$\gamma_{ds} = \frac{\gamma_{dl}(1 + \cos\theta_{CA})^2}{4} \quad (3.8)$$

which allows the dispersive component of the surface energy γ_{ds} to be calculated, provided the surface tension of the liquid (γ_{dl}) is known. Once γ_{ds} is known, the procedure can be repeated to calculate γ_{ps} by measuring the contact angle of another material with known dispersive and polar components (e.g. water). Finally, the total surface energy of the solid can be calculated using Equation 3.5. In Table 3.4, the dispersive and polar surface tension components of water and hexadecane are provided. These values were used for all surface energy estimates in this thesis.

	Water	Hexadecane
Surface Tension (mN/m)	72.8	27.5
Dispersive Component (mN/m)	21.8	27.5
Polar Component (mN/m)	51	0

Table 3.4: Table of dispersive and polar surface tension components for water and hexadecane [164].

3.6 Surface Profilometry and Microscopy

3.6.1 Dektak Profilometry

In this thesis, the thickness of films deposited on transparent substrates were measured using Dektak profilometry. A simplified illustration of Dektak profilometry on a thin film sample is displayed in Figure 3.15. A series of straight scratches is first made across the width of the film using a razor blade. A Veeco Dektak surface profiler then measures the vertical displacement of a stylus as it moves across the surface of the samples. Thickness values are extracted from the outputted line profile by measuring the width of the valley at the scratch position. For each sample, a minimum of 3 line profiles were typically measured across the film and averaged.

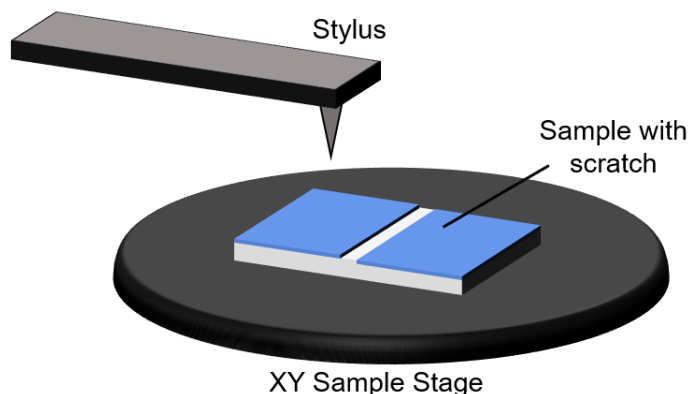


Figure 3.15: An illustration of a thin film Dektak profilometry measurement.

3.6.2 Atomic Force Microscopy

Atomic force microscopy (AFM) is a scanning probe, real-space imaging technique that maps the nanoscale surface topography of a sample. All AFM measurements in this thesis were performed on thin film samples in tapping mode. Tapping mode AFM is ideal for mapping organic BHJ films because it is non-destructive and higher resolution (1-5nm) compared to other AFM modes (e.g. contact mode).

A typical experimental setup of an AFM instrument operating in tapping mode is displayed in Figure 3.16. A small tip secured to an oscillating cantilever is scanned across the film surface. The cantilever oscillates just below its resonance frequency and gently *taps* the surface of the film. As the sample is scanned, a laser focused onto the back of the tip is deflected due to the surface topography of the sample. Changes in amplitude are

3.7 Spectroscopy

In the simplest terms, spectroscopy is the study of the interaction between matter and electromagnetic radiation as a function of wavelength or frequency. Various spectroscopic techniques are used throughout this thesis, allowing a diverse range of optical and material properties to be characterised. An overview of each technique is provided below but more comprehensive reviews can be found elsewhere [165, 166].

3.7.1 Ultraviolet-Visible Spectroscopy

Ultraviolet-visible (UV-Vis) spectroscopy was used in this thesis to study the absorption of light by thin film samples deposited onto quartz-coated glass substrates (Ossila). A white light beam from a deuterium/tungsten-halogen lamp (Ocean Optics - DH-2000-BAL) is directed through the thin film sample in transmission geometry and the transmitted light is collected by optical fibre cables (Ocean Optics) connected in series with a spectrometer (Ocean Optics - HR2000+ES) (Figure 3.17). The transmittance of the thin film is determined by comparing the transmission signal of the entire sample $I(L)$ with the transmission signal of an uncoated substrate $I(0)$. This allows the absorbance (A) or optical density to be determined using:

$$A = -\log\left(\frac{I(L)}{I_0}\right) \quad (3.9)$$

where L is the thickness of the film.

3.7.2 Steady-State Photoluminescence Spectroscopy

Steady-state photoluminescence (PL) spectroscopy was used in this thesis to study the emission of light from thin film samples deposited onto quartz-coated glass substrates (Ossila). Measurements were performed using a Horiba Fluoromax 4 fluorometer using an excitation wavelength of 400nm. A typical experimental setup for PL spectroscopy is shown in Figure 3.17. The sample is probed with an excitation source with a sufficient wavelength to probe the energy transitions of the sample. The resulting emission is collected and directed to a spectrometer.

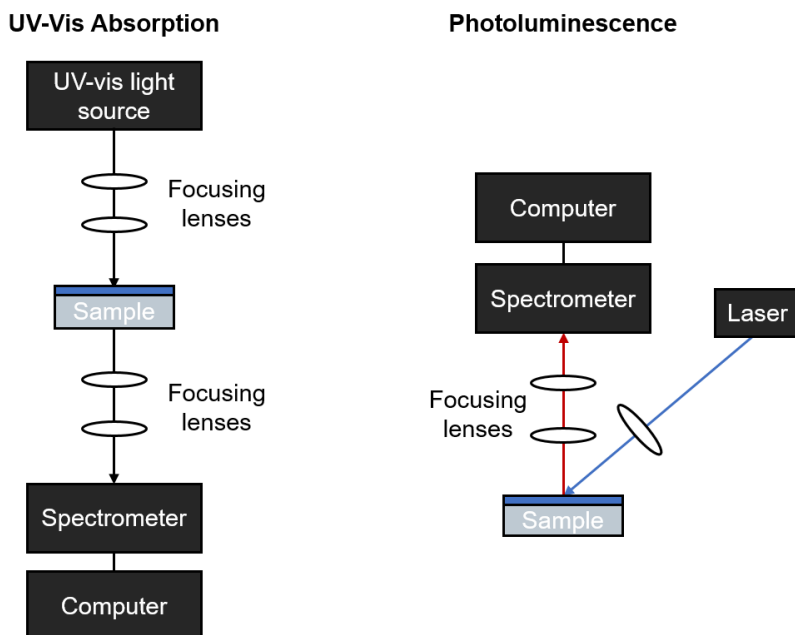


Figure 3.17: Optical setups for UV-Vis absorption and photoluminescence measurements

3.7.3 Exciton Diffusion Length Measurements

The exciton diffusion length (l_d) and its role in OPV device operation were discussed previously in Chapter 2. In this thesis, the exciton diffusion length of PBDB-T and ITIC pure films were measured by collaborators at The University of Minnesota (Russel J. Holmes, Kaicheng Shi, Janet A. Christenson and Ronald L. Christenson) following previously reported protocols [167, 168]. These measurements involve fabricating a series of *exciton-quenched* and *exciton-unquenched* samples composed of a number of stacked layers as shown in Figure 3.18.

The 2.5-nm-thick HfO_2 layer acts as an electron-blocking layer and was deposited via atomic layer deposition at 200°C. Pure PBDB-T and ITIC films were spin-coated from chlorobenzene solutions onto HfO_2 /quartz coated glass substrates using the processing parameters provided in Table 3.5. All films were annealed at 160°C for 10 minutes in a nitrogen-filled glovebox immediately after fabrication.

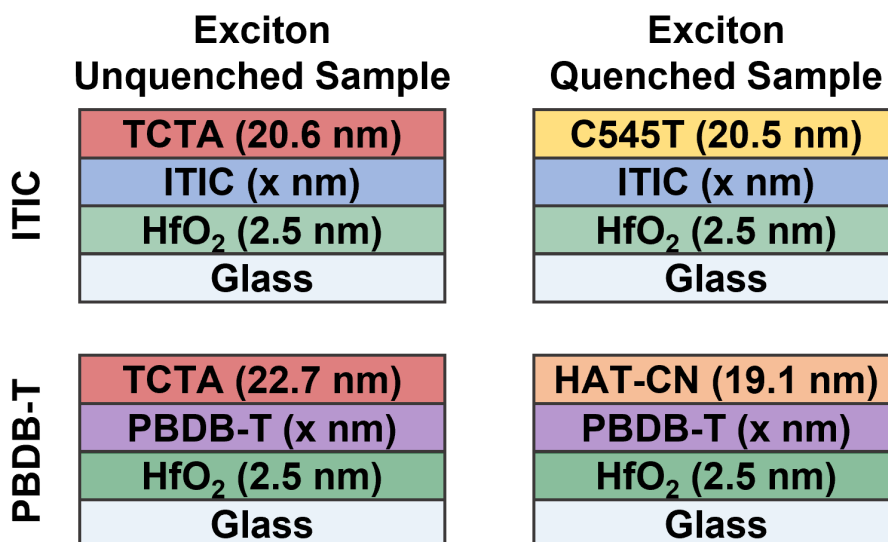


Figure 3.18: Exciton unquenched and quenched sample architectures for measuring the exciton diffusion length of ITIC and PBDB-T. Film thicknesses are shown in parenthesis.

Material	Solid Concentration (mg/mL)	Spin Speed (rpm)	Film Thickness (nm)
PBDB-T	8	3000	33.4
	10	2000	62.2
ITIC	10	1000	39.9
	15	1000	52.2

Table 3.5: Table of pure ITIC and PBDB-T film processing conditions for exciton diffusion measurements.

Capping layers were purchased from Luminescence Technology Corporation and deposited by high vacuum thermal evaporation at a pressure $< 7 \times 10^{-7}$ Torr. These include 4,4',4'-Tris(carbazol-9-yl)triphenylamine (TCTA, >99.5%), Dipyrazino[2,3-f :2',3'-h]quinoxaline-2,3,6,7,10,11-hexacarbonitrile (HAT-CN, >99%) and 2,3,6,7-Tetrahydro-1,1,7,7,-tetramethyl-1H,5H,11H-10-(2-benzothiazolyl)quinolizino[9,9a,1gh]coumarin (C545T, >99%).

The exciton diffusion length (l_d) was measured using spectrally-resolved PL quenching. (Note the term *quenching* is used here to describe exciton quenching and is different to the morphological quenching described previously). In this measurement, PL excitation spectra were collected in a nitrogen atmosphere using a Photon Technology International QuantaMaster 400 Fluorimeter equipped with a photomultiplier detection system. Spectra were collected at an emission wavelength of $\lambda = 720nm$ for PBDB-T and $\lambda = 820nm$ for ITIC. Samples were excited at an incident angle of 70° to the sample normal using a monochromatic Xenon lamp. Excitation spectra were collected for samples capped with non-quenching and quenching layers. The exciton unquenched spectrum permits an assessment of the exciton density under optical pumping, while the exciton quenching spectrum permits a measure of the number of excitons that are mobile enough to reach the top surface of the film. The ratio of these spectra (quenched/unquenched) is the PL ratio that is fit as a function of wavelength for (l_d) using a one-dimensional diffusion equation and a transfer matrix simulation of the optical field. Error bars for the extracted (l_d) represent a 95% confidence interval extracted from fitting. Non-quenching and quenching layers are selected based on the molecular orbital and exciton energies of each active material, while also minimising absorption overlap. While TCTA is used as a non-quenching layer for both PBDB-T and ITIC, HAT-CN is used as a quencher for PBDB-T while C545T is used as a quencher for ITIC. HAT-CN and C545T do not absorb strongly above $\lambda = 400nm$ and $\lambda = 550nm$ respectively. Fitting of photoluminescence ratios requires as input thin film thickness and optical constants. These values were extracted for thin films deposited on silicon substrates and glass respectively using spectroscopic ellipsometry (described below).

3.7.4 Spectroscopic Ellipsometry

Spectroscopic ellipsometry (SE) is a non-destructive, surface analysis technique used to characterise the thickness and optical properties of thin films. Incident light of known polarisation is either reflected from or transmitted through a thin film sample and the resultant change in polarisation state is measured. In general, when light is incident at an angle θ_i on a boundary between two materials with refractive indexes n_i and n_f respectively, there is a component of the light that is reflected and a component that is transmitted (Figure 3.19a). The transmitted component refracts at an angle θ_f defined by Snell's law [169]:

$$n_i \sin \theta_i = n_f \sin \theta_f \quad (3.10)$$

For visible light, $n_f > n_i$ (if the medium is air or a vacuum) so $\theta_f > \theta_i$ and there is a real angle of refraction θ_f for all incident angles θ_i . For X-rays and neutrons, the situation differs as typically $n_f < n_i$ and there is a real angle of refraction only for incidence angles larger than a critical angle θ_c . At the critical angle, Equation 3.10 reduces to:

$$\sin\theta_c = \frac{n_f}{n_i} \quad (3.11)$$

When $\theta_i < \theta_c$, total external reflection occurs, and only an evanescent wave penetrates into the material (this will be discussed further in Subsection 3.9.4).

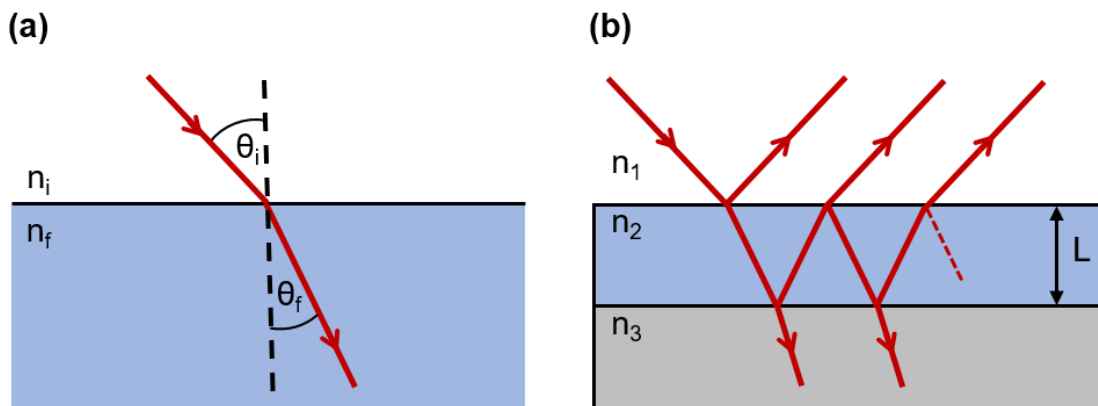


Figure 3.19: An illustration of wave propagation in the (a) single boundary scenario and (b) the double boundary scenario (e.g. for a thin film of thickness L on a semi-infinite substrate).

In the single boundary scenario shown in Figure 3.19a, the amplitude reflection coefficients (r) and amplitude transmitted coefficients t are each split into two components with the electric field orientated parallel and perpendicular to the plane of reflection (s and p polarised light respectively). Continuity of the tangential components of the E-fields at the interface give the Fresnel equations [169]:

$$r_s = \frac{n_i \cos\theta_i - n_f \cos\theta_f}{n_i \cos\theta_i + n_f \cos\theta_f} \quad (3.12)$$

$$r_p = \frac{n_f \cos\theta_i - n_i \cos\theta_f}{n_i \cos\theta_f + n_f \cos\theta_i} \quad (3.13)$$

$$t_s = \frac{2n_i \cos\theta_i}{n_i \cos\theta_i + n_f \cos\theta_f} \quad (3.14)$$

$$t_p = \frac{2n_i \cos\theta_i}{n_i \cos\theta_f + n_f \cos\theta_i} \quad (3.15)$$

In the case of a single layer film with thickness L on a silicon substrate, the system is now composed of three media (the ambient medium, the film medium and the substrate)

medium) with refractive indexes n_1 , n_2 and n_3 respectively (Figure 3.19b). In this scenario, the addition of a second boundary permits multiple reflections as the transmitted wave undergoes reflection and refraction at the boundary between mediums 2 and 3. This reflected wave then reflects and refracts at the surface boundary and so on. The substrate layer is considered to be semi-infinite such that waves transmitted through the substrate do not experience any further reflections. The composite reflection coefficients R_p and R_s can be calculated from a summation of each subsequent reflection in the film (derived elsewhere [170]). The complexity of the system increases as more and more layers are added but the total reflection coefficient can be calculated using numerical calculations. SE measures psi (Ψ) and delta (Δ) values that are related to the reflection coefficients according to:

$$\rho = \frac{R_p}{R_s} = \tan\Psi e^{i\Delta} \quad (3.16)$$

Measuring the ratio of the reflection coefficients makes SE a highly accurate and reproducible technique. Equation 3.16 is also a complex number containing phase information (Δ) which means SE is very sensitive to changes in film thickness and optical constants such that sub-monolayers can be detected.

The experimental setup for a typical SE measurement is displayed in Figure 3.20. Using a *polariser*, a linearly polarised, collimated beam of white light is directed onto a thin film sample. The reflected beam of light is passed through an *analyser* and a *detector*. The *analyser* measures the polarisation state of the reflected beam of light. Using a *monochromator*, a range of wavelengths are scanned so that Ψ and Δ are measured as a function of wavelength.

To measure the thickness of a thin film sample, it is necessary to have prior knowledge of the dispersion relation $n(\lambda)$. For many common materials, the dispersion relation is published elsewhere [171]. If $n(\lambda)$ of the material is unknown, an approximate mathematical model can be used instead. For transparent materials, a common model is the Cauchy model [172]:

$$n(\lambda) = A_n + \frac{B_n}{\lambda^2} + \frac{C_n}{\lambda^4} \quad (3.17)$$

where A_n represents the dimensionless refractive index of the material and B_n and C_n are constants which describe the curvature of the dispersion relation. For materials which absorb some wavelengths of the incident light, the Cauchy model can be used by restricting the wavelength range of the fit to wavelengths outside the absorption region (i.e. the transparent region). All SE measurements in this thesis were performed on single thin film layers spin coated onto silicon substrates using a M2000 ellipsometer (J.A. Woollam). For each measurement, the thickness of a native oxide layer of an uncoated silicon substrate was first measured (typically 1-2nm thick).

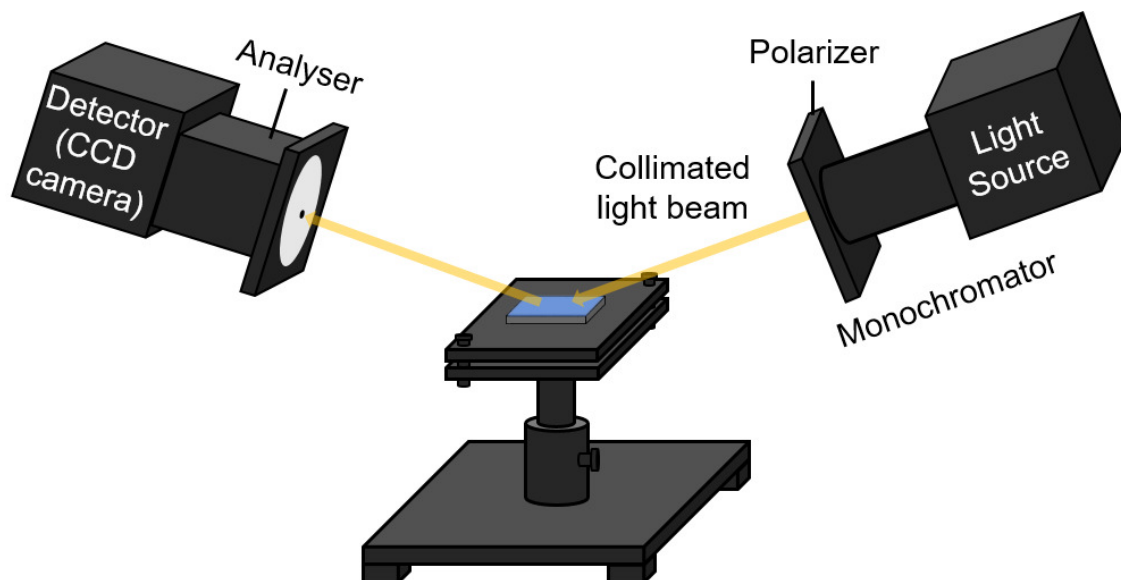


Figure 3.20: Spectroscopic ellipsometry setup for static sample measurements.

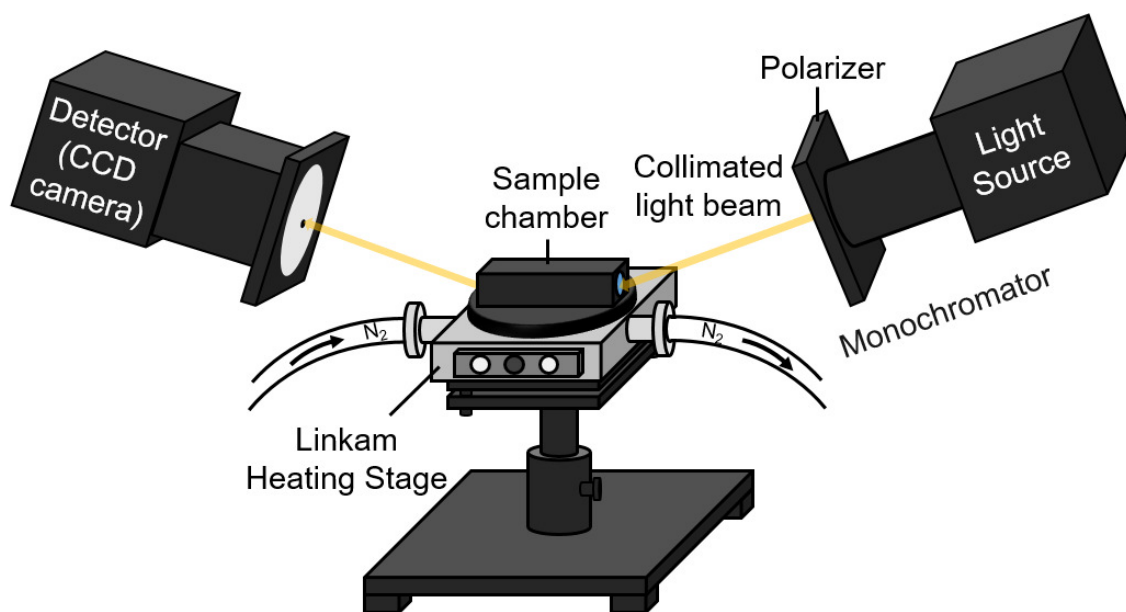


Figure 3.21: Spectroscopic ellipsometry setup for isothermal measurements.

In Chapter 5, SE measurements were performed during isothermal heating of thin film samples. For these measurements, the sample was mounted onto a linkam heating stage and enclosed in a nitrogen flow cell as shown in Figure 3.21. A heating rate of 90°C/min was used to rapidly heat the film to the appropriate temperature and measurements were performed every 10s for a duration of 10 minutes.

3.7.5 Nuclear Magnetic Resonance Spectroscopy

Proton nuclear magnetic resonance (NMR) measurements were used in Chapter 5 to identify chemical environments in solution with respect to ^1H . NMR spectroscopy relies on isotopes of certain elements having a different magnetic moment with different spin relaxation times after perturbation by a magnetic field [173].

In this thesis, NMR samples were prepared from thin films dissolved in deuterated chloroform (CDCl_3). Films were first fabricated following the same protocols used for device fabrication and subsequently dissolved in hydrogenated chloroform by dipping the films into solvent-filled vials. Vials were then stored in the glovebox with their lids removed for a few days so that the hydrogenated solvent evaporated. Once dried, the remaining solvent was dissolved in CDCl_3 and 600 μL was decanted into standard NMR tubes (supplier). ^1H NMR spectra were recorded on Bruker Avance AVIII 400 MHz NMR spectrometers equipped with a 5mm solution state BBO probe with Z-gradient at ambient temperature. Standard ^1H experiments were measured at 400.2MHz using a 30° pulse for excitation, 64 k acquisition points over a spectral width of 20ppm with 128 transients and a relaxation delay of 1s. Chemical shifts δ are given in ppm with respect to tetramethylsilane using the NMR solvent used as internal standards. All NMR data were analysed using TopSpin software (Bruker).

3.8 Thermal Characterisation of Bulk Samples

Differential scanning calorimetry (DSC) and thermogravimetric analysis (TGA) are thermoanalytical techniques used to characterise the thermal properties of bulk samples. Details regarding each technique is provided below.

3.8.1 Differential Scanning Calorimetry

DSC measures the difference in heat flow between a sample of interest and a reference sample as a function of time and temperature. Measurements are performed in a closed, inert atmosphere system isolated by a boundary that only permits the flow of heat and energy. It is useful for characterising a range of thermal properties such as melting points,

glass transitions, crystallisation, phase transitions, oxidation and specific heat capacity [174]. The DSC measurements in this thesis were performed on a Mettler Toledo DSC822 machine with a heating rate of 5°C/min or 10°C/min in a nitrogen-filled atmosphere. DSC samples were prepared by placing the neat solid directly into hermetic DSC pans prior to measurement.

3.8.2 Thermogravimetric Analysis

TGA measures the mass of a sample over a broad temperature range (typically 25°C to 900°C) in an inert atmosphere. It is useful for measuring the thermal stability of materials and determining decomposition temperatures. For example, the mass of an organic/ polymer sample will typically experience a sharp decline at the decomposition temperature as molecules begins to fragment and evaporate off. The TGA measurements in this thesis were performed using the thermal analysis services at the Department of Chemistry at The University of Sheffield.

3.9 Neutron and X-ray Scattering

The non-destructive, highly penetrating, isotope-specific nature of neutron-based scattering techniques make them an ideal probe for characterising organic thin films. X-ray scattering techniques on the other hand are often impeded by a lack of scattering contrast between the weakly scattering organic components and there is a much higher risk of beam damage to the sample. Nevertheless, the advancement of laboratory-based X-ray sources has increased the accessibility and quality of X-ray data achievable in the laboratory. Consequently, both neutron and X-ray scattering techniques are used frequently throughout this thesis to characterise self-assembled nanostructures in organic thin films. In this section, an overview of basic elastic scattering and diffraction theory is provided along with more specific details regarding the experimental setups and procedures. The theory discussed here is an overview of the more comprehensive treatments by Sivia [175] and Roe [176].

3.9.1 Basic Theory of Elastic Scattering

In an elastic scattering experiment a scattering probe is incident on a sample and the amount that is scattered in a particular direction defined by angles 2θ and ϕ is ascertained (Figure 3.22a). The factor of 2 is convention and algebraically convenient as discussed below. The incident probe with wavevector \mathbf{k}_i undergoes a change in momentum, scattering with a final wavevector \mathbf{k}_f as depicted in Figure 3.22b. This transfer of momentum can be expressed as:

$$\mathbf{P} = \hbar\mathbf{k}_i - \hbar\mathbf{k}_f = \hbar\mathbf{Q} \quad (3.18)$$

Where

$$\mathbf{Q} = \mathbf{k}_i - \mathbf{k}_f \quad (3.19)$$

In an elastic scattering experiment there is no exchange of energy ($E_i = E_f$) which means the wavevector and hence the wavelength of the scattering probe is unchanged upon scattering ($|\mathbf{k}_i| = |\mathbf{k}_f| = \frac{2\pi}{\lambda}$). For a probe which is scattered by a sample through an angle 2θ , the addition of vectors according to the vector diagram or "scattering triangle" depicted in Figure 3.22b allows Equation 3.20 to be rewritten as:

$$|\mathbf{Q}| = 2 \times |\mathbf{k}_i| \sin\theta = 2 \times \left| \frac{2\pi}{\lambda} \right| \sin\theta \quad (3.20)$$

$$Q = \frac{4\pi \sin\theta}{\lambda} \quad (3.21)$$

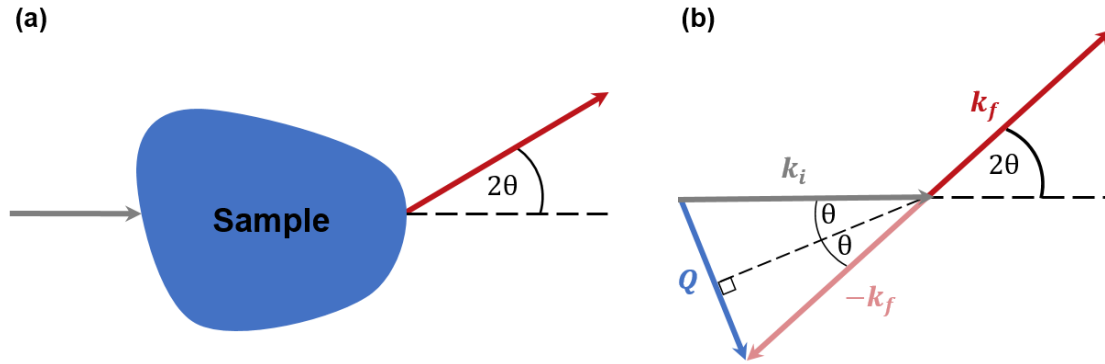


Figure 3.22: (a) The basic scattering principle. An incident probe interacts with the sample and is deflected at an angle 2θ . (b) The scattering vector triangle for an incident probe with wavevector \mathbf{k}_i and scattered wavevector \mathbf{k}_f . The difference $\mathbf{k}_i - \mathbf{k}_f$ is equal to the momentum transfer vector \mathbf{Q} .

Equation 3.21 describes two-dimensional scattering in the yz -plane with the incident beam direction oriented parallel to the z -axis. To describe the scattering of the probe completely, it is necessary to add a second angle ϕ which defines the scattering in the xy -plane (illustrated in Figure 3.23). Here, the incident wavevector is equal to $\mathbf{k}_i = (\frac{2\pi}{\lambda}, 0, 0)$ and the final wavevector is equal to $\mathbf{k}_f = \frac{2\pi}{\lambda}(\sin 2\theta \cos \phi, \sin 2\theta \sin \phi, \cos 2\theta)$. The momentum transfer of a scattered probe is then given by:

Where $\Phi = |\psi_0|^2$, r is the radial distance from the origin of scattering and $f(\lambda, \theta)$ is a function describing the probability that the sample will deflect the scattering probe in a particular direction. As the origin of scattering for X-rays and neutrons is different, $f(\lambda, \theta)$ has different properties for each probe (discussed later). From Equation 3.24, the number of particles deflected per unit time and area in the direction defined by 2θ and ϕ is given by the modulus squared of ψ_f :

$$|\psi_f|^2 = \frac{\Phi}{r^2} \left| f(\lambda, \theta) e^{i\mathbf{Q} \cdot \mathbf{R}_j} \right|^2 \quad (3.25)$$

Following on from this, the scattering rate R taken over angles is therefore given by:

$$R = \int_{2\theta=0}^{\pi} \int_{\phi=0}^{2\pi} |\psi_f|^2 dA \quad (3.26)$$

Where $dA = r^2 \sin 2\theta d\phi d2\theta$ is the area element generated in the direction of $(2\theta, \phi)$. Using Equation 3.26, the scattering cross-section σ , defined by $\frac{R}{\Phi}$ can be expressed as:

$$\sigma(\lambda) = 2\pi \int_{2\theta=0}^{\pi} |f(\lambda, \theta)|^2 \sin 2\theta d2\theta \quad (3.27)$$

The connection between the scattering cross-section and the structure of the sample will be discussed later. Before that, Equation 3.24 is first expanded to an assembly of atoms rather than a single fixed atom to represent a physical sample. Here, the scattered signal is characterised by the summation of the j^{th} deflection from a sample containing a total of N scattering entities located at \mathbf{R}_j :

$$|\psi_f|^2 = \frac{\Phi}{r^2} \left| \sum_{j=1}^N f_j(\lambda, \theta) e^{i\mathbf{Q} \cdot \mathbf{R}_j} \right|^2 \quad (3.28)$$

Where the scattering is assumed to be weak such that scattered probe has a negligible effect on the incident beam (The *Born* or *kinematical* approximation). Additionally, multiple scattering events are assumed to be negligible and the distance between the sample and the detector is assumed to be much larger than the sample size such that $|\mathbf{r} - \mathbf{R}_j| = r$ (The *Fraunhofer* or *far-field* limit). This therefore provides a relation between the differential cross-section for scattering from an assembly of atoms and the structure of the sample:

$$\frac{d\sigma}{d\Omega} \propto \left| \sum_{j=1}^N f_j(\lambda, \theta) e^{i\mathbf{Q} \cdot \mathbf{R}_j} \right|^2 \quad (3.29)$$

In principle, the differential cross-section has contributions from both inelastic and elastic neutron scattering. In most experiments, the inelastic scattering contribution is negligible and can be ignored. In this thesis, reference to the differential cross-section is taken to be equal to the elastic differential cross-section. To further understand the relation between

the structural properties of the sample and the differential cross-section, it is necessary to detail the characteristics of $f(\lambda, \theta)$ for neutrons and X-rays as discussed below.

Scattering Lengths

As mentioned previously, the scattering factor is different for X-ray and neutron scattering. For neutron scattering, $f(\lambda, \theta)$ is independent of both wavelength (except at resonances) and the scattering angle and so is typically written as:

$$f(\lambda, \theta) = -b \quad (3.30)$$

Where the nuclear scattering length b determines the strength of the scattering. In principle, scattering lengths are complex numbers but the imaginary part is typically negligible (except for nuclei with high neutron absorption cross-sections). Neutron scattering occurs as a result of the interaction between the incident neutron beam and the nuclei of the sample via the strong nuclear force. This scattering interaction is not well understood but it is clear that it depends on the composition of the nucleus and the orientation of its spin relative to the incident neutron. It is therefore isotope specific, spin-dependent and does not vary across the periodic table in a simple way. For example the scattering lengths between hydrogen and its isotope deuterium differ significantly. Following the rules of angular momentum addition from quantum mechanics, the average scattering length of hydrogen is equal to $\langle b \rangle_H = -0.374 \times 10^{-14}m$ with a standard deviation of $\Delta b_H = 2.527 \times 10^{-14}m$ ($\Delta b = \sqrt{\langle b^2 \rangle - \langle b \rangle^2}$). In the case of deuterium, $\langle b \rangle_D = 0.668 \times 10^{-14}m$ and $\Delta b_D = 0.403 \times 10^{-14}m$. The differing scattering lengths of hydrogen and deuterium are frequently exploited in neutron scattering through a method known as deuterium-labelling (discussed later in this Section). In contrast to neutron scattering, X-ray scattering is the result of the long-range electromagnetic interaction between an incident X-ray and the orbital electrons of the scattering entity. Here, the scattering factor $f(\lambda, \theta)$ is more complicated in comparison to neutrons and is expressed as:

$$f(\lambda, \theta) = Zg(Q)r_e \quad (3.31)$$

Where Z is the atomic number of the scattering entity, r_e is the radius of an electron (the Thomson scattering length) and $g(Q)$ describes the decay of the scattering factor for increasing Q . The magnitude of the scattering is therefore proportional to atomic number Z and the size of an atom but also decreases with increasing scattering angle.

Coherent and Incoherent Neutron Scattering

Returning to Equation 3.27, the cross-section for a neutron scattering experiment with $f(\lambda, \theta) = -b$ is given as:

$$\sigma = 4\pi|b|^2 \quad (3.32)$$

As described previously, the scattering length b is equal to $\langle b \rangle \pm \Delta b$, which allows the average neutron scattering cross-section to be written as:

$$\langle \sigma \rangle = 4\pi(\langle b \rangle^2 + \Delta b^2) = \langle \sigma_{coh} \rangle + \langle \sigma_{incoh} \rangle \quad (3.33)$$

Where $\langle \sigma_{coh} \rangle$ and $\langle \sigma_{incoh} \rangle$ are the coherent and incoherent cross-sections respectively. The coherent component of the scattering cross-section contains the structural information of the sample of interest whilst the incoherent component contributes a featureless background. Earlier in this section, the scattering lengths of hydrogen and deuterium were calculated. The much larger Δb of the hydrogen atom indicates that samples containing large concentrations of hydrogen suffer from a larger incoherent scattering background compared to samples containing high levels of deuterium. However, provided $\langle \sigma_{coh} \rangle$ is still sufficiently large, this is not an issue for most experiments and the background can be fitted appropriately during data fitting.

Scattering Length Density

The scattering length density (SLD) of material is essentially a measure of the *scattering power* per unit volume of a scattering entity. Mathematically, the SLD β_n of a material is given by the sum of scattering length contributions ($\langle b \rangle_i$) from the N atoms within a unit cell divided by the volume \mathcal{V} of the unit cell:

$$\beta_n = \frac{\sum_{i=1}^N \langle b \rangle_i}{\mathcal{V}} \quad (3.34)$$

For example, the SLD of a molecule with N atoms and molecular volume \mathcal{V}_m is the summation of atomic scattering lengths given by $\beta_n = \frac{\sum_{i=1}^N \langle b \rangle_i}{\mathcal{V}_m}$. The molecular volume \mathcal{V}_m is usually unknown but can be calculated if the mass density ρ and molecular weight M_w of the material is known. M_w is equal to the summation of the atomic molar mass m_i for each element. Combining all of the above, the SLD for a molecule can be written as:

$$\beta_n = \frac{\sum_{i=1}^N \langle b \rangle_i}{\mathcal{V}_m} = \frac{\rho N_A}{M_w} \sum_{i=1}^N \langle b \rangle_i = \rho N_A \sum_{i=1}^N \frac{\langle b \rangle_i}{m_i} \quad (3.35)$$

This is a trivial calculation for small molecules but for larger molecules containing many atoms of different elements, there are a number of useful online SLD calculators available. The X-ray and neutron SLD of materials studied in this thesis are presented in Table 3.6. Some values were determined from experimental data and others were estimated using the NIST online SLD calculator [177].

Material	Chemical Formula	ρ (g/cm^3)	β_n ($\times 10^{-6} \text{ \AA}^{-2}$)	β_x ($\times 10^{-6} \text{ \AA}^{-2}$)
PBDB-T	$(C_{68}H_{78}O_2S_8)_n$	1.16	1.15	10.54
PTB7-Th	$(C_{49}H_{57}FO_2S_6)_n$	1.15	1.14	10.43
PC ₇₁ BM	$C_{82}H_{14}O_2$	1.58	4.65	13.62
ITIC	$C_{94}H_{82}N_4O_2S_4$	1.11	1.77	9.99
d8-ITIC	$C_{94}H_{74}D_8N_4O_2S_4$	1.11	2.15	9.94
d52-ITIC	$C_{94}H_{30}D_{52}N_4O_2S_4$	1.11	4.16	9.64
EH-IDTBR	$C_{72}H_{88}N_6O_2S_8$	1.23	1.34	11.18
d-EH-IDTBR	$C_{72}H_{20}D_{68}N_6O_2S_8$	1.23	5.03	10.63
O-IDTBR	$C_{72}H_{88}N_6O_2S_8$	1.20	1.31	10.91
d-O-IDTBR	$C_{72}H_{20}D_{68}N_6O_2S_8$	1.20	4.91	10.37
O-IDTBCN	$C_{68}H_{78}N_8S_4$	1.16	1.52	10.56
d-O-IDTBCN	$C_{68}H_{10}D_{68}N_8S_4$	1.16	5.53	9.96

Table 3.6: Table of mass density (ρ), neutron scattering length density (β_n) and X-ray scattering length density (β_x) values for materials used in this thesis. β_n values for deuterated materials were extracted from the neutron reflectivity measurements presented in Chapter 5 and Chapter 6. Using these values, ρ values for each material were calculated by working backwards using Equation 3.35. It was assumed that the mass density of hydrogenated materials and their deuterated analogues is the same. β_n values for hydrogenated materials and β_x values were therefore estimated with the calculated ρ values using the NIST SLD calculator [177].

Deuterium Labelling

In a scattering experiment, it is important to have sufficient SLD contrast between the scattering entities of interest. For example, to characterise a binary organic BHJ blend film, it is essential that the SLD of the conjugated donor polymer and small molecule acceptor are sufficiently different so that each component can be identified and the scattering signal is measurable. For X-ray scattering, SLD contrast originates from differences in electron density and so the X-ray SLD of a material cannot be changed without significantly altering the chemistry of the molecule. In contrast, neutron scattering lengths are isotope specific. This means that the hydrogen atoms of a molecule can be substituted with deuterium atoms without altering the chemistry or structure of the molecule. As discussed previously, the scattering lengths of hydrogen and deuterium are very different (see Equation 3.9.1) and so altering the degree of deuterium-substitution in a molecule provides a method to control the neutron SLD of a molecule. This allows the neutron SLD contrast between scattering entities in a sample to be increased (or decreased in the case of contrast-matching). The

ability to deuterium-label parts or all of a molecule underpins the basis of most soft-matter neutron scattering experiments and has revolutionised a wide range of experimental research fields.

Neutron scattering techniques have been and still are used frequently to characterise fullerene-based OPV blends. The large C:H ratio of fullerene acceptors such as PC₇₁BM provides a significant natural neutron SLD contrast with most conjugated polymers (see Table 3.6). The rise of NFAs in OPV has presented a structural characterisation challenge. Unlike most hydrogenated polymer:fullerene blends, in polymer:NFA blends the natural neutron SLD contrast is insufficient because the neutron SLD of the donor polymer is typically very similar to that of the NFA (Table 3.6). To use the same neutron scattering techniques as have been used to characterise fullerene-based blends, it is necessary to increase the neutron SLD contrast in polymer:NFA samples. In this thesis, this is achieved by substituting the hydrogen atoms on side-chain or end-group moieties with deuterium atoms to form partially deuterated NFAs (d-NFAs). For example, deuteration of the linear n-octyl side chains of O-IDTBR increases the neutron SLD contrast from $\Delta_{\beta_n} = 0.16 \times 10^{-6} \text{Å}^{-2}$ in the PTB7-Th : O-IDTBR blend to $\Delta_{\beta_n} = 3.76 \times 10^{-6} \text{Å}^{-2}$ for the PTB7-Th : d-O-IDTBR blend.

Fourier Transforms

The characteristics of $f(\lambda, \theta)$ are related to the size and shape of the scattering entity which can be quantified through the three-dimensional SLD function $\beta(\mathbf{R}) = \beta(x, y, z)$. Using Equation 3.29, this allows the differential cross-section to be written as:

$$\frac{d\sigma}{d\Omega} = \left| \iiint_V \beta(\mathbf{R}) e^{i\mathbf{Q}\cdot\mathbf{R}} d^3\mathbf{R} \right|^2 \quad (3.36)$$

Where it becomes clear that the elastic differential cross-section is related to the structure of the sample through the Fourier transform of its SLD distribution. It therefore provides a more physical insight into the relationship between real and reciprocal space, forming the basis of all scattering techniques detailed below.

3.9.2 Basic Principles of Diffraction

The majority of studies presented in this thesis focus on characterising amorphous or semi-crystalline films where it is more useful to apply the elastic scattering concepts discussed in section previously. However, in Chapter 7, the samples of interest are highly crystalline and crystallographic information is gained using basic principles of diffraction. Diffraction is a subset of scattering and typically refers to the constructive interference of a scattering probe in a crystalline solid with long-range periodicity. The SLD function of a crystalline solid with long-range periodicity can be expressed as:

$$\beta(\mathbf{r}) = \beta(\mathbf{r} + n_1\mathbf{a} + n_2\mathbf{b} + n_3\mathbf{c}) \quad (3.37)$$

Where n_1 , n_2 and n_3 are integers. Equation 3.37 shows that the SLD at any location \mathbf{r} is the same as the SLD at any point translated by integer multiples of the lattice vectors \mathbf{a} , \mathbf{b} and \mathbf{c} . This gives rise to the crystallographic unit cell with axial lengths (a, b, c) and axial angles (α, β, γ) as shown in Figure 3.24.

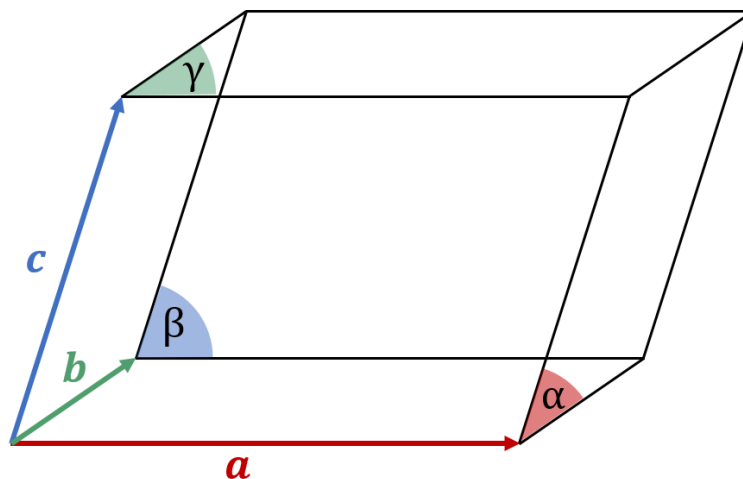


Figure 3.24: The crystal unit cell with lattice constants a , b , c , α , β and γ .

Using Equation 3.36, the differential cross-section is given as:

$$\frac{d\sigma}{d\Omega} = \left| L_R(\mathbf{Q}) \iiint_{\mathcal{V}_{cell}} \beta(\mathbf{R}) e^{i\mathbf{Q}\cdot\mathbf{R}} d^3\mathbf{R} \right|^2 \quad (3.38)$$

Where \mathcal{V}_{cell} is the volume of the unit cell and $L_R(\mathbf{Q})$ is equal to:

$$L_R(\mathbf{Q}) = \sum_{n_1} \sum_{n_2} \sum_{n_3} e^{i\mathbf{Q}\cdot(n_1\mathbf{a}+n_2\mathbf{b}+n_3\mathbf{c})} \quad (3.39)$$

Here, the properties of constructive interference are enforced as the summation in Equation 3.39 will cancel out to zero unless:

$$\mathbf{Q} \cdot (n_1\mathbf{a} + n_2\mathbf{b} + n_3\mathbf{c}) = \phi_0 + 2\pi n \quad (3.40)$$

Where ϕ_0 is a constant and n is an integer. The condition in Equation 3.40 can only be satisfied when

$$\mathbf{Q} = h\mathbf{a}^* + k\mathbf{b}^* + l\mathbf{c}^* \quad (3.41)$$

Where hkl are the miller indices and a^* , b^* and c^* are the reciprocal lattice vectors defined as:

$$\mathbf{a}^* = \frac{2\pi\mathbf{b} \times \mathbf{c}}{\mathbf{a} \cdot (\mathbf{b} \times \mathbf{c})}, \quad \mathbf{b}^* = \frac{2\pi\mathbf{c} \times \mathbf{a}}{\mathbf{a} \cdot (\mathbf{b} \times \mathbf{c})}, \quad \mathbf{c}^* = \frac{2\pi\mathbf{a} \times \mathbf{b}}{\mathbf{a} \cdot (\mathbf{b} \times \mathbf{c})}$$

a^* , b^* and c^* obey the following vector product rules:

$$\begin{aligned} \mathbf{a} \cdot \mathbf{a}^* &= \mathbf{b} \cdot \mathbf{b}^* = \mathbf{c} \cdot \mathbf{c}^* = 2\pi \\ \mathbf{a} \cdot \mathbf{b}^* &= \mathbf{a} \cdot \mathbf{c}^* = \mathbf{b} \cdot \mathbf{a}^* = \mathbf{b} \cdot \mathbf{c}^* = \mathbf{c} \cdot \mathbf{a}^* = \mathbf{c} \cdot \mathbf{b}^* = 0 \end{aligned}$$

This means that for constructive interference, the integer n must be equal to $n = n_1h + n_2k + n_3l$ such that the array of non-zero points of $L_R(\mathbf{Q})$ form a periodic lattice in Q space known as the *reciprocal lattice*:

$$L_R(\mathbf{Q}) = \sum_h \sum_k \sum_l \delta(\mathbf{Q} - (h\mathbf{a}^* + k\mathbf{b}^* + l\mathbf{c}^*)) \quad (3.42)$$

The consequence of this reciprocal lattice results in non-zero scattering at well-defined Q values called Bragg spots.

Diffraction can also be considered by treating the assembly of crystallographic planes as a diffraction grating such that an incident probe with a wavelength comparable to the interatomic spacings of the crystal, constructively interferes producing a diffraction pattern. If the wavelength of the incident probe is known, the interatomic spacings of the crystal can be determined from the resultant diffraction pattern [175]. This can be demonstrated by considering a coherent beam of X-rays with wavelength λ impinging at an angle θ onto a series of crystal lattice planes separated by a distance d (Figure 3.25). Here, the scalar product between the unit vector normal $\hat{\mathbf{n}}$ and position vector \mathbf{r} is given as:

$$\mathbf{r} \cdot \hat{\mathbf{n}} = nd + \Delta \quad (3.43)$$

Where $n = 0, \pm 1, \pm 2, \pm 3 \dots$ and Δ is an offset. This produces diffraction features as a result of constructive interference at scattering vectors equal to:

$$\mathbf{Q} = \frac{2\pi n}{d} \hat{\mathbf{n}} \quad (3.44)$$

The modulus of the scattering vector in Equation 3.44 can be equated to Equation 3.21 to give:

$$Q = \frac{4\pi \sin\theta}{\lambda} = \frac{2\pi n}{d} \quad (3.45)$$

Simplifying Equation 3.45 leads to:

$$n\lambda = 2d\sin\theta \quad (3.46)$$

Which is known as the Bragg condition or Bragg's law after Lawrence Bragg and his father William Henry Bragg who first discovered it in 1913 [178]. Here the path difference between the incident beam and reflected beam from successive planes is equal to $2d\sin\theta$ as shown in Figure 3.25. Constructive interference therefore occurs when this path difference is equal to an integer multiple of wavelengths $n\lambda$. Fourier analysis also shows that the d -spacing of the crystallographic planes is reciprocally related to the scattering vector through:

$$d = \frac{2\pi}{Q} \quad (3.47)$$

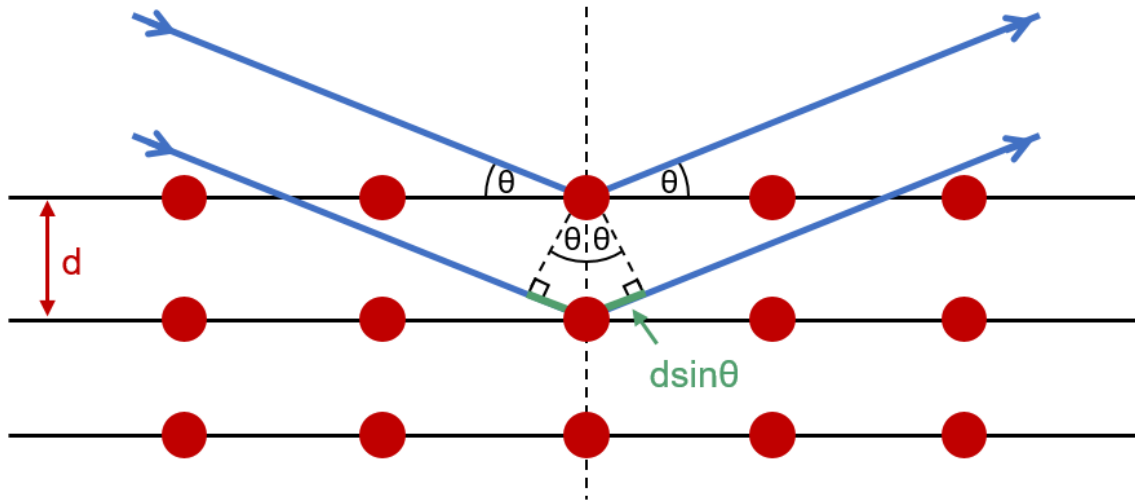


Figure 3.25: Diffraction of an incident wave front from a series of parallel crystal lattice planes. Constructive interference occurs according to the Bragg condition (Equation 3.46).

This means that the direction of \mathbf{Q} is orthogonal to the periodic lattice planes such that the observed Bragg spots correspond to lattice planes with a unit normal vector defined by:

$$\hat{\mathbf{n}}_{hkl} = \frac{\lambda}{4\pi\sin\theta_{hkl}}(h\mathbf{a}^* + k\mathbf{b}^* + l\mathbf{c}^*) \quad (3.48)$$

Which when substituted into Equation 3.43 gives [175]:

$$\mathbf{r} = u\mathbf{a} + v\mathbf{b} + w\mathbf{c} \quad (3.49)$$

Where u , v and w are integers which describe a translation or direction through a crystal $[u, v, w]$.

In crystallography, there are seven crystal systems based on rotational symmetry: triclinic, monoclinic, orthorhombic, tetragonal, trigonal, hexagonal and cubic [175]. Within each system, translational symmetry is described using four different atomic centre positions [179]: primitive (P), base-centred (C), body-centred (I) and face-centred (F). Together these configurations form the conventional *Bravais lattices* that are the building blocks for all three-dimensional crystal structures. Considering all possible symmetries of a crystal unit cell gives the possible *point symmetry groups*, which combined with the Bravais lattices, permit a total of 230 crystallographic *space groups* (summarised in Table 3.7).

Crystal System	Unit Cell Geometry	Space Groups
Triclinic	$a \neq b \neq c; \alpha \neq \beta \neq \gamma$	1 - 2
Monoclinic	$a \neq b \neq c; \alpha = \gamma = 90^\circ \neq \beta$	3 - 15
Orthorhombic	$a \neq b \neq c; \alpha = \beta = \gamma = 90^\circ$	16 - 74
Tetragonal	$a = b \neq c; \alpha = \beta = \gamma = 90^\circ$	75 - 142
Trigonal	$a = b = c; \alpha = \beta = \gamma \neq 90^\circ$	143 - 167
Hexagonal	$a = b \neq c; \alpha = \beta = 90^\circ, \gamma = 120^\circ$	168 - 194
Cubic	$a = b = c; \alpha = \beta = \gamma = 90^\circ$	195 - 230

Table 3.7: A summary of the unit cell lattice parameters for the seven possible crystal systems for the 230 space groups as defined by the International Tables of Crystallography [180]

Ewald Sphere

For elastic scattering ($|\mathbf{k}_i| = |\mathbf{k}_f|$), the observed diffraction reflections are often considered in terms of the *Ewald sphere* configuration (Figure 3.26). Here, a sphere is defined in real space centred at the origin of scattering with a radius equal to $2\pi/\lambda$. In this configuration, the incident wavevector \mathbf{k}_i starts at the origin of scattering and ends at the edge of the Ewald sphere where a reciprocal lattice point is located. All of the reciprocal lattice points located on the surface of the Ewald sphere satisfy the Bragg condition (Equation 3.46) resulting in constructive interference with scattering vector $\mathbf{Q} = \mathbf{k}_i - \mathbf{k}_f$.

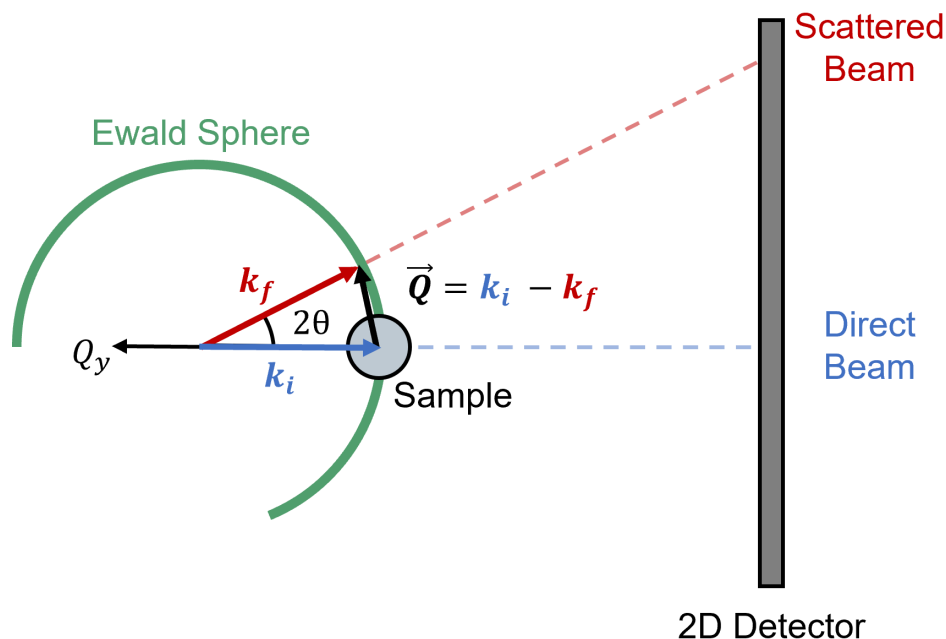


Figure 3.26: Ewald sphere configuration of elastic scattering. The centre of the sphere is defined as the origin of scattering and the radius is equal to the incident wavevector k_i .

3.9.3 Neutron and X-ray Sources

For a neutron or X-ray scattering experiment, it is necessary to have a source of neutrons or X-rays. The method used to generate these probes determines the experimental setup and variables such as the counting time necessary for sufficient statistics. Neutrons are produced using either a spallation source (e.g. ISIS neutron spallation source) or from nuclear fission reactors (e.g. Institut-Laue-Langevin (ILL)). X-rays can be produced at synchrotron facilities (e.g. Diamond Light Source and European Synchrotron Radiation Facility (ESRF)) or using laboratory setups with solid-state targets (typically copper) or more recently, liquid-metal jet targets (e.g. liquid gallium). The underlying principles to generate Neutrons or X-rays for each of these sources is detailed below.

Neutron Sources

Neutron reactor sources rely on the fission reaction of enriched uranium-235 (U^{235}) in the fuel rods. A U^{235} atom absorbs a neutron forming an unstable U^{236} atom that decays via several possible mechanisms. One possible decay route is:



The decay of U^{236} produces more neutrons (typically 2.5 neutrons per event) which can then be absorbed by more U^{235} atoms producing more unstable U^{236} atoms which subsequently decay to produce more neutrons and so on leading to a self-sustained chain reaction. This chain reaction yields a constant neutron flux of approximately $10^{15} \text{ s}^{-1} \text{ cm}^{-2}$ at research reactor facilities. The energies of these neutrons are controlled through the use of moderators (typically D_2O or graphite) which decreases (or increases) the speed of the neutrons through the loss (or gain) of kinetic energy via collisions. The resulting neutron energy distribution is determined by the temperature of the moderator according to a Maxwell-Boltzmann distribution. This allows neutron energies to be tuned by controlling the temperature of the moderator. For example, a moderator at 330K produces neutrons with an average wavelength of 1.7\AA , whereas a cold source using a moderator at 25K generates neutrons with an average wavelength of 6\AA . Reactor-based sources produce a high flux of neutrons but typically require the beam to be monochromated so much of the potential flux is lost.

In a neutron spallation source, bunches of high energy protons are periodically accelerated by a synchrotron towards a heavy metal solid target. The protons violently interact with the target nuclei producing a variety of nuclear fragments along with high-energy neutrons which are then slowed down by a moderator. At the ISIS spallation source, the world's most intense pulsed neutron source, accelerated protons have an energy of 800MeV and bunches are fired at a tungsten target 50 times every second producing a 50Hz pulsed neutron beam.

Accelerator-based sources are well suited to the time-of-flight (TOF) technique. Here, the time t taken for a neutron to travel the total flight path L from the moderator to the detector via the sample is given by:

$$t = \frac{L}{v} = \frac{m_n L \lambda}{h} \quad (3.50)$$

Where the speed of the neutron v with mass m_n is related to the de Broglie wavelength λ via $\lambda = h/m_n v$. The TOF technique removes the need to monochromate the beam increasing the amount of usable neutron flux. Although the raw flux produced from a spallation source is much lower than a reactor source, using the TOF technique means the final flux available for scattering experiments is of a comparable order of magnitude. For many neutron instruments, the distribution of neutron velocities and consequently the observable wavelength range is controlled using high-frequency rotating discs with two transparent windows called choppers. As their name suggests, choppers 'chop up' the neutron beam, by blocking the incident beam in short, well-defined intervals. This prevents

faster neutrons from damaging the sample and also mitigates the problem of frame overlap where a neutron in one pulse catches up with the lower energy tail of the previous pulse. Choppers also allow the TOF technique to be used at reactor sources where the continuous, moderated neutron beam is broken up into shorter pulses.

X-ray Sources

All objects emit electromagnetic radiation called blackbody radiation. The wavelength of the emitted radiation is inversely proportional to the temperature of the object $T(K)$ according to Wien's law:

$$\lambda_{max} = \frac{2.90 \times 10^{-3}(m \cdot K)}{T(K)} \quad (3.51)$$

Where λ_{max} (m) is the peak emission wavelength of the blackbody curve. This means, that for an object to emit X-rays with a wavelength $\lambda = 1.34\text{\AA}$, would require a temperature of around 22 million degrees. Fortunately, rather than generating X-rays using thermal energy, there is another way. The generation of X-rays in most laboratory sources relies on accelerating an electron with charge $-e$ through a voltage V onto a metal target. Any X-rays that are emitted have an energy limited to:

$$hf \geq eV \quad (3.52)$$

This approach produces X-rays via two different mechanisms. The first is the emission of Bremsstrahlung or 'braking' radiation when the electron is deflected or stopped by atomic nuclei in the target resulting in rapid deceleration. This produces a continuous distribution of X-ray energies limited by the equality in Equation 3.53. The second mechanism is an indirect process producing a discrete set of X-ray wavelengths. Here, the accelerated electron knocks off an inner shell electron from an atom in the metal target. To minimise the energy of the atom, an electron from an outer shell with energy E_j relaxes to the lower shell vacancy with energy E_i emitting a photon with an energy equal to the difference between the two energy levels:

$$hf_{ij} = E_j - E_i \quad (3.53)$$

The dominant energy level transition is typically the relaxation of an electron from the second energy level ($n = 2$) to the ground state $n = 1$ often referred to as the K_α spectral line. For a typical solid-state copper laboratory X-ray source, this corresponds to a wavelength of 1.5406\AA . The X-ray flux in laboratory-based X-ray sources is proportional to the electron flux. However, the majority of the input kinetic energy is converted into thermal energy rather than X-rays so an increase in electron flux also leads to a rise in the temperature of the target. For solid-state laboratory-based sources, this limits the achievable

X-ray flux to the melting point of the target. This can be mitigated by replacing the solid-state target with a rapid flow of liquid metal (typically indium or gallium alloys). This method prevents the target from melting as the source is constantly replenished, allowing much higher X-ray fluxes to be achieved. Liquid metal jet systems are a relatively new development and have opened up a wealth of laboratory-based materials experiments that were once only possible at synchrotron sources.

The work in this thesis benefitted greatly from the liquid gallium MetalJet source (Excillum) as part of the Xeuss 2.0 system (Xenocs) in the Department of Chemistry at The University of Sheffield. The Xeuss 2.0 instrument is capable of much faster acquisition times (1-3 minutes) compared to traditional solid-state laboratory sources. It is also the ideal X-ray instrument for measuring delicate organic/ polymer samples because the low X-ray flux (compared to synchrotrons) does not damage the sample and the entire beam path can be held under vacuum, reducing air scatter that would otherwise saturate the weak scattering signal from the sample.

For experiments requiring much faster acquisition times on the order of seconds, a synchrotron source is necessary. When a charged particle is accelerated, it emits electromagnetic radiation. Acceleration is defined as a change in velocity so a change in acceleration can be either a change in speed or direction. At synchrotrons, electrons orbit in a circular motion at relativistic speeds in response to a magnetic field. Here, the X-ray flux is several orders of magnitude higher than laboratory-based sources and instruments are typically equipped with advanced X-ray optics to produce an extremely monochromatic, well-collimated, low divergence beam concentrated in a small area at the sample. Although this allows rapid kinetic processes to be measured *in-situ*, there is also a much higher risk of beam damage for organic/ polymer samples and so it is often necessary to significantly attenuate the beam.

3.9.4 Neutron Reflectivity

Neutron reflectivity (NR) is a non-destructive, high-resolution depth profiling technique, capable of characterising the chemical composition of thin films and interfaces in the plane perpendicular to the substrate. In reflectivity experiments, the z direction (Q_z direction in real and reciprocal space) is conventionally defined differently to the scattering geometries described previously (it is now normal to the substrate). In a NR experiment, neutrons with wavevector k_i impinge the thin film surface at an angle θ_i and the amount that is reflected with the same attributes is ascertained (Figure 3.27). Specular NR probes the reflection of neutrons for which the angle of reflection (θ_f) is equivalent to the incident angle ($\theta_i = \theta_f$). If the surface of the sample is not completely flat or if there are some lateral, in-plane SLD inhomogeneities, the sample will also exhibit off-specular or diffuse

scattering ($\theta_i \neq \theta_f$). The NR studies in this thesis concern the measurement of specular reflectivity only. The reflectivity R is equal to the ratio of the reflected beam and the incident beam:

$$R = \frac{\text{Rate of specular scattering}}{\text{Rate of incidence}} \quad (3.54)$$

In an NR experiment, this rate is calculated as a function of Q ($R(Q)$) by repeating the measurement at multiple incident angles at a fixed wavelength or using a range of neutron wavelengths at a fixed angle (in practice, a combination of the two is typically performed to generate a large Q range according to Equation 3.21). The wavelength-dependent refractive index of neutrons is approximated by the following equation:

$$n(\lambda) \approx 1 - \frac{\beta_n \lambda^2}{2\pi} \quad (3.55)$$

As the majority of elements have positive scattering lengths, this means that $n(\lambda) < 1$. From Snell's law (Equation 3.10), neutrons are therefore only refracted at incident angles larger than the critical angle of the film ($\theta_i > \theta_c$) where the reflectivity falls with increasing incident angle ($R < 1$). At incident angles below the critical angle of the thin film ($\theta_i < \theta_c$) neutrons undergo total external reflection ($R = 1$) and only an evanescent wave penetrates into the material. In a reflectivity experiment, the transition point between these two behaviours is called the critical edge and is located at Q_c . Due to the very small deviation in the ratio n_f/n_i from 1, total external reflection is typically only observed at very small incident angles ($\theta_i < 1^\circ$).

There are two mathematical theories that describe NR: *Kinematic* theory and *Dynamic* theory. Dynamic theory offers an exact method for determining reflectivity curves and is derived from geometrical optics using Snell's and Fresnel's laws (Equation 3.10 to Equation 3.15). Although the Dynamic theory approach offers an exact solution, the method is entirely numerical and offers no physical insight into the connection between the scattering length density profile of a sample and the measured reflectivity curve. Kinematic theory on the other hand originates from the basic elastic scattering theory discussed previously. It is not an exact solution as it relies on the Born approximation and becomes invalid below the critical edge in the regime of total external reflection. However, the kinematic approximation is valid for incident angles much greater than the critical angle, when the scattering interactions are weak and interactions between the incident and reflected waves are negligible. Kinematic theory also has the advantage of offering a more physical interpretation of the link between the observed reflectivity curve and the interior structure of the sample. Detailed derivations of both Kinematic and Dynamic theories of reflectivity can be found elsewhere [175, 176]. Here, the key equations of Kinematic theory are provided to aid with interpretation of the NR presented in this thesis.

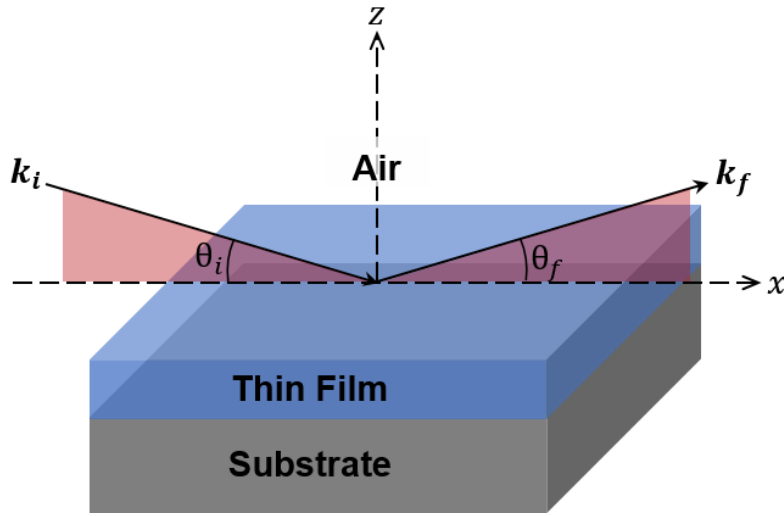


Figure 3.27: Specular neutron reflectivity geometry. A neutron incident on a thin film sample at an angle

In Kinematic theory, the measured specular reflectivity $R(Q)$ is approximated as:

$$R(Q) \approx \frac{16\pi^2}{Q^4} \left| \int_{-\infty}^{\infty} \frac{d\beta}{dz} e^{izQ} dz \right|^2 \quad (3.56)$$

Equation 3.56 shows that the measured reflectivity $R(Q)$ can be interpreted as the Fourier transform of the SLD gradient $(\frac{d\beta}{dz})$ in the plane normal to the surface of the sample.

In Figure 3.28 a series of simulated NR curves are presented where each layer is simulated as a slab with a sharp interface. For a smooth substrate layer (Figure 3.28a), the reflectivity curve exhibits a distinct $R(Q) \propto Q^{-4}$ relation at $Q > Q_c$. The position of the critical edge Q_c of the reflectivity curve is related to the SLD of the substrate β_s by:

$$Q_c = 4\sqrt{\pi\beta_s} \quad (3.57)$$

For a single uniform slab on a silicon substrate, the reflectivity curve consists of a sinusoidal Q variation superimposed onto the expected Q^{-4} decay. The Q spacing (ΔQ) between these *kiesseg* fringes follows a reciprocal relationship with the thickness of the film L :

$$\Delta Q = \frac{2\pi}{L} \quad (3.58)$$

Simulations show how the NR curve changes depending on the SLD β_1 and thickness L of the slab. The amplitude of the *kiesseg* fringes increases as the difference between β_1 and

β_s increases (Figure 3.28b). As L increases, ΔQ decreases (Figure 3.28c).

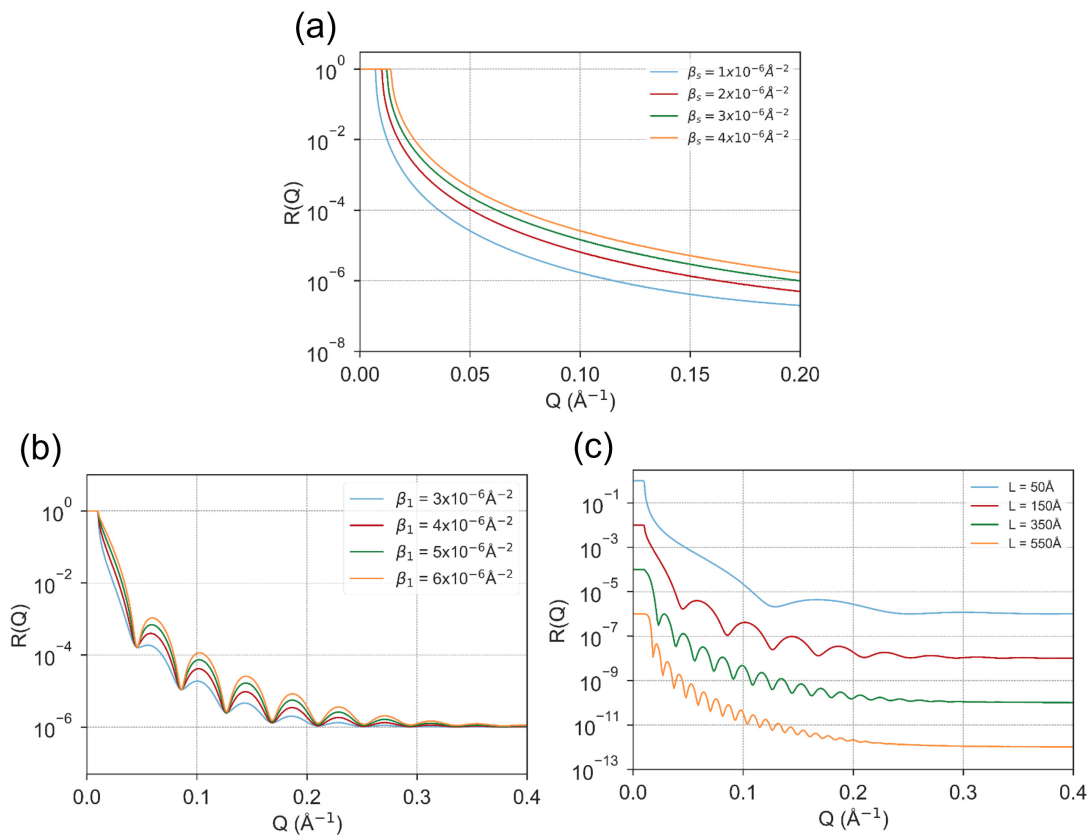


Figure 3.28: Specular neutron reflectivity simulations of (a) a substrate with various SLD values (β_s). (b) A 15nm single layer film on a silicon substrate ($\beta_s = 2.07 \times 10^{-6} \text{\AA}^{-2}$) with various SLD values (β_1). (c) A single layer film with $\beta_1 = 4 \times 10^{-6} \text{\AA}^{-2}$ on a silicon substrate with various film thicknesses (L). In (c), data has been offset by two decades for clarity.

For rough or diffuse interfaces in thin film samples, the SLD gradient $\frac{d\beta}{dz}$ is modelled as a Gaussian function with width σ . For a rough substrate, this corresponds to:

$$\frac{d\beta}{dz} = -\frac{\beta_s}{\sigma\sqrt{2\pi}} e^{-\frac{z^2}{2\sigma^2}} \quad (3.59)$$

Increasing the roughness of a substrate results in a more rapid reflectivity decay with increasing Q such that the reflectivity curve is modelled as:

$$R(Q) \approx \frac{16\pi^2\beta_s^2}{Q^4} \times e^{-\sigma^2Q^2} \quad (3.60)$$

Neutron Reflectivity Modelling

In an NR experiment, a $R(Q)$ vs Q curve is produced. Although this reflectivity curve can give some initial indications about the properties of the sample such as approximate film thicknesses (Equation 3.58), it is necessary to fit the reflectivity data using a mathematical model to gain detailed structural information about the sample. This is especially true for complex multilayer samples for which the reflectivity curve is calculated from the summation of reflected and transmitted waves as discussed previously. Reflectivity is therefore *model-dependent* and $R(Q)$ data is typically presented alongside the corresponding SLD profile simulated from the mathematical model. For a composite layer film, the effective SLD is calculated from the volume fraction of each material. For example, consider a two-phase OPV blend film composed of donor polymer and small molecule acceptor phases with SLDs β_D and β_A and volume fractions ϕ_D and ϕ_A respectively ($\phi_A + \phi_D = 1$). The effective SLD of the blend layer simulated from the reflectivity model is equal to:

$$\beta_n = \phi_A\beta_A + \phi_D\beta_D \quad (3.61)$$

where the volume fraction of each phase is given by:

$$\phi_A = \frac{\beta_n - \beta_D}{\beta_A - \beta_D} \quad (3.62)$$

NR fitting in this thesis was evaluated based on the $\chi^2/Npts$ value which is related to the difference between *observed* and *expected* reflectivity values according to:

$$\chi^2 = \frac{(\text{observed} - \text{expected})^2}{Npts \times \text{expected}} \quad (3.63)$$

where $Npts$ is the number of points in the data set.

Neutron Reflectivity Measurements at Institut-Laue-Langevin

All NR measurements in this thesis were performed using the D17 reflectometer at ILL in TOF, non-polarised mode (Figure 3.29a). The double chopper system at D17 selectively controls the neutron wavelengths from 2 to 27Å, enabling an order of magnitude in Q to be measured in less than a minute. Samples were mounted vertically onto a sample stage (Figure 3.29b) and scattered neutrons were measured using a 2D detector capable of detecting both specular and off-specular scattering. Measurements were performed in air on solid thin film samples deposited onto circular silicon substrates (5cm in diameter,

Figure 3.29c). Incident angles of 1° and 4° were measured for 30 minutes and 100 minutes respectively providing a total measurable Q range of $0.008 < Q(\text{\AA}^{-1}) < 3.4$. The TOF wavelength distribution of a collimated, pulsed beam without the sample present (i.e. the direct beam) is first measured. The neutron intensity reflected from a sample is then measured using the TOF wavelength distribution and the reflectivity $R(Q)$ is ascertained as the ratio of the reflected and incident neutron intensities. The partial reflectivity curves measured at different angles are stitched together and scaled according to the instrumental scale factor (I_0).

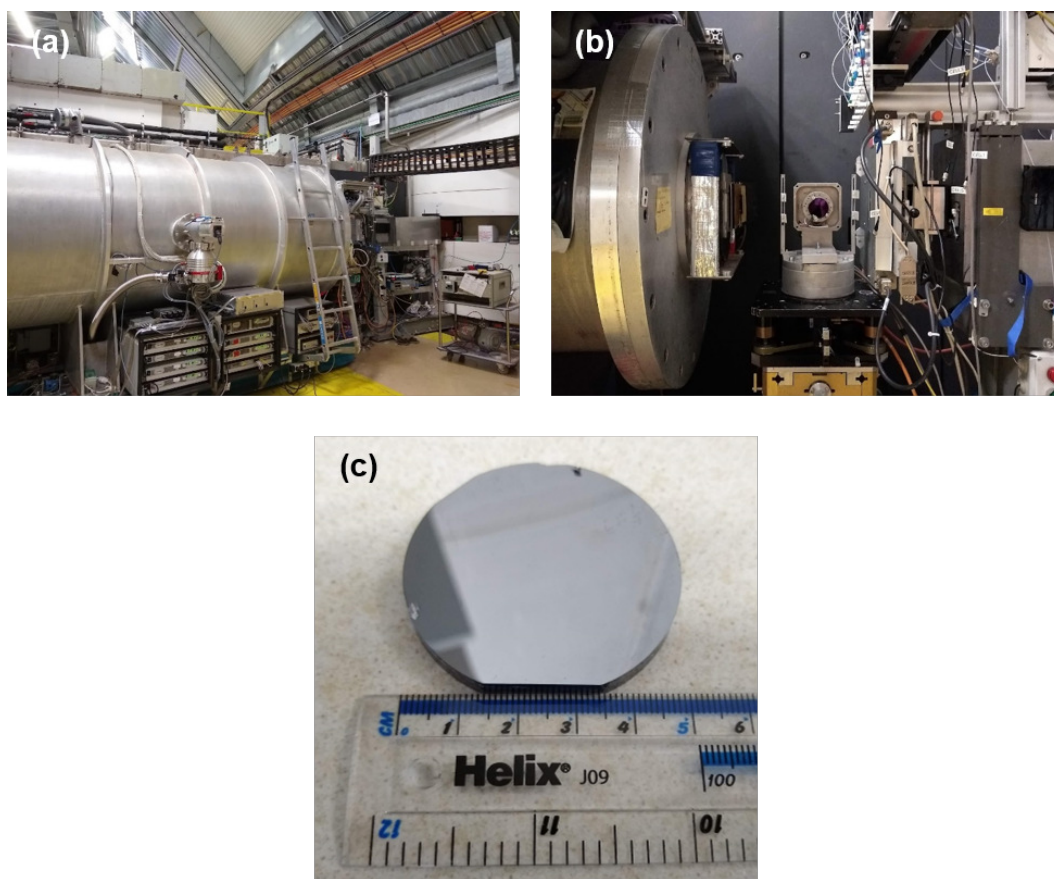


Figure 3.29: (a) The D17 reflectometer at Institut-Langevin. (b) A thin film sample mounted for measurement on D17. (c) A typical silicon substrate used for neutron reflectivity measurements. The sample measures 5mm in diameter and is approximately 0.5cm thick.

NR data fitting was performed using the open-software package GenX version 2.4 [181]. Samples were modelled by treating each layer as a single slab defined by three fit param-

ters: SLD (β_n), roughness (σ), and thickness (L). The instrumental resolution (dQ/Q) was kept constant at 2%. In practice, resolution varies with wavelength but changes between varying (dQ/Q) resolution and a fixed value produced insignificant changes in the fit parameters. Specific fit parameters are provided in the experimental chapters. The NR measurements in this thesis benefitted from beamtime awarded at the ILL under experiment numbers 9-11-1975 (DOI:10.5291/ILL-DATA.9-11-1927) and 9-11-1957 (DOI:10.5291/ILL-DATA.9-11-1957).

3.9.5 Small Angle Neutron Scattering

Small angle X-ray scattering (SAXS) and small angle neutron scattering (SANS) are characterisation techniques that probe the size, shape and number of scattering entities in a sample in transmission geometry. They have a broad range of applications for accessing the interior structure of samples from a few nanometers to a few microns [182]. X-rays or neutrons scattered by the sample are recorded with a 2D detector. The 2D scattering pattern is then radially averaged to produce a 1D $I(Q)$ vs Q intensity profile. In general, all small angle scattering studies concerns the analysis of this 1D intensity profile, which is usually modelled with a mathematical function to gain insight about the structure of the sample.

In this thesis, SANS was used to probe the two-phase system of BHJ blend films. The Lorentz-corrected scattering intensity (IQ^2 versus Q , also termed a *Kratky plot*) was used to identify a characteristic phase-separation length scale or long period L_p [183, 184]. For example, it has previously been used to characterise the long period of P3HT lamellae crystals, which corresponds to the mean average distance between lamellae domains, including the length of the P3HT crystals and the amorphous domains between them [105]. Here, the Q position of a correlation peak in the Lorentz-corrected intensity is related to L_p via:

$$Q = \frac{2\pi}{L_p} \quad (3.64)$$

Changes in the Lorentz-corrected scattering intensity are most easily understood by considering the integral of IQ^2 , known as the invariant [185, 186]. The invariant Q^* is linearly related to the electron density variance $\Delta\beta_x^2$ in the system:

$$Q^* = \int_0^\infty IQ^2 dQ \propto \langle \Delta\beta_x^2 \rangle \quad (3.65)$$

In the case of a two-phase OPV blend film, $\langle \Delta\beta_x^2 \rangle = \phi_A\phi_D(\beta_A - \beta_D)^2$ where ϕ_A and ϕ_D are the volume fractions of the donor and acceptor components and β_A and β_D are the corresponding SLDs. Given that, the measured scattering intensity is the result of

differences in SLD, a larger invariant corresponds to a higher degree of phase separation and domain purity.

To fit the 1D SANS intensity profiles of two-phase blend thin films, three, shape-independent models were used as outlined below. These models were chosen because they are relatively simple models with few parameters. Using such oversimplified models was necessary for the samples in this thesis as there was often limited or no a-priori structural knowledge of the blend films. Additionally, SANS measurements were performed on a stack of 15 samples which means the resultant scattering is an *average* representation of the thin film morphology. It should therefore be noted that the fit parameters extracted are characteristic of the *average* morphology but in reality, there is likely a distribution of these values.

1. Power Law Model

A power law model was used to extract the scattering exponent (α) values from the SANS curves. The scattering exponent contains information related to the interfaces of scattering entities. The model has the form [187]:

$$I(Q) = scale \times Q^{-\alpha} + B \quad (3.66)$$

where B is a flat background intensity and *scale* is simply a multiplication factor, not related to volume fraction. In a log-log $I(Q)$ vs Q plot, α is equivalent to the gradient of the SANS curve at high Q . α is related to the surface fractal dimension of the system D_s through $\alpha = 6 - D_s$ [105]. Systems characterised by sharp interfaces have a scattering exponent of $\alpha = 4$ and are said to exhibit *Porod behaviour*.

2. Debye-Anderson-Beuche (DAB) Model

The DAB model, a development of the earlier Debye-Bueche (DB) model, calculates the scattering from an ideal, random, non-particulate, two-phase system characterised by a correlation length ξ [188, 189, 190]. ξ is a measure of the average spacing between regions of two phases (1 and 2). The scattering intensity is expressed as:

$$I(Q) = scale \times \frac{\xi^3}{(1 + (Q\xi)^2)^2} + B \quad (3.67)$$

where B is the background intensity and *scale* is dependent on the SLD contrast or *scattering power* of the sample $\Delta\beta^2$ characterised by two phases with volume fractions ϕ_1 and ϕ_2 respectively:

$$scale = 8\phi_1\phi_2\Delta\beta^2 \quad (3.68)$$

The DAB model assumes a two-phase system containing only two regions of constant SLD with sharp phase boundaries of no measurable thickness. It therefore exhibits Porod behaviour ($I(Q) \sim Q^{-4}$) at large Q ($Q\xi \gg 1$). The DAB model was used in this thesis to characterise highly phase-separated, two-phase blend thin films for which the phases 1 and 2 represent the phases of the conjugated donor polymer and small molecule electron acceptor. However, caution should be taken as in reality no real material systems fulfils the criteria of an *ideal* two-phase system. For example, the assumption of sharp phase boundaries does not hold for systems that demonstrate diffuse interfaces or a high degree of intermixing so there will likely be deviations from the DAB model. In these cases, alternative models are used to characterise interfacial sharpness (e.g. Power Law, Guinier-Porod, Mass-Fractal and Unified Fit models). In addition, the DAB model, models two-phase systems using a single length scale and is therefore not suitable for systems that are composed of multiple characteristic length scales (e.g. hierarchical morphologies). Nevertheless, the simplicity of the DAB model is an attractive approach for modelling small angle scattering of two-phase OPV blend thin films as it relies only on three parameters and divergences from the model often manifest as systematic deviations [101, 191, 192, 193, 194].

To understand how ξ relates to the morphology of an irregular two-phase blend film, consider a two-phase random (non-particulate) system as shown in Figure 3.30. Here, transversal chords of alternating length L_1 and L_2 are defined as the distance that a line crossing the system in any arbitrary direction travels inside domains of phase 1 and 2 respectively [185, 191, 101]. Given the irregular shape of domains, there will be a distribution of chord length values. The average of these values ($\langle L_1 \rangle$ and $\langle L_2 \rangle$) and termed the *average chord length* (sometimes referred to as a *Porod length* or *transversal length*) can be calculated if the volume fraction of the phases is known by dividing the three-dimensional value of the correlation length ξ by the volume fraction of the *opposite* phase. This calculation makes several assumptions and should only be considered as a first-order estimation (e.g. the blend ratio of components in solution is often assumed to be the same as the volume fraction in the blend film). The summation of the average chord length of each phase is approximately equal to the *Porod length of inhomogeneity* [176]:

$$\frac{1}{l_p} = \frac{1}{\langle L_1 \rangle} + \frac{1}{\langle L_2 \rangle} \quad (3.69)$$

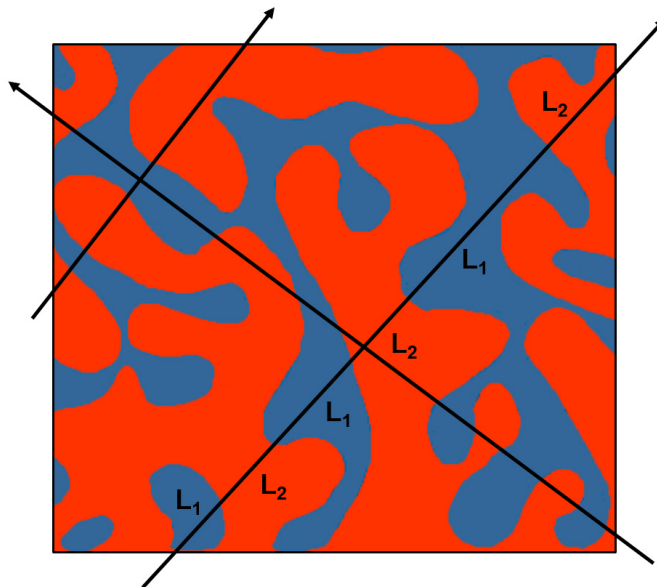


Figure 3.30: A two-phase random (non-particulate) system characterised by transversal chords of alternating length L_1 and L_2 between phase boundaries.

3. Guinier-Porod Model

The Guinier-Porod model is an empirical model that calculates the scattering for a generalised Guinier/power law object [195, 196, 197]. It can be used to determine the size and dimensionality of scattering entities and has the general form:

$$I(Q) = \begin{cases} \frac{G}{Q^s} e^{\left(\frac{-Q^2 R_g^2}{3-s}\right)} & Q \leq Q_1 \\ \frac{D}{Q^\alpha} & Q \geq Q_1 \end{cases} \quad (3.70)$$

where Q_1 , D and G are defined as:

$$Q_1 = \frac{1}{R_g} \sqrt{\frac{(\alpha - s)(3 - s)}{2}} \quad (3.71)$$

$$D = G e^{\left(\frac{-Q_1^2 R_g^2}{3-s}\right)} Q_1^{\alpha-s} = \frac{G}{R_g^{\alpha-s}} e^{\left(-\frac{\alpha-s}{2}\right)} \left(\frac{(\alpha - s)(3 - s)}{2}\right)^{\frac{\alpha-s}{2}} \quad (3.72)$$

α is the scattering exponent described above and R_g is the radius of gyration. R_g describes the SLD distribution from the scattering entity's SLD centre of mass [198]:

$$R_g^2 = \frac{\sum_i \beta_i (r_i - r_0)^2}{\sum_i \beta_i} \quad (3.73)$$

where β_i is the SLD at point i and r_i is the distance of point i from the centre of mass r_0 . R_g is well-known for common shapes such as solid sphere of radius R ($R_g = \sqrt{\frac{3}{5}}R$), a thin rod of length L ($R_g = \sqrt{\frac{1}{12}}L$) or a thin disk of radius R ($R_g = \sqrt{\frac{1}{2}}R$). The s parameter in Equation 3.70 is a dimensionality factor where $s = 0$ recovers the standard Guinier formula for 3D globular objects [198]:

$$I(Q) = scale \times e^{\left(\frac{-Q^2 R_g^2}{3}\right)} + B \quad (3.74)$$

$s = 1$ is for 2D symmetry and $s = 2$ for 1D symmetry.

The Guinier-Porod model was used in Chapter 5 to model 1D GISAXS data of OPV blends. For systems where the DAB model fails (e.g. intermixed systems with $\alpha < 4$), models such as the Guinier-Porod which fit a scattering exponent in addition to a characteristic length scale should be used. Given no a-priori information was known concerning the shape of scattering entities, only radii of gyration are provided.

Small Angle Neutron Scattering at ISIS

To provide a sufficient scattering volume, the majority of SANS measurements on solid films as reported in the literature have been performed on films that are much thicker ($1 - 2\mu m$) than those used in OPV devices ($\sim 80 - 100nm$) [183, 192, 105]. Although this is a relatively facile approach to enhancing the scattering volume, the processing conditions used to produce micron-thick films are often different to those used for device-relevant thicknesses (80-100nm). Such changes in processing conditions (e.g. deposition method, solid concentration etc.) can drastically affect the blend film nanostructure and any conclusions which relate back to device performance may be unreliable.

In this thesis the same method used by others is implemented [194, 101, 199], whereby a vertical stack of 15 device-relevant thick films are mounted in a holder. Assuming a beam diameter of 10mm and film thickness of 100nm gives a total active layer thickness of $\sim 1.5\mu m$ ($15 \times 100nm$) and a total sample volume of approximately $\sim 1.2 \times 10^8 \mu m^3$ ($1.5\mu m \times \pi \times 5mm^2$) which is much greater than the sample volume probed in grazing incidence and surface microscopy techniques and indeed that of SANS on a single micron-thick film ($\sim 7.9 \times 10^7 \mu m^3$). This approach whilst providing a sufficient scattering volume also crucially uses films that are processed in the same way as OPV device active layers allowing film nanostructure to be correlated with device performance more reliably. In this thesis, all OPV blend films prepared for SANS measurements were spin-coated onto either PEDOT:PSS or ZnO coated, 0.5mm thick, 15mm diameter quartz discs (Knight Optical WHQ 1500-C) (Figure 3.31b) following the same processing conditions as for OPV device

fabrication. 15 samples were then stacked vertically and mounted in an aluminium holder (Figure 3.31a) to generate a good signal to noise statistics in the SANS signal.

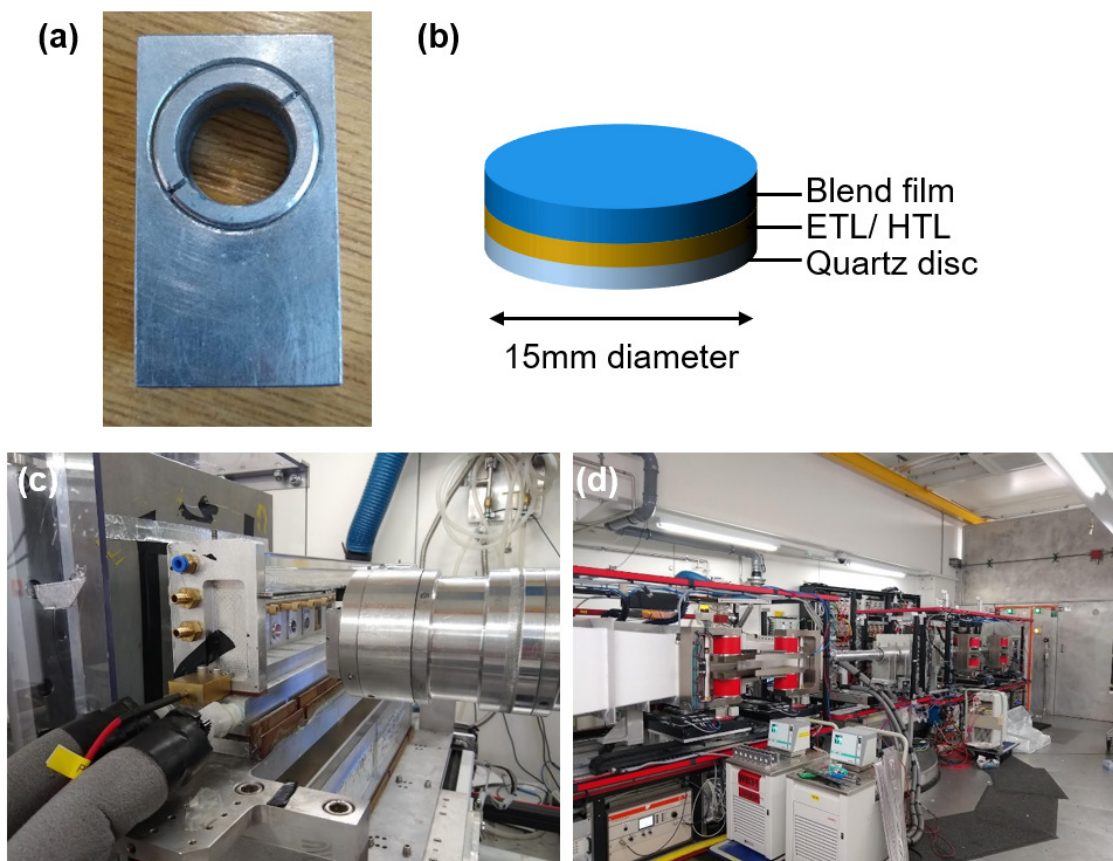


Figure 3.31: (a) Aluminium SANS sample holder for mounting quartz disc sample stacks. (b) An illustration of a single sample used in a sample stack. The blend film is deposited onto an ETL/HTL coated quartz disc. (c) SANS samples ready to be measured on Larmor. (d) The Larmor diffractometer at the ISIS neutron and muon spallation source.

All SANS measurements in this thesis were performed using the Larmor time-of-flight diffractometer at the ISIS neutron and muon spallation source (Figure 3.31) in Oxfordshire. Larmor utilises neutrons with a wavelength between 0.9 and 13.0\AA and is capable of probing a Q -range of $0.003 \leq Q (\text{\AA}^{-1}) \leq 0.7$. For all measurements, the beam diameter was collimated to 10mm at the sample. Each sample was measured for approximately 4 hours to provide high statistical precision. The background sample consisted of a stack of 15 PEDOT:PSS or ZnO coated quartz discs without active layer films.

Each raw scattering data set was radially averaged and corrected for sample transmission, background scattering and detector efficiency. Corrected data was converted to scattering cross-sectional ($\partial\sigma/\partial\Omega$) data using Mantid software [200] and plotted on an absolute scale (cm^{-1}). Initially, the data was reduced by the total thickness of the quartz ($15 \times 0.5mm$) and so it was necessary to scale the SANS signal to account for the total active layer film thickness. To do this, the thickness of a few films from each sample were measured using Dektak profilometry and averaged. SANS intensities were then multiplied by a factor of $(15 \times 0.5mm)/(15 \times L)$ where L is the average film thickness for each sample (see [201] for more details about data reduction at ISIS). Finally, the corrected, scaled data was fitted with appropriate models using SasView software (Version 4.1.2) [202] and evaluated based on the χ^2/N_{pts} value (Equation 3.63). The SANS measurements in this thesis were made possible through beamtime awarded under experiment numbers RB1920285 (DOI:10.5286/ISIS.E.RB1920285) and RB201389 (DOI:10.5286/ISIS.E.RB201389) at the ISIS neutron and muon spallation source.

3.9.6 Grazing Incidence X-Ray Scattering

The same diffraction and scattering principles discussed previously can be applied to thin film samples in grazing-incidence geometry. The experimental geometry for grazing incidence X-ray wide angle scattering (GIWAXS) and grazing incidence small angle scattering (GISAXS) measurements is shown in Figure 3.32. The translation of transmission SAXS to a grazing incidence geometry measurement emerged in the late 1980s as a method for studying nanoparticle self-assembly in weakly scattering organic thin films [203]. This has since been extended to studying a diverse range of material systems and thin film morphologies [204]. The ability to capture a large area of reciprocal space in a single measurement has improved diffraction studies, with the development of *GIWAXS* [104, 205]. In a typical experiment, X-rays impinge a thin film sample at a *grazing* angle θ_i ($\sim 0.1 - 0.2^\circ$ for organic films), and the scattering is defined by an out-of-plane angle θ_f and in-plane angle ϕ . The scattered X-rays are detected by a 2D detector positioned $\sim 300mm$ and $\sim 1200mm$ from the sample for GIWAXS and GISAXS respectively allowing a broad range of length scales to be probed ($\sim 0.1 - 10nm$ for GIWAXS and $\sim 10 - 200nm$ for GISAXS). In this geometry, the scattering vector Q is defined as $\mathbf{Q} = (Q_x, Q_y, Q_z)$ where the components are equal to:

$$Q_x = \frac{2\pi}{\lambda}(\cos(\phi)\cos(\theta_f) - \cos(\theta_i)) \quad (3.75)$$

$$Q_y = \frac{2\pi}{\lambda}(\sin(\phi)\cos(\theta_f)) \quad (3.76)$$

$$Q_z = \frac{2\pi}{\lambda}(\sin(\theta_i) + \sin(\theta_f)) \quad (3.77)$$

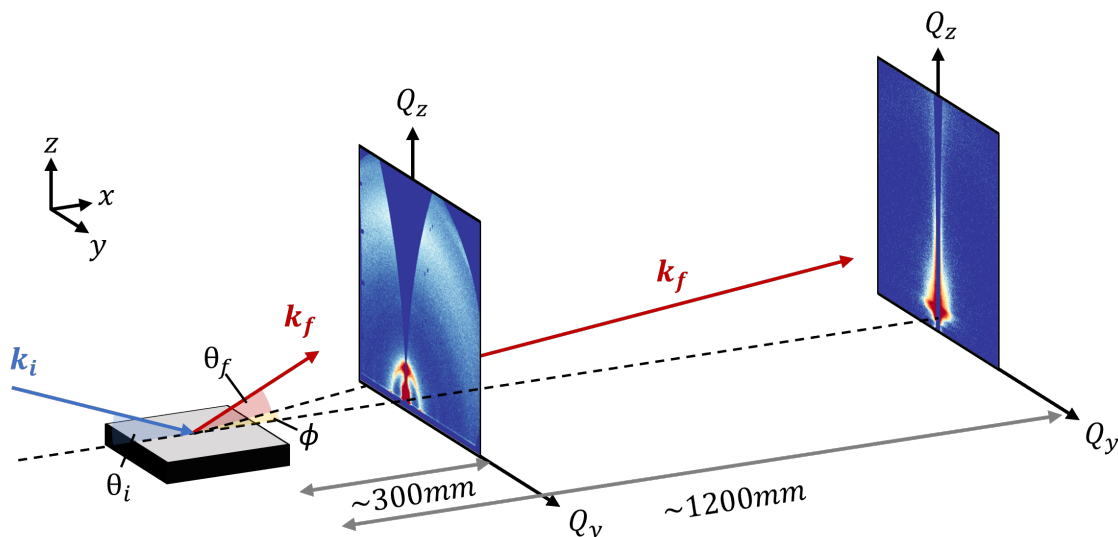


Figure 3.32: The scattering geometry for grazing incidence X-ray scattering measurements. The sample is inclined at an angle θ_i with respect to the incident beam with wave vector \mathbf{k}_i . X-rays are scattered with wavevector \mathbf{k}_f in a direction defined by angles 2θ and ϕ and are detected by a detector positioned $\sim 300\text{mm}$ and $\sim 1200\text{mm}$ from the sample for GIWAXS and GISAXS respectively.

In addition to probing a broad range of characteristic length scales in a sample, grazing incidence X-ray scattering measurements also allow depth-dependent information to be collected. The incident X-ray beam can be strongly refracted at the film/vacuum interface and can be reflected at the film-vacuum and/or film/substrate interfaces. These effects give rise to waveguiding or standing wave effects. For example, consider the following cases concerning the incident X-ray angle (θ_i) and critical angle of the material (θ_c):

- $\theta_i < \theta_c$: The X-ray beam is totally reflected but the transmitted beam travels in the plane of the film, trapped at the film/vacuum interface. X-rays do not penetrate into the film except for a short-range evanescent wave that travels through the top few nanometers of the film. Scattering intensity arises only from surface structures.
- $\theta_i \sim \theta_c$: The X-ray beam is refracted such that it travels within the plane of the film leading to a strong increase in scattering intensity. A waveguiding effect is produced due to strong reflection from the film/vacuum and film/substrate interfaces.
- $\theta_i > \theta_c$: The X-ray beam is refracted penetrating the film. Depending on the refractive index of the substrate and the incident angle, the X-ray beam will likely

be completely reflected at the film/substrate interface and partially reflected at the film/vacuum interface as it exits the film. The high probability of multiple-reflection events between the top and bottom interfaces results in interference giving rise to a standing wave within the film. Scattering intensity therefore arises from the bulk structure of the film.

This is demonstrated by considering the penetration depth of an X-ray into a typical OPV film such as pure ITIC (Figure 3.33). At incident angles below the critical angle $\theta_c \sim 0.14^\circ$, X-rays only penetrate the top $\sim 5\text{nm}$ of the film and so the measurement is *surface-sensitive*. At incident angles greater than the critical angle, X-rays can penetrate $\sim 10 - 100\mu\text{m}$ into the film, probing the entire film thickness and so the measurement is *bulk-sensitive*. For most grazing incidence X-ray scattering measurements in this thesis, incident angles approximately equal to the critical angle of the sample were chosen to probe the entire film thickness and maximise scattering intensity.

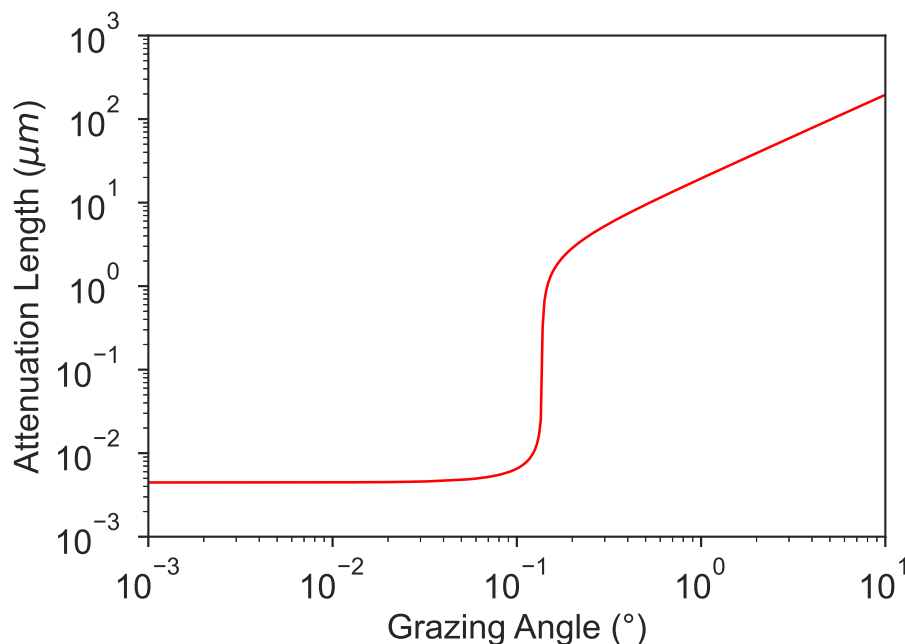


Figure 3.33: X-ray attenuation length as a function of grazing angle for pure ITIC with $\rho = 1.11\text{g}/\text{cm}^3$ and an X-ray energy of 9.24keV . Data was calculated using an online tool [206].

Grazing incidence X-ray scattering is a particularly useful technique for probing the degree of order and orientation of scattering entities within a film. This is demonstrated in

Figure 3.34 where the relationship between real and reciprocal space is considered for a face-on arrangement of lattice planes with various degrees of orientational order. A film consisting of randomly aligned planes (i.e. unoriented) does not exhibit any dependence on the azimuthal angle (χ) away from the normal, out-of-plane direction and the 2D scattering pattern is composed of isotropic Debye-Scherrer rings. A film which is composed of predominantly face-on oriented planes will scatter more strongly out-of-plane (Q_z direction in reciprocal space) and the scattering will appear as broad arcs. For a highly oriented film with a high degree of face-on orientational order, the scattering is centred out-of-plane, appearing as well-defined Bragg spots. This concept can be extended to planes aligned in other orientations. For example, a highly oriented edge-on assembly of planes will scatter in-plane (the Q_y direction in reciprocal space).

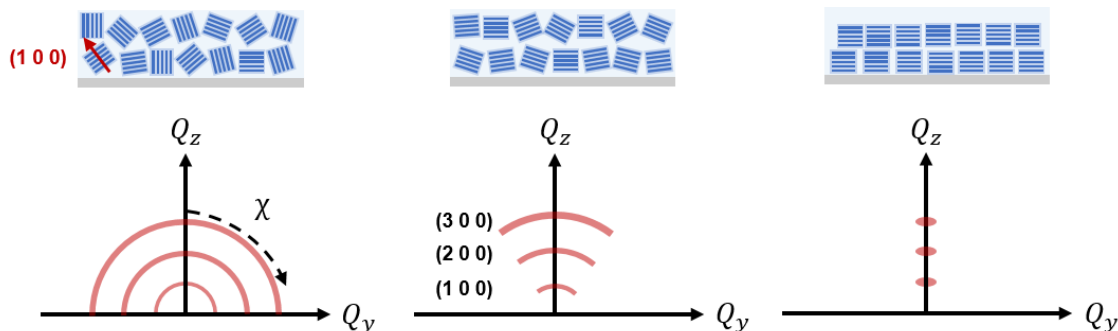


Figure 3.34: An illustration of the relationship between lattice plane orientation in real space (top row) and the resulting angular distribution of scattering in reciprocal space (bottom row) for a random orientation of planes (left), a predominantly face-on orientation (centre) and a highly ordered face-on orientation (right).

3.9.7 Grazing Incidence X-ray Scattering at Sheffield

All GIWAXS and GISAXS measurements in this thesis were performed in The Department of Chemistry at The University of Sheffield using a Xenocs Xeuss 2.0 SAXS/WAXS beamline. The layout of the instrument is displayed in Figure 3.35. This instrument is equipped with a liquid gallium MetalJet source (Excillum) capable of producing 9.24keV ($\lambda = 1.34\text{\AA}$) X-rays. X-rays were collimated onto the sample at an incident angle of $\theta_i = 0.16^\circ$ for all measurements in Chapter 4, Chapter 5 and Chapter 6 and $\theta_i = 0.15^\circ$ for measurements in Chapter 7.

Scattered X-rays were detected using a Pilatus 1M (Dectris) detector positioned approximately 300mm and 1200mm from the sample position for GIWAXS and GISAXS measurements respectively. Sample to detector distances were calibrated using a silver behenate (AgBe) standard and all measurements were performed with the sample chamber and flight path under vacuum to reduce background air scatter. Typically, samples were deposited onto quartz coated glass substrates (Ossila - S211) or unpatterned ITO glass substrates (Ossila).

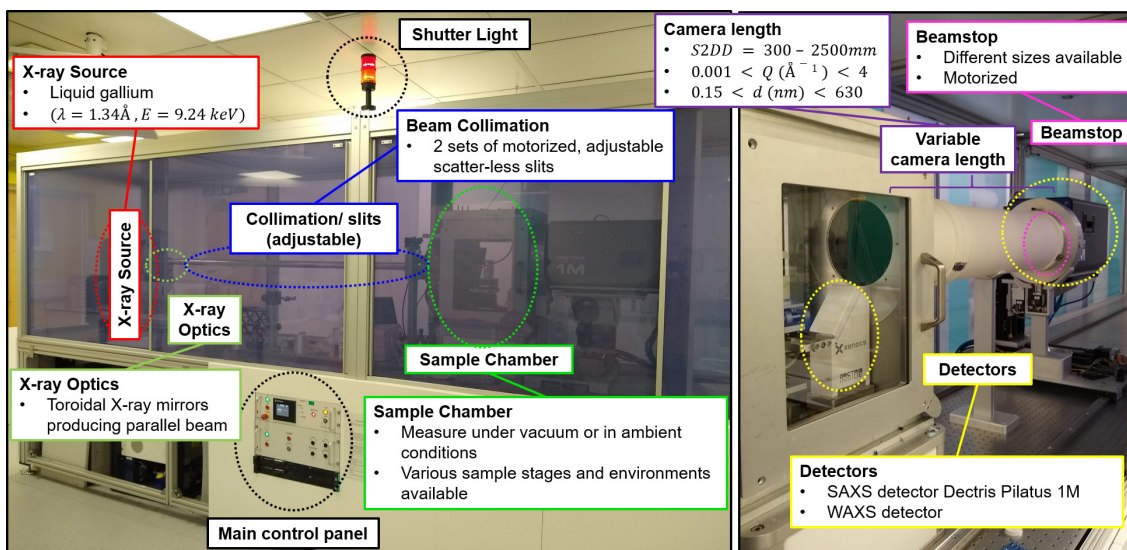


Figure 3.35: Layout of the Xeuss 2.0 SAXS/WAXS instrument.

Data Processing

Data processing for GIWAXS and GISAXS measurements can be divided into two parts: (1) 2D image correcting and reshaping and (2) extracting 1D intensity profiles. All grazing incidence X-ray scattering data in this thesis were processed using the GIXSGUI Matlab toolbox [207].

A typical corrected, reshaped 2D GIWAXS pattern is shown in Figure 3.36a. In a GIWAXS experiment, the intensity measured by the detector is the projection of the reciprocal lattice intercepted by the Ewald sphere onto the detector plane. To represent the 2D GIWAXS pattern using orthogonal reciprocal space axes (e.g. Q_z vs Q_r), it is necessary to reshape the image. This leads to a blank space or *missing wedge* on the 2D image which represents the Q region which cannot be probed at a fixed incident angle [207] (Figure 3.36a). Other image corrections account for the detector efficiency, path attenuation and pixel-to-pixel sensitivity.

After the 2D GIWAXS pattern has been corrected and reshaped, the image is typically azimuthally integrated in some way to generate 1D intensity profiles. Common integration areas are shown in Figure 3.36a along with the corresponding 1D intensity profiles in Figure 3.36b and Figure 3.36c. For Q -dependent intensity profiles, integrations are often performed across out-of-plane and in-plane sectors to probe scattering from planes aligned parallel and perpendicular to the substrate respectively (i.e. face-on and edge-on) (Figure 3.36b). For samples that exhibit preferential orientation, χ -dependent profiles are useful for probing the orientation of scattering entities with the same Q value such as those from equivalent lattice planes in a unit cell or from samples which contain multiple orientations (Figure 3.36c).

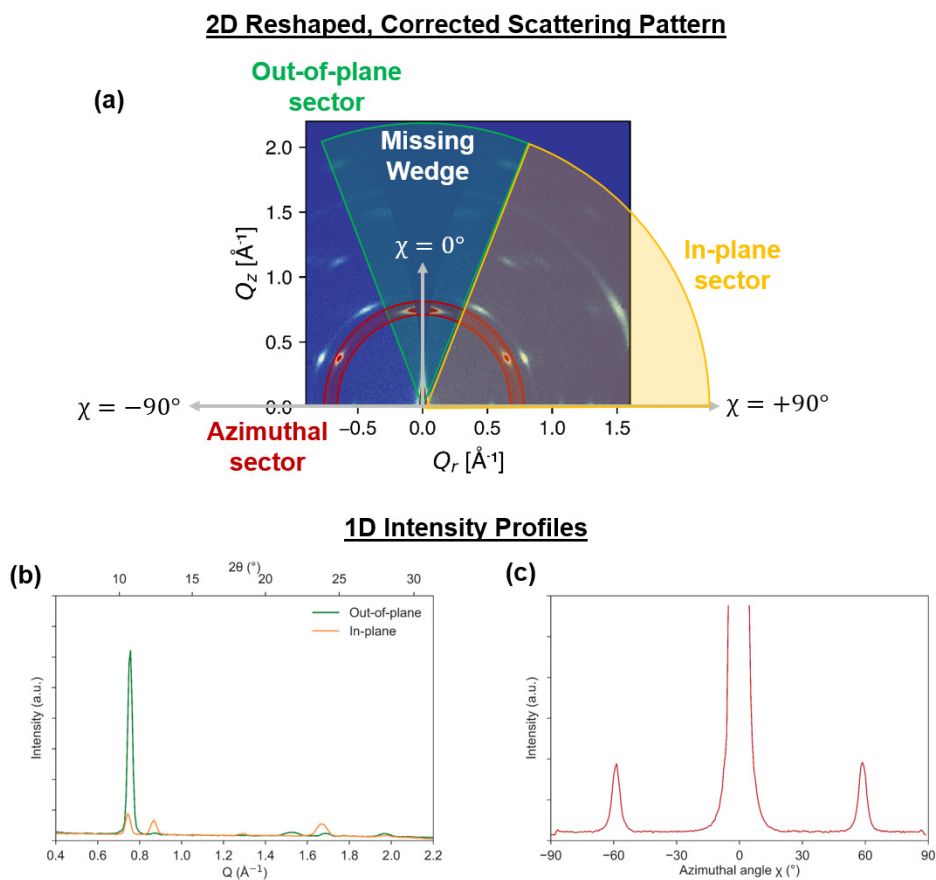


Figure 3.36: (a) A diagram showing typical integration areas of a 2D GIWAXS pattern. (b) Azimuthally integrated Q -dependent intensity profiles corresponding to the out-of-plane and in-plane sectors in (a). (c) Azimuthally integrated χ -dependent intensity profile corresponding to the azimuthal sector in (a).

Crystalline coherence lengths CCL were estimated from peaks in the 1D GIWAXS Q -dependent intensity profiles using Scherrer analysis [208]. CCL is an estimate of the average size of coherently scattering regions within the film calculated using the Scherrer equation:

$$CCL = \frac{\kappa\lambda}{W\cos\theta} \quad (3.78)$$

where W is the full width half maximum (FWHM) of the peak, θ is the scattering angle associated with the peak, λ is the X-ray wavelength and κ is a dimensionless shape factor equal to 0.94 for most organic materials [209]. Values for W and θ were extracted from fitting the GIWAXS peak with either a Gaussian or a Lorentzian function.

For GISAXS, 2D patterns were corrected in the same way as 2D GIWAXS patterns. A typical processed 2D GISAXS pattern is shown in Figure 3.37a. At smaller scattering angles (i.e. smaller Q values), the missing wedge correction discussed above becomes less important. The scattering enhancement highlighted in the red shaded box is the Yoneda region [210, 106]. This enhancement arises when $\theta_i = \theta_c$ because the incident and reflected standing waves reach a maximum [106].

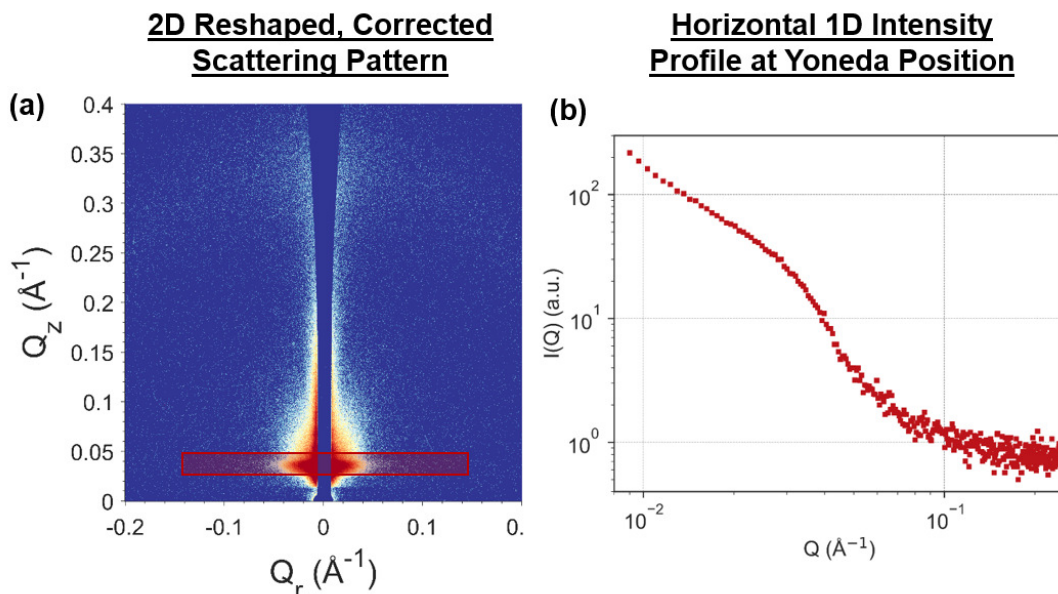


Figure 3.37: (a) A typical 2D GISAXS image with the Yoneda region shaded in red. (b) A 1D GISAXS horizontal linecut performed by integrating across the Yoneda region shown in (a).

Analysis of GISAXS typically involves taking a horizontal linecut at the Yoneda region, generating a 1D intensity profile (Figure 3.37b). For two-phase blend systems, the 1D intensity profile is then typically modelled using similar functions as for small angle scattering data (see Subsection 3.9.5). For thin films with well-defined nanoparticle assemblies, the 2D GIWAXS data can be modelled using various software (e.g. *BornAgain* [211], *IsGISAXS* [212], *SimDiffraction* [213]). It should be noted that in this thesis, GISAXS and GIWAXS profiles are the scattering intensities after applying standard corrections to the 2D image (detector efficiency, path attenuation, polarization etc. [207]). They have not been corrected for background and are therefore displayed in arbitrary units (*a.u.*). This is in contrast to SANS measurements which are shown in absolute units (cm^{-1}) as it was possible to correct the SANS intensities for background, transmission and film thickness.

Peak Indexing

The majority of GIWAXS data presented in this thesis was collected on amorphous or semi-crystalline organic thin films that often do not exhibit the same molecular arrangement as their reported bulk crystal structures. This can make peak indexing difficult. For these samples, peak indexing was performed by comparing with literature results and previously indexed molecular structures. In Chapter 7, the samples of interest are considerably more crystalline and peaks could be indexed using the crystallographic information file (CIF) of the reported bulk crystal structure. This was done using the three-dimensional nanostructure indexing application in GIXSGUI [207]. This program allows the expected scattering reflections to be simulated for any of the unit cells in the 230 crystallographic space groups described previously. In comparison to standard crystallographic indexing, the refraction and reflection effects at interfaces in thin film samples are considered. This is done using the *Diffraction* analysis tool (Figure 3.38a) where the unit cell parameters (a , b , c , α , β , and γ) can be inputted along with a unit cell orientation vector $[uvw]$. After inputting suitable parameters, the expected reflection positions in reciprocal space are calculated (i.e. Q_{xy} and Q_z values) and can be overlaid onto an experimental 2D scattering pattern (Figure 3.38b).

2D Simulations

In addition to 2D peak indexing in GIXSGUI, 2D diffraction patterns can be simulated using *WAXS* mode in *SimDiffraction*, a Matlab toolbox created and maintained by Dag Breiby [213]. This software was particularly useful for understanding the experimental GIWAXS data presented in Chapter 7. For the 2D simulations performed in Chapter 7, all samples were simulated using a uniaxial model with a pseudo-Voigt (PSV) distribution in the out-of-plane direction. The following corrections were applied: specular Lorentz correction, isotropic polarisation correction, Yoneda correction and structure factor correction

determined from relative atomic positions. Additionally, the following *SimDiffraction* parameters were kept constant for each simulation: the instrumental peak width (0.03\AA^{-1}), peak shape (0.2). See the *SimDiffraction* software manual for further details [213]. Key simulation parameters relating to the molecular order and orientation of the sample are discussed in Chapter 7.

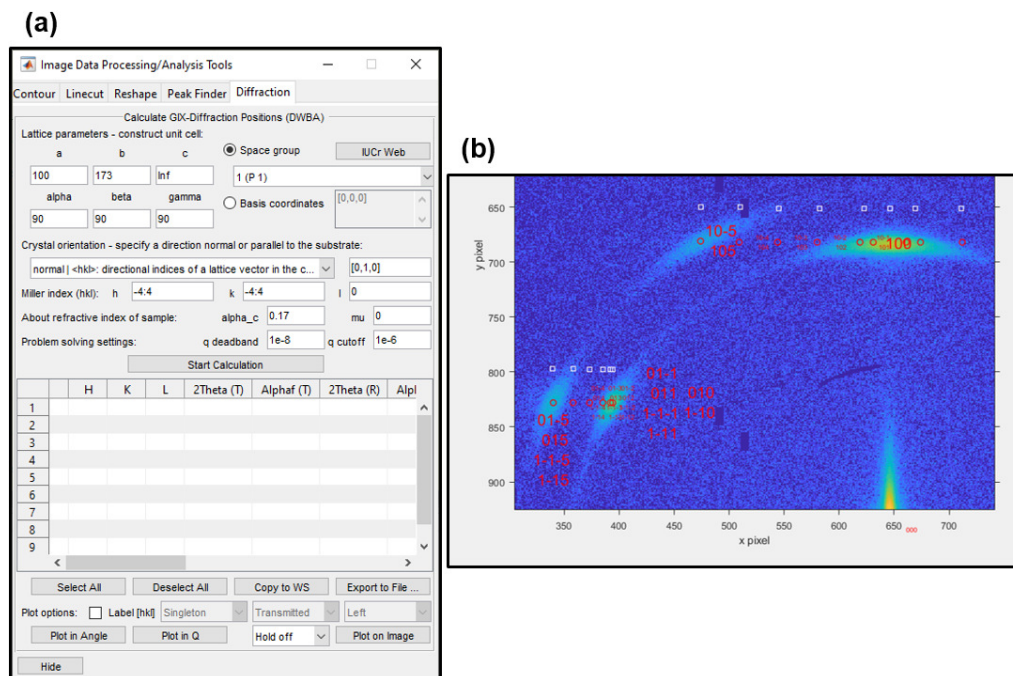


Figure 3.38: (a) The 2D nanostructure indexing application using the *Diffraction* analysis tool in GIXSGUI [207]. (b) An example of reflections simulated using a hexagonal crystal structure, which are overlaid on an experimental 2D GIWAXS pattern.

The general workflow for *SimDiffraction* consists of the following steps:

1. Load the 2D GIWAXS image and configure the image in the correct rotation and beam centre (Figure 3.39a).
2. Input instrument settings such as the sample-to-detector distance, beam centre, incidence angle, pixel size and X-ray wavelength (Figure 3.39c).
3. Input image settings such as the image size, Q_{xy} range and Q_z range (Figure 3.39c).
4. Apply any necessary corrections such as Lorentz correction, polarisation, Yoneda correction etc. (Figure 3.39c).

5. Read in CIF file and input appropriate hkl ranges and axis oriented along Q_z (Figure 3.39b).
6. Input simulation settings such as the preferred orientation model and out-of-plane parameters (Figure 3.39d).
7. Simulate 2D GIWAXS pattern using the polycrystalline film function (Figure 3.39e).

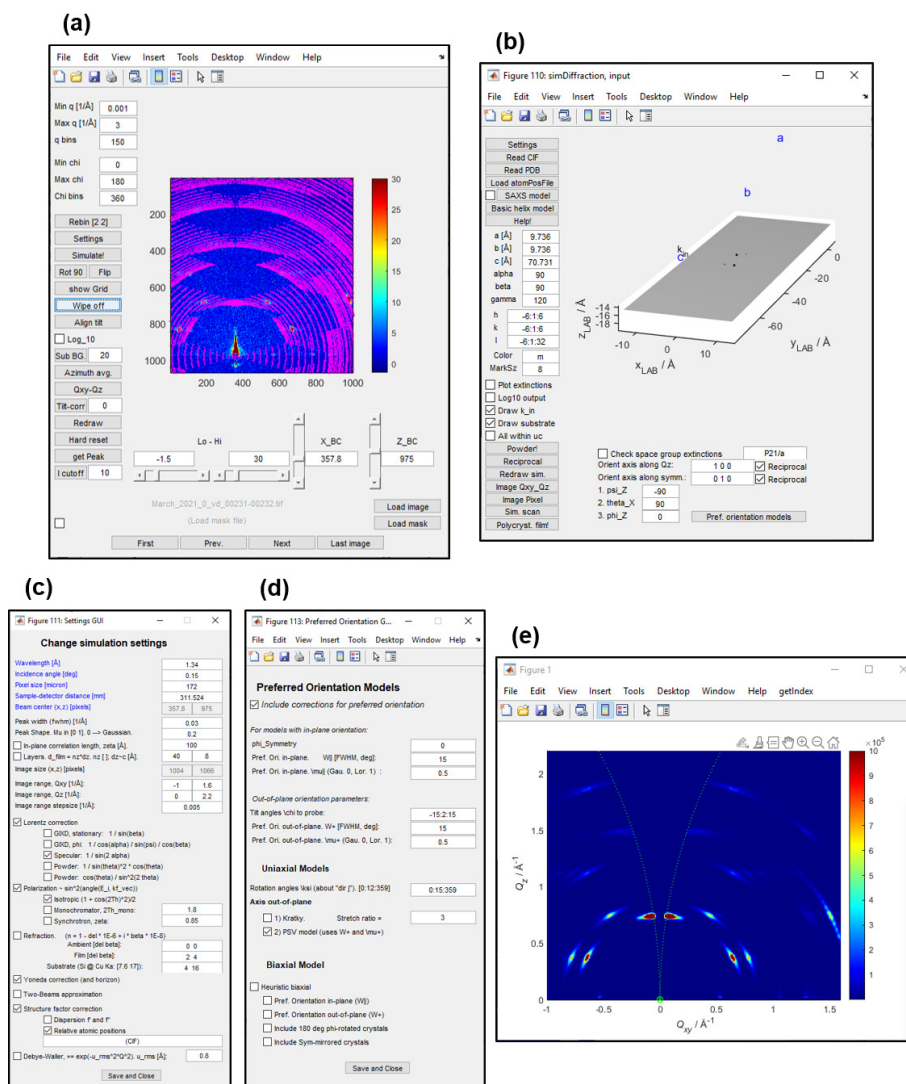


Figure 3.39: Screenshots of the *simDiffraction* Matlab package used to simulated 2D GIWAXS patterns.

Correlating Nanostructure with Optoelectronic Functionality in PBDB-T : ITIC Organic Photovoltaics with Non-Halogenated Solvents

4.1 Foreword

The fabrication of high efficiency polymer : NFA OPV devices typically relies on the use of halogenated processing solvents which have health and cost related concerns. To ensure large-area solution processing is practically viable, the environmental and health-related impact of halogenated solvents must be addressed. However, finding safer, more environmentally-benign processing solvents that deliver the same PV performance and operational lifetime remains one of the greatest challenges to industrial scale OPV manufacture.

In this chapter, I investigate the impact of processing solvent on the morphology and optoelectronic functionality of PBDB-T : ITIC based OPV devices. Specifically, two non-halogenated processing solvent systems (o-xylene and a carbon disulfide : acetone co-solvent blend) are compared to two halogenated processing solvents (chlorobenzene and chloroform). The findings demonstrate the feasibility of non-halogenated solvents for rapid, large throughput manufacturing, necessary for the commercialisation of OPV.

4.2 Author Contributions

In this chapter, all structural characterisation measurements (GIWAXS, GISAXS and AFM) were performed and analysed by myself. OPV devices were fabricated and tested by Emma L. K. Spooner. Samples for PL and UV-Vis absorption studies were made by myself and measurements were performed by Emma L. K. Spooner. The analysis and interpretation of PL and absorption measurements was performed by myself. Exciton diffusion measurements and modelling were performed by collaborators at Minnesota University (Kaicheng Shi, Janet A. Christenson, Ronald L. Christenson and Russel J. Holmes). DSC and TGA measurements were collected through the Thermal Analysis Service at The Department of Chemistry, University of Sheffield. The interpretation and write-up of all results detailed in this chapter was performed by myself under the supervision of Andrew J. Parnell.

4.3 Introduction

The highest efficiency organic solar cells typically rely on the use of pernicious halogenated processing solvents and solvent additives [32, 214, 215, 216, 217, 33]. To be commercially viable, it is critical that the fabrication of devices can be made rapid, scalable and inexpensive. Each of these requirements are made more complex through the use of halogenated processing solvents. As a result, there is currently a large research effort focused on sourcing OPV processing solvents which do not contain halogen atoms (F, Cl, Br and I) (i.e. non-halogenated) that deliver a comparable (or improved) PV performance and operational stability to halogenated alternatives. In the literature, non-halogenated solvents are often labelled as *green* or *eco-friendly* [218, 219, 220] but this can be misleading given that they also possess their own potential health, cost and environmental risks.

OPV processing solvents can be separated into four groups: (1) Halogenated solvents, (2) Aromatic non-halogenated solvents, (3) Non-aromatic non-halogenated solvents and (4) Linear polar solvents (alcohols and water). Halogenated solvents can be both aromatic (e.g. chlorobenzene) and non-aromatic (e.g. chloroform) but they are grouped together here for simplicity. The highest efficiency organic solar cells typically rely on the use of pernicious aromatic Group 1 solvents and solvent additives [32, 214, 215, 216, 217, 33] because they are compatible with the extended aromatic structures of most active layer components. However, the harmful, health-related impact of these solvents is an increasing concern as OPV technologies push towards commercialisation [221].

Chloroform, for example is regarded as a human carcinogenic substance [222] and other noxious halogenated solvents such as chlorobenzene, o-dichlorobenzene and dichloromethane can be harmful to specific vital organs in animals and humans [223, 224, 225, 226]. The toxicity of a solvent is often described using a median lethal dose (LD50) value. This is defined as the dose of a substance (per kilogram of body weight) required to kill half of the tested animal population (usually rats) within a certain time period. The LD50 values for a range of solvents from each of the four groups described above is presented in Figure 4.1. Here a low LD50 value corresponds to a smaller dose required to kill 50% of the population (i.e. more toxic). As can be seen halogenation generally leads to solvents with a higher toxicity, however lack of halogenation alone does not ensure less toxicity. For example, tetrahydrofuran (THF) is a Group 3 solvent but has a lower LD50 value than dichloromethane (DCM), a Group 1 solvent. Other health-related risks should also be considered such as the potential damage to the reproductive system associated with N-methyl-2-pyrrolidone (NMP) and CS₂ [227, 228] or the risk of blindness from methanol inhalation [229].

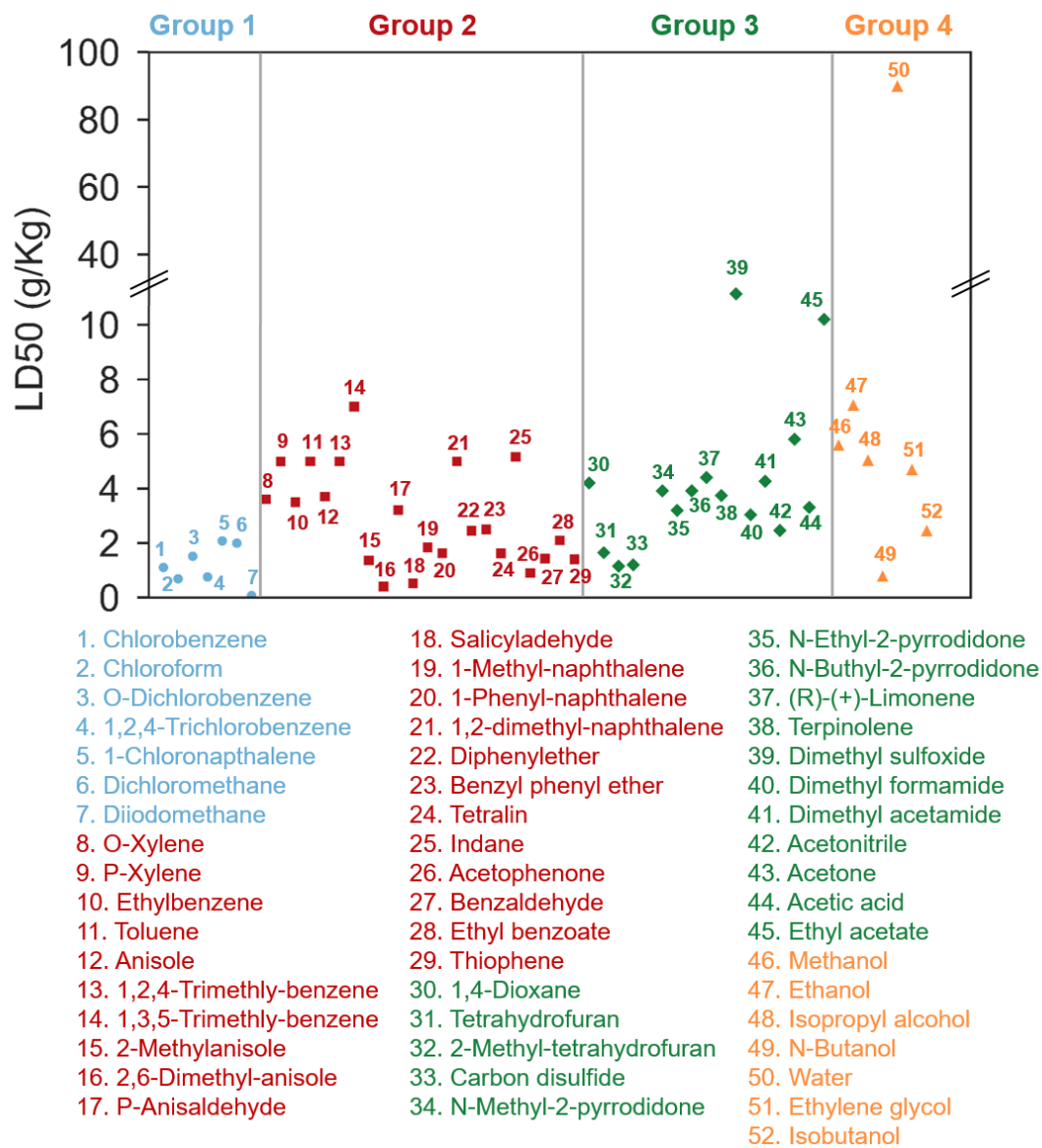


Figure 4.1: LD50 values for halogenated solvents (Group 1), aromatic non-halogenated solvents (Group 2), non-aromatic non-halogenated solvents (Group 3) and linear polar solvents (Group 4). Data was compiled from various sources [218, 230, 231].

In addition to negative health effects and toxicity, it has recently been reported that rises in global chloroform emissions are detrimental to the recovery of the stratospheric ozone layer [232, 233]. The management of such hazardous substances at the quantities required for large-scale production will therefore require strict industrial regulations and waste handling protocols to avoid severe eco-toxicological effects. Whilst there are safe ways to use dangerous solvents in industrial processes, they add significant cost and complexity. [221, 234, 235].

The economic impact of halogenated processing solvents should also be considered. It has been estimated that the cumulative thermal energy required to produce 16 million litres of chlorobenzene for 1GW of power through the Process one method [27] is 880TJ compared to 17TJ if water is used instead [26]. Such differences in embedded energy impact the EPBT of the solar cell with chlorobenzene contributing an additional 10 days and water adding only 4h [26]. It is therefore of industrial importance to phase-out the use of halogenated processing solvents to improve the cost, scalability and practical viability of OPV technologies.

The PV performance of OPV devices processed from non-halogenated solvents is typically inferior to those processed from halogenated solvents. However, both solvent groups have shared similar surges in *PCE* over the last decade as discussed in several review articles [218, 236, 237, 220, 219]. The selection of processing solvent must be carefully considered as there are a number of properties which can impact the film drying kinetics and morphology (e.g. boiling point, vapour pressure, polarity, miscibility, solubility and surface tension). The primary consideration is the solubility of the solute in the solvent. This is often determined through a trial and error approach [238] but a more empirical evaluation is to use Hansen Solubility Parameters (HSPs) [239, 240]. The HSPs of a material are δ_D , δ_D and δ_D , which correspond to the dispersive, permanent dipole-dipole and hydrogen bonding intermolecular forces respectively. The three parameters define coordinates in three-dimensional Hansen space. The distance between two points 1 and 2 in Hansen space (e.g. for a solute and solvent) is termed the radius of interaction R_a and is expressed as:

$$R_a = \sqrt{4(\delta_{D1} - \delta_{D2})^2 + (\delta_{P1} - \delta_{P2})^2 + (\delta_{H1} - \delta_{H2})^2} \quad (4.1)$$

where the subscripts 1 and 2 represent the two substances respectively [238]. A small R_a value is representative of substances with similar chemical properties (e.g. a solute that is soluble in an appropriate solvent). Each substance is also defined by its own radius of solubility in Hansen space (R_0). If the HSP coordinates of a solvent are located within the Hansen sphere of the solute it is considered a good solvent whereas those located outside are considered poor solvents. This is often quantified geometrically through the relative energy difference (*RED*) value given by:

$$RED = \frac{R_a}{R_0} \quad (4.2)$$

$RED > 1$ indicates poor solubility whereas $RED < 1$ indicates good solubility. In general, substances which have similar chemical properties to each other (e.g. an aromatic solvent and aromatic solute or a non-polar solvent and non-polar solute) are considered compatible due to strong molecular interactions.

Studies focusing on non-halogenated processing solvents have therefore primarily focused on aromatic Group 2 solvents as they have similar chemical properties to most conjugated, aromatic organic materials. For polymer : fullerene systems, $>10\%$ $PCEs$ have been achieved using Group 2 solvents such as o-xylene [241, 242, 243, 244], toluene [245] and 1,2,4-trimethylbenzene [246]. However, for some systems, the BHJ morphology is non-ideal [247, 248] and high $PCEs$ are often only achieved through the use of solvent additives which are often halogenated [101] and detrimental to the long-term operational stability of the device [126, 123]. There has also been some success using non-aromatic, non-halogenated (Group 3) solvents such as CS_2 [249] and a CS_2 : acetone blend [239] in polymer : fullerene systems. However, the poorer solubility of fullerenes in non-aromatic solvents and restricted chemical modification has limited further advancements.

With the advent NFAs, there is a greater potential for chemical modification providing strategies to improve the solubility and processability of NFA systems with both aromatic and non-aromatic halogenated solvents. Polymer : NFA systems have achieved $PCEs >16\%$ for devices processed using Group 2 solvents such as o-xylene [250, 251, 252] and toluene [253, 254]. In addition to this, several systems processed from Group 3 solvents such as THF [255, 256, 257, 258], anisole [259], 2-MTHF [260, 261] and limonene [262] have demonstrated promising $PCEs >10\%$. Further efforts to improve performance in Group 3 solvents focuses on the chemical design of NFAs and conjugated polymers to improve their solubility in less harmful solvents whilst maintaining high PV performance. A key research focus is the alteration of side-chain chemical moieties given their role in determining the solubility, crystallinity and optoelectronic properties of a molecule [263].

The performance of OPVs processed from the ultimate eco-friendly, Group 4 polar solvents such as water or alcohols remains largely inferior to devices processed from the other solvent groups due to poor solubility. However, over the past decade there have been pioneering research efforts to improve this. For example, OPVs incorporating water-dispersible nanoparticles (NPs) as the photoactive layer have recently demonstrated $PCEs$ as high as 7.50% for a polymer : NFA based system [264]. In a separate study, the substitution of polymer side-chains with hydrophilic moieties achieved a PCE of 2.51% in a fullerene-based system processed from a water : ethanol blend [265]. Although these achievements

are promising, the *PCE* of water/alcohol processed devices remains significantly lower than devices processed from Group 1-3 solvents.

The primary obstacle in finding compatible solvents appears to be the trade-off between solubility and morphology. As side-chains are extended or functionalised to increase solubility, the molecular π - π stacking is often disrupted leading to an unfavourable nanomorphology that is detrimental to device performance. On the other hand, solubility that is too high can lead to nanomorphologies that are too finely intermixed and suffer from severe charge carrier recombination [218]. In addition to solubility, the drying dynamics of the photoactive film are strongly linked to the properties of the processing solvent. For example, high boiling point solvents increase the film drying time, which can lead to excessive crystallisation, domain over-purification and domain sizes that are much larger than the exciton diffusion length [102, 123]. As a result, additional strategies such as solvent additives [101], thermal annealing [153] and solvent annealing [154] are often employed to finely tune the drying kinetics of the film and gain further control of the self-assembled morphology.

In this chapter, the impact of four different processing solvent systems (chlorobenzene, chloroform, o-xylene and a CS₂ : acetone solvent blend) on the nanostructure, PV performance and optical properties of a prototypical polymer : NFA blend (PBDB-T : ITIC) are investigated. The thermal properties of PBDB-T and ITIC solid materials are first characterised to inform the choice of anneal temperature during thin film fabrication. Following on from this, the optoelectronic performance of PBDB-T : ITIC blend films are compared using spectroscopy and device-based measurements. Grazing incidence X-ray scattering measurements was then performed to correlate differences in optoelectronic performance with changes in the nanomorphology of the thin film. The findings presented here, further the understanding of processing-structure-performance relationships for non-halogenated polymer : NFA systems. This is critical to improving the eco-compatibility and ultimately the commercialisation of high-efficiency OPV technologies.

4.4 Experimental

The samples of interest in this chapter concern pure and blend films of PBDB-T : ITIC processed from various solvents (chlorobenzene, chloroform, o-xylene and CS₂ : acetone). In this chapter PBDB-T (batch M1001) from Ossila was used with $M_w = 117,406$, $M_n = 58,737$ and $PDI = 2.0$. The selected processing solvents allow a range of solvent properties to be compared between halogenated and non-halogenated systems. For example, chlorobenzene and o-xylene have comparably high boiling points, (132°C and 144°C respectively) and low vapour pressures (9mmHg and 7mmHg respectively). Similarly, chloroform, acetone and CS₂ are all low boiling point ($b_p = 61.2$ °C, 46.3°C and 56.2°C respectively),

highly volatile solvents ($P_v = 194\text{mmHg}$, 100mmHg and 230mmHg respectively). O-xylene was selected as a suitable candidate to investigate given its compatibility with other polymer : NFA systems [250, 251, 252] and its high boiling point makes it a promising candidate for large-scale roll-to-roll processing [26]. A CS_2 : acetone solvent blend was also selected as previous work demonstrated its similar HSP parameters to chlorobenzene [239] suggesting it will be a good solvent for polymer : NFA systems. The film processing conditions used for pure and blend film samples are provided below in Table 4.1 and Table 4.2 respectively. PBDB-T : ITIC solutions were prepared in a 1:1 blend ratio (by weight) at the appropriate solid concentration. The CS_2 : acetone co-solvent blend was prepared in a 4:1 ratio by volume. Films processed from chloroform and CS_2 : acetone were spin-coated statically and films processed from chlorobenzene and o-xylene were spin-coated dynamically to produce films that were $\sim 80\text{-}90\text{nm}$ thick. It should be noted that PBDB-T showed a considerably poorer solubility in o-xylene solutions and films contained numerous particulates as can be seen in the optical microscopy images shown in (Figure 4.20). All films were thermally annealed immediately after fabrication at 160°C for 10 minutes in a nitrogen-filled glovebox.

Solvent	Material	Solid Concentration (mg/mL)	Spin Speed (rpm)
Chlorobenzene	PBDB-T	10	2000
	ITIC	15	1000
Chloroform	PBDB-T	10	2000
	ITIC	15	3000
O-Xylene	PBDB-T	7.5	2000
	ITIC	15	1000
CS_2 : Acetone	PBDB-T	10	2000
	ITIC	15	3000

Table 4.1: A summary of the processing conditions used to spin-coat pure PBDB-T and ITIC thin films from various solvents.

Solvent	Solid Concentration (mg/mL)	Spin Speed (rpm)
Chlorobenzene	18	2000
Chloroform	9	3000
O-Xylene	13	1000
CS_2 : Acetone	8	2000

Table 4.2: A summary of the processing conditions used to spin-coat PBDB-T : ITIC blend thin films from various solvents.

4.5 Thermal Characterisation of PBDB-T and ITIC

An anneal temperature of 160°C was informed by DSC and TGA measurements of pure PBDB-T and ITIC (Figure 4.2, Figure 4.3 and Figure 4.4) and has been used as an optimum anneal temperature in other studies [94]. The glass transition temperature (T_g) of ITIC has previously been measured to be $\sim 180^\circ\text{C}$ [266] where it was hypothesised that diffusion-limited crystallisation can occur at temperatures below T_g . This conclusion has been used in other studies to justify the formation of multiple polymorphic phases in the temperature range $150 < T(^{\circ}\text{C}) < 350$ [267, 112]. Similar thermal behaviour has been reported for a number of pharmaceutical small-molecules [268, 269, 270] but given the large molecular structure of ITIC (and other large conjugated materials), mobility in a vitrified state at $T < T_g$ seems unlikely. Upon further inspection, it should also be noted that previous T_g measurements of ITIC were performed following isothermal heating of films at 450°C [266]. My TGA measurements show that this temperature is considerably higher than the decomposition temperature of ITIC with a transient mass loss of $\sim 15\%$ at 450°C (Figure 4.4a). Any T_g measurements performed after such intensive heating will likely contain molecular fragments of decomposed ITIC and are therefore inaccurate.

In this study, the DSC thermogram from the first heating ramp exhibits a small endothermic peak with a maximum at 180°C, characteristic of a crystallisation temperature (T_c) and a stronger exothermic peak at $\sim 210^\circ\text{C}$ indicative of a melting temperature (T_m) (Figure 4.2a). Additionally, there appears to be a step-like feature visible in both the heating and cooling ramps, characteristic of a glass transition in the range $\sim 100\text{--}120^\circ\text{C}$ (Figure 4.2). Combining this with the TGA thermogram in (Figure 4.4a), it is therefore concluded that ITIC undergoes a glass transition at $\sim 100\text{--}120^\circ\text{C}$, crystallisation at $\sim 180^\circ\text{C}$, melting at $\sim 210^\circ\text{C}$ and begins to decompose at $\sim 355^\circ\text{C}$. At $T > T_g$, the increased molecular mobility leads to the formation of multiple polymorphic phases as reported elsewhere [267, 112].

For PBDB-T, there are fewer thermal transitions in the DSC thermograms compared to ITIC and they are much less distinct in agreement with other studies [266, 128] (Figure 4.3). There is a step-like feature characteristic of a glass transition visible at $\sim 80^\circ\text{C}$ in the first heating ramp (Figure 4.3a) but this is not visible in the cooling thermogram (Figure 4.3b) which makes it difficult to discern if this a true glass transition. The only clear feature is the broad peak at $\sim 252^\circ\text{C}$ characteristic of a melting temperature. TGA measurements also show that the onset of decomposition occurs at $\sim 437^\circ\text{C}$ (Figure 4.4b).

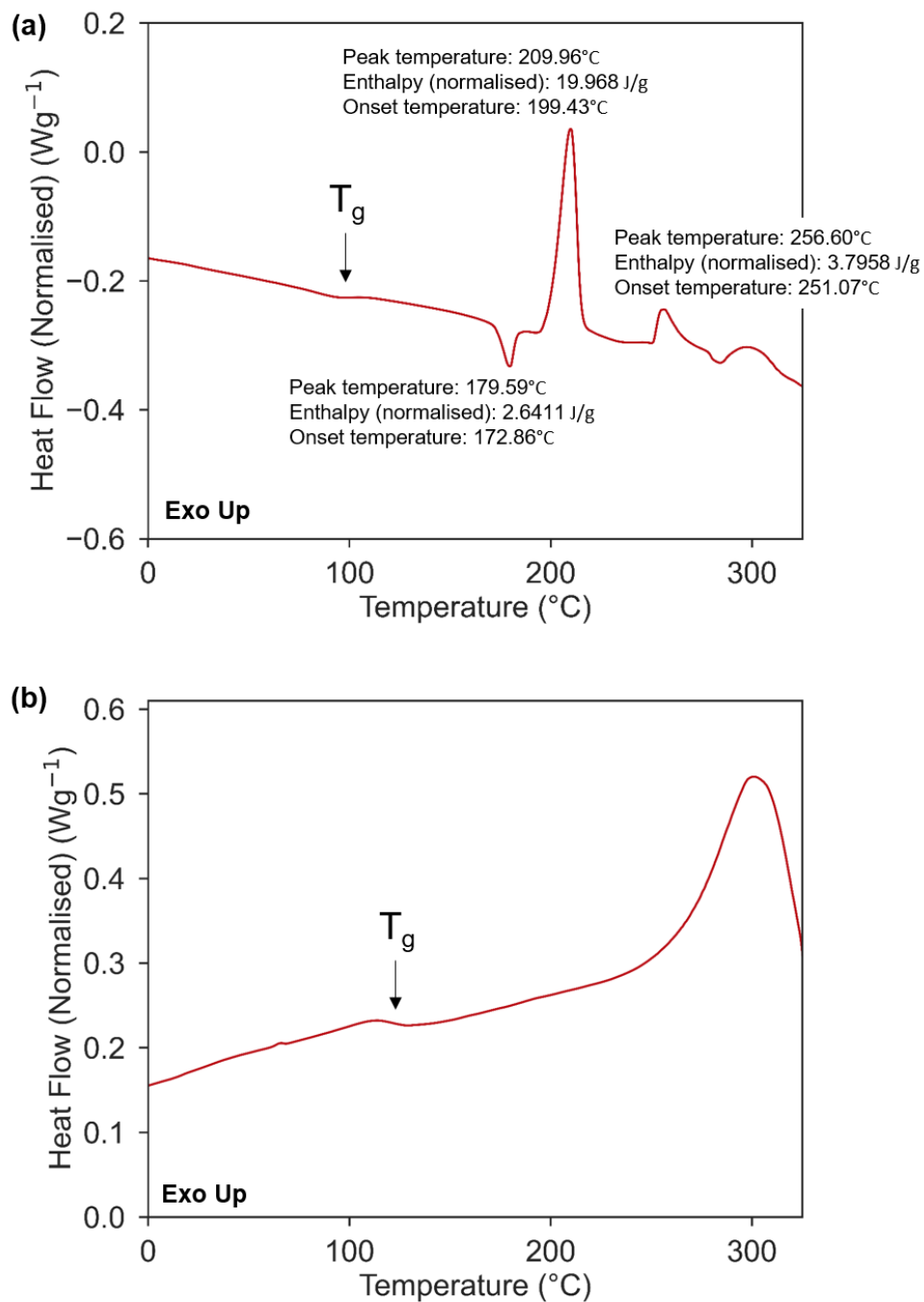


Figure 4.2: DSC thermogram of pure ITIC solid collected using a rate of $10^{\circ}\text{C}/\text{min}$ for (a) the first heating ramp from 0°C to 325°C , and (b) the first cooling ramp from 325°C to 0°C . Note the step-like transition at $T_g = 121^{\circ}\text{C}$ in the cooling stage.

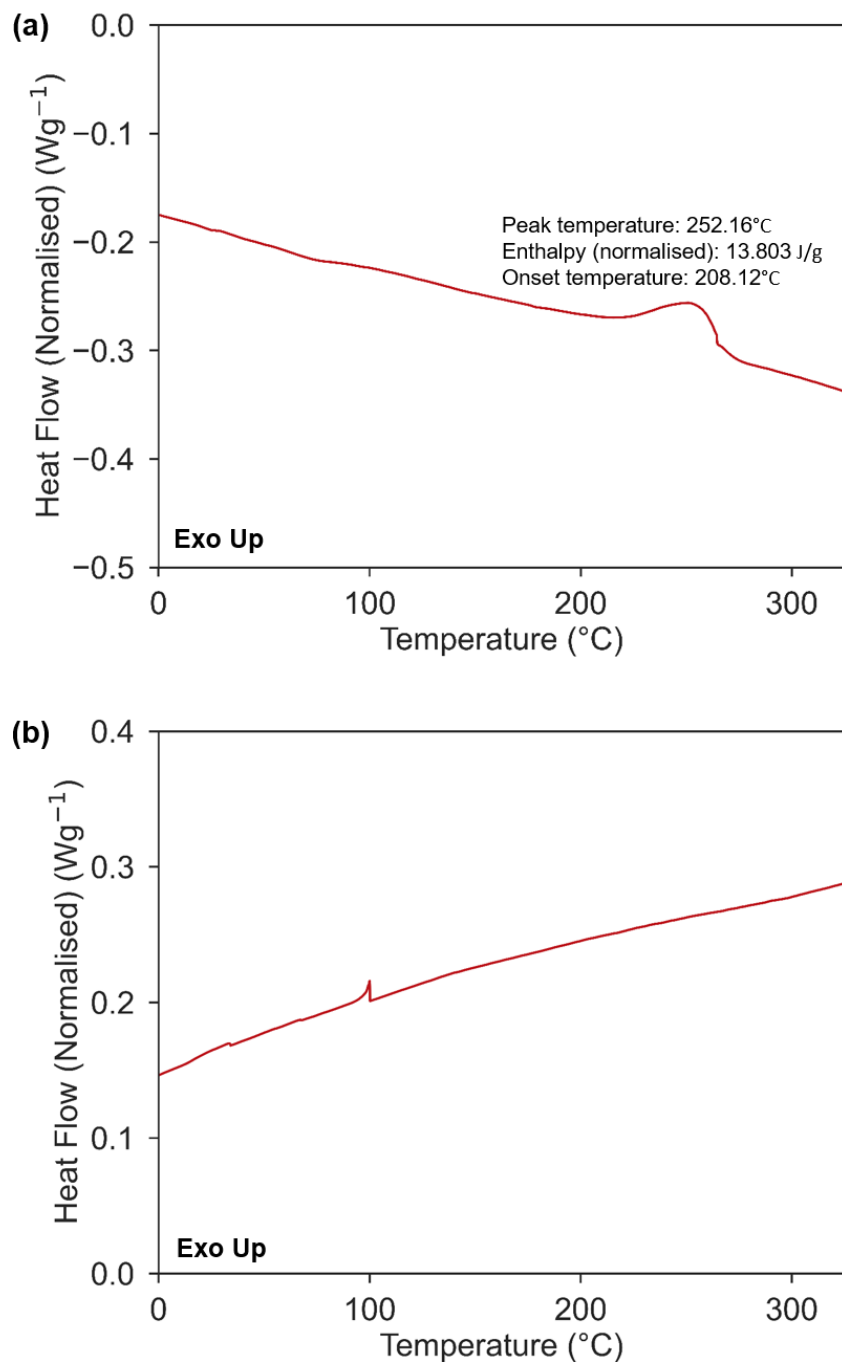


Figure 4.3: DSC thermogram of pure PBDB-T solid collected using a rate of $10^{\circ}\text{C}/\text{min}$ for (a) the first heating ramp from 0°C to 325°C , and (b) the first cooling ramp from 325°C to 0°C .

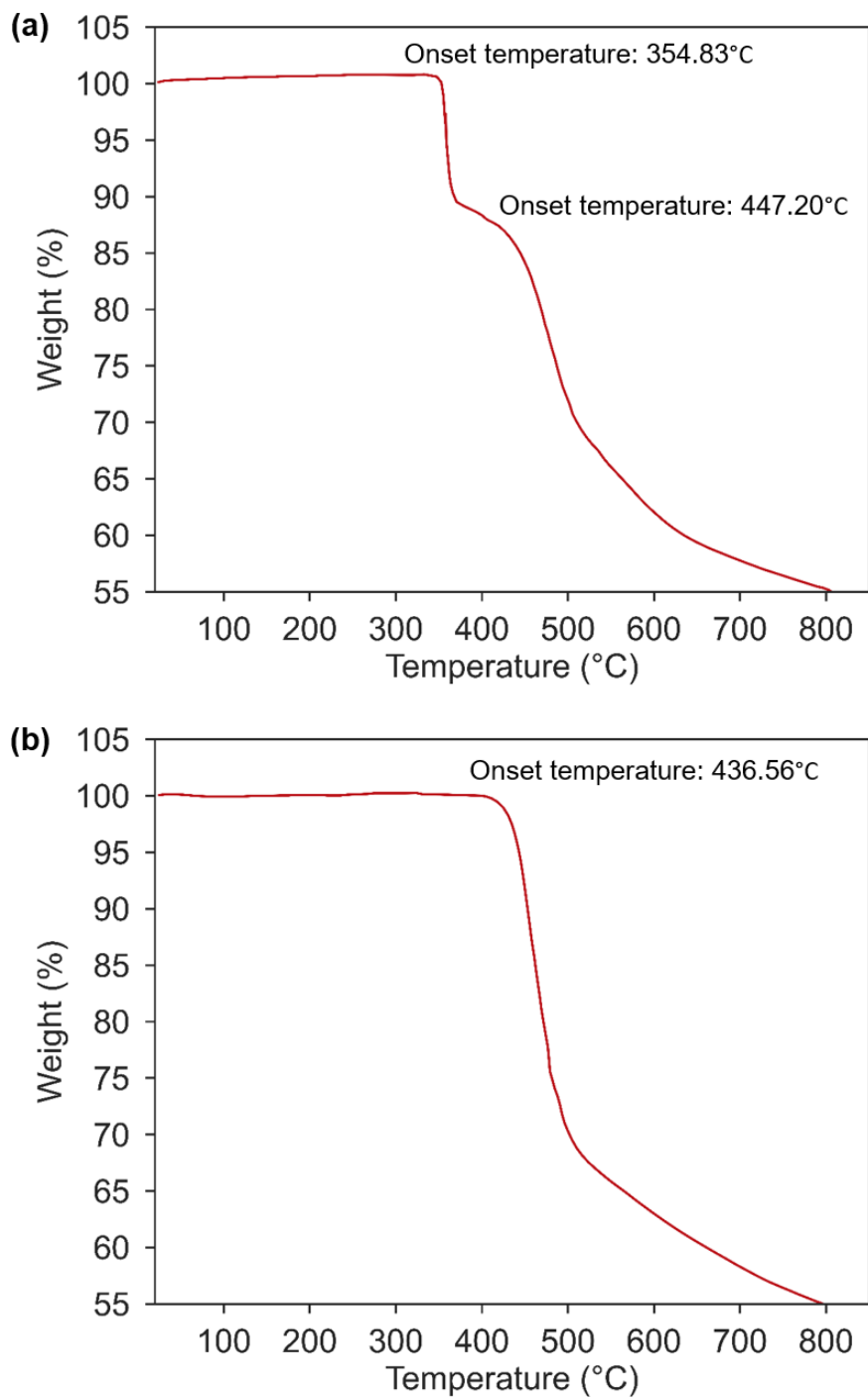


Figure 4.4: TGA thermogram of (a) pure ITIC solid and (b) pure PBDB-T solid. Mass loss was measured during heating from room temperature to 800°C.

4.6 Optoelectronic Properties

The normalised UV-Vis absorption of pure ITIC and pure PBDB-T thin films along with blend thin films of PBDB-T : ITIC processed from various solvents are shown in Figure 4.5, Figure 4.6 and Figure 4.7 respectively. The absorption profile of ITIC consists of two strong absorption bands in the 600-800nm wavelength range with maxima at $\sim 650\text{nm}$ $\sim 700\text{nm}$, consistent with previous reports [93, 271] (Figure 4.5). The absorption peak at 700nm has previously been identified as a high-energy π - π^* transition and intramolecular charge transfer from the core IDTT unit to the flanking INCN moieties [271]. The optical bandgap of ITIC calculated from the onset of absorption according to Equation 2.3 is equal to 1.60eV. The spectra of chlorobenzene and o-xylene-processed ITIC films appear to undergo a bathochromic shift relative to the absorption spectra of chloroform and CS_2 : acetone-processed films, which are potentially indicative of enhanced molecular π - π stacking through the formation of J-aggregates [272].

In the case of pure PBDB-T films, the absorption spectrum of all solvent processed films exhibit a maximum at $\sim 630\text{nm}$ along with a lower intensity band centred at $\sim 580\text{nm}$ in agreement with previous reports [94, 95] and the optical band gap is calculated to be 1.83eV (Figure 4.6). For the o-xylene-processed PBDB-T film, the intensity of the lower absorption transition at $\sim 580\text{nm}$ is significantly lower relative to the $\sim 630\text{nm}$ peak. In the blend, the absorption contributions of PBDB-T and ITIC combine to produce a spectra with strong absorption in the 500-800nm wavelength range (Figure 4.7). The ITIC absorption peak at $\sim 700\text{nm}$ for the o-xylene-processed blend film, is much more pronounced relative to the PBDB-T peak at $\sim 630\text{nm}$, which is again indicative of poor PBDB-T solubility and a greater absorption contribution from the acceptor component.

In addition to changes in light absorption, the impact of processing solvent on light emission was investigated. The degree of PL quenching in an OPV blend film is related to the efficiency of exciton dissociation at donor-acceptor interfaces. In an ideal OPV BHJ device, excitons are separated into free charge carriers at heterointerfaces before radiative recombination can occur (i.e. the potential emission of photons is *quenched*). In Figure 4.8, the steady-PL of pure ITIC, pure PBDB-T and PBDB-T : ITIC blend thin films processed from various solvents are presented. PL intensities have been corrected for photon absorption by normalizing each dataset to the absorption coefficient at the excitation wavelength. The PL intensities of the pure films are much higher compared to the blend thin films because there are no donor-acceptor interfaces to pull away free charge carriers during exciton dissociation. The PL signal of the chlorobenzene-processed blend film is the most quenched relative to the emission of the pure component films processed from the same solvent (Figure 4.8a). In comparison, there are clear emission peaks in the blend PL at $\sim 760\text{nm}$ for chloroform, o-xylene and CS_2 : acetone-processed blend films (Figure 4.8b-d).

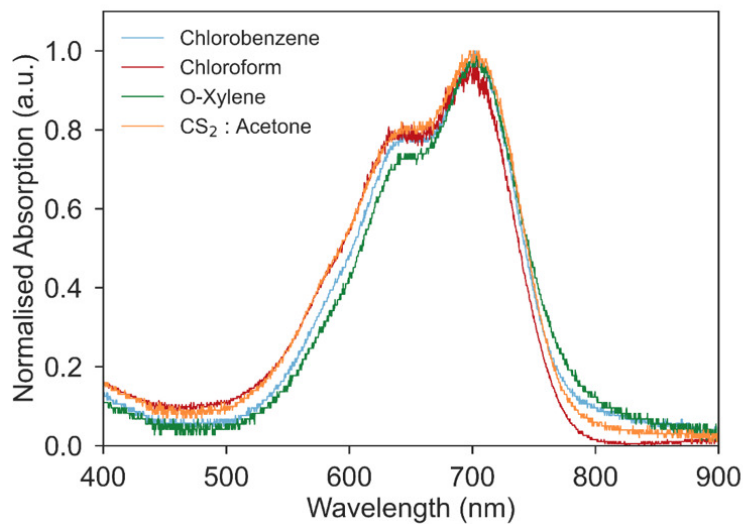


Figure 4.5: Normalised UV-Vis absorption of pure ITIC films processed from chlorobenzene, chloroform, o-xylene, and CS₂ : acetone.

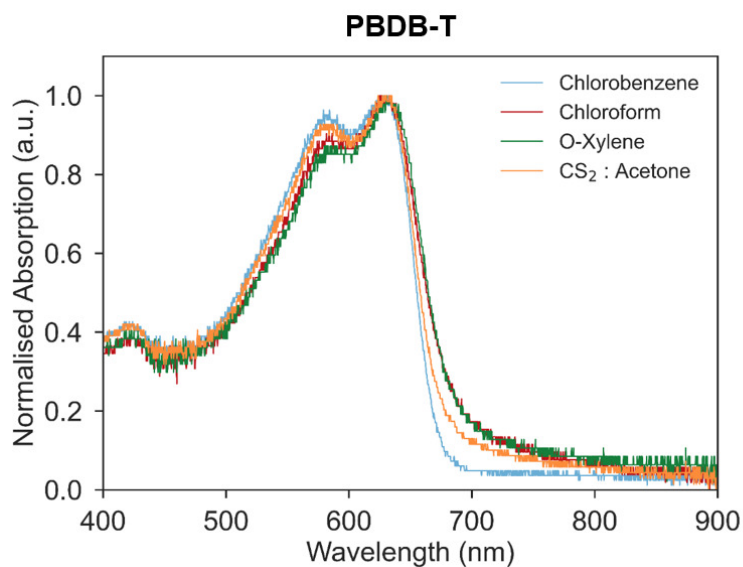


Figure 4.6: Normalised UV-Vis absorption of pure PBDB-T films processed from chlorobenzene, chloroform, o-xylene, and CS₂ : acetone. Note the PBDB-T used here had $M_W=142,718$, $M_N=60,189$ and $PDI=2.3$ (batch M1001A2 from Ossila).

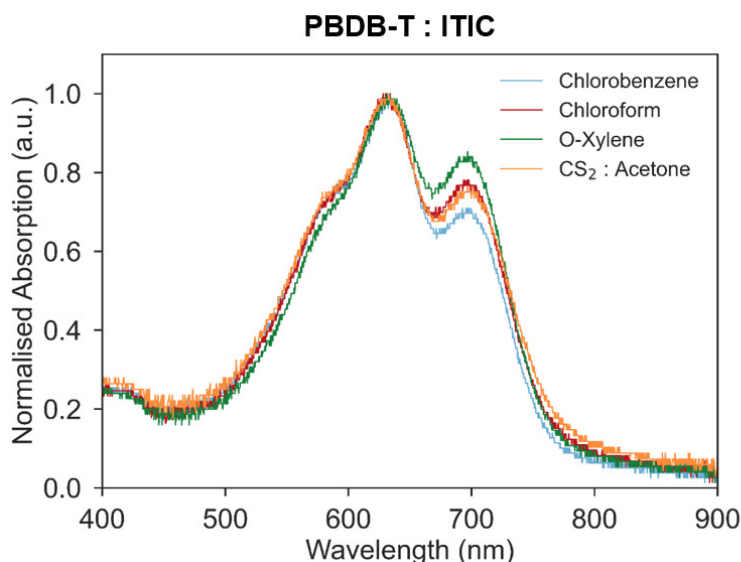


Figure 4.7: Normalised UV-Vis absorption of PBDB-T : ITIC blend films processed from chlorobenzene, chloroform, o-xylene, and CS₂ : acetone.

The exciton diffusion length (l_d) of PBDB-T and ITIC films processed from chlorobenzene was measured using PL quenching measurements (Figure 4.22 and Figure 4.21), giving values equal to $11.60 \pm 0.60\text{nm}$ and $12.65 \pm 0.35\text{nm}$ respectively. It should be noted that l_d values as high as 25-32nm have been reported for ITIC elsewhere [29] suggesting values are dependent on measurement technique and film processing conditions. Nevertheless, it provides a rough target for the optimisation of the blend nanostructure. The superior PL quenching exhibited by the chlorobenzene-processed PBDB-T : ITIC blend is indicative of a more favourable nanomorphology either due to a domain size comparable to l_d or an optimised donor-acceptor interfacial area permitting efficient exciton dissociation.

Next, the impact of processing solvent on the PV performance of PBDB-T : ITIC based OPV devices was investigated. OPV devices were fabricated using a conventional device architecture (glass/ ITO/ PEDOT:PSS/ PBDB-T : ITIC/ PFN-Br/ Ag) following the protocols described in Chapter 2. The J - V curves of champion devices are displayed in Figure 4.9 along with device statistics in Figure 4.10 and Table 4.3. The highest PCE of 8.84% was achieved for the chlorobenzene-processed device as a result of a superior J_{SC} and FF of $16.62\text{mA}/\text{cm}^2$ and 62.7% respectively. Followed behind this was the CS₂ : acetone-processed device achieving a maximum PCE of 7.30%.

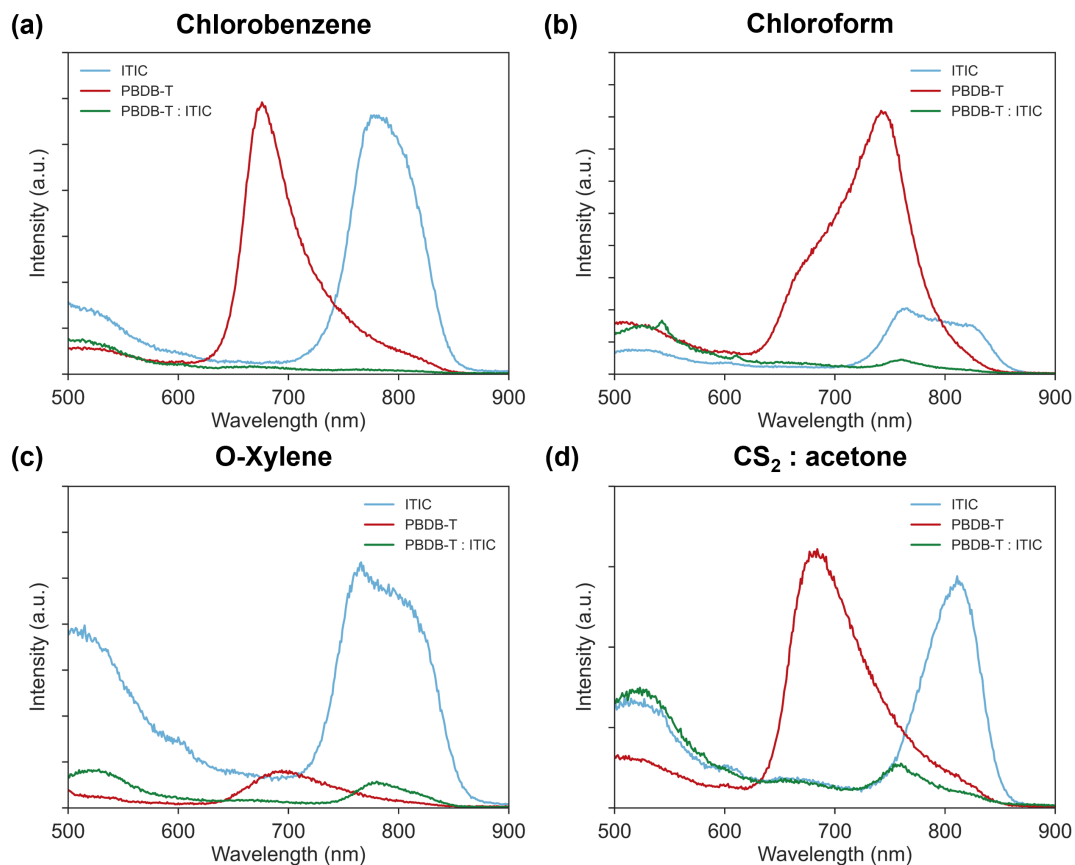


Figure 4.8: Steady-state PL spectra of neat PBDB-T and ITIC thin films and PBDB-T : ITIC blend thin films processed from (a) chlorobenzene, (b) chloroform, (c) o-xylene, and (d) CS₂ : acetone measured using an excitation wavelength of 405nm. PL intensities have been corrected for photon absorption.

Despite suffering from a relatively lower J_{SC} and FF , the overall PCE of the CS₂ : acetone-processed device is boosted by a remarkably high V_{OC} of 0.92V, which is amongst the highest open-circuit voltages achieved for PBDB-T : ITIC systems in the literature [94, 273, 274, 275]. The PCE of o-xylene and chloroform-processed devices were comparable, achieving a maximum PCE of 5.81% and 6.10% respectively. In comparison to the chlorobenzene and CS₂ : acetone-processed devices, the main performance limitations appear to originate in a reduced J_{SC} for the o-xylene-processed device and a reduced FF for the device processed from chloroform.

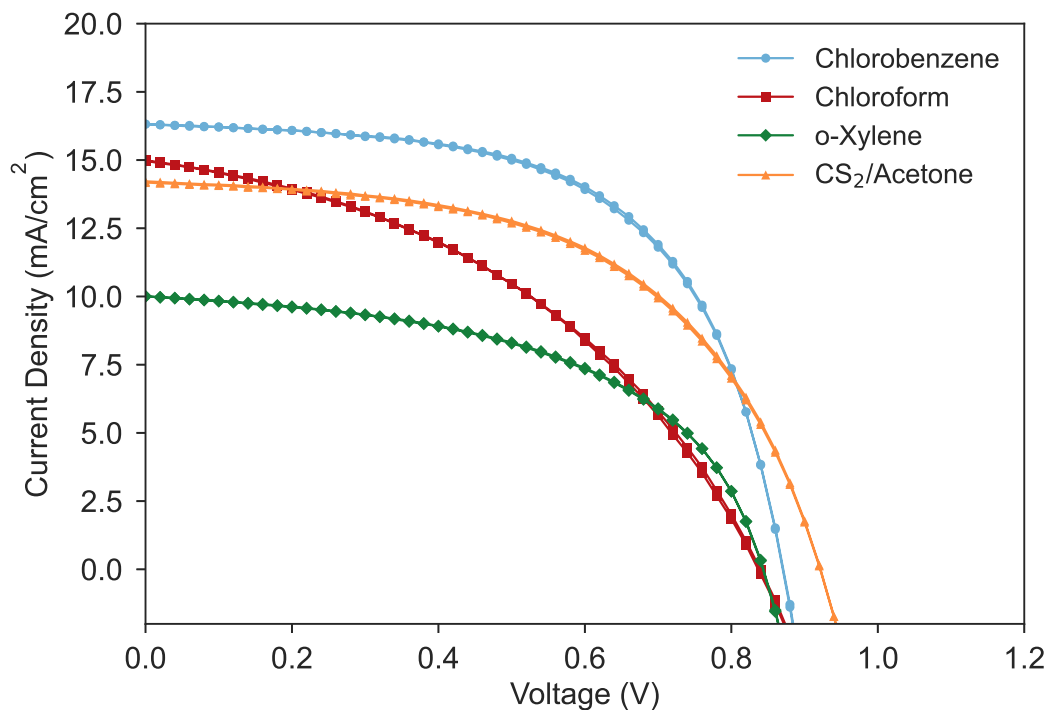


Figure 4.9: J - V performance of champion PBDB-T : ITIC devices processed from chlorobenzene, chloroform, *o*-xylene, and CS_2 : acetone.

Solvent	J_{sc} (mA/cm^2)	V_{oc} (V)	FF (%)	PCE (%)
Chlorobenzene	16.39 ± 0.31 (16.62)	0.82 ± 0.14 (0.88)	55.79 ± 9.96 (62.72)	7.73 ± 2.07 (8.84)
Chloroform	14.56 ± 0.64 (15.11)	0.85 ± 0.01 (0.86)	43.13 ± 0.99 50.15 ± 2.23	5.29 ± 0.31 (5.81)
O-Xylene	12.05 ± 1.04 (13.45)	0.85 ± 0.01 (0.86)	(54.28) (54.28)	4.90 ± 0.73 (6.10)
CS_2 : Acetone	14.32 ± 0.24 (14.93)	0.91 ± 0.01 (0.92)	49.84 ± 2.99 (54.67)	6.49 ± 0.49 (7.30)

Table 4.3: Summary of device metrics presented in Figure 4.10, averaged across 10 devices ± 1 standard deviation. Champion values are shown in parenthesis.

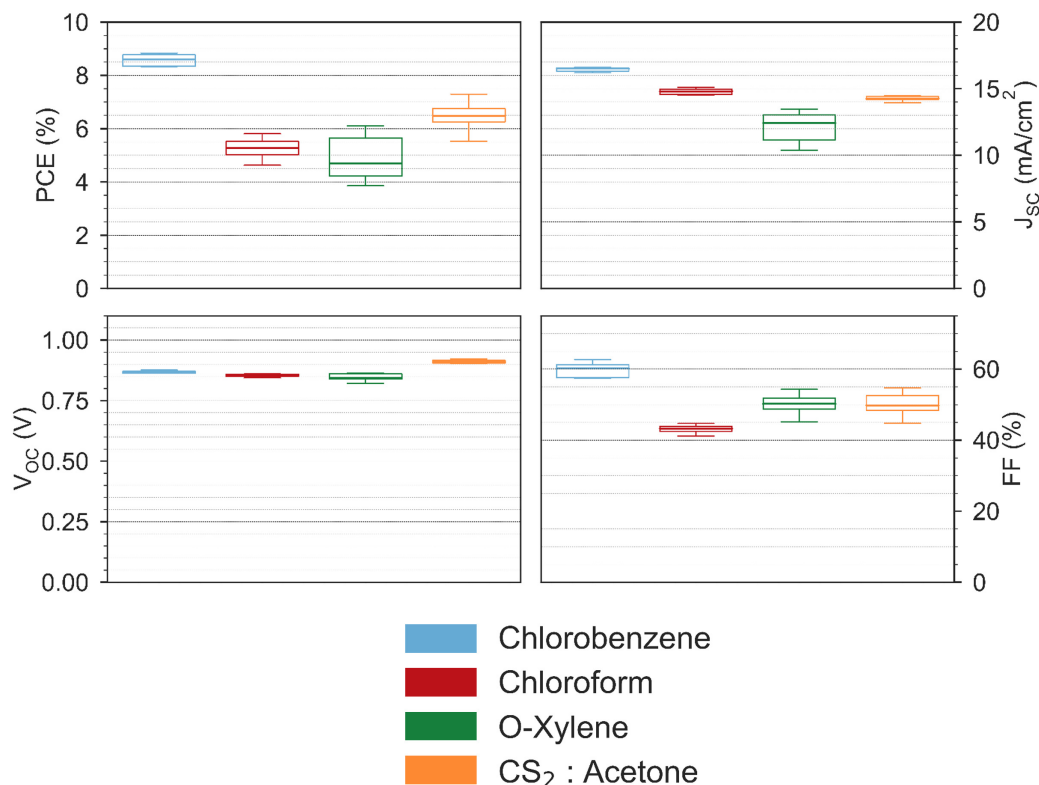


Figure 4.10: Boxplot of device metrics for the 10 highest performing PBDB-T : ITIC devices processed from chlorobenzene, chloroform, o-xylene, and CS₂ : acetone.

The *EQE* spectra of PBDB-T : ITIC films processed from various solvents is displayed in Figure 4.11. Each device displays a broad photoelectric conversion efficiency in the range 300-800nm, which is consistent with the UV-Vis absorption measurements discussed previously (Figure 4.7). The suboptimal light absorption of both PBDB-T and ITIC in the wavelength range 300-500nm results in a lower *EQE* across the same range. For the chlorobenzene-processed device, the *EQE* is slightly higher as a result of enhanced light absorption, in agreement with the superior J_{SC} (Table 4.3). In comparison, o-xylene-processed devices suffer from a decreased *EQE* due to relatively low light absorption, indicative of a higher number of charge trap states or poor exciton dissociation efficiency [276]. The integrated J_{SC} values calculated from the *EQE* spectra in Figure 4.11 are compared in Table 4.4 to the champion values extracted from the *J-V* curves shown in Figure 4.9. The errors between calculated and measured J_{SC} values are less than $\sim 10\%$.

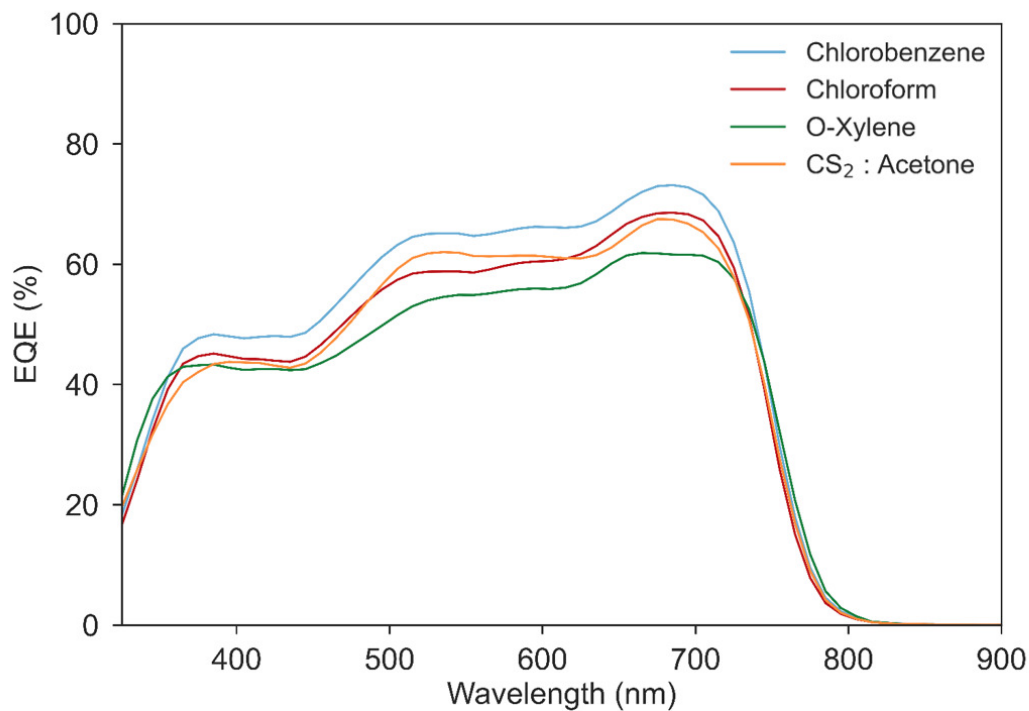


Figure 4.11: *EQE* spectra of PBDB-T : ITIC devices processed from chlorobenzene, chloroform, o-xylene, and CS₂ : acetone.

Solvent	Device J_{SC} (mA/cm^2)	Integrated J_{SC} from <i>EQE</i> (mA/cm^2)
Chlorobenzene	16.62	15.04
Chloroform	14.98	13.85
O-Xylene	13.20	13.06
CS₂ : Acetone	14.93	13.87

Table 4.4: A summary of J_{SC} values for PBDB-T : ITIC devices processed from chlorobenzene, chloroform, o-xylene, and CS₂ : acetone. Values were extracted from the champion J - V curves (Figure 4.9) and from integrating the *EQE* spectra (Figure 4.11).

4.6.1 Small Scale Structures

To understand the apparent differences in PV performance and the optical properties discussed above, the impact of processing solvent on the three-dimensional blend thin film nanostructure was investigated using X-ray scattering and microscopy-based techniques. Firstly, the crystallinity and molecular orientation of PBDB-T and ITIC in the blend was characterised using GIWAXS measurements. The 2D GIWAXS scattering patterns are displayed in Figure 4.12. Each scattering pattern consists of two noticeable features: a high intensity feature at $Q \sim 0.3\text{\AA}^{-1}$ ($d \sim 21\text{\AA}$) and a broad diffuse feature in the out-of-plane direction at $Q \sim 1.7\text{\AA}^{-1}$ ($d \sim 3.65\text{\AA}$). These features have previously been attributed to lamellar stacking and π - π -stacking of both PBDB-T and ITIC [109, 277]. Unfortunately the lamellar and π - π -stacking length scales of PBDB-T and ITIC are too similar to deconvolve the individual scattering contributions from each component.

To further understand the GIWAXS data, azimuthally integrated Q -dependent 1D profiles were extracted from the 2D scattering patterns in the out-of-plane and in-plane directions (Figure 4.13). For the chlorobenzene-processed blend film, the lamellar stacking and π - π -stacking intensities are considerably higher in both the out-of-plane and in-plane directions suggesting a greater degree of molecular order. The crystalline coherence length CCL corresponding to lamellar stacking was estimated from the width and position of the out-of-plane lamellar peak at $Q \sim 0.3\text{\AA}^{-1}$ using the Scherrer equation Equation 3.78. These values are summarised in Table 4.5. The chlorobenzene and o-xylene-processed films are composed of the largest coherently scattering regions with CCL values of 4.31 and 5.49nm respectively. In comparison, chloroform and CS_2 : acetone-processed films exhibit smaller coherence lengths of 3.65nm and 3.92nm respectively. The differences in CCL are likely related to the boiling point of the processing solvent. Processing from high boiling solvents such as chlorobenzene and o-xylene slows the drying kinetics of the film, allowing more time for the components to aggregate. Films processed from low boiling point solvents dry rapidly, resulting in a more disordered molecular packing.

Solvent	Q (\AA^{-1})	d (\AA)	$FWHM$ (\AA^{-1})	CCL (nm)
Chlorobenzene	0.310	20.3	0.136	4.31
Chloroform	0.296	21.3	0.161	3.65
O-Xylene	0.306	20.6	0.107	5.49
CS_2 : Acetone	0.313	20.1	0.150	3.92

Table 4.5: Table of Q -values, d -spacing, FWHM and crystallite size extracted from the out-of-plane GIWAXS Q -dependent 1D intensity profiles (Figure 4.13a).

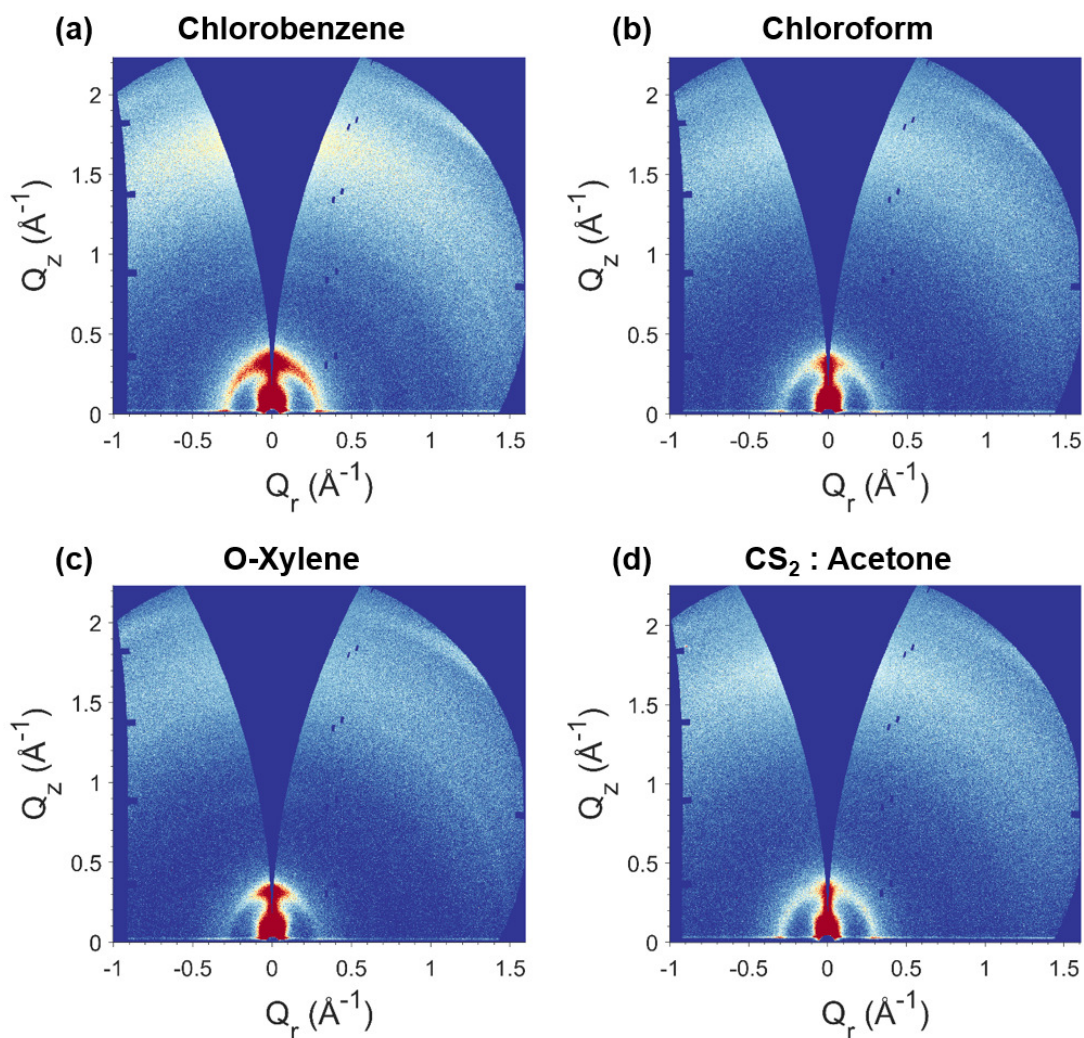
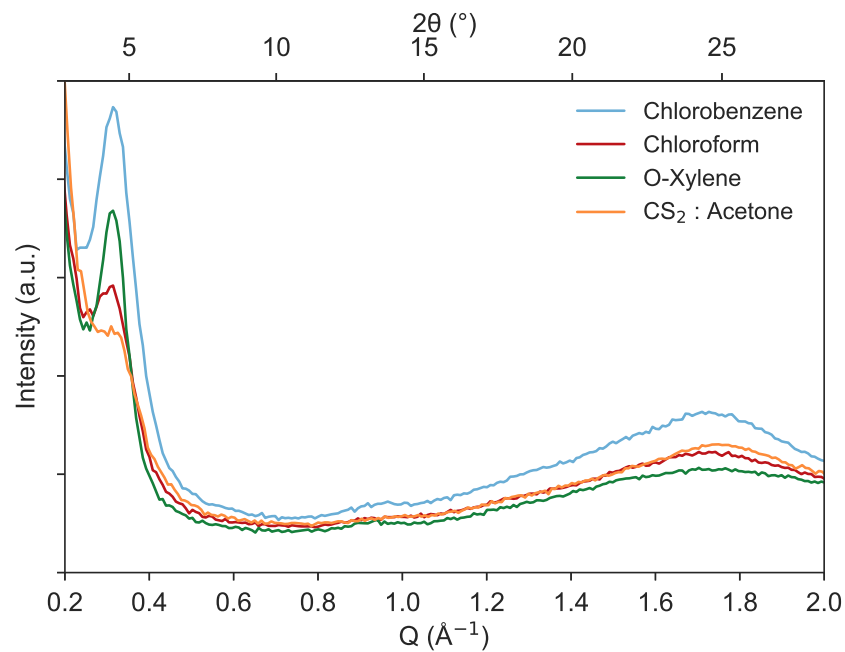
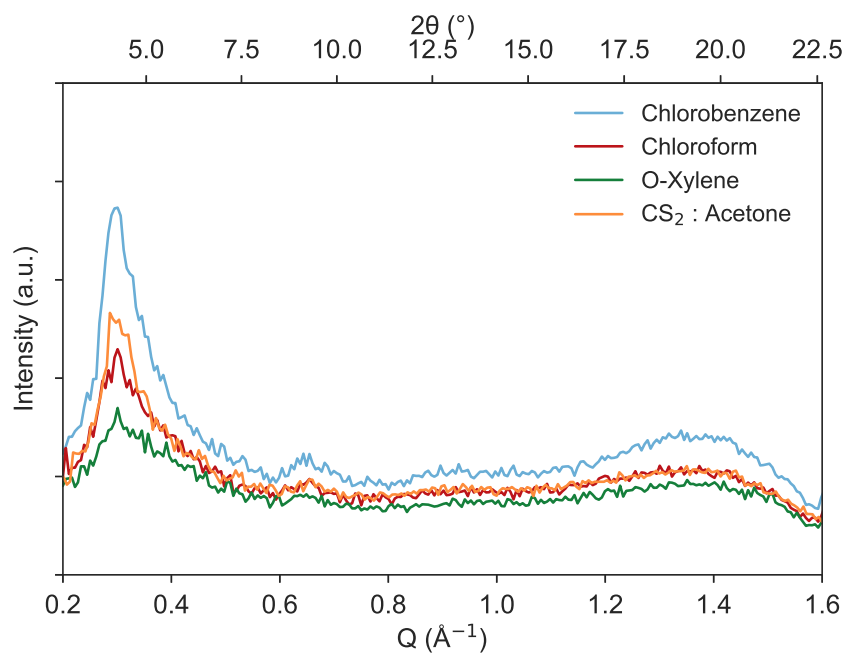


Figure 4.12: 2D GIWAXS patterns of PBDB-T : ITIC blend thin films processed from (a) chlorobenzene, (b) chloroform, (c) o-xylene, and (d) CS_2 : acetone. Measurements were taken using an incident angle of $\theta_i=0.16^\circ$.



(a)



(b)

Figure 4.13: Azimuthally integrated Q -dependent GIWAXS intensity profiles in the (a) out-of-plane and (b) in-plane directions of PBDB-T : ITIC blend thin films processed from chlorobenzene, chloroform, o-xylene, and CS₂ : acetone.

4.7 Large Scale Structures

Next, AFM and GISAXS measurements were performed to probe the impact of processing solvent on the characteristics of large-scale structures in the blend thin films such as the size, shape and intermixing of domains. As discussed in Chapter 2, these properties are critical to understanding the efficiency of exciton dissociation and the percolation of free charges to the electrodes in an OPV device. AFM topography images of PBDB-T : ITIC films processed from halogenated and non-halogenated solvents are shown in Figure 4.14 and RMS surface roughness values (σ_{RMS}) are summarised in Table 4.6. The AFM images of films processed from chlorobenzene and chloroform appear very similar with comparable height scales (Figure 4.14a and Figure 4.14b) and both films exhibit a similar RMS surface roughness of $2.01nm$ and $1.86nm$ respectively. In comparison, the surface of the o-xylene film appears to be composed of more distinct domains and the height scale range is a factor of ~ 3 times greater than the other AFM images leading to an increased RMS surface roughness of $5.12nm$ (Figure 4.14c). For the CS_2 : acetone-processed film, the surface is ultra-smooth with a RMS roughness of $1.29nm$ (Figure 4.14d).

Solvent	σ_{RMS} (nm)
Chlorobenzene	2.01
Chloroform	1.86
O-Xylene	5.12
CS₂ : Acetone	1.29

Table 4.6: Table of RMS film roughness σ_{RMS} values extracted from the AFM data shown in Figure 4.14

Although AFM measurements give an initial indication of the blend morphology, it is only the surface of the film that is probed and interpretation often relies on visual, qualitative comparisons of the images. GISAXS measurements were consequently performed to probe large-scale structures across the full *three-dimensional* morphology of the film. The 2D GISAXS scattering patterns shown in Figure 4.15 exhibit intense scattering in the small angle region with an in-plane Yoneda enhancement [210] at $Q_z \sim 0.03\text{\AA}^{-1}$ and weak intensity scattering at $Q \sim 0.3\text{\AA}^{-1}$ corresponding to the lamellar stacking peak identified previously in GIWAXS measurements. The higher surface roughness of the o-xylene-processed film measured by AFM is also apparent from the broad, diffuse scattering visible in the out-of-plane direction.

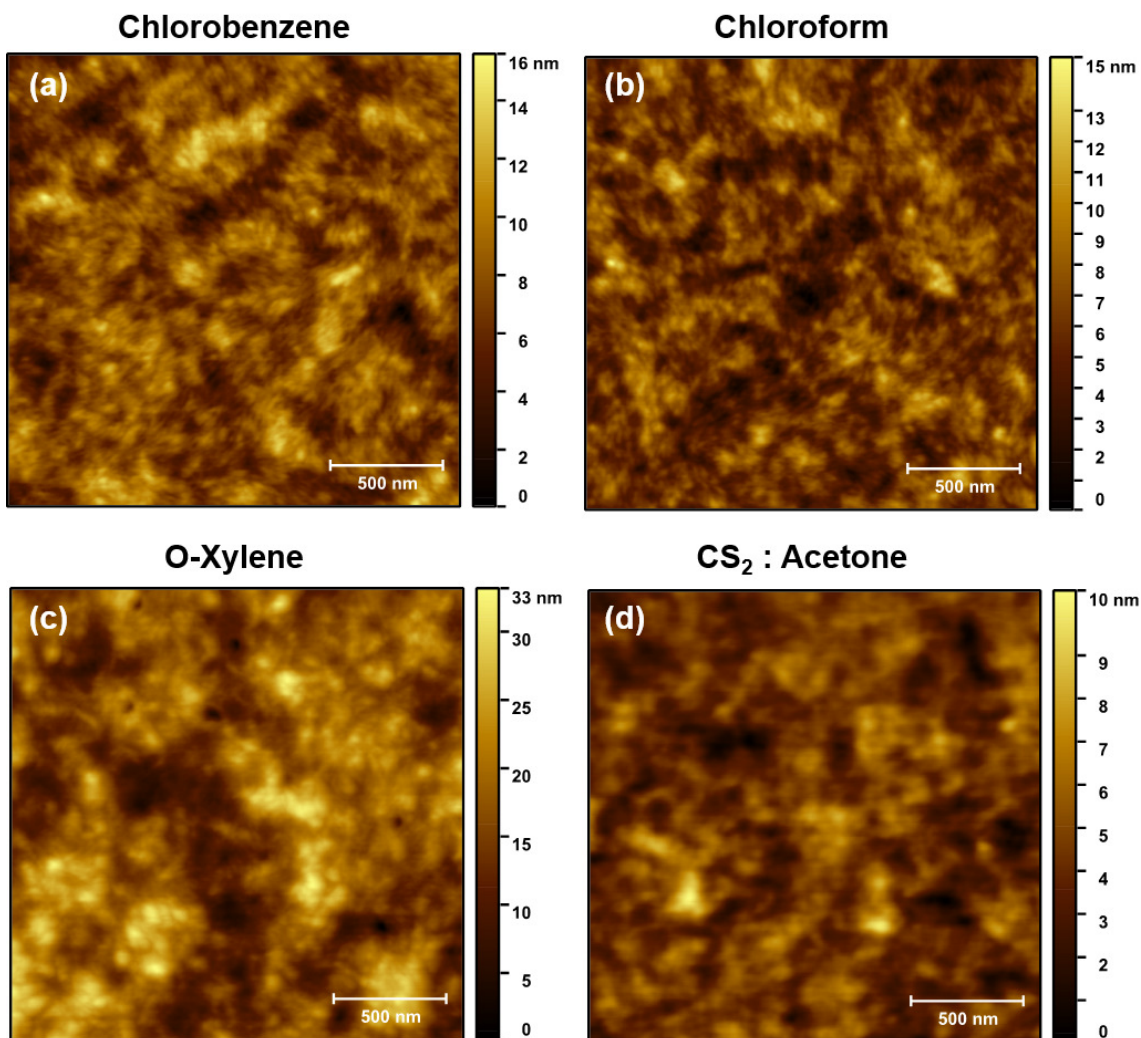


Figure 4.14: AFM height topography images of PBDB-T : ITIC blend thin films processed from (a) chlorobenzene, (b) chloroform, (c) o-xylene, and (d) CS₂ : acetone. The scale bar is 500nm. Note the variation in height scale particularly for the o-xylene-processed film blend film (c).

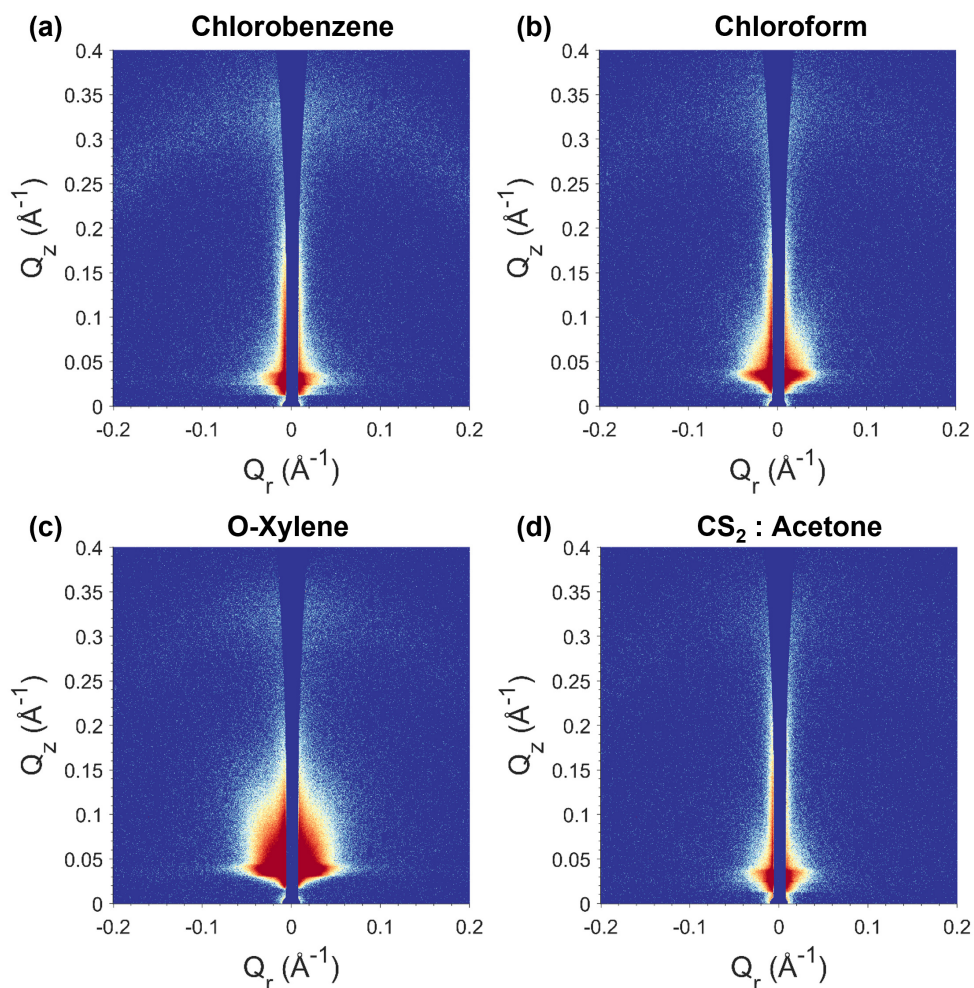


Figure 4.15: 2D GISAXS patterns of PBDB-T : ITIC blend thin films processed from (a) chlorobenzene, (b) chloroform, (c) o-xylene, and (d) CS₂ : acetone. An incident angle of $\theta_i = 0.16^\circ$ was chosen as it close to the critical angle of the material.

To further analyse the 2D GISAXS patterns, horizontal linecuts were performed at the Yoneda region corresponding to the critical angle of the thin film (Figure 4.16). This data has also been plotted as IQ^2 versus Q , termed the Lorentz scattered intensity (Figure 4.17). Here, the appearance of a peak in the 1D GISAXS profiles is made clearer and the peak position can be measured more easily without aberrations arising from the scattering geometry [186]. As discussed in Subsection 3.9.5, peaks in the Lorentz-corrected scattering intensity for OPV systems have previously been identified as a phase-separation length scale or long period L_p [183, 105]. Chloroform, o-xylene and CS₂ : acetone-processed

blend thin films have a peak in the Lorentz-corrected GISAXS intensity corresponding to L_p values of 26.0nm, 27.0nm and 28.7nm respectively (see Table 4.7 for Q values). In the case of the chlorobenzene-processed film, a peak is not observed suggesting the observable Q -range is either too small to capture the characteristic length scale or there is insufficient electron density contrast in the system resulting in a low scattering signal.

Changes in the Lorentz-corrected scattering intensity can be understood by considering the integral of IQ^2 , known as the invariant (see Subsection 3.9.5 for further details). A larger invariant corresponds to a greater electron density contrast in the sample, indicative of phase-separated system with high domain purity. By comparing the area under the Lorentz-corrected scattering curves in Figure 4.17 it is clearly seen that chloroform and o-xylene-processed blend films have a larger invariant compared to chlorobenzene and CS₂ : acetone-processed blend films. Given the superior PV performance of chlorobenzene and CS₂ : acetone-processed, this suggests that a more finely intermixed PBDB-T : ITIC morphology with a large interfacial area is desirable for efficient PV performance.

To understand this further, the 1D horizontal linecuts in Figure 4.16 were fitted using a Guinier-Porod model (see Figure 3.9.5) in the Q range $0.015 \leq Q (\text{\AA}^{-1}) \leq 0.25$ (Figure 4.18). The Guinier-Porod model was chosen as it can be used to fit small angle scattering from systems which are more intermixed and therefore do not exhibit Porod behaviour (scattering exponent = 4). Fit parameters are summarised in Table 4.8. Here a lower scattering exponent (α) corresponds to a larger interfacial area with $\alpha \sim 4$ representative of a system with sharp, phase-separated interfaces [196, 197]. Chlorobenzene and CS₂ : acetone-processed blend thin films exhibit scattering exponent values of 2.35 and 2.64 respectively, characteristic of intermixed systems with large interfacial areas in agreement with the reduced Lorentz invariant discussed above. In comparison, the scattering exponent values of the chloroform and o-xylene-processed films are significantly higher (3.92 and 4.50 respectively) suggesting these systems have a higher degree of phase-separation with sharp interfaces.

The radius of gyration (R_g) and dimensionality factor (s) parameters contain information related to the size and shape of domains. For example, the R_g of spherical domains with radius R is given by $R_g^2 = \frac{3}{5}R^2$. s is related to the dimensionality of the scattering entity ($s = 0$ for 3D symmetry, $s = 1$ for 2D symmetry etc.) [196, 197]. The chloroform and o-xylene-processed films exhibit R_g values of 7.19 and 7.35nm respectively and s values close to zero, indicative of globular, three-dimensional domains. In comparison, blend films processed from chlorobenzene and CS₂ : acetone exhibit larger R_g values of 9.15nm and 8.06nm respectively and higher s values suggesting a more interpenetrating network-like structure. The correlation between R_g and PV performance can be rationalised by considering the exciton diffusion length (l_d) of PBDB-T and ITIC (12.65 ± 0.35 nm and

$11.60 \pm 0.60\text{nm}$ respectively). For chlorobenzene and CS_2 : acetone-processed films, R_g is comparable to l_d permitting more efficient exciton dissociation at the donor-acceptor interfaces compared to chloroform, o-xylene-processed films.

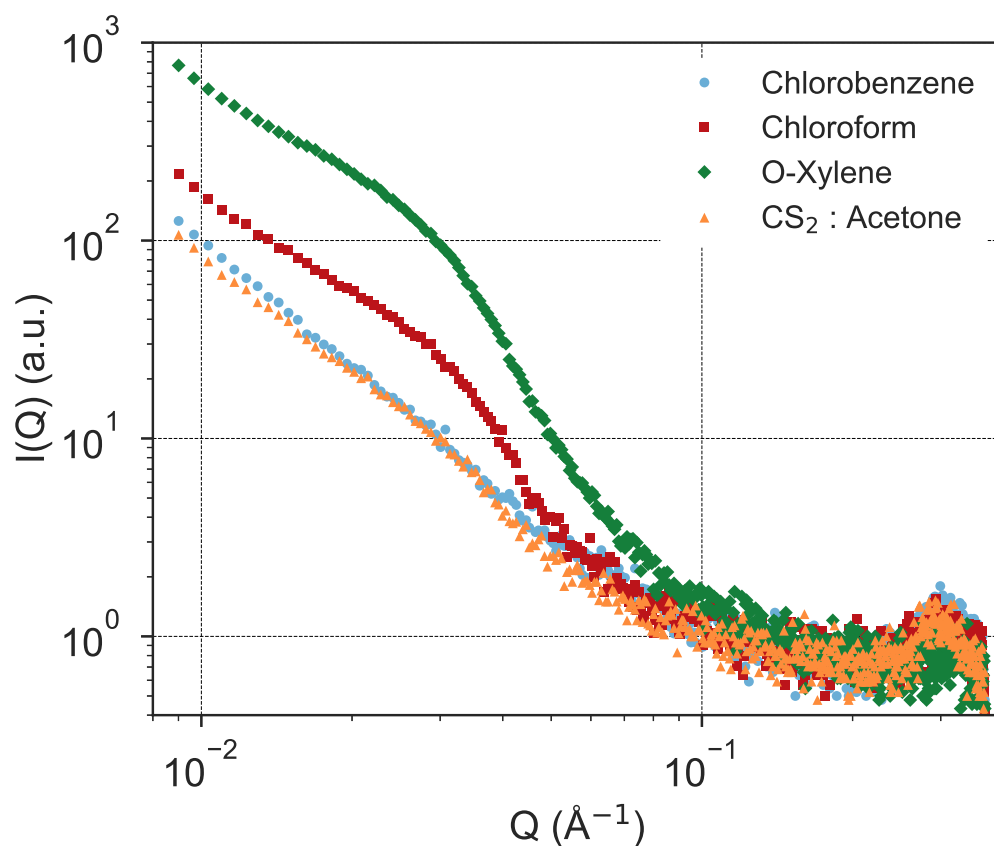


Figure 4.16: 1D GISAXS intensity of PBDB-T : ITIC blend thin films processed from (a) chlorobenzene, (b) chloroform, (c) o-xylene, and (d) CS_2 : acetone. Data was extracted by taking horizontal linecuts at the Yoneda position in the Q_{xy} range $0.2\text{\AA}^{-1} \leq Q \leq 1.0\text{\AA}^{-1}$. Note the peak at $Q \sim 0.3\text{\AA}^{-1}$ corresponds to the lamellar scattering peak characterised in GIWAXS measurements above.

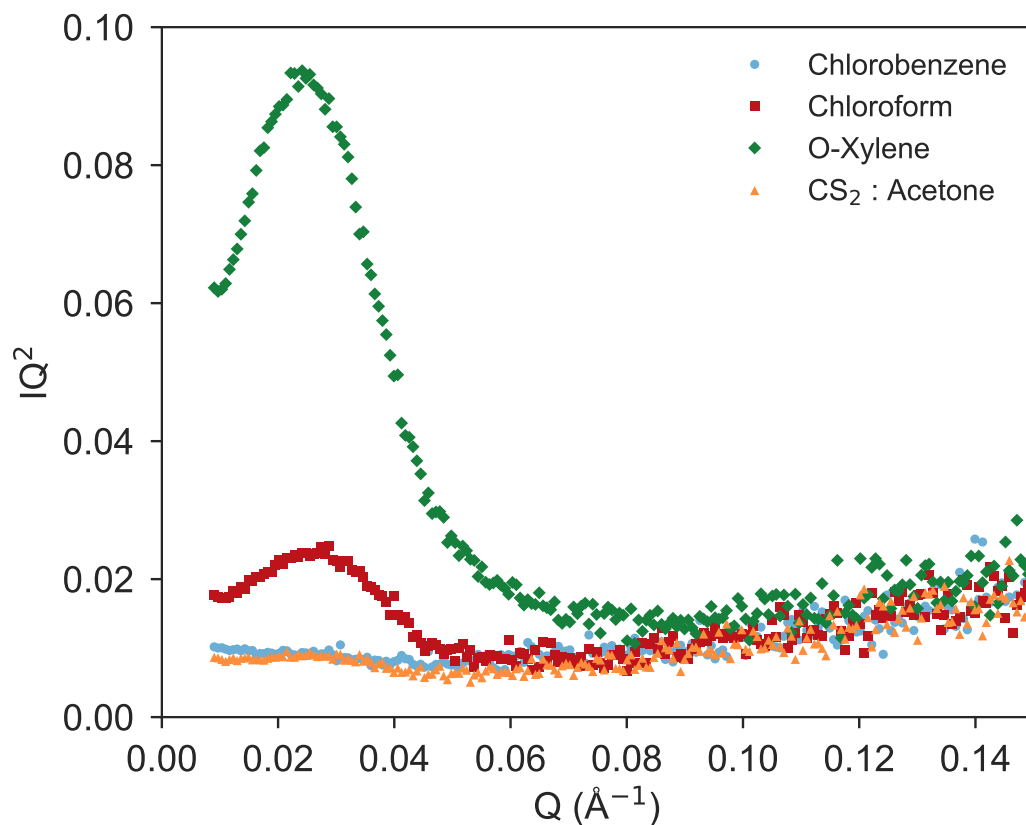


Figure 4.17: Lorentz-corrected GISAXS intensity across the full Q -range for PBDB-T : ITIC blend thin films processed from chlorobenzene, chloroform, o-xylene, and CS_2 : acetone. Data is repeated from Figure 4.16 but plotted as IQ^2 vs Q .

Solvent	Q_{max} (\AA^{-1})	L_p (nm)
Chlorobenzene	–	–
Chloroform	0.0241	26.0
O-Xylene	0.0232	27.0
CS_2 : Acetone	0.0219	28.7

Table 4.7: Table of Q -values and corresponding long period L_p calculated from the correlation peaks in the Lorentz-corrected GISAXS patterns for PBDB-T : ITIC blend films processed from various solvents (Figure 4.17). A value could not be extracted for the chlorobenzene-processed film as a peak was not observed. (Blue trace in Figure 4.17.)

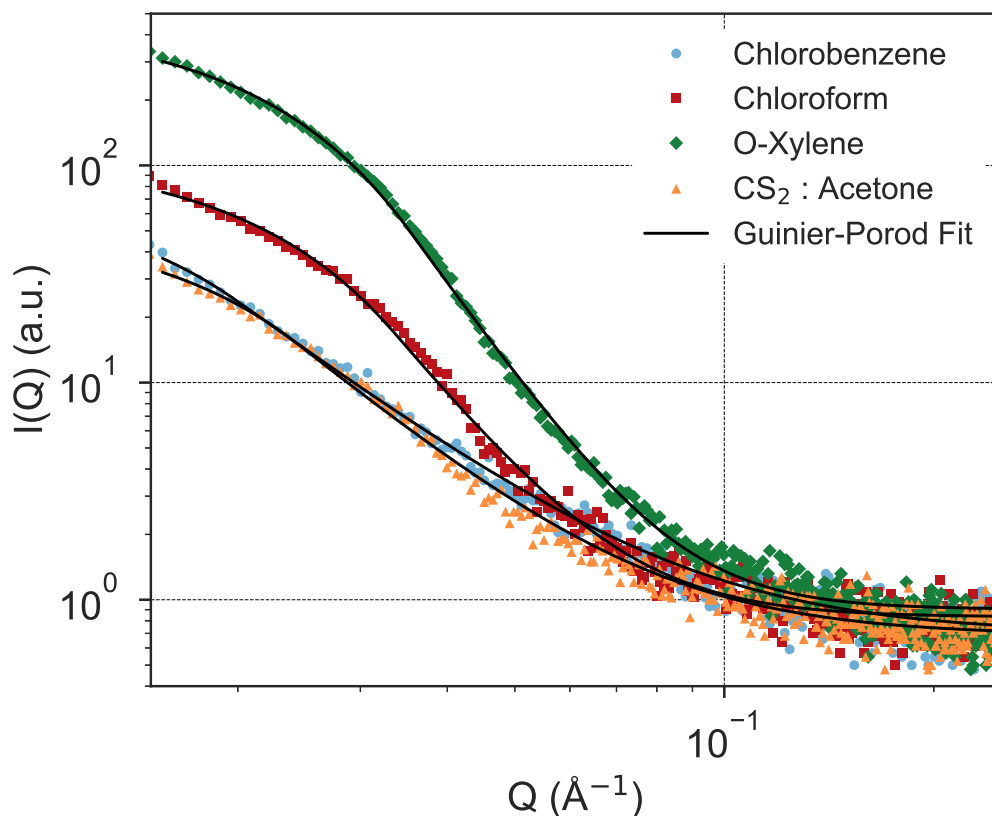


Figure 4.18: Guinier-porod GISAXS fits in the Q -range $0.015 \leq Q \text{ (\AA}^{-1}\text{)} \leq 0.25$ for PBDB-T : ITIC blend thin films processed from chlorobenzene, chloroform, o-xylene, and CS_2 : acetone. Data is repeated from Figure 4.16 but Guinier-Porod fitting is overlaid.

Solvent	Scale ($\times 10^2$)	B	R_g (nm)	α	s ($\times 10^{-2}$)	χ^2/N_{pts}
Chlorobenzene	0.54 ± 0.01	0.70 ± 0.06	9.15 ± 0.24	2.35 ± 0.05	8.0 ± 1.0	0.10
Chloroform	1.11 ± 0.01	0.83 ± 0.06	7.19 ± 0.03	3.92 ± 0.12	0.5 ± 0.2	0.44
O-Xylene	4.60 ± 0.01	0.90 ± 0.06	7.35 ± 0.01	4.50 ± 0.05	0.3 ± 0.1	2.56
CS_2 : Acetone	0.46 ± 0.01	0.69 ± 0.06	8.06 ± 0.14	2.64 ± 0.09	3.5 ± 0.8	0.09

Table 4.8: Table of Guinier-Porod GISAXS fit parameters for the data shown in Figure 4.18.

4.8 Discussion

Taken together, the GIWAXS, GISAXS and AFM measurements reveal distinct solvent-induced morphologies. Chlorobenzene and CS₂ : acetone-processed PBDB-T : ITIC blend films are characterised by a nanostructure that has a large interfacial area with length scales comparable to the exciton diffusion length of PBDB-T and ITIC. This is beneficial for efficient exciton dissociation and PL quenching. At the molecular level, the chlorobenzene blend film exhibits a high degree of order, which is advantageous for good charge transport and reduced non-geminate recombination. In comparison, PBDB-T : ITIC blend films processed from chloroform and o-xylene, form highly phase-separated morphologies with small interfacial areas. Although blend films processed from o-xylene demonstrate a high degree of molecular order, the unfavourable nanomorphology combined with large surface roughness due to poor PBDB-T solubility, ultimately leads to poor PV performance.

The impact of processing solvent on the relationship between film nanostructure and PV performance is demonstrated more clearly in Figure 4.19. Here, R_g and α values extracted from the GISAXS data (Table 4.8) are plotted alongside the average *PCE* of PBDB-T : ITIC devices. The highest *PCE* is achieved for systems characterised by a large interfacial area (small α) and a length scale close to the exciton diffusion length ($R_g \sim l_d$). For highly phase-separated systems (large α) with small domains ($R_g < l_d$), device *PCE* drops significantly.

In addition to the size and purity of domains, their distribution in the plane perpendicular to the substrate can also have a significant impact on PV performance [107, 278]. To investigate the surface properties of the blend thin films, the contact angle of a water droplet on the film surface was measured using contact angle goniometry (Figure 4.24). Reference films of pure ITIC and pure PBDB-T films were first measured giving water contact angles equal to 99° and 105° respectively (Figure 4.23). For PBDB-T : ITIC blend thin films processed from chlorobenzene, chloroform, o-xylene and CS₂ : acetone, the measured water contact angles are 103°, 100°, 101° and 102° respectively. The more hydrophobic surface of the chlorobenzene-processed film suggests the surface is enriched PBDB-T, in agreement with other studies [117, 116, 279]. A PBDB-T enriched surface layer of significant interfacial width would be detrimental to conventional architecture devices, acting as a blocking layer to electrons diffusing to the PFN-Br ETL. This may contribute to the relatively low V_{OC} observed in *J-V* measurements for the chlorobenzene-processed device (Table 4.3), however the effect seems to be minimal, implying the interfacial width is not thick enough to severely impede device performance. Interestingly, the lack of substantial differences in the water contact angle for the chloroform, o-xylene and CS₂ : acetone-processed films does not explain the high V_{OC} achieved for the CS₂ : acetone blend film and its exact origin remains unclear.

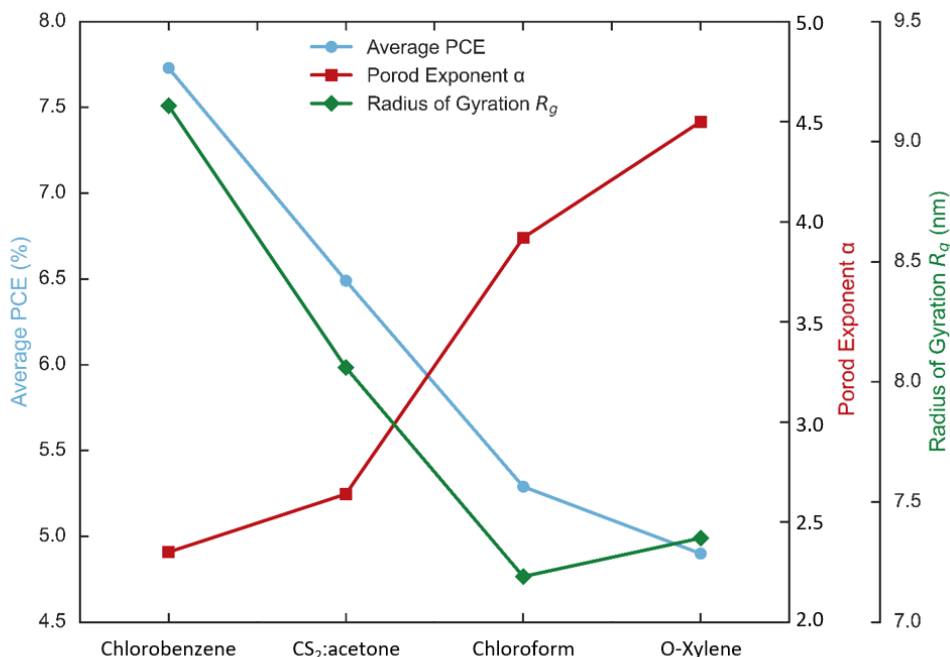


Figure 4.19: Comparison of the average PCE , radius of gyration and scattering exponent values for PBDB-T : ITIC films processed from chlorobenzene, chloroform, o-xylene, and CS₂ : acetone.

Voltage losses in OPV materials occur due to radiative and non-radiative charge carrier recombination at the donor-acceptor interface and at active layer/electrode contacts. A reduction in voltage losses has previously been linked to a reduction in non-radiative and radiative recombination through an optimised interfacial area [280, 281, 282] and beneficial segregation of component materials to the electrical contacts [117, 116] (e.g. ITIC segregation at the top contact). Although water contact angle measurements do not suggest severe interfacial segregation at the surface, a more thorough characterisation of the full vertical composition of the blend films in the plane perpendicular to the substrate by a suitable depth-profiling technique such as neutron reflectivity [107, 278], XPS [129] or ion beam analysis [101] would help clarify this. Additionally, other possible origins for reduced voltage losses should not be discounted. For example, the significantly smoother surface of the CS₂ : acetone blend film measured by AFM (Table 4.6) could aid PFN-Br adhesion to the blend film, enhancing carrier diffusion to the electrical contact.

4.9 Summary

In this chapter, the impact of processing solvent on the BHJ nanomorphology and optoelectronic functionality of PBDB-T : ITIC OPV systems was investigated. The study aimed to address the potential use of more environmentally benign, non-halogenated solvents such as o-xylene and a CS₂ : acetone blend as alternatives to the commonly used pernicious, halogenated processing solvents such as chlorobenzene and chloroform. Although chlorobenzene-processed PBDB-T : ITIC devices exhibited a superior *PCE*, it was found that devices processed from CS₂ : acetone resulted in efficiencies as high as 7.30% and a surprisingly high V_{OC} of 0.92V. Both systems demonstrated efficient PL quenching and GISAXS measurements revealed a highly intermixed morphology with characteristic length scales close to the exciton diffusion length of PBDB-T and ITIC. In comparison, the *PCE* of PBDB-T : ITIC devices processed from o-xylene and chloroform was significantly lower. In these systems, domains were over-purified leading to a reduction in interfacial area and poor PL quenching. The results therefore demonstrate the significant role of the processing solvent in determining the BHJ nanomorphology and resulting optoelectronic properties of PBDB-T : ITIC blend systems. Additionally, they highlight the high level of structural detail attainable from grazing incidence X-ray scattering measurements using a laboratory-based X-ray system. However, it should be noted that for blend nanomorphologies which are finely intermixed, a higher degree of contrast would be beneficial to increase the scattering intensity. Such contrast could be achieved in neutron scattering techniques through deuterium labelling. The structure-performance relationships explored here will be advantageous for developing fabrication routes compatible with large-scale manufacture, essential for the commercialisation OPV.

4.10 Supplementary Data

4.10.1 Optical Microscopy

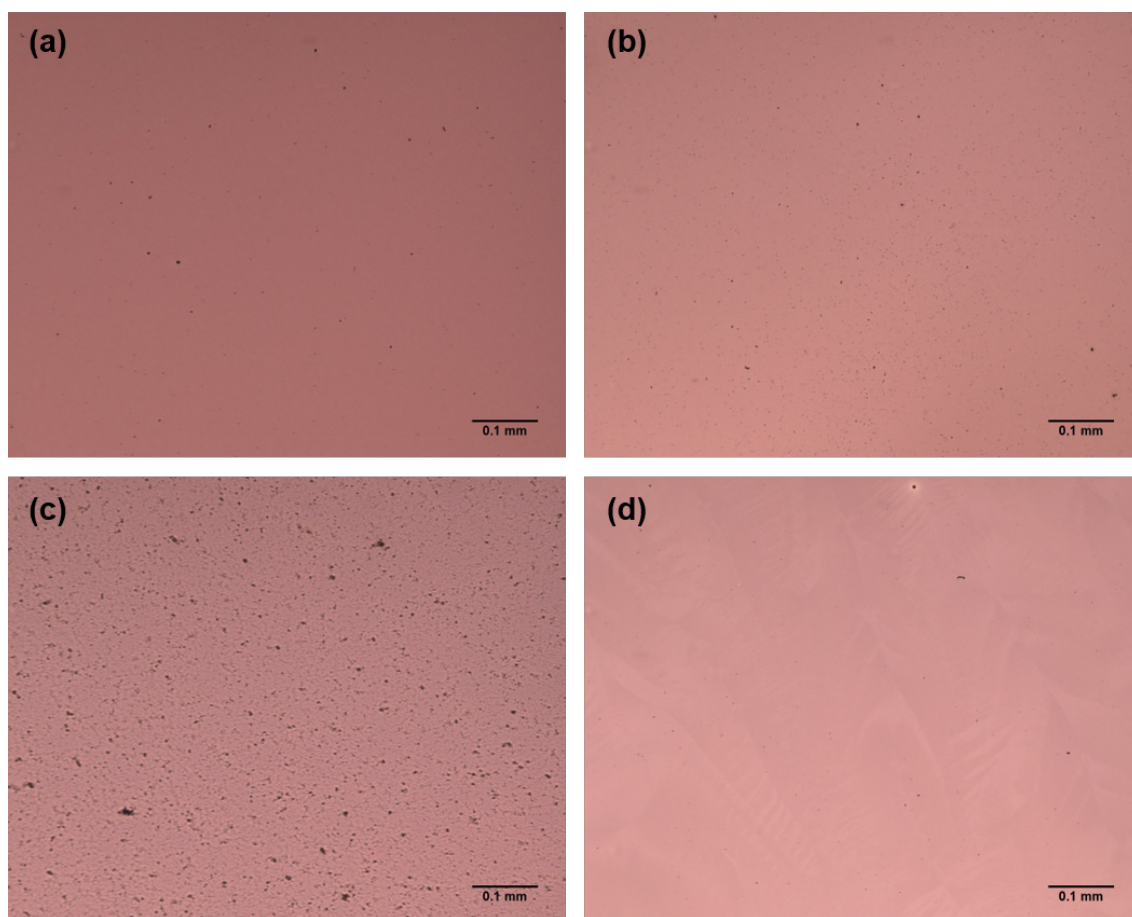


Figure 4.20: Optical microscope images of PBDB-T : ITIC blend thin films processed from (a) chlorobenzene, (b) chloroform, (c) o-xylene, and (d) CS_2 : acetone. The scale bar is 0.1mm.

4.10.2 Exciton Diffusion Length of PBDB-T and ITIC

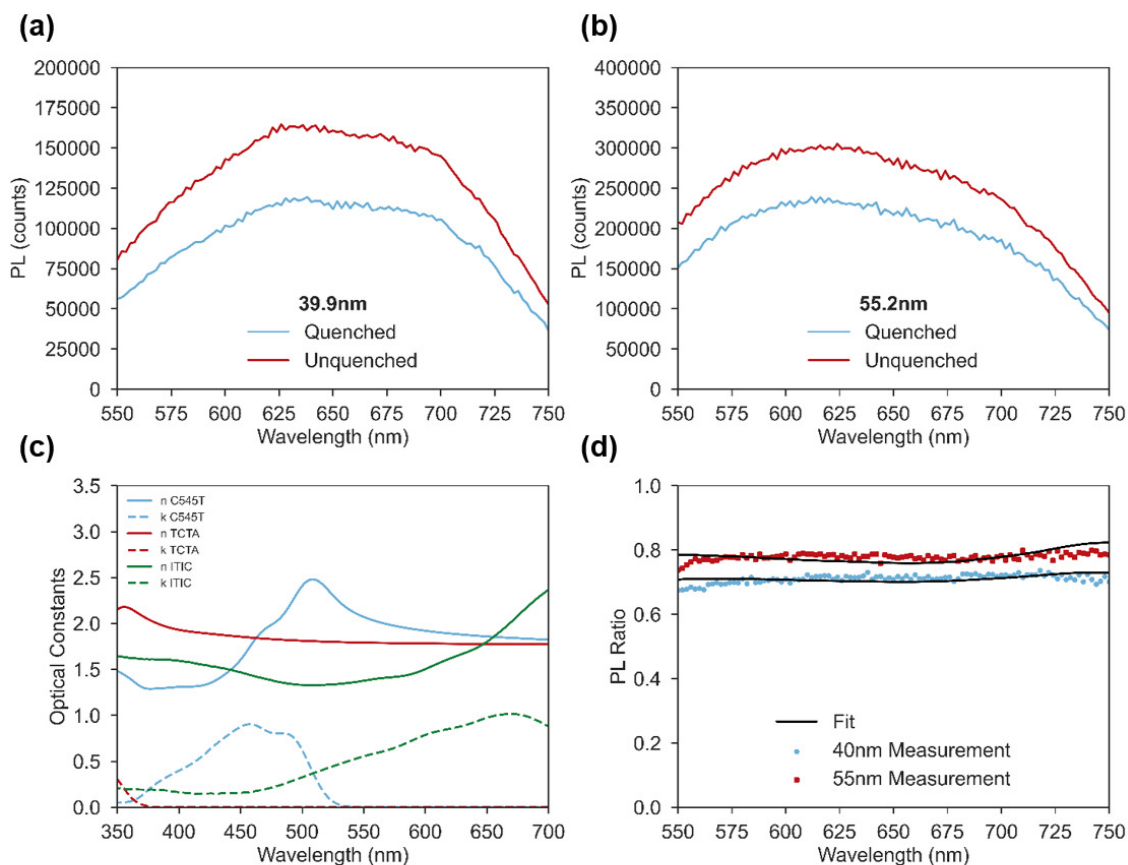


Figure 4.21: Steady-state photoluminescence measurements of quenched and unquenched ITIC thin films processed from chlorobenzene with film thicknesses of (a) 39.9nm and (b) 55.2nm. (c) The optical constants (n, k) of C545T, TCTA and ITIC. (d) The PL ratio and corresponding fit for extracting the exciton diffusion length from ITIC thin films. ($l_d = 11.60 \pm 0.60\text{nm}$).

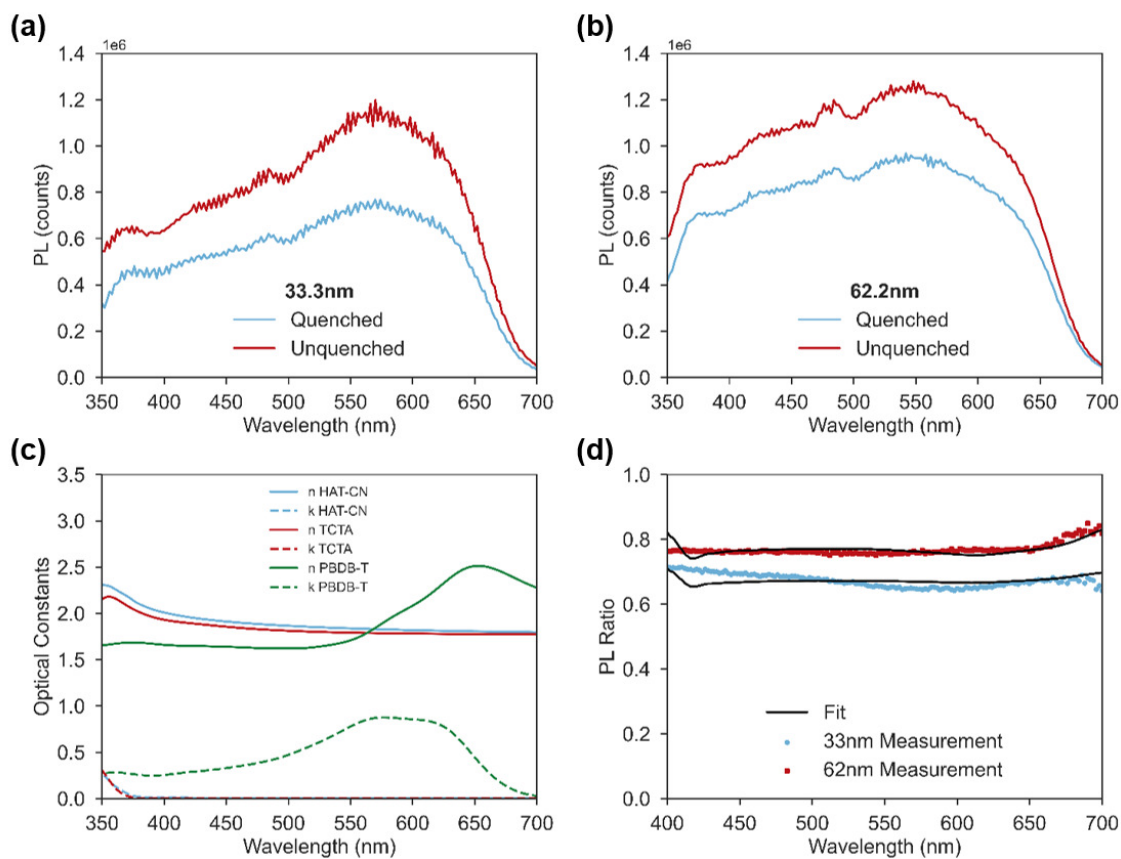


Figure 4.22: Steady-state photoluminescence measurements of quenched and unquenched PBDB-T thin films processed from chlorobenzene with film thicknesses of (a) 33.3nm and (b) 62.2nm. (c) The optical constants (n, k) of HAT-CN, TCTA and PBDB-T. (d) The PL ratio and corresponding fit for extracting the exciton diffusion length from PBDB-T thin films. ($l_d = 12.65 \pm 0.35$ nm).

4.10.3 Contact Angle Measurements

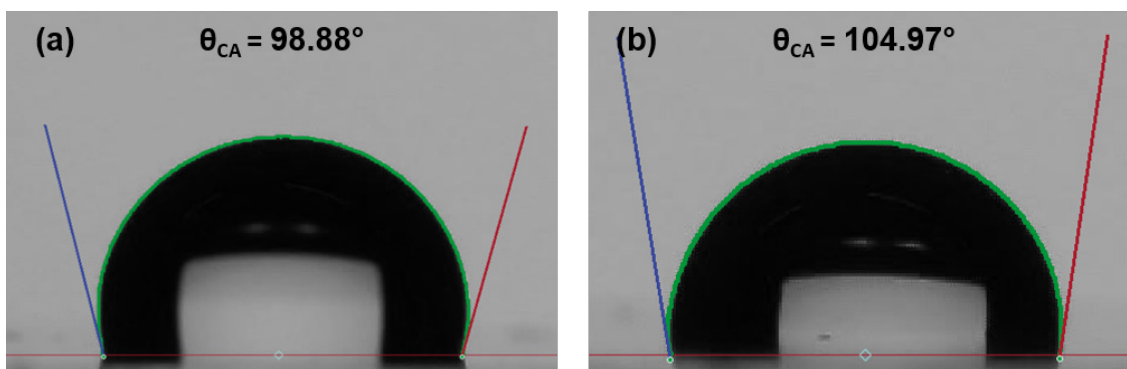


Figure 4.23: Measured contact angles of a water droplet on the surface of (a) pure ITIC and (b) pure PBDB-T thin films processed from chlorobenzene.

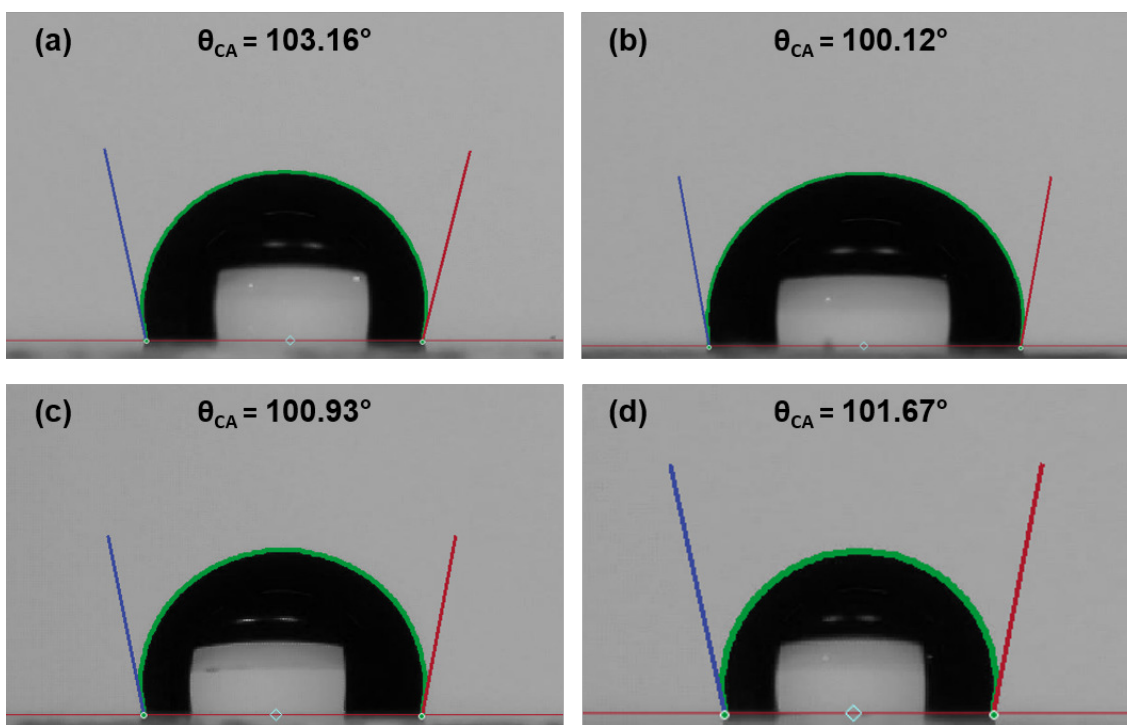


Figure 4.24: Measured contact angles of a water droplet on the surface of PBDB-T : ITIC blend thin films processed from (a) chlorobenzene, (b) chloroform, (c) o-xylene, and (d) CS_2 : acetone.

The Impact of 1,8-diiodooctane on the Morphology, Performance and Stability of Organic Photovoltaics

5.1 Foreword

Over the past decade, small molecule solvent additives such as 1,8-diiodooctane (DIO) have been used extensively to optimise the morphology and consequently the performance of fullerene-based OPVs. This approach has naturally been translated to polymer : NFA systems but with limited success. Additionally, there are growing concerns of the potentially detrimental nature of DIO to the long-term operational stability of PV devices due to degradation routes associated with residual DIO in the film after processing.

In this chapter, I evaluate the benefit of DIO as an OPV processing treatment by comparing its impact between polymer : fullerene (PBDB-T : PC₇₁BM) and polymer : NFA (PBDB-T : ITIC) systems. Initially, the chapter focuses on understanding how DIO impacts the morphology, PV performance and optical properties of *fresh* samples, comparing how this differs between fullerene and NFA-based systems. A particular focus is paid to characterising the three-dimensional self-assembled blend nanostructure of each system using X-ray and neutron scattering techniques. These results are then expanded to explore the stability of each system under different conditions to probe both extrinsic and intrinsic degradation factors. To understand the origin of device instabilities, the removal of DIO from the film is tracked using spectroscopic ellipsometry and ¹H NMR measurements. Taken together, the results demonstrate the complex relationships between solvent-additive-induced morphologies and the resulting optoelectronic functionality and stability. Furthermore, they emphasise that the same methods used to optimise fullerene-based blends are not necessarily applicable to NFA-based systems, prompting the need to source alternative optimisation protocols that deliver both high-efficiency and long-term operational stability.

5.2 Author Contributions

The work in this chapter was performed in collaboration with Emma L. K. Spooner. All structural characterisation measurements (GIWAXS, SANS, NR and AFM) were performed, analysed and interpreted primarily by myself unless otherwise stated below. Emma L. K. Spooner fabricated, tested and processed all devices and related data (EQE, stability). SANS measurements were assisted by Robert M. Dalgliesh, Emma L. K. Spooner, Stephanie L. Burg and Derick L. K. Liew. NR measurements were assisted by Phillip Gut-

freund and performed through a remote access beamtime. Spectroscopic ellipsometry, UV-Vis absorption, contact angle goniometry and film stability photographs were performed, processed and analysed by myself. Emma L. K. Spooner assisted with sample preparation for various measurements. NMR measurements were performed by Khalid A. Doudin and analysis was assisted by Khalid A. Doudin and Mary O’Kane. The interpretation of all data was performed primarily by myself with assistance from Emma L. K. Spooner for device related data. Deuterated ITIC (d8-ITIC and d52-ITIC) were synthesised by collaborators at Wuhan University of Technology and The University of Porto. The project was supervised by Andrew J. Parnell, Richard A. L. Jones and David G. Lidzey.

5.3 Introduction

The inclusion of low volume concentrations of high boiling point, small molecule solvent additives in OPV casting solutions is a common processing method used to fine-tune the BHJ film nanomorphology, providing an easy method to optimise device performance. Since the first demonstration of this optimisation technique using alkane dithiols such as 1,8-octanedithiol (ODT) [283], various alternatives such as 1-chloronaphthalene [284, 285, 286], N-methyl-2-pyrrolidone (NMP) [284, 287], diphenyl ether (DPE) [238, 250] and 1,8-diiodooctane (DIO) [284, 94, 101] have emerged. DIO in particular has been the additive of choice over the past decade, proving to be a successful morphological optimisation tool for fullerene-based blends [101, 238]. With the emergence of high-efficiency NFAs, solvent additive processing has naturally been translated to polymer : NFA systems but their success has been limited, often leading to decreases in device performance rather than enhancements [288]. In addition to this, there are a growing number of reports linking the use of solvent additives to a number of degradation routes, limiting device stability in both polymer : fullerene and polymer : NFA systems [123, 126]. With power conversion efficiencies of organic solar cells now approaching 20% [32, 214, 215, 216, 217, 33], the primary limitation to their commercialisation is the long-term operational stability of devices. It is therefore essential that the impact of solvent additives on the intricate processing-morphology-performance-stability relationships are well-understood and the key differences of how these relationships manifest in both polymer : fullerene and polymer : NFA systems are identified and addressed.

DIO has been used extensively in OPV systems with contrasting morphological effects depending on the thermodynamic and kinetic factors at play during film formation. As discussed in Subsection 2.4.2, kinetic factors include the processing conditions and solvent vapour pressure which determine the film drying kinetics. Thermodynamic factors concern the properties of the material such as the solubilities and interactions of the blend components in the casting solvents and their crystallisation behaviour [102]. The phase-separation

process of the three component system (solvent:donor:acceptor) has been modelled in previous studies using the homogenous Flory-Huggins free energy theory [289, 290, 291, 292]. Here, the morphology of the blend is determined by competing liquid-liquid (L-L) or solid-liquid (S-L) phase separation processes and the quench depth of the system [102].

In OPV blend systems where L-L phase separation dominates, it is reported that solvent additives reduce the extent of component demixing by inducing aggregation in solution in favour of S-L demixing instead [102]. Additionally, the quench depth may also be reduced into the unstable two-phase region of the phase diagram through extended solvent evaporation. Both processes occur when using solvent additives that are poorer solvents for the donor and acceptor components compared to the casting solvent. Solvent additives that are good solvents for the donor and acceptor components mostly reduce demixing by reducing the quench depth through slow solvent evaporation rate. Solvent additives may also hinder L-L demixing by acting as compatibilizers and reducing unfavourable interactions between donor and acceptor components. In the literature, it is reported that in some polymer : fullerene blends such as PTB7-Th : PC₇₁BM [293, 294] and PCDTBT : PC₇₁BM [238], the use of DIO reduces component demixing .

For blend systems where phase separation is governed predominantly by S-L phase demixing, the nucleation and growth of the solid phase limits phase separation. Using solvent additives in such systems therefore increases the degree of phase separation by prolonging film drying and promoting crystal growth either by inducing early nucleation in the case of poor solvents or by increasing the diffusion of solutes for enhanced crystallisation in the case of good solvents [102]. Systems which demonstrate this type of behaviour during DIO processing include P3HT : PC₇₁BM [238] and PffBT4T-2OD : PC₇₁BM [101] where larger domains are formed and interfacial area is reduced. More recent studies have demonstrated the same phase-separation enhancement occurs in polymer : NFA systems such as PBDB-T-SF : IT-4F [295] and PBDB-T : ITIC [116]. Given the rich DIO-induced phase-behaviour apparent in the literature, it is important to identify the driving forces responsible for such effects and characterise how this affects the hierarchical morphological length scales in different systems from molecular-scale packing to aggregate self-assembly to device-scale phase segregation. This is key to improving device optimisation strategies and the resultant optoelectronic functionality.

Although processing with DIO can lead to boosts in the initial performance of devices through greater morphological control, it is important to also consider the impact on device stability. Previous studies have demonstrated the detrimental impact of DIO processing to the operational lifetime of numerous polymer : fullerene systems [296, 127]. The most notable concern is the potentially detrimental impact of residual DIO to the photo-stability of the active layer organic materials during irradiation in ambient conditions [127, 297, 123].

Residual DIO in the film can accelerate UV-induced degradation through the formation of highly reactive iodine and iodoctane free radicals via photolysis [127, 126, 123]. These radicals act as a photo-acid, attacking the conjugated active layer materials and the formation of hydroiodic (HI) acid can be detrimental to device interlayers such as PEDOT:PSS, severely inhibiting charge collection at the electrical contacts [127, 298]. A potentially more influential degradation factor is the risk of oxygen diffusion into the photoactive film which is increased for films containing large amounts of residual DIO as the rate of oxygen diffusion is higher in organic solvents [123].

In response to this, several studies have presented methods to remove DIO from the film via additional processing steps such as thermal annealing [101, 126, 297], high-vacuum exposure [297], methanol rinsing [297, 299], IPA rinsing [300] and light-soaking [301]. The efficacy of these solvent removal methods has been debated in the literature and largely depends on the method used to detect residual DIO. For example, X-ray fluorescence (XRF) measurements have been used previously to show thermal annealing at temperatures of 175°C for 30 minutes and high-vacuum treatments are sufficient to completely remove DIO from PTB7-Th : PC₇₁BM blend films [297]. However, using ¹H NMR measurements this was recently shown to not necessarily be true as substantial amounts of DIO are retained in P3HT : PC₇₁BM films after high vacuum exposure and even after high temperature treatments, sub-ppt concentrations can remain [126].

Even in the absence of oxygen and light, OPV degradation can still occur through morphological and chemical degradation factors. For example, residual DIO in the film after processing is a particular concern to morphological stability as it increases the mobility of the active layer components in the film [302, 303] permitting molecular rearrangement and phase evolution. Retained DIO solvent can also undergo undesirable chemical reactions with device components even in the absence of light and oxygen [298]. To date, the majority of studies in the literature have focused on studying the impact of DIO processing on the photo-stability of organic materials by ageing devices under illumination in inert and/ or ambient conditions [296, 123, 127, 304]. In such experiments, it is difficult to disentangle the primary degradation routes as there are potentially a number of extrinsic factors (e.g. light, oxygen, heat) and intrinsic factors (e.g. morphological, chemical instabilities) involved. Additionally, these studies have primarily focused on polymer : fullerene systems and there is a lack of understanding of how degradation differs in polymer : NFA systems. It is therefore important to explore the impact of DIO on the stability of both polymer : fullerene and polymer : NFA systems under a range of stress conditions. This is necessary to identify the primary degradation routes in both systems and to effectively link degradation to processing conditions and film nanomorphology.

The work presented in this chapter aims to clarify the efficacy of DIO processing as a

suitable optimisation methods for OPV systems by comparing its impact in polymer : fullerene and polymer : NFA systems. This was done by firstly comparing the impact of DIO on the optoelectronic properties of PBDB-T : ITIC and PBDB-T : PC₇₁BM blends processed with various DIO volume concentrations (0-3 Vol%). Using a range of characterisation techniques (GIWAXS, SANS, AFM and NR) these results were then correlated with DIO-induced changes to the full, three-dimensional nanostructure of each blend system. Importantly, deuterated ITIC was synthesised for neutron scattering techniques to increase the SLD contrast in the blend with PBDB-T. To the best of the authors knowledge, using deuterium-labelled NFAs to characterise the thin film nanostructure of OPV systems has not been reported elsewhere. Following on from this, the impact of DIO on the stability of each system is investigated under different stress conditions. This firstly involved tracking the removal of DIO during thermal annealing using spectroscopic ellipsometry and ¹H NMR measurements. Primary degradation routes for each system were then explored by ageing films and devices in various environments (e.g. in the dark and under illumination). Taken together, the results presented in this chapter provide understanding of the relationships between processing, morphology, performance and stability, and highlight the need to develop alternative optimisation protocols to fabricate systems that are both efficient *and* stable.

5.4 Experimental

Measurements in this chapter were performed on PBDB-T : ITIC and PBDB-T : PC₇₁BM blend films along with reference pure material films of ITIC, PC₇₁BM and PBDB-T. PBDB-T (batch M1001A2) from Ossila was used with $M_w = 142,718$, $M_n = 60,189$ and $PDI = 2.37$). Film processing conditions for pure and blend films are provided in Table 5.1 and Table 5.2 respectively. All active layer solutions were prepared in a solvent mixture of chlorobenzene with the addition of DIO in volume concentrations of 0, 0.5, 1 and 3 Vol%. All films were spun dynamically and annealed in a nitrogen-filled glovebox at 160°C for 10 minutes, informed by the thermal measurements discussed in Chapter 4. Blend thin films were $\sim 80 - 100nm$ thick.

Material	Solid Concentration (mg/mL)	Spin Speed (rpm)
ITIC	15	1000
PC ₇₁ BM	15	1000
PBDB-T	10	2000

Table 5.1: Table of film processing conditions for pure ITIC, PC₇₁BM and PBDB-T films.

Blend	Solid Concentration (mg/mL)	Spin Speed (rpm)
PBDB-T : ITIC	18	2050
PBDB-T : PC ₇₁ BM	15	1000

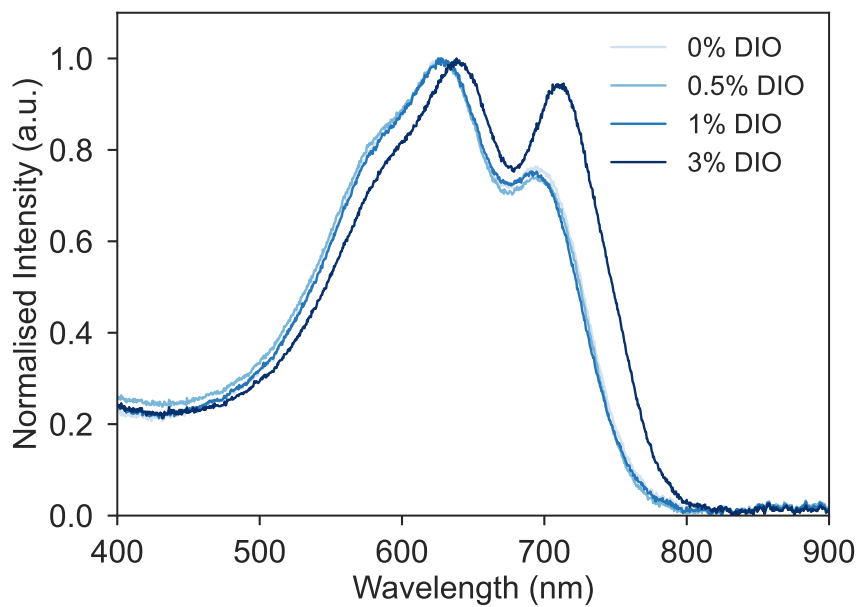
Table 5.2: Table of film processing conditions for PBDB-T : ITIC and PBDB-T : PC₇₁BM blend films.

5.5 Optoelectronic Properties and Structural Characterisation of Fresh Films

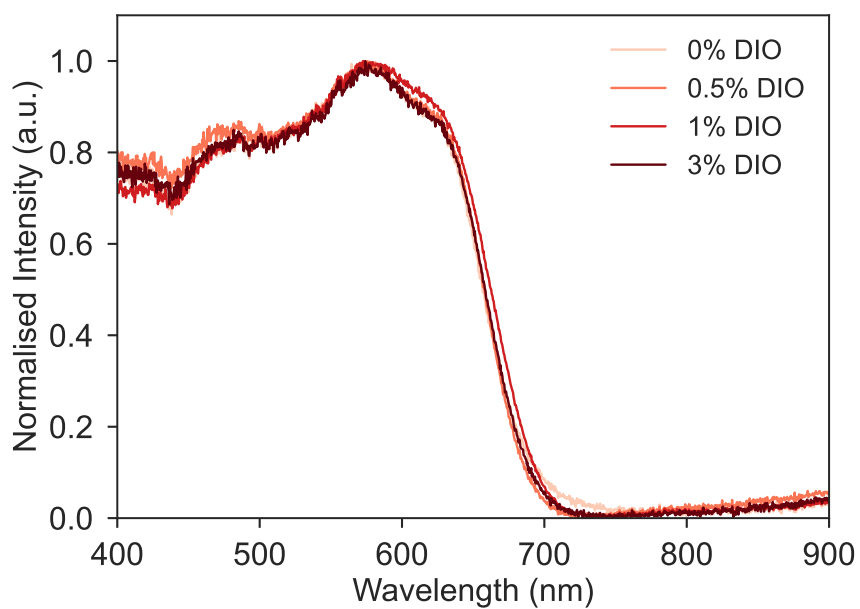
5.5.1 Optoelectronic Properties

The normalised UV-Vis absorption spectra of PBDB-T : ITIC and PBDB-T : PC₇₁BM blend thin films processed from 0, 0.5, 1 and 3 Vol% DIO are displayed in Figure 5.1 and corresponding reference spectra of pure ITIC, PC₇₁BM and PBDB-T films are provided in the supplementary data (Figure 5.29, Figure 5.30 and Figure 5.31 respectively). In the case of PBDB-T : ITIC, the UV-Vis absorption profiles of films processed from 0-1 Vol% DIO are comparable, exhibiting an absorption maximum at $\sim 627\text{nm}$ and absorption edge at $\sim 762\text{nm}$ (Figure 5.1a). Comparing with pure ITIC and PBDB-T reference films, the contributions of each component can be identified (Subsection 5.10.1). The high-energy shoulder at $\sim 580\text{nm}$ originates from PBDB-T absorption, the peak at $\sim 700\text{nm}$ is from an ITIC absorption band and the peak at $\sim 627\text{nm}$ is a superposition of the transitions at $\sim 625\text{nm}$ and $\sim 650\text{nm}$ for PBDB-T and ITIC respectively (Figure 5.29 and Figure 5.31). For the PBDB-T : ITIC film processed with 3 Vol% DIO, the absorption spectrum appears to have undergone a bathochromic shift of $\sim 10\text{nm}$ relative to films processed with lower DIO concentrations and the shifted ITIC peak at $\sim 710\text{nm}$ exhibits a considerably higher intensity relative to the maximum absorption. Upon inspection of the pure reference films, a similar bathochromic shift of $\sim 7\text{nm}$ occurs for the ITIC film processed from 3 Vol% indicative of enhanced molecular packing through the formation of J-aggregates [272, 110].

In the case of PBDB-T : PC₇₁BM blend films, stronger absorption is observed at wavelengths $< 500\text{nm}$ compared to PBDB-T : ITIC films. However, the significantly reduced absorption at wavelengths $> 700\text{nm}$ leads to a poorer spectral overlap with the solar spectrum (Figure 5.1b). Comparing to the reference spectra of pure PC₇₁BM and PBDB-T, absorption $< 500\text{nm}$ is dominated by PC₇₁BM, whereas the low energy absorption contribution ($> 500\text{nm}$) is dominated by PBDB-T, exhibiting an absorption maximum at $\sim 580\text{nm}$ and absorption edge at $\sim 695\text{nm}$ (Figure 5.30, Figure 5.31). With increasing DIO concentration, the absorption profiles of PBDB-T : PC₇₁BM blend films do not change significantly.



(a)



(b)

Figure 5.1: Normalised UV-Vis absorption of (a) PBDB-T : ITIC and (b) PBDB-T : PC₇₁BM blend thin films processed with 0, 0.5, 1 and 3 Vol% DIO.

Next, the impact of DIO concentration on the J - V characteristics of PBDB-T : ITIC and PBDB-T : PC₇₁BM OPV devices was investigated. Devices were fabricated in a conventional device architecture (glass/ITO/PEDOT:PSS/active layer/PFN-Br/Ag) following the fabrication protocols outlined in Chapter 3. Champion J - V curves are presented in Figure 5.2 along with a box plot of device statistics in Figure 5.3 and summary in Table 5.3. The performance of PBDB-T : ITIC solar cells processed without DIO is in agreement with literature values [94], achieving a champion PCE of 10.62%, J_{SC} of $17.76\text{mA}/\text{cm}^2$, V_{OC} of 0.91V and FF of 67.01%. With the addition of 0.5 Vol% DIO, there is a noticeable increase in PCE from 10.63% to 11.05% primarily resulting from enhancements in FF and J_{SC} . Processing with higher concentrations of DIO (1 Vol% and 3 Vol%) appears to be detrimental to the PV performance of PBDB-T : ITIC devices with champion PCE s dropping to 9.94% and 5.08% respectively. The performance of the 3 Vol% DIO film in particular seems to suffer from drastic losses across all device metrics and the appearance of an inflection point near V_{OC} giving the curve a prominent 'S-shape'. S-shaped J - V curves have been reported in OPV systems elsewhere and are indicative of significantly reduced charge carrier extraction at the electrical contacts [305, 306, 307].

In comparison, PBDB-T : PC₇₁BM devices generally exhibit inferior PV performance to PBDB-T : ITIC cells as the weaker absorption of the solar spectrum (demonstrated in the UV-Vis measurements above Figure 5.1) severely limits device photocurrent (i.e. J_{SC}). PBDB-T : PC₇₁BM devices processed without DIO exhibit a champion PCE of 7.33%, J_{SC} of $13.15\text{mA}/\text{cm}^2$, V_{OC} of 0.86V and FF of 68.77%. With the addition of 0.5 Vol% DIO, there is a significant boost in PV performance with the champion PCE increasing to 8.48% primarily due to enhancements in J_{SC} and FF . As DIO concentration is increased to 1 Vol%, further improvements in J_{SC} and FF results in a slightly increased champion PCE of 8.84% and an impressive FF of 71.40%. Similarly to PBDB-T : ITIC devices, at larger DIO concentrations (3 Vol%) there is a decrease in V_{OC} suggesting a reduction in charge extraction. However, the effect is much less severe in PBDB-T : PC₇₁BM devices, achieving a champion PCE of 7.94%. Importantly, S-shaped J - V curves are only observed in the 3 Vol% DIO PBDB-T : ITIC system with PBDB-T : PC₇₁BM systems exhibiting normal diode-like J - V characteristics for all DIO concentrations.

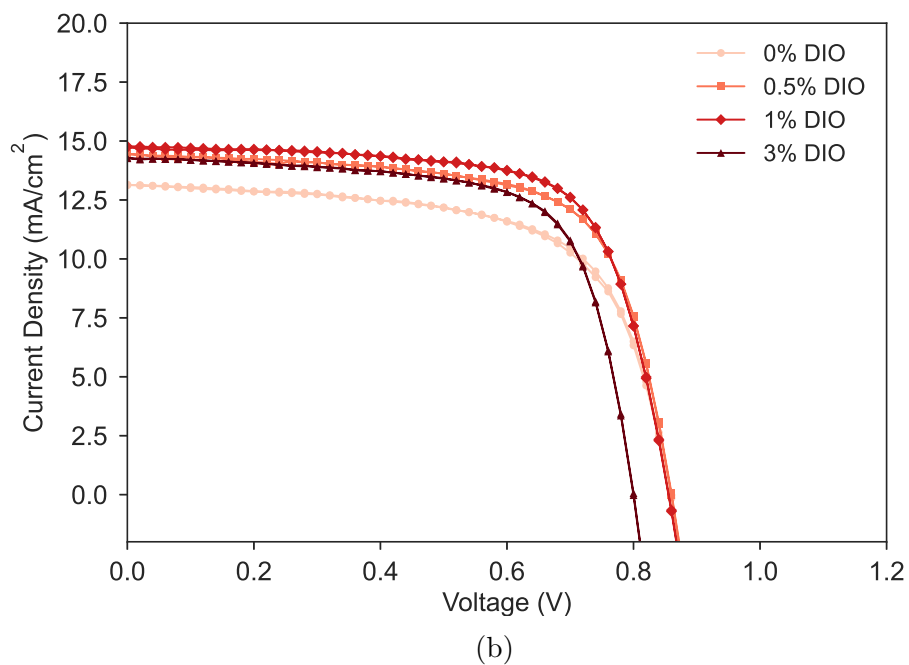
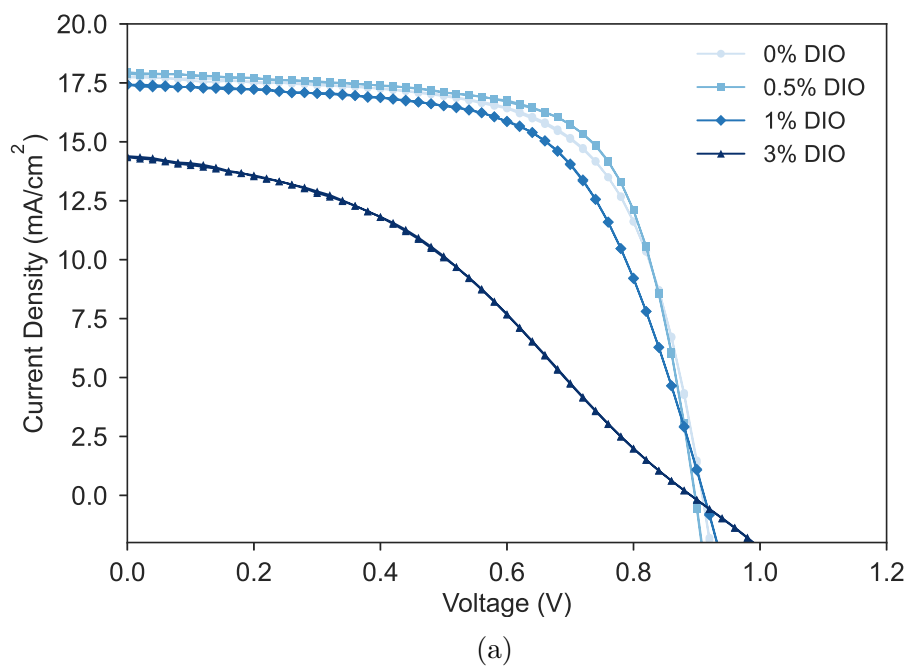
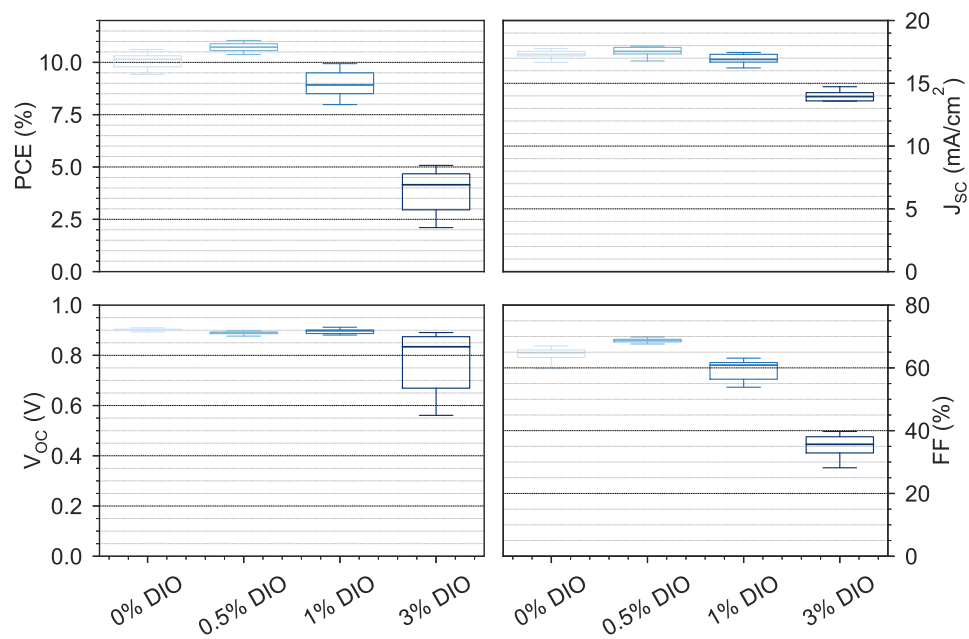
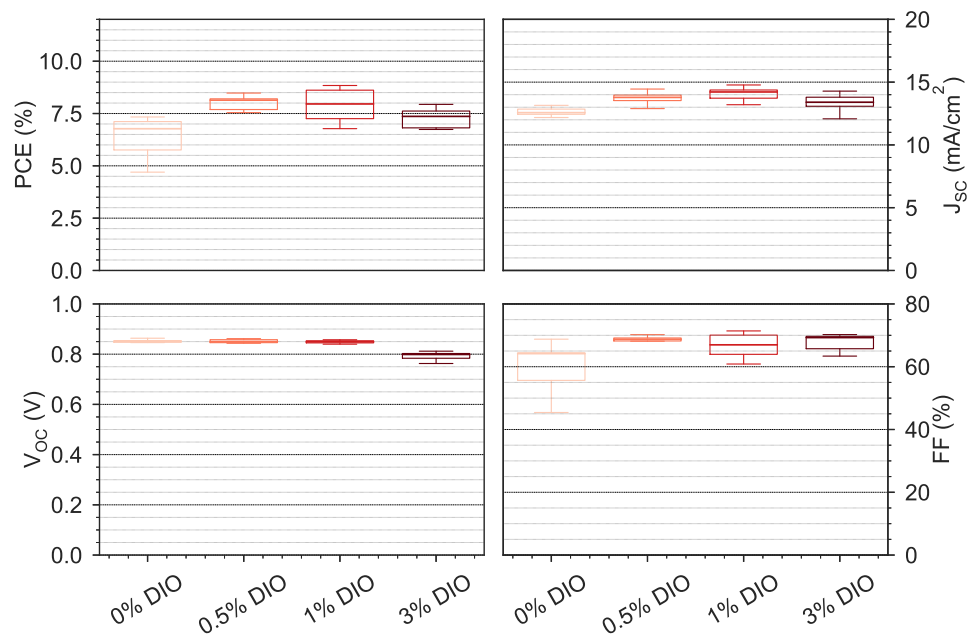


Figure 5.2: Champion J - V curves of (a) PBDB-T : ITIC and PBDB-T : PC₇₁BM solar cells processed from chlorobenzene with 0-3 Vol% DIO.



(a)



(b)

Figure 5.3: Boxplot of device metrics for (a) PBDB-T : ITIC and PBDB-T : PC₇₁BM solar cells processed from chlorobenzene with 0-3 Vol% DIO. Approximately 25 devices are included for each split.

System	DIO (Vol%)	J_{SC} (mA/cm^2)	V_{OC} (V)	FF (%)	PCE (%)
PBDB-T : ITIC	0	17.34 ± 0.26 (17.76)	0.88 ± 0.10 (0.91)	62.48 ± 8.50 (67.01)	9.67 ± 1.82 (10.62)
	0.5	17.52 ± 0.33 (17.95)	0.88 ± 0.05 (0.90)	65.52 ± 10.63 (69.83)	10.18 ± 1.88 (11.05)
	1	16.93 ± 0.38 (17.45)	0.89 ± 0.02 (0.91)	58.47 ± 5.09 (63.10)	8.84 ± 0.95 (9.94)
	3	13.65 ± 0.89 (14.73)	0.78 ± 0.89 (0.86)	35.21 ± 3.05 (39.74)	3.84 ± 0.98 (5.08)
PBDB-T : PC ₇₁ BM	0	12.61 ± 0.34 (13.15)	0.85 ± 0.01 (0.86)	60.60 ± 6.0 (68.77)	6.51 ± 0.76 (7.33)
	0.5	13.68 ± 0.48 (14.44)	0.80 ± 0.16 (0.86)	63.37 ± 13.9 (70.22)	7.24 ± 2.23 (8.48)
	1	14.06 ± 0.49 (14.77)	0.82 ± 0.07 (0.86)	64.07 ± 10.9 (71.40)	7.53 ± 1.71 (8.84)
	3	13.28 ± 0.74 (14.28)	0.74 ± 0.17 (0.81)	61.77 ± 15.01 (70.24)	6.43 ± 2.21 (7.94)

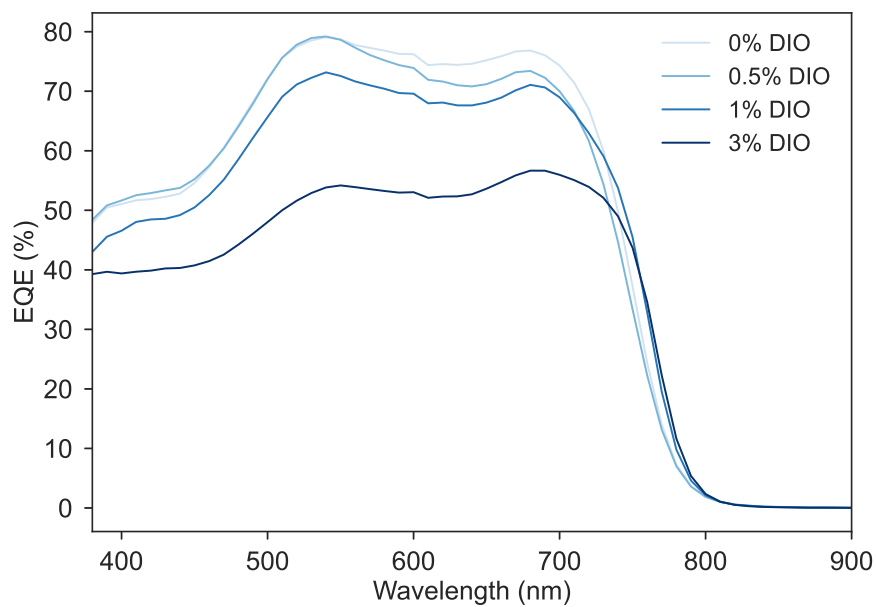
Table 5.3: Summary of the average and champion OPV device metrics for PBDB-T : ITIC and PBDB-T : PC₇₁BM solar cells processed from chlorobenzene with 0-3 Vol% DIO. Averages are given for ~ 25 devices ± 1 standard deviation, with metrics relating to the champion PCE shown in parenthesis.

The EQE spectra of PBDB-T : ITIC and PBDB-T : PC₇₁BM devices processed from various concentrations of DIO is displayed in Figure 5.4. Integrated J_{SC} values from the EQE spectra show $<10\%$ discrepancy between values extracted from J - V measurements of the same devices (Table 5.4). PBDB-T : ITIC devices exhibit a broad photo conversion response in the wavelength range 500-750nm in agreement with the UV-Vis absorption measurements described above (Figure 5.1a). In this wavelength range, devices processed from 0 and 0.5 Vol% DIO exhibit EQEs over 70% with maximum EQE values close to 80% (Figure 5.4a). For DIO concentrations >0.5 Vol%, EQE decreases particularly for devices processed from 3 Vol% with EQE limited to a maximum of $\sim 55\%$. In comparison to PBDB-T : ITIC systems, the EQE at wavelengths <500 nm is much greater for PBDB-T : PC₇₁BM devices due to the low-wavelength absorption of PC₇₁BM discussed previously (Figure 5.1b). However, as a result of limited absorption at higher wavelengths, EQE falls off sharply at wavelengths >700 nm. In agreement with the J - V measurements described above, devices processed from 1 Vol% DIO exhibit the highest integrated J_{SC} with a

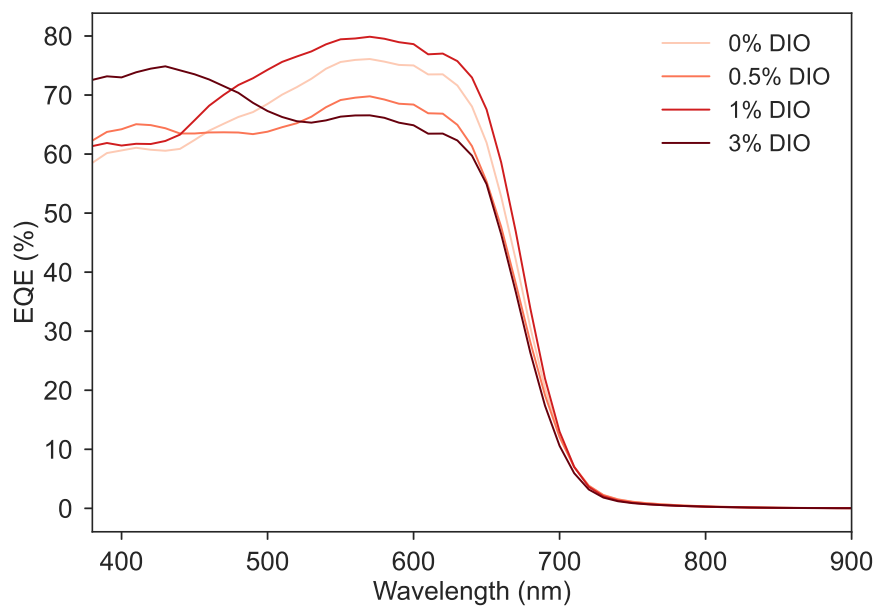
maximum EQE of $\sim 80\%$. For devices processed with 0, 0.5 and 3 Vol% DIO, the lower EQE in the region 500-700nm compared to the 1 Vol% device is in agreement with the weaker absorption and lower J_{SC} values discussed above. Interestingly, PBDB-T : PC₇₁BM devices processed from 3 Vol% DIO display an enhanced EQE at wavelengths $< 500\text{nm}$. The origin of this enhancement is unclear given that it does not relate to similar enhancements in the UV-Vis absorption of either component of the blend film.

System	DIO (Vol%)	J_{SCJV} (mA/cm^2)	J_{SCEQE} (mA/cm^2)
PBDB-T : ITIC	0	17.10	16.50
	0.5	17.15	16.00
	1	16.22	15.40
	3	12.46	12.30
PBDB-T : PC ₇₁ BM	0	13.48	12.60
	0.5	12.78	11.80
	1	13.49	13.30
	3	13.00	12.00

Table 5.4: A summary of J_{SC} values for PBDB-T : ITIC and PBDB-T : PC₇₁BM devices processed from various concentrations of DIO (0-3 Vol%). Values were extracted from J - V measurements (J_{SCJV}) and from integrating the EQE spectra in Figure 5.4 (J_{SCEQE}).



(a)



(b)

Figure 5.4: EQE spectra from a representative run of (a) PBDB-T : ITIC and (b) PBDB-T : PC₇₁BM devices processed with various concentrations of DIO (0-3 Vol%).

5.5.2 Small-Scale Structures

The changes in optical properties and device performance discussed above provide an initial indication that the morphology and nanostructure of the blend films is also likely to be influenced by the presence of DIO. To investigate this, GIWAXS measurements were performed to characterise DIO-induced changes in the molecular self-assembly of both pure reference films and corresponding blend thin films. To identify scattering peaks in the blend data, GIWAXS of pure ITIC, PC₇₁BM and PBDB-T reference films processed from chlorobenzene with 0-3 Vol% DIO were collected. All pure reference film GIWAXS data are provided in the supplementary information at the end of the chapter (Subsection 5.10.2). 2D GIWAXS patterns of PBDB-T : ITIC and PBDB-T : PC₇₁BM films processed from chlorobenzene with 0-3 Vol% DIO are displayed in Figure 5.5 and Figure 5.6 respectively. In Figure 5.7, corresponding azimuthally integrated Q -dependent and χ -dependent 1D intensity profiles are plotted. To generate Q -dependent intensity profiles, the 2D scattering patterns were integrated in the Q range $0.2 < Q(\text{\AA}^{-1}) < 2.0$ through various χ angles; out-of-plane (in the Q_z direction, $-20 < \chi(^{\circ}) < 20$) and in-plane ($70 < \chi(^{\circ}) < 90$). For χ -dependent intensity profiles, the 2D scattering patterns were integrated across the full χ range $-90 < \chi(^{\circ}) < 90$ in the Q range $0.25 < Q(\text{\AA}^{-1}) < 0.45$. A summary of peak positions, d -spacings and crystalline coherence lengths CCL for the most prominent scattering features in the blend film data are provided in Table 5.5 where CCL values were estimated using the Scherrer equation Equation 3.78.

For PBDB-T : ITIC blend films, it is evident from the 2D scattering patterns that DIO concentration has a significant impact on molecular self-assembly (Figure 5.5). To understand these changes, it is first necessary to compare the changes in molecular packing of pure ITIC and PBDB-T reference films processed using the same DIO concentration series. The 2D GIWAXS patterns of pure ITIC films processed from chlorobenzene with 0-3 Vol% DIO are composed of a broad scattering feature at $Q \sim 1.7\text{\AA}^{-1}$ in the out-of-plane direction and a number of orientated features at low Q in the range $0.3 < Q(\text{\AA}^{-1}) < 0.55$ (Figure 5.32). Currently two bulk ITIC crystal structures have been reported; an edge-to-face crystal structure [111], and a face-to-face crystal structure [308]. Despite exhibiting well-determined crystallographic phases in the bulk, the molecular self-assembly of ITIC in a thin film geometry is complex and multiple processing-dependent polymorphs and packing motifs that are different to the bulk crystal structures have been reported [267, 112].

In the thin film, molecular self-assembly is dominated by π - π stacking of the terminal IC groups which have previously demonstrated a diverse range of chain-like and cluster-like molecular structures [111] in coexisting face-on and edge-on orientations relative to the substrate [109]. In this study, the previously reported bimodal lamellar stacking is apparent in pure ITIC films processed without DIO from the appearance of two in-plane

peaks at $Q = 0.34\text{\AA}^{-1}$ ($d = 18.6\text{\AA}$) and $Q = 0.44\text{\AA}^{-1}$ ($d = 14.2\text{\AA}$) in addition to two out-of-plane peaks at $Q = 0.54\text{\AA}^{-1}$ ($d = 11.6\text{\AA}$) and $Q = 1.67\text{\AA}^{-1}$ ($d = 3.76\text{\AA}$) [109] (Figure 5.33, and Table 5.11). The scattering feature at $Q = 0.34\text{\AA}^{-1}$ is consistent with the (001) backbone stacking peak [109] and is close to the c -crystallographic lattice constant in one of the reported bulk crystal structure ($c = 17.5\text{\AA}$) [111]. The in-plane peak at $Q = 0.44\text{\AA}^{-1}$ originates from face-on lamellar stacking (100) whilst the out-of-plane peak at $Q = 0.54\text{\AA}^{-1}$ has been previously indexed as edge-on lamellar stacking ($a = 11.5\text{\AA}$) [111, 109]. The broad scattering feature in the out-of-plane direction at $Q = 1.67\text{\AA}^{-1}$ originates from π - π stacking between the terminal aromatic groups.

With the inclusion of DIO, a number of additional scattering features appear and scattering intensities increase, indicative of enhanced molecular order and crystallinity. For example, the 1 Vol% DIO processed film shows an additional π - π stacking peak at $Q = 1.54\text{\AA}^{-1}$ ($d = 4.08\text{\AA}$) which increases in intensity for films processed using higher DIO concentrations (3 Vol%). The enhanced molecular packing of ITIC films processed from 3 Vol% DIO is identifiable from the appearance of multiple higher order peaks in the in-plane direction at $Q = 0.63, 0.73$ and 0.84\AA^{-1} (Figure 5.33b) and large increases in intensity and CCL for several characteristic length scales (e.g. CCL increases from 0.9nm to 18.8nm for the π - π stacking peak at $Q \sim 1.67 - 1.69\text{\AA}^{-1}$ Table 5.11). The enhanced intensity of the edge-on lamellar stacking peak in the out-of-plane direction at $Q = 0.54\text{\AA}^{-1}$ and the backbone and face-on lamellar stacking peaks at $Q \sim 0.34\text{\AA}^{-1}$ and $Q \sim 0.44\text{\AA}^{-1}$ respectively in the in-plane direction suggest DIO induces preferential orientation of *both* face-on and edge-on orientated ITIC (Figure 5.33). This is also evident in the angular distribution intensity profiles where there is a higher intensity in the in-plane direction ($\chi \sim 70^\circ$) due to preferential orientation of both the backbone and face-on lamellar stacking peaks, characteristic of preferentially edge-on orientated and face-on orientated ITIC respectively (Figure 5.33c). The GIWAXS data of pure ITIC films presented here is therefore not representative of either reported bulk crystal structure in agreement with results reported elsewhere [111, 308] and the inclusion of DIO in the casting solution enhances the crystallinity in both face-on and edge-on molecular orientations.

The 2D scattering patterns of pure PBDB-T reference films processed with 0-3 Vol% are similar to results reported elsewhere [109, 116] with all films exhibiting two prominent scattering features; a ring-like feature at $Q \sim 0.3\text{\AA}^{-1}$ from lamellar (100) stacking and a diffuse broad arc in the out-of-plane direction at $Q \sim 1.7\text{\AA}^{-1}$ resulting from π - π stacking (Figure 5.34). For the film processed without DIO, the lamellar stacking and π - π stacking peaks are positioned at $Q = 0.29\text{\AA}^{-1}$ (in the in-plane direction) and $Q = 1.69\text{\AA}^{-1}$ respectively (Figure 5.35, Table 5.12). The lamellar peak in the out-of-plane direction is considerably stronger than the in-plane contribution suggesting there is a greater number of edge-on orientated crystallites. As DIO concentration increases, the simultaneous increase

in intensity of the π - π stacking peak and decrease in lamellar stacking intensity in the out-of-plane direction, combined with an increase in lamellar stacking intensity in the in-plane direction is indicative of a change in molecular orientation from an edge-on orientation to a predominantly face-on orientated system (Figure 5.35). This is also demonstrated in the χ -dependent intensity profiles where the in-plane intensity ($\chi \sim \pm 90^\circ$) increases with increasing DIO concentration due to stronger in-plane scattering from lamellae aligned face-on to the substrate (Figure 5.35c). In addition to a DIO-induced change in molecular orientation, the *CCL* values relating to the in-plane lamellar peak and π - π stacking peak increase from 6.24nm to 11.13nm and from 1.19nm to 2.01nm respectively for films processed with 0 and 3 Vol% DIO (Table 5.12). Taken together, the observed differences in GIWAXS intensities, angular distribution and crystallite sizes demonstrate that processing with DIO enhances the molecular order of PBDB-T, increasing the relative proportion of favourable face-on orientated crystallites and lateral grain size.

Using the GIWAXS data of pure ITIC and pure PBDB-T films discussed above, DIO-induced changes observed in GIWAXS of PBDB-T : ITIC blend films are now more easily identifiable. For PBDB-T : ITIC blend films processed without DIO (0 Vol%), two prominent scattering features are visible; a ring-like feature at $Q = 0.31\text{\AA}^{-1}$ ($d = 20.3\text{\AA}$) with preferential orientation in the out-of-plane direction and a broad, diffuse arc also in the out-of-plane direction at $Q = 1.73\text{\AA}^{-1}$ ($d = 3.63\text{\AA}$) (Figure 5.5a, Table 5.5). The preferential orientation of the scattering feature at $Q = 0.31\text{\AA}^{-1}$ in the out-of-plane direction is similar to the lamellar peak observed for pure PBDB-T films processed without DIO suggesting PBDB-T adopts the same edge-on orientation at low DIO concentrations in both the pure film and the blend film (Figure 5.7). With the inclusion of 0.5 Vol% DIO, the same two characteristic scattering features observed for the blend film without DIO are visible but intensities are stronger, indicating a higher degree of molecular order. Furthermore, an additional weak intensity peak at $Q = 0.36\text{\AA}^{-1}$ ($d = 17.4\text{\AA}$) in the in-plane direction is observed which was previously indexed as backbone (001) stacking in pure ITIC films (Figure 5.7b). As DIO concentration is increased to 1 Vol%, the lamellar stacking peak associated with edge-on orientated ITIC emerges at $Q = 0.49\text{\AA}^{-1}$ ($d = 13.0\text{\AA}$) in the out-of-plane direction and PBDB-T appears to undergo the same transition in molecular orientation as observed for the pure films, from a predominantly edge-on arrangement to a more favourable face-on preferential orientation. This is demonstrated by the decrease in lamellar stacking scattering intensity in the out-of-plane direction and simultaneous increase in the in-plane direction at $Q \sim 0.3\text{\AA}^{-1}$. For 3 Vol% DIO, the same DIO-induced changes observed for pure ITIC films are also apparent in the blend film with the emergence of a secondary π - π stacking peak at $Q = 1.56\text{\AA}^{-1}$ ($d = 4.02\text{\AA}$) and a number of higher order peaks in the in-plane direction. Additionally, the χ -dependent 1D intensity profile of the blend film is representative of the combined increases in in-plane scattering observed for the pure ITIC and pure PBDB-T films.

In comparison to PBDB-T : ITIC, the lack of significant changes in the 2D GIWAXS patterns of PBDB-T : PC₇₁BM blend films processed from chlorobenzene with 0-3 Vol% DIO suggests DIO concentration is less influential on the molecular self-assembly of PC₇₁BM (Figure 5.6). This is demonstrated in the 2D GIWAXS of pure PC₇₁BM films, which each consist of weakly scattering isotropic rings, indicative of an amorphous PC₇₁BM molecular arrangement (Figure 5.34). In general, pure PC₇₁BM films exhibit GIWAXS features at $Q \sim 0.38, 0.69, 1.30$ and 1.87 \AA^{-1} ($d = 16.5, 9.1, 4.8$ and 3.4 \AA) (Figure 5.35, Table 5.13). The most prominent of these is the isotropic ring at $Q \sim 1.3$ which corresponds to the approximate spherical diameter of PC₇₁BM molecules as reported elsewhere [309, 310]. With the inclusion of DIO, the d -spacing and CCL of each characteristic pure PC₇₁BM peak does not change significantly. However, scattering intensities fluctuate the higher intensities observed for films processed with 1 Vol%, indicative of enhanced molecular order. In PBDB-T : PC₇₁BM blend films, the 2D GIWAXS patterns show three distinct scattering features; lamellar (100) PBDB-T stacking at $Q \sim 0.3 \text{ \AA}^{-1}$, an amorphous PC₇₁BM isotropic ring at $Q \sim 1.3 \text{ \AA}^{-1}$ and PBDB-T π - π stacking at $Q \sim 1.75 \text{ \AA}^{-1}$ (Figure 5.6, Figure 5.7). In agreement with GIWAXS of pure films, the CCL related to characteristic PC₇₁BM length scales does not change significantly with DIO concentration (Figure 5.7). For PBDB-T lamellar stacking length scales, CCL increases from 7.5nm and 5.3nm to 14.4 and 7.9nm in the in-plane and out-of-plane directions respectively, which is similar to the DIO-induced crystallite growth observed in pure PBDB-T films. However, in contrast to both pure PBDB-T and PBDB-T : ITIC films, the edge-on to face-on orientational rearrangement of PBDB-T with increasing DIO concentration is not observed for PBDB-T : PC₇₁BM blend films. Instead, films processed with DIO show enhanced lamellar stacking intensities in both the in-plane and out-of-plane direction and the lack of angular dependence in the χ -dependent intensity profiles suggests the system contains a mixture of edge-on and face-on orientated PBDB-T, which is largely unchanged with increasing DIO concentration.

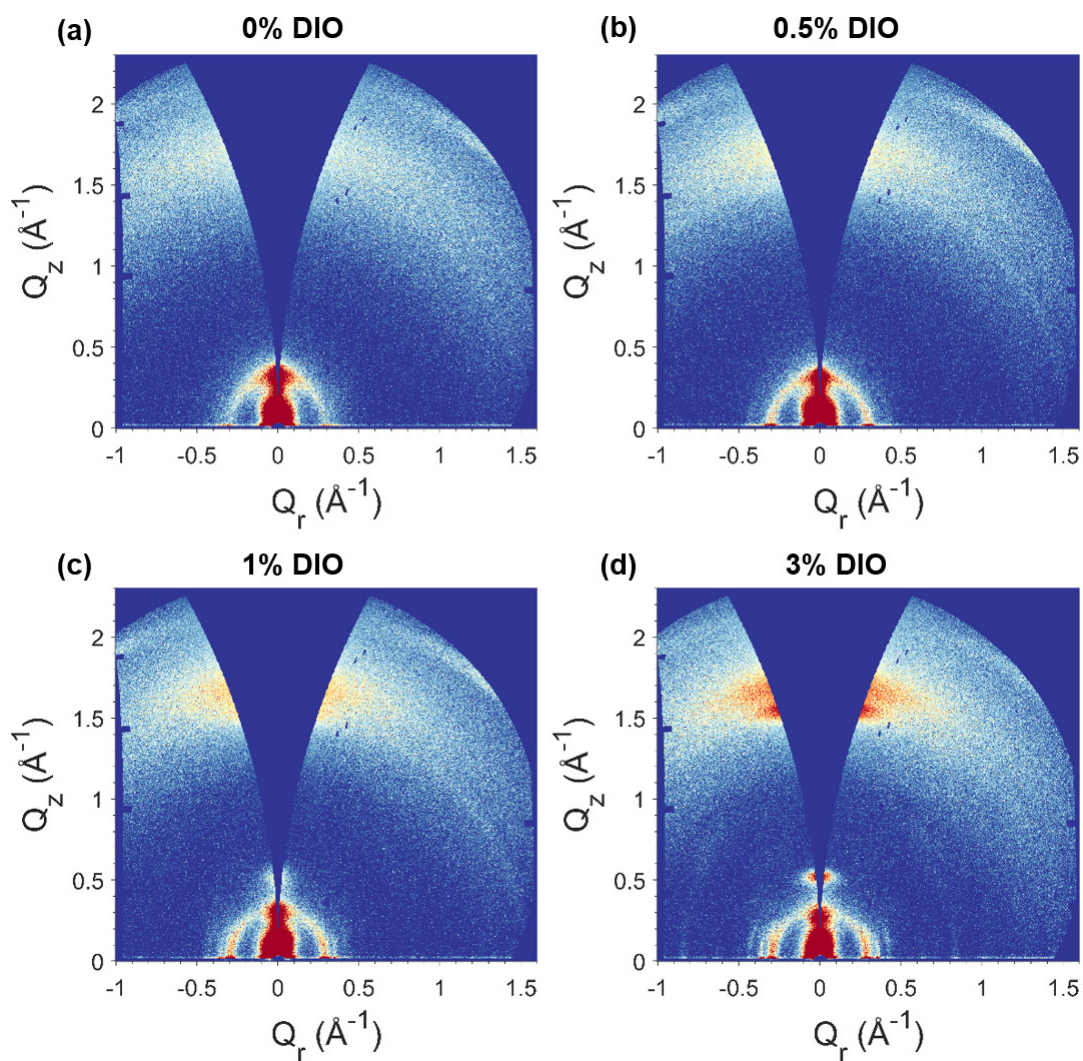


Figure 5.5: 2D GIWAXS patterns of PBDB-T : ITIC blend films processed with (a) 0 (b) 0.5 (c) 1 and (d) 3 Vol% DIO.

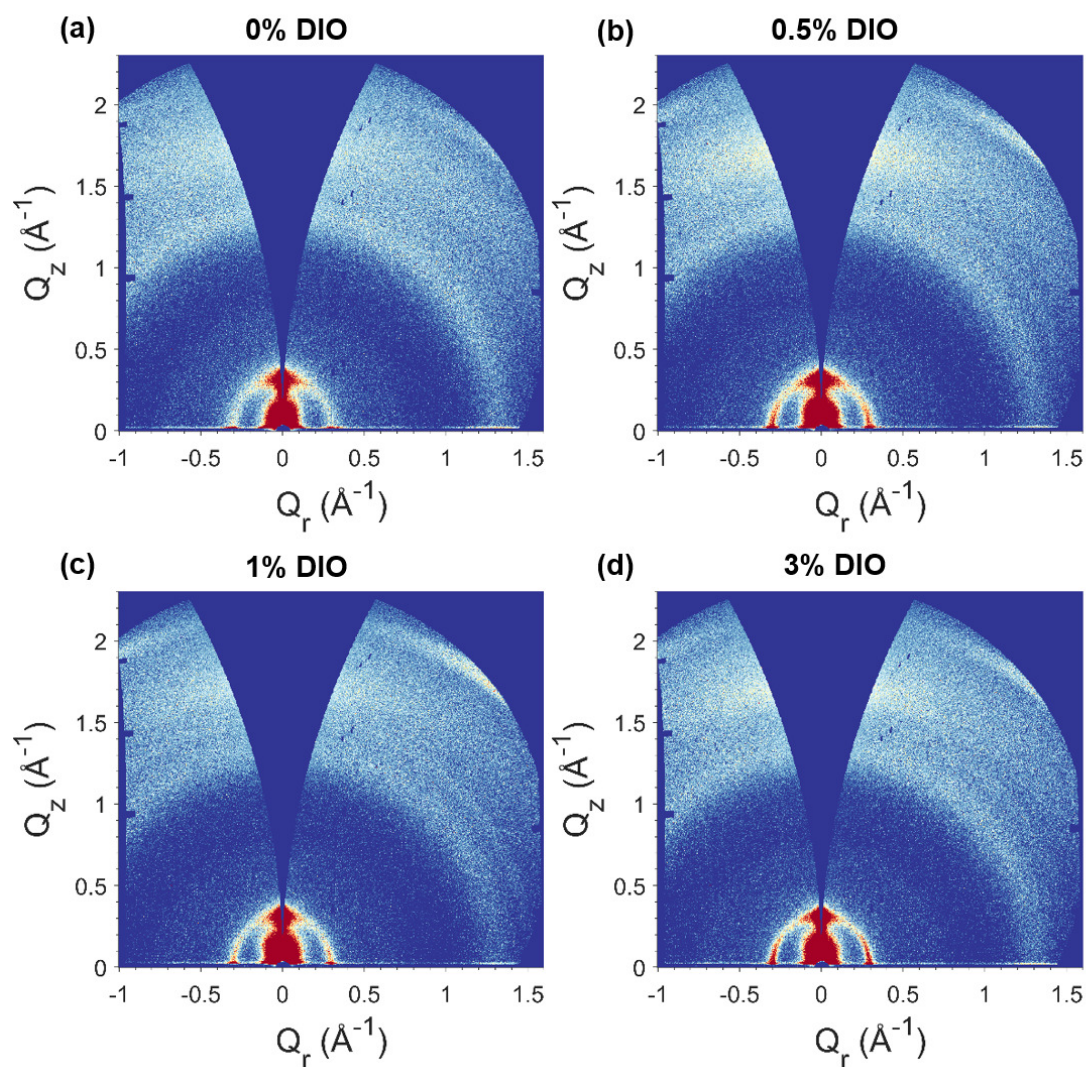


Figure 5.6: 2D GIWAXS patterns of PBDB-T : ITIC blend films processed with (a) 0 (b) 0.5 (c) 1 and (d) 3 Vol% DIO.

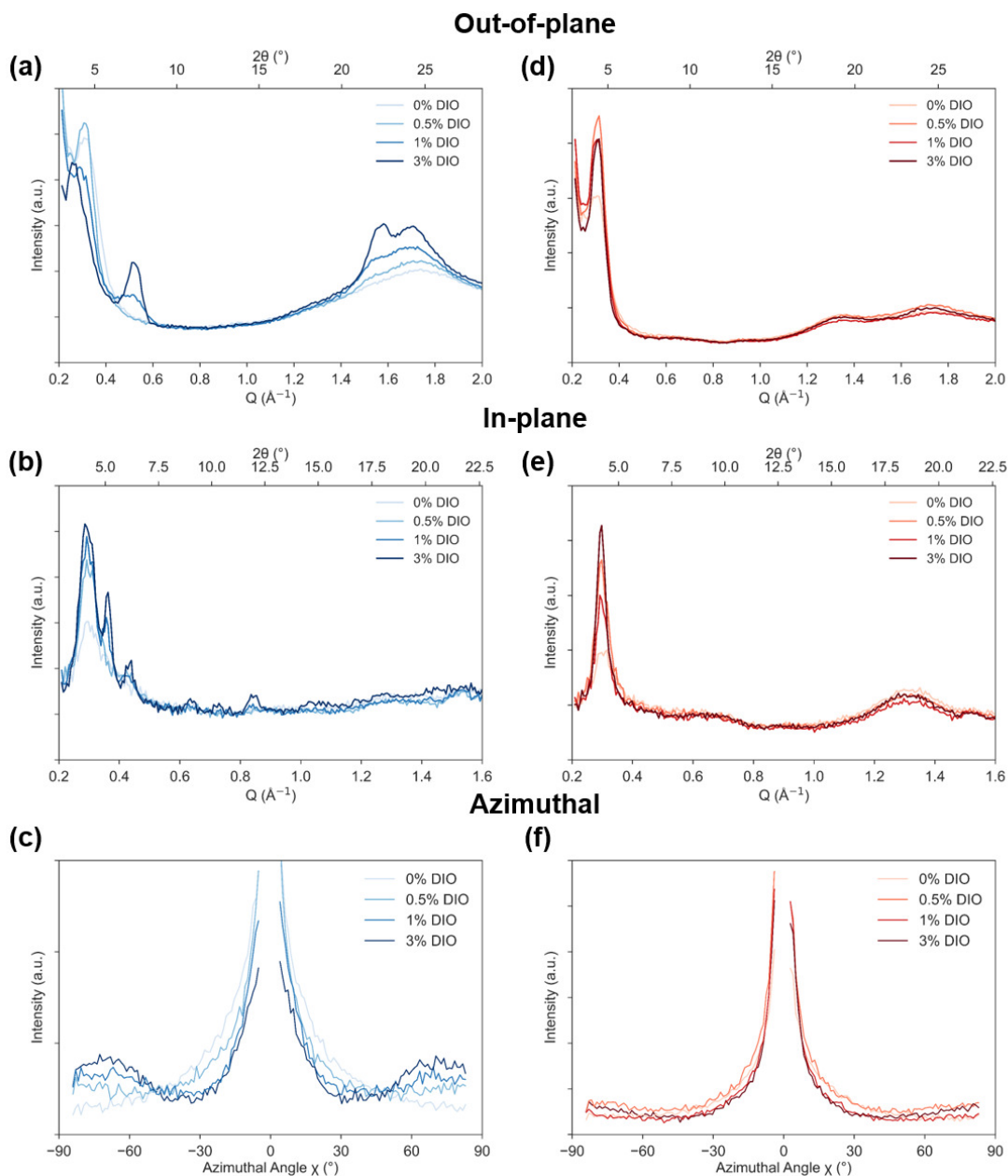


Figure 5.7: Azimuthally integrated 1D GIWAXS profiles of (a-c) PBDB-T : ITIC and (d-f) PBDB-T : PC₇₁BM films processed with various concentrations of DIO. Q -dependent integrations were performed across the full Q range through various χ angles; out-of-plane (in the Q_z direction, $-20 < \chi(^{\circ}) < 20$) and in-plane ($70 < \chi(^{\circ}) < 90$). χ -dependent integrations were performed across the full χ range in the Q range $0.25 < Q(\text{\AA}^{-1}) < 0.45$.

System	DIO (Vol%)	Direction	Q (\AA^{-1})	d (\AA)	CCL (nm)
PBDB-T : ITIC	0	In-plane	0.310	20.27	3.77
		Out-of-plane	0.307	20.49	4.25
			1.732	3.63	0.84
	0.5	In-plane	0.298	21.11	6.99
			0.416	15.12	6.06
		Out-of-plane	0.303	20.8	5.30
	1.717		3.72	1.00	
	1		In-plane	0.294	21.39
		0.360		17.44	20.50
		0.417		15.06	7.46
		Out-of-plane	0.289	21.73	4.54
			0.485	12.95	3.25
			1.690	3.72	1.10
	3	In-plane	0.294	21.38	8.74
			0.363	17.29	14.85
			0.430	14.61	10.76
			0.634	9.91	16.64
			0.726	8.66	23.92
		Out-of-plane	0.844	7.44	15.58
			0.241	21.73	2.96
0.516			12.95	7.24	
1.563			4.02	8.56	
PBDB-T : PC ₇₁ BM	0	In-plane	0.306	20.53	7.51
			1.320	4.76	2.17
		Out-of-plane	0.299	20.99	5.29
			1.313	4.79	2.63
			1.748	3.59	0.77
	0.5	In-plane	0.306	21.03	7.51
			1.320	4.76	2.17
		Out-of-plane	0.299	20.53	5.29
			1.313	4.79	2.63
			1.748	3.60	0.77
	1	In-plane	0.298	21.06	10.80
			1.314	4.78	2.33
		Out-of-plane	0.303	20.74	6.95
			1.310	4.80	2.49
			1.743	3.59	0.89
	3	In-plane	0.296	21.19	14.43
			1.316	4.77	2.31
		Out-of-plane	0.306	20.56	7.92
			1.312	4.79	2.41
			1.751	3.59	1.04

Table 5.5: GIWAXS peak positions, d -spacings and CCL values extracted from the out-of-plane and in-plane Q -dependent intensity profiles shown in Figure 5.7.

The GIWAXS measurements discussed above demonstrate that DIO has a greater impact on the molecular self-assembly of PBDB-T : ITIC blend films compared to PBDB-T : PC₇₁BM. In PBDB-T : ITIC systems, DIO induces a favourable face-on PBDB-T orientation and enhanced π - π stacking and lamellar stacking of both PBDB-T and ITIC. This is in agreement with the spectral UV-Vis absorption shifts discussed above, characteristic of aggregation and a higher degree of molecular order. Although improvements in crystallinity are beneficial for efficient charge transport and reduced recombination, given the reduced J_{SC} and FF of devices processed using larger DIO concentrations (3 Vol%) it is likely that enhanced ITIC crystallinity leads to excessive aggregation and phase separation as reported elsewhere [116]. For PBDB-T : PC₇₁BM systems, DIO does not appear to impact the molecular arrangement of PC₇₁BM and changes are driven by PBDB-T aggregation only.

5.5.3 Large-Scale Structures

Excessive crystallisation and aggregation of the organic components in BHJ thin films can lead to a higher purity of domains, reduced interfacial area and the formation of structures with length scales much larger than the exciton diffusion length [110]. Each of these factors significantly limits exciton dissociation and charge separation at the interfaces with severe consequences for the resulting PV performance of the device. The exciton diffusion length for PBDB-T and ITIC was measured previously to be 12.65nm and 11.60nm respectively (Chapter 4). For PC₇₁BM, values of the order \sim 5-10nm have been reported elsewhere [29]. To investigate the impact of DIO on large-scale structures in PBDB-T : ITIC and PBDB-T : PC₇₁BM systems in further detail, SANS and AFM measurements were performed.

AFM height topography images of PBDB-T : ITIC and PBDB-T : PC₇₁BM blend films processed from chlorobenzene with 0-3 Vol% DIO are displayed in Figure 5.8 and Figure 5.9 respectively and RMS roughness (σ_{RMS}) values are summarised in Table 5.6. For PBDB-T : ITIC blend films, the lateral surface features of PBDB-T : ITIC blend films processed from 0, 0.5 and 1 Vol% DIO appear comparable, exhibiting a finely intermixed surface structure with some small surface grains visible. Notably however, RMS surface roughness (σ_{RMS}) increases with increasing DIO concentration from 1.60nm for the blend film without DIO to 1.80nm and 4.27nm for films processed with 0.5 and 1 Vol% respectively (Table 5.6). The 3 Vol% blend film appears drastically different to those processed from lower DIO concentrations, with the vertical height scale increasing by a factor of 10, corresponding to a significantly higher RMS surface roughness of 30.6nm (Figure 5.8d). Additionally, the surface of the film appears to be composed of large aggregates, due to excessive ITIC crystallisation as discussed in the GIWAXS measurements above. In comparison to PBDB-T : ITIC systems, PBDB-T : PC₇₁BM blend films appear considerably more tolerant to DIO concentration exhibiting comparable finely intermixed surface morphologies (Figure 5.9).

Similar to PBDB-T : ITIC systems, the RMS surface roughness of PBDB-T : PC₇₁BM also increases with increasing DIO concentration but the effect is much less severe, rising from 1.00nm for the film without DIO to a maximum of 2.44nm for the 3 Vol% DIO film. This suggests the higher surface roughness of PBDB-T : ITIC films processed with 3 Vol% DIO is the result of ITIC crystallisation. In comparison, small increases in surface roughness with increasing DIO content for PBDB-T : PC₇₁BM systems, are most likely the result of enhanced PBDB-T molecular packing and aggregation.

Blend System	DIO (Vol%)	σ_{RMS} (nm)
PBDB-T : ITIC	0	1.60
	0.5	1.80
	1	4.27
	3	30.6
PBDB-T : PC₇₁BM	0	1.00
	0.5	1.32
	1	1.53
	3	2.44

Table 5.6: Summary of RMS roughness (σ_{RMS}) values extracted from the AFM data shown in Figure 5.8 and Figure 5.9 for PBDB-T : ITIC and PBDB-T : PC₇₁BM films processed with various concentrations of DIO respectively.

To confirm this, AFM measurements of pure ITIC, PC₇₁BM and PBDB-T films were performed (Subsection 5.10.3). The surface of pure ITIC films processed from chlorobenzene with 0-3 Vol% DIO are composed of protruding, fibre-like strands which seem to aggregate and increase in size as DIO concentration increases (Figure 5.38). This coincides with an increase in RMS surface roughness from 13.2nm for the film processed without DIO to 20.7nm for the 3 Vol% DIO film (Table 5.14).

In contrast, DIO concentration does not appear to have a noticeable effect on the surface topography of pure PC₇₁BM films, with all surfaces displaying an ultra-smooth RMS roughness of \sim 3nm with few distinct surface features (Figure 5.39). For pure PBDB-T films, there is a significant increase in lateral surface grain size as DIO concentration increases and RMS surface roughness values rise from 2.04nm for the film processed without DIO to 3.84nm for the film processed with 3 Vol% DIO (Figure 5.40). This is in agreement with the increase in in-plane lamellar stacking *CCL* and enhanced face-on molecular orientation with increasing DIO concentration measured previously with GIWAXS.

It can therefore be concluded that in PBDB-T : ITIC systems the combined aggregation of PBDB-T and excessive crystallisation of ITIC results in significantly rougher films when processed with higher DIO concentrations. In PBDB-T : PC₇₁BM systems, surface roughness also increases with higher DIO concentrations but the effect is much less severe as only PBDB-T aggregation contributes, with PC₇₁BM remaining largely unaffected.

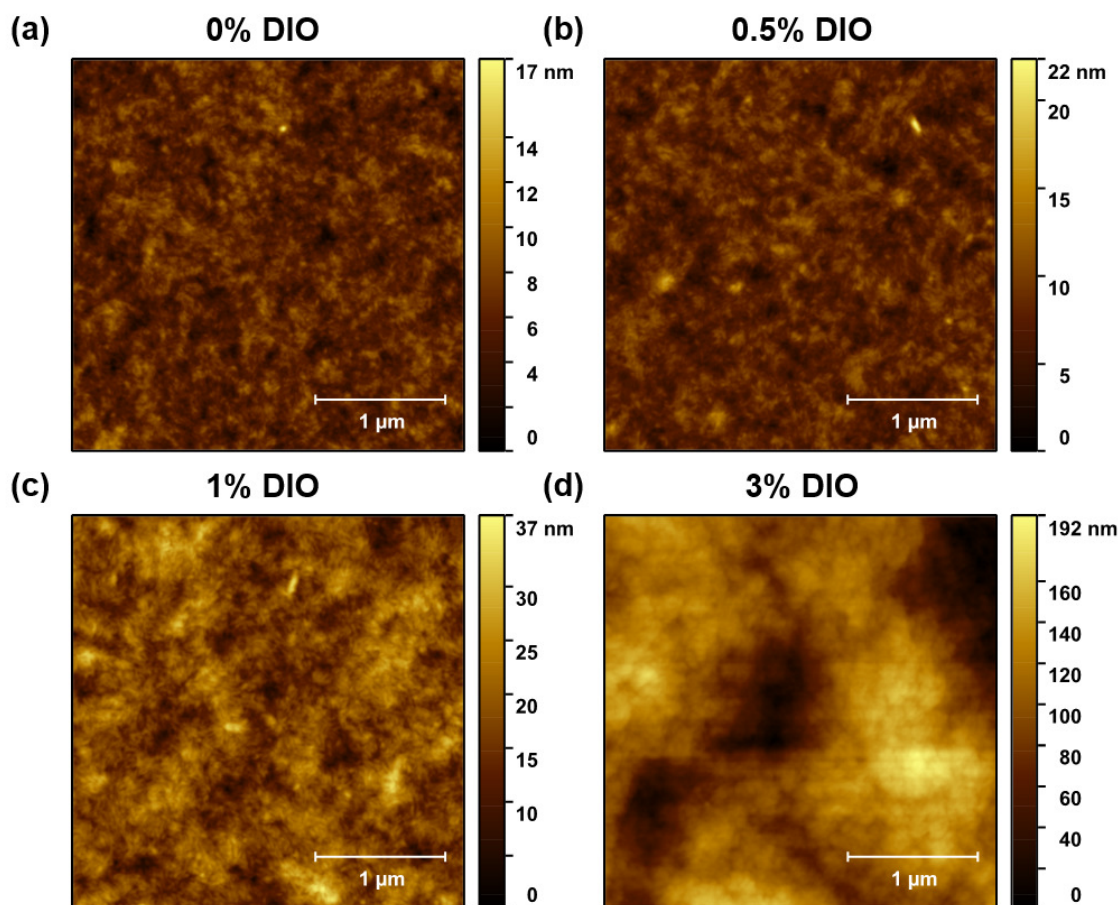


Figure 5.8: AFM height topography images of PBDB-T : ITIC films processed with (a) 0, (b) 0.5, (c) 1 and (d) 3 Vol% DIO. The scale bar is $1\mu\text{m}$. Note the significantly increased height scale for the blend film processed with 3 Vol% DIO (Image (d)).

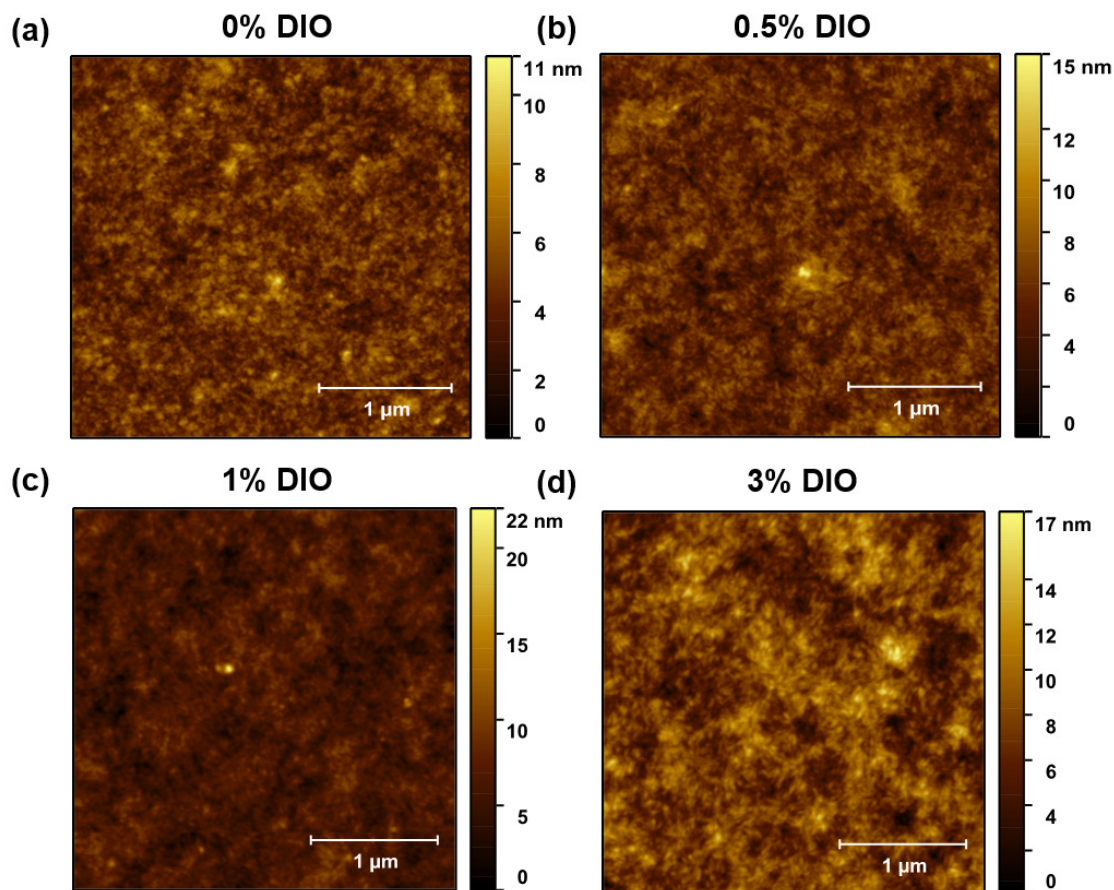


Figure 5.9: AFM height topography images of PBDB-T : PC₇₁BM films processed with (a) 0, (b) 0.5, (c) 1 and (d) 3 Vol% DIO. The scale bar is 1 μm .

Next, SANS measurements were performed to probe the bulk, three-dimensional nanomorphology of the entire thickness of PBDB-T : ITIC and PBDB-T : PC₇₁BM films processed with DIO. A series of blend films were stacked together to generate an appropriate scattering volume as described in Chapter 3 and deuterated ITIC (d52-ITIC) was used to provide sufficient contrast with PBDB-T in the blend. Unfortunately only a small amount of d52-ITIC was synthesised, limiting the sample series to PBDB-T : d52-ITIC blend films processed from 0, 0.5 and 3 Vol% DIO. In the PBDB-T : PC₇₁BM blend films there is naturally sufficient neutron contrast due to the large C:H ratio of PC₇₁BM such that deuterium-labelling is not necessary. A full list of SLD values is provided in Table 3.6.

The absolute SANS intensities of PBDB-T : d52-ITIC and PBDB-T : PC₇₁BM blend films processed from chlorobenzene with 0-3 Vol% DIO are shown in Figure 5.10. A small peak at $Q \sim 0.3 \text{\AA}^{-1}$ from PBDB-T lamellar stacking is visible in both blend systems. This data

has also been plotted as the Lorentz-corrected SANS intensity (IQ^2 versus Q), where a peak is visible for each sample relating to a characteristic long-period (L_p) length scale [183, 105] (Figure 5.11). In Table 5.7, peak positions and L_p values from the Lorentz-corrected intensities are provided.

For PBDB-T : d52-ITIC, the characteristic length scale for blend films processed from 0, 0.5 and 3 Vol% DIO are 35.8nm, 54.5nm and 57.1nm respectively. For PBDB-T : PC₇₁BM systems, films processed without DIO exhibit the largest length scale of 62.8nm. This decreases to 23.8nm with the inclusion of 0.5 Vol% DIO and steadily increases again to 32.3nm and 47.3nm for films processed from 1 and 3 Vol% DIO respectively. In Figure 5.12, the SANS data is fitted with a DAB model (see Subsection 3.9.5) to extract values for the correlation length (ξ) of each system. Full fit parameters are provided in Section A.1 and ξ values are summarised in Table 5.7. For PBDB-T : d52-ITIC systems processed without DIO, a correlation length of 5.05nm is extracted from the DAB model fit in agreement with GISAXS measurements reported elsewhere [311]. Processing with 0.5 and 3 Vol% DIO increases this value to 8.01 and 7.92nm respectively. This is in agreement with the increase in L_p and the enhanced aggregation of PBDB-T and ITIC revealed by GIWAXS measurements. For PBDB-T : PC₇₁BM systems, a correlation length of 7.68nm is extracted for films processed without DIO. With the inclusion of small concentrations of DIO (0.5 Vol%), ξ decreases considerably to 4.06nm and increases gradually to 4.56nm and 6.03nm for DIO volume concentrations of 1 and 3 Vol% respectively.

In the DAB model, sharp interfaces between domains are characterised by a scattering exponent of $\alpha = 4$ are assumed. Deviations from the DAB model therefore arise due to diffuse interfaces ($\alpha \neq 4$) or due to the existence of multiple characteristic length scales in the system. To probe the interfacial area of domains, a power law was fitted to the SANS data according to Equation 3.66 (Figure 5.13). Values for the power law exponents for PBDB-T : d52-ITIC and PBDB-T : PC₇₁BM blends processed from chlorobenzene with 0-3 Vol% DIO are summarised in Table 5.7. For PBDB-T : d52-ITIC, exponent values do not change significantly as a result of DIO processing with values of $\alpha = 3.54$, 3.55 and 3.48 extracted for films processed with 0, 0.5 and 3 Vol% DIO respectively. This suggests that each sample exhibits a comparable degree of intermixing between phases and DIO mostly influences the size of characteristic length scales. In comparison, PBDB-T : PC₇₁BM films generally exhibit smaller exponent values compared to PBDB-T : d52-ITIC systems. For PBDB-T : PC₇₁BM films processed without DIO, an exponent of 2.83 was extracted from power law fitting, indicative of a highly intermixed system with large a interfacial area.

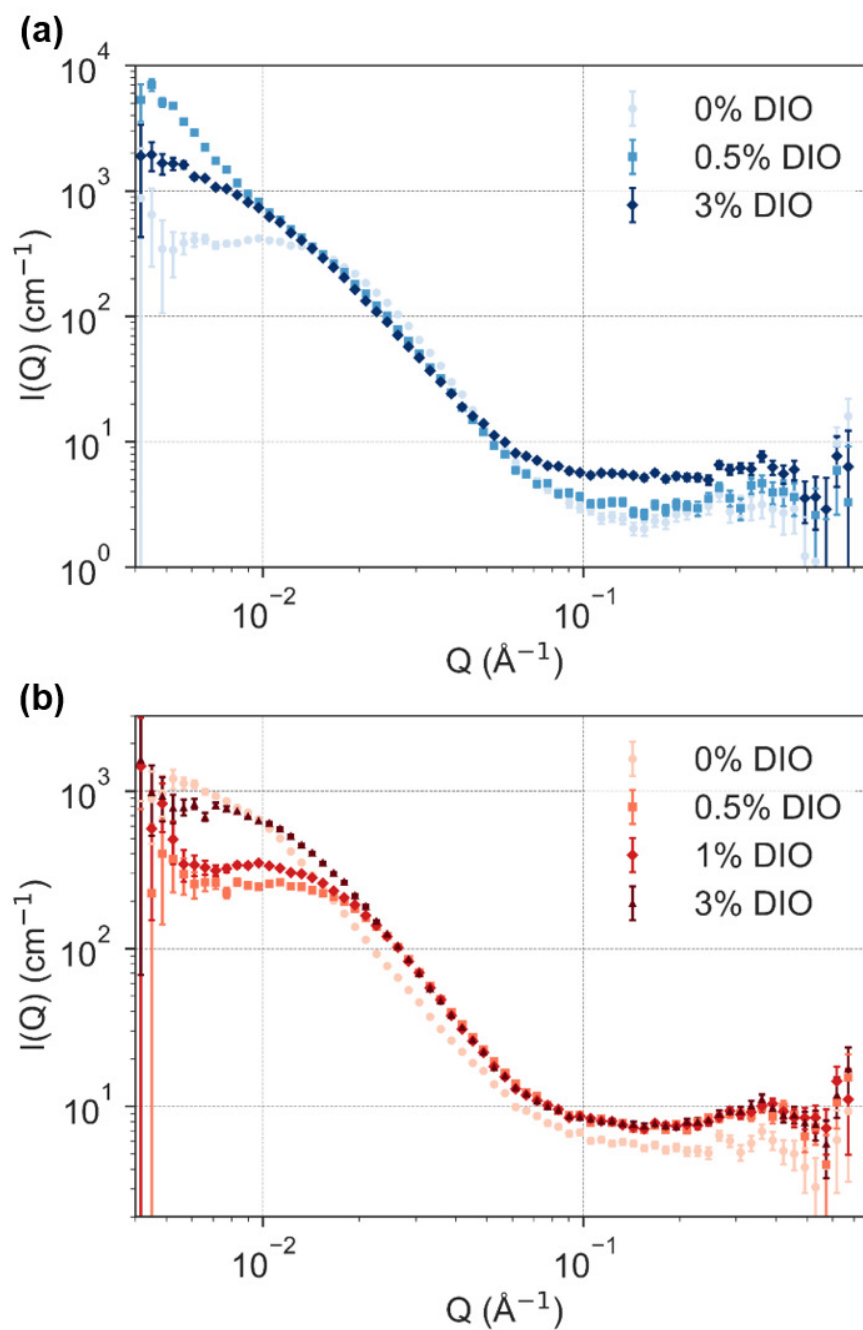


Figure 5.10: Absolute SANS intensity of (a) PBDB-T : d52-ITIC and (b) PBDB-T : PC₇₁BM blend films processed from chlorobenzene with 0-3 Vol% DIO in the full measurable Q range.

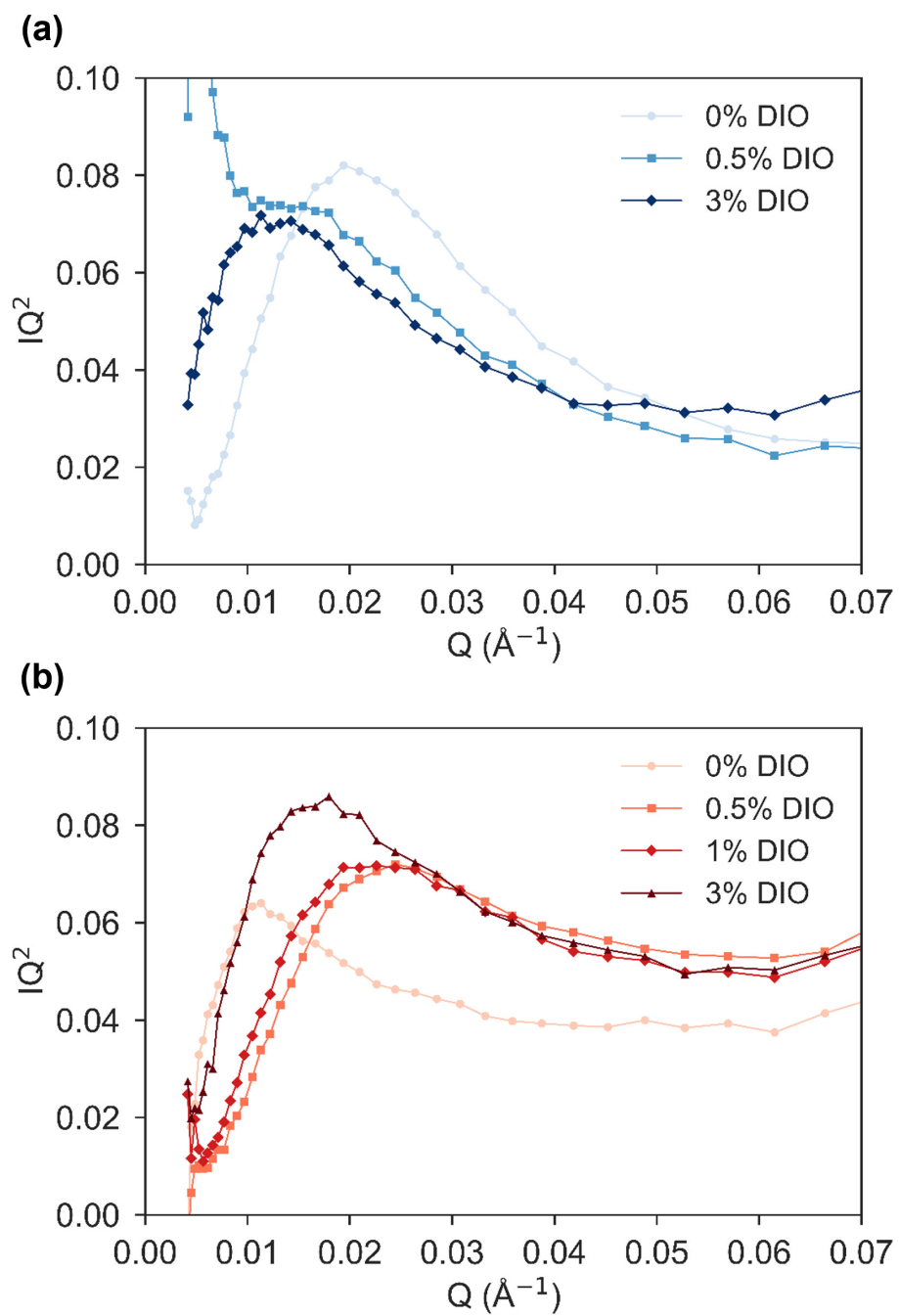


Figure 5.11: Lorentz-corrected SANS intensity ($I(Q)$ vs Q) of (a) PBDB-T : d52-ITIC and (b) PBDB-T : PC₇₁BM blend films processed from chlorobenzene with 0-3 Vol% DIO.

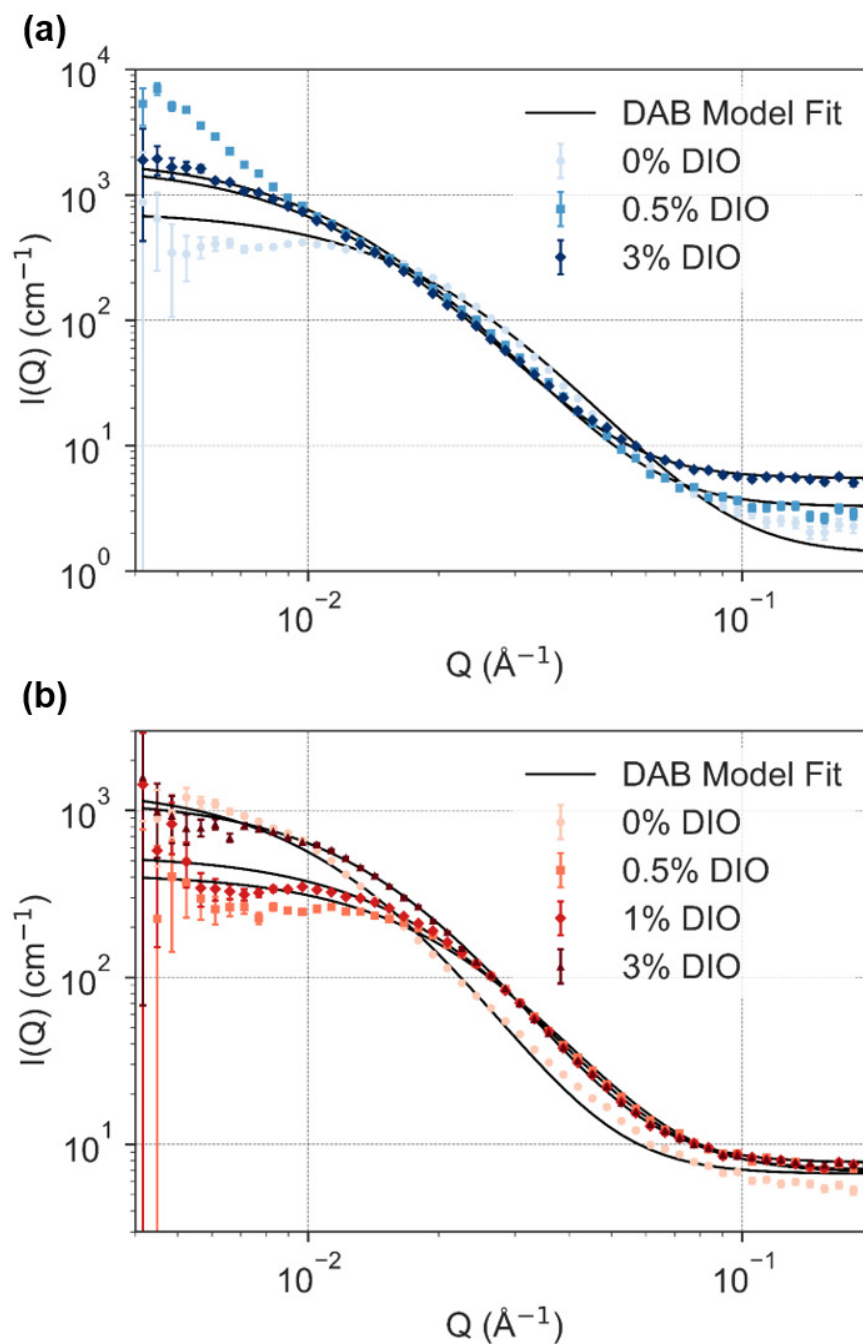


Figure 5.12: SANS DAB fits (Equation 3.67) in the interval $0.004 < Q \text{ \AA}^{-1} < 0.2$ for (a) PBDB-T : d52-ITIC and (b) PBDB-T : PC₇₁BM blend films processed from chlorobenzene with 0-3 Vol% DIO.

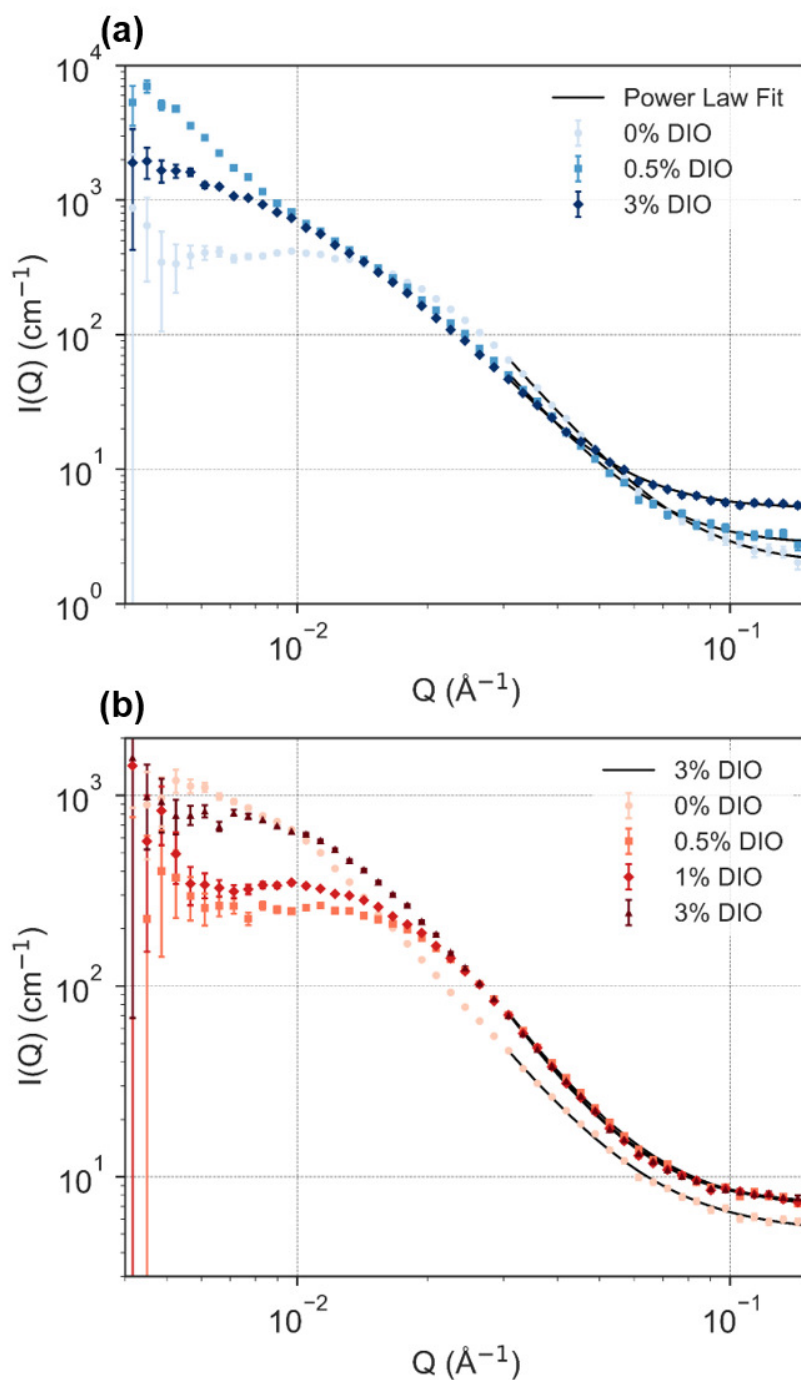


Figure 5.13: SANS power law fits (Equation 3.66) in the interval $0.03 < Q \text{ \AA}^{-1} < 0.2$ for (a) PBDB-T : d52-ITIC and (b) PBDB-T : PC₇₁BM blend films processed from chlorobenzene with 0-3 Vol% DIO.

Blend System	DIO (Vol %)	Lorentz Peak		DAB Model	Power Law
		Q (\AA^{-1})	L_p (nm)	ξ (nm)	α
PBDB-T : d52-ITIC	0	0.0176 ± 0.0003	35.8 ± 0.6	5.05 ± 0.02	3.54 ± 0.04
	0.5	0.0115 ± 0.0003	54.5 ± 0.3	8.01 ± 0.03	3.55 ± 0.05
	3	0.0110 ± 0.0003	57.1 ± 1.6	7.92 ± 0.03	3.48 ± 0.06
PBDB-T : PC ₇₁ BM	0	0.0100 ± 0.0002	62.8 ± 1.3	7.68 ± 0.04	2.83 ± 0.05
	0.5	0.0264 ± 0.0006	23.8 ± 0.5	4.06 ± 0.02	3.03 ± 0.03
	1	0.0195 ± 0.0005	32.3 ± 1.0	4.56 ± 0.02	3.22 ± 0.04
	3	0.0133 ± 0.0004	47.3 ± 1.5	6.03 ± 0.02	3.18 ± 0.04

Table 5.7: A summary of SANS fit parameters relating to size and purity of domains. Long-period (L_p) values were extracted from the Lorentz-corrected scattering peaks in Figure 5.11 using Equation 3.64. Correlation lengths (ξ) are from the DAB fits in Figure 5.12. scattering exponents (α) were extracted from the power law fits in Figure 5.13. Full fit parameters are provided in Section A.1.

Processing PBDB-T : PC₇₁BM films with DIO increases exponent values to $\alpha = 3.03$, 3.22 and 3.18 for DIO volume concentrations of 0.5, 1 and 3 Vol% respectively. This demonstrates that processing with DIO increases the degree of phase separation in PBDB-T : PC₇₁BM systems, reducing the intermixing of domains.

The majority of samples have similar Guinier-like SANS profiles typical for two-phase binary blend films for which the DAB model works reasonably well. However, for PBDB-T : d52-ITIC films processed from 0.5 Vol% DIO, there is a distinct increase in scattering intensity at low Q ($Q < 0.008 \text{\AA}^{-1}$) suggesting the existence of larger macroscopic aggregates or some larger length scale. Fitting the interval $0.005 < Q \text{\AA}^{-1} < 0.01$ with a power law model (Equation 3.66), gives an exponent value of $\alpha = 3.14 \pm 0.15$ (Figure 5.41). The size of this structure is outside of the Q range of the SANS instrument and cannot be fully characterised. However, similar DIO-induced scattering profiles have been observed for other binary blend systems indicative of a multi-length-scale phase-separated morphology [312, 313]. Such hierarchical morphologies can form mesh-like, continuous networks of polymer fibrils and aggregated acceptor-rich domains, beneficial for efficient exciton dissociation and charge transport in a PV device [312, 105].

Taken together the AFM and SANS results demonstrate the influence of DIO processing on the characteristics of large scale structures in polymer : fullerene and polymer : NFA blends. The results demonstrate that DIO can induce a rich, hierarchical phase behaviour in OPV systems but morphological changes can be overlooked in surface microscopy techniques such as AFM. Instead, SANS can be used to probe the intricate changes to the three-dimensional nanomorphology. For PBDB-T : ITIC systems, processing with DIO in-

creases the aggregation of PBDB-T and ITIC. However, the degree of intermixing does not change significantly. For low DIO concentrations (0.5 Vol%) this results in a hierarchical morphology which facilitates efficient charge transport and reduced recombination leading to an enhanced J_{SC} and FF . Processing with larger concentrations of DIO (3 Vol%) results in excessive ITIC crystallisation and characteristic length scales larger than l_d of both component materials, inhibiting efficient exciton dissociation at heterointerfaces. In comparison, although AFM measurements of PBDB-T : PC₇₁BM systems revealed only slight morphological changes with DIO processing, SANS measurements show that in reality there are significant changes to interfacial area and characteristic length scales. PBDB-T : PC₇₁BM films processed without DIO are finely intermixed but when processed with DIO the degree of phase separation is enhanced and domain size can be optimised by changing the volume concentration of DIO in the casting solution.

5.5.4 Vertical Chemical Composition

The appearance of S-shaped J - V curves in PBDB-T : ITIC devices processed from 3 Vol% DIO (Figure 5.2) suggests charge carrier recombination and extraction at the electrical contacts is inhibited [305, 306, 307]. Such effects can occur due to vertical phase segregation of donor and acceptor materials forming a charge transport blocking layer at an interface. For example, an acceptor-rich layer at the bottom electrode interface in the conventional architecture devices used in this work would restrict hole transport to the PEDOT:PSS interface. Similarly, a donor-rich surface layer would inhibit electron transport to the PFN-Br ETL. To investigate this, the vertical chemical composition of PBDB-T : ITIC and PBDB-T : PC₇₁BM blend films processed from various concentrations of DIO (0-3 Vol%) was characterised using neutron reflectivity (NR) and contact angle goniometry as discussed below.

To estimate the surface energy of ITIC, PC₇₁BM and PBDB-T, the contact angles of water and hexadecane droplets on the surface of pure films were measured (Figure 5.42). Using the Fowkes surface energy model, the dispersive (γ_{sd}), polar (γ_{sp}) and total surface (γ_s) energies of each component material were then calculated following the methodology described in Subsection 3.5.2. These values are summarised in Table 5.8. The surface energy of PBDB-T is slightly lower than the surface energy of ITIC and PC₇₁BM giving an initial indication that it is more energetically favourable for PBDB-T to segregate to the surface in a blend film.

To gain a preliminary insight into the impact of DIO on the vertical chemical composition of blend films, contact angles of water and hexadecane droplets on PBDB-T : ITIC and PBDB-T : PC₇₁BM surfaces processed from chlorobenzene with 0-3 Vol% DIO were measured (Figure 5.43 and Figure 5.44 respectively). The corresponding surface energies

estimated using the Fowkes model are provided in Table 5.9. The estimated total surface energy of both blend systems appears to decrease with larger DIO concentrations suggesting an increasing surface enrichment of PBDB-T in agreement with results reported elsewhere [116, 117]. This is observed more clearly in the graphical representation shown in Figure 5.14. In general, the surface energy of PBDB-T : ITIC blend films is lower than PBDB-T : PC₇₁BM films processed using the same DIO concentration suggesting the surface enrichment of PBDB-T is greater for PBDB-T : ITIC system.

Material	Surface Energy (mN/m)		
	γ_{ds}	γ_{ps}	γ_s
PBDB-T	26.81	0.16	26.97
ITIC	26.83	0.85	27.68
PC₇₁BM	26.92	1.15	28.07

Table 5.8: Summary of surface energy values estimated using the Fowkes model for pure PBDB-T, ITIC and PC₇₁BM films from the water and hexadecane contact angle measurements shown in Figure 5.42.

Blend System	DIO Vol%	Surface Energy (mN/m)		
		γ_{ds}	γ_{ps}	γ_s
PBDB-T : ITIC	0	26.94	0.34	27.16
	0.5	26.89	0.17	27.06
	1	26.87	0.06	26.93
	3	26.87	0.03	26.91
PBDB-T : PC₇₁BM	0	26.89	0.27	27.28
	0.5	26.94	0.18	27.12
	1	26.91	0.08	26.99
	3	26.89	0.05	26.94

Table 5.9: Summary of surface energy values calculated using the Fowkes model for PBDB-T : ITIC and PBDB-T : PC₇₁BM blend thin films processed with various volume concentrations of DIO (0-3 Vol%) using the contact angle measurements shown in Figure 5.43 and Figure 5.44.

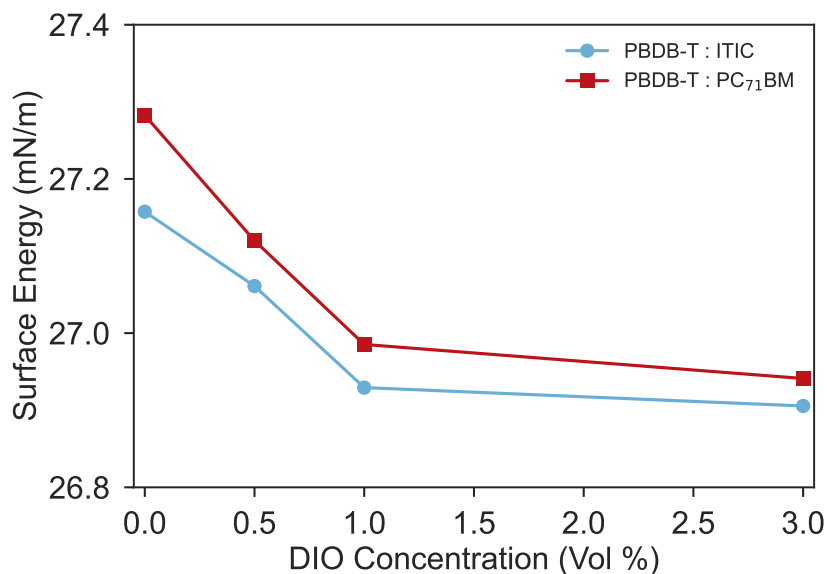


Figure 5.14: Total surface energy γ_s of PBDB-T : ITIC and PBDB-T : PC₇₁BM blend films as a function of DIO concentration, estimated from contact angle goniometry measurements using the Fowkes model.

To investigate this further, the entire depth of PBDB-T : ITIC and PBDB-T : PC₇₁BM blend films processed from chlorobenzene with 0-3 Vol% DIO was characterised in detail using NR. Deuterated ITIC (d8-ITIC) was used to provide sufficient contrast with PBDB-T in the blend. To characterise the SLD values of each component material, NR of pure PEDOT:PSS, PBDB-T, d8-ITIC and PC₇₁BM films were collected and modelled (Section A.2). All samples were made fresh and stored in nitrogen sealed bags before transit to D17 at ILL for measurement ~ 1 week later.

NR of PBDB-T : ITIC and PBDB-T : PC₇₁BM blend films processed from chlorobenzene with 0-3 Vol% DIO are plotted as $R(Q)$ versus Q in Figure 5.15. In Figure 5.16, the SLD profiles corresponding to the modelled NR data are plotted as a function of OPV blend thickness such that the midpoints of the air/film interface and the film/PEDOT:PSS interface are positioned at 0 and 1 respectively. All blend film NR data was modelled as a stack of Si/SiO₂/PEDOT:PSS/OPV blend/Air where each layer in the sample represents a slab characterised by a thickness L , roughness σ and SLD β_n . For the OPV blend film, a single homogenous slab layer was insufficient to appropriately model the data. After trialling various models, an acceptor-rich layer at the film/PEDOT:PSS interface was added to model all blend films. The fit parameters relating to the OPV blend layer

are summarised in Table 5.10. Further information about the various trialled fitting models and full fitting parameters can be found in Section A.2.

For PBDB-T : d8-ITIC blends, the NR data was modelled reasonably well for films processed from 0, 0.5 and 1 Vol% DIO with $\chi^2/N_{pts} < 4$ (Figure 5.15a). For the 3 Vol%, the fit is slightly worse with χ^2/N_{pts} increasing to ~ 7 , most likely due to a considerably higher surface roughness resulting from large aggregates on the film surface (Table 5.6). For each PBDB-T : d8-ITIC sample, it was necessary to fix the upper-bound of the buried interface SLD to the SLD of pure d8-ITIC ($2.15 \times 10^{-6} \text{\AA}^{-2}$) to ensure fits remained physical. For each sample, the fitting program progressed to the upper SLD bound for each sample suggesting the buried interface is composed entirely of pure d8-ITIC. The SLD profiles of blend films processed from 0 and 0.5 Vol% DIO appear very similar with the OPV film composed of a $\sim 60 \text{\AA}$ pure d8-ITIC buried interface layer and a $\sim 700 \text{\AA}$ mixed bulk layer (Figure 5.16b).

To understand the observed changes in SLD as a function of film depth, the volume concentration of the acceptor ϕ_A as a function of OPV blend thickness was calculated for each sample using Equation 3.62 (Figure 5.17). In the case of PBDB-T : ITIC films processed from 0 and 0.5%, the buried interface is 100% d8-ITIC as expected and the bulk layer is composed of $\sim 53\%$ PBDB-T and $\sim 47\%$ d8-ITIC by volume (Figure 5.17a), which is close to the weight ratio of the materials in solution (1:1). For the blend film processed from 1% DIO, the interfacial width of the buried interface appears to broaden and the composition of the bulk layer changes to $\sim 59\%$ PBDB-T and $\sim 41\%$ d8-ITIC. As DIO concentration is increased further to 3 Vol% DIO, the vertical segregation between components becomes more severe, with the volume concentration of PBDB-T in the bulk layer increasing to $\sim 93\%$. Additionally, there is a large increase in surface roughness compared to films processed from lower concentrations of DIO, which is in agreement with the AFM measurements discussed above (Table 5.6).

The formation of such a broad, pure d8-ITIC interfacial barrier and the low concentration of d8-ITIC in the bulk of the film severely inhibits charge extraction at the electrical contacts, resulting in S-shaped J - V characteristics as described above (Figure 5.2). For PBDB-T : ITIC based devices processed from lower concentrations of DIO (0-1 Vol%), although the buried interface is also composed of pure d8-ITIC it is perhaps not sufficiently thick or the bulk layer has a sufficiently high d8-ITIC concentration that S-shaped J - V characteristics are not observed. In comparison to literature results, ϕ_A of the buried interfacial barrier reported here is much higher [116, 117]. For example, acceptor volume concentrations at the buried interface of $\sim 70 - 80\%$ have been reported elsewhere for PBDB-T : ITIC devices processed with 1 Vol% DIO in an inverted architecture (ITO/ZnO/PBDB-T : ITIC/MoO₃/Ag) [117]. It should be noted however, that other studies did not use deuter-

ated ITIC, limiting the contrast in the blend and samples were fabricated using different processing conditions.

For NR data fitting of PBDB-T : d8-ITIC blend films, the vertical segregation was sufficient to remove any ambiguity in the position of the acceptor-rich buried interface as other models (e.g. an acceptor-rich surface layer or single uniform layer) were not capable of appropriately fitting the data, producing high χ^2/N_{pts} values. In the case of PBDB-T : PC₇₁BM blend films, although it was clear that a single homogenous layer could not effectively model the NR data, there was more ambiguity in the position of a second interface compared to PBDB-T : ITIC samples (i.e. positioned on the surface of the film or at the film/PEDOT:PSS interface). Despite offering high-resolution characterisation of interfacial phenomena, this is a common issue when modelling NR of multi-layered samples without prior knowledge of the vertical composition. Consequently, the OPV blend film of all PBDB-T : PC₇₁BM NR samples were modelled in three different ways; as a single homogenous bulk slab, as a bulk slab with an acceptor-rich buried interface and as a bulk slab with an acceptor-rich surface interface (Appendix A).

The ambiguity in interfacial position is most clearly demonstrated for the PBDB-T : PC₇₁BM film processed without DIO (Appendix A) where each model produces comparable fits. Given that contact angle measurements suggest a PBDB-T enrichment at the surface for both PBDB-T : ITIC and PBDB-T : PC₇₁BM systems (Figure 5.14) and similar vertical segregation has been reported elsewhere [116, 117], a system composed of an acceptor-rich buried interface and a mixed bulk layer was selected as the most physical model (Figure 5.15b). From the corresponding SLD profiles presented in Figure 5.16b, the concentration of PC₇₁BM at the buried interface increases with increasing DIO concentration. For the film processed without DIO, the bulk layer is $\sim 44\%$ PC₇₁BM by volume and there is a small enriched layer at the film/PEDOT:PSS interface, which is composed of $\sim 48\%$ PC₇₁BM. As DIO concentration is increased, the acceptor volume concentration at the film/PEDOT:PSS interface rises to $\sim 61\%$, $\sim 64\%$ and $\sim 68\%$ for films processed with 0.5, 1 and 3 Vol% DIO respectively. In comparison to PBDB-T : d8-ITIC systems, vertical segregation of the active layer components in PBDB-T : PC₇₁BM also increases with increasing DIO concentration and the interfacial width of the acceptor-rich buried interfaces are comparable. Despite this, the change in acceptor volume concentration in the bulk layer of PBDB-T : PC₇₁BM systems is much less severe and the acceptor volume concentration of the buried-interface layer is much lower, only rising to a maximum of $\sim 68\%$ (compared to 100% for PBDB-T : d8-ITIC).

The vertical segregation measured with NR explains the changes in $J-V$ characteristics described previously. As DIO volume concentration increases, the degree of vertical segregation increases in both the polymer : fullerene and polymer : NFA systems, inhibiting

hole transport at the PEDOT:PSS interface and reducing V_{OC} values. In inverted architecture devices this effect has led to improvements in device performance as the increased acceptor volume concentration at the bottom ETL facilitates efficient electron transport and extraction [116, 117]. However, when processed with large concentrations of DIO (3 Vol%) interfacial segregation is so significant in polymer : NFA systems that devices exhibit S-shaped J - V characteristics.

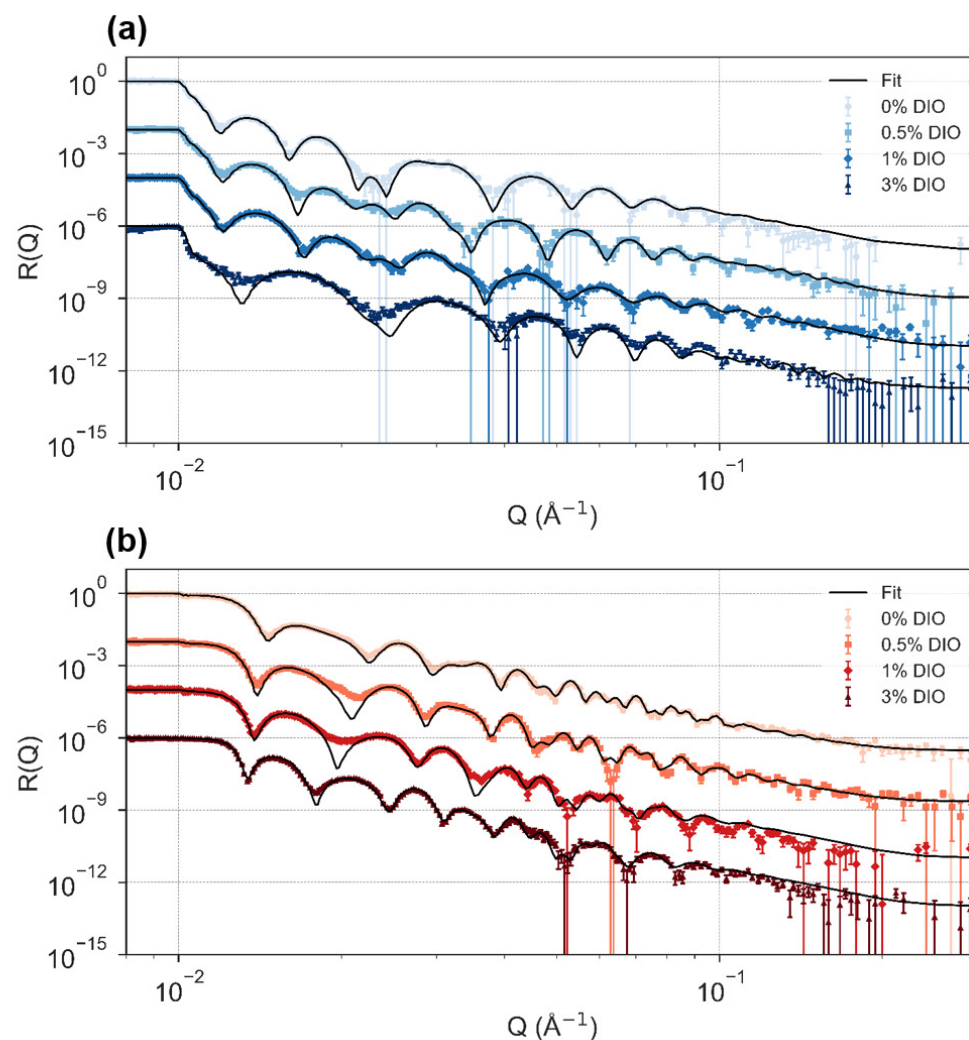


Figure 5.15: NR of (a) PBDB-T : d8-ITIC and (b) PBDB-T : PC₇₁BM blend thin films processed with various concentrations of DIO (0-3 Vol%) on PEDOT:PSS coated silicon substrates. Data has been offset by two decades for clarity.

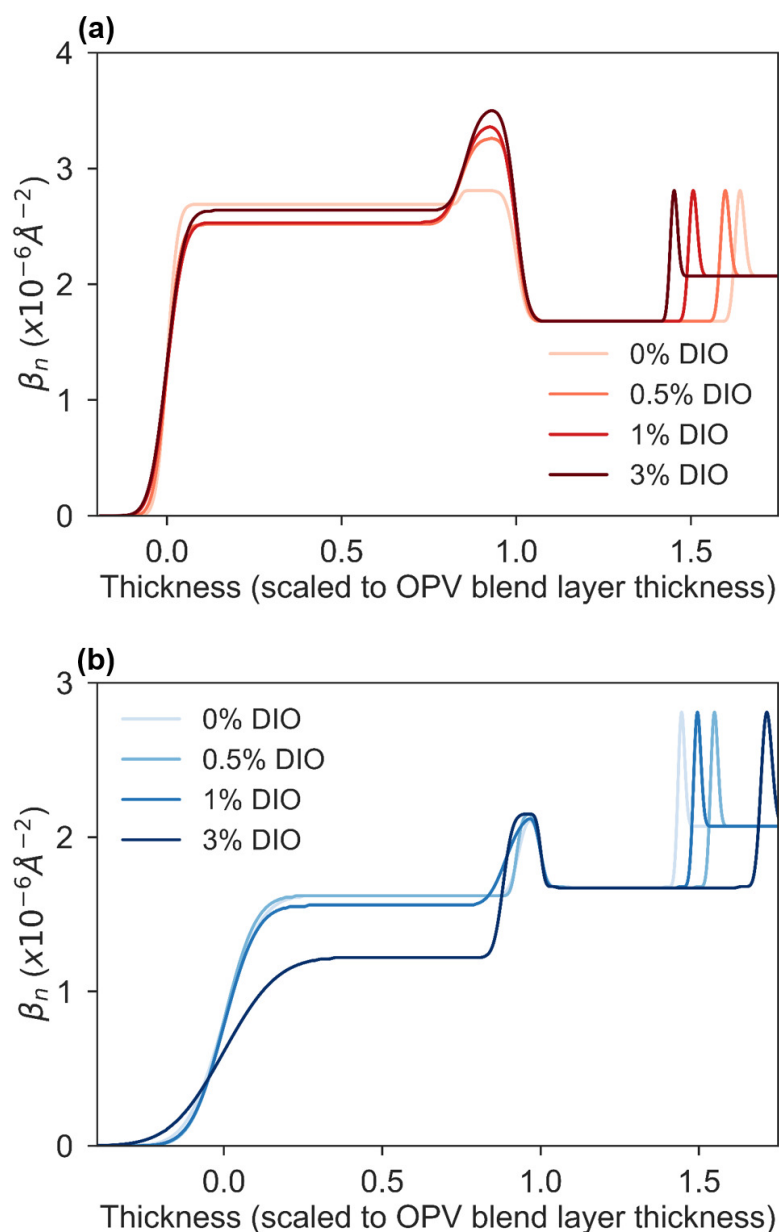


Figure 5.16: SLD profiles corresponding to the NR modelling shown in Figure 5.15 for (a) PBDB-T : d8-ITIC (1:1 by wt) and (b) PBDB-T : PC₇₁BM (1:1 by wt) blend thin films processed with various concentrations of DIO (0-3 Vol%) on PEDOT:PSS coated silicon substrates. Thickness has been scaled to the thickness of the OPV blend film where 0 is midpoint of the air/film interface and 1 is the midpoint of the film/PEDOT:PSS interface.

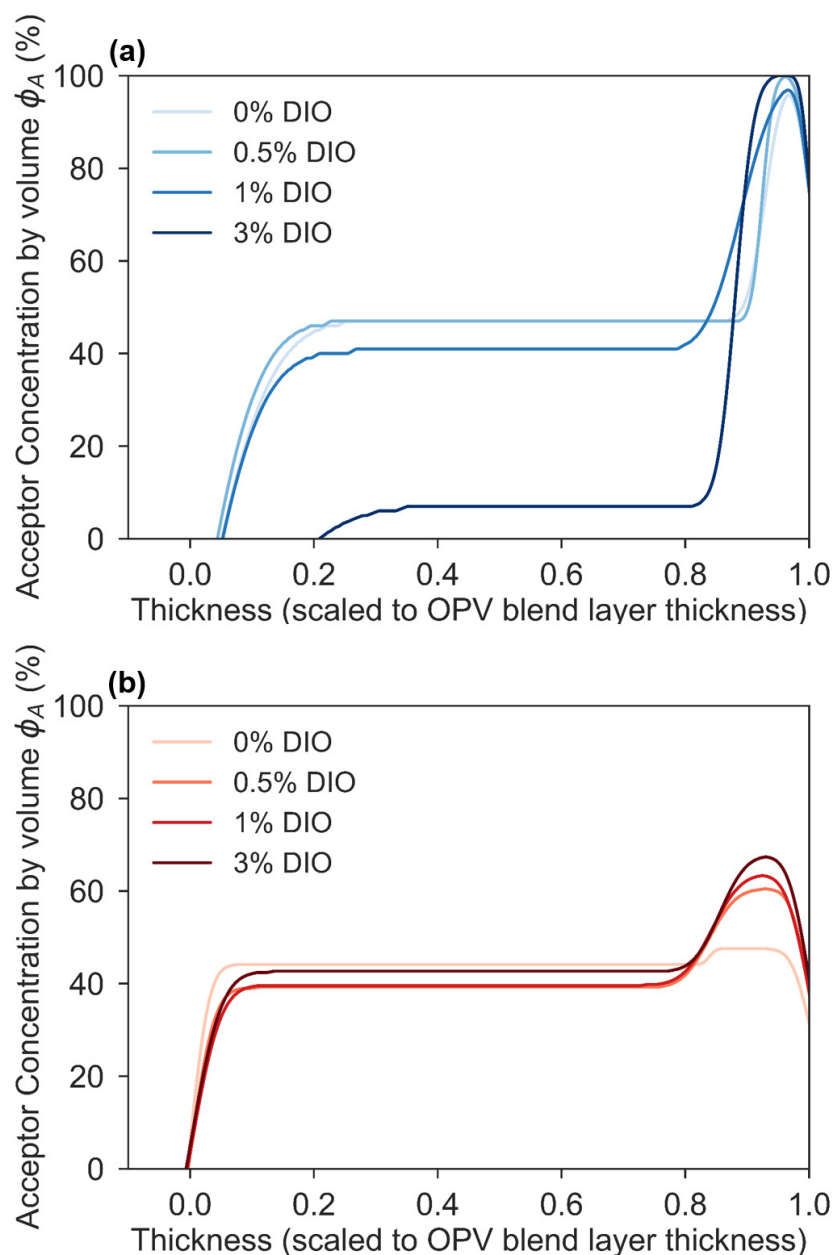


Figure 5.17: Acceptor concentration by volume as a function of film depth calculated from the SLD profiles shown in Figure 5.16 using Equation 3.62 for (a) PBDB-T : d8-ITIC (1:1 by wt) and (b) PBDB-T : PC₇₁BM (1:1 by wt) blend thin films processed with various concentrations of DIO (0-3 Vol%). Thickness has been scaled to the thickness of the OPV blend film where 0 is midpoint of the air/film interface and 1 is the midpoint of the film/PEDOT:PSS interface.

Blend System	DIO	Bulk Layer			Interface Layer			χ^2/N_{pts}
	(Vol%)	L (Å)	σ (Å)	β_n ($\times 10^{-6}\text{Å}^{-2}$)	L (Å)	σ (Å)	β_n ($\times 10^{-6}\text{Å}^{-2}$)	
PBDB-T : d8-ITIC	0	376	15	1.62	60	19	2.15	2.88
	0.5	723	59	1.62	59	11	2.15	3.73
	1	692	86	1.56	86	34	2.15	2.19
	3	462	70	1.22	62	12	2.15	6.15
PBDB-T : PC ₇₁ BM	0	566	16	2.69	109	5	2.81	5.04
	0.5	597	21	2.52	115	24	3.26	17.50
	1	635	29	2.53	117	28	3.38	16.68
	3	754	35	2.64	127	29	3.52	6.20

Table 5.10: Table of neutron reflectivity fit parameters corresponding to the reflectivity data and SLD profiles shown in Figure 5.15 and Figure 5.16 respectively. Here, the OPV blend layer has been modelled with an acceptor-rich buried region at the film/PEDOT:PSS interface. Full fit parameters and additional modelling information are provided in Section A.2.

5.6 Tracking the Removal of DIO

The impact of DIO on the hierarchical morphology, vertical chemical composition and optoelectronic performance of fresh PBDB-T : ITIC and PBDB-T : PC₇₁BM blend systems has been investigated in detail above. To investigate the impact of DIO on the stability of the same systems, it is first necessary to confirm if DIO is fully removed from the film during processing as numerous studies have shown that this can be a primary degradation route as discussed previously. To test the efficacy of the thermal annealing protocols used in this work, the removal of DIO from blend films was tracked using spectroscopic ellipsometry (SE) and residual amounts were detected using ¹H NMR measurements.

For SE measurements, films were isothermally annealed at 160°C in a nitrogen-filled atmosphere. To track the removal of DIO, the change in film thickness during annealing was measured as a function of time (Figure 5.18). As-cast films processed from DIO-containing solutions are considerably thicker than films processed without DIO because they are swollen by the high boiling solvent. During thermal annealing, all DIO-processed films undergo a rapid reduction in film thickness within the first 90 seconds as DIO evaporates from the film. For films processed without DIO, film thickness increases slightly due to thermal expansion. Interestingly the thickness of PBDB-T : PC₇₁BM films processed with DIO relative to the film thickness after 10 minutes of annealing is much greater than PBDB-T : ITIC systems processed from the same volume concentrations of DIO. This is either because PBDB-T : PC₇₁BM films swell by a greater amount or because a greater amount of DIO is removed from the film during thermal annealing. SE measurements demonstrate that thermal annealing is capable of rapidly removing a large volume of DIO.

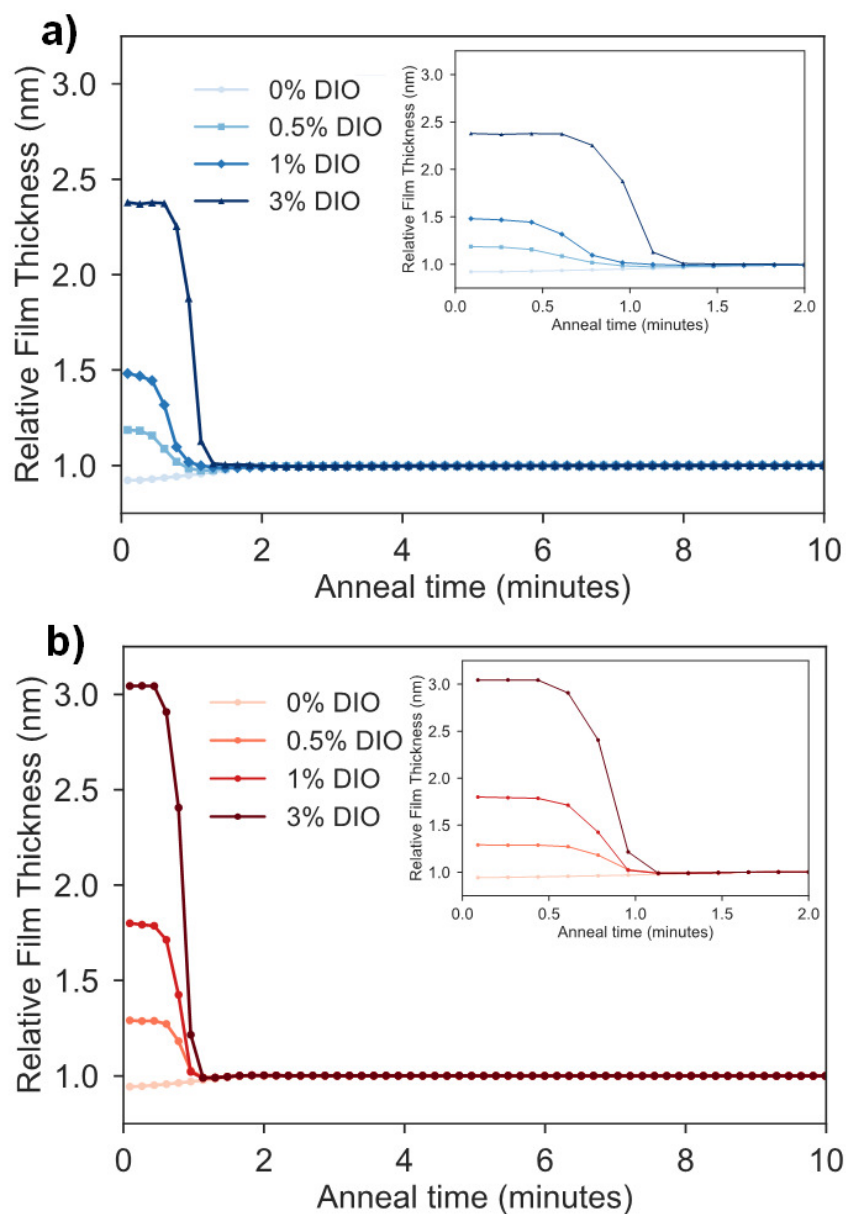


Figure 5.18: The change in film thickness during the isothermal annealing at 160°C of (a) PBDB-T : ITIC and (b) PBDB-T : PC₇₁BM blend films processed with various amounts of DIO. The insets show the first 2 minutes of annealing. Film thickness values were extracted by fitting spectroscopic ellipsometry measurements using a Cauchy model (Equation 3.17) in the transparent wavelength range $850 - 1000\text{nm}$. Data is normalised to the final film thickness after 10 minutes.

Given that residual amounts will not significantly contribute to the final film thickness, it is unclear if DIO is removed entirely from the film from SE measurements. ^1H NMR measurements were performed to further investigate the impact of thermal annealing on DIO removal in PBDB-T :ITIC and PBDB-T : PC₇₁BM blend films. Although it is difficult to determine the exact amount of residual DIO from ^1H NMR measurements without internal calibrants, it is a useful method for firstly determining if there is any DIO trace at all in a sample and secondly for comparing relative amounts between samples [126].

For the ^1H NMR measurements in this work it was necessary to dissolve ~ 15 films per sample in an appropriate deuterated solvent (deuterated chloroform, CDCl_3). Three samples were measured for each blend system; an annealed control film processed without DIO (0 Vol%), an as-cast film processed with 3 Vol% DIO and an annealed film processed with 3 Vol% DIO. To locate a characteristic DIO NMR peak, a reference sample of dilute DIO in CDCl_3 was measured (Figure 5.45a). The distinct triplet NMR peak centred at ~ 3.19 ppm was selected as the characteristic peak for identifying trace amounts of DIO in the samples (Figure 5.45b). In Figure 5.19a the ^1H NMR signal corresponding to the DIO peak in the blend samples of interest is displayed. As expected, the highest NMR signals are observed for the as-cast PBDB-T : ITIC and PBDB-T : PC₇₁BM samples processed from 3 Vol%. The DIO NMR signal for annealed samples is significantly lower demonstrating the effectiveness of thermal annealing for removing large amounts of DIO from thin films. However, upon closer inspection of the annealed DIO NMR peak (Figure 5.19b), there is a clear DIO signal from the annealed PBDB-T : ITIC sample processed using 3 Vol% and there also appears to be a weak DIO signature in the analogous annealed PBDB-T : PC₇₁BM sample processed with 3 Vol%.

To compare relative quantities of DIO between samples, it was necessary to calibrate the integrated peak area of the DIO NMR signal to another peak in the NMR spectra. This was determined by measuring ^1H NMR of dissolved films of pure ITIC, PC₇₁BM and PBDB-T (Figure 5.46a). The characteristic PBDB-T NMR signal centred at ~ 7.055 ppm was chosen as it does not overlap with the NMR features of ITIC, PC₇₁BM or DIO. The relative concentration of DIO was then calculated by calibrating the peak area of the DIO signal to the peak area of the PBDB-T peak through multiple Gaussian peak fitting. The calculated peak area ratio was then normalised to the value of the as-cast sample processed with 3 Vol% and compared to the values calculated for the annealed samples processed with 0 and 3 Vol% DIO as shown in Figure 5.19c. For blend films processed with 3 Vol% DIO, thermal annealing reduces the concentration of DIO relative to that of the as-cast film by $\sim 95\%$ and $\sim 99\%$ for PBDB-T : ITIC and PBDB-T : PC₇₁BM systems respectively. This calculation makes several assumptions (e.g. that there is the same relative proportion of PBDB-T in each sample) and so should only be considered as a rough estimation. Nevertheless, the ^1H NMR analysis suggests that ITIC-based systems trap more DIO

compared to PC₇₁BM-based systems. The origin of this effect is unclear but could be related to either an increased chemical affinity or the molecular structure of each acceptor. ITIC, like many other NFAs has an extended conjugated molecular structure which could act as a thermodynamic or physical barrier to DIO evaporation. This would be especially effective in highly crystalline blend films such as PBDB-T : ITIC films processed from 3 Vol% DIO which exhibit enhanced ITIC crystallinity and as described previously. In contrast, the smaller, spherical fullerene structure of PC₇₁BM in its amorphous molecular arrangement could permit the evaporation of DIO more easily, reducing the amount of retained DIO solvent.

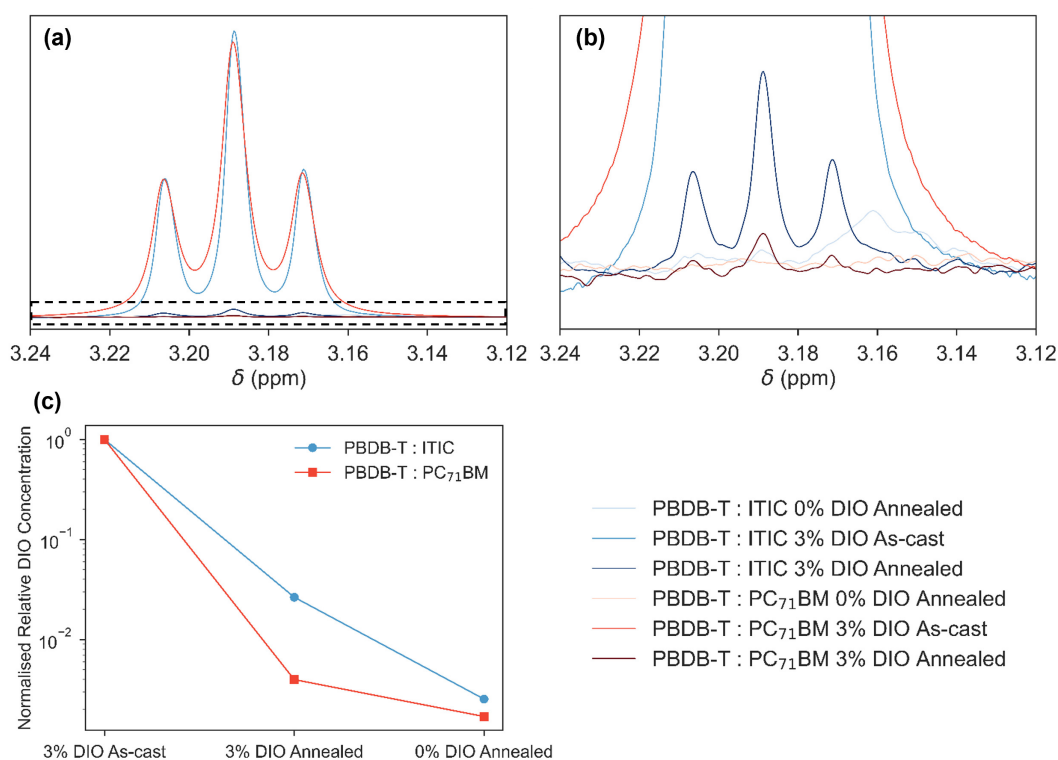


Figure 5.19: (a) DIO ¹H NMR signal for dissolved as-cast and annealed PBDB-T : ITIC and PBDB-T : PC₇₁BM films in CDCl₃ processed with 0 and 3 Vol% DIO. (b) A closer inspection of the weaker NMR signals highlighted in the dotted box in (a). (c) The normalised, relative concentration of DIO, calculated by calibrating the peak area of the DIO signal to the peak area of the PBDB-T NMR peak centred at ~ 7.055 ppm (Figure 5.46b). Values were normalised to the value of the as-cast sample processed with 3 Vol% DIO. The vertical axis is plotted on a log scale due to the large differences in values between as-cast and annealed samples.

5.7 Stability in Ambient Conditions

As discussed previously, residual DIO retained in films after processing has been shown to be detrimental to device stability. Given that ^1H NMR measurements indicate PBDB-T : ITIC based systems trap more DIO compared to PBDB-T : PC₇₁BM systems, it is important to understand how this influences the stability of devices under both extrinsic and intrinsic factors. The primary risk of DIO-induced film degradation is through the formation of highly reactive radicals and increased rate of oxygen diffusion into the film when aged under illumination in ambient conditions. Consequently, the impact of DIO processing on the photo-stability of each material was first investigated using UV-Vis absorption and device ageing measurements.

To compare rates of photo-degradation, UV-Vis absorption measurements of pure films and blend thin films were performed at 4 hour intervals during irradiation at 1 Sun in ambient conditions (i.e. in an ATLAS lifetime tester) for a total duration of 24h. Measurements of films stored in the dark in ambient conditions were also performed at the same time intervals to act as a control. Absorption spectra during ageing for pure ITIC, PC₇₁BM and PBDB-T films along with PBDB-T : ITIC and PBDB-T : PC₇₁BM blend films processed from chlorobenzene with 0-3 Vol% DIO are displayed in Appendix B). To compare the photo-stability of each material, the maximum absorption normalised to the initial measurement before ageing was plotted as a function of irradiation time for pure and blend thin films (Figure 5.20, Figure 5.21).

Starting first with the pure films, it is apparent that there are drastically different rates of photo-degradation between materials. In particular, ITIC films processed without DIO degrade rapidly, appearing completely photo-bleached after 12-16h of irradiation (Figure 5.20a) whilst films aged in the dark show no signs of absorption loss (Figure 5.20b). The intrinsic photo-instability of ITIC has been reported previously and linked to instability of the vinylene linkage between the donor core and acceptor units [124]. Interestingly, although all pure ITIC films appear equally photo-bleached after 24h, processing with DIO significantly decreases the initial rate of photo-degradation. For example, the maximum absorption of pure ITIC films processed without DIO after 12 hours of irradiation drops to $\sim 10\%$ of the initial value but for films processed with 3 Vol% DIO, absorption is $\sim 45\%$ of the initial value. This is surprising given the wealth of literature linking residual DIO to accelerated UV-induced degradation [297, 126, 123]. However, a potential explanation can be rationalised by considering DIO-induced changes to the nanostructure of pure ITIC films.

As demonstrated in the GIWAXS measurements above, DIO processing enhances the crystallinity of ITIC, offering a more densely packed crystalline nanostructure. This reduces

the rate of oxygen diffusion into the film, preventing a number of potential UV-induced degradation routes such as irreversible conjugation loss and photo-oxidation [314, 124]. Similar crystallinity-related photo-stability improvements have been observed in other systems [315, 316, 317, 318]. Interestingly, the results presented here suggest that enhanced ITIC crystallinity has a much greater effect on reducing the rate of oxygen diffusion compared to any opposing effect associated with residual DIO retained in the film. However, ultimately the intrinsic photo-stability of ITIC is so poor that all films experience drastic photobleaching within 24h.

In comparison to pure ITIC, pure PC₇₁BM and PBDB-T films exhibit considerably superior photo-stabilities, with the normalised maximum absorption of all films processed with and without DIO remaining >80% of the initial value after 24h of irradiation (Figure 5.20c and Figure 5.20e). For pure PC₇₁BM films, there does not appear to be any significant DIO-related dependence on the resultant photo-stability. Pure PBDB-T films appear to exhibit slightly improved photo-stabilities as DIO volume concentration increases. While this effect is much weaker compared to ITIC, it likely originates via a similar mechanism; DIO-induced aggregation limits the rate of oxygen diffusion into the film reducing photo-degradation. This is in agreement with the enhanced face-on PBDB-T molecular packing and aggregation demonstrated in the GIWAXS measurements discussed above.

For PBDB-T : ITIC blend films, the presence of PBDB-T appears to suppress ITIC photo-degradation with all films retaining a maximum absorption above ~70% of the initial value after 24h irradiation exposure (Figure 5.21a). The same DIO-dependent photo-stability observed for pure PBDB-T and ITIC films is also apparent here with films processed without DIO undergoing slightly faster rates of photo-degradation compared to films processed with DIO. This is unsurprising given the DIO-induced molecular packing enhancement demonstrated in the GIWAXS studies of both pure PBDB-T and ITIC films and PBDB-T : ITIC blend films. Additionally, in PBDB-T : ITIC blends processed with higher concentrations of DIO, photo-stability is also likely to be improved due the formation of a PBDB-T-rich surface layer (discussed above) which could act as a protective barrier to the more intrinsically unstable ITIC molecules accumulated at the film/substrate interface. In comparison, the superior photo-stability of pure PBDB-T and PC₇₁BM relative to pure ITIC are reflected in UV-vis measurements of PBDB-T : PC₇₁BM blend films (Figure 5.21b). Here, the maximum absorption value of remains above 85% of the initial value after 24h and there are no indications of any significant DIO-dependent photo-degradation. In the dark, both blend systems exhibit good stability with only minimal changes in maximum absorption observed after 24h (Figure 5.21c, Figure 5.21d).

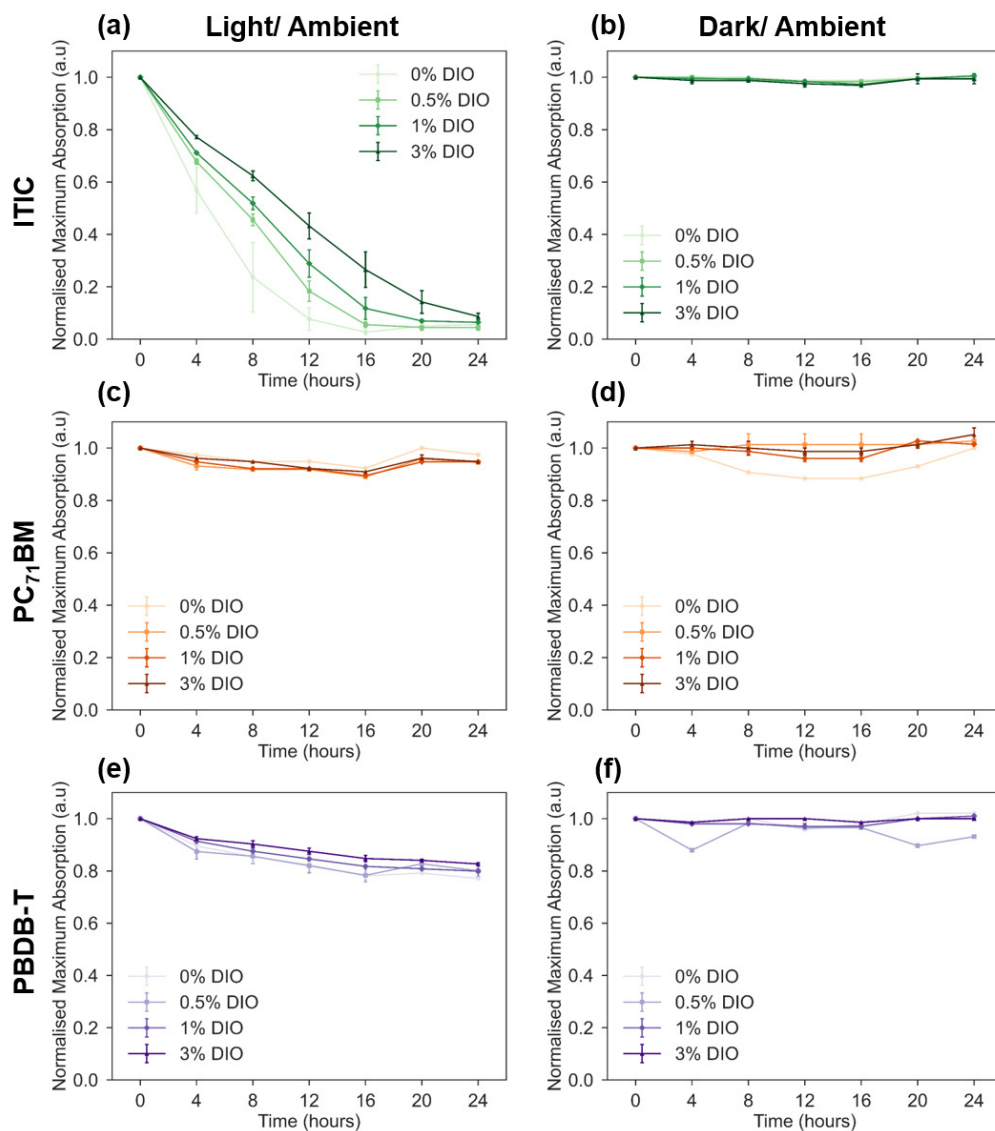


Figure 5.20: Normalised maximum absorption of pure (a,b) ITIC, (c,d) PC₇₁BM and (e,f) PBDB-T films processed from chlorobenzene with 0-3 Vol% DIO and aged in ambient conditions during 1 Sun irradiation (Light/ Ambient conditions) and in the dark (Dark/ Ambient conditions). Measurements were performed at 4h intervals for a total duration of 24h. Values are normalised to the initial maximum absorption of each film measured immediately after fabrication before ageing. The wavelengths at which absorption maxima occurred are $\sim 705\text{nm}$ and $\sim 711\text{nm}$ for pure ITIC films processed from 0-1 Vol% DIO and 3 Vol% respectively, $\sim 484\text{nm}$ for pure PC₇₁BM films, and $\sim 581\text{nm}$ for pure PBDB-T films. Full UV-Vis spectra are provided in Appendix B.

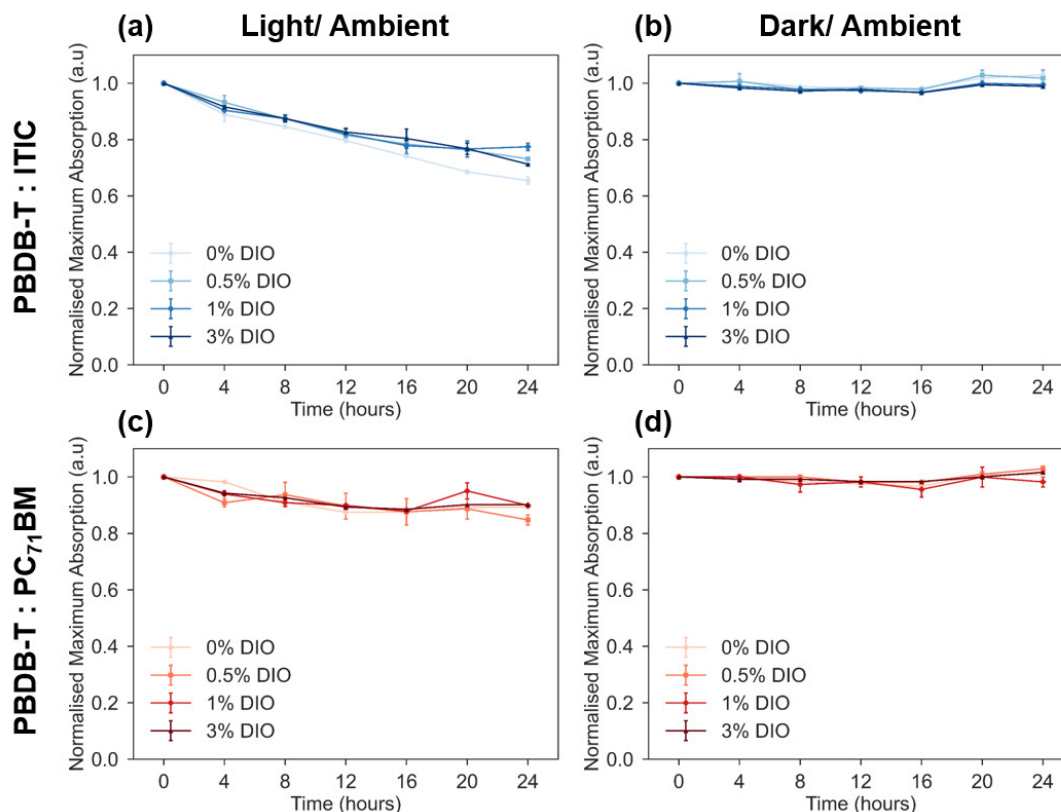


Figure 5.21: Normalised maximum absorption of (a,b) PBDB-T : ITIC and (c,d) PBDB-T : PC₇₁BM blend films processed from chlorobenzene with 0-3 Vol% DIO and aged in ambient conditions during 1 Sun irradiation (Light/ Ambient conditions) and in the dark (Dark/ Ambient conditions). Measurements were performed at 4h intervals for a total duration of 24h. Values are normalised to the initial maximum absorption of each film measured immediately after fabrication before ageing. The wavelengths at which absorption maxima occurred are $\sim 628\text{nm}$ and $\sim 639\text{nm}$ for PBDB-T : ITIC blend films processed from 0-1 Vol% DIO and 3 Vol% respectively, and 577nm for PBDB-T : PC₇₁BM blend films. Full UV-Vis spectra are provided in Appendix B.

The differences in rates of photo-degradation for each sample can also be tracked visually, simply by photographing films during ageing (Figure 5.22). For each sample, photographs were taken every 12h for a duration of 96h (4 days) whilst exposed to 1 Sun irradiation in ambient conditions. In agreement with the UV-Vis measurements described above, all films appear to undergo some level of photobleaching but the rate of degradation differs drastically across materials. For pure ITIC films, the same DIO dependence observed in UV-Vis absorption measurements is also apparent in the film photographs. ITIC films processed without DIO undergo rapid photobleaching within 12h of irradiation but DIO-processed films take a further 12h before the distinctive blue films appear completely photo-bleached. Signs of photobleaching are also observed in pure PBDB-T films after 48-72h irradiation exposure. However, the DIO-dependent photo-degradation is less apparent compared to UV-measurements. For pure PC₇₁BM, all films retain their characteristic orange colour after 96h irradiation exposure, regardless of DIO concentration.

In the blend films, the superior photo-stability of PBDB-T : PC₇₁BM systems is clearly visible with all films appearing visually unchanged after 4 days of irradiation exposure. In comparison, all PBDB-T : ITIC blend films show signs of photobleaching after 24-48h of irradiation exposure and films processed without DIO exhibit a faster rate of photo-degradation. However, regardless of DIO concentration, the poor intrinsic stability of ITIC results in all films appearing completely photo-bleached after 96h. Whilst photographing films during irradiation exposure is a quick and easy method for gaining an initial comparison of the photo-stability of each material, it is only a qualitative approach and does not take into account differences in film thickness.

Next, the impact of DIO on the photo-stability of PBDB-T : ITIC and PBDB-T : PC₇₁BM blends was further investigated by tracking the *J-V* characteristics of OPV devices during 1 Sun irradiation in ambient conditions. These measurements were performed using an ATLAS lifetime tester using unencapsulated devices. Device performance metrics (*PCE*, *J_{SC}*, *V_{OC}* and *FF*) normalised to their initial value are displayed as a function of hours tested in Figure 5.23. All devices experience a substantial burn-in process primarily due to *J_{SC}* losses (Figure 5.23b).

For PBDB-T : ITIC devices processed with 0, 0.5 and 1 Vol% DIO, rapid burn-in drastically reduces *PCEs* to <20% of their initial values after 10 hours of irradiation as the active layer materials undergo significant photobleaching (Figure 5.23a). In agreement with the UV-Vis measurements described above, the rate of photo-degradation of PBDB-T : ITIC devices processed with 3 Vol% DIO is considerably slower with *PCEs* dropping to ~40% of their initial value after 10 hours of irradiation (Figure 5.23a). This is attributed to reduced oxygen diffusion as a result of a more densely packed nanostructure and enhanced accumulation of PBDB-T at the surface of the film.

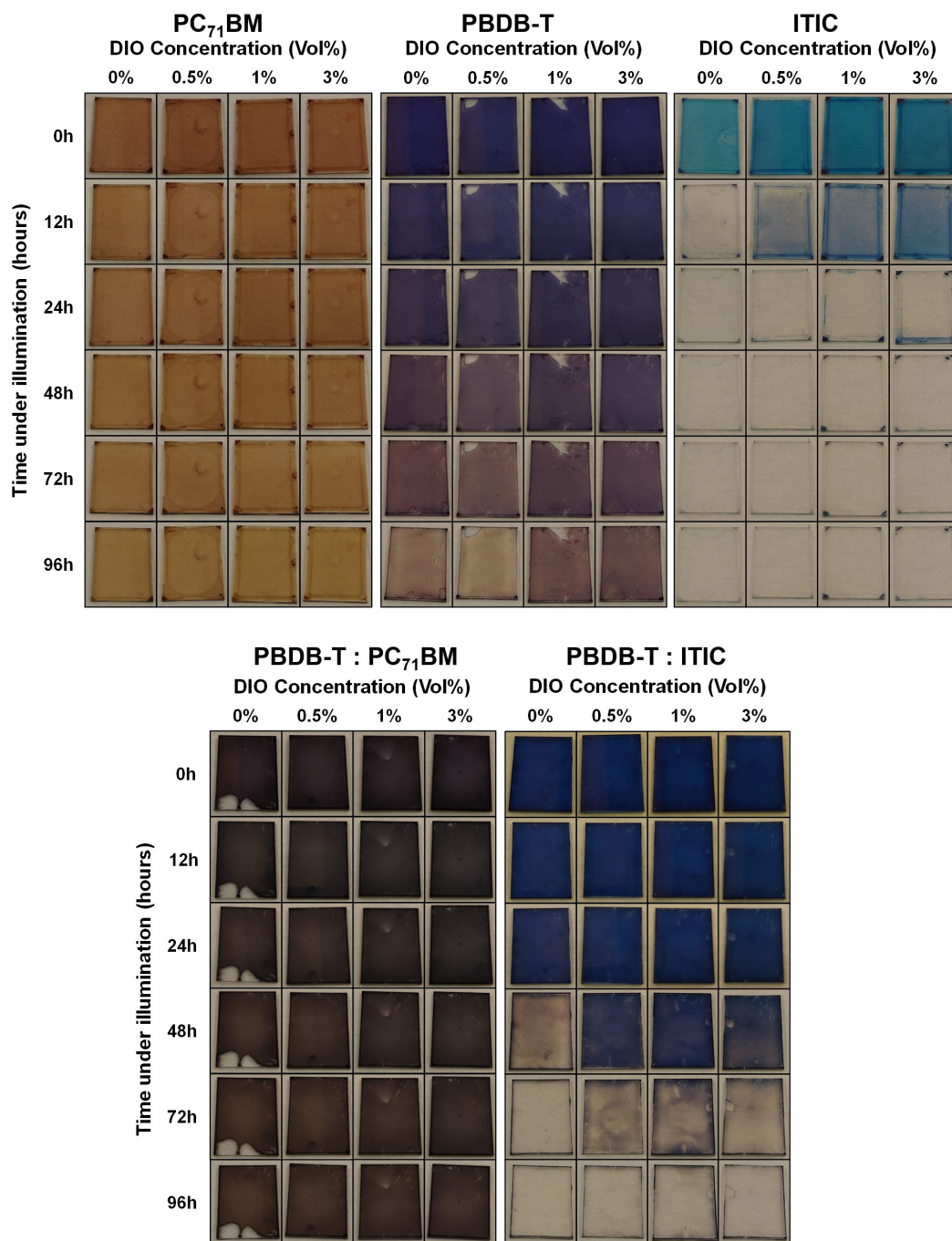
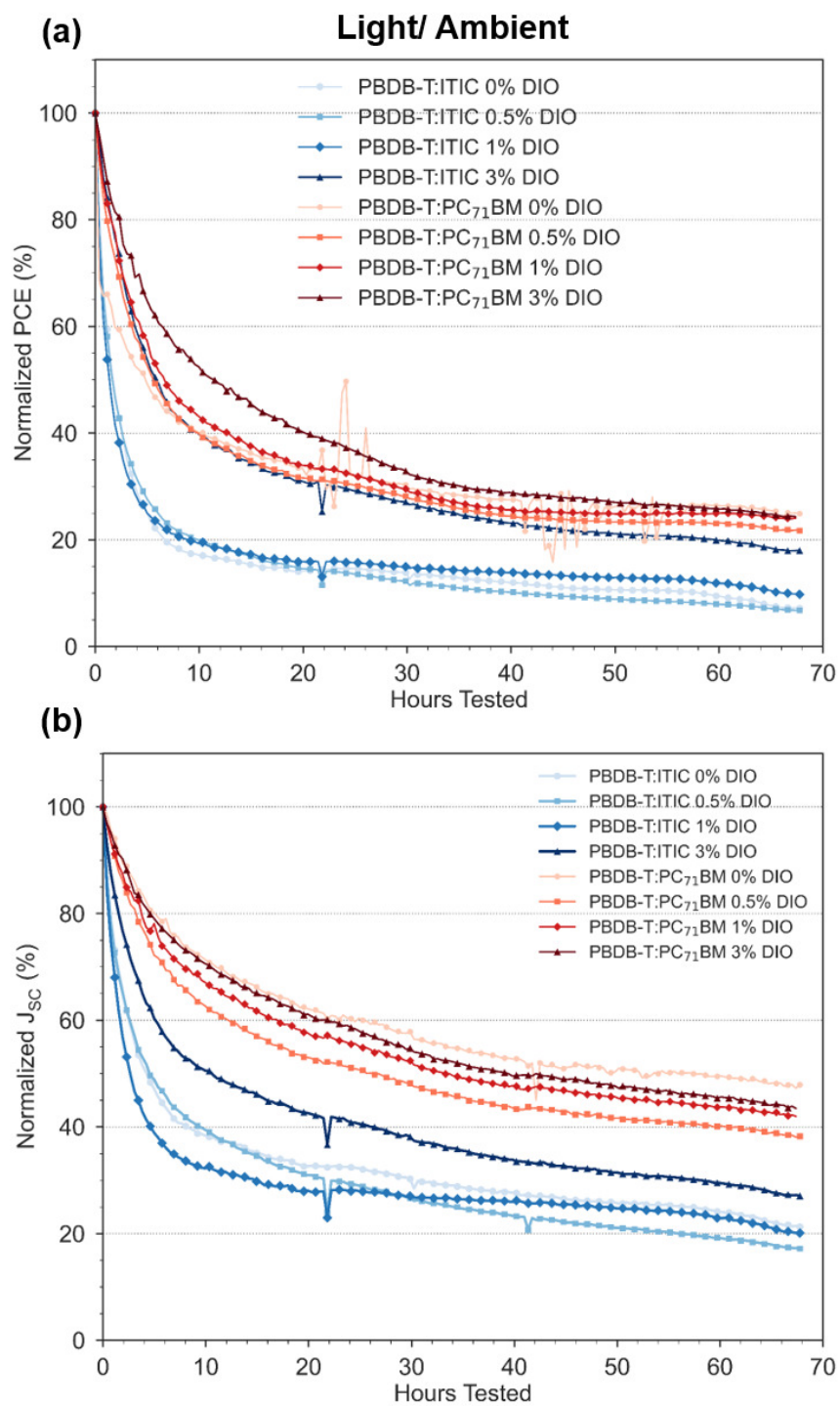


Figure 5.22: Photographs of pure material and blend films processed with various amounts of DIO (0, 0.5, 1 and 3%) and aged by light irradiation for increasing amounts of time in an ATLAS lifetime tester under ambient conditions.

In comparison, PBDB-T : PC₇₁BM devices display considerably better photo-stabilities compared to PBDB-T : ITIC devices, due to reduced photobleaching in agreement with previous studies [319, 314]. PBDB-T : PC₇₁BM devices processed with 3 Vol% DIO are particularly photo-stable, likely due to the combined effect of superior intrinsic photo-stability and a reduced rate of oxygen diffusion facilitated by PBDB-T aggregation and vertical segregation. Interestingly, higher concentrations of DIO seem to generally result in larger FF losses for both blend systems during irradiation, suggesting other degradation factors are at play (Figure 5.23c). However, in these ageing conditions, photobleaching is so severe that J_{SC} losses dominate the overall device stability.

To disentangle the primary degradation factors, devices were also aged in the dark in ambient conditions to remove any light-induced ageing effects. Device metrics as a function of ageing time for PBDB-T : ITIC and PBDB-T : PC₇₁BM devices processed from chlorobenzene with 0-3 Vol% DIO are displayed in Figure 5.24. In the absence of solar irradiation, DIO volume concentration has a significant impact on the stability of PBDB-T : ITIC devices whereas the stability of PBDB-T : PC₇₁BM devices is much less dependent. PBDB-T : ITIC devices processed with 1 and 3 Vol% DIO undergo drastic burn-in losses within the first 10 days of ageing, with PCE dropping to $\sim 80\%$ and $\sim 50\%$ of its initial value respectively (Figure 5.24a). This is mostly attributed to changes in V_{OC} and FF (and J_{SC} for 3 Vol% DIO) (Figure 5.24b-d). In comparison, PBDB-T : ITIC devices processed with lower concentrations of DIO (0 and 0.5 Vol%) are considerably more stable with PCE maintaining above $\sim 85\%$ after 90 days of ageing (Figure 5.24a) and losses mostly originate from changes in FF .

For PBDB-T : PC₇₁BM devices, the superior stability is clear with PCE s only decreasing to $\sim 90 - 95\%$ of their initial values after 90 days of ageing, regardless of DIO volume concentration (Figure 5.24a). Interestingly, the PCE of PBDB-T : PC₇₁BM devices processed with 3 Vol% DIO increases by $\sim 5\%$ due to an initial boost in FF and remains above the initial value after ~ 40 days of ageing. Similar increases in device performance during ageing has been reported for other OPV systems elsewhere [114, 128, 115] and they have been attributed to an increase in domain purity as the film morphology evolves to its thermal equilibrium and passes through the percolation threshold. These concepts will be discussed in further detail in the following section where devices are aged in inert conditions to remove oxygen related degradation effects.



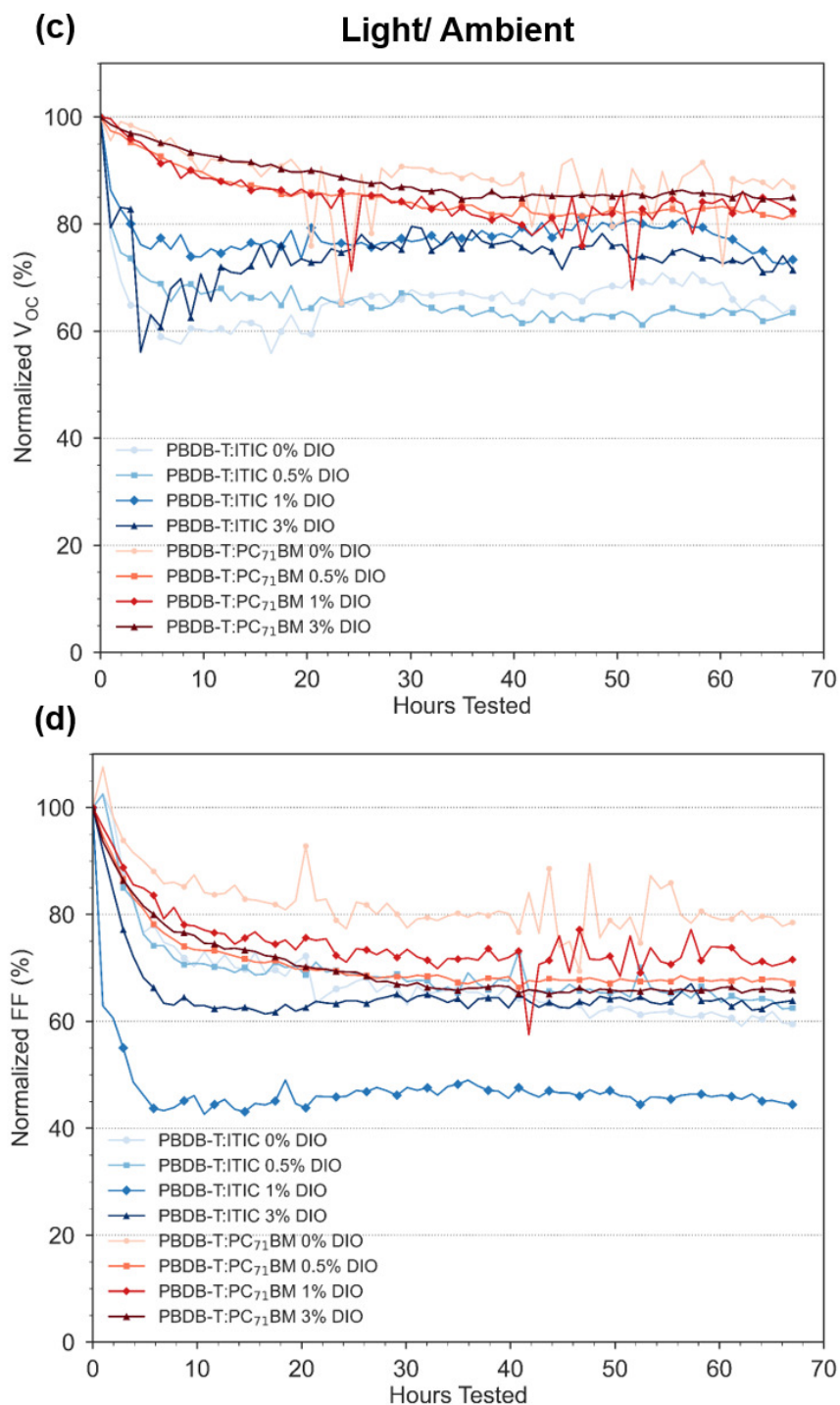
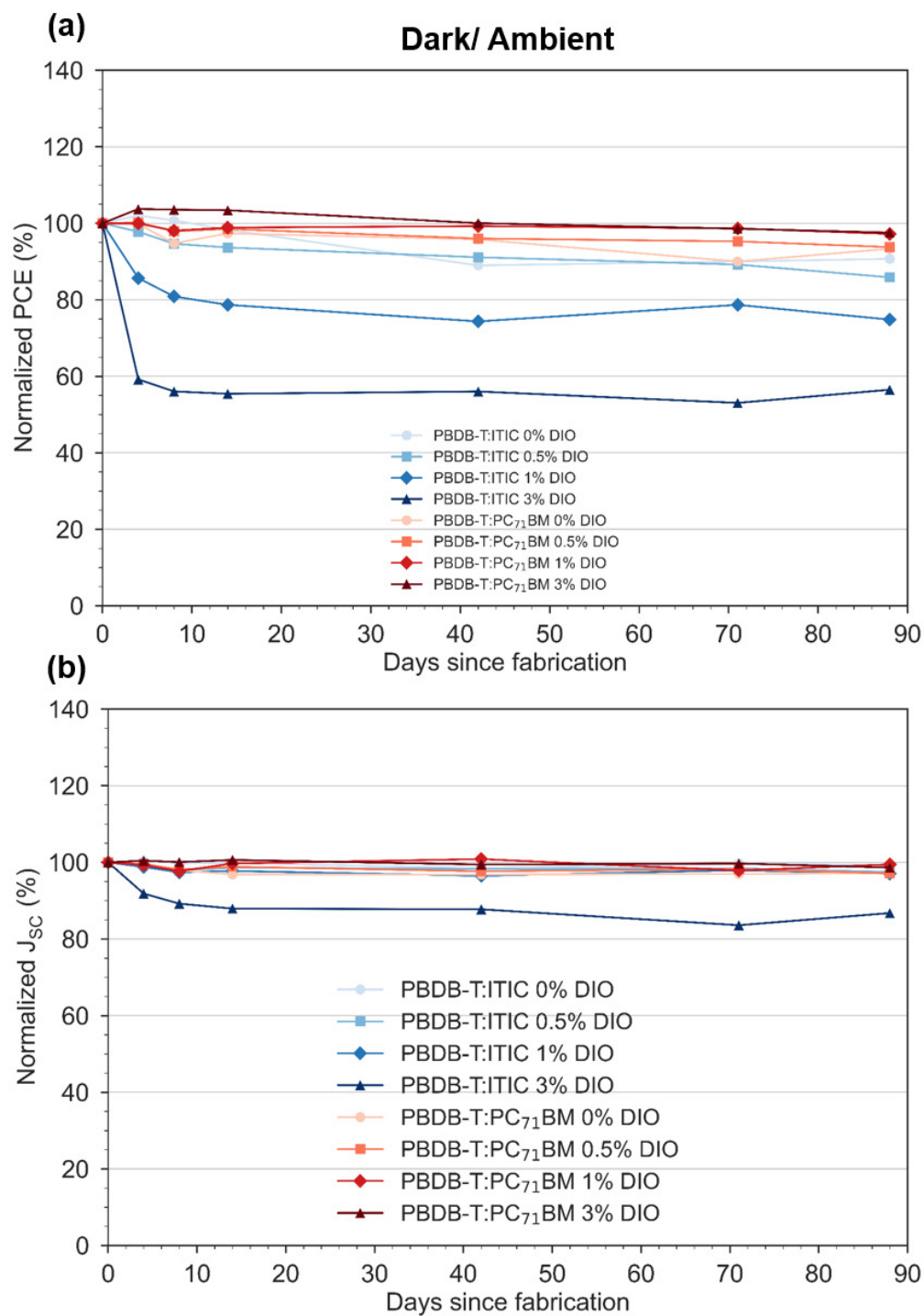


Figure 5.23: Normalised (a) PCE , (b) J_{sc} , (c) V_{oc} and (d) FF of PBDB-T : ITIC and PBDB-T : $PC_{71}BM$ devices processed from chlorobenzene with 0-3 Vol% DIO and aged in an ATLAS lifetime tester (light/ambient conditions) for 70 hours.



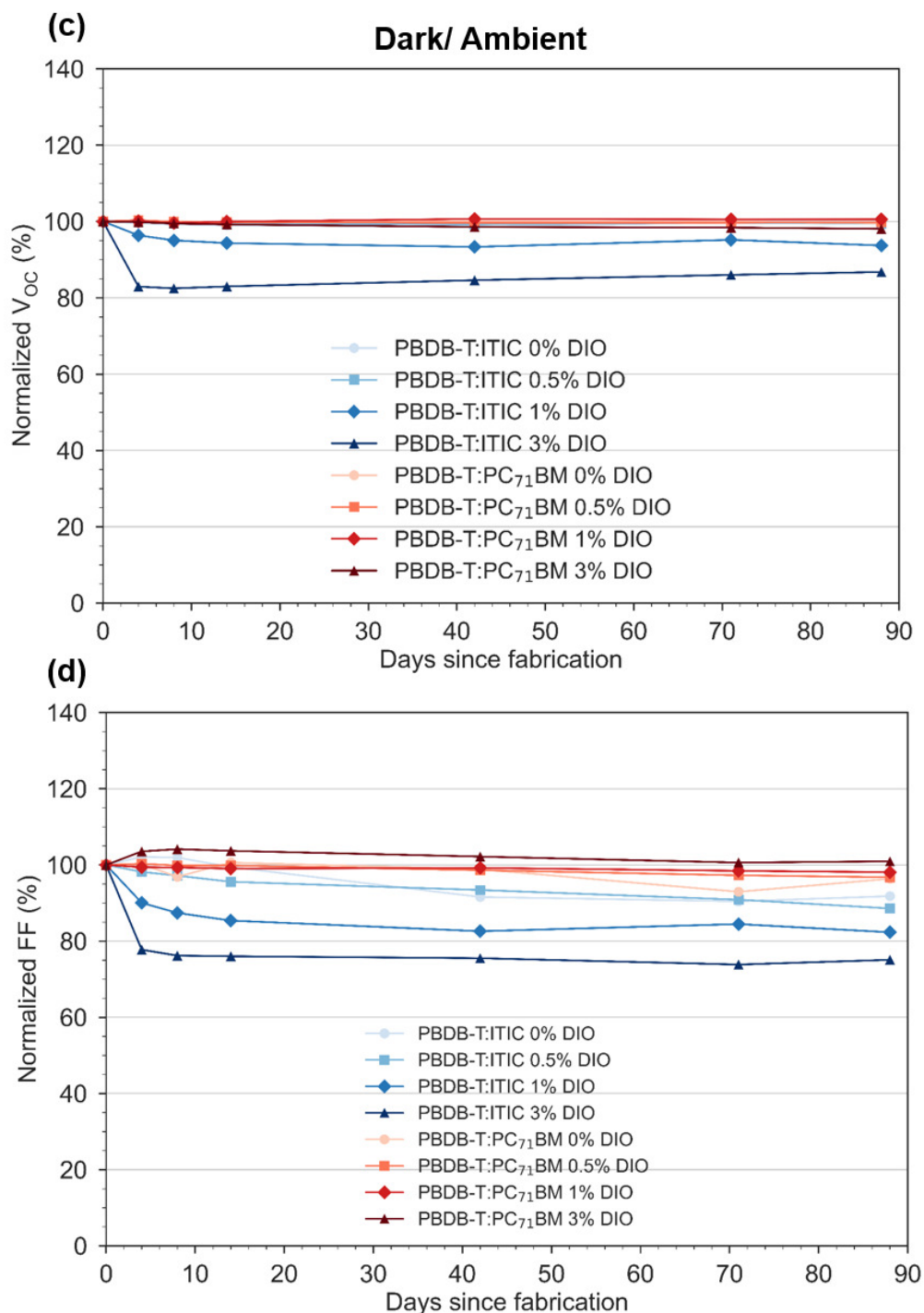


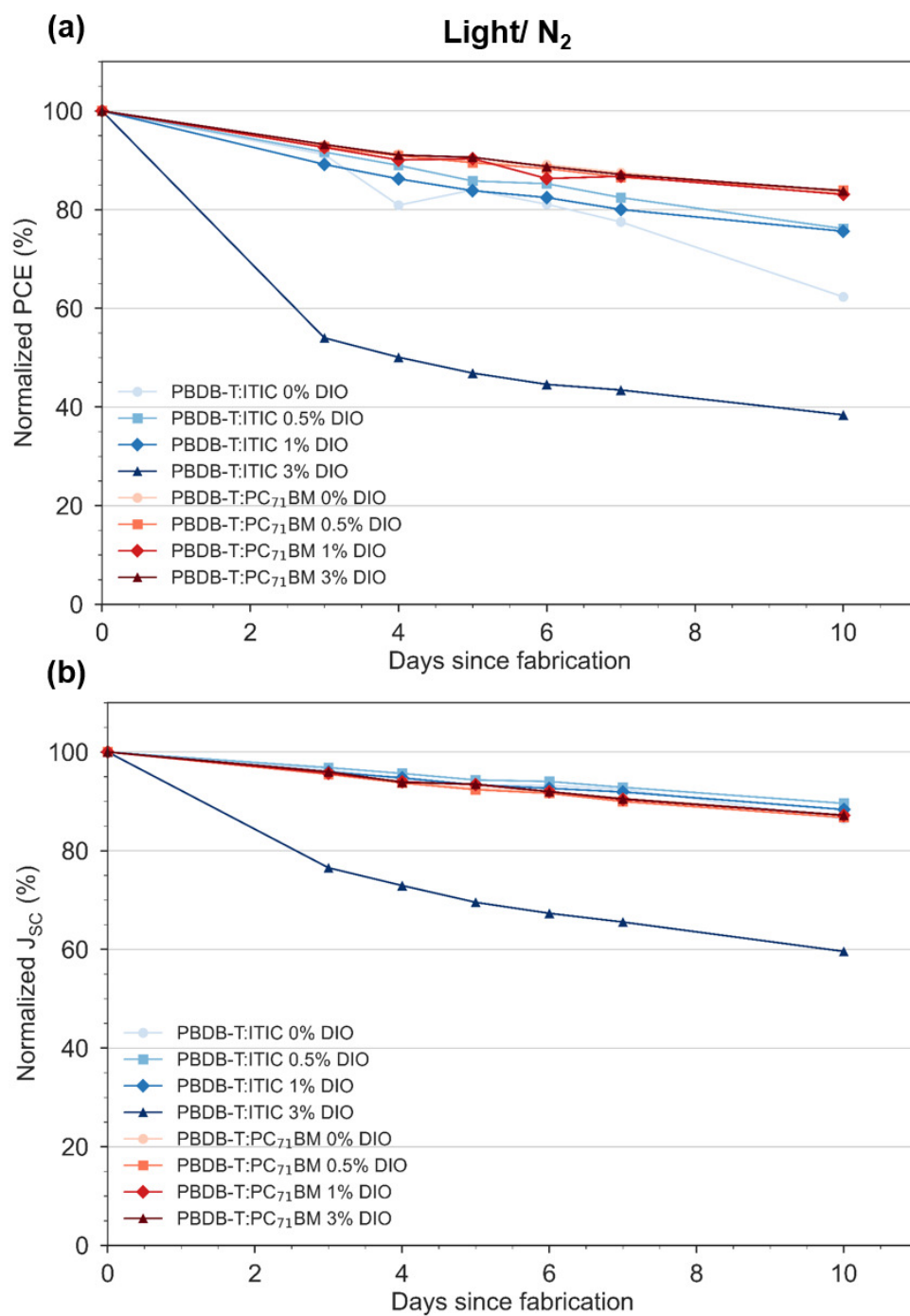
Figure 5.24: Normalised (a) PCE , (b) J_{SC} , (c) V_{OC} and (d) FF of PBDB-T : ITIC and PBDB-T : PC₇₁BM devices processed from chlorobenzene with 0-3 Vol% DIO and aged in the dark in ambient conditions for 90 days.

5.8 Stability in Inert Conditions

A primary DIO-induced OPV degradation route is the enhanced diffusion of oxygen into the film as a result of retained DIO solvent in the film after processing [123]. To remove any oxygen-related effects and explore other degradation pathways, the stability of devices aged in inert conditions was investigated. Following the ageing protocols discussed in Subsection 3.4.5, devices were aged during 1 Sun irradiation in a nitrogen-filled glovebox (Figure 5.25).

For PBDB-T : ITIC devices, processing with 3 Vol% DIO results in a similar rapid burn-in as observed for devices aged in ambient conditions with PCE plummeting to $\sim 55\%$ of the initial value after 3 days during 1 Sun irradiation in inert conditions (Figure 5.25a). Degradation is observed for all PV metrics but J_{SC} losses are the most significant (Figure 5.25b). This rapid decrease in performance in the absence of oxygen is likely linked to UV-induced photo-degradation, accelerated by larger amounts of trapped DIO solvent as previously indicated by ^1H NMR measurements. Morphological instabilities should also not be discounted but these will be considered later. For PBDB-T : ITIC devices processed with 0-1% DIO, the lower volume of residual DIO in the films after processing, results in reduced burn-in losses and significantly improved stability across all PV metrics (Figure 5.25). In comparison, PBDB-T : PC₇₁BM devices exhibit superior stability with all devices processed with and without DIO retaining $>80\%$ of their initial PCE value after 10 days of 1 Sun irradiation in inert conditions (Figure 5.25a). Primary losses originate from reductions in J_{SC} with FF and V_{OC} maintaining values $>95\%$ of the initial values.

To further understand the degradation routes linked to morphological instabilities, devices were aged in the dark during storage in a nitrogen-filled glovebox for 90 days after fabrication (Figure 5.26). PBDB-T : ITIC devices processed with 1 and 3 Vol% DIO degrade rapidly within the first 5 days of storage with PCE values dropping to $\sim 70\%$ of the initial value (Figure 5.26a). Devices processed with 0 and 0.5% DIO demonstrate improved stability maintaining PCE values $>85\%$ of the initial value after 90 days of storage. In comparison, PBDB-T : PC₇₁BM devices demonstrate superior stability and for some devices, PCE increases during dark storage ((Figure 5.26a)). This is most significant for devices processed with 0 and 3 Vol% with PCE increasing by $\sim 25\%$ and $\sim 7.5\%$ respectively. PCE enhancements during ageing correspond to increases in J_{SC} and FF , indicative of changes in film nanomorphology [114, 128, 115] (Figure 5.26b,d).



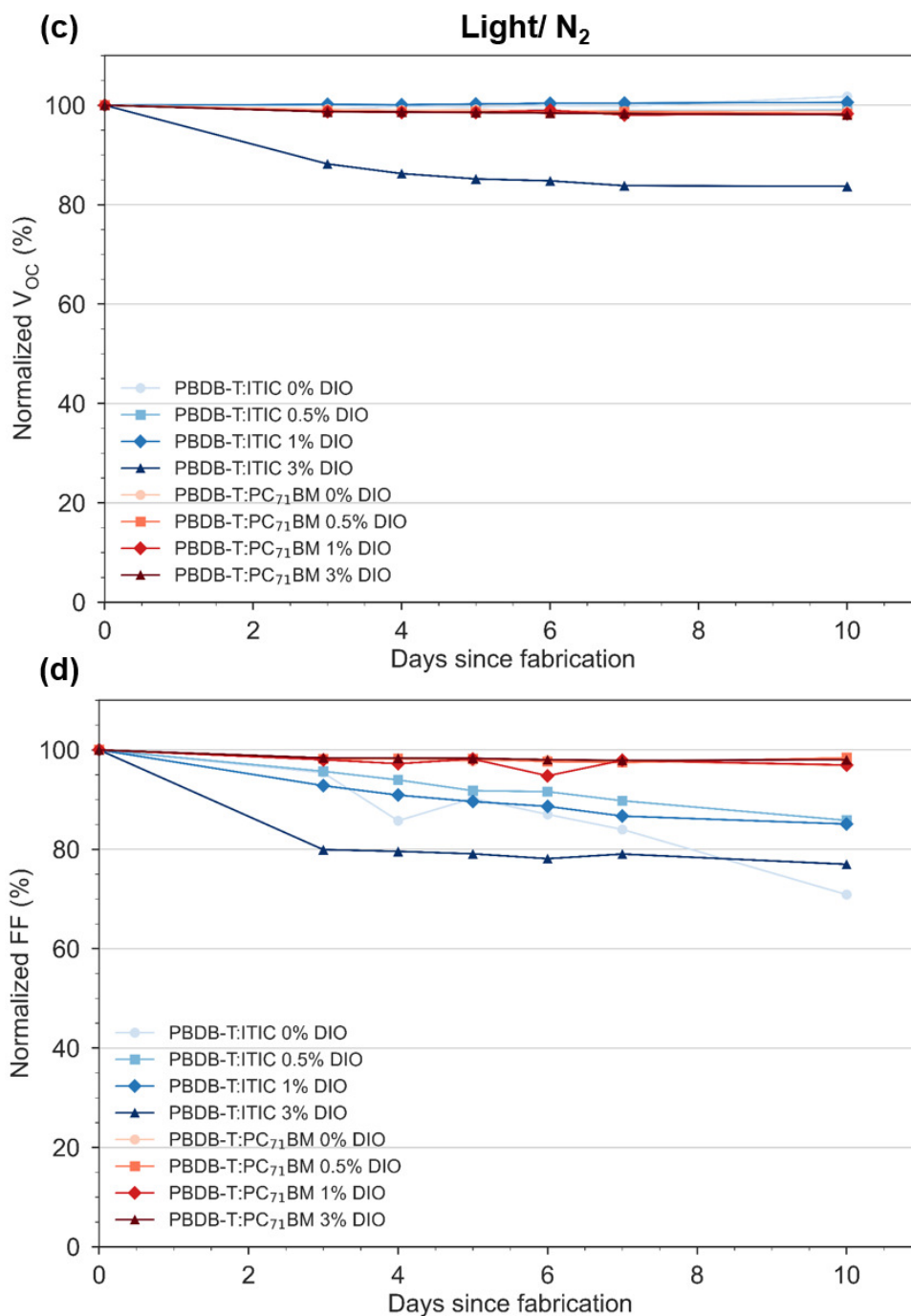
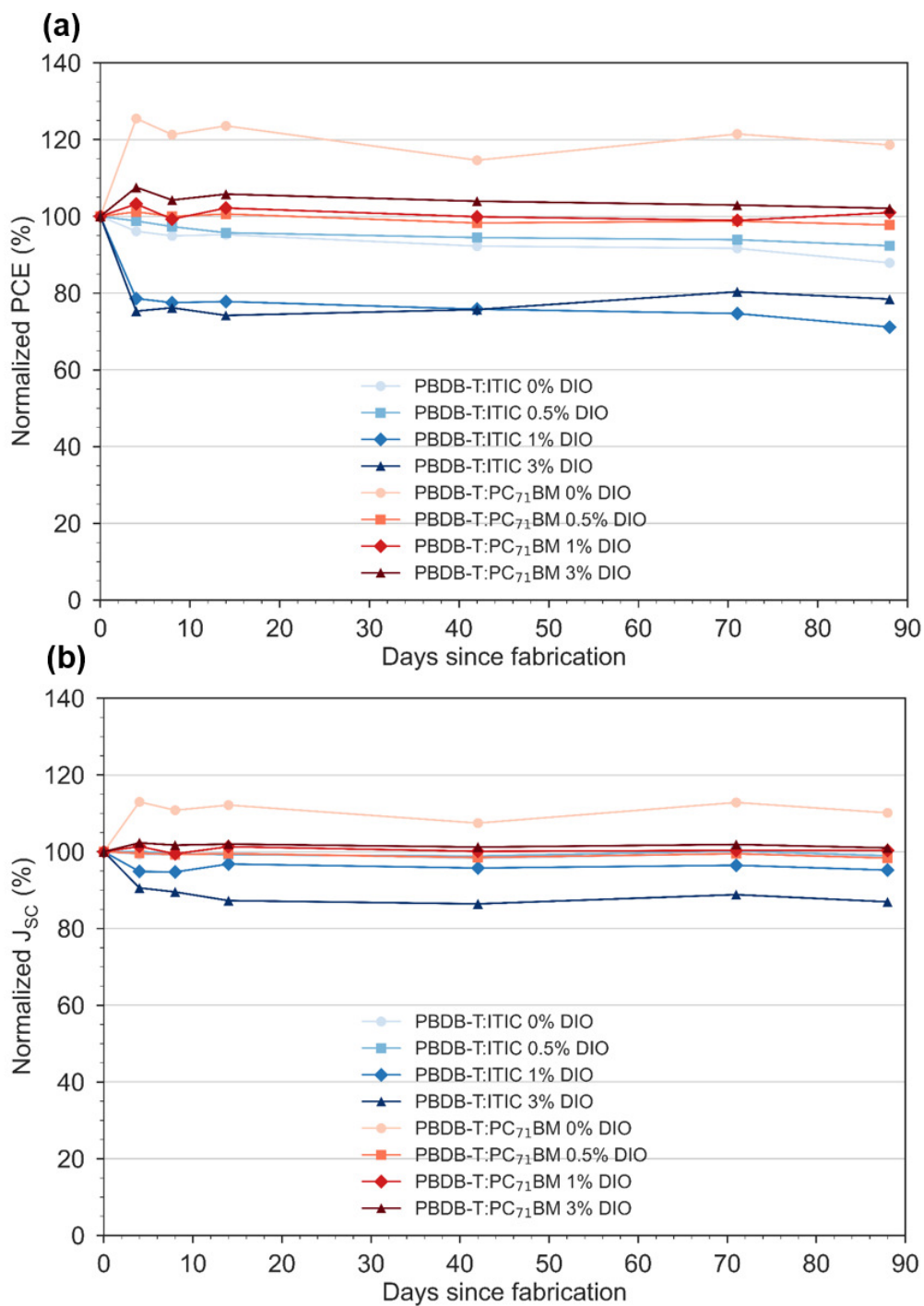


Figure 5.25: Normalised (a) PCE , (b) J_{SC} , (c) V_{OC} and (d) FF of PBDB-T : ITIC and PBDB-T : PC₇₁BM devices processed from chlorobenzene with 0-3 Vol% DIO and aged under illumination in a nitrogen-filled glovebox (light/ N₂ conditions) for 10 days.



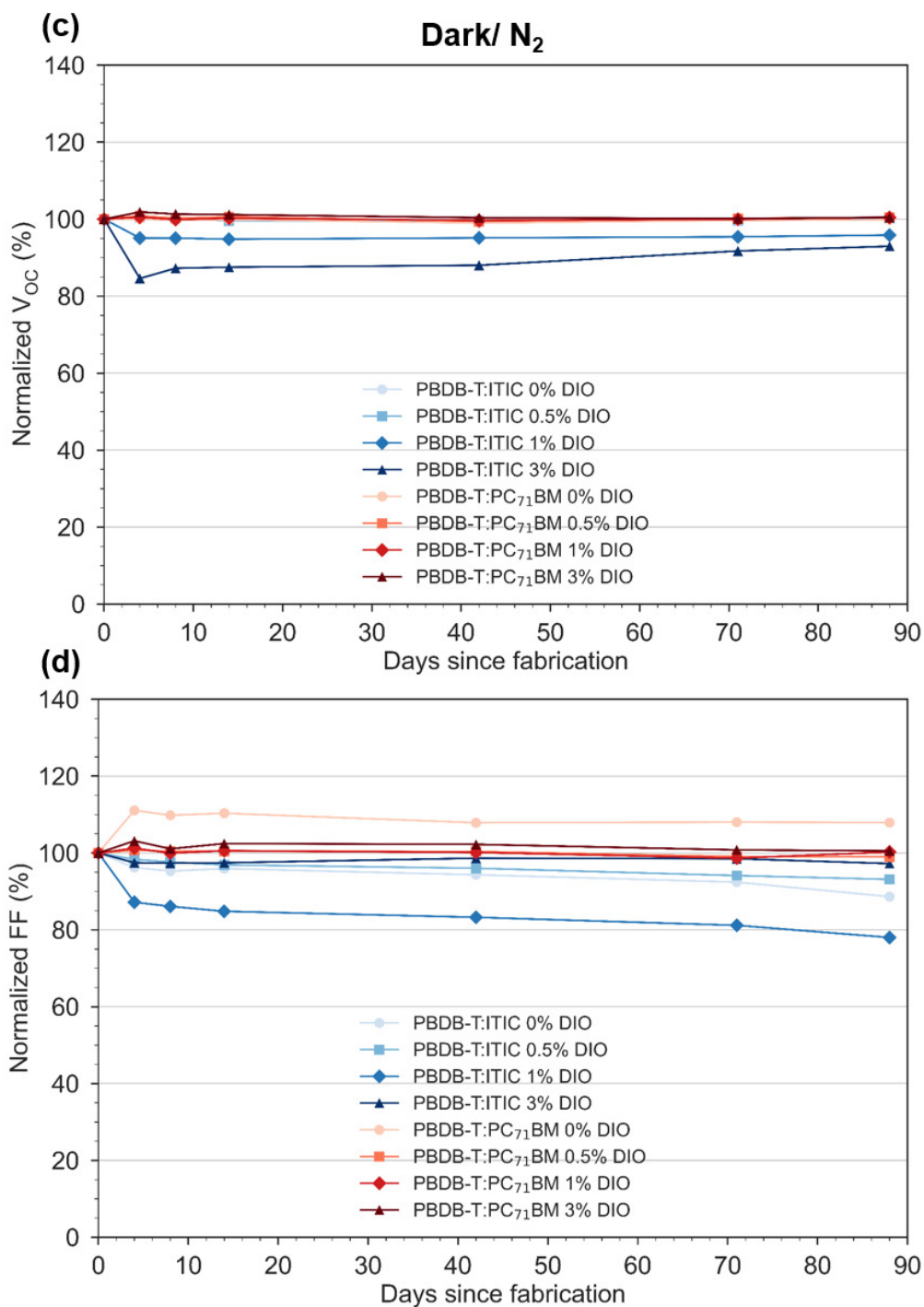


Figure 5.26: Normalised (a) PCE , (b) J_{SC} , (c) V_{OC} and (d) FF of PBDB-T : ITIC and PBDB-T : PC₇₁BM devices processed from chlorobenzene with 0-3 Vol% DIO and aged in the dark in a nitrogen-filled glovebox (dark/ N₂ conditions) for 90 days.

To investigate the apparent morphological changes during ageing, indicated by device measurements, AFM measurements of fresh PBDB-T : ITIC and PBDB-T : PC₇₁BM films processed from 0 and 3 Vol% DIO, were compared with films exposed to 1 Sun irradiation in an inert atmosphere for 24h (Figure 5.27, Figure 5.28). For PBDB-T : ITIC films, surface domains appear more well-defined after ageing, indicative of a higher degree of phase separation (Figure 5.27). This is most apparent for the surface topography of aged PBDB-T : ITIC films processed with 3 Vol% DIO, which are composed of distinct, aggregated domains (Figure 5.27d). For PBDB-T : PC₇₁BM films, the surface nanomorphology is much smaller making it difficult to discern morphological changes (Figure 5.28). Films processed without DIO do not appear to have changed significantly after ageing (Figure 5.28a,b). For PBDB-T : PC₇₁BM films processed with 3 Vol% DIO, the surface of the fresh film consists of a intermixed nanomorphology (Figure 5.28c). After ageing, domains appear more distinct and globular in shape indicating the blend components have phase separated (Figure 5.28d).

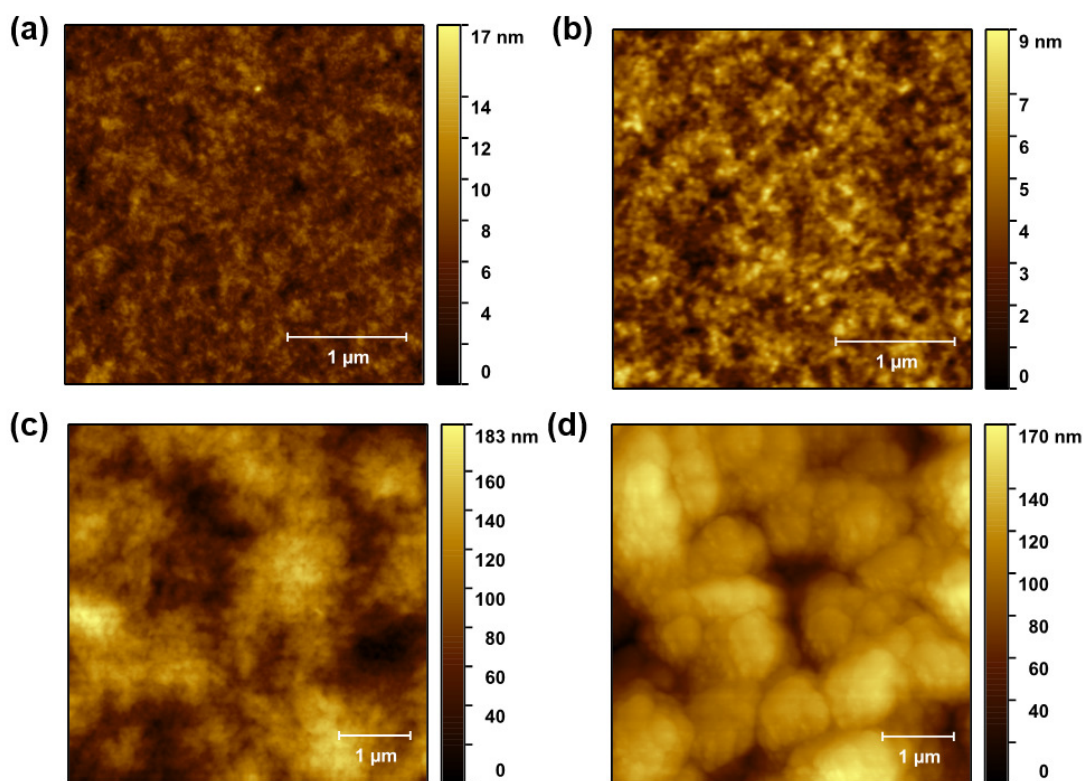


Figure 5.27: AFM height topography images of PBDB-T : ITIC films processed with (a,b) 0 and (c,d) 3 Vol% DIO measured fresh immediately after fabrication (a,c) and after 1 Sun irradiation in inert conditions for 24h (b,d). The scale bar is 1 μm . Parts (a) and (c) are repeated from Figure 5.8.

To understand changes in the *bulk* film nanomorphology during ageing, further structural characterisation using scattering methods (e.g. GIWAXS and SANS) of fresh and aged films is required.

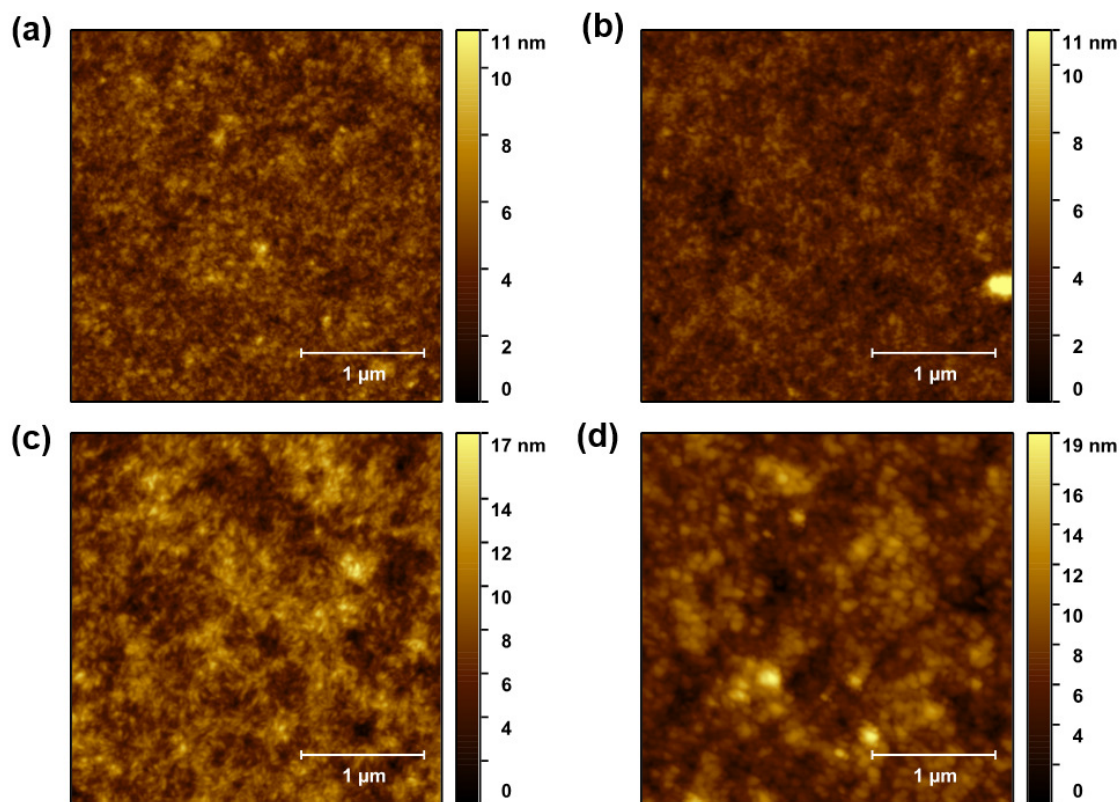


Figure 5.28: AFM height topography images of PBDB-T : PC₇₁BM films processed with (a,b) 0 and (c,d) 3 Vol% DIO measured fresh immediately after fabrication (a,c) and after 1 Sun irradiation in inert conditions for 24h (b,d). The scale bar is 1 μ m. Parts (a) and (c) are repeated from Figure 5.9.

During device ageing, it was noted that S-shaped J - V curves that were initially only visible for freshly fabricated PBDB-T : ITIC devices processed with 3 Vol% DIO appeared in devices processed with 1 Vol % DIO within 4 days of ageing in the dark in inert conditions (Figure 5.47c) and within 3 days of ageing during 1 Sun irradiation in inert conditions (Figure 5.48c). Additionally, the J - V curves for PBDB-T : ITIC devices processed with 3 Vol% becomes more *S-shaped* during ageing (Figure 5.47d, Figure 5.48d). In comparison, PBDB-T : PC₇₁BM devices retain normal diode-like J - V characteristics regardless of DIO concentration or ageing environment (Figure 5.47e-h, Figure 5.48e-h).

As previously discussed, the appearance of S-shaped J - V curves are indicative of a charge extraction barrier at the electrodes. NR measurements revealed DIO induces severe vertical segregation in PBDB-T : ITIC systems, with an ITIC-rich layer forming at the PEDOT:PSS/ film interface and a PBDB-T-rich layer at the film surface. The evolution of S-shaped J - V curves in 1 and 3 Vol% DIO devices, therefore suggest that this vertical segregation effect becomes more exaggerated during ageing with the active layer components continuing to accumulate at interfaces after fabrication. This is in agreement with the rapid degradation in V_{OC} observed for PBDB-T : ITIC devices processed with 1 and 3 Vol% DIO, aged in the dark (Figure 5.24d, Figure 5.26d).

Although the films are expected to be vitrified at room temperature, residual DIO retained in the film after processing, likely provides sufficient mobility for phase-segregation to continue to evolve to thermodynamic equilibrium. To verify this, the vertical composition of fresh and aged films should be compared using a suitable high-resolution depth-profiling techniques such as NR.

5.9 Discussion and Summary

In summary, the impact of DIO on the morphology, performance and stability of PBDB-T : ITIC and PBDB-T : PC₇₁BM organic photovoltaic systems has been investigated in detail, demonstrating that the same nanostructure optimisation protocols used extensively for fullerene-based systems are not easily translated to NFA systems.

The chapter opened with a comparison of the optoelectronic properties of each blend system after processing with 0, 0.5, 1 and 3 Vol% DIO. In general, ITIC-based systems exhibit superior device performance due to a stronger absorption of the solar spectrum compared to PC₇₁BM. When processed with small amounts of DIO (0.5 Vol%) a maximum PCE of 11.05% is achieved for PBDB-T : ITIC systems. However, processing with higher concentrations of DIO severely impacts all device metrics with average PCE s dropping to 3.84%. In comparison, the performance of PBDB-T : PC₇₁BM devices is much more tolerable to higher concentrations of DIO and a more significant boost in performance is observed with a maximum PCE of 8.84% achieved for devices processed with 1 Vol% DIO.

Using a combination of GIWAXS, SANS, AFM and NR measurements, DIO-induced changes in optoelectronic properties were then correlated to the self-assembled, hierarchical morphology of the blend films. Importantly, deuterated ITIC was synthesised for neutron scattering measurements to improve the contrast in the blend film with PBDB-T. For PBDB-T : ITIC systems, using small concentrations of DIO induces a favourable face-on PBDB-T molecular orientation and enhances the crystallinity of both components,

which is beneficial for efficient charge transport and reduced non-geminate recombination. However, when larger amounts of DIO are added to the casting solvent, ITIC undergoes excessive crystallisation forming large, phase-separated aggregates. Additionally, the blend films undergo catastrophic vertical segregation forming a thick ITIC-pure hole-blocking barrier at the film/PEDOT:PSS interface and a bulk layer, which is severely depleted in ITIC. Consequently, charge-extraction is significantly restricted at the electrical contacts, resulting in S-shaped J - V curves.

In the case of PBDB-T : PC₇₁BM, PC₇₁BM molecular packing is not significantly impacted by DIO and changes in morphology are driven by PBDB-T aggregation. From SANS measurements, processing with DIO provides greater control of large-scale structural properties, allowing the degree of domain coarsening and domain size to be optimised. Furthermore, as DIO concentration is increased, vertical segregation occurs with PBDB-T-accumulating at the film surface and PC₇₁BM at the PEDOT:PSS/ film interface. However, in comparison to ITIC-based systems, this vertical phase segregation effect is much less severe and S-shaped J - V curves are not observed.

Next, the impact of DIO on the stability of PBDB-T : ITIC and PBDB-T : PC₇₁BM films was investigated under different environmental conditions. Spectroscopic ellipsometry and ¹H NMR measurements revealed that whilst thermal annealing rapidly removes the majority of DIO from the blend films, residual amounts remain and ITIC-based films appear to trap a larger amount compared to PC₇₁BM-based blends, possibly due to the extended conjugated NFA molecular structure and enhanced crystallinity at larger DIO concentrations. Despite this, when irradiated in ambient conditions, ITIC-based cells processed from higher concentrations exhibit improved photo-stabilities. This is attributed to reduced oxygen diffusion into the film as a result of a more densely packed, crystalline nanostructure.

In inert conditions, processing with large volume concentrations (1 and 3 Vol%) DIO is detrimental to the stability of PBDB-T : ITIC devices. On the other hand, the stability of PBDB-T : PC₇₁BM devices is significantly superior with device PCE even increasing for systems processed without DIO. Differences in inert stability between polymer : NFA and polymer : fullerene systems are most likely linked to morphological and chemical instabilities which are accelerated by residual DIO. The larger amounts of trapped DIO solvent in PBDB-T : ITIC systems potentially undergoes undesirable chemical reactions with device components. Additionally, the increased mobility of the active layer components permits extended lateral and vertical phase separation leading to a reduction in interfacial area and the formation of component-rich interfaces which act as blocking layers.

In conclusion, this chapter highlights the need to develop alternative structural optimisation protocols which provide a method to fine-tune the active-layer morphology of polymer : NFA films whilst importantly maintaining the long-term operational stability of devices. At present, there are considerable research efforts focused on pushing *PCEs* beyond current records with stability often a secondary thought [43]. Whilst high-efficiency is important for commercialisation and can often be achieved through the use of solvent additives, it is essential that the impact of such processing methods on the long-term operational stability of devices is considered. A boost in initial performance does not imply promising stability.

If optimisation protocols for high-efficiency devices insist on the use of solvent additives, it is essential that more suitable methods for removing residual amounts from the film are sourced or alternative solvent additives are used which are easier to remove from the film and prevent rapid device degradation. At present, there are some studies investigating alternative, lower boiling point additive materials which are iodine-free making them easier to remove from the film and less susceptible to undesirable chemical reactions [320, 321, 123, 301, 322]. However, given that it is difficult to completely remove residual solvent additive with 100% certainty [126] and that NFAs offer a wealth of chemical tunability possibilities through the modification of side-chain and end-group chemical moieties, a potentially more successful route is to optimise morphology through chemical design alone. This removes the risk of detrimental chemical reactions between residual high-boiling solvents and materials within the device entirely, and allows additional material properties such as energy levels, absorption, solubility and thermal properties to be optimised.

Promisingly, the field appears to be gradually shifting away from solvent-additive processing, with the focus centred on the design of new high performance, stable materials. Additionally, there are a growing number of studies focused on improving device stability through the design of more stable, high-performing NFAs. For example the IDTBR family of molecules have demonstrated considerably better intrinsic photo-stabilities compared to ITIC [125, 124, 314] and a number of solvent-additive-free polymer : NFA systems based on the Y6 family of acceptors have recently reported *PCEs* > 16% [250, 251]. Whilst this is encouraging, the highest efficiency devices (*PCE* > 19%) still rely on DIO processing [32, 33]. The results presented in this chapter therefore highlight the need for more-detailed studies correlating morphology to device performance and stability. This will inform the design of new materials that are both high-performing *and* stable, critical aspects for the commercialisation of OPV.

5.10 Supplementary Data

5.10.1 Absorption of Fresh Pure Material Films

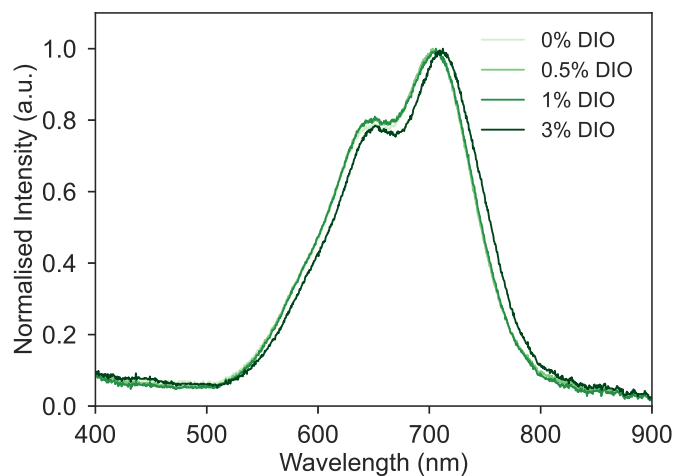


Figure 5.29: Normalised UV-Vis absorption of pure ITIC films processed from chlorobenzene with 0-3 Vol% DIO.

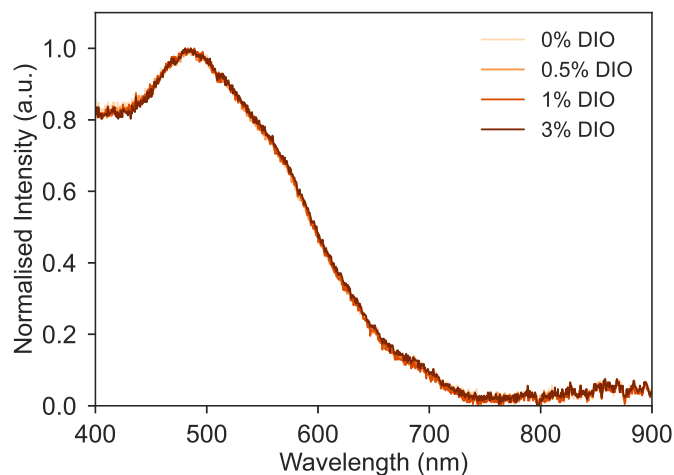


Figure 5.30: Normalised UV-Vis absorption of pure PC₇₁BM films processed from chlorobenzene with 0-3 Vol% DIO.

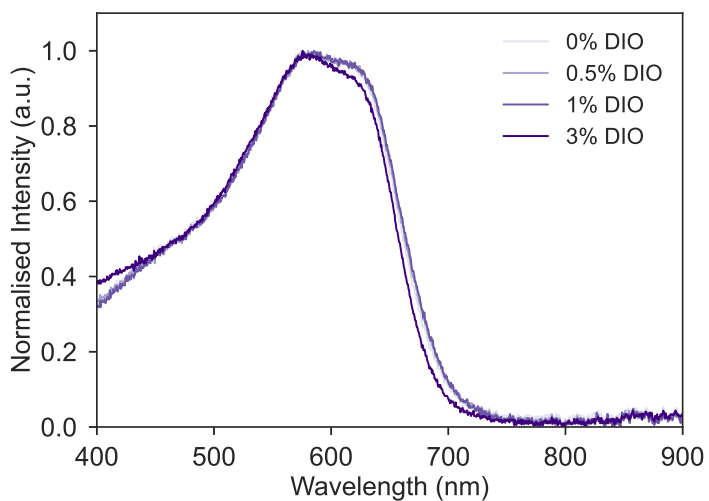


Figure 5.31: Normalised UV-Vis absorption of pure PBDB-T films processed from chlorobenzene with 0-3 Vol% DIO. Note the PBDB-T used here had $M_W=70,532$, $M_N=33,138$ and $PDI=2.1$ (batch M1002 from Ossila).

5.10.2 GIWAXS of Pure Material Films

2D GIWAXS patterns, azimuthally integrated 1D line profiles and a summary of peak positions, d -spacings and crystalline coherence lengths CCL for the most prominent scattering features of pure ITIC, PC₇₁BM and PBDB-T films processed from 0, 0.5, 1 and 3 Vol% are shown below. Q -dependent 1D intensity profiles are integrations in the Q range $0.2 < Q(\text{\AA}^{-1}) < 2.0$ through various χ angles; out-of-plane (in the Q_z direction, $-20 < \chi(^{\circ}) < 20$) and in-plane ($70 < \chi(^{\circ}) < 90$). For χ -dependent 1D intensity profiles are integrations across the full χ range $-90 < \chi(^{\circ}) < 90$ in the Q range $0.25 < Q(\text{\AA}^{-1}) < 0.45$.

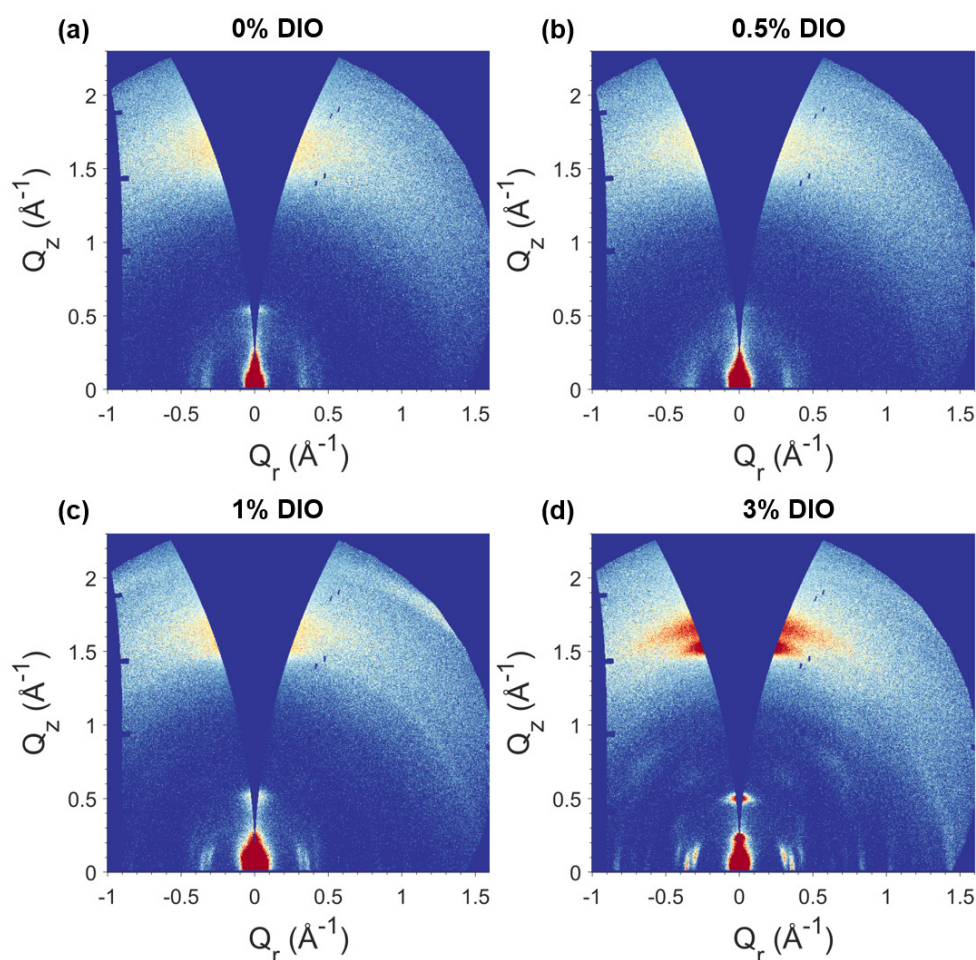


Figure 5.32: 2D GIWAXS patterns of pure ITIC films processed with various concentrations of DIO (0-3 Vol%).

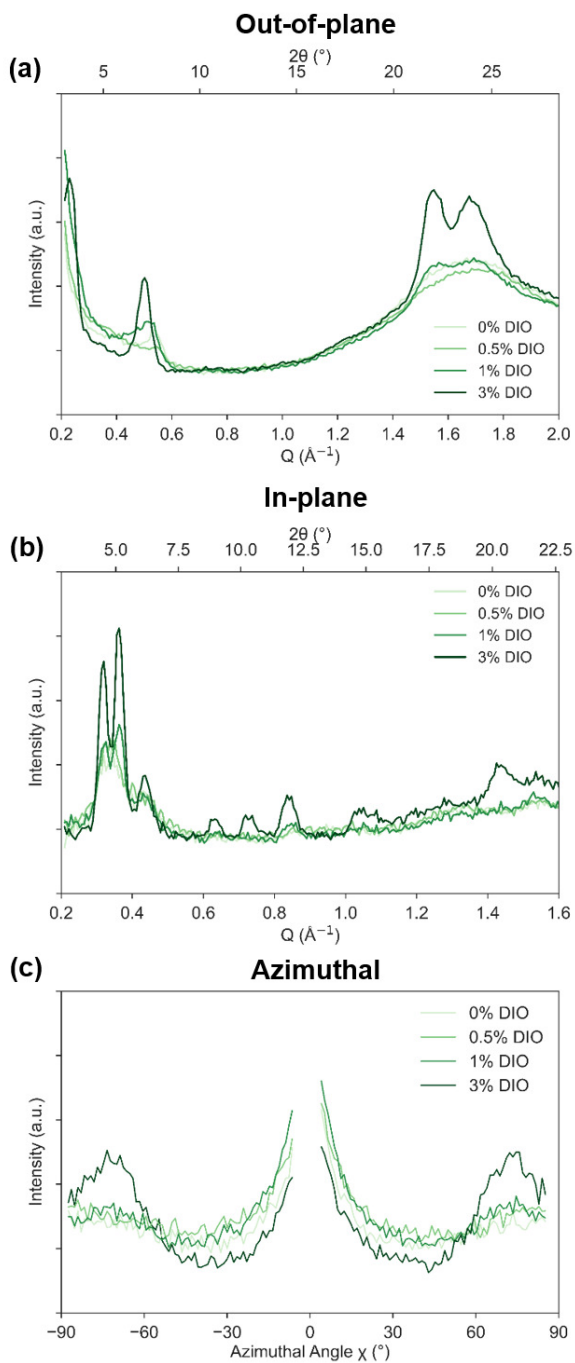


Figure 5.33: 1D GIWAXS intensity profiles of pure ITIC films processed with various concentrations of DIO (0-3 Vol%).

DIO (Vol%)	Direction	Q (\AA^{-1})	d (\AA)	CCL (nm)
0	In-plane	0.339	18.55	7.21
		0.441	14.24	8.87
	Out-of-plane	0.534	11.77	7.90
		1.694	3.70	0.91
0.5	In-plane	0.334	18.82	8.22
		0.426	14.74	6.02
	Out-of-plane	0.541	11.62	8.64
		1.703	3.69	0.93
1	In-plane	0.321	19.58	12.21
		0.364	14.24	19.74
		0.427	14.72	6.95
	Out-of-plane	0.500	12.57	4.70
		1.541	4.08	6.11
		1.693	3.71	1.21
3	In-plane	0.318	19.77	1.98
		0.363	17.31	18.87
		0.434	14.48	12.67
		0.632	9.94	19.16
		0.729	8.62	15.34
		0.841	7.48	6.90
	Out-of-plane	0.228	27.57	10.53
		0.499	12.60	10.41
		1.538	4.09	9.62
		1.693	3.77	1.81

Table 5.11: Table of GIWAXS peak positions, d -spacings and crystalline coherence lengths (CCL) extracted from the out-of-plane and in-plane Q -dependent intensity profiles shown in Figure 5.33 for pure ITIC films processed from chlorobenzene with 0-3 Vol% DIO. CCL values were estimated using Scherrer analysis (Equation 3.78).

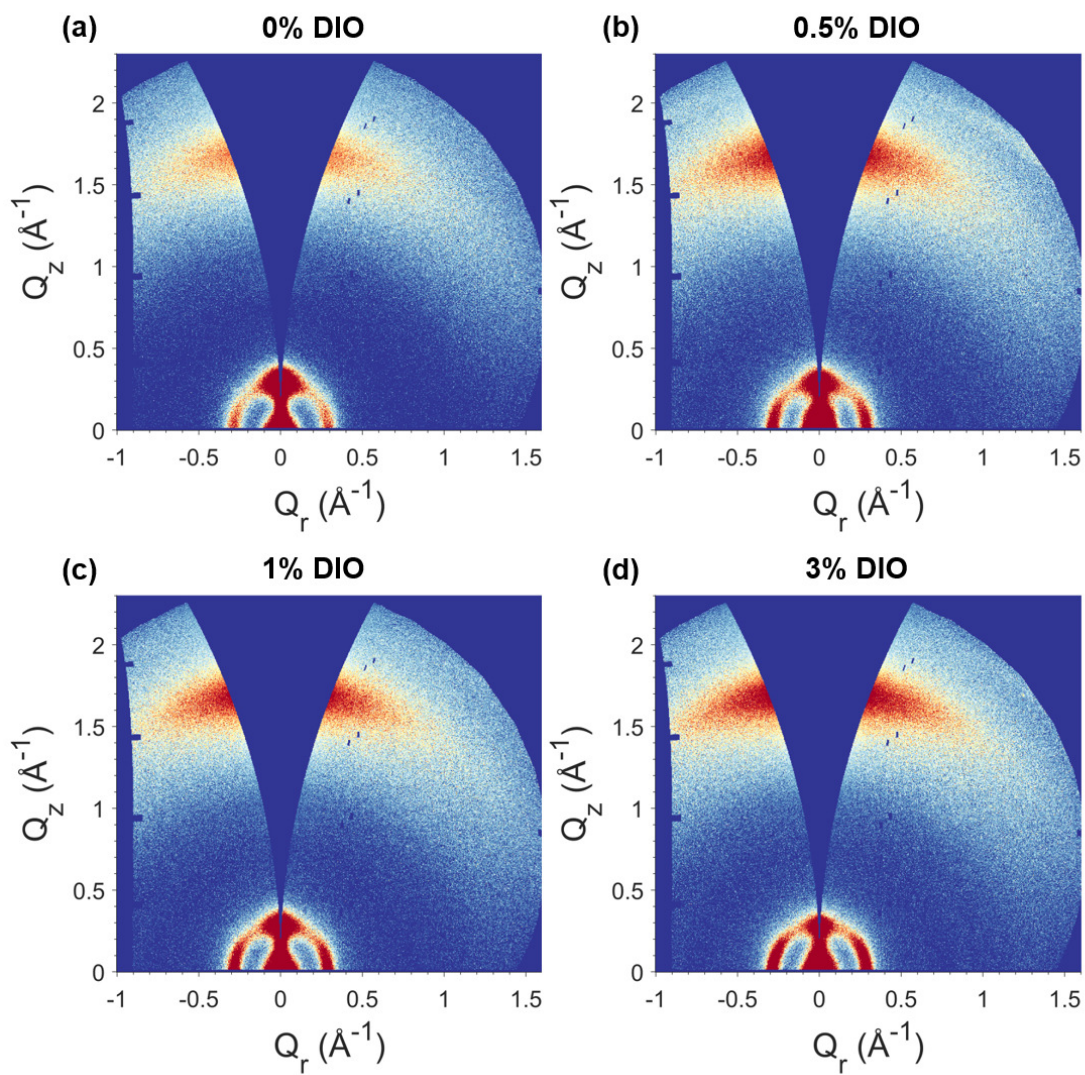


Figure 5.34: 2D GIWAXS patterns of pure PBDB-T films processed with various concentrations of DIO (0-3 Vol%).

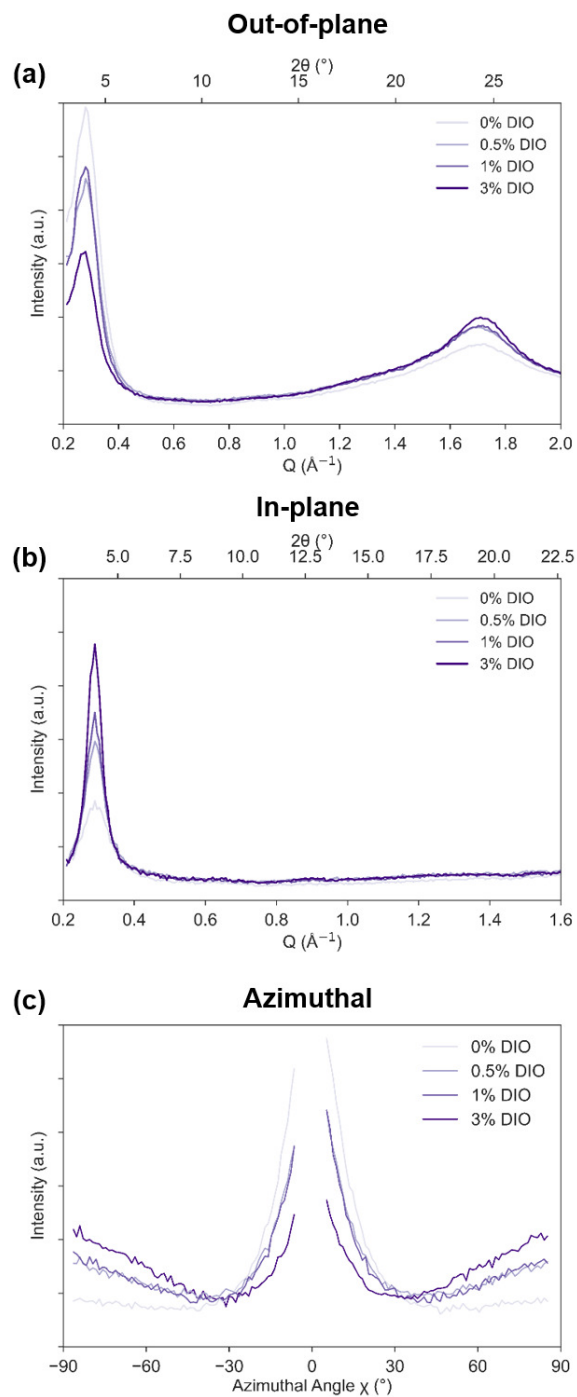


Figure 5.35: 1D GIWAXS intensity profiles of pure PBDB-T films processed with various concentrations of DIO (0-3 Vol%).

DIO (Vol%)	Direction	Q (\AA^{-1})	d (\AA)	CCL (nm)
0	In-plane	0.291	21.6	6.24
	Out-of-plane	0.278	22.6	4.90
		1.693	3.71	1.19
0.5	In-plane	0.289	21.7	8.38
	Out-of-plane	0.275	22.8	4.87
		1.687	3.72	1.36
1	In-plane	0.289	21.8	9.34
	Out-of-plane	0.274	22.9	5.29
		1.696	3.71	1.83
3	In-plane	0.288	21.8	11.13
	Out-of-plane	0.271	23.2	5.22
		1.702	3.69	2.01

Table 5.12: Table of GIWAXS peak positions, d -spacings and crystalline coherence lengths (CCL) extracted from the out-of-plane and in-plane Q -dependent intensity profiles shown in Figure 5.35 for pure PBDB-T films processed from chlorobenzene with 0-3 Vol% DIO. CCL values were estimated using Scherrer analysis (Equation 3.78).

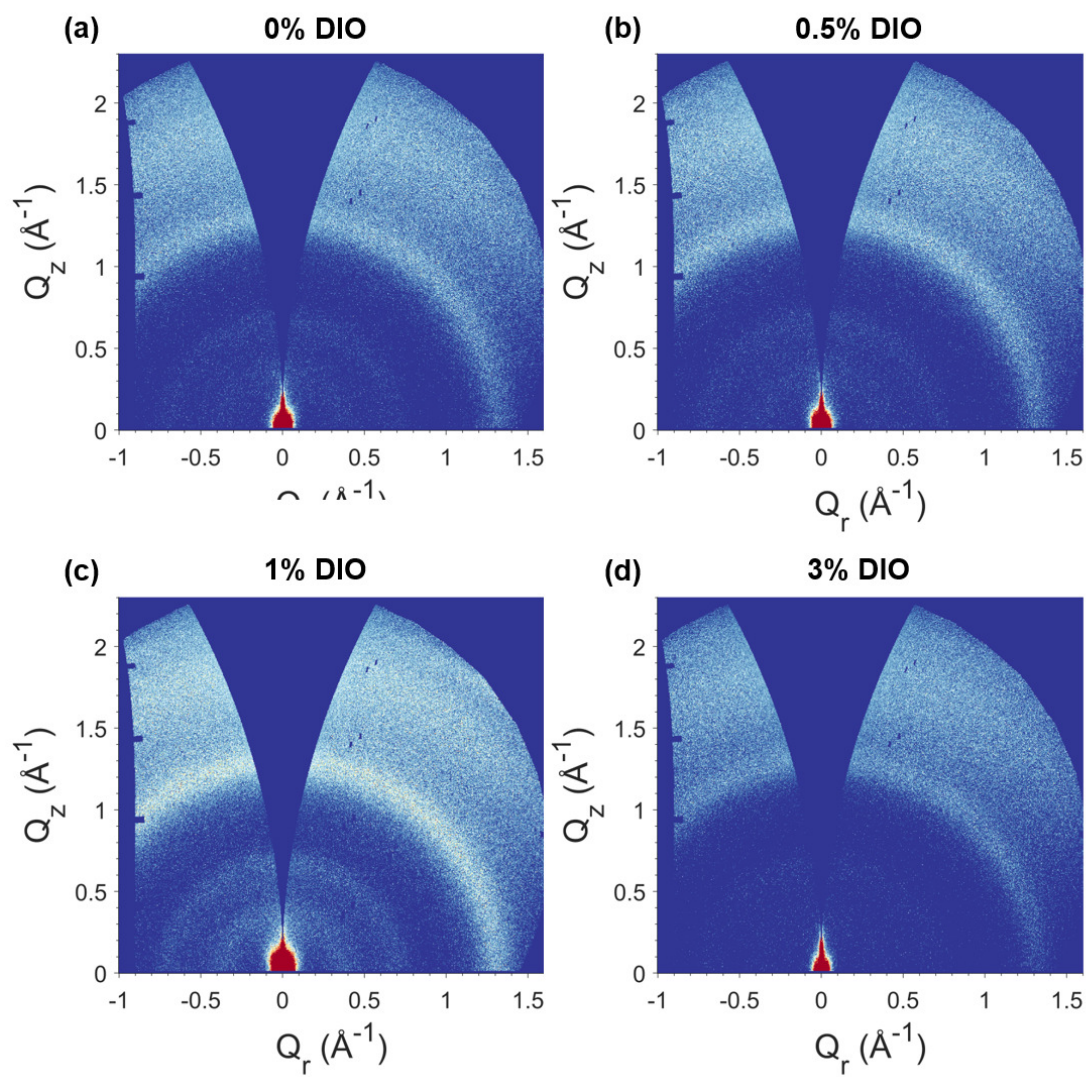


Figure 5.36: 2D GIWAXS patterns of pure PC₇₁BM films processed with various concentrations of DIO (0-3 Vol%).

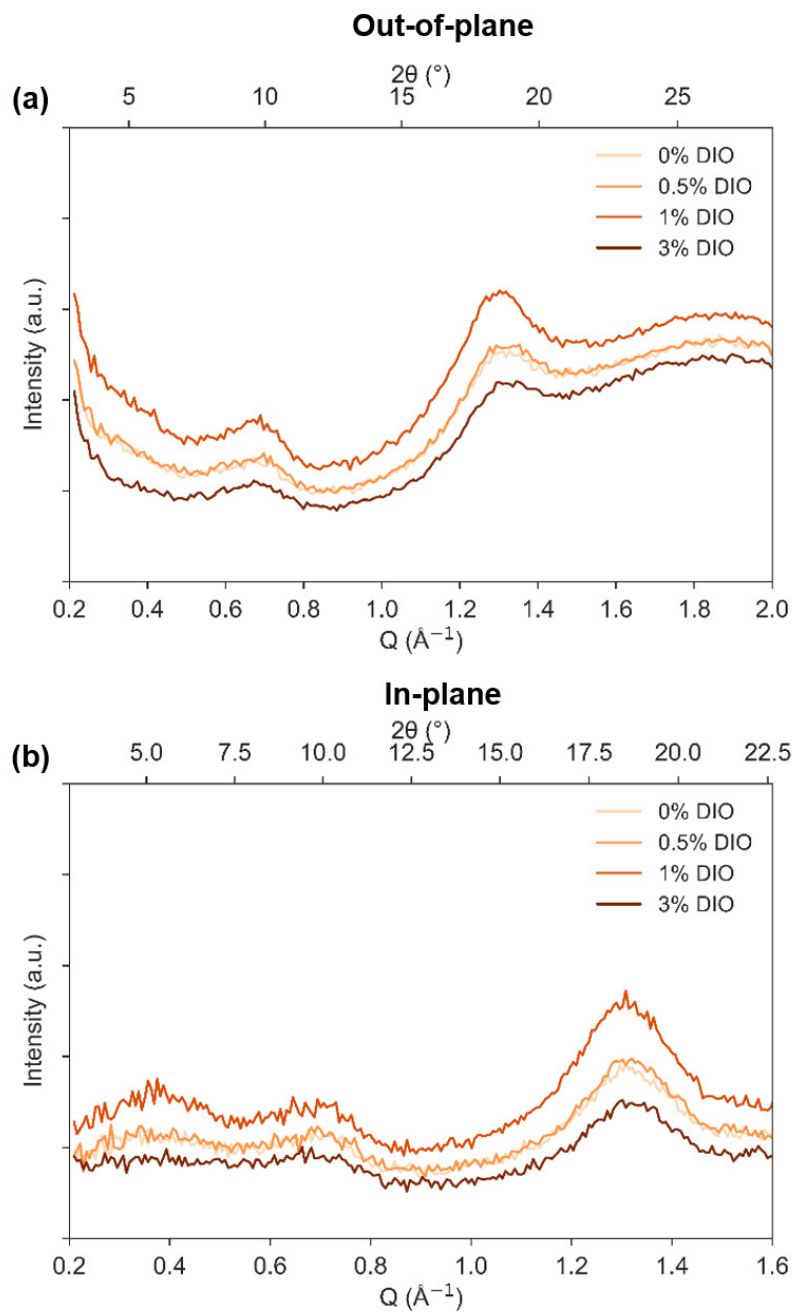


Figure 5.37: 1D GIWAXS intensity profiles of pure PC₇₁BM films processed with various concentrations of DIO (0-3 Vol%).

DIO (Vol%)	Direction	Q (\AA^{-1})	d (\AA)	CCL (nm)
0	In-plane	0.381	16.50	1.94
		0.688	9.14	3.71
		1.319	4.76	2.30
	Out-of-plane	0.669	9.39	3.11
		1.295	4.85	2.81
		1.871	3.36	0.46
0.5	In-plane	0.384	16.38	1.93
		0.691	9.10	3.65
		1.321	4.75	2.30
	Out-of-plane	0.645	9.74	2.08
		1.299	4.84	2.81
		1.866	3.37	0.48
1	In-plane	0.376	16.71	2.26
		0.681	9.22	3.55
		1.311	4.79	2.25
	Out-of-plane	0.667	9.42	3.35
		1.296	4.85	2.78
		1.871	3.36	0.42
3	In-plane	0.371	16.92	1.28
		0.691	9.09	3.71
		1.323	4.75	2.32
	Out-of-plane	0.651	9.65	2.55
		1.301	4.83	2.91
		1.861	3.38	0.51

Table 5.13: Table of GIWAXS peak positions, d -spacings and crystalline coherence lengths (CCL) extracted from the out-of-plane and in-plane Q -dependent intensity profiles shown in Figure 5.37 for pure PC_{71}BM films processed from chlorobenzene with 0-3 Vol% DIO. CCL values were estimated using Scherrer analysis (Equation 3.78).

5.10.3 AFM of Fresh Pure Material Films

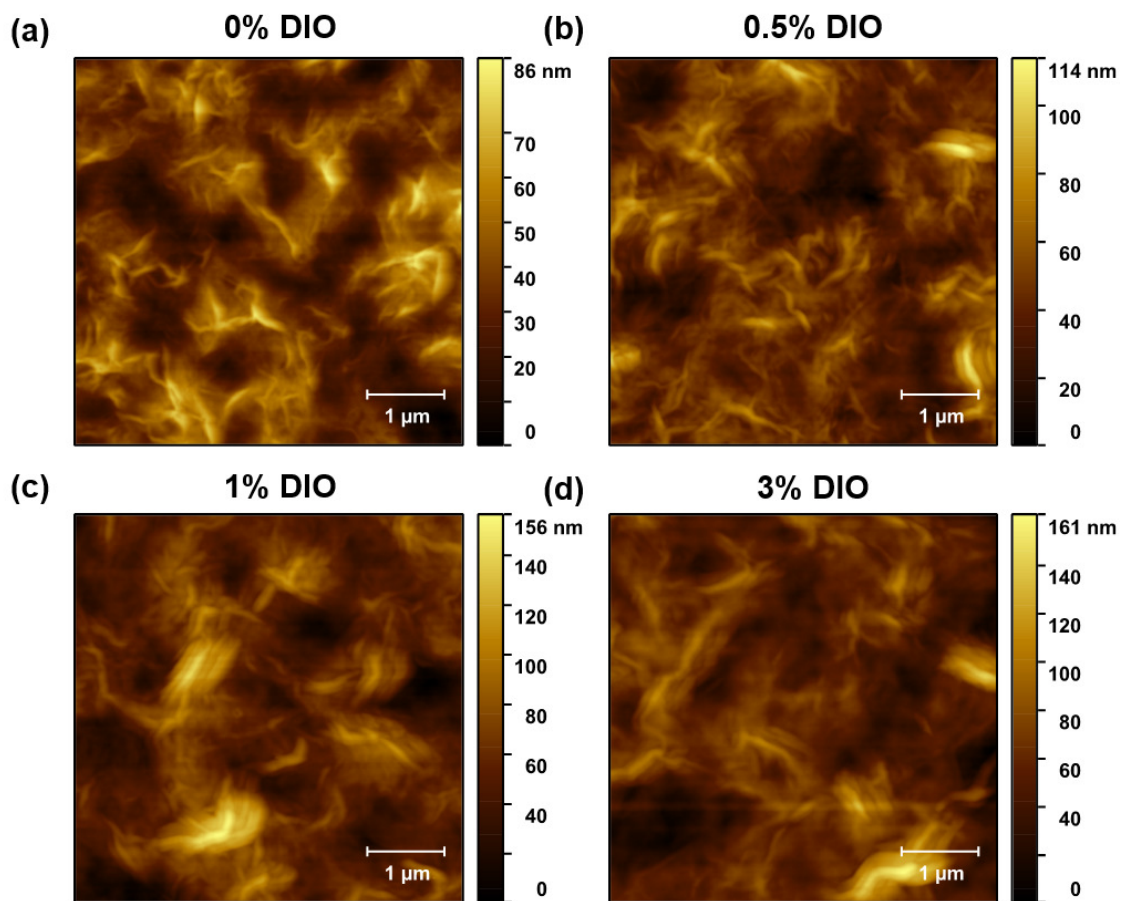


Figure 5.38: AFM height topography images of pure ITIC thin films processed with (a) 0, (b) 0.5, (c) 1 and (d) 3 Vol% DIO. The scale bar is $1\mu\text{m}$.

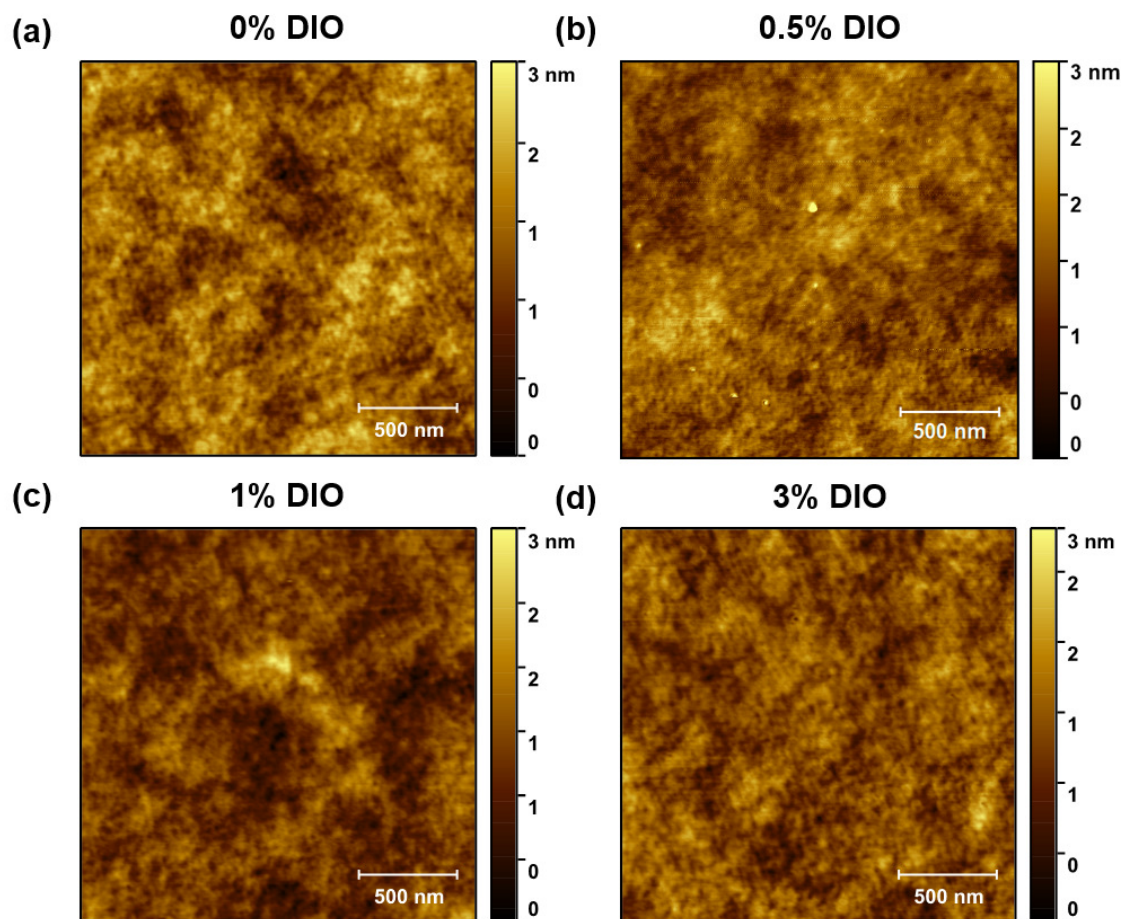


Figure 5.39: AFM height topography images of pure PC₇₁BM thin films processed with (a) 0, (b) 0.5, (c) 1 and (d) 3 Vol% DIO. The scale bar is 500nm.

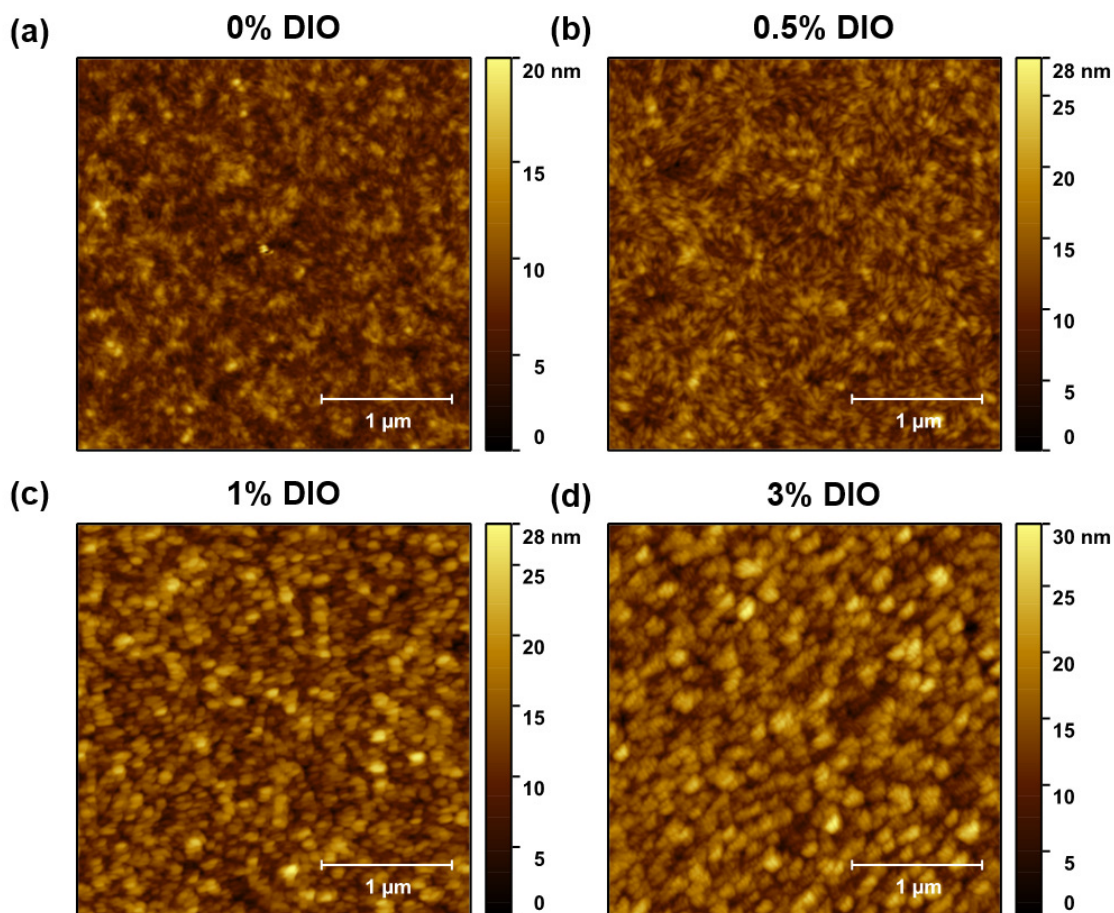


Figure 5.40: AFM height topography images of PBDB-T films processed with (a) 0, (b) 0.5, (c) 1 and (d) 3 Vol% DIO. The scale bar is $1\mu m$.

DIO Vol%	σ_{RMS} (nm)		
	ITIC	PCBM	PBDB-T
0	13.2	0.32	2.04
0.5	14.7	0.34	2.80
1	21.7	0.35	3.50
3	20.7	0.31	3.84

Table 5.14: Summary of RMS roughness (σ_{RMS}) values extracted from the AFM data shown in Figure 5.38, Figure 5.39 and Figure 5.40 for pure ITIC, PC₇₁BM and PBDB-T thin films processed with various concentrations of DIO.

5.10.4 Additional SANS Data

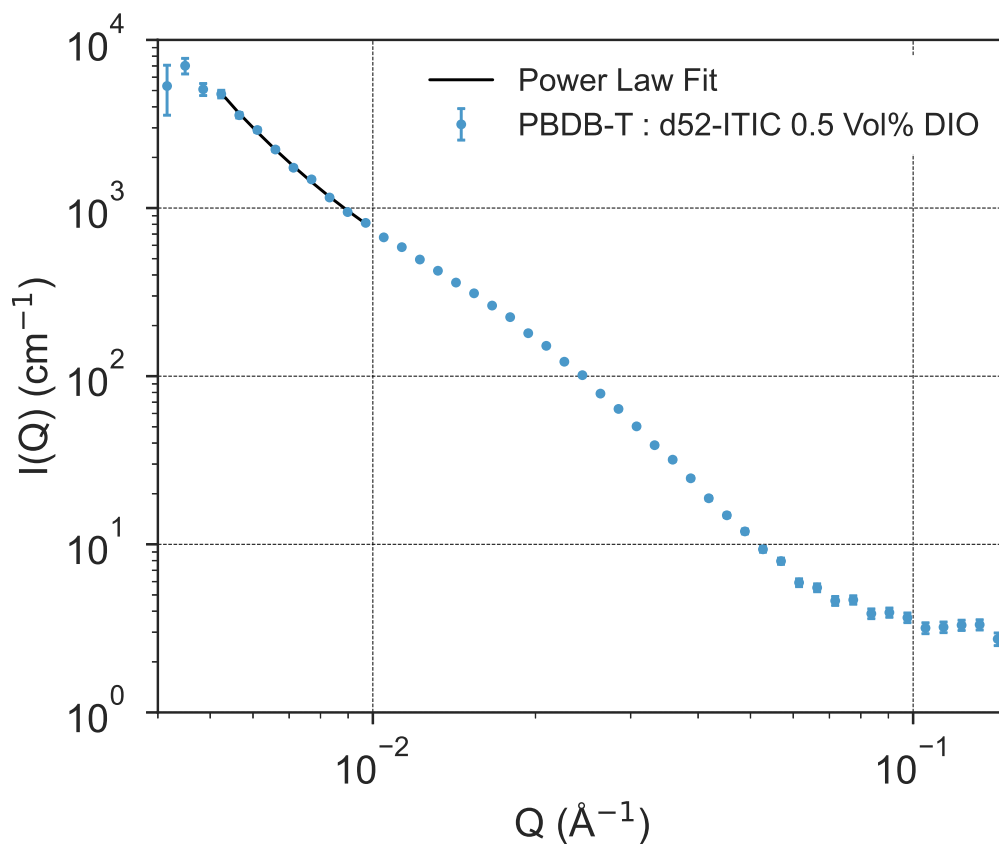


Figure 5.41: SANS power law fitting in the Q range $0.005 < Q \text{ \AA}^{-1} < 0.01$ for PBDB-T : d52-ITIC films processed with 0.5 Vol% DIO. The fitting parameters are: scale = $(2.18 \pm 1.73) \times 10^{-4}$, $B = 259 \pm 58 \text{ cm}^{-1}$ and $\alpha = 3.14 \pm 0.15$ with $\chi^2/N_{pts} = 1.51$.

5.10.5 Contact Angle Measurements

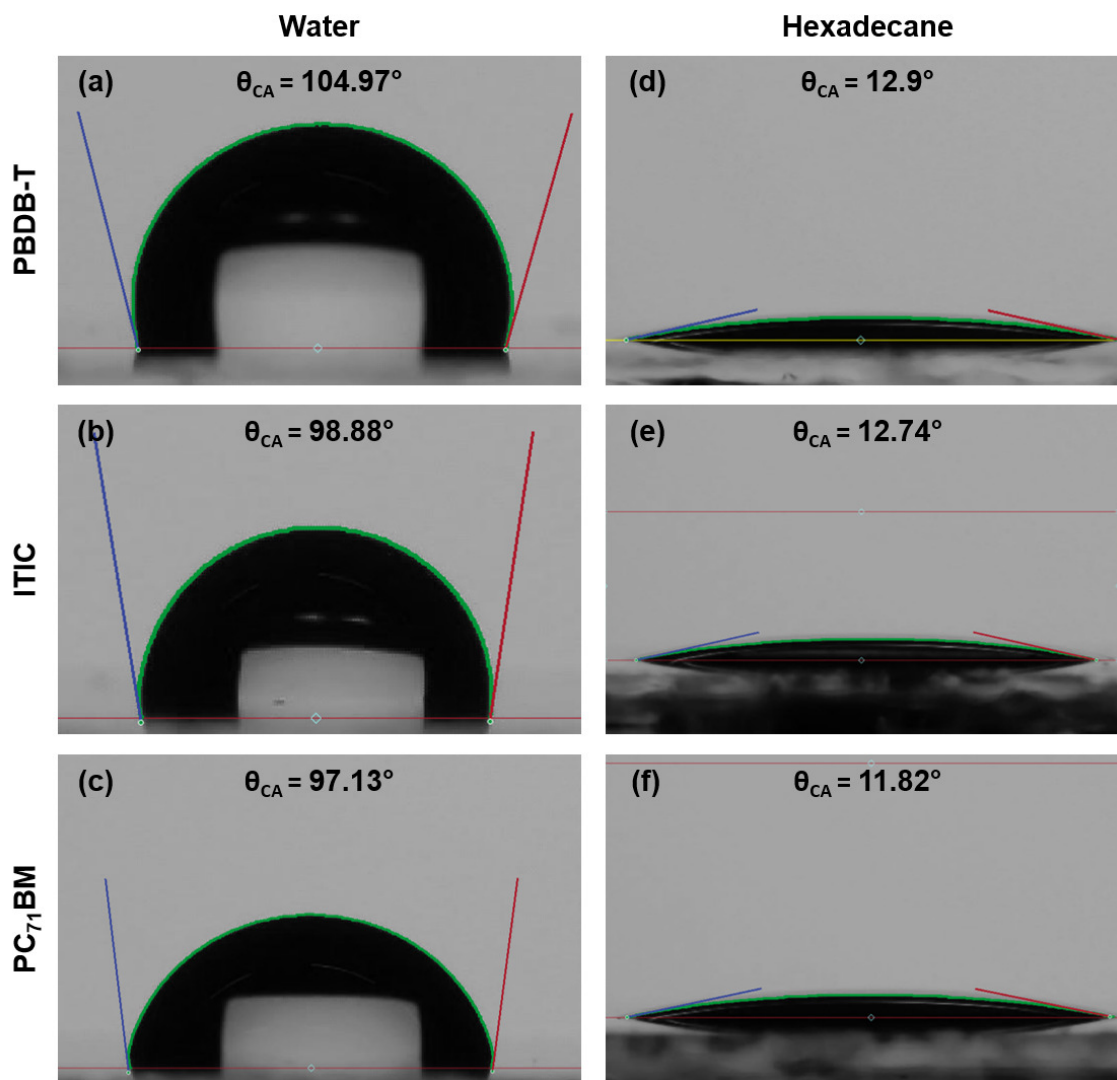


Figure 5.42: Measured contact angles of a water droplet (a-c) and a hexadecane droplet (d-f) on the surface of pure PBDB-T, ITIC and PC₇₁BM thin films processed from various volume concentrations of DIO (0-3 Vol%).

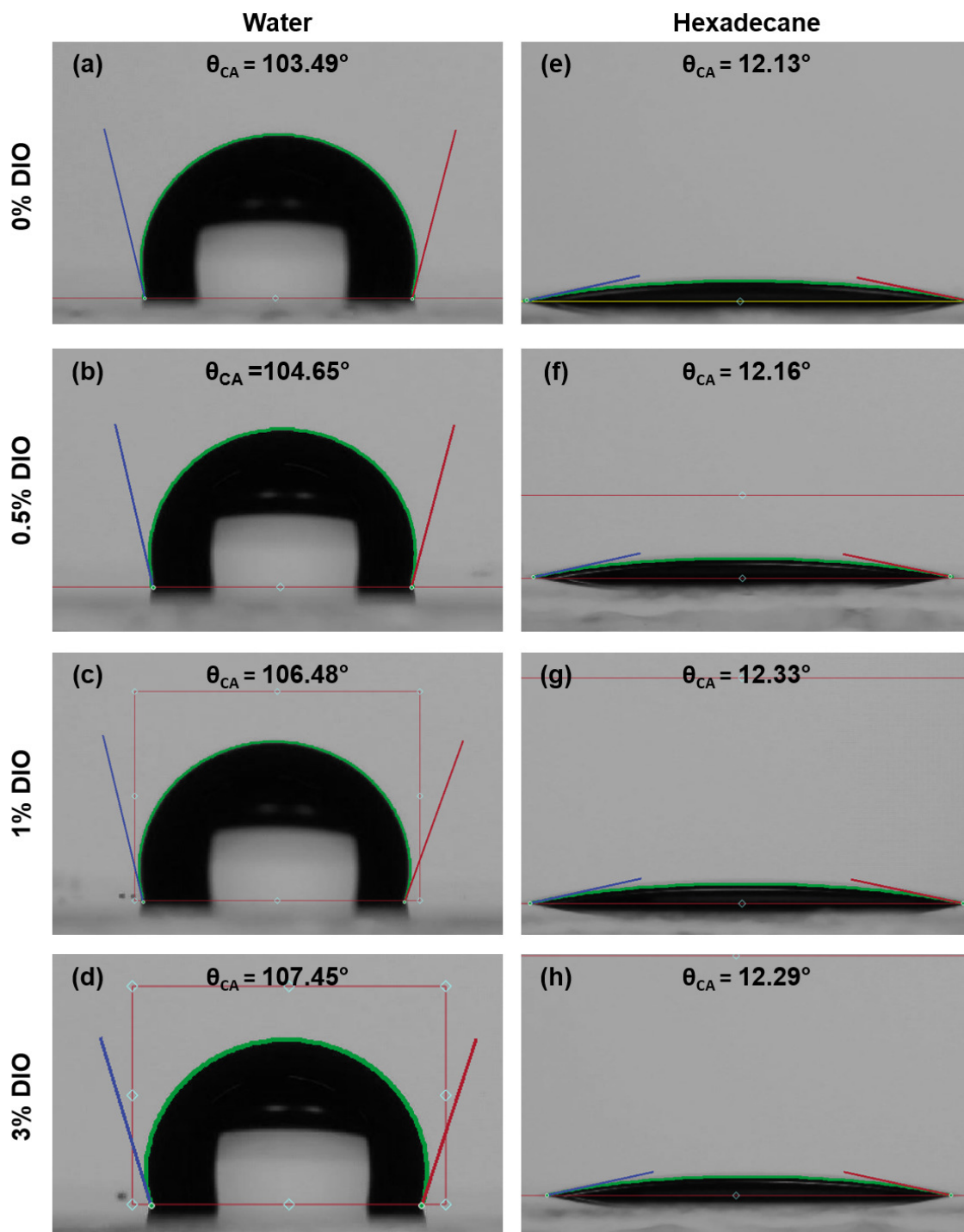


Figure 5.43: Measured contact angles of a water droplet (a-d) and a hexadecane droplet (e-h) on the surface of PBDB-T : ITIC blend thin films processed from various volume concentrations of DIO (0-3 Vol%).

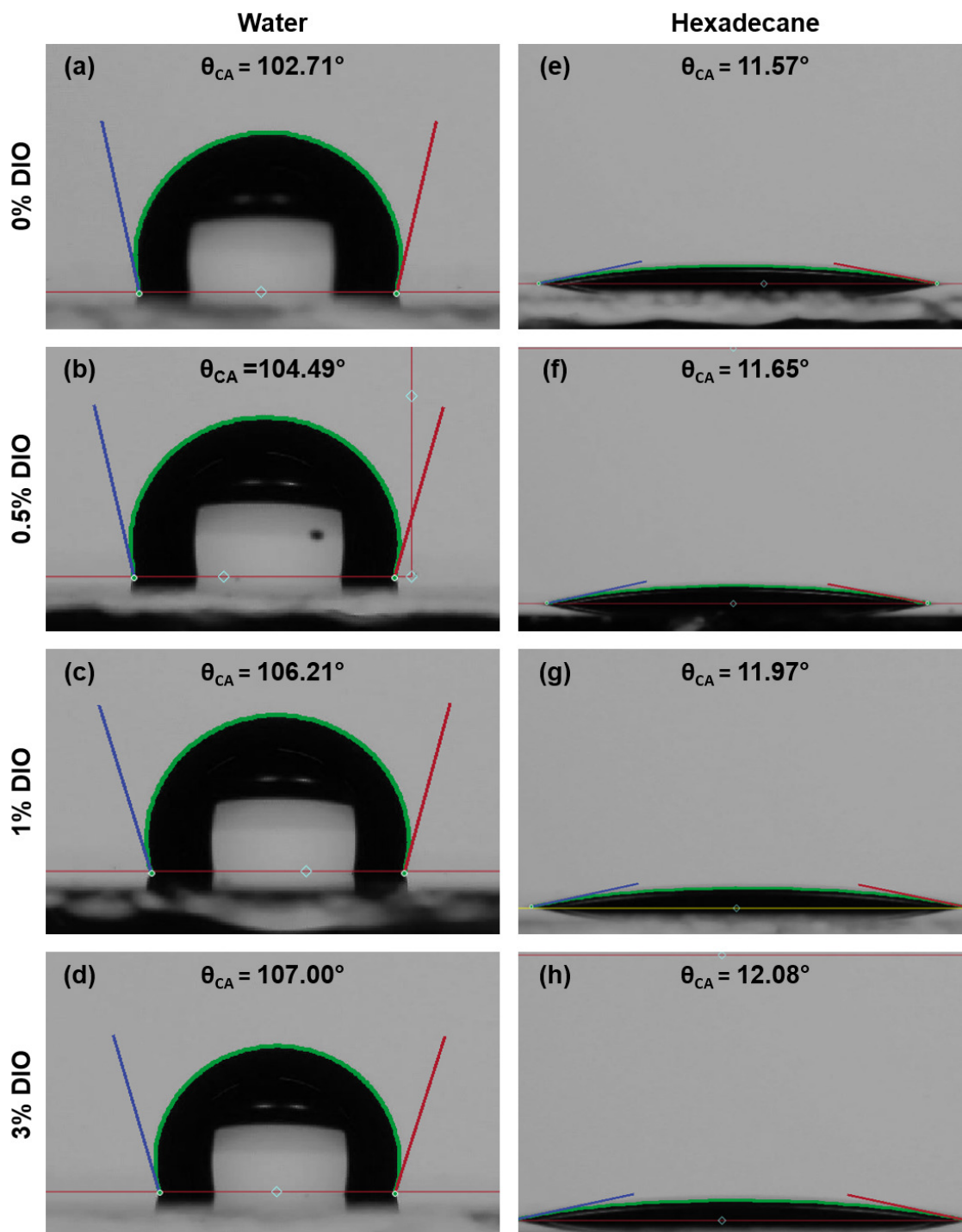


Figure 5.44: Measured contact angles of a water droplet (a-d) and a hexadecane droplet (e-h) on the surface of PBDB-T : PC₇₁BM blend thin films processed from various volume concentrations of DIO (0-3 Vol%).

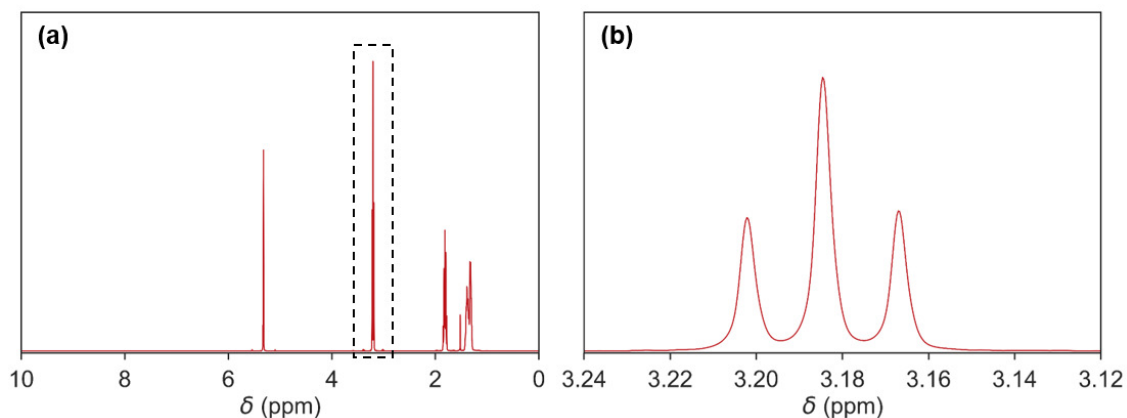
5.10.6 ^1H NMR of Reference Materials

Figure 5.45: (a) ^1H NMR of dilute DIO in CDCl_3 where the position of the most prominent DIO peak is enclosed in the dotted box. (b) The DIO ^1H NMR peak shown in (a) used for detecting residual amounts in PBDB-T : ITIC and PBDB-T : PC_{71}BM blend films.

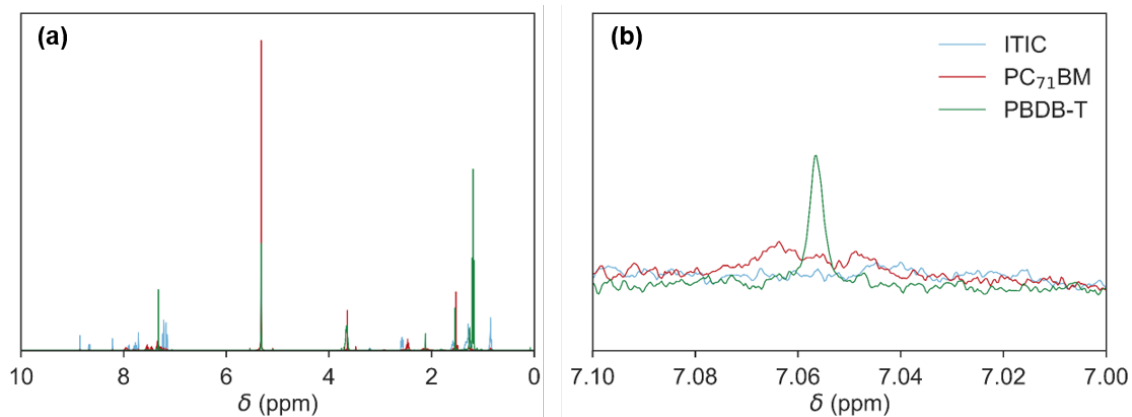


Figure 5.46: (a) ^1H NMR of dissolved reference films of ITIC, PC_{71}BM and PBDB-T in CDCl_3 . (b) The PBDB-T peak centred at ~ 7.055 ppm used for comparing relative amounts of DIO in blend thin films.

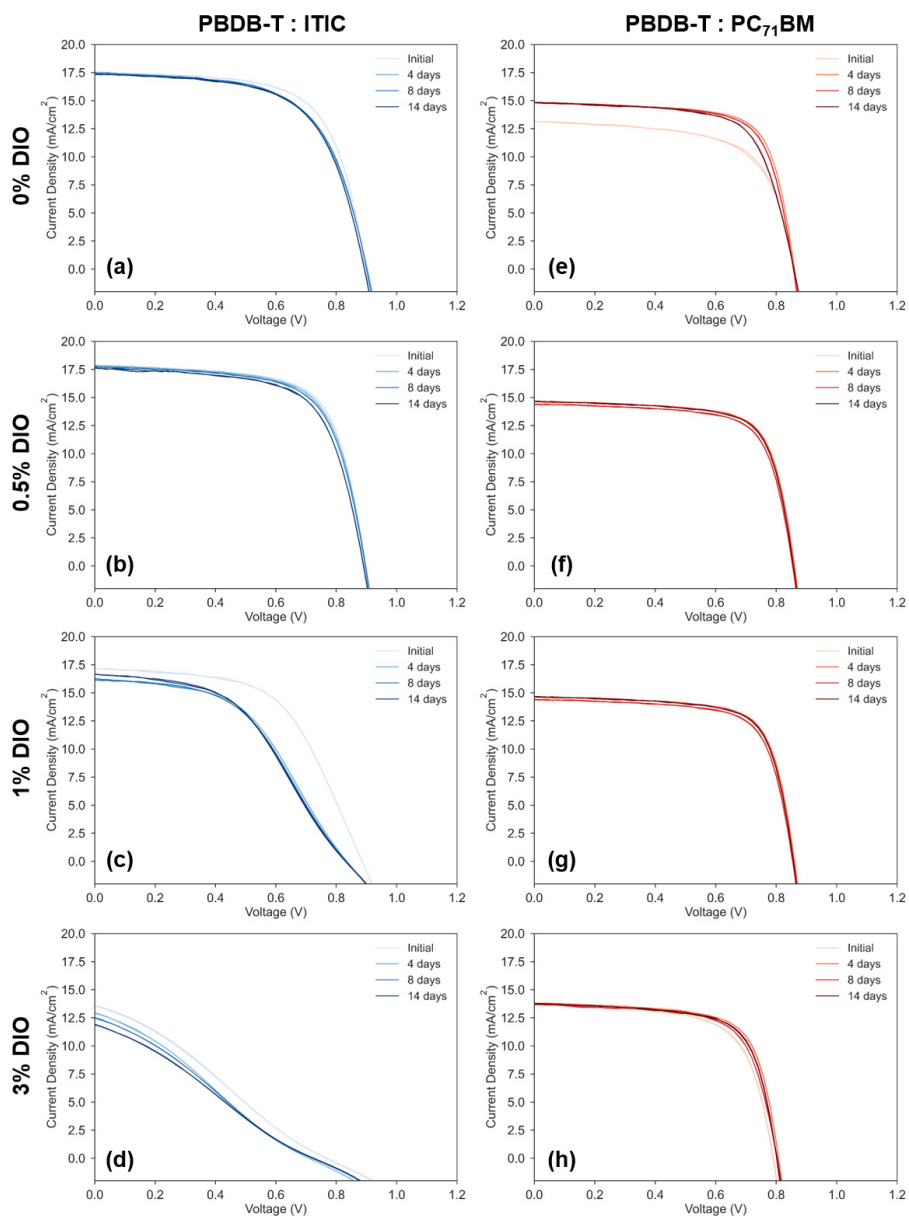
5.10.7 The Evolution of S-shaped J - V Curves During Ageing

Figure 5.47: J - V characteristics of (a-d) PBDB-T : ITIC and PBDB-T : PC₇₁BM devices processed from chlorobenzene with 0-3 Vol% DIO, measured after ageing in the dark in an inert atmosphere for 0, 4, 8 and 14 days. Note the appearance of S-shaped J - V curves for PBDB-T : ITIC devices processed from 1 and 3 Vol% DIO.

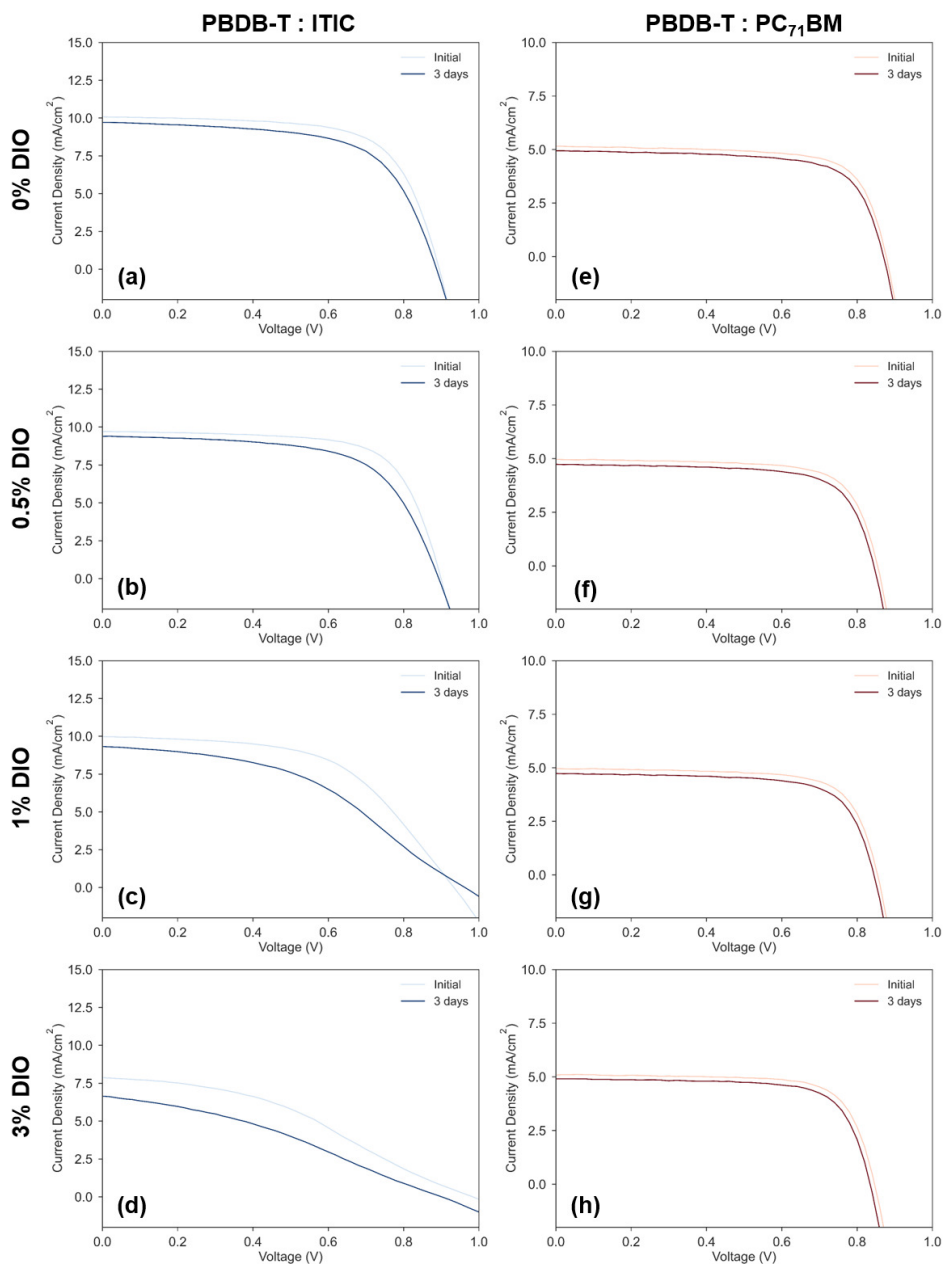


Figure 5.48: $J-V$ characteristics of (a-d) PBDB-T : ITIC and PBDB-T : PC₇₁BM films processed from chlorobenzene with 0-3 Vol% DIO, measured after ageing during 1 Sun irradiation in an inert atmosphere for 0 and 3 days. Note the appearance of S-shaped $J-V$ curves for PBDB-T : ITIC devices processed from 1 and 3 Vol% DIO.

The Effect of Chemical Design on the Morphology, Performance and Stability of Non-fullerene Acceptor Organic Photovoltaics

6.1 Foreword

The advent of high-efficiency NFAs has resulted in an explosion of new molecular structures and synthesising strategies incorporating a diverse range of chemical moieties. This has afforded a greater degree of molecular tunability, providing substantial control of numerous material properties such as solubility, optical properties, thermal properties and more. Despite this, there is a lack of understanding concerning the more fundamental relationships between chemical structure, film nanomorphology, device performance and stability. In this chapter, I explore these relationships for three IDT based NFA systems (EH-IDTBR, O-IDTBR and O-IDTBCN) in blends with a high-performing conjugated polymer (PTB7-Th). The thermal properties of each NFA are first investigated using temperature-dependent UV-Vis spectroscopy and AFM measurements. This is followed by a detailed characterisation of the three-dimensional nanomorphology of PTB7-Th : NFA and PTB7-Th : PC₇₁BM blend films using a broad range of structural characterisation techniques (GIWAXS, SANS, AFM and NR). Importantly, deuterated analogues of the three NFAs were synthesised for NR and SANS measurements to improve the neutron SLD contrast in the blend with PTB7-Th. Structural characterisation is then correlated with the optoelectronic functionality and stability of each system to explore the influence of different NFA side-chain and terminal chemical groups. The work in this chapter will aid with the design of more stable, high-performing materials, critical to the commercialisation of OPVs.

6.2 Author Contributions

In this chapter, the bulk of characterisation measurements, data interpretation and analysis was performed by myself including UV-Vis, AFM, GIWAXS, NR analysis and SANS analysis. Deuterated NFAs used for NR and SANS were synthesised by Matthew Bidwell under the supervision of Iain McCulloch. Emma L. K. Spooner fabricated, tested and processed all devices and related data. SANS and NR measurements were performed by Robert Dalglish and Philip Gutfreund respectively via remote beamtimes. The project was supervised by Andrew J. Parnell and Richard A. L. Jones.

6.3 Introduction

For an OPV device to be considered *optimised* it is important to consider both the initial performance *and* the long-term operational stability of devices. Many optimisation protocols only focus on the prior of these objectives and the potentially detrimental impact to device stability is often ignored. The importance of this concept was demonstrated previously in Chapter 5 where although a small boost in initial device *PCE* could be achieved through solvent additive processing, it typically led to accelerated device degradation in certain conditions. A potentially more successful optimisation method is to design materials that are both high-performing and intrinsically stable. NFAs based on an A-D-A architecture with an IDT core are among some of the most successful OPVs in terms of both efficiency and long-term operational stability [97, 323, 128, 114]. In this study, the film nanomorphology, device performance and stability of a series of IDT based A-D-A architecture NFAs (EH-IDTBR, O-IDTBR and O-IDTBCN, Figure 3.3) was investigated to probe the impact of different side-chain (linear or branched), and terminal (rhodanine or dicyanovinyl) chemical groups.

The IDT-based NFAs investigated in this study are relatively new molecules that are still in the early stages of development with structure-performance-stability relationships emerging. Initial studies have demonstrated both promising device performance and good operational stability that is far superior to analogous fullerene-based systems. For example, O-IDTBR and EH-IDTBR were first synthesised in 2016 and tested in P3HT OPV blend systems demonstrating superior oxidative stability and significantly reduced burn-in losses compared to P3HT : PC₇₁BM systems [97, 98]. Since then, their superior robustness has been demonstrated repeatedly in OPV systems with a wide variety of conjugated polymers such as PffBT4T-20D [324, 124, 325], FTAZ [114], PBDB-T [128], PBDB-T-2F [128] and PTB7-Th [326, 325, 124].

IDT-based NFAs have also demonstrated impressive intrinsic photostabilities, outperforming fullerene-based acceptors and many other NFAs such as ITIC and its derivatives [314, 124]. This increased photostability has been attributed to the planarity of the conjugated backbone and enhanced crystallinity [125]. However, it is suspected that the BT terminal group is a potential degradation route due to its intrinsic instability [125]. O-IDTBCN is one of the newest additions to the IDT NFA family. It was first synthesised in 2019 by substituting the terminal rhodanine group of O-IDTBR with dicyanovinyl units [139]. In OPV blend systems with PTB7-Th, impressive fill factors and short-circuit current densities as high as 73% and $19.8\text{mA}/\text{cm}^{-1}$ respectively were achieved [139]. However, the deeper lying LUMO level compared to O-IDTBR and EH-IDTBR resulted in a lower open-circuit voltage (0.72V). Interestingly, the authors tentatively suggested device performance enhancements were in part due to a more finely intermixed morphology, indicated

by AFM measurements and more efficient PL quenching [139].

In this work, initial studies focus on characterising the thermal properties and crystallisation behaviour of the three IDT-based NFAs (EH-IDTBR, O-IDTBR and O-IDTBCN). This is followed by a detailed characterisation of the film nanostructure and optoelectronic properties of four PTB7-Th based OPV systems: PTB7-Th : PC₇₁BM, PTB7-Th : EH-IDTBR, PTB7-Th : O-IDTBR and PTB7-Th : O-IDTBCN. Using a combination of structural characterisation techniques (GIWAXS, AFM, SANS, NR), the full three-dimensional morphology is characterised both laterally and perpendicular to the substrate, covering a broad range of characteristic length scales from molecular-scale packing to nanoscale phase-separation. Importantly, deuterium labelled analogues of each NFA (d-EH-IDTBR, d-O-IDTBR and d-O-IDTBCN, Figure 3.4) were synthesised to increase the neutron SLD contrast in the blend with PTB7-Th (see Subsection 3.2.3). Following on from this, stability of each system is explored in inert conditions. Taken together, the study aims to develop understanding of the relationships between chemical structure, film nanomorphology, and OPV device stability and operation.

6.4 Experimental

Measurements in this chapter were performed on both pure material films and blend films. Film processing conditions for pure and blend samples are provided in Table 6.1 and Table 6.2 respectively. All solutions were prepared in chlorobenzene and left stirring overnight in a nitrogen-filled glovebox at 60°C. Films were spun statically in ambient conditions and annealed in the glovebox. In Section 6.5 various annealing temperatures between 40-200°C are used for temperature-dependent studies. In Section 6.6 and Section 6.7 all pure and blend films were annealed at 80°C. All thermal annealing was performed for 10 minutes in a nitrogen-filled glovebox. Device fabrication followed the same protocols reported elsewhere [326].

Blend	Solid Concentration (mg/mL)	Spin Speed (rpm)
PC ₇₁ BM	15	1000
EH-IDTBR	15	2000
O-IDTBR	15	2000
O-IDTBCN	15	2000
PTB7-Th	10	2000

Table 6.1: Table of film processing conditions for pure films.

Blend	Donor : Acceptor Mass Ratio	Solid Concentration (mg/mL)	Spin Speed (rpm)
PTB7-Th : PC ₇₁ BM	1:1.5	24	1250
PTB7-Th : EH-IDTBR	1:2.5	24	2000
PTB7-Th : O-IDTBR	1:2.5	24	2000
PTB7-Th : O-IDTBCN	1:2.5	24	2000

Table 6.2: Table of film processing conditions for blend films.

6.5 Characterising the Thermal Behaviour of Non-fullerene Acceptors

In this section, the thermal properties of pure EH-IDTBR, O-IDTBR and O-IDTBCN films are characterised using temperature-dependent UV-Vis spectroscopy. These changes are then linked to structural changes of the thin film nanostructure using AFM measurements.

6.5.1 Temperature-dependent UV-Vis

Temperature-dependent UV-Vis spectroscopy was used to measure changes in absorption resulting from the molecular rearrangement of NFAs following protocols reported elsewhere [327]. The typical absorption spectrum shift that occurs for many conjugated systems due to enhanced molecular order and aggregation [97] is tracked as a function of annealing temperature. Previous studies have shown that at annealing temperatures above the glass transition temperature (T_g), there is an easily discernible change in the absorption spectrum [327, 128]. To quantify this change, a deviation metric (DM_T) is defined as the sum of the squared deviation in the absorption spectrum of the as-cast ($I_{RT}(\lambda)$) and annealed samples ($I_T(\lambda)$) [327]:

$$DM_T = \sum_{\lambda_{min}}^{\lambda_{max}} [I_{RT}(\lambda) - I_T(\lambda)]^2 \quad (6.1)$$

Using Equation 6.1, DM_T was calculated as a function of annealing temperature for each NFA (Figure 6.1d-f). All films were spin-coated and annealed in a nitrogen-filled glovebox to eliminate degradation effects, particularly at elevated temperatures. UV-Vis measurements were performed ex-situ by thermally cycling NFA films at increased annealing temperatures in a temperature range of 40 - 200°C at 5°C intervals. After each thermal annealing step, films were left in the glovebox for 10 minutes to cool back to room temperature.

The absorption profile of as-cast films of EH-IDTBR, O-IDTBR and O-IDTBCN are all similar in shape but with absorption maxima centred at 671nm, 688nm and 722nm respectively in agreement with previous studies [97, 139] Figure 6.1a-c). As annealing temperature increases, each NFA experiences an overall bathochromic shift which has previously been linked to enhanced molecular order and the formation of J-aggregates [272, 110]. For EH-IDTBR, there is first a gradual hypochromic shift of ~ 10 nm as annealing temperature increases from 40°C to 160°C . At $T = 180^\circ\text{C}$, a competing bathochromic shift begins to dominate, broadening the UV-Vis spectra. At $T = 200^\circ\text{C}$, the UV-Vis spectrum is very noisy and the total bathochromic shift of the maxima previously positioned at 671nm for the as-cast sample is ~ 36 nm. The increased noise in the absorption profile at 200°C is attributed to an increased level of diffuse scattering due to the formation of large crystallites on the film surface (Figure 6.1g). Calculating DM_T as a function of temperature reveals a distinct thermal transition at $\sim 130^\circ\text{C}$ and a broader transition in the temperature range $\sim 150 - 200^\circ\text{C}$ (Figure 6.1d).

In comparison to EH-IDTBR, the bathochromic shifts of the linear chain analogues (O-IDTBR and O-IDTBCN) is much more distinct and the magnitude of the change in DM_T is considerably larger indicating a greater degree of molecular mobility and a greater tendency to crystallise (Figure 6.1e,f). The spectral shift is so significant that it is observed visually as a change in film colour from blue to green as annealing temperature increases (Figure 6.1g). For O-IDTBR, a distinct thermal transition is observed at $\sim 125^\circ\text{C}$ originating from a large bathochromic shift of ~ 40 nm (Figure 6.1b,e). At $T > 125^\circ\text{C}$, the absorption profile continues to shift gradually until a total bathochromic shift of ~ 44 nm is achieved (Figure 6.1b). For O-IDTBCN, there are two clear transitions at $\sim 80^\circ\text{C}$ and $\sim 150^\circ\text{C}$ (Figure 6.1c,f). These originate from separate bathochromic shifts in the absorption profiles of ~ 50 nm and ~ 36 nm respectively (Figure 6.1c).

Previous studies investigating the thermal properties of conjugated materials using temperature-dependent UV-Vis spectroscopy have attributed sharp transitions in the DM_T vs temperature plots to the glass transition or cold crystallisation onset of the material [327, 128]. Ghasemi et al. suggested that exothermal cold crystallisation can obscure the weaker glass transition signal in DSC measurements and that the two thermal transitions will occur at similar temperatures [128]. For EH-IDTBR, the authors identified an exothermic peak at 113°C in the DSC thermogram and a transition in their DM_T vs temperature plot at 116°C as T_g or T_c . Despite this, there is a noticeable step-like feature at $\sim 80^\circ\text{C}$ in their DSC thermogram, characteristic of a glass transition. In other studies, DSC measurements have revealed a crystallisation temperature T_C at 115°C for O-IDTBR whilst no crystallisation was observed for EH-IDTBR [97]. There is therefore a lack of clarity concerning the identification of the thermal transitions of IDT-based NFA materials in the literature, particularly from DSC and temperature-dependent UV-Vis spectroscopy.

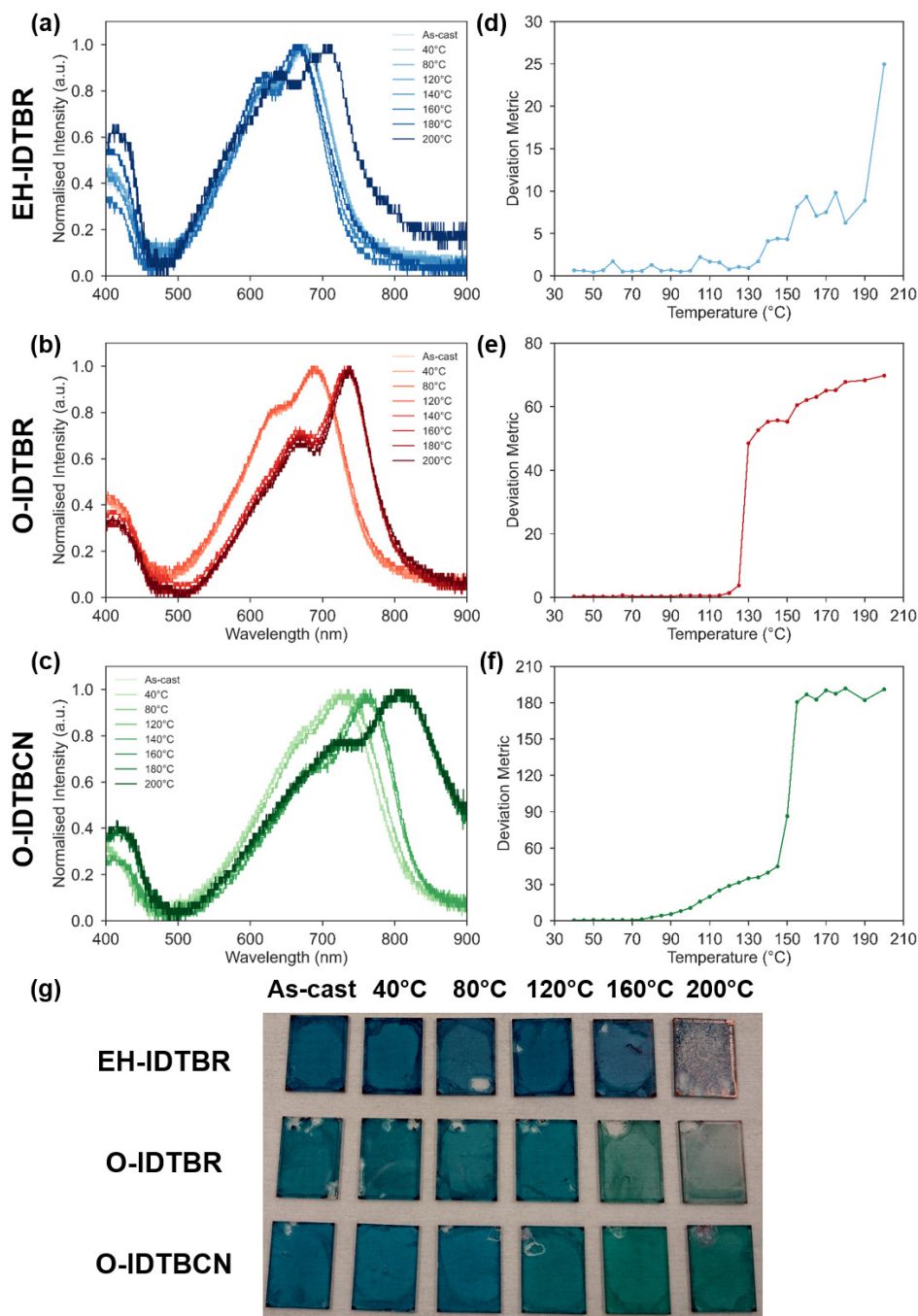


Figure 6.1: (a-c) Temperature-dependent UV-Vis spectra of as-cast and thermally annealed thin films at annealing temperatures between 40-200°C. (d-f) Deviation metric as a function of annealing temperature. (g) Photographs of as-cast and thermally annealed films.

From the temperature-dependent UV-Vis measurements presented in this chapter it is tentatively suspected that the weaker transition at $\sim 80^\circ\text{C}$ for O-IDTBCN is a glass transition and the higher temperature transition at $\sim 150^\circ\text{C}$ is crystallisation. For EH-IDTBR and O-IDTBR the transitions at $\sim 130^\circ\text{C}$ and $\sim 125^\circ\text{C}$ are most likely the result of crystallisation. Additionally, it is suspected that the glass transition temperature of both materials occurs in a similar temperature range to the potential T_g for O-IDTBCN at ($\sim 80^\circ\text{C}$) but the transitions are too weak to detect. Further temperature-dependent measurements such as DSC, spectroscopic ellipsometry or X-ray reflectivity are necessary to fully characterise the origin of the observed transitions.

6.5.2 Temperature-Dependent AFM Studies

To correlate the temperature-dependent changes observed in UV-Vis spectroscopy to structural changes, AFM measurements were performed on as-cast and thermally annealed films, annealed in the temperature range $80\text{-}200^\circ\text{C}$ (Figure 6.2). RMS roughness values (σ_{RMS}) are summarised in Table 6.3.

As-cast films of EH-IDTBR, O-IDTBR and O-IDTBCN display significantly different surface morphologies. For O-IDTBCN, as-cast films are ultra smooth ($<0.5\text{nm}$) and no distinct grains are visible suggesting films are largely amorphous (Figure 6.2k). In comparison, the surface of O-IDTBR films are composed of distinct globular-like, domains and films are considerably rougher than O-IDTBCN with $\sigma_{RMS}=3.87\text{nm}$ (Figure 6.2f). For as-cast EH-IDTBR films, the surface morphology seems to be intermediate between the amorphous surface of O-IDTBCN and the aggregated surface of O-IDTBR (Figure 6.2a). Although some structure is visible, domain interfaces are not well-defined, resulting in a surface roughness of 1.06nm . For annealed films, there are distinct temperature-dependent changes of the surface morphology for each NFA as discussed below.

Compared with as-cast films, EH-IDTBR and O-IDTBR films annealed at 80°C and 120°C , do not exhibit significant changes in the surface morphology and surface roughness remains largely unchanged (Figure 6.2a-c and Figure 6.2f-h). As annealing temperature is increased to 160°C , there is a distinct change in surface morphology and a simultaneous increase in surface roughness for both NFAs. For EH-IDTBR, long needle-like crystals or fibrils appear on the surface and surface roughness increases to 5.77nm (Figure 6.2d). For O-IDTBR, the surface is still composed of globular-like domains but the size of these features increases dramatically and surface roughness rises to 16.19nm (Figure 6.2i). At 200°C , surface roughness continues to increase significantly for both NFAs and the lateral morphology becomes too large to appropriately image using the same scan size as films annealed at lower annealing temperatures (Figure 6.2e and Figure 6.2j). AFM images across larger scan sizes along with optical microscopy images of films annealed at 200°C are provided

in the Supplementary Data (Figure 6.22 and Figure 6.23 respectively). The surface of EH-IDTBR films annealed at 200°C are composed of macroscopic crystals that are of the order $\sim 10 - 100\mu m$ in size (Figure 6.23b). For O-IDTBR, the surface of films annealed at 200°C are composed of large spherulite crystals but these are significantly smaller in size ($\sim 1 - 10\mu m$) compared to the macroscopic crystals formed on the surface of EH-IDTBR films.

For O-IDTBCN, as-cast films and films annealed at 80°C are comparable with both topography images appearing featureless and exhibiting similar surface roughness values (Figure 6.2k-l). As annealing temperature is increased to 120°C, small island-like domains appear and surface roughness increases substantially to 3.74nm. This is in agreement with the suspected glass transition observed in the UV-measurements discussed above at $\sim 80^\circ\text{C}$. As annealing temperature increases these isolated domains seem to act as nucleation sites for the formation of larger aggregates which increase in size as annealing temperature increases. At 200°C the film is significantly rougher (15.02nm) compared to the as-cast film and large crystalline domains are visible. Comparing the larger AFM scans (Figure 6.22) and optical microscopy images (Figure 6.23) of films annealed at 200°C, O-IDTBCN crystallites are considerably smaller than O-IDTBR and O-IDTBR. This can be attributed to a higher crystallisation temperature as indicated in the UV-Vis measurements described above. It should also be stressed that the onset temperatures for crystallisation are kinetic in character for each NFA. At temperatures close to T_g (i.e. $< 120^\circ\text{C}$), the crystallisation rate is slow as the kinetics are slow. As annealing temperature increases, the crystallisation rate rises steeply, and crystal size increases rapidly. At temperatures approaches the melting temperature, crystallisation rate slows as thermodynamic driving forces are smaller closer to the melting temperature.

Annealing temperature (°C)	RMS Roughness σ_{RMS} (nm)		
	EH-IDTBR	O-IDTBR	O-IDTBCN
As-cast	1.06	3.87	0.27
40	1.11	3.98	0.29
80	0.97	2.91	0.30
120	1.03	3.65	3.74
160	5.77	16.19	6.80
200	29.23	20.74	15.02

Table 6.3: Table of RMS film roughness values extracted from the AFM images shown in Figure 6.2.

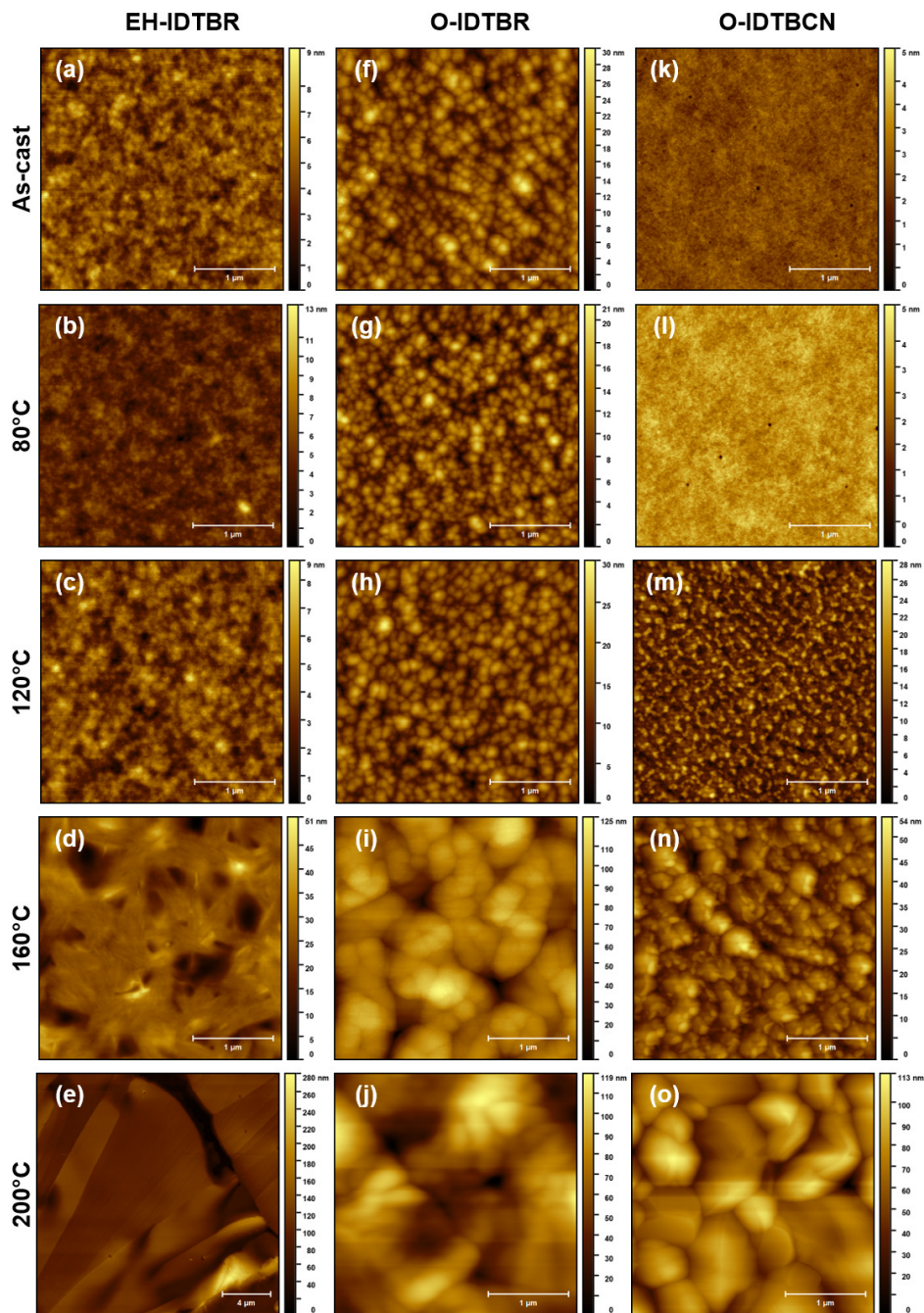


Figure 6.2: AFM height topography images of (a-e) EH-IDTBR, (f-j) O-IDTBR and (k-o) O-IDTBCN thin films measured as-cast and after thermal annealing for 10 minutes at 80, 120, 160 and 200°C. The scale bar is $1\mu\text{m}$. Note the AFM images of films annealed at 40°C are not included here as they were very similar to the as-cast and 80°C films for each NFA.

The temperature-dependent AFM and UV-Vis measurements presented here demonstrate the significant impact of chemical structure on the thermal properties and crystallisation behaviour of each NFA. Both branched and linear side-chain IDTBR exhibit crystallisation behaviour at similar temperatures ($T_C \sim 125\text{-}130^\circ\text{C}$) whilst O-IDTBCN crystallises at a slightly higher temperature ($T_C \sim 150^\circ\text{C}$). However, the linear alkyl side-chains of O-IDTBR and O-IDTBCN result in a greater UV-Vis spectral shift in suggesting a greater degree of crystallisation compared to EH-IDTBR suggesting the branched ethylhexyl side-chains inhibit molecular mobility. To further understand the temperature-dependent structural changes in the films across the full depth of the film, further measurements such as GIWAXS are required.

6.6 Initial Optoelectronic Properties and Morphology

In the previous section, the impact of chemical design on the thermal properties and crystallisation of NFAs was investigated. Next, these concepts are applied to polymer : NFA BHJ blends to explore the relationship between molecular structure, nanomorphology and optoelectronic functionality.

6.6.1 Optoelectronic Properties

UV-Vis absorption spectra of pure PC₇₁BM EH-IDTBR, O-IDTBR, O-IDTBCN and PTB7-Th films are displayed in Figure 6.3. As discussed previously in Chapter 5 PC₇₁BM is weakly absorbing at wavelengths $>550\text{nm}$ resulting in a poor spectral overlap with the solar spectrum. In comparison, the absorption profile of the NFAs and PTB7-Th offers a considerably greater spectral overlap with the solar spectrum and can therefore contribute more significantly to the photocurrent of an OPV device compared to fullerene acceptors. For EH-IDTBR, O-IDTBR, PTB7-Th and O-IDTBCN the absorption profiles between 550 and 900nm are composed of two primary contributions with a maximum at $\sim 669\text{nm}$, $\sim 683\text{nm}$, $\sim 699\text{nm}$ and $\sim 717\text{nm}$ respectively which is in agreement with results reported elsewhere [97, 139]. It is also noted that the weaker intensity shoulder at ($\sim 400\text{nm}$) is more pronounced for IDTBR based NFAs. This feature has previously been attributed to aggregation in IDT-BT polymers [328]. For linear O-IDTBR and O-IDTBCN, the position of the highest intensity absorption peak is red-shifted by 14nm and 66nm relative to the branched EH-IDTBR respectively. The significant bathochromic shift of the absorption profile of O-IDTBCN relative to EH-IDTBR would be preferable in affording a more complementary absorption profile with most conjugated polymers, particularly high bandgap polymers such as P3HT [97].

The UV-Vis absorption profiles of PTB7-Th based blend films are representative of the superposition of contributions from each individual component (Figure 6.4). For PTB7-Th : PC₇₁BM, absorption is strongest at wavelengths <550nm due to PC₇₁BM and the addition of PTB7-Th offers a more complementary spectrum, improving absorption capabilities in the range 600-750nm. In comparison, the PTB7-Th : NFA blends display strong absorption in the wavelength range 550 - 800nm with maxima at ~668nm, ~683nm and ~710nm for EH-IDTBR, O-IDTBR and O-IDTBCN based PTB7-Th blend films respectively. The narrow band gap of O-IDTBCN is particularly effective at increasing the spectral overlap of the blend absorption to the solar spectrum. For EH-IDTBR and O-IDTBR, although both acceptors provide strong absorption in the region of the solar spectrum, they both absorb at similar wavelengths to PTB7-Th which could reduce the combined spectral overlap compared to PTB7-Th : O-IDTBCN, limiting their contribution to the photocurrent.

Next, the PV performance of each blend system was evaluated by comparing their *J-V* characteristics. Devices were fabricated with an inverted device architecture (glass/ITO/ZnO/PTB7-Th : acceptor/MoO₃/Ag) following the protocols outlined in Chapter 3. Champion *J-V* curves are displayed in Figure 6.5 along with a boxplot of device metric statistics in Figure 6.6. A full summary of average and champion device metrics is provided in Table 6.4. PTB7-Th : EH-IDTBR devices achieved the highest champion *PCE* of 9.06% due to a high V_{OC} of 1.02V, J_{SC} of 15.04mA/cm² and *FF* of 69.52%. PTB7-Th : O-IDTBCN devices exhibited marginally higher J_{SC} and *FF* values compared to PTB7-Th : EH-IDTBR systems but large V_{OC} losses reduced the champion *PCE* to 8.05%. Following on from this, PTB7-Th : O-IDTBR devices achieved a champion *PCE* of 7.75% but there is a strikingly large distribution in performance. Losses here originate from a significantly reduced J_{SC} and lower *FF* compared to EH-IDTBR and O-IDTBCN systems. Finally, PTB7-Th : PC₇₁BM devices achieved the lowest champion *PCE* of 6.55% with the primary source of losses originating from a reduced J_{SC} and V_{OC} . J_{SC} losses are expected here due to the weaker absorption and poor spectral overlap afforded by PC₇₁BM as demonstrated in the UV-Vis measurements above. Although morphological factors may contribute, the primary origin of the reduced V_{OC} in both PTB7-Th : O-IDTBCN and PTB7-Th : PC₇₁BM systems results from the deeper lying LUMO levels of O-IDTBCN and PC₇₁BM compared to O-IDTBR and EH-IDTBR (Table 3.1)[139].

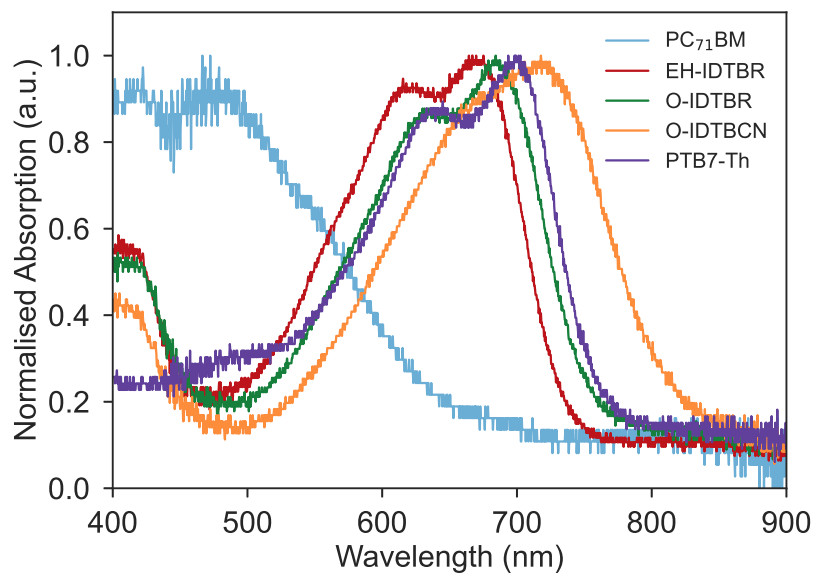


Figure 6.3: Normalised UV-Vis absorption spectra of pure materials.

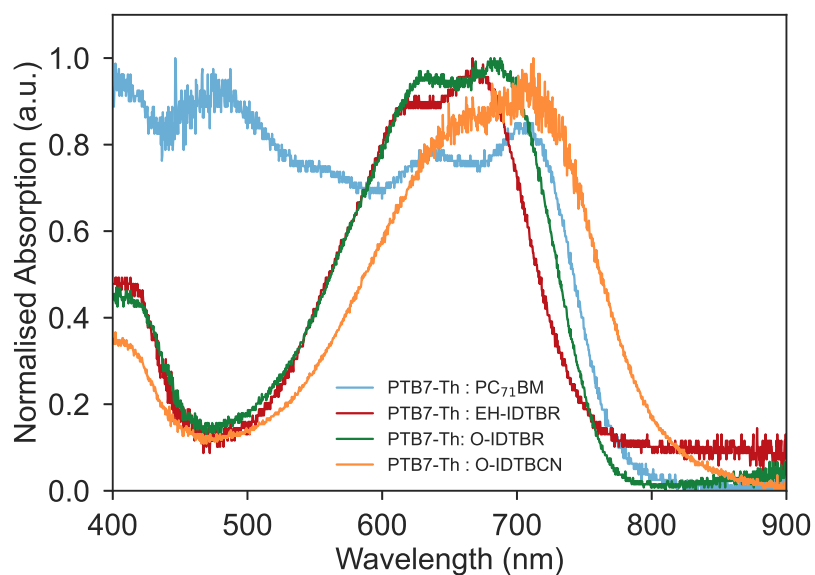


Figure 6.4: Normalised UV-Vis absorption spectra of PTB7-Th based blend films.

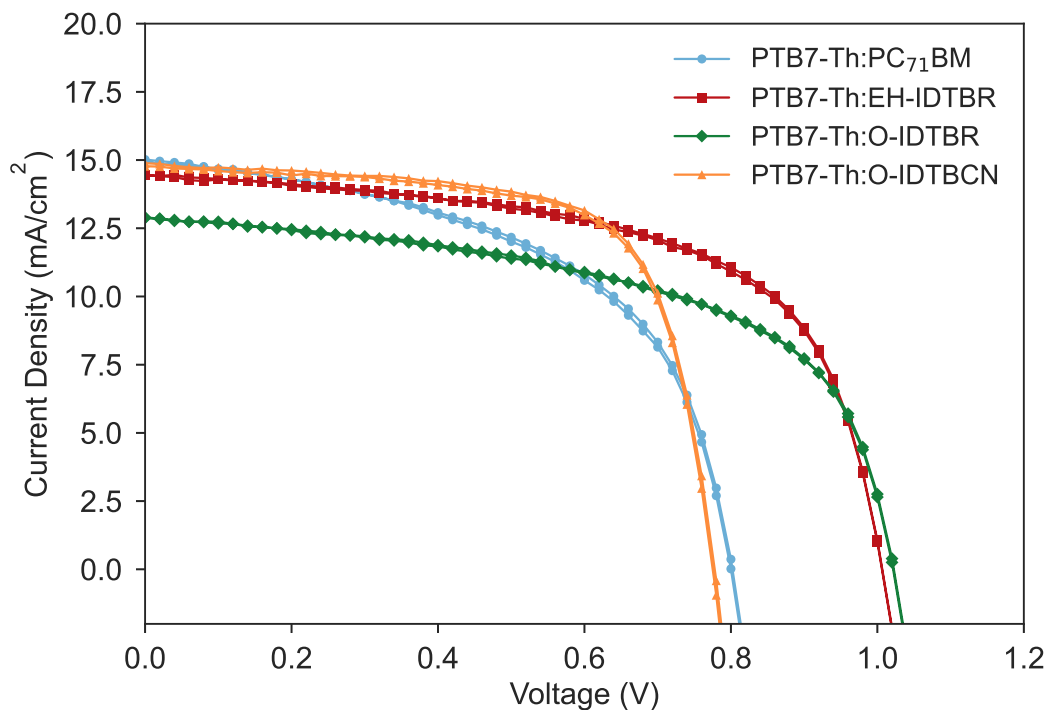


Figure 6.5: Champion J - V curves of PTB7-Th based solar cells.

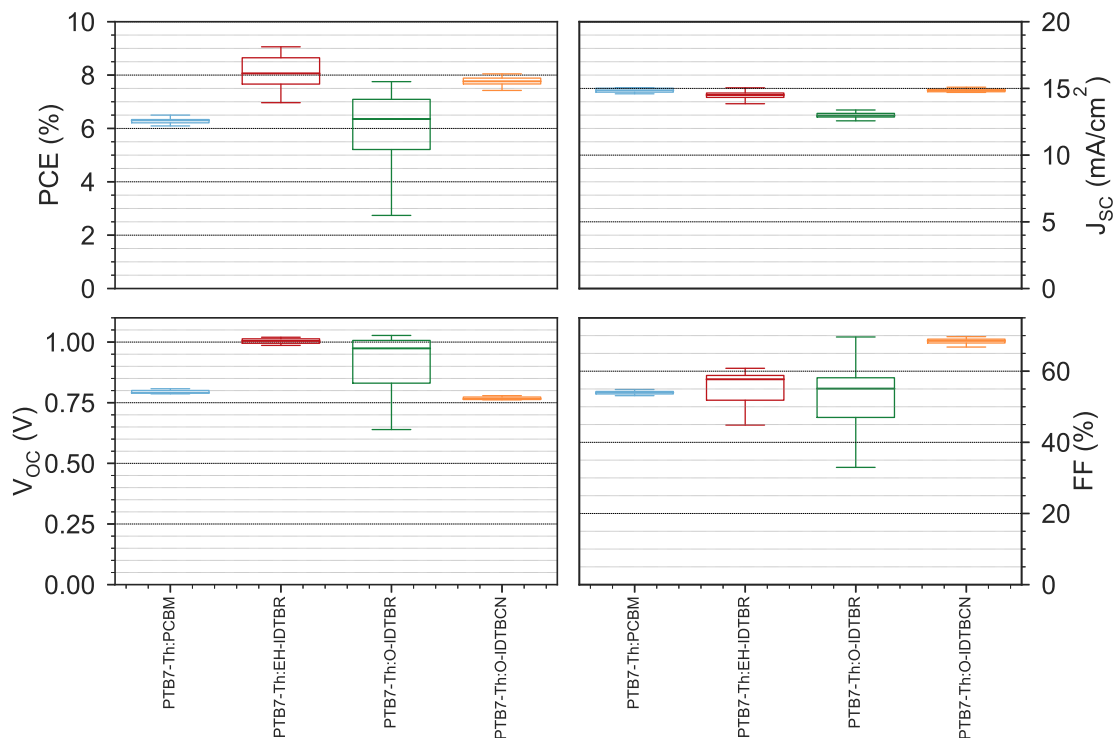


Figure 6.6: Boxplot of device metrics for PTB7-Th based solar cells. Data includes the top 10 devices for each split.

Blend System	J_{sc} (mA/cm^2)	V_{oc} (V)	FF (%)	PCE (%)
PTB7-Th : PC₇₁BM	14.85 ± 0.16 (15.06)	0.79 ± 0.01 (0.81)	53.43 ± 2.29 (54.85)	6.25 ± 0.30 (6.55)
PTB7-Th : EH-IDTBR	14.49 ± 0.29 (15.04)	0.99 ± 0.06 (1.02)	55.44 ± 6.45 (69.52)	7.77 ± 1.31 (9.06)
PTB7-Th : O-IDTBR	12.97 ± 0.29 (13.61)	0.92 ± 0.12 (1.03)	52.96 ± 10.32 (69.62)	5.85 ± 1.58 (7.75)
PTB7-Th : O-IDTBCN	14.86 ± 0.11 (15.09)	0.77 ± 0.01 (0.78)	68.01 ± 1.69 (69.70)	7.73 ± 0.22 (8.05)

Table 6.4: Summary of the average and champion OPV device metrics for PTB7-Th based solar cells. Averages are given for the top 10 devices ± 1 standard deviation, with metrics relating to the champion PCE shown in parenthesis.

The EQE spectra of PTB7-Th based systems is displayed in Figure 6.7. J_{SC} values extracted from integrating the EQE spectra are comparable to J_{SC} values from J - V measurements of devices with less than 15% discrepancy (Table 6.5). The EQE profiles of each blend largely follow their UV-Vis profiles as discussed previously (Figure 6.4). The narrower bandgap of O-IDTBCN allows PTB7-Th : O-IDTBCN devices to harvest a greater fraction of the incident photon flux, displaying a broad EQE profile which extends past 800nm and exhibits a maximum photon conversion of $\sim 70\%$. This partially explains the superior integrated J_{SC} for PTB7-Th : O-IDTBCN devices. In comparison, PTB7-Th : EH-IDTBR and PTB7-Th : O-IDTBR devices both display a broad photon conversion response in the wavelength range 500 - 750nm but EQE values are limited to a maximum of 67% and 61%. For PTB7-Th : PC₇₁BM systems, EQE is slightly enhanced compared to PTB7-Th : NFA systems in the region 450-550nm but maximum EQE is limited to 62%.

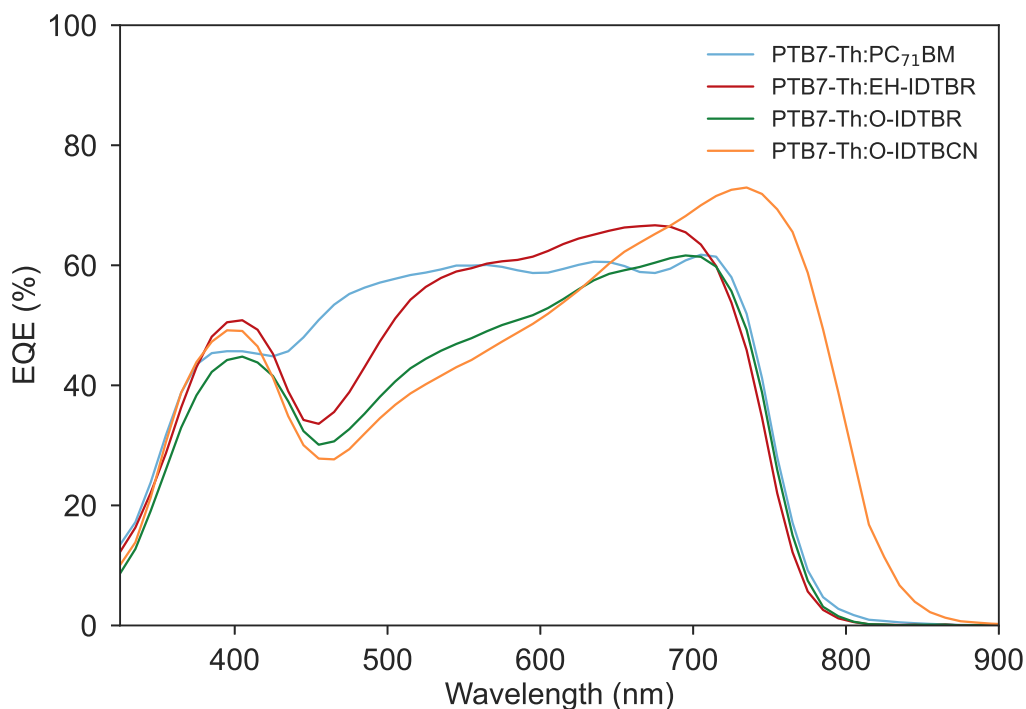


Figure 6.7: EQE spectra of PTB7-Th based solar cells.

Blend System	Device J_{SC} (mA/cm^2)	Integrated J_{SC} from EQE (mA/cm^2)
PTB7-Th : PC₇₁BM	15.05	13.57
PTB7-Th : EH-IDTBR	15.00	13.17
PTB7-Th : O-IDTBR	13.48	11.71
PTB7-Th : O-IDTBCN	14.83	14.22

Table 6.5: J_{SC} values for PTB7-Th based solar cells extracted from J - V measurements and from integrating the EQE spectra (Figure 6.7).

6.6.2 Small-Scale Structures

Given the apparent differences in optical properties and device performance, GIWAXS measurements were performed to probe the molecular packing and crystallinity of each pure material and blend system. The 2D GIWAXS scattering patterns of the pure materials are shown in Figure 6.8.

The 2D scattering pattern of pure PC₇₁BM consists of weak intensity diffraction rings at $Q \sim 0.7\text{\AA}^{-1}$ ($d = 9.0\text{\AA}$) $Q \sim 1.3\text{\AA}^{-1}$ ($d = 4.8\text{\AA}$) indicating an amorphous arrangement of PC₇₁BM molecules in agreement with previous measurements discussed in Chapter 5 (Figure 6.8a). The 2D GIWAXS patterns of EH-IDTBR, O-IDTBR, O-IDTBCN and PTB7-Th each exhibit two distinctive scattering features arising from π - π stacking in the out-of-plane direction at approximately $Q = 1.6 - 1.8\text{\AA}^{-1}$ and lamellar stacking in the in-plane direction at approximately $Q = 0.25 - 0.4\text{\AA}^{-1}$. This molecular packing is indicative of a face-on molecular orientation which is beneficial for OPV systems as charge transport typically occurs along the π - π stacking direction (i.e. perpendicular to the substrate). The scattering intensity of PTB7-Th and O-IDTBR in particular seem to be higher than the other samples suggesting a higher degree of molecular order. Although single crystal structures have been reported for EH-IDTBR and O-IDTBR [329], GIWAXS measurements show the thin film packing is different to the bulk single crystal structure with films only exhibiting lamellar and π - π stacking peaks, in agreement with other studies [97].

To further understand the differences in molecular packing between the pure films, 1D profiles were extracted from the 2D GIWAXS patterns by azimuthally integrating through various χ angles in the out-of-plane and in-plane directions (Figure 6.9). The in-plane lamellar peaks and out-of-plane π - π peaks were modelled with Lorentzian curve functions to extract peak width and peak position values. These values were then used to calculate the d -spacing and crystalline coherence length CCL related to each scattering feature according to Equation 3.47 and Equation 3.78 respectively (Table 6.6).

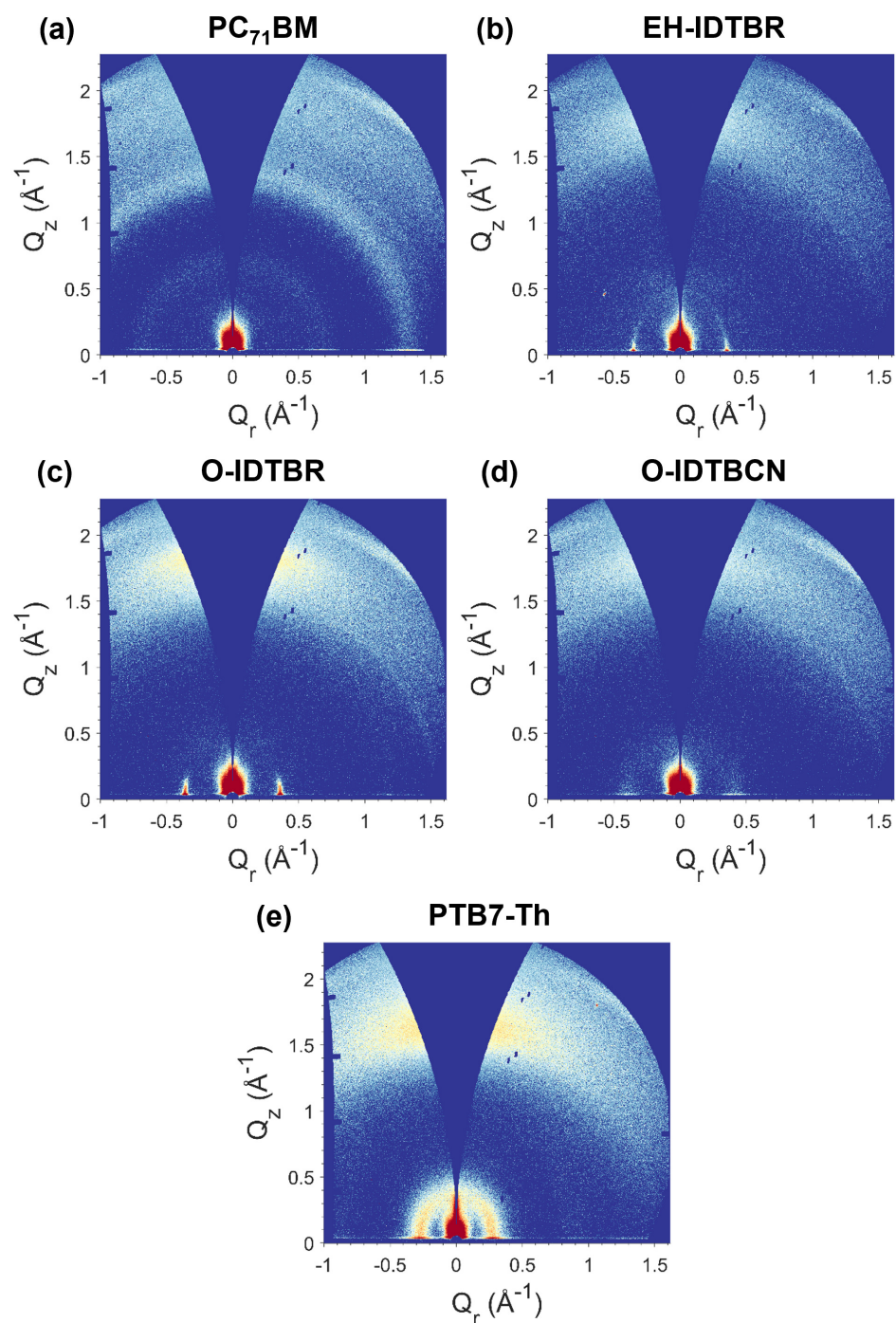


Figure 6.8: 2D GIWAXS patterns of fresh (a) PC₇₁BM, (b) EH-IDTBR, (c) O-IDTBR, (d) O-IDTBCN and (e) PTB7-Th thin films annealed at 80°C for 10 minutes. Data was collected at an incident angle of $\theta_i = 0.16^\circ$.

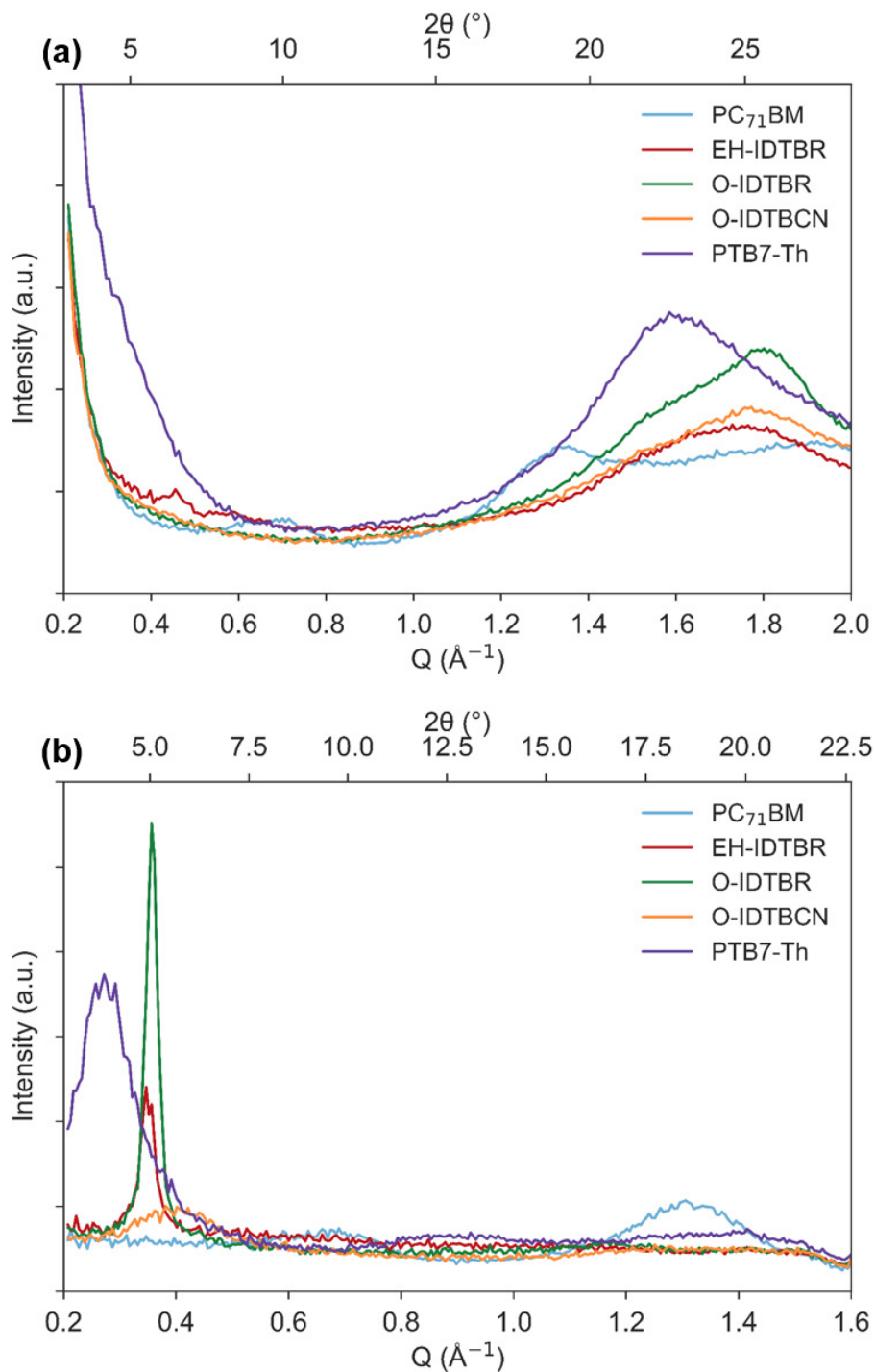


Figure 6.9: Azimuthally integrated Q -dependent intensity profiles of fresh annealed thin films of PC₇₁BM, EH-IDTBR, O-IDTBR, O-IDTBCN and PTB7-Th in the (a) out-of-plane and (b) in-plane directions.

Pure Material	In-plane Lamellar Peak			Out-of-plane π - π Stacking Peak		
	Q (\AA^{-1})	d (\AA)	CCL (nm)	Q (\AA^{-1})	d (\AA)	CCL (nm)
EH-IDTBR	0.356	17.6	20.1	1.78	3.52	0.88
O-IDTBR	0.364	17.3	23.6	1.81	3.48	0.88
O-IDTBCN	0.400	15.7	2.68	1.82	3.46	0.73
PTB7-Th	0.282	22.3	4.70	1.67	3.76	1.03

Table 6.6: Table of characteristic length scales relating to in-plane lamellar stacking and out-of-plane π - π stacking of pure EH-IDTBR, O-IDTBR, O-IDTBCN and PTB7-Th films. Q values are extracted from fitting the GIWAXS peaks in the 1D intensity profiles shown in Figure 6.9. d -spacings are calculated using Equation 3.47 and CCL values are estimated using the Scherrer equation Equation 3.78.

For EH-IDTBR and O-IDTBR, the lamellar d -spacings are 17.6 \AA and 17.3 \AA and π - π d -spacings are 3.53 \AA and 3.47 \AA respectively, indicating the linear side-chain analogue self-assembles into a more tightly packed configuration. This corresponds to a higher degree of crystalline order with a CCL of 23.7nm estimated from Scherrer analysis of the in-plane lamellar peak. In comparison, the dicyanovinyl terminal groups of O-IDTBCN results in a smaller lamellar stacking distance ($d = 15.7\text{\AA}$) compared to the rhodanine end group analogue (O-IDTBR). Additionally, the smaller CCL values extracted from the 1D intensity profiles indicate O-IDTBCN self-assembles into a considerably less ordered arrangement compared to both EH-IDTBR and O-IDTBR. For the polymer, the lamellar stacking and π - π stacking d -spacings are 22.3 \AA and 3.76 \AA , corresponding to CCL values of 4.70nm and 1.03nm respectively.

In Figure 6.10, 2D scattering patterns of PTB7-Th based blends films are displayed. Each scattering pattern consists of weak intensity, diffuse features indicative of a low degree of molecular order. For PTB7-Th : PC₇₁BM, amorphous PC₇₁BM scattering features are visible at $Q \sim 0.7\text{\AA}^{-1}$ and $Q \sim 1.3\text{\AA}^{-1}$, along with the lamellar stacking characteristic of PTB7-Th at $Q \sim 0.3\text{\AA}^{-1}$ (Figure 6.10a). For PTB7-Th : NFA blend films, the low Q regions at $0.2 < Q$ (\AA^{-1}) < 0.5 appear to be composed of multiple low intensity scattering features. To investigate this further, azimuthally integrated 1D intensity profiles were extracted from the 2D scattering patterns in the in-plane and out-of-plane direction (Figure 6.11). Although scattering intensities are low, it is clear that the low Q feature in the in-plane intensity profiles for PTB7-Th : NFA blend films are each the superposition of scattering from two different contributions (Figure 6.11b). Given the lamellar stacking Q position of PTB7-Th and the NFAs are substantially different as described above, these contributions most likely originate from the lamellar stacking of the polymer and the NFA.

To confirm this, the low Q feature was deconvolved into two separate Lorentzian functions to extract values for peak position, peak width and CCL (Table 6.7).

For PTB7-Th : PC₇₁BM blends, the lamellar CCL value corresponding to the size of coherently diffracting regions of PTB7-Th is equal to 2.99nm. For the PTB7-Th : NFA blends, this increases slightly to $\sim 3.4 - 3.9nm$ suggesting the molecular order of the polymer is enhanced in the NFA blends. In the PTB7-Th : NFA blends, the lamellar CCL relating to the acceptor regions is equal to 9.7nm, 19.1nm and 7.1nm for EH-IDTBR, O-IDTBR and O-IDTBCN respectively. Interestingly, comparing with the CCL of the pure films (Table 6.6), the presence of the polymer appears to suppress the molecular order of EH-IDTBR and O-IDTBR lamellar stacking but enhance that of O-IDTBCN. For the π - π stacking features in the Q range $Q \sim 1.70 - 1.85\text{\AA}^{-1}$, the contributions from each individual component cannot be discerned. Instead a single, broad Lorentzian function is used to fit the scattering feature for each blend film and the extracted peak characteristics and estimated CCL values are summarised in Table 6.8. In comparison to the pure films, the π - π stacking CCL of EH-IDTBR and O-IDTBR blend systems is considerably suppressed whereas O-IDTBCN CCL remains largely unchanged.

Blend System	PTB7-Th			Acceptor		
	Q (\AA^{-1})	d (\AA)	CCL (nm)	Q (\AA^{-1})	d (\AA)	CCL (nm)
PTB7-Th : PC₇₁BM	0.308	20.4	2.99	–	–	–
PTB7-Th : EH-IDTBR	0.293	21.5	3.45	0.354	17.8	9.7
PTB7-Th : O-IDTBR	0.304	20.6	3.62	0.363	17.3	19.1
PTB7-Th : O-IDTBCN	0.298	21.1	3.82	0.403	15.6	7.1

Table 6.7: Table of GIWAXS parameters extracted from fitting the in-plane lamellar stacking peak (Figure 6.9b). d -spacings are calculated using Equation 3.47 and CCL values are estimated using the Scherrer equation (Equation 3.78).

Blend System	Q (\AA^{-1})	d (\AA)	CCL (nm)
PTB7-Th : PC₇₁BM	1.868	3.36	0.52
PTB7-Th : EH-IDTBR	1.738	3.62	0.70
PTB7-Th : O-IDTBR	1.751	3.59	0.63
PTB7-Th : O-IDTBCN	1.762	3.57	0.74

Table 6.8: Table of GIWAXS parameters extracted from fitting the out-of-plane π - π stacking peak (Figure 6.9a). d -spacings are calculated using Equation 3.47 and CCL values are estimated using the Scherrer equation (Equation 3.78).

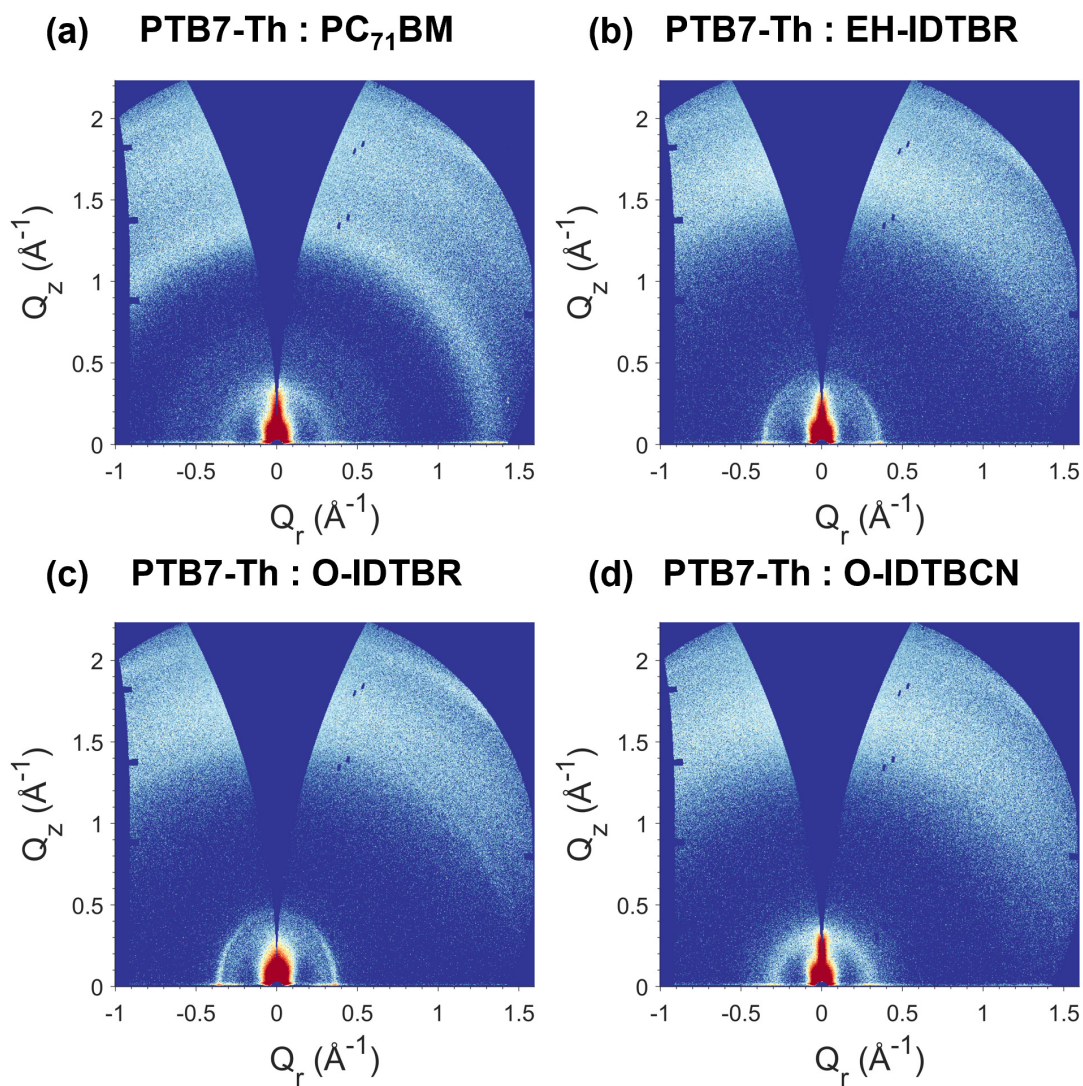


Figure 6.10: 2D GIWAXS patterns of fresh (a) PTB7-Th : PC₇₁BM, (b) PTB7-Th : EH-IDTBR, (c) PTB7-Th : O-IDTBR and (d) PTB7-Th : O-IDTBCN thin films annealed at 80°C for 10 minutes.

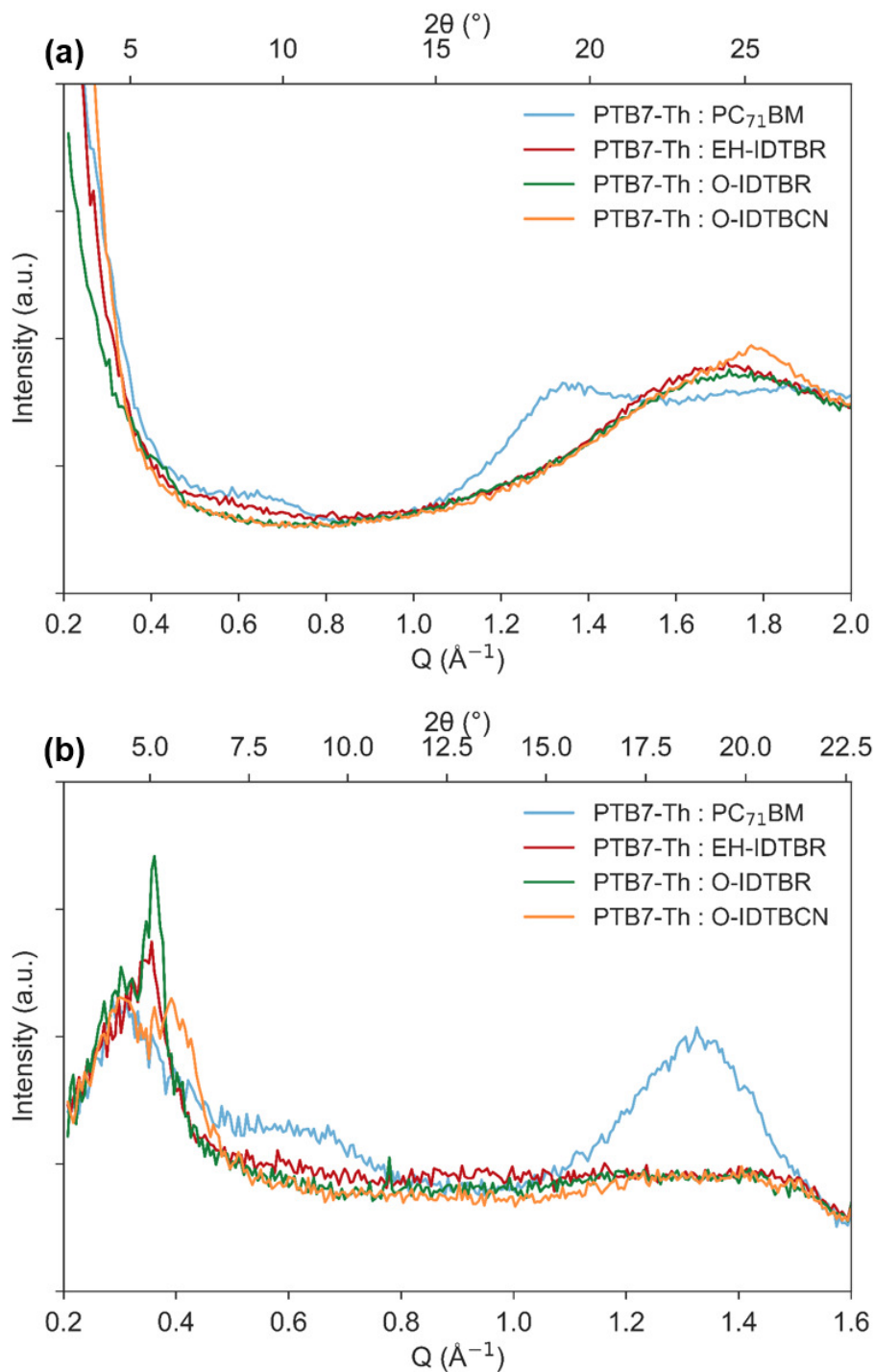


Figure 6.11: Azimuthally integrated Q -dependent intensity profiles of fresh annealed PTB7-Th : acceptor blends in the (a) out-of-plane and (b) in-plane direction.

6.6.3 Large-Scale Structures

From GIWAXS measurements, it is apparent that the choice of side-chain and end-group have a significant effect on the crystallinity of both the pure and blend film. For efficient charge transport in an OPV device, it is desirable to have small molecular stacking distances and large crystalline coherence lengths. However, in achieving this, materials that have a high degree of molecular order are often susceptible to aggregation [110], forming domains much larger than the exciton diffusion length (l_d) [116]. The exciton diffusion length of EH-IDTBR has been previously measured as 15nm [29] which gives an initial indication of the optimum nanomorphology in the blend films. l_D values of O-IDTBR and O-IDTBR are expected to be a similar order of magnitude to EH-IDTBR. In this section, the properties of larger scale structures in the blend films such as the size and purity of domains are investigated using SANS and AFM.

AFM height topography images of PTB7-Th based blends are displayed in (Figure 6.12) and root-mean-squared (RMS) surface roughness (σ_{RMS}) values are summarised in Table 6.9. The surface of PTB7-Th : PC₇₁BM blend films are composed of distinct, uniform domains with an RMS roughness of 1.12 nm (Figure 6.12a). In comparison, PTB7-Th : EH-IDTBR and PTB7-Th : O-IDTBCN blend film are slightly rougher with $\sigma_{RMS} \sim 2 - 3nm$ and domains seem to be a comparable size but the interfaces are much less distinct particularly for the O-IDTBCN blend suggesting a more finely intermixed morphology (Figure 6.12b,d). The surface morphology of PTB7-Th : O-IDTBR blend films appear significantly different compared to the other samples, with much larger domains visible suggesting significant aggregation and phase separation. This is further reflected in a much greater RMS roughness value of 10.97nm and likely contributes to the large dispersion in device performance (Figure 6.6).

Although the AFM measurements discussed above provide an initial indication of the larger length scales present in PTB7-Th based blend films, it is only a small area on the film surface which has been probed. In an OPV device the entire BHJ thin film is capable of absorbing sunlight and generating excitons. As such, to correlate film nanostructure with device operation it is necessary to characterise the *three-dimensional* blend film morphology, both in the lateral direction and vertical direction. SANS measurements provide the capabilities to do this as the entire film is probed and the resultant scattering is representative of the *average* nanostructure present in the sample. As described previously in Subsection 3.9.5, in this work the averaging properties of SANS measurements are exploited further and performed on a stack of 15 films per sample. To provide sufficient neutron SLD contrast in the PTB7-Th : NFA blend films a series of deuterium labelled NFA analogues were synthesised by collaborators at Imperial College (Figure 3.4). The neutron SLD of each of these materials can be found in Table 3.6.

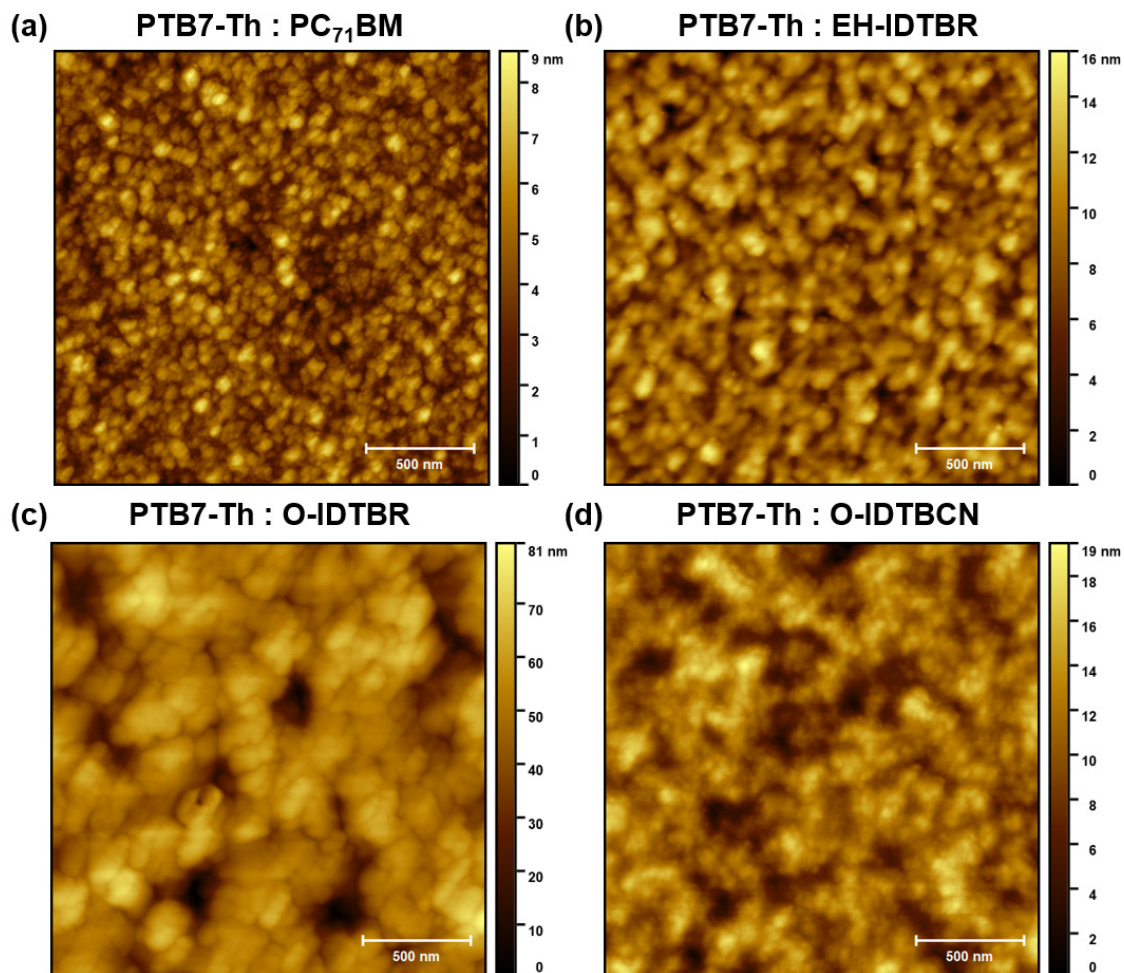


Figure 6.12: AFM height topography images of fresh (a) PTB7-Th : PC₇₁BM, (b) PTB7-Th : EH-IDTBR, (c) PTB7-Th : O-IDTBR and (d) PTB7-Th : O-IDTBCN. The lateral scale bar is 500nm.

Sample	σ_{RMS} (nm)
PTB7-Th : PC ₇₁ BM	1.12
PTB7-Th : EH-IDTBR	2.10
PTB7-Th : O-IDTBR	10.97
PTB7-Th : O-IDTBCN	2.87

Table 6.9: Table of root-mean-squared roughness (σ_{RMS}) values extracted from the AFM data shown in Figure 6.12.

The absolute SANS intensities in the full observable Q range of PTB7-Th based blends are presented in Figure 6.13. The most prominent differences between samples occur at low Q ($Q < 0.01 \text{ \AA}^{-1}$). Here, the scattering intensities of PC₇₁BM, d-EH-IDTBR and d-O-IDTBCN blend systems are comparable and begin to flatten off whilst the PTB7-Th : d-O-IDTBR blend film shows much higher scattering intensity.

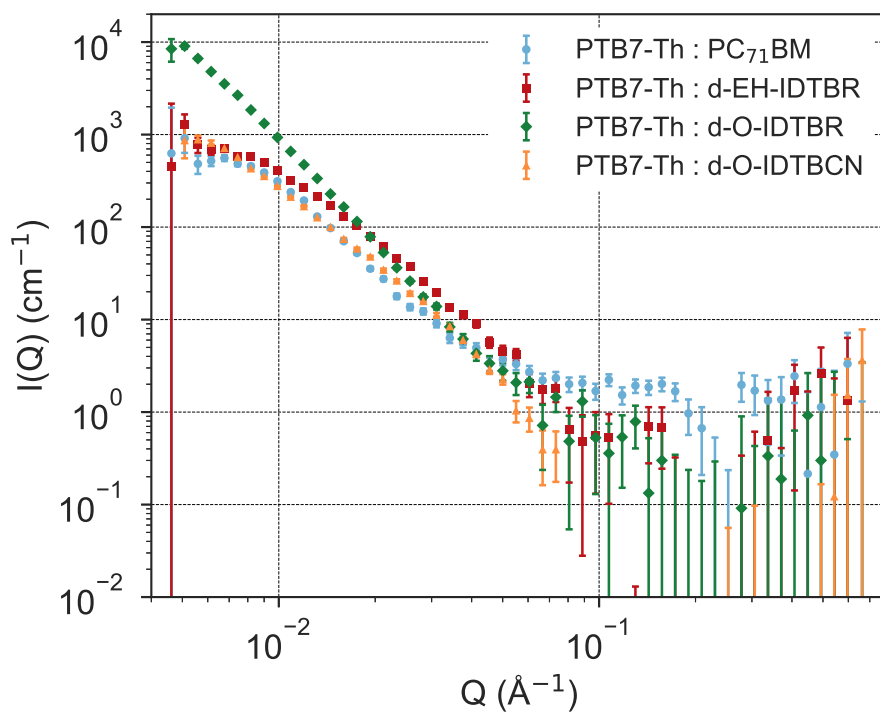


Figure 6.13: Absolute SANS intensity of PTB7-Th : PC₇₁BM, PTB7-Th : d-EH-IDTBR, PTB7-Th : d-O-IDTBR and PTB7-Th : d-O-IDTBCN blend films in the full measurable Q range.

To understand these apparent changes, the Lorentz-corrected SANS intensity (IQ^2 vs Q) is shown in Figure 6.14. A characteristic peak is not observed for the PTB7-Th : d-O-IDTBR blend system suggesting the characteristic length scale is outside of the observable Q range of the diffractometer. For the PC₇₁BM, d-EH-IDTBR and d-O-IDTBCN blend systems, distinct characteristic peaks are observed corresponding to long-period (L_p) values of 92.9nm, 70.8nm and 69.3nm respectively (Table 6.10). These values are related to the long-period of lamellae crystals defined as the mean average distance between lamellae domains including the length of the crystal and the amorphous domains between the crystals [105]. The area under the Lorentz-corrected scattering intensity (the invariant, Equa-

tion 3.65) is related to the contrast in the system contrast in the system and hence the domain composition of the blend film. The invariant is considerably higher for the PTB7-Th : d-O-IDTBR blend system compared to PC₇₁BM, d-EH-IDTBR and d-O-IDTBCN blend systems, suggesting a greater amount of contrast and hence a greater degree of phase separation.

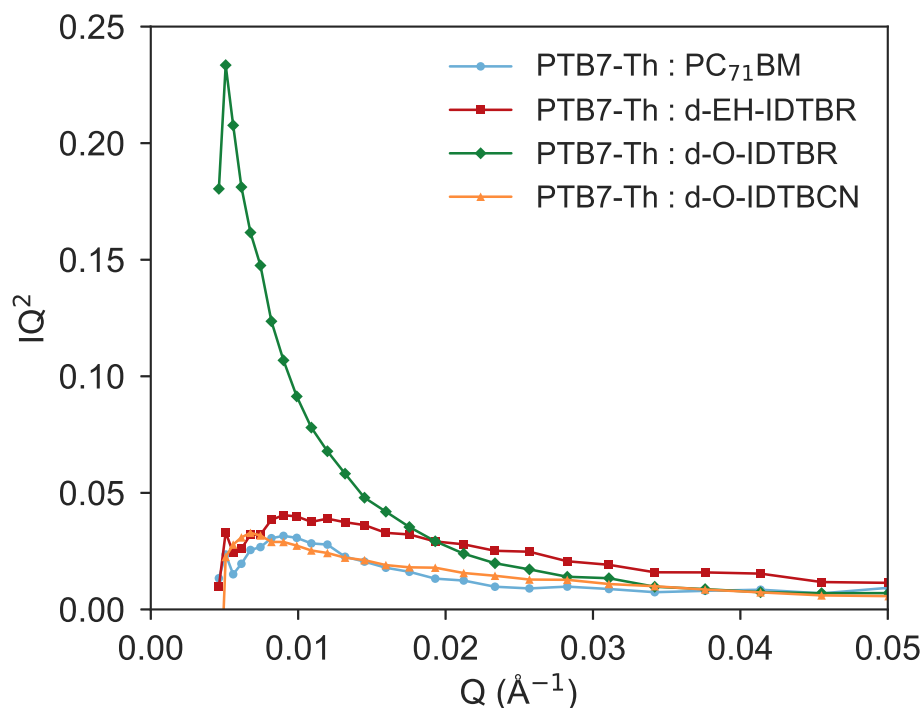


Figure 6.14: Lorentz-corrected SANS intensity of PTB7-Th : PC₇₁BM, PTB7-Th : d-EH-IDTBR, PTB7-Th : d-O-IDTBR and PTB7-Th : d-O-IDTBCN blend films. Data is repeated from Figure 6.13 but plotted as IQ^2 vs Q .

In Figure 6.15, the SANS data are modelled using a DAB model (see Subsection 3.9.5) where correlation lengths (ξ) of 13.61nm, 8.90nm, 29.69nm and 10.95nm are extracted for PTB7-Th : PC₇₁BM, PTB7-Th : d-EH-IDTBR, PTB7-Th : d-O-IDTBR and PTB7-Th : d-O-IDTBCN blend films respectively (Table 6.10). Using the values for ξ , an average *chord length* (see Equation 3.9.5) can be roughly estimated for the donor (polymer) and acceptor phases by dividing the three-dimensional correlation length by the volume fraction of the opposite phase [185, 191, 101]. Assuming the volume fraction is the same as the weight ratio of the materials in solution (Table 6.2), the volume fractions of the acceptor phase

(ϕ_A) are 0.6 and 0.71 for PTB7-Th : PC₇₁BM and PTB7-Th : NFA blends respectively. The volume fractions of the donor phase (ϕ_D) are therefore 0.4 and 0.29 for PTB7-Th : PC₇₁BM and PTB7-Th : NFA blends respectively as $\phi_A + \phi_D = 1$. Using these values for ϕ_A and ϕ_D , approximate value for the chord length of the acceptor phases (l_A) in each system are calculated to be ~ 34 nm, ~ 31 nm, ~ 104 nm and ~ 38 nm for PC₇₁BM, d-EH-IDTBR, d-O-IDTBR and d-O-IDTBCN based blends respectively. For the PTB7-Th phase, chord lengths are equal to ~ 23 nm, ~ 12 nm, ~ 42 nm and ~ 15 nm for PC₇₁BM, d-EH-IDTBR, d-O-IDTBR and d-O-IDTBCN based blends respectively. These trends are consistent with the long-period analysis described above.

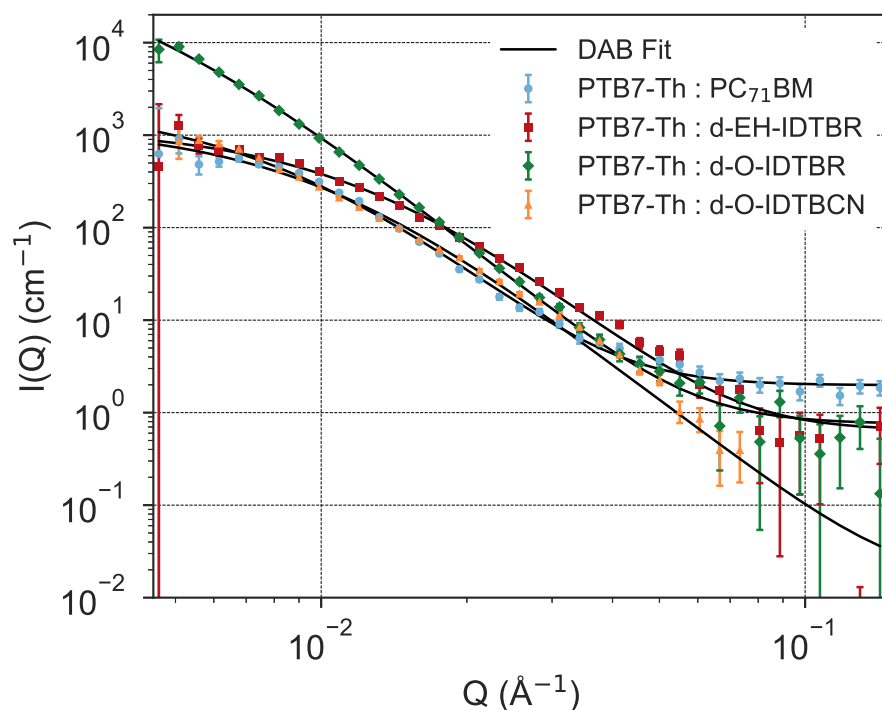


Figure 6.15: DAB SANS fits in the interval $0.004 \leq Q \text{ (\AA}^{-1}\text{)} \leq 0.15$ for PTB7-Th : PC₇₁BM, PTB7-Th : d-EH-IDTBR, PTB7-Th : d-O-IDTBR and PTB7-Th : d-O-IDTBCN blend films. Data is repeated from Figure 6.13 but shows the DAB model fits.

Given ξ values are similar to the *CCL* values extracted from GIWAXS analysis of the acceptor lamellar peak described above (Table 6.7), it is suspected that the DAB model is more sensitive to the acceptor crystallites rather than the amorphous regions in between them. For this reason, *absolute* length scales from the DAB model should be treated with

caution as it is an over-simplified model which assumes a two-phase system. In reality, the blend films are much more complicated as they are likely composed of three phases: a crystalline acceptor phase, an amorphous acceptor phase and an amorphous polymer phase. The reader should therefore treat average chord length values with caution as the calculation makes several assumptions and should only be considered as a first-order estimation (e.g. a two-phase system is assumed and the the blend ratio of components in solution is often assumed to be the same as the volume fraction in the blend film). Nevertheless, SANS measurements show that PTB7-Th : d-O-IDTBR systems form much larger characteristic length scales compared to PC₇₁BM, d-EH-IDTBR, and d-O-IDTBCN based blends, which results in a reduced exciton dissociation efficiency and consequently lower PV performance.

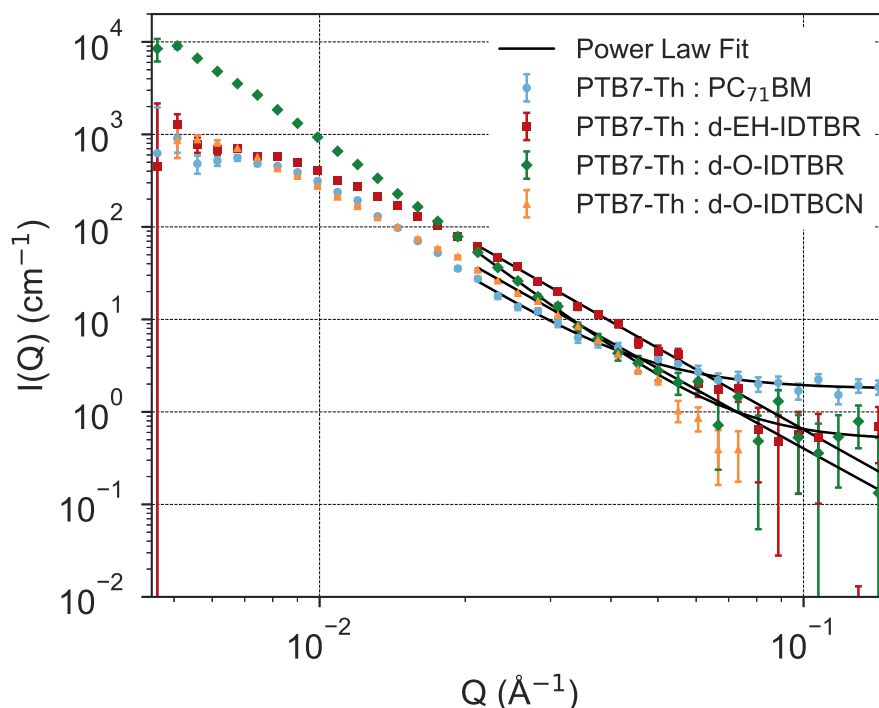


Figure 6.16: Power law fits in the interval $0.02 \leq Q$ (\AA^{-1}) ≤ 0.15 of PTB7-Th : PC₇₁BM, PTB7-Th : d-EH-IDTBR, PTB7-Th : d-O-IDTBR and PTB7-Th : d-O-IDTBCN blend films.

To investigate the interfacial area and purity of domains in each blend system, the SANS data were modelled using a simple power law model (Equation 3.9.5) to extract scattering exponent (α) values (Figure 6.17, Table 6.10). Here, it is worth remembering that a value of $\alpha = 4$ is representative of sharp domain boundaries, indicative of a system with a high degree of phase separation. Exponent values < 4 suggest that domain boundaries are diffuse, resulting in an increase in interfacial area. PTB7-Th : d-O-IDTBR blend films exhibit the highest scattering exponent of 3.68 which is in agreement with the aggregated surface morphology observed in AFM measurements. Similarly, PTB7-Th : PC₇₁BM systems are also characterised by a relatively high scattering exponent of 3.13 as expected by the appearance of well-defined surface domains in the AFM measurements discussed above. For PTB7-Th : d-EH-IDTBR and PTB7-Th : d-O-IDTBCN, the power law fits produce exponents of 2.91 and 2.86 respectively, indicative of a more finely intermixed morphology and larger interfacial area.

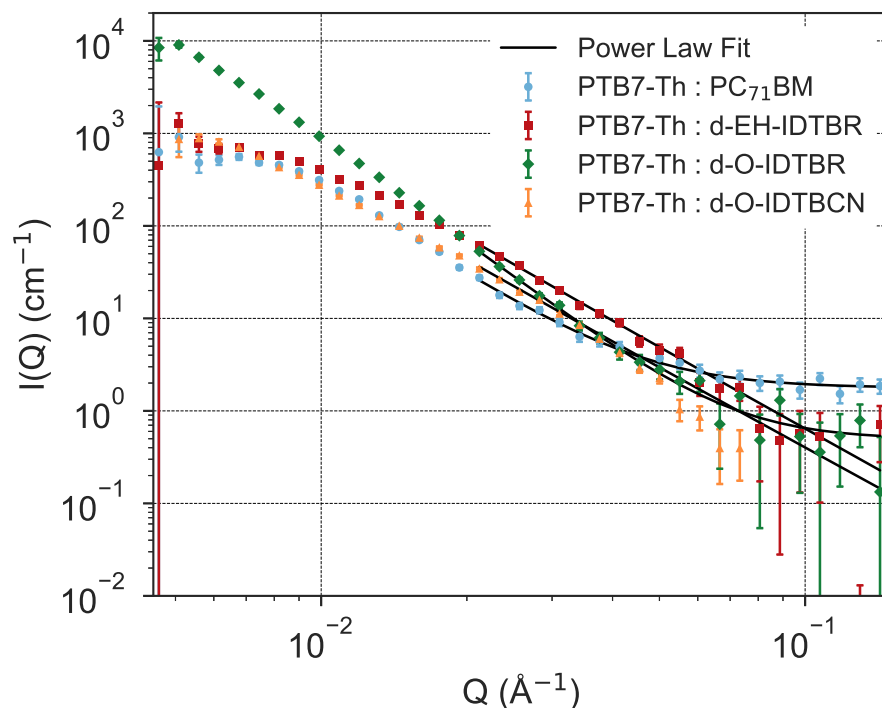


Figure 6.17: Power law fits in the interval $0.02 \leq Q \text{ (\AA}^{-1}\text{)} \leq 0.15$ of PTB7-Th : PC₇₁BM, PTB7-Th : d-EH-IDTBR, PTB7-Th : d-O-IDTBR and PTB7-Th : d-O-IDTBCN blend films.

Blend system	Lorentz Peak		DAB Model	Power Law
	Q (\AA^{-1})	L_p (nm)	ξ (nm)	α
PTB7-Th : PC₇₁BM	0.00676	92.9	13.61 ± 0.26	3.13 ± 0.17
PTB7-Th : d-EH-IDTBR	0.00888	70.8	8.90 ± 0.12	2.91 ± 0.08
PTB7-Th : d-O-IDTBR	–	–	29.67 ± 0.51	3.68 ± 0.12
PTB7-Th : d-O-IDTBCN	0.00907	69.3	10.95 ± 0.12	2.86 ± 0.06

Table 6.10: A summary of SANS fit parameters relating to the size and interfacial sharpness of domains. Long-period (L_p) values were extracted from the Lorentz-corrected scattering peaks in Figure 6.14 using Equation 3.64. Correlation lengths (ξ) are from the DAB fits in Figure 6.15. Scattering exponents (α) were extracted from the power law fits in Figure 6.17. Full fit parameters are provided in Section A.3.

6.6.4 Vertical Chemical Composition

The GIWAXS, AFM and SANS analysis discussed above of PTB7-Th based blend systems provides a detailed characterisation of the hierarchical structures present from the packing of individual molecules at the small scale to the phase separated domains they form on the larger scale. Another important morphological factor is the vertical distribution of domains in the plane perpendicular to the substrate. A build-up of donor or acceptor material at the top or bottom electrode interface can have a significant impact on the resulting device performance. For the device architecture implemented in this work, an accumulation of acceptor material at the active layer surface or donor material at the film/ZnO interface could inhibit free carrier transport and extraction. Comparatively, an accumulation of donor and acceptor materials in the opposite configuration (donor material at the surface, acceptor material at the film/ZnO interface), could potentially facilitate charge transport and extraction. For each of these scenarios, the impact of any enriched layer is related to its interfacial width and volume concentration [107, 303]. In many multi-phase thin film systems, vertical stratification of the component materials is often driven by differences in surface energy where the material with the lower surface energy segregates to the top of the film as it is more energetically favourable.

Before measuring the vertical composition profile of each blend using neutron reflectivity, the surface energies of each material were estimated using contact angle goniometry measurements. The water and hexadecane contact angles for each material are provided in the supplementary information (Subsection 6.9.3) and surface energies estimated using the Fowkes model (see Subsection 3.5.2) are summarised in Table 6.11. The surface energy of PTB7-Th is lower than the surface energies of the acceptor materials, indicating it is to be

expected that PTB7-Th might segregate to the surface of the film (Table 6.11).

Pure Material	Surface Energy (mN/m)		
	Dispersive	Polar	Total
PC₇₁BM	26.74	1.20	27.94
EH-IDTBR	26.93	1.36	28.29
O-IDTBR	26.73	1.05	27.77
O-IDTBCN	26.84	1.07	27.91
PTB7-Th	26.68	0.18	26.86

Table 6.11: Summary of surface energy values calculated using the Fowkes model (see Subsection 3.5.2) for pure PC₇₁BM, EH-IDTBR, O-IDTBR, O-IDTBCN and PTB7-Th films using the contact angle measurements shown in Subsection 6.9.3

To investigate this, NR measurements were performed to probe the chemical composition of the entire film thickness. As for the SANS measurements described above, deuterated NFAs (d-EH-IDTBR, d-O-IDTBR and d-O-IDTBCN) were again used to increase the SLD contrast with PTB7-Th in the blend. Before measuring the blend thin films, pure PC₇₁BM, d-EH-IDTBR, d-O-IDTBR, d-O-IDTBCN, PTB7-Th and ZnO films were first measured to extract SLD values for each material. NR data of the pure reference films and full fit parameters are provided in Section A.4.

The reflectivity curves of PTB7-Th : PC₇₁BM, PTB7-Th : d-EH-IDTBR, PTB7-Th : d-O-IDTBR and PTB7-Th : d-O-IDTBCN blend films on ZnO coated silicon substrates are displayed in Figure 6.18. In Figure 6.19, the SLD profiles corresponding to the modelled NR data are plotted as a function of OPV blend thickness such that the midpoints of the air/film interface and the film/ZnO interface are positioned at 0 and 1 respectively. Each blend film was modelled as a stack of Si/SiO₂/ZnO/OPV blend/Air where each layer in the sample represents a slab characterised by a thickness L , roughness σ and SLD β_n . For the OPV blend film, a single homogenous slab layer was insufficient to appropriately model the data. After trialling various models, an acceptor-rich layer was added at the film/ZnO interface to model all blend films. The fit parameters relating to the OPV blend layer are summarised in Table 6.12. Further information about the various trialled fitting models and full fitting parameters can be found in Section A.4.

For PTB7-Th : PC₇₁BM systems, the blend film is representative of a bilayer layer system with a 333nm thick PC₇₁BM-rich layer at the film/ZnO interface and a 314nm thick PTB7-

Th-rich layer at the film/air interface. Using Equation 3.62, the acceptor concentration by volume (ϕ_A) as a function of film depth was extracted from the SLD profiles (Figure 6.20). At the film/ZnO interface, the PC₇₁BM-rich layer has an SLD of $4.11 \times 10^{-6} \text{ \AA}^{-1}$ which corresponds to a composition of $\sim 85\%$ PC₇₁BM and $\sim 15\%$ PTB7-Th. For the surface layer, the acceptor and donor concentrations are more comparable with the fitted SLD value of $2.74 \times 10^{-6} \text{ \AA}^{-1}$ corresponding to a PC₇₁BM concentration of $\sim 45\%$ and PTB7-Th concentration of $\sim 55\%$. Although PC₇₁BM enrichment at the ZnO interface is likely to be beneficial for charge transport, the considerable thickness of the layer could be detrimental to the extraction pathway of electrons to the ETL. In addition to the smaller HOMO-LUMO offset, an interface which is too thick and enriched in a single component likely contributes to the lower V_{OC} values observed for PTB7-Th : PC₇₁BM devices (Table 6.4).

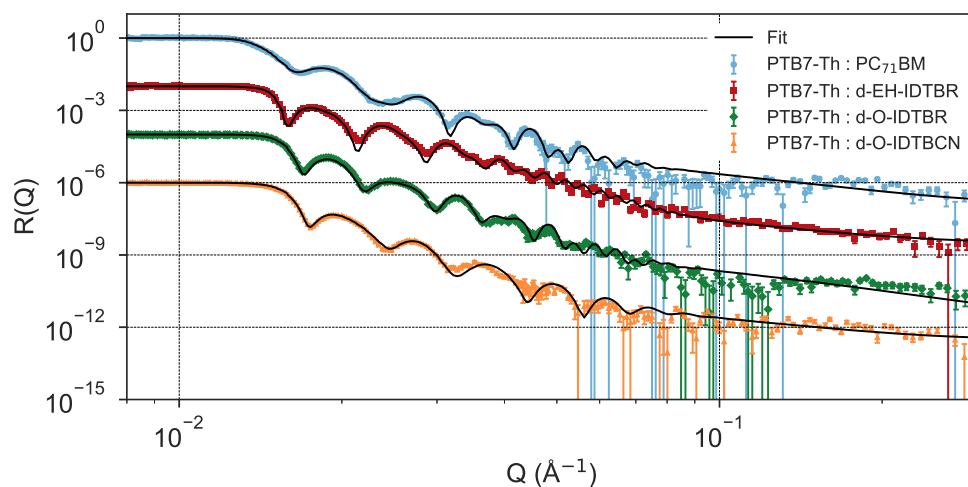


Figure 6.18: Neutron reflectivity of PTB7-Th blend thin films deposited on ZnO coated silicon substrates. Data has been offset by two decades for clarity.

From the SLD profiles, each PTB7-Th : NFA blend film consists of a thick bulk layer and a thinner NFA-rich layer at the film/ZnO interface (Figure 6.19). Similar interfacial segregation has been reported elsewhere for P3HT: O-IDTBR blends [330]. For PTB7-Th : d-EH-IDTBR and PTB7-Th : d-O-IDTBCN, the SLDs of the bulk layer correspond to similar NFA volume concentrations of 68% and 70% respectively which is close to the weight ratio of the dry materials in solution (D:A of 1:2.5). At the film/ZnO interface, the modelled SLD values of the NFA-rich layer corresponds to acceptor concentrations of $\sim 90\%$ and $\sim 79\%$ by volume for PTB7-Th : d-EH-IDTBR and PTB7-Th : d-O-IDTBR blend films respectively.

The SLD profile of the PTB7-Th : d-O-IDTBR blend film is notably different to the other NFA-based blends films. The film surface is significantly rougher with $\sigma = 75\text{\AA}$ in agreement with the AFM measurements discussed above (Table 6.9), and the model which produced the best fit consists of a bulk layer with a very broad NFA-rich interface at the film/ZnO interface. The SLD values of the bulk layer and NFA-rich buried interface correspond to d-O-IDTBR volume concentrations of $\sim 78\%$ and $\sim 99\%$ respectively. The higher acceptor concentrations at the film/ ZnO interface for EH-IDTBR and O-IDTBR based blend films likely contributes to the higher V_{OC} in device measurements (Table 6.4).

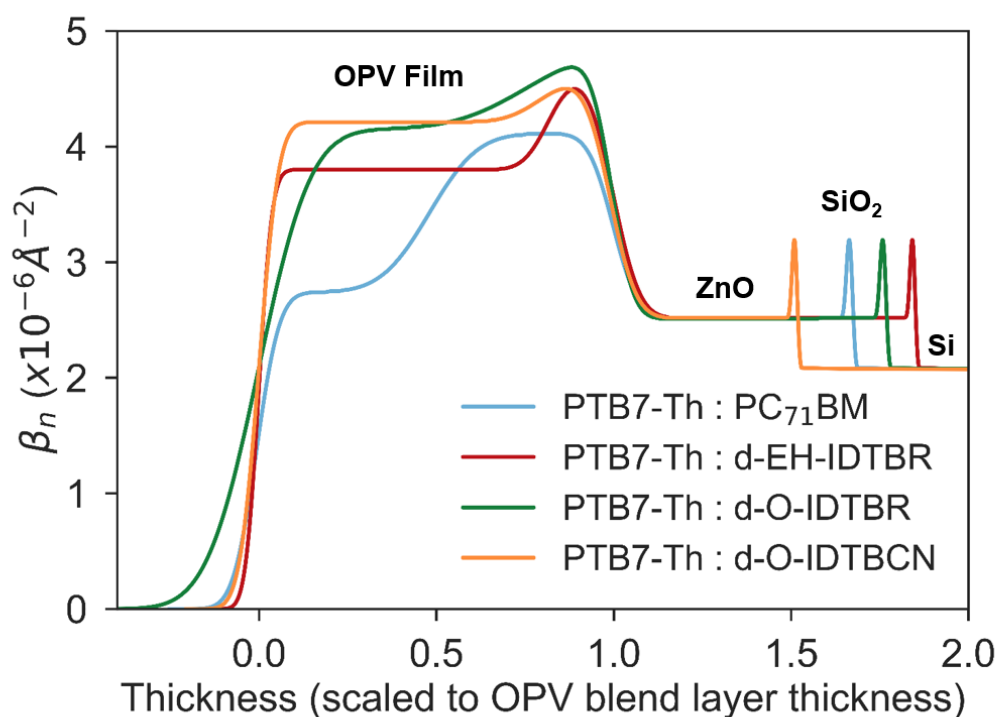


Figure 6.19: SLD profiles corresponding to the NR modelling shown in Figure 6.18 for PTB7-Th blend thin films deposited on ZnO coated silicon substrates. Thickness has been scaled to the thickness of the OPV blend film where 0 is midpoint of the air/film interface and 1 is the midpoint of the film/ZnO interface.

Sample	Bulk Layer			Interface Layer			χ^2/N_{pts}
	L (Å)	σ (Å)	β_n ($\times 10^{-6} \text{Å}^{-2}$)	L (Å)	σ (Å)	β_n ($\times 10^{-6} \text{Å}^{-2}$)	
PTB7-Th : PC₇₁BM	314	33	2.74	333	69	4.11	7.45
PTB7-Th : d-EH-IDTBR	629	23	3.80	141	43	4.64	9.47
PTB7-Th : d-O-IDTBR	491	75	4.15	155	104	4.86	6.78
PTB7-Th : d-O-IDTBCN	594	32	4.21	146	58	4.60	8.26

Table 6.12: Table of neutron reflectivity fit parameters corresponding to the reflectivity data shown in Section A.4 where each sample has been modelled with an acceptor-rich buried region at the film/ZnO interface.

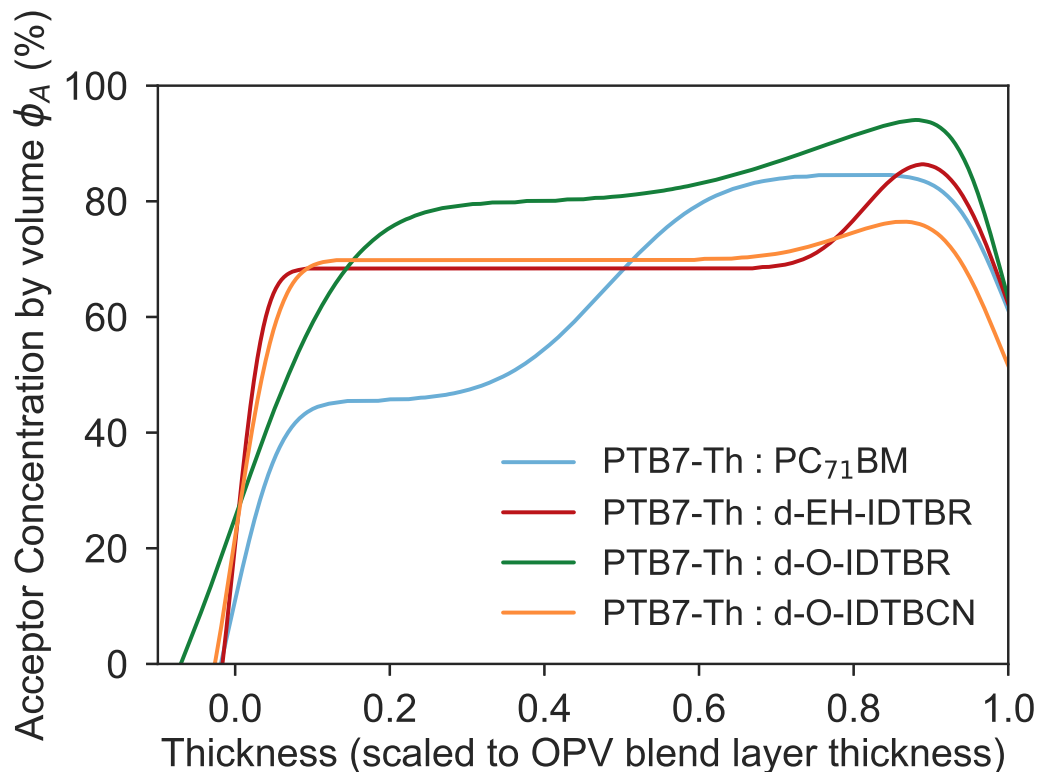


Figure 6.20: Acceptor concentration by volume as a function of film depth calculated from the SLD profiles shown in Figure 6.19 using Equation 3.62 for PTB7-Th based blend thin films. Thickness has been scaled to the thickness of the OPV blend film where 0 is midpoint of the air/film interface and 1 is the midpoint of the film/ZnO interface.

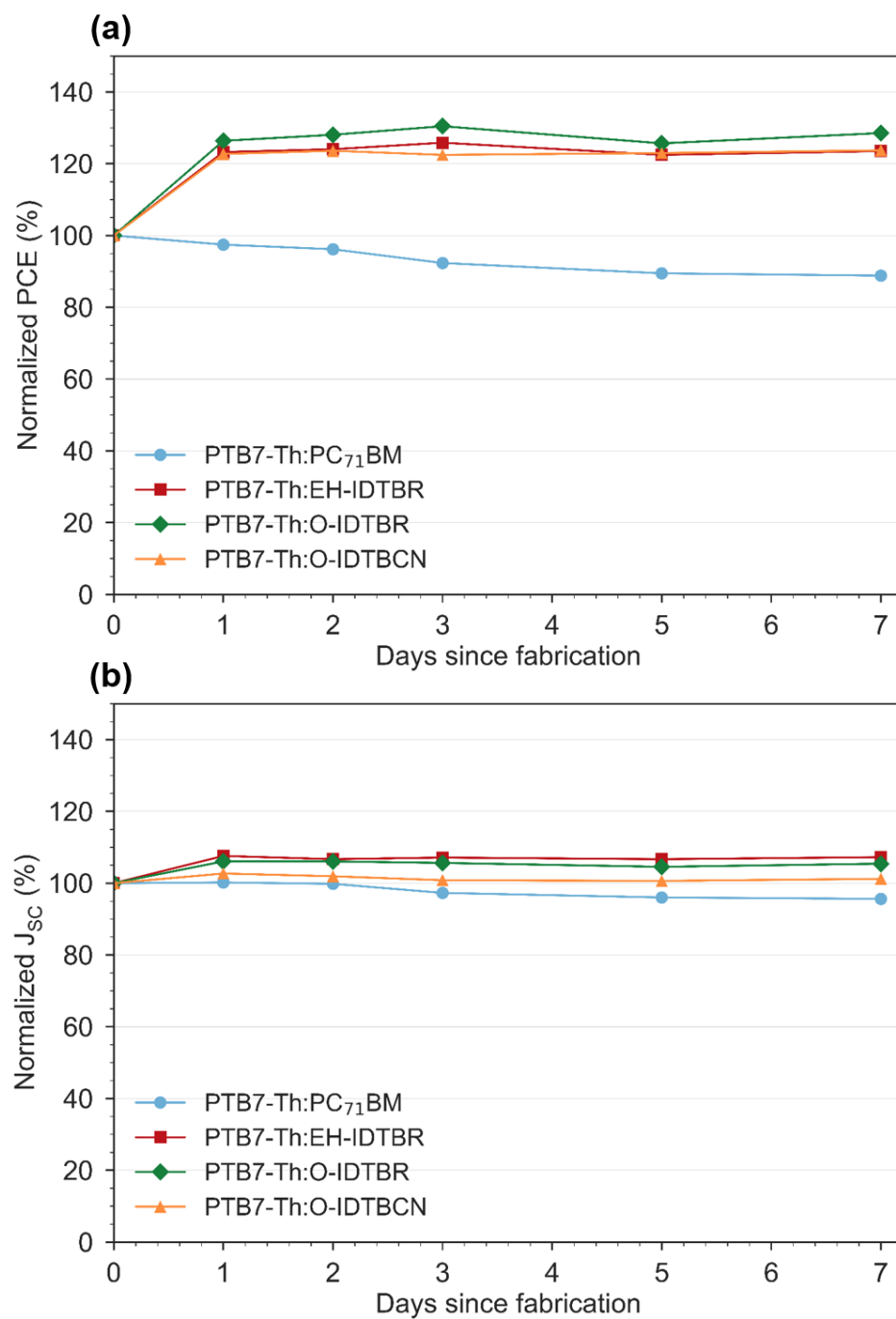
6.7 Device Stability

The device performance metrics of PTB7-Th based solar cells measured every 24h for a period of 1 week during constant exposure to 1 Sun irradiation in an inert atmosphere are displayed in Figure 6.21. Interestingly, the *PCE* of PTB7-Th : NFA devices increases substantially by a factor of 20-30% within the first day of ageing (Figure 6.21a). This is mostly driven by increases in *FF* (Figure 6.21d) and small increases in *J_{SC}* (Figure 6.21b). The *V_{OC}* of each PTB7-Th : NFA system remains largely unchanged after 1 week of ageing (Figure 6.21c).

In the case of PTB7-Th : PC₇₁BM devices, an extended burn-in period is observed during the first 3 days of ageing and after 1 week of exposure to 1 Sun irradiation, *PCE* is ~90% of its initial value (Figure 6.21a). Degradation mostly originates from small decreases in *J_{SC}* (Figure 6.21b) and *FF* (Figure 6.21c).

The differences in stability of PTB7-Th : PC₇₁BM and PTB7-Th : NFA blends are striking. For the PTB7-Th : NFA blends, similar *FF* driven *PCE* enhancements have been observed elsewhere for PTB7-Th : EH-IDTBR [128] and FTAZ : EH-IDTBR [114] OPV blend systems. Such increases in *FF* upon ageing have been linked to domain coarsening and stronger phase separation [115]. PTB7-Th : EH-IDTBR is considered to be a vitrified, hypo-miscible system (i.e. high interaction parameter χ) with a low diffusion coefficient [114]. It is therefore surprising that the *PCE* of each PTB7-Th : NFA system increases so significantly as it suggests they are not completely vitrified, exhibiting sufficient mobility to diffuse to thermodynamic equilibrium. Additionally, SANS measurements revealed that PTB7-Th : EH-IDTBR and PTB7-Th : O-IDTBCN blend films are more finely intermixed compared to PTB7-Th : O-IDTBR. However, given each system undergoes a comparable *PCE* enhancement during 1 Sun irradiation, changes are likely to be driven more by differences in thermal behaviour rather than miscibility in agreement with other results [128].

Further studies are required to fully understand the apparent morphological changes during ageing and other degradation factors should not be discounted. For example, PC₇₁BM is known to undergo UV-induced dimerization in inert conditions [331] and can undergo photochemical reactions which are detrimental to device performance [332].



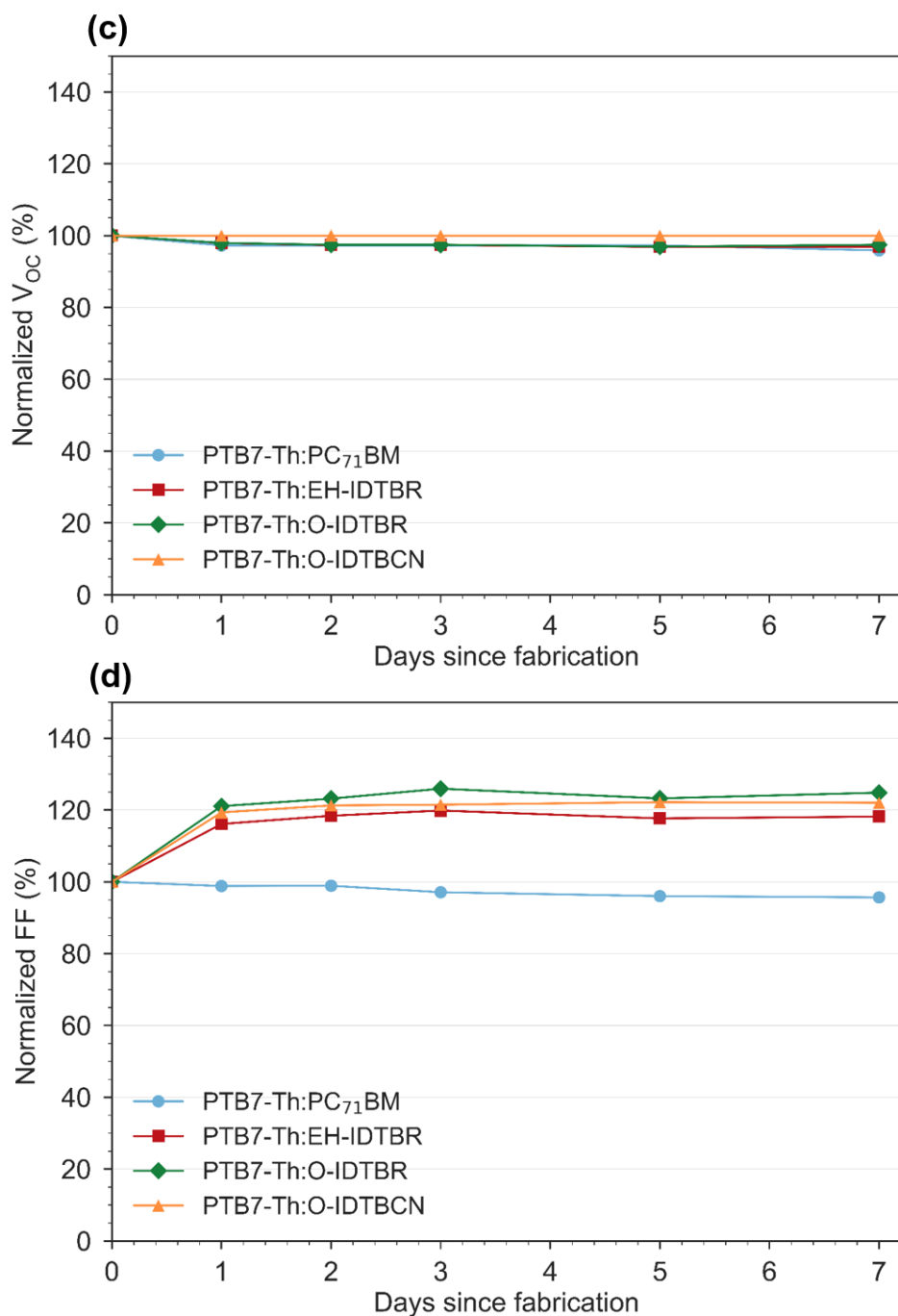


Figure 6.21: Normalised (a) PCE , (b) J_{SC} , (c) V_{OC} and (d) FF of PTB7-Th based devices aged in a nitrogen-filled glovebox under 1 Sun irradiation (light/ N_2 conditions) for 7 days.

6.8 Summary

In this chapter, the thermal properties, optoelectronic performance, film morphology and operational stability of PTB7-Th based blends incorporating various electron acceptors (PC₇₁BM, EH-IDTBR, O-IDTBR, O-IDTBCN) has been studied. The choice of NFAs allowed the impact of different side-chain and end-group chemical moieties to be investigated. Importantly, the synthesis of deuterated analogues of each NFA provided a way to use neutron scattering techniques (SANS and NR) to probe the full three-dimensional morphology of each blend system.

Taken together, the GIWAXS, AFM, SANS and NR measurements indicate distinct hierarchical morphologies for each PTB7-Th blend system. For PTB7-Th : PC₇₁BM systems, although the system exhibits a low degree of molecular order, films are composed of regular, phase-separated domains. PTB7-Th : EH-IDTBR and PTB7-Th : O-IDTBCN blend films are composed of small crystalline NFA domains, finely intermixed in a PTB7-Th matrix. For PTB7-Th : O-IDTBCN systems, the degree of intermixing is slightly enhanced. In comparison, PTB7-Th : O-IDTBR blend films are drastically different to all other systems. At the molecular level, the film is composed of highly ordered NFA domains, beneficial for efficient charge transport. However, characterising the larger length scales in the systems reveals a large phase-separated morphology with sharp interfaces and characteristic length scales much greater than the exciton diffusion length for IDTBR-type NFAs ($l_d \sim 15nm$, [29]). This likely contributes to the reduced J_{SC} and FF values observed in the J - V measurements of OPV devices (Table 6.4). NR measurements revealed that the vertical chemical composition of each blend film consists of an acceptor-rich region at the film/ZnO interface which is likely to impact electron extraction and consequently device V_{OC} .

Tracking device performance during 1 Sun irradiance in inert conditions revealed PTB7-Th : NFA systems exhibit superior stability compared to PTB7-Th : PC₇₁BM blends. For PTB7-Th : NFA systems, device PCE increased by ~ 20 - 30% during the first day of ageing due to FF driven enhancements. Previous studies have linked increases in FF to an increase in domain purity and a higher degree of phase separation. To further understand this, more detailed morphological measurements (e.g. SANS of fresh and aged films) should be carried out to probe changes in the three-dimensional film nanomorphology during ageing. Understanding these intricate morphological changes are crucial to developing more stable material systems suitable for commercialisation.

6.9 Supplementary Data

6.9.1 AFM studies at an annealing temperature of 200°C

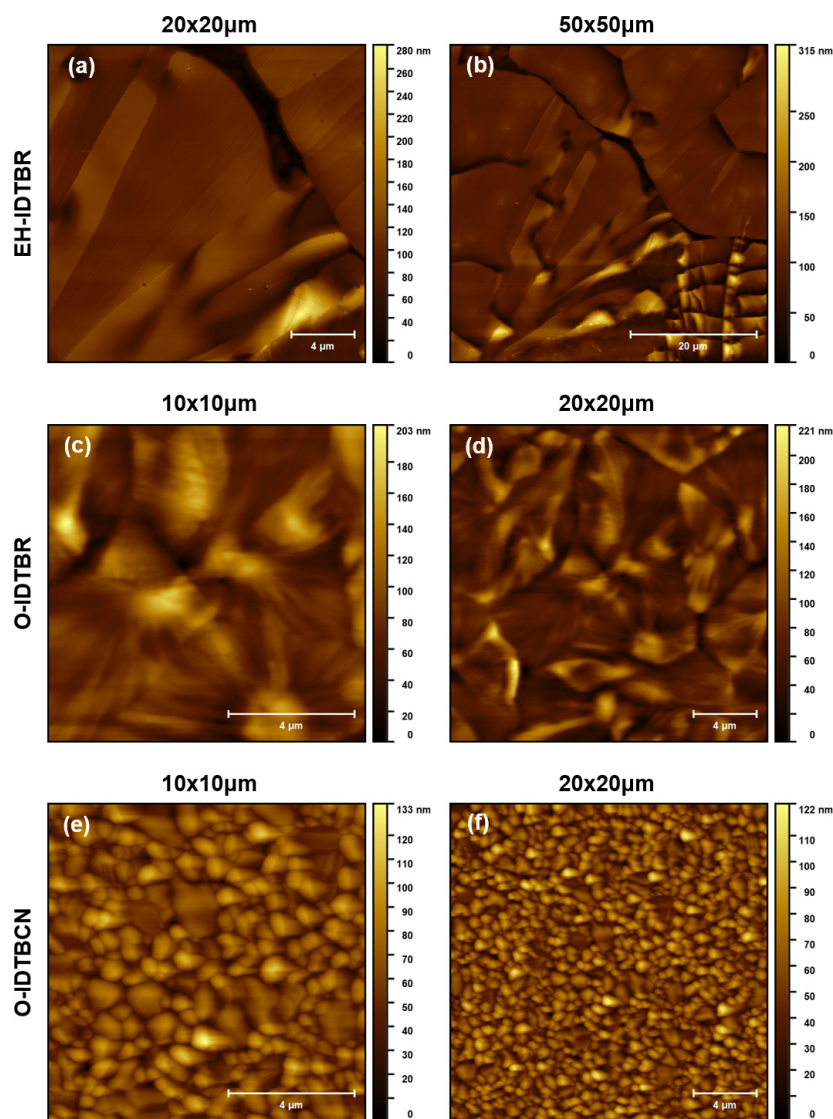


Figure 6.22: AFM measurements of EH-IDTBR, O-IDTBR and O-IDTBCN annealed at 200°C for 10 minutes. Measurements were taken at scan sizes of either 10x10 μm , 20x20 μm or 50x50 μm depending on the lateral size of film features. The lateral scale bar is 20 μm for 50x50 μm scans and 4 μm for all other measurements.

6.9.2 Optical Microscopy

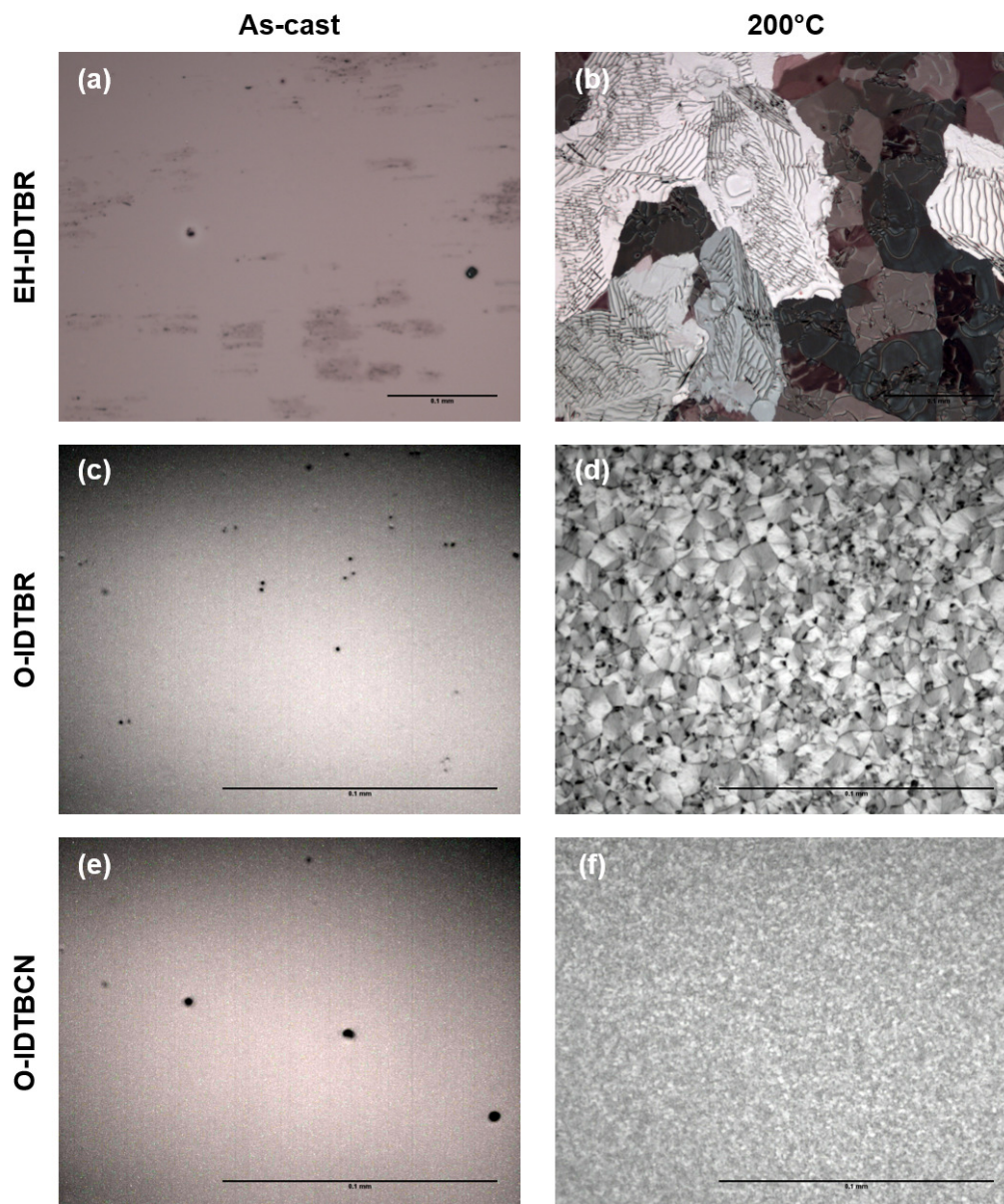


Figure 6.23: Optical microscopy images of EH-IDTBR, O-IDTBR and O-IDTBCN films imaged as-cast and after thermal annealing at 200°C for 10 minutes. EH-IDTBR images were at magnification of $\times 20$. O-IDTBR and O-IDTBCN were at a magnification of $\times 50$. The lateral scale bar for all images is 0.1mm.

6.9.3 Contact Angle Goniometry of Pure Materials

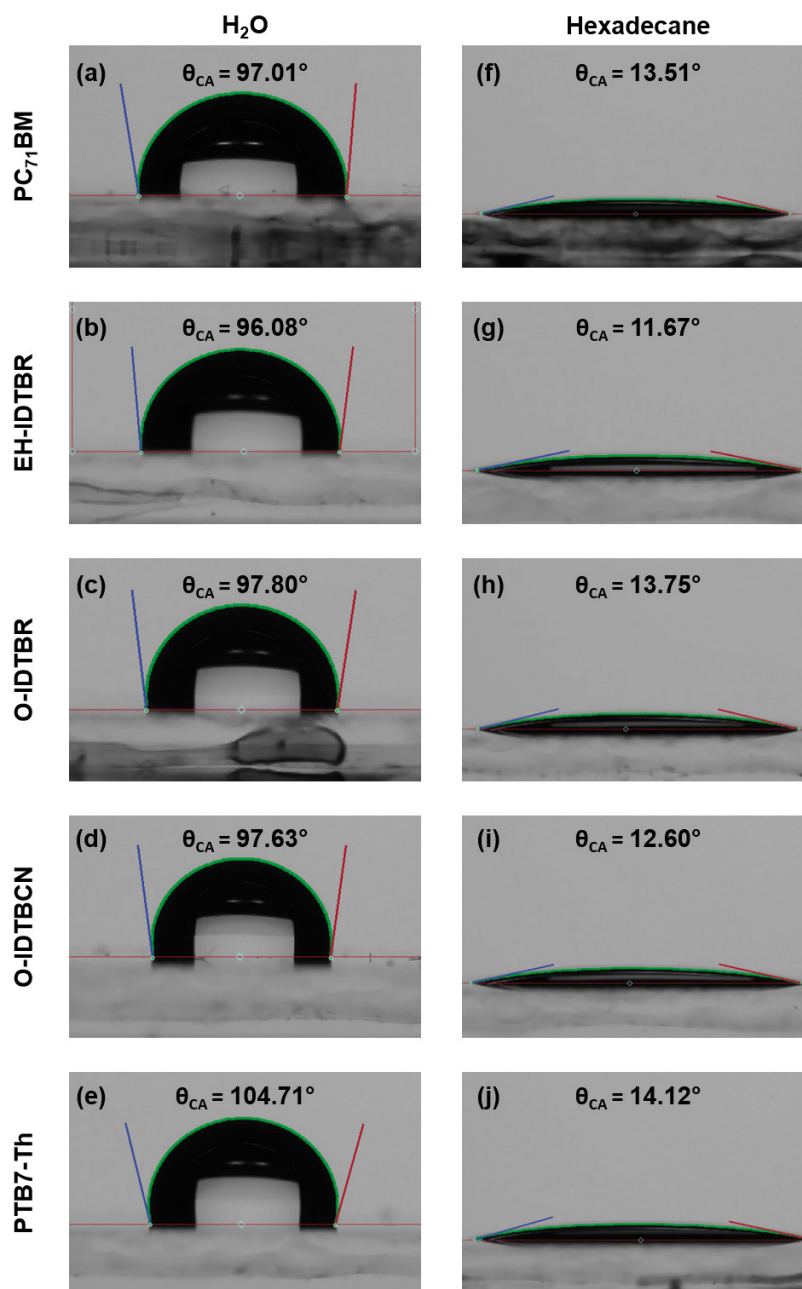


Figure 6.24: Measured contact angles of a water droplet (a-e) and a hexadecane droplet (f-j) on the surface of pure reference films.

Controlling Anisotropic Properties Through Manipulation of Chiral Small Molecule Orientation in the Bulk

7.1 Foreword

The chiroptical properties of chiral π -conjugated molecular systems such as the absorption and emission of circularly polarised light or transport of spin-polarised electrons are highly anisotropic. Consequently, the performance of chiral-based optoelectronic devices strongly depends on the molecular packing and orientation of the chiral molecule within the thin film. In this chapter I will detail a novel approach to control the molecular self-assembly of a chiral small molecule (2,2'-dicyano[6]helicene, **CN6H**) in thin films using both organic and inorganic structural templating layers. Specifically, I investigate the impact of two templating layers, 3,4,9,10-perylenetetracarboxylic dianhydride (PTCDA) and copper(I) iodide (CuI) where the structural templating arises from π - π interactions for PTCDA and dipole-dipole interactions for CuI. GIWAXS measurements reveal that these driving forces induce **CN6H** supramolecular columns to adopt a face-on, upright orientation on PTCDA and an edge-on, flat-lying orientation on CuI. Given the highly anisotropic crystal structure of **CN6H**, such significant changes in molecular orientation have a profound impact on the chiroptical response. The templating methodologies described here open material engineering routes to control the orientation and functional properties of chiral small molecules. The detailed structural characterisation performed also highlights the level of insight achievable for such systems. The findings will be beneficial to a range of emerging chiroptical technologies and will contribute to an exciting, rapidly expanding area of research on chiroptical functionality.

7.2 Author Contributions

The work in this chapter forms part of a manuscript currently in preparation in collaboration with Imperial College London. My contribution to this work includes performing, analysing and interpreting the GIWAXS measurements, 2D GIWAXS simulations and PXRD simulations. 2D GIWAXS simulations were done with the assistance of Joel A. Smith at The University of Oxford. All authors have contributed to writing and proof-reading the manuscript. Sample preparation and all other characterisation measurements and simulations were performed by collaborators at Imperial College London, Osaka Uni-

versity and Dalhousie University. The most recent author list can be found in Section 0.5. Here, the manuscript has been adapted into the style of a thesis chapter with emphasis on my own individual contribution.

7.3 Introduction

Chapter 4, Chapter 5 and Chapter 6 focused on characterising the self-assembly of π -conjugated materials for OPV systems and correlating structural properties with optoelectronic functionality and stability. Conjugated organic thin films have a number of desirable characteristics because they are inexpensive, have tuneable optoelectronic properties and are compatible with large-area, flexible device architectures. As a result, their use is not confined to OPV and their processing properties are beneficial to a broad range of organic electronic device applications. Such applications typically require the fabrication of an organic thin film in which the self-assembly of the molecular constituents has a significant impact on the performance and efficiency of the electronic device. Here, the molecular assembly and orientation of chiral small molecules in thin films with respect to device-relevant interfaces is explored and correlated with chiroptical properties. Exploiting molecular chirality is an emerging strategy to expand the functionality of organic electronic devices, enabling the fabrication of next-generation displays, polarisation selective photodetectors, enantioselective biosensors and room-temperature spintronic devices [333, 334, 335, 336, 337, 338].

In chemistry, a molecule is said to be *chiral* or possess *molecular chirality* if it cannot be superimposed onto its mirror image by any form of rotation or translation. The chiral molecule and its mirror image exist as distinguishable *enantiomers*. Molecular chirality in organic electronics typically focuses on the archetypal class of molecules called *helicenes* which are composed of $n \geq 5$ *ortho*-fused angularly arranged benzene rings in a helical, non-planar scaffold [339]. The intrinsic chirality and conjugated nature of helicene molecules result in impressive chiroptical and charge transport properties that are highly anisotropic [340, 341, 342, 343, 344, 345, 346]. These structure-property relationships are yet to be fully understood. However, it is clear that the alignment of the helical molecular axis and corresponding supramolecular assembly relative to other interfaces has a significant impact on the chiroptical response. For example, monolayers of chiral molecules have been shown to act as efficient spin filters, preferentially transmitting electrons with a specific spin orientation known as the chiral induced spin selectivity (CISS) effect [347]. In devices which make use of the CISS effect, the orientation of the chiral molecule with respect to the charge injection electrodes dictates the spin polarisation of the transmitted electrons [348]. Additionally, chiral cholesteric liquid crystalline materials have been incorporated into photonic devices where the thickness, pitch and orientation of the helical assembly

determines the chiroptical properties through Bragg reflection and scattering [349, 350]. In these systems, liquid crystalline alignment layers such as rubbed polyimide are required to guide the growth of an ordered chiral structure [351, 352, 353]. Although there is a clear relationship between molecular orientation and the optoelectronic properties of chiral thin films, effective control of molecular orientation with respect to the substrate remains challenging. This is particularly true in films which do not exhibit liquid crystalline behaviour or involve monolayer self-assembly on conductive surfaces [354, 355, 356, 357, 340, 343]. Strategies to control chiral molecule orientation, particularly in bulk helicene-based thin films are yet to be established.

The molecular order and orientation of a terminally functionalised helicene molecule (2,2'-dicyano[6]helicene, **CN6H**) was investigated using the structural characterisation techniques implemented in previous chapters, namely GIWAXS and AFM. In Figure 7.1a,b, the chemical structures of both **CN6H** enantiomers are displayed, denoted [*P*] and [*M*] as is the convention for helical molecules where [*P*] (plus) is a right-handed helix and [*M*] (minus) is a left-handed helix. Films of **CN6H** can be prepared in the enantiopure state consisting of a pure film of either [*P*] or [*M*] enantiomers, or from a racemic mixture composed of an equal blend of each enantiomer. A novel approach to control **CN6H** molecular orientation uses both organic (3,4,9,10-perylenetetracarboxylic dianhydride, PTCDA) and inorganic (copper(I) iodide (1 1 1), CuI) structural templating layers (Figure 7.1c and Figure 7.1d respectively). The use of templating layers to control molecular orientation has been demonstrated previously for aromatic systems with molecules typically adopting an edge-on or face-on orientation [358, 359, 360] (Figure 7.1e). Here their use was extended to control the orientation of chiral π -conjugated small molecules. It was found that the use of PTCDA and CuI templating layers had a significant impact on the molecular orientation of **CN6H** with helices either adopting an upright, face-on orientation for the case of PTCDA or a flat-lying edge-on orientation for CuI. Such drastic changes in molecular orientation had a profound influence on the chiroptical response with templated **CN6H** exhibiting intense circular dichroism (CD) that was dependent on the orientation of the **CN6H** helical axis. Edge-on oriented **CN6H** demonstrates intense CD for electronic transitions polarised parallel to the helical axis whereas face-on orientated **CN6H** demonstrates strong CD transitions for transitions polarised perpendicular. This elegant approach to control the orientation of chiral π -conjugated molecules can be easily transferred to device fabrication protocols for a range of next-generation technologies.

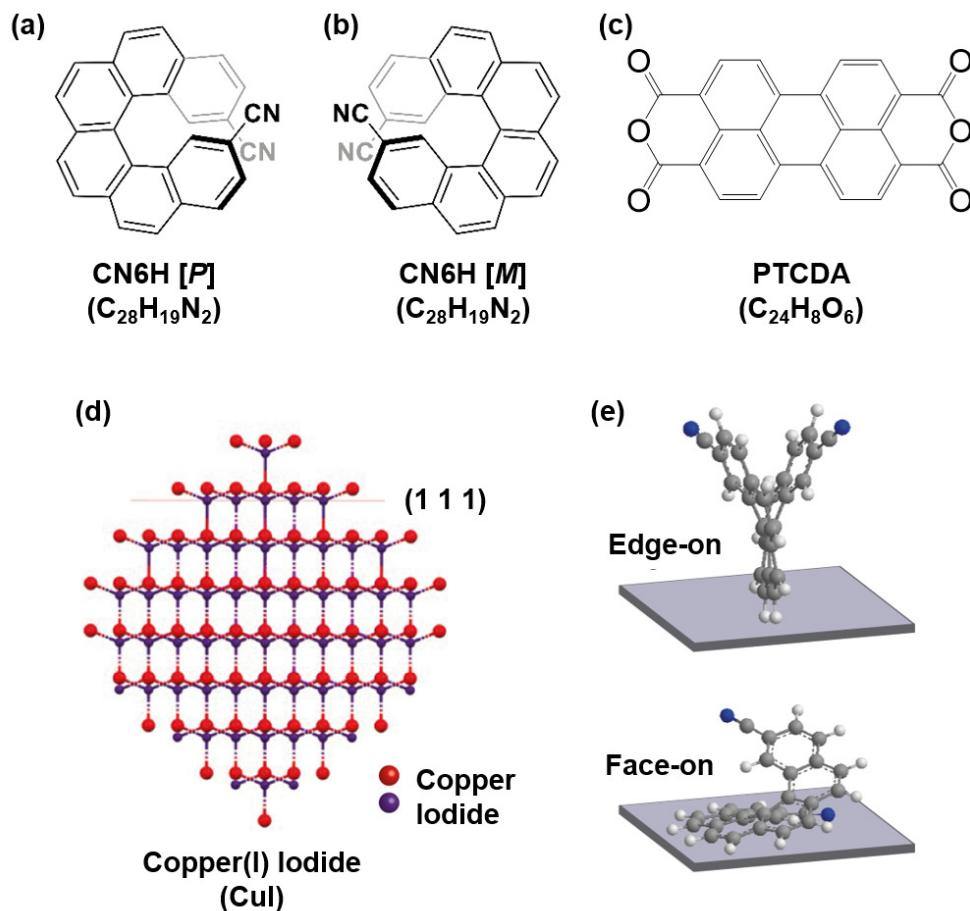


Figure 7.1: Chemical structures of (a) the *[P]* and *[M]* enantiomers of 2,2'-dicyano[6]helicene (CN6H) and the structural templating layers (c) 3,4,9,10-perylenetetracarboxylic dianhydride (PTCDA) and (d) copper(I) iodide (CuI). The edge-on and face-on orientations of CN6H with respect to the substrate are illustrated in (e).

7.4 Experimental

7.4.1 Sample Preparation

Samples were prepared at Imperial College London and measured as received in Sheffield. Each thin film of PTCDA, CuI (111) and CN6H, were grown by Organic Molecular Beam Deposition (OMBD) (Kurt J. Lesker Spectros 100 system) following previously reported optimisation protocols [359]. OMBD involves the evaporation of powdered materials for the

fabrication of reproducible, ultra-uniform, high-purity organic thin films. This technique is particularly applicable for materials which are difficult to dissolve or for samples composed of several complex layers. PTCDA and **CN6H** films were deposited at room temperature and CuI films were grown at 100°C to promote the growth of large grains and provide films that are pinhole free.

7.4.2 Crystal Structure Simulations

Crystal structure prediction was performed using the CrystalPredictorII [361, 362]/DMACRYS [363] workflow. The tentative crystal structures were subsequently relaxed at the B86bPBE/DZP level with exchange-hole dipole moment (XDM) dispersion correction [364] and using the projector augmented-wave (PAW) [365] method. PXRD simulations and crystal packing images were simulated in VESTA using the previously reported CIF [366].

7.4.3 GIWAXS and AFM

GIWAXS measurements and simulations were performed following procedures discussed in Chapter 3. All 2D simulations were performed using the *simDiffraction* Matlab toolbox [213] and implemented a uniaxial model with a pseudo-Voight (PSV) distribution in the out-of-plane direction. AFM surface characterisation was carried out in tapping mode following the same procedures described in Chapter 3 using an Asylum Research MFP-3D microscope. Roughness values were extracted using the open-source software Gwyddion with the standard deviation of three separate images quoted as the error. Lateral grain sizes were calculated using a watershed to define grain boundaries.

7.4.4 Circular Dichroism Measurements

Circular dichroism (CD) spectra were collected using a Chirascan (Applied Photophysics) instrument.

7.5 Results and Discussion

7.5.1 CN6H Crystal Structure

The bulk packing of helicenes is often complex. For this study, a helicene molecule with a well-defined crystal packing structure was required so that any control of molecular orientation could be characterised and effectively understood. **CN6H** was identified through the Cambridge Structural Database as a suitable candidate with a well-documented crystal packing (CSD reference: UJOCOL)[366]. **CN6H** is a member of the $P6_122$ (178) crystallographic space group, crystallising in the solid-state with highly anisotropic, supramolecular

columns with a uniaxial hexagonal unit cell (Figure 7.2). The hexagonal unit cell lattice parameters are $a = 9.736\text{\AA}$, $b = 9.736\text{\AA}$, $c = 70.731\text{\AA}$, $\alpha = 90^\circ$, $\beta = 90^\circ$, $\gamma = 120^\circ$ and volume $V = 5806.3282\text{\AA}^3$. The extended c -axis makes **CN6H** particularly anisotropic which suggests any changes in molecular orientation will have a strong influence on the chiroptical properties. The supramolecular columns are homochiral, possessing the same handedness as the enantiopure molecule and they are assembled such that the helical axis is orientated along the c -axis. Each helical supramolecular column is composed of helicene molecules interlocked through face-to-face π - π interactions between adjacent aromatic units with neighbouring ring centres separated by an average spacing of 3.75\AA [366].

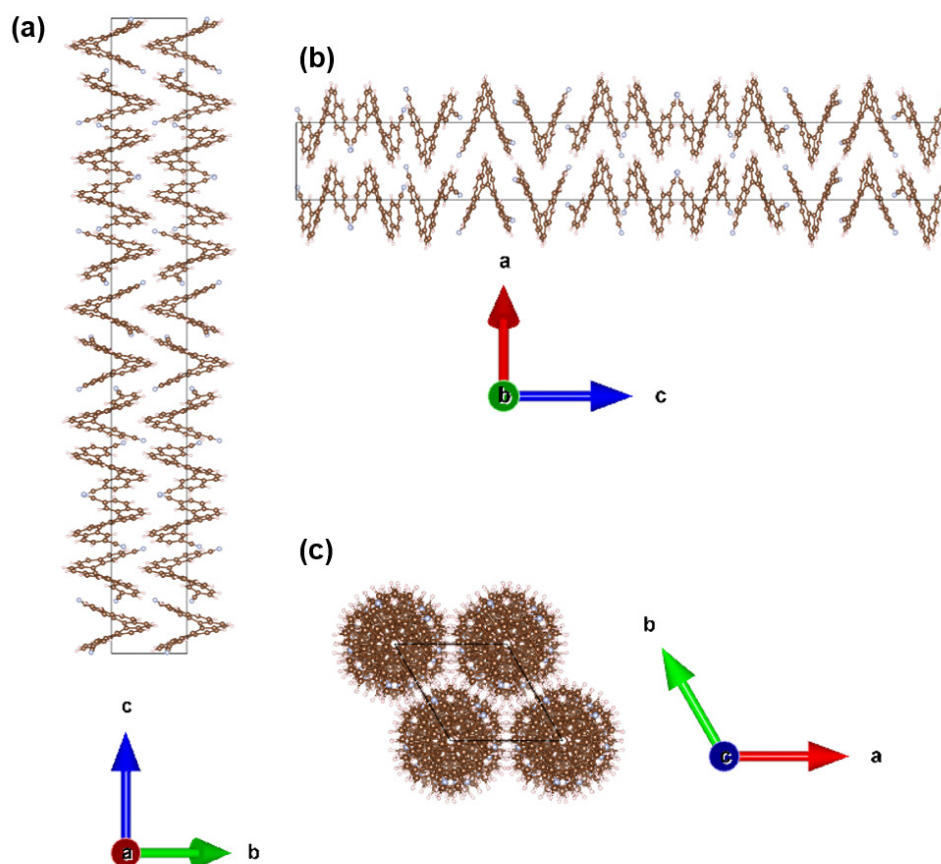


Figure 7.2: Illustrations of the reported **CN6H** single crystal structure [366] extracted from VESTA. The crystal packing from different viewpoints is displayed with the (a) a , (b) b and (c) c crystallographic axes aligned parallel to the line of sight.

A crystal structure prediction (CSP) search was performed to evaluate how the potential crystal packing in a thin film geometry differs to the experimentally observed bulk crystal structure (i.e. polymorphism). In Figure 7.3 the crystal-energy landscape for each polymorph from the CSP search is displayed as a function of mass density. The search found a number of potential racemic and enantiopure crystal structures some of which undergo columnar packing. It also revealed that the experimentally observed $P6_122$ (178) polymorph is the most thermodynamically stable with an energy 3.3 kJ mol^{-1} lower than all other potential polymorphs. Interestingly, it was also the only polymorph which undergoes homochiral columnar packing with all other polymorphs assembling into heterochiral structures.

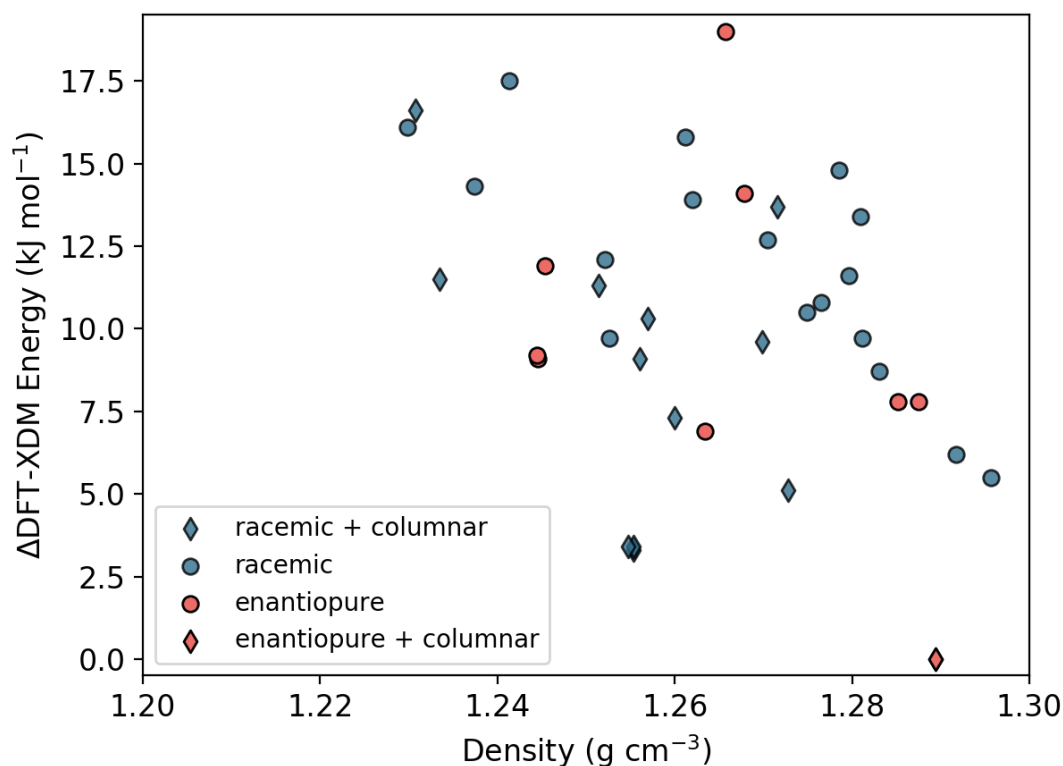


Figure 7.3: Crystal-energy landscape of the lowest lying polymorphs from the **CN6H** CSP search and relaxed at density functional theory - XDM (DFT-XDM) level of theory. Racemic polymorphs are shown in blue whilst enantiopure polymorphs are shown in red. If the polymorph contains columnar packing, a diamond shape is used. If it does not, a circular shape is used. The experimentally observed $P6_122$ (178) polymorph (red diamond- lower right) is the only polymorph which exhibits homochiral columnar packing.

This helical solid-state packing is uncommon for helicenes and supramolecular self-assembly typically requires more complex approaches such as chemical derivatization involving dipole moments and/ or alkyl chains. Before probing the thin film molecular orientation of **CN6H** using GIWAXS measurements, the single crystal structure was first simulated to identify the positions of the individual lattice planes in reciprocal space. Here, 1D PXRD simulations were performed in VESTA using the previously reported CIF [366] (Figure 7.4). The miller indices (hkl), d -spacings and relative intensities of the highest intensity reflections are displayed in Table 7.1. For the most prominent reflections, the alignment of the corresponding lattice planes for face-on and edge-on orientated **CN6H** is illustrated in Figure 7.5.

In GIWAXS measurements, lattice planes that are aligned perpendicular to the substrate produce in-plane scattering (Q_{xy} direction) and lattice planes that are aligned parallel to the substrate scatter out-of-plane (Q_z direction). The PXRD simulation and lattice plane illustration therefore provides an initial indication of the expected reciprocal scattering positions of each lattice plane for face-on and edge-on oriented **CN6H**. For example, in a face-on arrangement of supramolecular columns, the (1 0 0) plane is orthogonal to the substrate so in-plane scattering is expected and the (0 0 6) and (1 0 17) lattice planes are expected to scatter out-of-plane because they are aligned either parallel or *almost* parallel to the substrate. Similarly, in an edge-on **CN6H** arrangement, the opposite is true. The (1 0 0) plane would be aligned parallel to the substrate resulting in out-of-plane scattering and the (0 0 6) and (1 0 17) lattice planes would scatter in-plane as they are aligned either perpendicular or *almost* perpendicular to the substrate.

h	k	l	d (Å)	2θ (°)	Q (Å ⁻¹)	Normalised Intensity	Multiplicity
1	0	17	3.731109	23.82907	1.683992	100	12
1	0	0	8.431623	10.48348	0.74519	67.62944	6
1	0	5	7.242698	12.21047	0.867516	36.28711	12
1	0	22	3.004065	29.71525	2.091551	13.08895	12
1	1	0	4.868	18.20913	1.290706	3.95533	6
0	0	6	11.7885	7.4931	0.53299	3.30109	2

Table 7.1: Table of the highest intensity reflections from the simulated PXRD data shown in Figure 7.4.

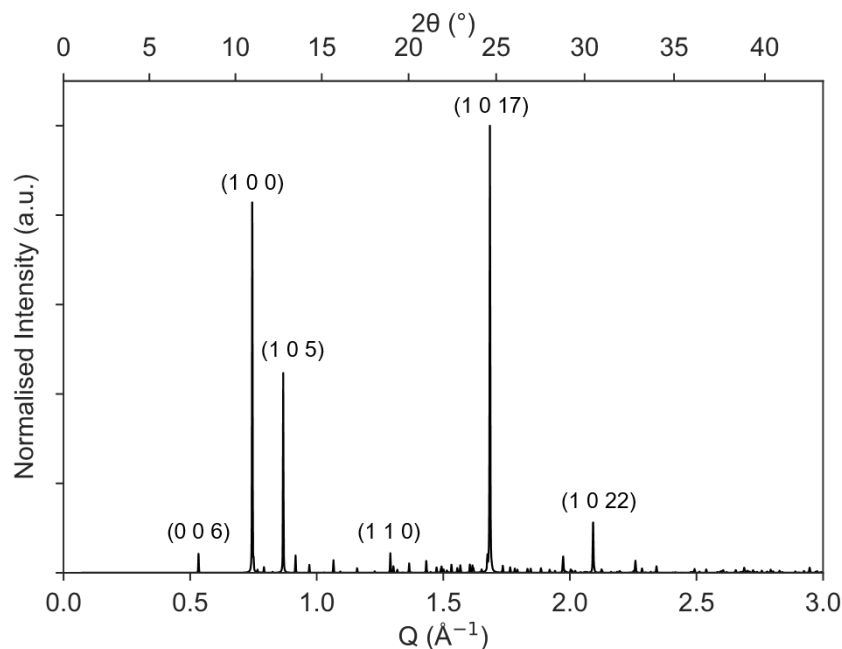


Figure 7.4: PXRD simulation of **CN6H** crystal structure [366]. Intensities are normalised to the highest intensity reflection and the miller indices (hkl) of the most prominent scattering reflections are labelled.

7.5.2 Probing Molecular Orientation Using GIWAXS

The simulated PXRD analysis of the single crystal structure of **CN6H** discussed above and the illustration shown in Figure 7.5 provided a preliminary insight into the expected prominent reflections and their orientation with respect to the substrate. Next, GIWAXS measurements were performed to experimentally determine the crystallographic orientation of **CN6H** thin films deposited on the structural templating layers PTCDA and CuI. The lack of polymorphism and previously reported CIF [366] also allowed the 2D GIWAXS patterns to be replicated in simulations using the *simDiffraction* Matlab toolbox as discussed in Subsection 3.9.7.

Background measurements of the bare substrates were performed first to identify any prominent scattering features. The 2D GIWAXS patterns and corresponding Q -dependent intensity profiles in the out-of-plane and in-plane directions for silicon, PTCDA and CuI are presented in Figure 7.6. Silicon and CuI display no prominent scattering features in the observable Q -range. For PTCDA, two in-plane peaks are visible at $Q = 0.65\text{\AA}^{-1}$ and $Q = 0.88\text{\AA}^{-1}$, as well as two out-of-plane peaks at $Q = 1.76\text{\AA}^{-1}$ and $Q = 1.95\text{\AA}^{-1}$.

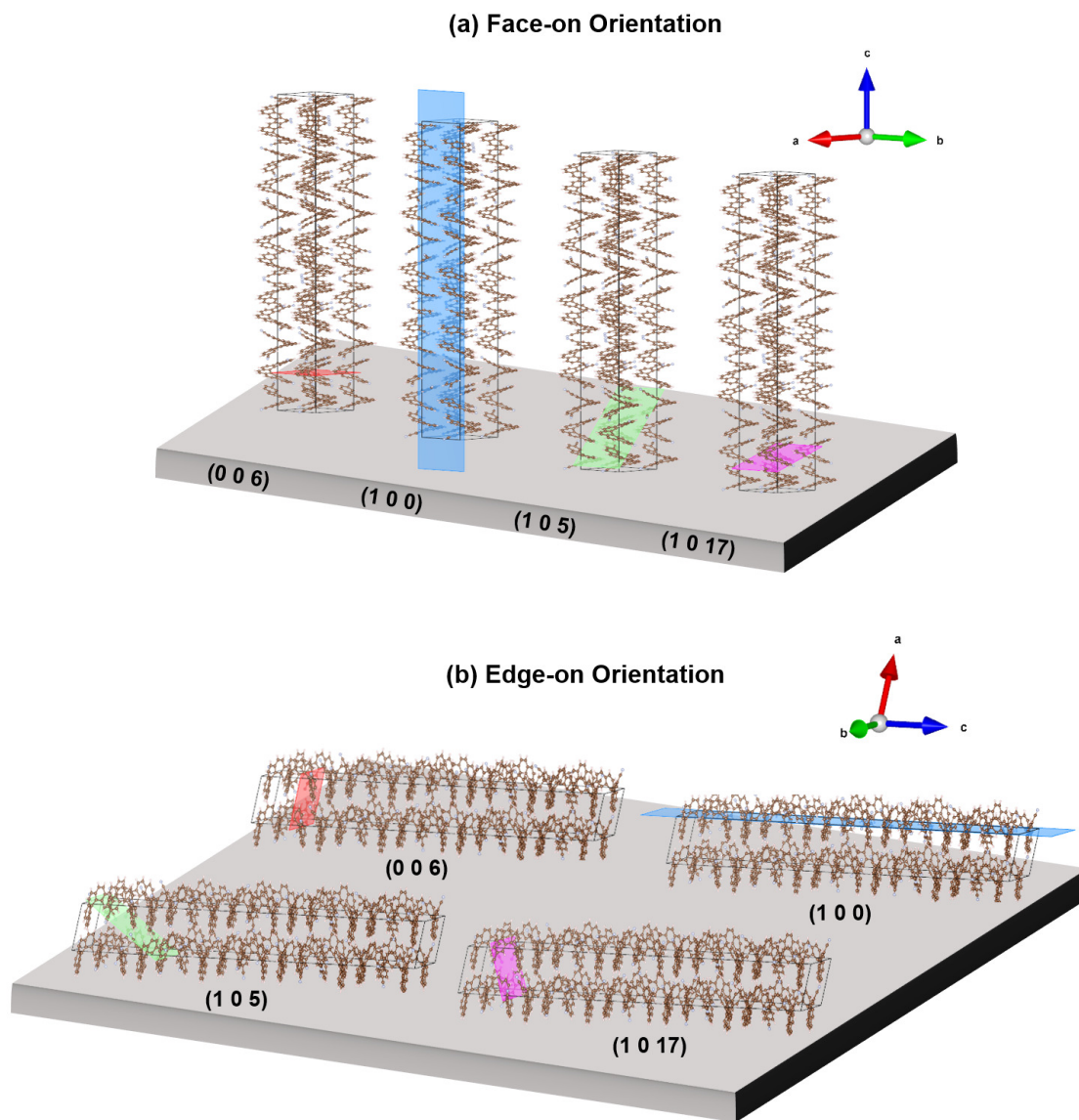


Figure 7.5: Illustration of the $(0\ 0\ 6)$, $(1\ 0\ 0)$, $(1\ 0\ 5)$ and $(1\ 0\ 17)$ lattice planes in (a) face-on and (b) edge-on oriented CN6H supramolecular columns.

Previous studies have reported the existence of two crystalline PTCDA polymorphs which exhibit herringbone-like structures [367]. The GIWAXS peaks observed for PTCDA in this work (Figure 7.6b) are consistent with the previously reported α -crystalline structure in the monoclinic $P2_1/c$ space group. In a thin film, PTCDA molecules adopt a flat-lying orientation with the planar conjugated core aligned parallel to the substrate. The out-of-plane peak at $Q = 1.95\text{\AA}^{-1}$ arises from π - π stacking between adjacent molecules separated by an intermolecular spacing of $d = 3.22\text{\AA}$ in agreement with previous studies [358].

The 2D GIWAXS patterns of untemplated and templated **CN6H** [*M*] and **CN6H** [*P*] and corresponding 2D simulations are shown in Figure 7.7 and Figure 7.8 respectively. To index scattering features, the in-plane and out-of-plane Q -dependent intensity profiles are compared with the simulated PXRD 1D intensity profile discussed previously and prominent peaks are labelled with their respective miller indices (Figure 7.9). It is apparent from the 2D GIWAXS patterns that the choice of templating layer has a significant impact on the molecular packing of **CN6H**. The 2D GIWAXS pattern of **CN6H** on bare silicon (Figure 7.7a and Figure 7.8a) consist of a number of weak intensity Debye-Scherrer rings with the highest intensities originating from the (1 0 0), (1 0 5) and (1 0 17) lattice planes at Q values of 0.76\AA^{-1} , 0.88\AA^{-1} and 1.68\AA^{-1} respectively. The appearance of complete diffraction rings indicates a low degree of molecular order and an almost randomly oriented arrangement of **CN6H**. Although both **CN6H** [*M*] and **CN6H** [*P*] films on bare silicon exhibit a disordered arrangement of **CN6H** helices, the (100) reflection for **CN6H** [*P*] has a stronger out-of-plane intensity compared to **CN6H** [*M*]. In contrast, the (1 0 17) reflection for **CN6H** [*M*] has a stronger out-of-plane intensity compared to **CN6H** [*P*]. As a result, the 2D simulations of **CN6H** [*M*] and **CN6H** [*P*] are replicated by simulating 2D GIWAXS patterns as a very broad distribution that is primarily orientated with the (1 0 17) and (1 0 0) planes parallel to the substrate respectively (Figure 7.7d and Figure 7.8d). The 2D simulation parameters are provided in Table 7.2. Differences in the scattering patterns of **CN6H** [*M*] and **CN6H** [*P*] films on non-interacting, bare silicon surfaces are attributed to sample-to-sample variation and both films exhibit a high degree of disorder with multiple **CN6H** orientations.

For PTCDA templated **CN6H**, the increased scattering intensity indicates an enhancement of the molecular order and the appearance of broad arcs rather than complete rings suggests there is some preferential orientation (Figure 7.7b and Figure 7.8b). In particular, the (1 0 17) and (0 0 *l*) family of lattice planes are higher in intensity in the out-of-plane direction whilst the (1 0 0) reflection is more prominent in the in-plane direction. This is indicative of a face-on orientation of **CN6H** supramolecular columns (Figure 7.5a). The scattering intensity of PTCDA templated **CN6H** [*P*] is stronger compared to **CN6H** [*M*] but both scattering patterns are replicated by simulating a dominant face-on orientation with scattering from the (0 0 6) plane centred out-of-plane with a reasonably broad distribution of crystallite orientations (Figure 7.7e and Figure 7.8e).

The 2D GIWAXS patterns of CuI templated **CN6H** consist of the distinctive high intensity diffraction features (Bragg spots) typically observed for systems with a high degree of molecular order and preferential orientation (Figure 7.7c and Figure 7.8c). These Bragg spots occupy *layer lines* in Q -space parallel to the substrates and are indexed in Figure 7.10 as $(0\ 0\ l)$, $(1\ \bar{1}\ l)$, $(1\ 0\ l)$, $(2\ \bar{1}\ l)$ etc. in the out-of-plane direction. Layer lines are typically observed in fibre diffraction experiments for samples containing fibres or filaments with uniaxial orientation [213, 368] and is further evidence of a highly ordered arrangement of uniaxially orientated **CN6H** supramolecular columns. The appearance of the $(1\ 0\ 0)$ plane in the out-of-plane direction at $Q = 0.76\text{\AA}^{-1}$ is indicative of edge-on oriented **CN6H** (Figure 7.5a) and indeed both enantiomers are simulated using a uniaxial model with the $(1\ 0\ 0)$ plane oriented parallel to the substrate (Figure 7.7f and Figure 7.8f). The distribution around the dominant orientation is considerably narrower compared to untemplated and PTCDA templated **CN6H**, characteristic of a significantly higher degree of molecular order (see Table 7.2).

Sample	Reciprocal axis oriented along Q_z	χ angles to probe ($^\circ$)	W_\perp ($^\circ$)	μ_\perp ($^\circ$)
CN6H [<i>M</i>] on bare silicon	1 0 17	-90:1:90	360	0.9
CN6H [<i>P</i>] on bare silicon	0 0 1 (0 0 6)	-90:1:90	360	0.9
CN6H [<i>M</i>] on PTCDA	0 0 1 (0 0 6)	-60:1:60	120	0.5
CN6H [<i>M</i>] on CuI	1 0 0	-35:0.5:35	15	0.4

Table 7.2: *simDiffraction* parameters used to simulate 2D GIWAXS scattering patterns with a Pseudo-Voigt (PSV) model. Here the reciprocal axis along Q_z describes the primary orientation, χ angles are the range of probed crystallite tilts away from this orientation, W_\perp describes the width of the PSV distribution and μ_\perp is the proportion of Gaussian or Lorentzian contribution to the PSV model ($\mu_\perp = 0$ is Gaussian and $\mu_\perp = 1$ is Lorentzian). See the *simDiffraction* software manual for further details [213].

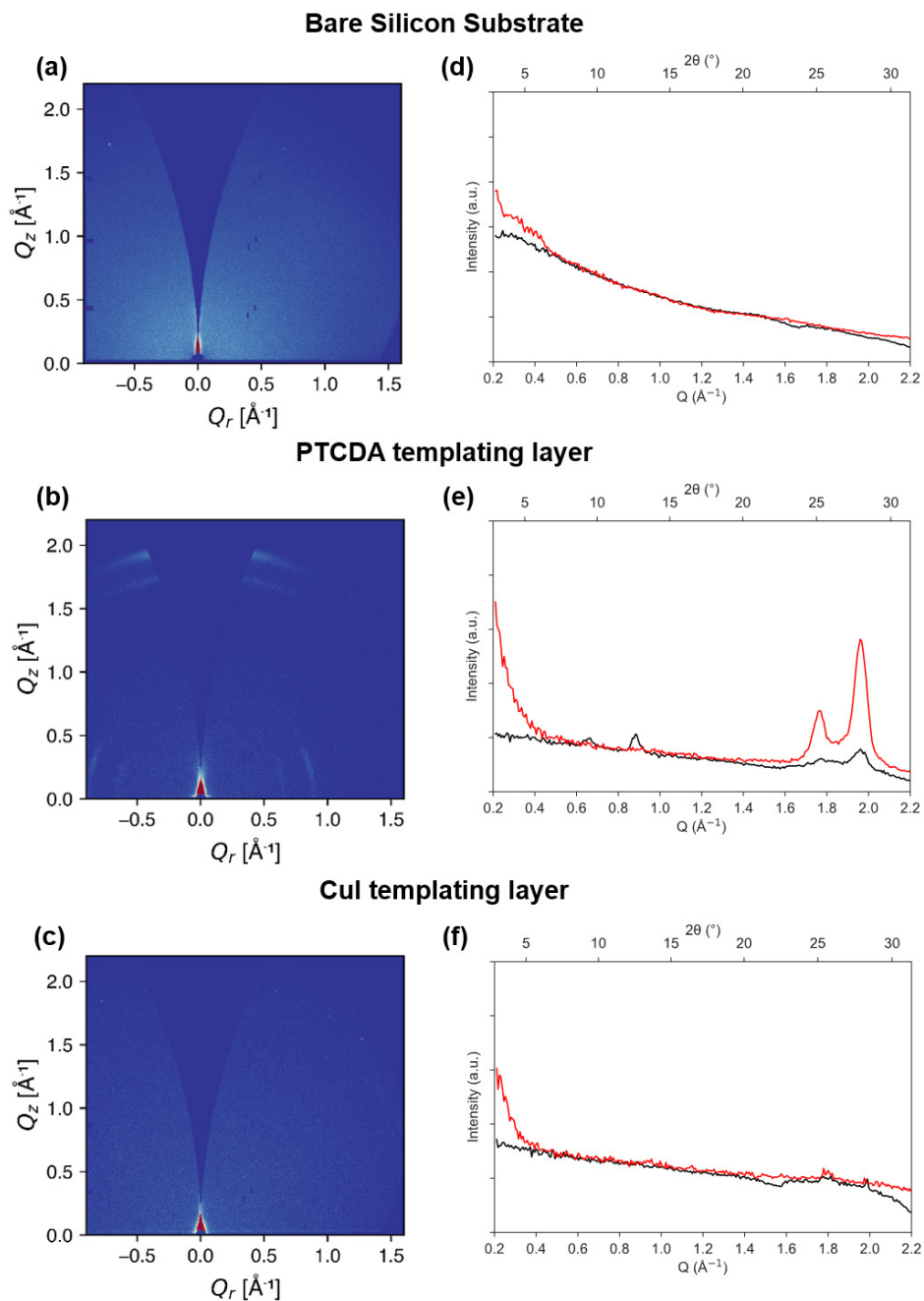


Figure 7.6: (a-c) 2D GIWAXS scattering patterns of bare silicon, PTCDA and CuI. (d-f) Corresponding Q -dependent 1D intensity profiles in the out-of-plane (red line) and in-plane (black line) directions.

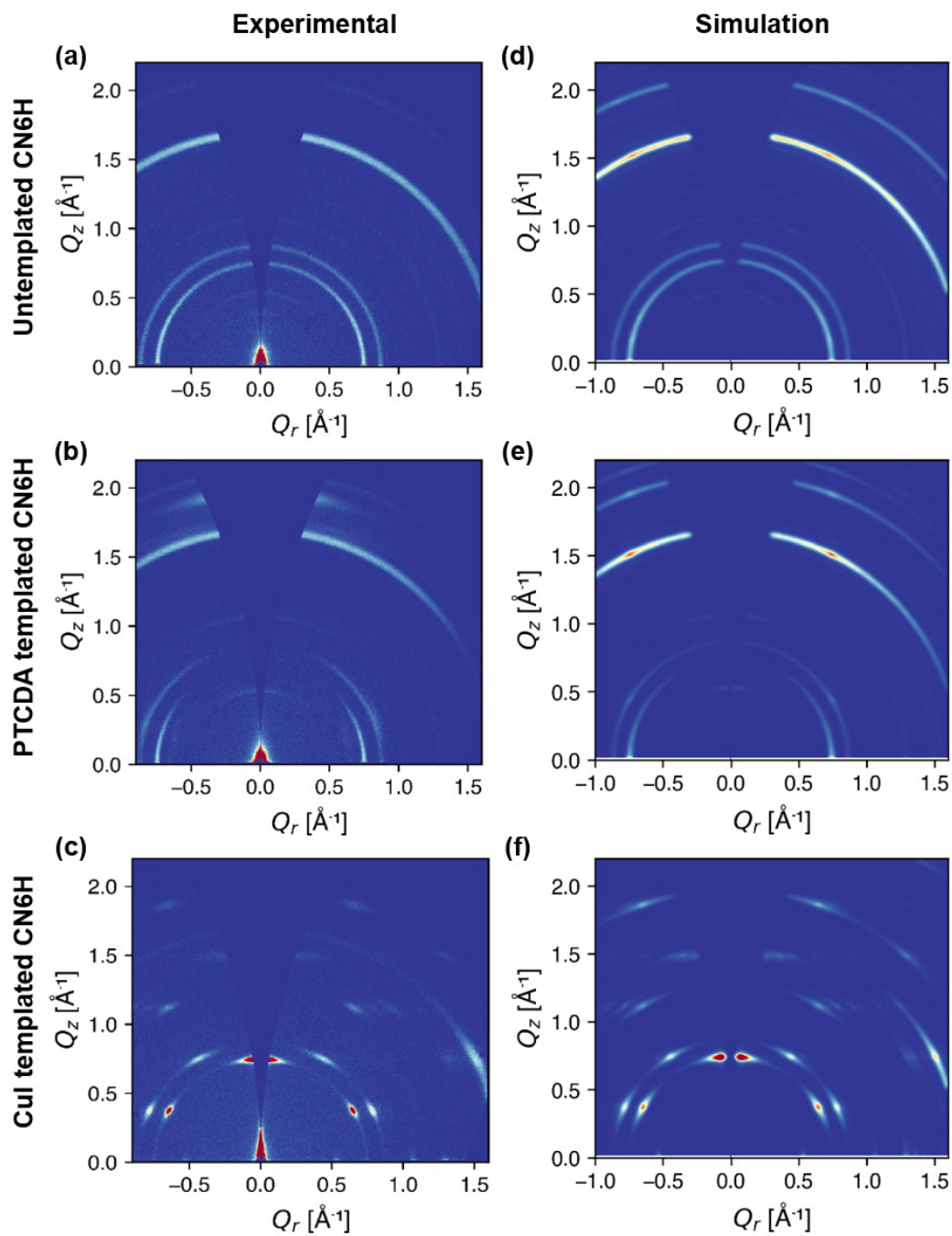


Figure 7.7: Experimental and simulated 2D GIWAXS diffraction patterns of untemplated and templated **CN6H** [M]. Comparable data for **CN6H** [P] is provided in Figure 7.8

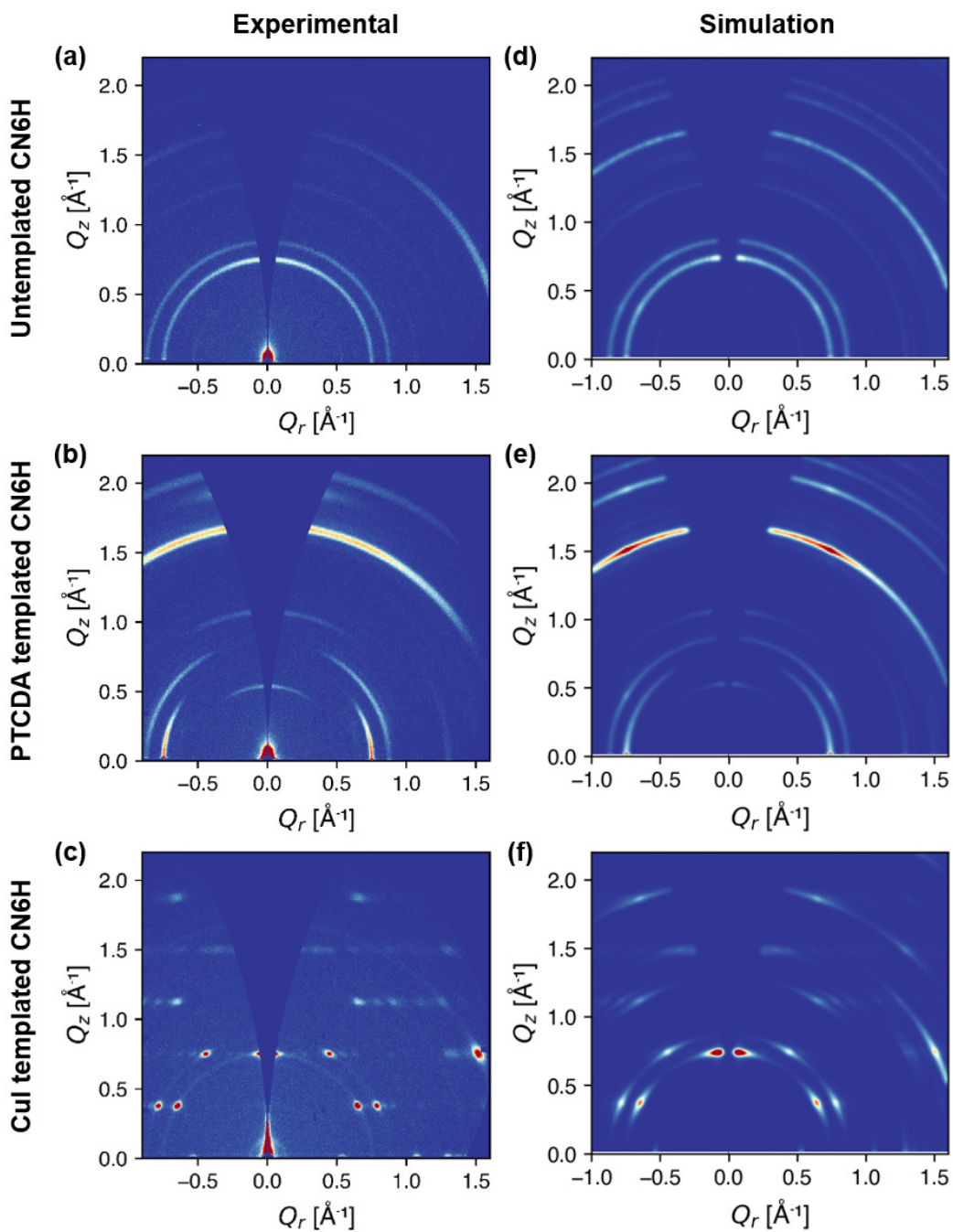


Figure 7.8: Experimental and simulated 2D GIWAXS diffraction patterns of untemplated and templated **CN6H** [*P*]. Parts (e) and part (f) are repeated from Figure 7.7

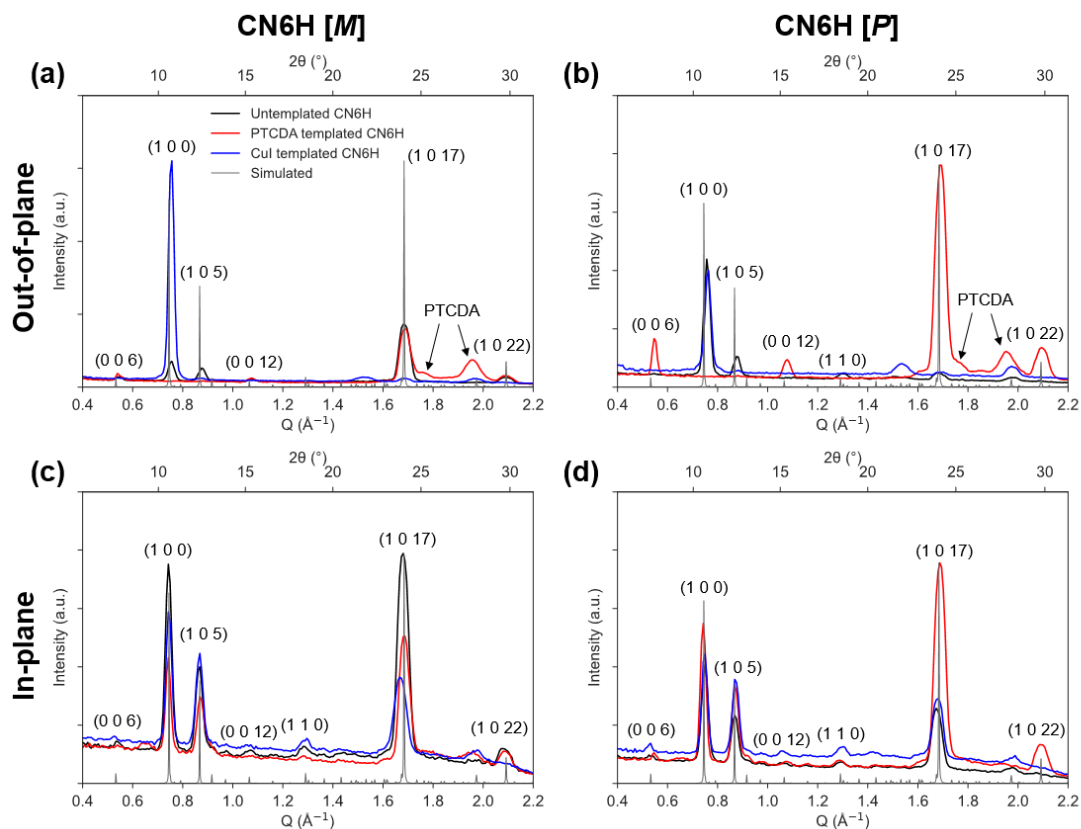


Figure 7.9: Azimuthally integrated Q -dependent out-of-plane and in-plane 1D GIWAXS profiles of untemplated and templated **CN6H [M]** and **CN6H [P]**. Simulated PXRDR is overlaid and the highest intensity reflections are labelled with the corresponding miller indices (hkl)

The degree of molecular order and orientation of **CN6H** supramolecular columns is further evaluated by considering the angular distribution of the scattering intensity from specific lattice planes. An unoriented film will exhibit little dependence on the azimuthal angle χ away from the normal, out-of-plane direction (appearing as completely isotropic scattering rings in the 2D scattering pattern). In contrast, an oriented film will exhibit angular dependence in a particular direction depending on the specific molecular orientation. In Figure 7.11, the 2D GIWAXS patterns are remapped as a function of χ for untemplated and templated **CN6H**. The high intensity (1 0 0), (1 0 5) and (1 0 17) reflections each now appear as horizontal lines or Bragg spots positioned at the same Q -value (red shaded region in Figure 7.11). To probe the angular dependence of each high intensity reflection, 1D χ -dependent intensity profiles are compared for untemplated and templated **CN6H** (Figure 7.11).

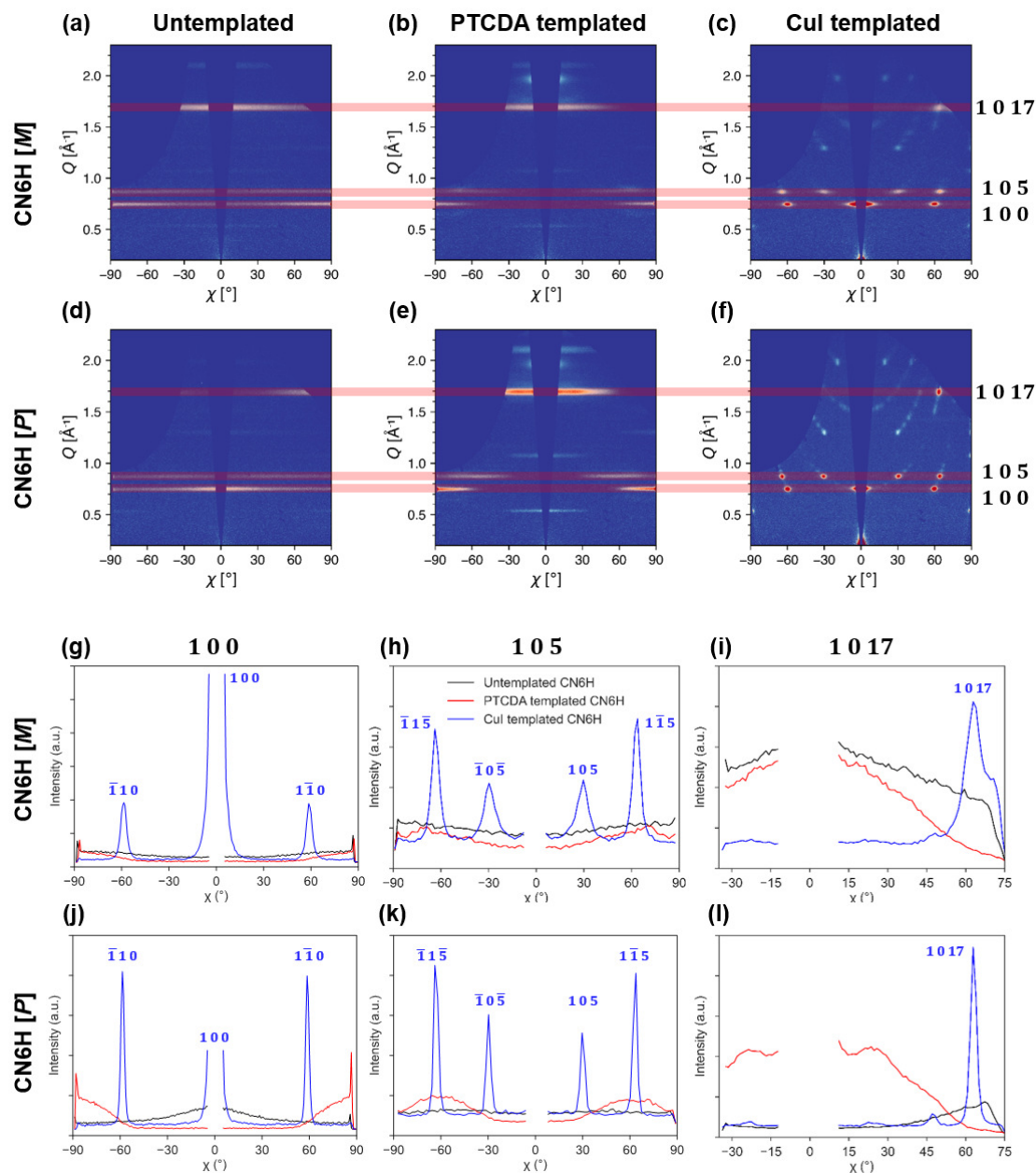


Figure 7.11: (a-f) 2D azimuthal (χ -remapped) GIWAXS images of untemplated and templated **CN6H [M]** and **CN6H [P]**. (g-l) Azimuthally integrated χ -dependent 1D intensity profiles performed in the red shaded regions shown, to probe the orientation of the $(1\ 0\ 0)$ and $(1\ 0\ 5)$ and $(1\ 0\ 17)$ lattice planes.

In contrast, the χ -dependent intensity profiles of CuI templated **CN6H** consist of sharp, high intensity peaks, confirming the highly oriented, ordered arrangement of **CN6H** discussed previously. In the (1 0 0) profile, peaks are observed in the out-of-plane direction ($\chi = 0^\circ$) and at $\chi \sim \pm 60^\circ$. This is expected for a uniaxial, edge-on orientated **CN6H** and is understood by considering symmetry equivalent planes for the 1 0 0 reflection which has a multiplicity of 6 in the hexagonal system (Figure 7.11g,j). These are (1 0 0), (0 1 0), (-1 0 0), (0 -1 0), (1 -1 0) and (-1 1 0) which are separated by a reciprocal angle $\gamma^* = 60^\circ$ (i.e. separated by $\chi = 60^\circ$ on the detector). Similarly, the 1 0 5 reflection has a multiplicity of 12 in the hexagonal system so additional peaks are observed in the 1 0 5 profiles due to the symmetry equivalent planes. This includes the (1 -1 5) plane indexed in Figure 7.10. With only weak scattering away from the primary orientations both **CN6H** [*M*] and **CN6H** [*P*] CuI templated films are close to uniaxially oriented (Figure 7.11h,k).

7.5.3 Atomic Force Microscopy

The GIWAXS measurements and simulations discussed above indicate three distinct morphologies. In the absence of templating layers (i.e. for non-templating/interacting bare silicon surfaces), there is a disordered arrangement of **CN6H** supramolecular columns with multiple **CN6H** orientations. On PTCDA, the helical axis is primarily aligned orthogonal to the substrate adopting a predominantly face-on arrangement of **CN6H** supramolecular columns. On CuI, the helical axis is aligned parallel to the substrate in a highly ordered, edge-on orientation. Next, large scale film structures such as the size and shape of **CN6H** crystalline grains are evaluated using AFM. In Figure 7.12 the nanoscale topography of untemplated and templated **CN6H** [*M*] and **CN6H** [*P*] is displayed. Untemplated **CN6H** forms small, uniform domains with an average lateral grain size of $58 \pm 12\text{nm}$ and RMS roughness of $6.9 \pm 0.6\text{nm}$. On PTCDA surfaces, the face-on oriented **CN6H** supramolecular columns form larger clusters that exhibit a broad range of shapes and surface profiles. This results in an increased lateral grain size of $105 \pm 59\text{nm}$ and RMS roughness of $10.8 \pm 0.6\text{nm}$. In the case of CuI templated **CN6H**, edge-on orientated supramolecular columns form a platelet-like morphology with grains appearing elongated and rectangular shaped. Such a regular domain consistency results in a large lateral grain size of $153 \pm 42\text{nm}$ and ultra-smooth films with an RMS roughness of $1.5 \pm 0.3\text{nm}$. The topography of the neat CuI templating layers fabricated following the same protocols as this study has been reported elsewhere with neat CuI films exhibiting a smooth and pinhole free surface [359]. The neat PTCDA films in this study were too sticky to successfully image which likely contributes to the higher molecular disorder and broader angular distribution of **CN6H** supramolecular columns on PTCDA compared to CuI templating layers.

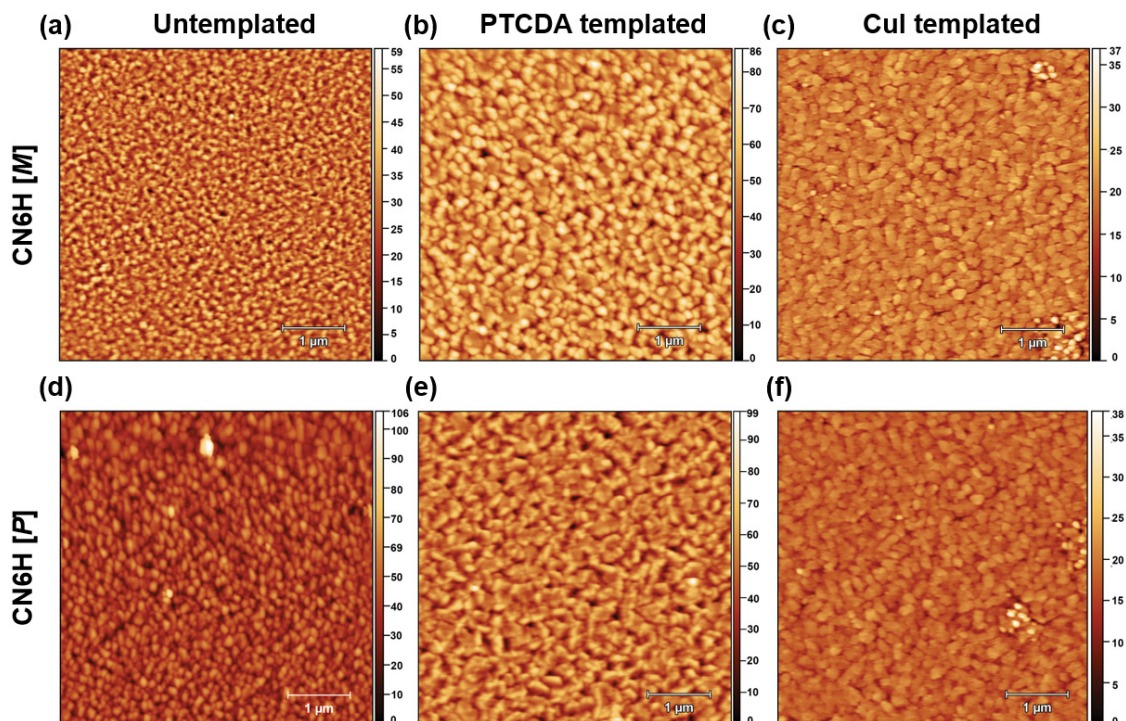


Figure 7.12: AFM height topography images of untemplated (a and d) and templated films (b and e) **CN6H [M]** and (e and f) **CN6H [P]**. The lateral scale bar is $1\mu\text{m}$.

7.5.4 Chiroptical Properties

The GIWAXS and AFM described above provide a detailed structural characterisation of the influence of CuI and PTCDA templating layers on the molecular order and orientation of **CN6H** supramolecular columns. Finally, the influence of the observed changes in molecular orientation on the chiroptical properties of untemplated and templated **CN6H** films is evaluated by measuring the CD response. CD is a spectroscopic absorption technique used to investigate the differential absorption of left and right-handed circularly polarised light (denoted LHCP and RHCP light) by optically active chiral molecules. It is useful for characterising the chirality of molecular systems, recording a non-zero spectrum for chiral molecules with enantiomers producing spectra that are equal in magnitude and opposite in sign. The CD response is defined as the difference between the absorption of LHCP and RHCP light:

$$CD = A_l - A_r \quad (7.1)$$

where A_l and A_r are the absorbances of LHCP and RCHP light respectively. The measured CD does not solely depend on the chirality of the system but additionally on a wide range of factors such as molecular conformation, temperature, concentration and the chemical environment. The CD spectra in Figure 7.13 were obtained with the following procedure: the incoming light was assumed to travel along the x -axis and the substrate to lie on the yz -plane. The intensity of the circular dichroism for the lowest 20 excited states was calculated for two different orientations: $(0^\circ, 20^\circ, 20^\circ)$ and $(0^\circ, 90^\circ, 90^\circ)$ where (α, β, γ) indicate the rotation angle around the x -, y - and z -axis. Therefore, the former orientation corresponds to the (slightly tilted) face-on and the latter orientation corresponds to the edge-on. The total components along the y -axis and the z -axis only (as the substrate lies on the yz -plane) were then calculated for the 20 lowest transitions and the spectra obtained by multicomponent Gaussian fitting. As an approximation, the FWHM was set to 0.25 eV for all transitions studied.

For the case of hexahelicenes, the CD spectra are characterised by two intensive bands of opposite sign at high and low energy (Figure 7.13b and Figure 7.13c) [369]. The transitions associated to the low energy bands (vibronic structure in the range 340-400 nm) are mainly B-symmetric, while the higher energy ones are mainly A-symmetric (range 270-340 nm, Figure 7.13a). These bands have been attributed to transitions mainly polarised along the bc -plane (B-band) or the a -axis (A-band) of **CN6H** [369]. In the case of untemplated **CN6H**, the lineshape and relative intensity of the A- and B-bands is comparable to CD spectra of the molecules in solution. The same is not true for the CD spectra of templated **CN6H**: with considerable suppression of either the A- (CuI templated **CN6H**) or B-bands (PTCDA templated **CN6H**). The suppressed B-band apparent in the CD spectra of PTCDA templated **CN6H** is consistent with the fact that transitions with components polarised along the c -axis of the unit cell cannot be excited when the helicenes are oriented face-on, as would be expected for upright supramolecular columns. Meanwhile the suppressed A-band observed in CuI templated **CN6H** is consistent with the **CN6H** adopting a more edge-on configuration, and flat-lying supramolecular columns.

7.5.5 Proposed Templating Mechanisms

The driving forces responsible for changes in the molecular orientation of **CN6H** can be rationalised by considering the interactions between the chiral columns and the structural templating surfaces. On non-interacting surface (i.e. bare silicon), PTCDA molecules are understood to lie flat such that the π -electron rich conjugated core is aligned parallel to the substrate. Consequently, π - π interactions between the π -electron clouds of PTCDA and **CN6H** force the supramolecular columns to assemble in an upright configuration with the helical axis aligned perpendicular to the substrate. The functionalised terminal cyano groups of **CN6H** are also likely to contribute to this templating effect given their electron-

withdrawing nature. The PTCDA templating mechanism is illustrated in Figure 7.14. Similar structural templating effects driven by PTCDA π - π interactions have been seen before in other aromatic systems [359]. The results presented here are the first to show such templating effects for chiral conjugated systems.

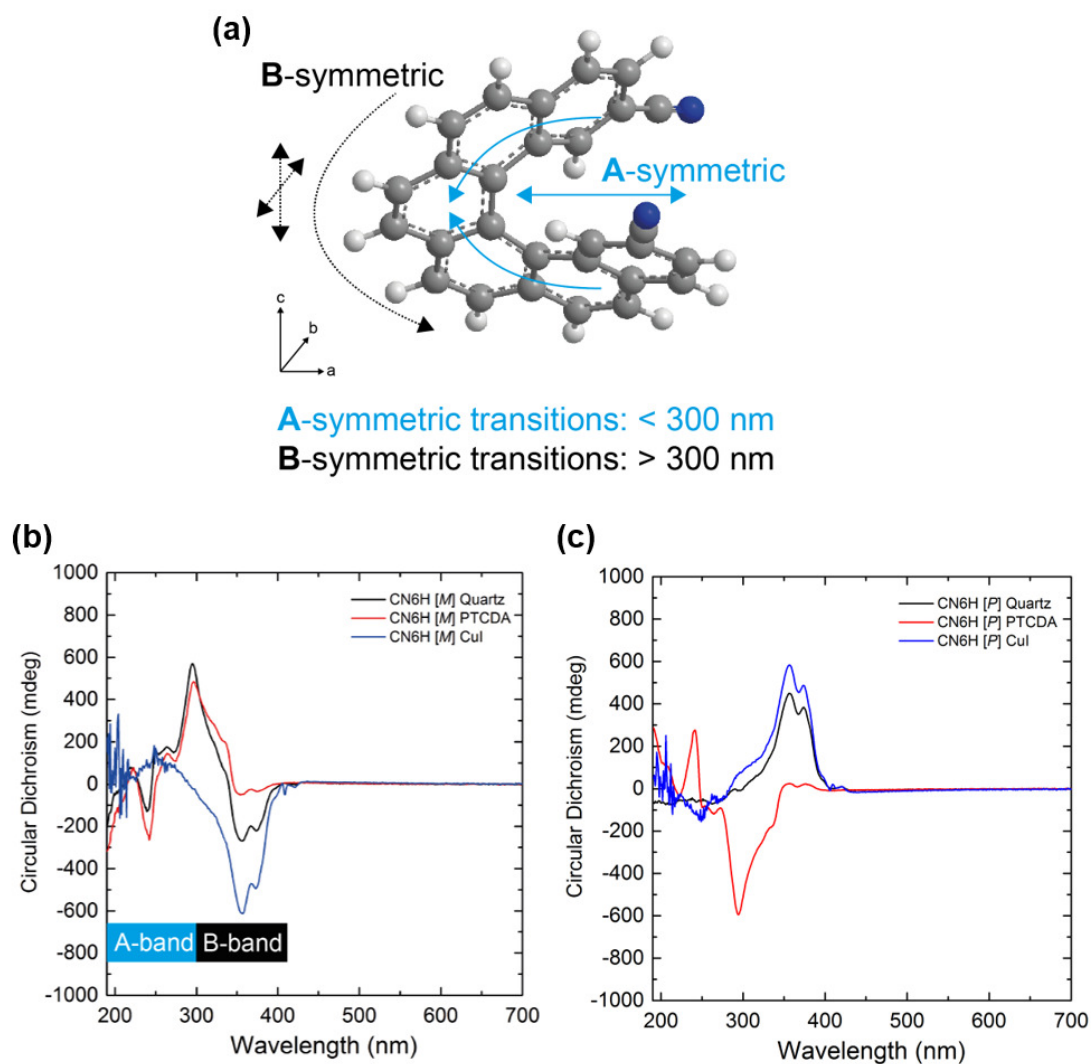


Figure 7.13: (a) Symmetries of the A- and B-symmetric transitions of **CN6H** orientated with respect to the crystallographic axes of the unit cell. CD spectra for untemplated and templated (b) **CN6H** [*M*] and (c) **CN6H** [*P*].

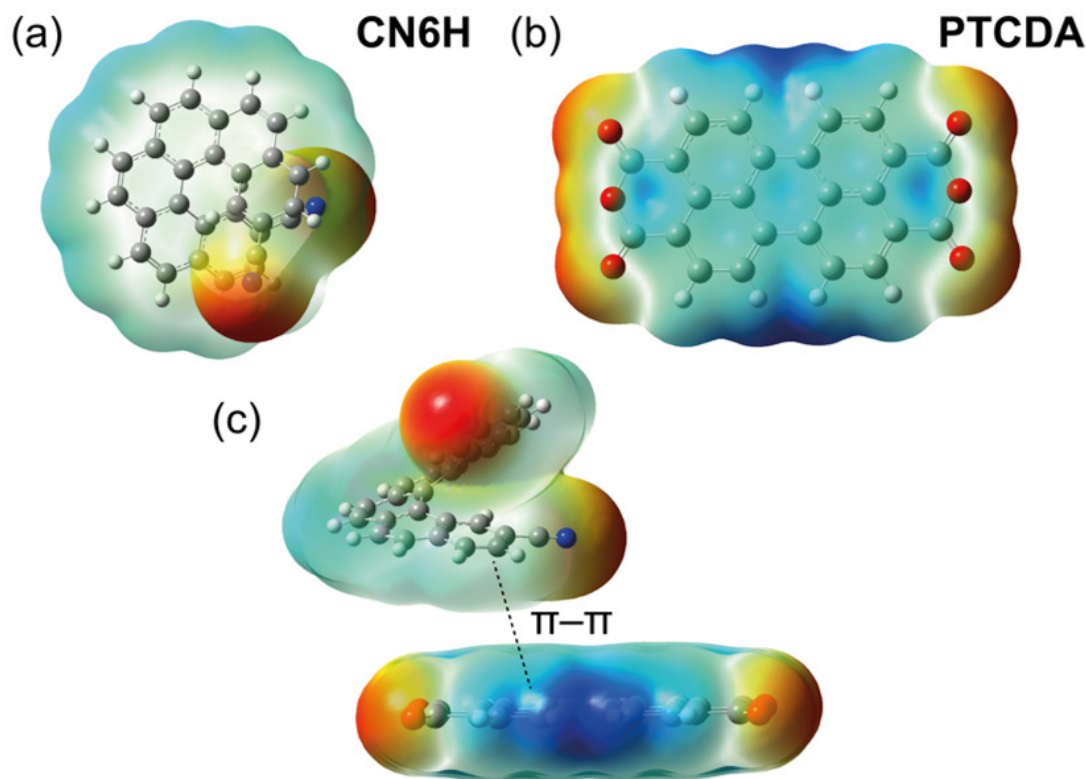


Figure 7.14: Electrostatic surface potentials of (a) **CN6H** and (b) PTCDA in a planar overview, and (c) an illustration of the π - π interactions between flat-lying PTCDA and **CN6H**. The red areas represent electron rich regions of the molecule, whilst the blue regions represent electron deficient regions.

CuI films grown at high temperatures (100°C) can contain surface grains with either Cu^+ or I^- terminations which persist when the films are cooled to room temperature [359, 370]. The CuI films used in this work were fabricated such that the (1 1 1) plane was orientated parallel to the surface. In this configuration, I^- termination is energetically favoured at the surface (Figure 7.15b). As a result, the surface of the CuI films have high electron densities with a weak dipole normal to the substrate surface (Figure 7.15c). Considering a typical quadrupolar model for **CN6H** molecules, the repulsive Coulomb interactions between the negatively charged CuI surface and the aromatic rings are minimised by arranging into a V-shape configuration (Figure 7.15c). This results in **CN6H** supramolecular columns assembling into a flat-lying, edge-on arrangement with the *c*-axis of the unit cell aligned parallel to the CuI surface.

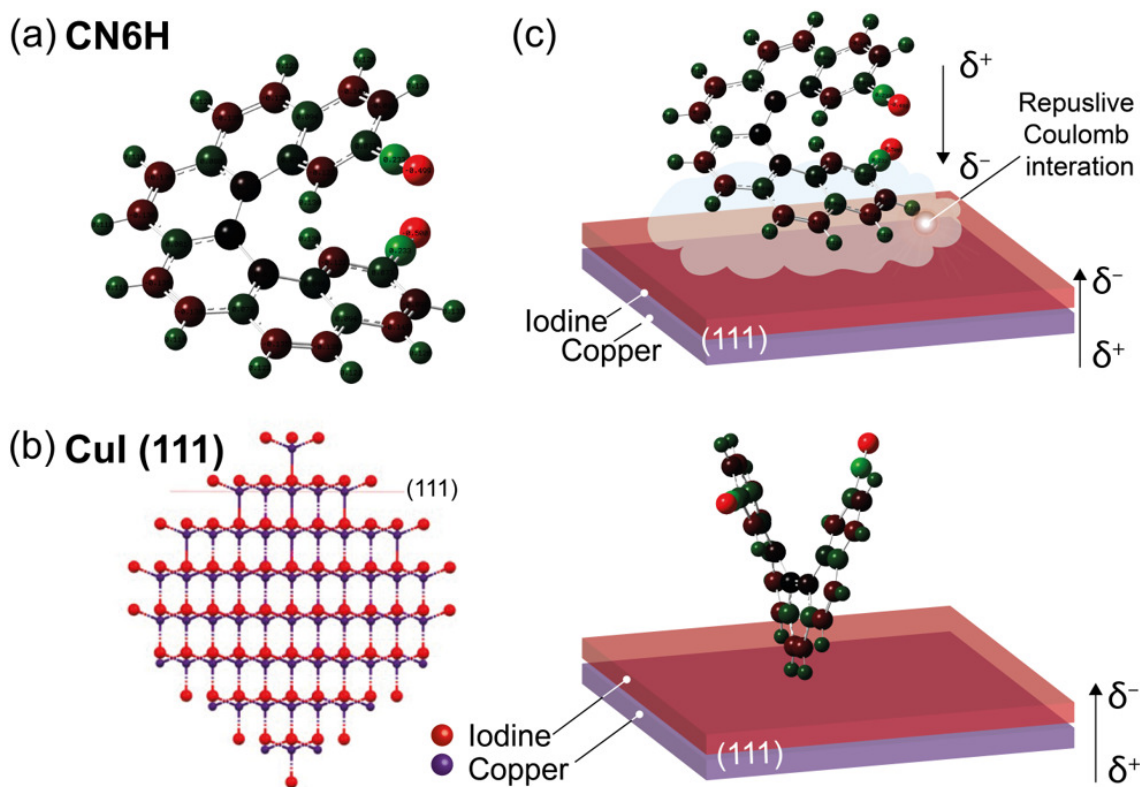


Figure 7.15: (a) Partial charges of **CN6H**. The red atoms have negative charge whilst the green atoms carry a positive charge. (b) Crystal packing of **CuI** along the (111) plane showing the relative positions of the iodine and copper atoms. The **CuI** surface primarily consists of iodine atoms. (c) An illustration of the electrostatic interactions which force an edge-on orientation of **CN6H**.

7.6 Summary

The results presented in this Chapter demonstrate an effective strategy to control the orientation of a chiral molecule in the solid state through the use of both organic and inorganic structural templating layers. On non-interacting surfaces, **CN6H** supramolecular columns are highly disordered exhibiting a wide range of orientations (Figure 7.16a). On PTCDA, **CN6H** adopts an upright, face-on orientation with the helical axis aligned orthogonal to the substrate (Figure 7.16b). This templating effect is driven by π - π interactions between **CN6H** aromatic units and the flat-lying PTCDA conjugated core. The rough PTCDA surface induces a small degree of disorder leading to several **CN6H** orientations tilted away from the orthogonal substrate axis. On **CuI**, dipole-dipole interactions force **CN6H**

supramolecular columns to adopt a flat-lying, edge-on orientation (Figure 7.16c). **CN6H** films on CuI are ultra-smooth with a high degree of molecular order and crystallinity. These dramatic changes in molecular orientation are characterised using GIWAXS and the experimentally observed scattering patterns are replicated by simulating different configurations of the single crystal structure. Given that the electronic transitions of **CN6H** are polarised along different axes of the unit cell, the significant changes in molecular orientation have a profound impact on the chiroptical response. The structural manipulation approaches described here will allow chiral molecules to be integrated into a diverse range of emerging technologies and devices which rely on chiroptical functionality.

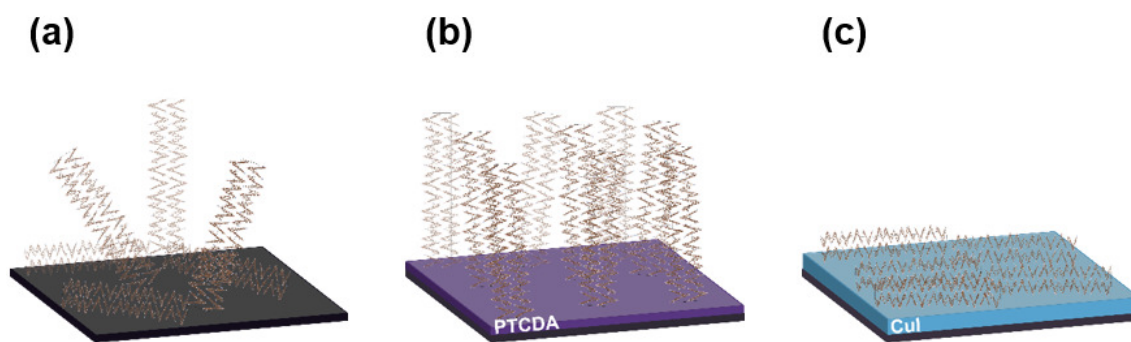


Figure 7.16: An illustration of the molecular assembly of (a) untemplated **CN6H** on bare silicon and templated **CN6H** on (b) PTCDA and (c) CuI templating layers.

Conclusion

In this thesis, I have studied self-assembled nanostructures in thin film systems for organic electronic applications. In each experimental chapter, I have characterised the structural properties of organic thin films using a range of X-ray and neutron scattering techniques. These findings have been correlated to the optoelectronic functionality and stability of a diverse range of systems. In this conclusion, the limitations and future studies specific to each experimental contribution are discussed. The thesis ends with concluding remarks concerning the future outlook of the overarching research topics presented in this work.

8.1 Summary of the Thesis and its Contributions

Chapter 4: Correlating Nanostructure with Optoelectronic Functionality in PBDB-T : ITIC Organic Photovoltaics with Non-Halogenated Solvents

In this chapter, I explored the impact of casting solvent on the nanostructure and optoelectronic functionality of PBDB-T : ITIC based systems. The research addressed the potential use of more environmentally-benign, non-halogenated solvents such as o-xylene and a CS₂ : acetone blend as alternatives to pernicious, halogenated processing solvents such as chlorobenzene and chloroform. Such studies are necessary for the commercialisation of OPV given the increased compatibility of non-halogenated solvents with industrial processes for large-scale fabrication. Although it was found that devices processed from chlorobenzene exhibit superior PCE, devices processed from CS₂ : acetone demonstrated comparable film nanomorphologies and PL quenching. Additionally the high V_{OC} achieved for CS₂ : acetone processed devices were the highest in the study. The origin of reduced voltage losses is currently unclear but it could be linked to the vertical composition of the film. To clarify this, further investigation is required using depth-profiling techniques such as NR, XPS or Rutherford backscattering. The use of grazing incidence X-ray scattering techniques (GIWAXS and GISAXS) in this chapter proved to be a powerful tool for characterising a broad range of characteristic length scales in the blend films. However, for two-phase systems which are finely intermixed or have large characteristic length scales, alternative measurements that are more sensitive to the contrast in the system (e.g. SANS) and probe larger Q ranges are necessary.

More broadly, the study emphasised the need for wider investigations into the use of non-halogenated solvents covering a larger material and solvent parameter space. This

could be aided by more rigorous solvent selection using the Hansen solubility parameters software HSPiP. Additionally, further studies should also take into consideration the impact of processing solvent on the stability of the device, ensuring systems exhibit both high-efficiency and long-term operational lifetime, critical for commercialisation.

Chapter 5: The Impact of 1,8-diiodooctane on the Morphology, Performance and Stability of Organic Photovoltaics

In this chapter, I investigated the impact of a high boiling point solvent additive (1,8-diiodooctane, DIO) on the morphology, performance and stability of PBDB-T : ITIC and PBDB-T : PC₇₁BM based organic photovoltaics using a broad range of structural and optoelectronic characterisation techniques. The inclusion of solvent additives in the casting solution has been a common approach used to control the morphology of bulk heterojunction films. However, numerous studies have demonstrated the detrimental impact of DIO to the stability of devices through various degradation mechanisms such as accelerated photo-degradation and morphological instabilities.

The work in this chapter, revealed that whilst DIO offered some benefits to NFA based systems (e.g. enhanced photo-stability in ambient conditions), the same optimisation protocols used for fullerene-based systems are not easily translated to NFA-based systems. Most notably, there is a greater risk of trapping residual DIO in the film which can accelerate degradation through increased oxygen diffusion and UV-induced reactions. Processing with larger DIO concentration can also lead to excessive NFA crystallisation and vertical phase-separation which severely limits device performance. The findings therefore highlight the need to design alternative methods for optimising device efficiency which also preserve the operational lifetime of devices. Future work should expand these results to explore alternative solvent additives and material systems. Additionally, more rigorous stability characterisation measurements should be performed to identify primary degradation routes and changes in morphology.

Chapter 6: The Effect of Chemical Design on the Morphology, Performance and Stability of Non-fullerene Acceptor Organic Photovoltaics

In Chapter 6, I explored the effect of chemical design on the morphology, performance and stability of NFA-based organic photovoltaics using a range of structural and optoelectronic characterisation techniques. More specifically, the study focused on characterising high-performing indacenothiophene (IDT) A-D-A based NFAs (EH-IDTBR, O-IDTBR and O-IDTBCN) in binary blend films with the conjugated polymer PTB7-Th. Comparison was

also made to a benchmark fullerene-based blend, PTB7-Th : PC₇₁BM. Using deuterated NFAs, an in-depth characterisation of the three-dimensional morphology of each blend system was performed using SANS and NR measurements. These measurements were combined with GIWAXS and AFM studies to correlate findings to optoelectronic properties and device stability.

Given the diverse range of NFA chemical structures now available, it is essential that the choice of chemical moieties and the resulting structure-performance-stability relationships are well understood to inform the design of new commercially-viable materials that are both efficient and stable. Although this chapter, addressed the stability of each system in inert conditions, future studies should perform more rigorous stability testing (i.e. under different stress factors and for longer ageing times). Furthermore, given the *FF* driven *PCE* enhancements, more in-depth morphological studies using techniques such as SANS should be performed to characterise changes in domain purity upon ageing. Additional thermal measurements such as DSC should also be performed to further understand the different thermal transitions and crystallisation behaviour of each NFA.

Chapter 7: Controlling Anisotropic Properties Through Manipulation of Chiral Small Molecule Orientation in the Bulk

In my final experimental contribution chapter, I presented a novel approach to control the molecular orientation of organic chiral small molecules in thin films using both inorganic (CuI) and organic (PTCDA) structural templating layers. The properties of chiral π -conjugated molecules such as the absorption and emission of circularly polarised light are highly anisotropic and consequently their molecular orientation in the solid-state has a significant impact on the performance and efficiency of chiral optoelectronic devices.

Using GIWAXS measurements and simulations, it was found that the molecular packing of a chiral small molecule (2,2'-dicyano[6]helicene, CN6H) could be switched from a face-on orientation on PTCDA to an edge-on orientation on CuI. Such templating methodologies offer a simple approach to engineering orientational control and consequently the anisotropic functional properties of chiral molecular systems. The results will therefore be beneficial for a range of emerging, next-generation technologies. Future studies should explore this structural templating effect in other chiral aromatic systems and further investigate the impact of molecular orientation in chiroptical devices.

8.2 Concluding Remarks

In general, it is hoped that the insights gained in this work will be of benefit to others in the field. A common trend throughout this thesis was the implementation of multiple, complementary characterisation techniques which when combined, probe a wide range of structures covering length scales from sub-nanometre to a few microns. This approach provided a high level of insight into the self-assembled hierarchical morphologies prevalent in many organic electronic thin film systems. In particular, the synthesis of deuterated non-fullerene acceptors for SANS and NR measurements combined with grazing incidence X-ray scattering techniques, proved to be a powerful approach to probe the full three-dimensional morphology of organic thin films. Linking these structural findings to the optoelectronic performance and stability of such systems is crucial to developing our understanding of the chemical design strategies and processing protocols necessary for the fabrication of highly efficient, stable devices.

At the time of writing, the 26th UN Climate Change Conference (COP26) has just concluded and it is clear that current efforts to reduce global CO₂ emissions are insufficient. Currently, it is unclear if organic photovoltaics will reach technological maturity in time to significantly contribute to reducing anthropogenic emissions, and it is clear that there are considerable research challenges remaining to be addressed. Nevertheless, the rapid developments over the past decade in material design, device efficiency and optimisation protocols indicate a promising future with plenty of research avenues yet to be explored.

References

- [1] IPCC. Climate Change 2021 The Physical Science Basis. 2021.
- [2] Nico Wunderling, Jonathan F. Donges, Jürgen Kurths, and Ricarda Winkelmann. Interacting tipping elements increase risk of climate domino effects under global warming. *Earth System Dynamics*, 12(2):601–619, jun 2021.
- [3] UNFCCC. PARIS AGREEMENT. 2015.
- [4] BloombergNEF. New Energy Outlook 2021 Executive Summary. 2021.
- [5] Bp. Full report – Statistical Review of World Energy 2021.
- [6] Marc J. R. Perez and Richard Perez. A fundamental look at supply side energy reserves for the planet. *International Energy Agency, Solar Heating and Cooling Program Newsletter*, 62, 2015.
- [7] Martin Rothbart. Energy Landscape: How is the energy sector influencing the future powertrain? 2019.
- [8] Richard M. Swanson. A vision for crystalline silicon photovoltaics. *Progress in Photovoltaics: Research and Applications*, 14(5):443–453, aug 2006.
- [9] VDMA. International Technology Roadmap for Photovoltaic (ITRPV). 12th Ed, 2021.
- [10] IRENA. Renewable Power Generation Costs in 2020. 2021.
- [11] NREL. Best Research-Cell Efficiency Chart | Photovoltaic Research | NREL.
- [12] Tetsuyuki Ishii and Atsushi Masuda. Annual degradation rates of recent crystalline silicon photovoltaic modules. *Progress in Photovoltaics: Research and Applications*, 25(12):953–967, dec 2017.
- [13] Alessandro Virtuani, Mauro Cacciavo, Eleonora Annigoni, Gabi Friesen, Domenico Chianese, Christophe Ballif, and Tony Sample. 35 years of photovoltaics: Analysis of the TISO-10-kW solar plant, lessons learnt in safety and performance—Part 1. *Progress in Photovoltaics: Research and Applications*, 27(4):328–339, apr 2019.
- [14] John A. Tsanakas, Long Ha, and Claudia Buerhop. Faults and infrared thermographic diagnosis in operating c-Si photovoltaic modules: A review of research and future challenges. *Renewable and Sustainable Energy Reviews*, 62:695–709, sep 2016.
- [15] J. Czochralski. Ein neues Verfahren zur Messung der Kristallisationsgeschwindigkeit der Metalle. *Zeitschrift für Physikalische Chemie*, 92U(1):219–221, nov 1918.
- [16] P. S. Dutta. Bulk Growth of Crystals of III-V Compound Semiconductors. *Comprehensive Semiconductor Science and Technology*, 1-6:36–80, jan 2011.
- [17] Fraunhofer ISE. Photovoltaics Report. 2021.

- [18] Tarkeshwar Sinha, Devjyoti Lilhare, and Ayush Khare. A review on the improvement in performance of CdTe/CdS thin-film solar cells through optimization of structural parameters. *Journal of Materials Science*, 54(19):12189–12205, oct 2019.
- [19] Mark Geoghegan and Georges Hadziioannou. *Polymer Electronics*. Oxford University Press, 1st edition, 2013.
- [20] Maximilian Moser, Andrew Wadsworth, Nicola Gasparini, Iain McCulloch, M Moser, A Wadsworth, I McCulloch, and N Gasparini. Challenges to the Success of Commercial Organic Photovoltaic Products. *Advanced Energy Materials*, 11(18):2100056, may 2021.
- [21] Yongxi Li, Xia Guo, Zhengxing Peng, Boning Qu, Hongping Yan, Harald Ade, Maojie Zhang, and Stephen R. Forrest. Color-neutral, semitransparent organic photovoltaics for power window applications. *Proceedings of the National Academy of Sciences of the United States of America*, 117:21147–21154, 9 2020.
- [22] Nan Cui, Yu Song, Ching Hong Tan, Kai Zhang, Xiye Yang, Sheng Dong, Boming Xie, and Fei Huang. Stretchable transparent electrodes for conformable wearable organic photovoltaic devices. *Flexible Electronics*, 5:1–8, 11 2021.
- [23] Kenjiro Fukuda, Kilho Yu, and Takao Someya. The future of flexible organic solar cells. *Advanced Energy Materials*, 10:2000765, 7 2020.
- [24] Yong Cui, Ling Hong, and Jianhui Hou. Organic photovoltaic cells for indoor applications: Opportunities and challenges. *ACS Applied Materials & Interfaces*, 12:38815–38828, 9 2020.
- [25] Moritz Riede, Donato Spoltore, and Karl Leo. Organic Solar Cells—The Path to Commercial Success. *Advanced Energy Materials*, 11(1):2002653, jan 2021.
- [26] Thomas R. Andersen, Thue T. Larsen-Olsen, Birgitta Andreasen, Arvid P. L. Böttiger, Jon E. Carlé, Martin Helgesen, Eva Bundgaard, Kion Norrman, Jens W. Andreasen, Mikkel Jørgensen, and Frederik C. Krebs. Aqueous Processing of Low-Band-Gap Polymer Solar Cells Using Roll-to-Roll Methods. *ACS Nano*, 5(5):4188–4196, may 2011.
- [27] Frederik C. Krebs, Suren A. Gevorgyan, and Jan Alstrup. A roll-to-roll process to flexible polymer solar cells: model studies, manufacture and operational stability studies. *Journal of Materials Chemistry*, 19(30):5442–5451, jul 2009.
- [28] Saqib Rafique, Shahino Mah Abdullah, Khaulah Sulaiman, and Mitsumasa Iwamoto. Fundamentals of bulk heterojunction organic solar cells: An overview of stability/degradation issues and strategies for improvement. *Renewable and Sustainable Energy Reviews*, 84:43–53, mar 2018.
- [29] Yuliar Firdaus, Vincent M. Le Corre, Safakath Karuthedath, Wenlan Liu, Anastasia Markina, Wentao Huang, Shirsopratim Chattopadhyay, Masrur Morshed Nahid, Mohamad I. Nugraha, Yuanbao Lin, Akmaral Seitkhan, Aniruddha Basu, Weimin

- Zhang, Iain McCulloch, Harald Ade, John Labram, Frédéric Laquai, Denis Andrienko, L. Jan Anton Koster, and Thomas D. Anthopoulos. Long-range exciton diffusion in molecular non-fullerene acceptors. *Nature Communications*, 11(1):1–10, oct 2020.
- [30] Ardanan Armin, Wei Li, Oskar J. Sandberg, Zuo Xiao, Liming Ding, Jenny Nelson, Dieter Neher, Koen Vandewal, Safa Shoaee, Tao Wang, Harald Ade, Thomas Heumüller, Christoph Brabec, and Paul Meredith. A history and perspective of non-fullerene electron acceptors for organic solar cells. *Advanced Energy Materials*, 11:2003570, 4 2021.
- [31] Sean E. Shaheen, Christoph J. Brabec, N. Serdar Sariciftci, Franz Padinger, Thomas Fromherz, and Jan C. Hummelen. 2.5% efficient organic plastic solar cells. *Applied Physics Letters*, 78:841, 2 2001.
- [32] Yong Cui, Ye Xu, Huifeng Yao, Pengqing Bi, Ling Hong, Jianqi Zhang, Yunfei Zu, Tao Zhang, Jinzhao Qin, Junzhen Ren, Zhihao Chen, Chang He, Xiaotao Hao, Zhixiang Wei, and Jianhui Hou. Single-Junction Organic Photovoltaic Cell with 19% Efficiency. *Advanced Materials*, 33(41):2102420, oct 2021.
- [33] Pengqing Bi, Shaoqing Zhang, Zhihao Chen, Ye Xu, Yong Cui, Tao Zhang, Junzhen Ren, Jinzhao Qin, Ling Hong, Xiaotao Hao, and Jianhui Hou. Reduced non-radiative charge recombination enables organic photovoltaic cell approaching 19% efficiency. *Joule*, 5(9):2408–2419, sep 2021.
- [34] Jingwen Wang, Huifeng Yao, Ye Xu, Lijiao Ma, and Jianhui Hou. Recent progress in reducing voltage loss in organic photovoltaic cells. *Materials Chemistry Frontiers*, 5:709–722, 1 2021.
- [35] Cenqi Yan, Stephen Barlow, Zhaohui Wang, He Yan, Alex K.Y. Jen, Seth R. Marder, and Xiaowei Zhan. Non-fullerene acceptors for organic solar cells. *Nature Reviews Materials*, 3:1–19, 2 2018.
- [36] Steven A. Lopez, Benjamin Sanchez-Lengeling, Julio de Goes Soares, and Alán Aspuru-Guzik. Design principles and top non-fullerene acceptor candidates for organic photovoltaics. *Joule*, 1:857–870, 12 2017.
- [37] Na Gyeong An, Jin Young Kim, and Doojin Vak. Machine learning-assisted development of organic photovoltaics via high-throughput in situ formulation. *Energy & Environmental Science*, 14(6):3438–3446, jun 2021.
- [38] Tudur Wyn David, Helder Anizelli, T. Jesper Jacobsson, Cameron Gray, William Teahan, and Jeff Kettle. Enhancing the stability of organic photovoltaics through machine learning. *Nano Energy*, 78:105342, dec 2020.
- [39] Xiaoyan Du, Larry Lüer, Thomas Heumueller, Jerrit Wagner, Christian Berger, Tobias Osterrieder, Jonas Wortmann, Stefan Langner, Uyxing Vongsaysy, Melanie

- Bertrand, Ning Li, Tobias Stubhan, Jens Hauch, and Christoph J. Brabec. Elucidating the Full Potential of OPV Materials Utilizing a High-Throughput Robot-Based Platform and Machine Learning. *Joule*, 5(2):495–506, feb 2021.
- [40] Nastaran Meftahi, Mykhailo Klymenko, Andrew J. Christofferson, Udo Bach, David A. Winkler, and Salvy P. Russo. Machine learning property prediction for organic photovoltaic devices. *Computational Materials*, 6(1):1–8, nov 2020.
- [41] Dimensions | the next evolution in linked scholarly information.
- [42] Yongxi Li, Xiaheng Huang, Kan Ding, Hafiz K.M. Sherif, Long Ye, Haoran Liu, Chang Zhi Li, Harald Ade, and Stephen R. Forrest. Non-fullerene acceptor organic photovoltaics with intrinsic operational lifetimes over 30 years. *Nature Communications*, 12(1):1–9, sep 2021.
- [43] Quinn Burlingame, Melissa Ball, and Yueh Lin Loo. It’s time to focus on organic solar cell stability. *Nature Energy*, 5(12):947–949, nov 2020.
- [44] J. R. Hook and H. E. Hall. *Solid state physics*. Wiley, 2nd edition, 1991.
- [45] Charles. Kittel. *Introduction to solid state physics*. Wiley, 8th edition, 2005.
- [46] Jenny. Nelson. *The physics of solar cells*. Imperial College Press, 1st edition, 2003.
- [47] Richard A. L. Jones and R. W. Richards. *Polymers at surfaces and interfaces*. Cambridge University Press, 1st edition, 1999.
- [48] Richard A. L. Jones. *Soft condensed matter*. Oxford University Press, 1st edition, 2002.
- [49] Shamim Ahmad. Organic semiconductors for device applications: Current trends and future prospects. *Journal of Polymer Engineering*, 34:279–338, 6 2014.
- [50] W. Kowalsky, E. Becker, T. Benstem, H.-H. Johannes, D. Metzdorf, H. Neuner, and J. Schöbel. *Organic semiconductors: fundamentals and applications*. Springer, Berlin, Heidelberg, 10 2000.
- [51] Jason D. Myers and Jiangeng Xue. Organic semiconductors and their applications in photovoltaic devices. *Polymer Reviews*, 52:1–37, 1 2012.
- [52] A. Einstein, Einstein, and A. Über einen die erzeugung und verwandlung des liches betreffenden heuristischen gesichtspunkt. *Annalen der Physik*, 322:132–148, 1905.
- [53] NREL. Solar Spectra | Grid Modernization | NREL.
- [54] William Shockley and Hans J. Queisser. Detailed balance limit of efficiency of p-n junction solar cells. *Journal of Applied Physics*, 32:510, 6 1961.
- [55] Bruno Ehrler, Esther Alarcón-Lladó, Stefan W. Tabernig, Tom Veeken, Erik C. Garnett, and Albert Polman. Photovoltaics Reaching for the Shockley–Queisser Limit. *ACS Energy Letters*, 5(9):3029–3033, sep 2020.
- [56] Armin Richter, Martin Hermle, and Stefan W. Glunz. Reassessment of the limiting efficiency for crystalline silicon solar cells. *IEEE Journal of Photovoltaics*, 3:1184–1191, 2013.

- [57] Safakath Karuthedath, Julien Gorenflot, Yuliar Firdaus, Neha Chaturvedi, Catherine S.P. De Castro, George T. Harrison, Jafar I. Khan, Anastasia Markina, Ahmed H. Balawi, Top Archie Dela Peña, Wenlan Liu, Ru Ze Liang, Anirudh Sharma, Sri H.K. Paleti, Weimin Zhang, Yuanbao Lin, Erkki Alarousu, Dalaver H. Anjum, Pierre M. Beaujuge, Stefaan De Wolf, Iain McCulloch, Thomas D. Anthopoulos, Derya Baran, Denis Andrienko, and Frédéric Laquai. Intrinsic efficiency limits in low-bandgap non-fullerene acceptor organic solar cells. *Nature Materials*, 20:378–384, 10 2020.
- [58] Deping Qian, Zilong Zheng, Huifeng Yao, Wolfgang Tress, Thomas R. Hopper, Shula Chen, Sunsun Li, Jing Liu, Shangshang Chen, Jiangbin Zhang, Xiao Ke Liu, Bowei Gao, Liangqi Ouyang, Yingzhi Jin, Galia Pozina, Irina A. Buyanova, Weimin M. Chen, Olle Inganäs, Veaceslav Coropceanu, Jean Luc Bredas, He Yan, Jianhui Hou, Fengling Zhang, Artem A. Bakulin, and Feng Gao. Design rules for minimizing voltage losses in high-efficiency organic solar cells. *Nature Materials*, 17:703–709, 7 2018.
- [59] Tony Blythe and David Bloor. *Electrical Properties of Polymers, Second Edition*. 2005.
- [60] G. G. Macfarlane, T. P. McLean, J. E. Quarrington, and V. Roberts. Exciton and phonon effects in the absorption spectra of germanium and silicon. *Journal of Physics and Chemistry of Solids*, 8:388–392, 1 1959.
- [61] W. C. Dunlap and R. L. Watters. Direct measurement of the dielectric constants of silicon and germanium. *Physical Review*, 92:1396, 12 1953.
- [62] Chengxi Zhang, Rugeng Liu, Chun Hong Mak, Xingli Zou, Hsin-Hui Shen, Shao-Yuan Leu, Li Ji, and hsien-Yi Hsu. Photophysics of organic photovoltaic devices: a review. *Journal of Photonics for Energy*, 8(2):021001, jun 2018.
- [63] Sergey V. Gaponenko and Hilmi Volkan Demir. *Applied Nanophotonics*. Cambridge University Press, 11 2018.
- [64] J. J.M. Halls, K. Pichler, R. H. Friend, S. C. Moratti, and A. B. Holmes. Exciton diffusion and dissociation in a poly(p-phenylenevinylene)/c60 heterojunction photovoltaic cell. *Applied Physics Letters*, 68:3120, 6 1998.
- [65] Muhammad T. Sajjad, Arvydas Ruseckas, Lethy Krishnan Jagadamma, Yiwei Zhang, and Ifor D.W. Samuel. Long-range exciton diffusion in non-fullerene acceptors and coarse bulk heterojunctions enable highly efficient organic photovoltaics. *Journal of Materials Chemistry A*, 8(31):15687–15694, aug 2020.
- [66] Weiwei Li, Koen H. Hendriks, Alice Furlan, Martijn M. Wienk, and René A.J. Janssen. High quantum efficiencies in polymer solar cells at energy losses below 0.6 eV. *Journal of the American Chemical Society*, 137:2231–2234, 2 2015.
- [67] Christopher G. Shuttle, Richard Hamilton, Jenny Nelson, Brian C. O’Regan, and James R. Durrant. Measurement of charge-density dependence of carrier mobility in an organic semiconductor blend. *Advanced Functional Materials*, 20:698–702, 3 2010.

- [68] Holger Spanggaard and Frederik C. Krebs. A brief history of the development of organic and polymeric photovoltaics. *Solar Energy Materials and Solar Cells*, 83:125–146, 6 2004.
- [69] A. Pochettino. *Atti reale accad. Lincei*, 1:355, 1906. cited By 1.
- [70] Max Volmer. Die verschiedenen lichtelektrischen erscheinungen am anthracen, ihre beziehungen zueinander, zur fluoreszenz und dianthracenbildung. *Annalen der Physik*, 345:775–796, 1 1913.
- [71] Richard H. Bube and 1927. Photoconductivity of solids. page 461, 1978.
- [72] C. W. Tang and A. C. Albrecht. Photovoltaic effects of metal–chlorophyll-a–metal sandwich cells. *The Journal of Chemical Physics*, 62:2139, 9 1975.
- [73] M. Mabrouki, A. Oueriagli, A. Outzourhit, E. L. Ameziane, S. Hotchandani, and R. M. LeBlanc. Dark signals and photovoltaic properties of al/chlorophyll a/ag cells. *Physica Status Solidi (A) Applied Research*, 191:345–354, 2002.
- [74] G. M. Delacote, J. P. Fillard, and F. J. Marco. Electron injection in thin films of copper phthalocyanine. *Solid State Communications*, 2:373–376, 12 1964.
- [75] David Keaens and Melvin Calvin. Photovoltaic effect and photoconductivity in laminated organic systems. *The Journal of Chemical Physics*, 29:950, 8 1958.
- [76] Donald A. Seanor. *Electrical Properties of Polymers*. Academic Press, 1982.
- [77] Alan J. Heeger. Semiconducting and metallic polymers: The fourth generation of polymeric materials. *Journal of Physical Chemistry B*, 105:8475–8491, 9 2001.
- [78] G. Yu, C. Zhang, and A. J. Heeger. Dual-function semiconducting polymer devices: Light-emitting and photodetecting diodes. *Applied Physics Letters*, 64:1540–1542, 1994.
- [79] Eugene Frankevich, Anvar Zakhidov, and Katsumi Yoshino. Photoconductivity of poly(2,5-diheptyloxy-p-phenylene vinylene) in the air atmosphere: Magnetic-field effect and mechanism of generation and recombination of charge carriers. *Physical Review B - Condensed Matter and Materials Physics*, 53:4498–4508, 1996.
- [80] S. Karg, W. Riess, V. Dyakonov, and M. Schwoerer. Electrical and optical characterization of poly(phenylene-vinylene) light emitting diodes. *Synthetic Metals*, 54:427–433, 3 1993.
- [81] H. Antoniadis, B. R. Hsieh, M. A. Abkowitz, S. A. Jenekhe, and M. Stolka. Photovoltaic and photoconductive properties of aluminum/poly(p-phenylene vinylene) interfaces. *Synthetic Metals*, 62:265–271, 2 1994.
- [82] R. N. Marks, J. J.M. Halls, D. D.C. Bradley, R. H. Friend, and A. B. Holmes. The photovoltaic response in poly(p-phenylene vinylene) thin-film devices. *Journal of Physics: Condensed Matter*, 6:1379, 2 1994.

- [83] C. W. Tang. Two-layer organic photovoltaic cell. *Applied Physics Letters*, 48:183, 8 1986.
- [84] N. S. Sariciftci, L. Smilowitz, A. J. Heeger, and F. Wudl. Semiconducting polymers (as donors) and buckminsterfullerene (as acceptor): photoinduced electron transfer and heterojunction devices. *Synthetic Metals*, 59:333–352, 8 1993.
- [85] J. J.M. Halls, K. Pichler, R. H. Friend, S. C. Moratti, and A. B. Holmes. Exciton dissociation at a poly(p-phenylenevinylene)/c60 heterojunction. *Synthetic Metals*, 77:277–280, 2 1996.
- [86] Masahiro Hiramoto, Hiroshi Fujiwara, and Masaaki Yokoyama. Three-layered organic solar cell with a photoactive interlayer of codeposited pigments. *Applied Physics Letters*, 58:1062, 6 1998.
- [87] G. Yu, K. Pakbaz, and A. J. Heeger. Semiconducting polymer diodes: Large size, low cost photodetectors with excellent visible-ultraviolet sensitivity. *Applied Physics Letters*, 64:3422–3424, 1994.
- [88] A. Köhler, H. F. Wittmann, R. H. Friend, M. S. Khan, and J. Lewis. Enhanced photocurrent response in photocells made with platinum-poly-yne/c60 blends by photoinduced electron transfer. *Synthetic Metals*, 77:147–150, 2 1996.
- [89] Jan C. Hummelen, Brian W. Knight, F. Lepeq, Fred Wudl, Jie Yao, and Charles L. Wilkins. Preparation and characterization of fulleroid and methanofullerene derivatives. *Journal of Organic Chemistry*, 60:532–538, 2 2002.
- [90] G. Yu, J. Gao, J. C. Hummelen, F. Wudl, and A. J. Heeger. Polymer photovoltaic cells: Enhanced efficiencies via a network of internal donor-acceptor heterojunctions. *Science*, 270:1789, 12 1995.
- [91] Artem A. Bakulin, Jan C. Hummelen, Maxim S. Pshenichnikov, and Paul H.M. Van Loosdrecht. Ultrafast hole-transfer dynamics in polymer/pcbm bulk heterojunctions. *Advanced Functional Materials*, 20:1653–1660, 5 2010.
- [92] Nicola Gasparini, Andrew Wadsworth, Maximilian Moser, Derya Baran, Iain McCulloch, and Christoph J. Brabec. The physics of small molecule acceptors for efficient and stable bulk heterojunction solar cells. *Advanced Energy Materials*, 8:1703298, 4 2018.
- [93] Yuze Lin, Jiayu Wang, Zhi-Guo Zhang, Huitao Bai, Yongfang Li, Daoben Zhu, and Xiaowei Zhan. An Electron Acceptor Challenging Fullerenes for Efficient Polymer Solar Cells. *Advanced Materials*, 27(7):1170–1174, feb 2015.
- [94] Wenchao Zhao, Deping Qian, Shaoqing Zhang, Sunsun Li, Olle Inganäs, Feng Gao, and Jianhui Hou. Fullerene-Free Polymer Solar Cells with over 11% Efficiency and Excellent Thermal Stability. *Advanced Materials*, 28(23):4734–4739, jun 2016.
- [95] Sunsun Li, Long Ye, Wenchao Zhao, Shaoqing Zhang, Subhrangsu Mukherjee, Harald Ade, and Jianhui Hou. Energy-Level Modulation of Small-Molecule Electron Acceptors to Achieve over 12% Efficiency in Polymer Solar Cells. *Advanced Materials*, 28(42):9423–9429, nov 2016.

- [96] Wenchao Zhao, Sunsun Li, Huifeng Yao, Shaoqing Zhang, Yun Zhang, Bei Yang, and Jianhui Hou. Molecular optimization enables over 13cells. *Journal of the American Chemical Society*, 139:7148–7151, 5 2017.
- [97] Sarah Holliday, Raja Shahid Ashraf, Andrew Wadsworth, Derya Baran, Syeda Amber Yousaf, Christian B. Nielsen, Ching-Hong Tan, Stoichko D. Dimitrov, Zhengrong Shang, Nicola Gasparini, Maha Alamoudi, Frédéric Laquai, Christoph J. Brabec, Alberto Salleo, James R. Durrant, and Iain McCulloch. High-efficiency and air-stable P3HT-based polymer solar cells with a new non-fullerene acceptor. *Nature Communications*, 7(1):1–11, jun 2016.
- [98] Nicola Gasparini, Michael Salvador, Sebastian Strohm, Thomas Heumueller, Ievgen Levchuk, Andrew Wadsworth, James H. Bannock, John C. de Mello, Hans Joachim Egelhaaf, Derya Baran, Iain McCulloch, and Christoph J. Brabec. Burn-in Free Nonfullerene-Based Organic Solar Cells. *Advanced Energy Materials*, 7(19):1700770, oct 2017.
- [99] Sara Marina, Edgar Gutierrez, Junkal Gutierrez, Marco Gobbi, Nicolas Ramos, Eduardo Solano, Jeromy Rech, Wei You, Luis E. Hueso, Agnieszka Tercjak, Harald Ade, and Jaime Martin. Semi-paracrystallinity in semi-conducting polymers. *Materials Horizons*, 5:311–580, 2022.
- [100] F. Van Antwerpen and D. W. Van Krevelen. Influence of crystallization temperature, molecular weight, and additives on the crystallization kinetics of poly(ethylene terephthalate). *Journal of Polymer Science: Polymer Physics Edition*, 10:2423–2435, 12 1972.
- [101] Yiwei Zhang, Andrew J. Parnell, Fabio Pontecchiani, Joshaniel F. K. Cooper, Richard L. Thompson, Richard A. L. Jones, Stephen M. King, David G. Lidzey, and Gabriel Bernardo. Understanding and controlling morphology evolution via DIO plasticization in PffBT4T-2OD/PC71BM devices. *Scientific Reports 2017 7:1*, 7(1):1–12, mar 2017.
- [102] Caitlin McDowell, Maged Abdelsamie, Michael F. Toney, and Guillermo C. Bazan. Solvent Additives: Key Morphology-Directing Agents for Solution-Processed Organic Solar Cells. *Advanced Materials*, 30(33):1707114, aug 2018.
- [103] Stefanie Rechberger, Nicola Gasparini, Ranbir Singh, Min Kim, Christos L. Chochos, Vasilis G. Gregoriou, Kilwon Cho, Christoph J. Brabec, Tayebbeh Ameri, and Erdmann Spiecker. Unraveling the complex nanomorphology of ternary organic solar cells with multimodal analytical transmission electron microscopy. *Solar RRL*, 4:2000114, 6 2020.
- [104] Peter Müller-Buschbaum and P Müller-Buschbaum. The active layer morphology of organic solar cells probed with grazing incidence scattering techniques. *Advanced Materials*, 26:7692–7709, 12 2014.

- [105] Wen Yin and Mark Dadmun. A New Model for the Morphology of P3HT/PCBM Organic Photovoltaics from Small-Angle Neutron Scattering: Rivers and Streams. *ACS Nano*, 5(6):4756–4768, jun 2011.
- [106] P. Müller-Buschbaum. *A Basic Introduction to Grazing Incidence Small-Angle X-Ray Scattering*, volume 776. Springer, 2009.
- [107] A. J. Parnell, Alan D.F. Dunbar, Andrew J. Pearson, Paul A. Staniec, Andrew J.C. Dennison, Hiroshi Hamamatsu, Maximilian W.A. Skoda, David C. Lidzey, and Richard A.L. Jones. Depletion of PCBM at the Cathode Interface in P3HT/PCBM Thin Films as Quantified via Neutron Reflectivity Measurements. *Advanced Materials*, 22(22):2444–2447, jun 2010.
- [108] E. L. Hynes, J. T. Cabral, A. J. Parnell, P. Gutfreund, R. J.L. Welbourn, A. D.F. Dunbar, D. M \hat{o} n, and A. M. Higgins. Interfacial width and phase equilibrium in polymer-fullerene thin-films. *Communications Physics*, 2:1–13, 9 2019.
- [109] Jiangquan Mai, Yiqun Xiao, Guodong Zhou, Jiayu Wang, Jingshuai Zhu, Ni Zhao, Xiaowei Zhan, and Xinhui Lu. Hidden Structure Ordering Along Backbone of Fused-Ring Electron Acceptors Enhanced by Ternary Bulk Heterojunction. *Advanced Materials*, 30(34):1802888, aug 2018.
- [110] Donghui Li, Xue Zhang, Dan Liu, and Tao Wang. Aggregation of non-fullerene acceptors in organic solar cells. *Journal of Materials Chemistry A*, 8(31):15607–15619, aug 2020.
- [111] Guangchao Han, Yuan Guo, Xiaoxian Song, Yue Wang, and Yuanping Yi. Terminal π - π stacking determines three-dimensional molecular packing and isotropic charge transport in an A- π -A electron acceptor for non-fullerene organic solar cells. *Journal of Materials Chemistry C*, 5(20):4852–4857, may 2017.
- [112] Sara Marina, Alberto D. Scaccabarozzi, Edgar Gutierrez-Fernandez, Eduardo Solano, Aditi Khirbat, Laura Ciammaruchi, Amaia Iturrospe, Alex Balzer, Liyang Yu, Elena Gabirondo, Xavier Monnier, Haritz Sardon, Thomas D. Anthopoulos, Mario Caironi, Mariano Campoy-Quiles, Christian M \ddot{u} ller, Daniele Cangialosi, Natalie Stingelin, and Jaime Martin. Polymorphism in Non-Fullerene Acceptors Based on Indacenodithienothiophene. *Advanced Functional Materials*, 31(29):2103784, jul 2021.
- [113] Long Ye, Sunsun Li, Xiaoyu Liu, Shaoqing Zhang, Masoud Ghasemi, Yuan Xiong, Jianhui Hou, and Harald Ade. Quenching to the percolation threshold in organic solar cells. *Joule*, 3:443–458, 2 2019.
- [114] Masoud Ghasemi, Huawei Hu, Zhengxing Peng, Jeromy James Rech, Indunil Angunawela, Joshua H. Carpenter, Samuel J. Stuard, Andrew Wadsworth, Iain McCulloch, Wei You, and Harald Ade. Delineation of Thermodynamic and Kinetic Factors that Control Stability in Non-fullerene Organic Solar Cells. *Joule*, 3(5):1328–1348, may 2019.

- [115] Long Ye, Huawei Hu, Masoud Ghasemi, Tonghui Wang, Brian A. Collins, Joo Hyun Kim, Kui Jiang, Joshua H. Carpenter, Hong Li, Zhengke Li, Terry McAfee, Jingbo Zhao, Xiankai Chen, Joshua Lin Yuk Lai, Tingxuan Ma, Jean Luc Bredas, He Yan, and Harald Ade. Quantitative relations between interaction parameter, miscibility and function in organic solar cells. *Nature Materials*, 17:253–260, 2 2018.
- [116] Li Ming Wang, Li Ming Wang, Qingduan Li, Shengjian Liu, Zhixiong Cao, Yue Peng Cai, Xuechen Jiao, Xuechen Jiao, Haojie Lai, Weiguang Xie, Xiaozhi Zhan, Xiaozhi Zhan, and Tao Zhu. Quantitative Determination of the Vertical Segregation and Molecular Ordering of PBDB-T/ITIC Blend Films with Solvent Additives. *ACS Applied Materials and Interfaces*, 12(21):24165–24173, may 2020.
- [117] Qingduan Li, Li Ming Wang, Shengjian Liu, Xiaozhi Zhan, Tao Zhu, Zhixiong Cao, Haojie Lai, Jiaji Zhao, Yuepeng Cai, Weiguang Xie, and Fei Huang. Impact of Donor-Acceptor Interaction and Solvent Additive on the Vertical Composition Distribution of Bulk Heterojunction Polymer Solar Cells. *ACS Applied Materials and Interfaces*, 11(49):45979–45990, dec 2019.
- [118] Jens A. Hauch, Pavel Schilinsky, Stelios A. Choulis, Richard Childers, Markus Biele, and Christoph J. Brabec. Flexible organic p3ht:pcbm bulk-heterojunction modules with more than 1 year outdoor lifetime. *Solar Energy Materials and Solar Cells*, 92:727–731, 7 2008.
- [119] Yiwei Zhang, Edward Bovill, James Kingsley, Alastair R. Buckley, Hunan Yi, Ahmed Iraqi, Tao Wang, and David G. Lidzey. Pcdtbt based solar cells: one year of operation under real-world conditions. *Scientific Reports 2016 6:1*, 6:1–8, 2 2016.
- [120] Ning Li, José Darío Perea, Thaer Kassar, Moses Richter, Thomas Heumueller, Gebhard J. Matt, Yi Hou, Nusret S. Güldal, Haiwei Chen, Shi Chen, Stefan Langner, Marvin Berlinghof, Tobias Unruh, and Christoph J. Brabec. Abnormal strong burn-in degradation of highly efficient polymer solar cells caused by spinodal donor-acceptor demixing. *Nature Communications*, 8:1–9, 2 2017.
- [121] Thomas Heumueller, William R. Mateker, Andreas Distler, Urs F. Fritze, Rongrong Cheacharoen, William H. Nguyen, Markus Biele, Michael Salvador, Max Von Delius, Hans Joachim Egelhaaf, Michael D. McGehee, and Christoph J. Brabec. Morphological and electrical control of fullerene dimerization determines organic photovoltaic stability. *Energy & Environmental Science*, 9:247–256, 1 2016.
- [122] Craig H. Peters, I. T. Sachs-Quintana, William R. Mateker, Thomas Heumueller, Jonathan Rivnay, Rodrigo Noriega, Zach M. Beiley, Eric T. Hoke, Alberto Salleo, and Michael D. McGehee. The mechanism of burn-in loss in a high efficiency polymer solar cell. *Advanced Materials*, 24:663–668, 2 2012.
- [123] Sarah Holliday, Christine K Luscombe, S Holliday, and C K Luscombe. Low Boiling Point Solvent Additives for Improved Photooxidative Stability in Organic Photovoltaics. *Advanced Electronic Materials*, 4(10):1700416, oct 2018.

- [124] Andrew J. Clarke, Joel Luke, Rico Meitzner, Jiaying Wu, Yuming Wang, Harrison K.H. Lee, Emily M. Speller, Helen Bristow, Hyojung Cha, Michael J. Newman, Katherine Hooper, Alex Evans, Feng Gao, Harald Hoppe, Iain McCulloch, Ulrich S. Schubert, Trystan M. Watson, James R. Durrant, Wing C. Tsoi, Ji Seon Kim, and Zhe Li. Non-fullerene acceptor photostability and its impact on organic solar cell lifetime. *Cell Reports Physical Science*, 2(7):100498, jul 2021.
- [125] Joel Luke, Emily M. Speller, Andrew Wadsworth, Mark F. Wyatt, Stoichko Dimitrov, Harrison K.H. Lee, Zhe Li, Wing C. Tsoi, Iain McCulloch, Diego Bagnis, James R. Durrant, and Ji Seon Kim. Twist and Degrade—Impact of Molecular Structure on the Photostability of Nonfullerene Acceptors and Their Photovoltaic Blends. *Advanced Energy Materials*, 9(15):1803755, apr 2019.
- [126] Ian E. Jacobs, Faustine Wang, Zaira I. Bedolla Valdez, Alejandra N. Ayala Oviedo, David J. Bilsky, and Adam J. Moulé. Photoinduced degradation from trace 1,8-diiodooctane in organic photovoltaics. *Journal of Materials Chemistry C*, 6(2):219–225, jan 2018.
- [127] Nutifafa Y. Doumon, Gongbao Wang, Xinkai Qiu, Adriaan J. Minnaard, Ryan C. Chiechi, and L. Jan Anton Koster. 1,8-diiodooctane acts as a photo-acid in organic solar cells. *Scientific Reports 2019 9:1*, 9(1):1–14, mar 2019.
- [128] Masoud Ghasemi, Nrup Balar, Zhengxing Peng, Huawei Hu, Yunpeng Qin, Taesoo Kim, Jeromy J. Rech, Matthew Bidwell, Walker Mask, Iain McCulloch, Wei You, Aram Amassian, Chad Risko, Brendan T. O’Connor, and Harald Ade. A molecular interaction–diffusion framework for predicting organic solar cell stability. *Nature Materials*, 20(4):525–532, apr 2021.
- [129] Mengxue Chen, Dan Liu, Wei Li, Robert S. Gurney, Donghui Li, Jinlong Cai, Emma L. K. Spooner, Rachel C. Kilbride, James D. McGettrick, Trystan M. Watson, Zhe Li, Richard A. L. Jones, David G. Lidzey, and Tao Wang. Influences of Non-fullerene Acceptor Fluorination on Three-Dimensional Morphology and Photovoltaic Properties of Organic Solar Cells. *ACS Applied Materials & Interfaces*, 11(29):26194–26203, jul 2019.
- [130] Wenchao Zhao, Sunsun Li, Shaoqing Zhang, Xiaoyu Liu, and Jianhui Hou. Ternary Polymer Solar Cells based on Two Acceptors and One Donor for Achieving 12.2% Efficiency. *Advanced Materials*, 29(2):1604059, jan 2017.
- [131] Qi Wang, Shaoqing Zhang, Bowei Xu, Sunsun Li, Bei Yang, Wenxia Yuan, and Jianhui Hou. Efficient Fullerene-Free Polymer Solar Cells Based on Alkylthio Substituted Conjugated Polymers. *Journal of Physical Chemistry C*, 121(9):4825–4833, mar 2017.
- [132] Trevor M. Grant, Kayden L.C. Kaller, Trevor J. Coathup, Nicole A. Rice, Karin Hinzer, and Benoît H. Lessard. High Voc solution-processed organic solar cells containing silicon phthalocyanine as a non-fullerene electron acceptor. *Organic Electronics*, 87:105976, dec 2020.

- [133] Yong Cui, Huifeng Yao, Bowei Gao, Yunpeng Qin, Shaoqing Zhang, Bei Yang, Chang He, Bowei Xu, and Jianhui Hou. Fine-Tuned Photoactive and Interconnection Layers for Achieving over 13% Efficiency in a Fullerene-Free Tandem Organic Solar Cell. *Journal of the American Chemical Society*, 139(21):7302–7309, may 2017.
- [134] Qing Ma, Xiaonan Xue, Lian Zhong, Indunil Angunawela, Shanshan Chen, Harald Ade, Lijun Huo, Zhanjun Zhang, and Yongfang Li. High voltage all polymer solar cells with a polymer acceptor based on NDI and benzotriazole. *Journal of Materials Chemistry C*, 7(29):9031–9037, jul 2019.
- [135] Haijun Bin, Liang Gao, Zhi-Guo Zhang, Yankang Yang, Yindong Zhang, Chunfeng Zhang, Shanshan Chen, Lingwei Xue, Changduk Yang, Min Xiao, and Yongfang Li. 11.4% Efficiency non-fullerene polymer solar cells with trialkylsilyl substituted 2D-conjugated polymer as donor. *Nature Communications*, 7(1):1–11, dec 2016.
- [136] Jafar I. Khan, Maha A. Alamoudi, Neha Chaturvedi, Raja S. Ashraf, Mohammed N. Nabi, Anastasia Markina, Wenlan Liu, Top Archie Dela Peña, Weimin Zhang, Olivier Alévêque, George T. Harrison, Wejdan Alsufyani, Eric Levillain, Stefaan De Wolf, Denis Andrienko, Iain McCulloch, and Frédéric Laquai. Impact of Acceptor Quadrupole Moment on Charge Generation and Recombination in Blends of IDT-Based Non-Fullerene Acceptors with PCE10 as Donor Polymer. *Advanced Energy Materials*, 11(28):2100839, jul 2021.
- [137] Zhi-Hao Chen, Peng-Qing Bi, Xiao-Yu Yang, Meng-Si Niu, Kang-Ning Zhang, Lin Feng, and Xiao-Tao Hao. Quantitatively Characterized Crystallization Effect on Recombination Energy Loss in Non-Fullerene Organic Solar Cells. *The Journal of Physical Chemistry C*, 123(20):12676–12683, may 2019.
- [138] Sachin Badgajar, Chang Eun Song, Sora Oh, Won Suk Shin, Sang-Jin Moon, Jong-Cheol Lee, In Hwan Jung, and Sang Kyu Lee. Highly efficient and thermally stable fullerene-free organic solar cells based on a small molecule donor and acceptor. *Journal of Materials Chemistry A*, 4(42):16335–16340, oct 2016.
- [139] Andrew Wadsworth, Helen Bristow, Zeinab Hamid, Maxime Babics, Nicola Gasparini, Colm W. Boyle, Weimin Zhang, Yifan Dong, Karl. J. Thorley, Marios Neophytou, Raja Shahid Ashraf, James R. Durrant, Derya Baran, and Iain McCulloch. End Group Tuning in Acceptor–Donor–Acceptor Nonfullerene Small Molecules for High Fill Factor Organic Solar Cells. *Advanced Functional Materials*, 29(47):1808429, nov 2019.
- [140] Steve Murov. Properties of Solvents Used in Organic Chemistry. <http://murov.info/orgsolvents.htm>.
- [141] ChemSpider. 1,8-DIODOOCTANE | C₈H₁₆I₂ | ChemSpider. <http://www.chemspider.com/Chemical-Structure.81807.html>.
- [142] American Chemical Society Division of Organic Chemistry. Common Solvents Used in Organic Chemistry: Table of Properties. <https://organicchemistrydata.org/solvents/>.

- [143] Microkat. Ethanolamine. <http://www.microkat.gr/msdspd90-99/Ethanolamine.html>.
- [144] Hin Lap Yip and Alex K.Y. Jen. Recent advances in solution-processed interfacial materials for efficient and stable polymer solar cells. *Energy & Environmental Science*, 5(3):5994–6011, mar 2012.
- [145] Roberto Sorrentino, Erika Kozma, Silvia Luzzati, and Riccardo Po. Interlayers for non-fullerene based polymer solar cells: distinctive features and challenges. *Energy & Environmental Science*, 14(1):180–223, jan 2021.
- [146] Yanming Sun, Jung Hwa Seo, Christopher J. Takacs, Jason Seifert, and Alan J. Heeger. Inverted Polymer Solar Cells Integrated with a Low-Temperature-Annealed Sol-Gel-Derived ZnO Film as an Electron Transport Layer. *Advanced Materials*, 23(14):1679–1683, apr 2011.
- [147] Werner Kern. The Evolution of Silicon Wafer Cleaning Technology. *Journal of The Electrochemical Society*, 137(6):1887, jun 1990.
- [148] Niranjana Sahu, B. Parija, and S. Panigrahi. Fundamental understanding and modeling of spin coating process: A review. *Indian Journal of Physics*, 83(4):493–502, aug 2009.
- [149] Yuhang Liu, Jingbo Zhao, Zhengke Li, Cheng Mu, Wei Ma, Huawei Hu, Kui Jiang, Haoran Lin, Harald Ade, and He Yan. Aggregation and morphology control enables multiple cases of high-efficiency polymer solar cells. *Nature Communications*, 5(1):1–8, nov 2014.
- [150] Austin L. Jones, Carr Hoi Yi Ho, Parand R. Riley, Indunil Angunawela, Harald Ade, Franky So, and John R. Reynolds. Investigating the active layer thickness dependence of non-fullerene organic solar cells based on PM7 derivatives. *Journal of Materials Chemistry C*, 8(43):15459–15469, nov 2020.
- [151] Alfred G. Emslie, Francis T. Bonner, and Leslie G. Peck. Flow of a Viscous Liquid on a Rotating Disk. *Journal of Applied Physics*, 29(5):858, jun 1958.
- [152] Dietrich Meyerhofer. Characteristics of resist films produced by spinning. *Journal of Applied Physics*, 49(7):3993, aug 1978.
- [153] Paul A. Staniec, Andrew J. Parnell, Alan D.F. Dunbar, Hunan Yi, Andrew J. Pearson, Tao Wang, Paul E. Hopkinson, Christy Kinane, Robert M. Dalgliesh, Athene M. Donald, Anthony J. Ryan, Ahmed Iraqi, Richard A.L. Jones, and David G. Lidzey. The Nanoscale Morphology of a PCDTBT:PCBM Photovoltaic Blend. *Advanced Energy Materials*, 1(4):499–504, jul 2011.
- [154] H. C. Liao, C. S. Tsao, Y. C. Huang, M. H. Jao, K. Y. Tien, C. M. Chuang, C. Y. Chen, C. J. Su, U. S. Jeng, Y. F. Chen, and W. F. Su. Insights into solvent vapor annealing on the performance of bulk heterojunction solar cells by a quantitative nanomorphology study. *RSC Advances*, 4(12):6246–6253, jan 2014.

- [155] Weiran Cao and Jiangeng Xue. Recent progress in organic photovoltaics: device architecture and optical design. *Energy & Environmental Science*, 7(7):2123–2144, jun 2014.
- [156] Getachew Adam, Battulga Munkhbat, Patrick Denk, Christoph Ulbricht, Calin Hrelescu, and Markus C. Scharber. Different device architectures for bulk-heterojunction solar cells. *Frontiers in Materials*, 3:39, aug 2016.
- [157] E. Bovill, N. Scarratt, J. Griffin, H. Yi, A. Iraqi, A. R. Buckley, J. W. Kingsley, and D. G. Lidzey. The role of the hole-extraction layer in determining the operational stability of a polycarbazole:fullerene bulk-heterojunction photovoltaic device. *Applied Physics Letters*, 106(7):073301, feb 2015.
- [158] W. A. ZISMAN. Relation of the equilibrium contact angle to liquid and solid constitution. 18:1–51, 1 1964.
- [159] Frederick M. Fowkes. ATTRACTIVE FORCES AT INTERFACES. *Industrial and Engineering Chemistry*, 56:40–52, 12 1964.
- [160] D. K. Owens and R. C. Wendt. Estimation of the surface free energy of polymers. *Journal of Applied Polymer Science*, 13:1741–1747, 8 1969.
- [161] D. H. Kaelble. Dispersion-polar surface tension properties of organic solids. <https://doi.org/10.1080/0021846708544582>, 2:66–81, 4 1969.
- [162] Robert J. Good and Carel J. van Oss. The modern theory of contact angles and the hydrogen bond components of surface energies. *Modern Approaches to Wettability*, pages 1–27, 1992.
- [163] Robert J. Good. A thermodynamic derivation of wenzel’s modification of young’s equation for contact angles; together with a theory of hysteresis1. *Journal of the American Chemical Society*, 74:5041–5042, 10 1952.
- [164] Bronisław Jańczuk and Tomasz Białłopiotrowicz. Surface free-energy components of liquids and low energy solids and contact angles. *Journal of Colloid and Interface Science*, 127:189–204, 1 1989.
- [165] Mark Fox. *Optical properties of solids*. Oxford University Press, 2nd edition, 2010.
- [166] Enric Garcia-Caurel, Antonello De Martino, Jean Paul Gaston, and Li Yan. Application of Spectroscopic Ellipsometry and Mueller Ellipsometry to Optical Characterization:. *Applied Spectroscopy*, 67(1):1–21, jan 2013.
- [167] Tao Zhang, Dana B. Dement, Vivian E. Ferry, and Russell J. Holmes. Intrinsic measurements of exciton transport in photovoltaic cells. *Nature Communications*, 10:1–10, 3 2019.
- [168] Deepesh Rai and Russell J. Holmes. Measurement of the triplet exciton diffusion length in organic semiconductors. *Journal of Materials Chemistry C*, 7:5695–5701, 5 2019.

- [169] Eugene Hecht. *Optics*. Pearson, 5th edition, 2017.
- [170] D. J. de Smet. A child's garden of ellipsometry. 2001.
- [171] D. E. Aspnes and A. A. Studna. Dielectric functions and optical parameters of si, ge, gap, gaas, gasb, inp, inas, and insb from 1.5 to 6.0 ev. *Physical Review B*, 27:985, 1 1983.
- [172] F. A. Jenkins and H. E. White. *Fundamentals of Optics*. McGraw-Hill, 4th edition, 2017.
- [173] Timothy D.W. Claridge. *High-Resolution NMR Techniques in Organic Chemistry*. Elsevier, 2016.
- [174] G. W. H. Höhne, W. Hemminger, and H.-J. Flammersheim. *Differential Scanning Calorimetry: An Introduction for Practitioners*. Springer Berlin Heidelberg, 1996.
- [175] D. S. Sivia. *Elementary Scattering Theory: For X-ray and Neutron Users*. Oxford University Press, 2011.
- [176] Ryong-Joon Roe. *Methods of X-Ray and Neutron Scattering in Polymer Science*. Oxford University Press, 2000.
- [177] NIST. Scattering Length Density Calculator.
- [178] W H Bragg, W L Bragg Apr, By W H Bragg, and Cavendish Professor of Physics. The reflection of x-rays by crystals. *Proceedings of the Royal Society of London. Series A, Containing Papers of a Mathematical and Physical Character*, 88:428–438, 7 1913.
- [179] J W Mullin. *Crystallization*. Butterworth-Heinemann, 4th edition, 2001.
- [180] International tables crystallography.
- [181] Matts Björck and Gabriella Andersson. GenX: an extensible X-ray reflectivity refinement program utilizing differential evolution. *Journal of Applied Crystallography*, 40(6):1174–1178, dec 2007.
- [182] Cy M. Jeffries, Jan Ilavsky, Anne Martel, Stephan Hinrichs, Andreas Meyer, Jan Skov Pedersen, Anna V. Sokolova, and Dmitri I. Svergun. Small-angle x-ray and neutron scattering. *Nature Reviews Methods Primers*, 1:1–39, 10 2021.
- [183] Andrew J. Parnell, Ashley J. Cadby, Oleksandr O. Mykhaylyk, Alan D. F. Dunbar, Paul E. Hopkinson, Athene M. Donald, and Richard A. L. Jones. Nanoscale Phase Separation of P3HT PCBM Thick Films As Measured by Small-Angle X-ray Scattering. *Macromolecules*, 44(16):6503–6508, aug 2011.
- [184] G. R. Strobl and M. Schneider. Direct evaluation of the electron density correlation function of partially crystalline polymers. *Journal of Polymer Science: Polymer Physics Edition*, 18:1343–1359, 6 1980.
- [185] O. Kratky. Possibilities of X-Ray Small Angle Analysis in the Investigation of Dissolved and Solid High Polymer Substances. *Pure and Applied Chemistry*, 12(1-4):483–524, jan 1966.

- [186] O Glatter and O Kratky. *Small angle x-ray scattering*. Academic Press, London ;;New York, 1982.
- [187] powerlaw — SasView 5.0.4 documentation.
- [188] P. Debye, H. R. Anderson, and H. Brumberger. Scattering by an Inhomogeneous Solid. II. The Correlation Function and Its Application. *Journal of Applied Physics*, 28(6):679, may 2004.
- [189] P. Debye and A. M. Bueche. Scattering by an Inhomogeneous Solid. *Journal of Applied Physics*, 20(6):518, apr 2004.
- [190] dab — SasView 5.0.4 documentation.
- [191] Dian Chen, Atsuhiko Nakahara, Dongguang Wei, Dennis Nordlund, and Thomas P. Russell. P3HT/PCBM bulk heterojunction organic photovoltaics: Correlating efficiency and morphology. *Nano Letters*, 11(2):561–567, feb 2011.
- [192] Huipeng Chen, Jihua Chen, Wen Yin, Xiang Yu, Ming Shao, Kai Xiao, Kunlun Hong, Deanna L. Pickel, W. Michael Kochemba, S. Michael Kilbey II, and Mark Dadmun. Correlation of polymeric compatibilizer structure to its impact on the morphology and function of P3HT:PCBM bulk heterojunctions. *Journal of Materials Chemistry A*, 1(17):5309–5319, apr 2013.
- [193] Yiwei Zhang, Andrew J. Parnell, Oskar Blaszczyk, Andrew J. Musser, Ifor D.W. Samuel, David G. Lidzey, and Gabriel Bernardo. Effect of fullerene acceptor on the performance of solar cells based on PffBT4T-2OD. *Physical Chemistry Chemical Physics*, 20(28):19023–19029, jul 2018.
- [194] Gabriel Bernardo, Hugo Gaspar, Gabriel E. Pérez, Alec S.D. Shackelford, Andrew J. Parnell, Markus Bleuel, Adélio Mendes, Stephen M. King, and Steven R. Parnell. Impact of 1,8-diiodooctane on the morphology of organic photovoltaic (OPV) devices – A Small Angle Neutron Scattering (SANS) study. *Polymer Testing*, 82:106305, feb 2020.
- [195] guinierporod — SasView 5.0.4 documentation.
- [196] Boualem Hammouda. A new Guinier–Porod model. *Journal of Applied Crystallography*, 43(4):716–719, aug 2010.
- [197] B. Hammouda and IUCr. Analysis of the Beaucage model. *Journal of Applied Crystallography*, 43(6):1474–1478, oct 2010.
- [198] guinier — SasView 5.0.4 documentation.
- [199] Dian Chen, Atsuhiko Nakahara, Dongguang Wei, Dennis Nordlund, and Thomas P. Russell. P3HT/PCBM Bulk Heterojunction Organic Photovoltaics: Correlating Efficiency and Morphology. *Nano Letters*, 11(2):561–567, feb 2010.
- [200] Mantid.
- [201] Sans isis data reduction - mantid project.

- [202] SasView - Small Angle Scattering Analysis.
- [203] J. R. Levine, J. B. Cohen, Y. W. Chung, and P. Georgopoulos. Grazing-incidence small-angle x-ray scattering: new tool for studying thin film growth. *Journal of Applied Crystallography*, 22:528–532, 12 1989.
- [204] Gilles Renaud, Rémi Lazzari, and Frédéric Leroy. Probing surface and interface morphology with grazing incidence small angle x-ray scattering. *Surface Science Reports*, 64:255–380, 8 2009.
- [205] Peter Müller-Buschbaum. Probing organic solar cells with grazing incidence scattering techniques. *Synchrotron Radiation in Materials Science*, pages 191–238, 2 2018.
- [206] CXRO X-Ray Interactions With Matter.
- [207] Zhang Jiang. GIXSGUI: A MATLAB toolbox for grazing-incidence X-ray scattering data visualization and reduction, and indexing of buried three-dimensional periodic nanostructured films. *Journal of Applied Crystallography*, 48(3):917–926, jun 2015.
- [208] A. L. Patterson. The Scherrer Formula for X-Ray Particle Size Determination. *Physical Review*, 56(10):978, nov 1939.
- [209] Yiwei Zhang, Muhammad T. Sajjad, Oskar Blaszczyk, Andrew J. Parnell, Arvydas Ruseckas, Luis A. Serrano, Graeme Cooke, and Ifor D.W. Samuel. Large Crystalline Domains and an Enhanced Exciton Diffusion Length Enable Efficient Organic Solar Cells. *Chemistry of Materials*, 31(17):6548–6557, sep 2019.
- [210] Y. Yoneda. Anomalous Surface Reflection of X Rays. *Physical Review*, 131(5):2010, sep 1963.
- [211] Gennady Pospelov, Walter Van Herck, Jan Burle, Juan M. Carmona Loaiza, Céline Durniak, Jonathan M. Fisher, Marina Ganeva, Dmitry Yurov, and Joachim Wuttke. Bornagain: software for simulating and fitting grazing-incidence small-angle scattering. *Journal of Applied Crystallography*, 53:262–276, 2 2020.
- [212] R. Lazzari and IUCr. Isgisaxs: a program for grazing-incidence small-angle x-ray scattering analysis of supported islands. *Journal of Applied Crystallography*, 35:406–421, 7 2002.
- [213] Dag W. Breiby, Oliver Bunk, Jens W. Andreasen, Henrik T. Lemke, and Martin M. Nielsen. Simulating X-ray diffraction of textured films. *Journal of Applied Crystallography*, 41(2):262–271, mar 2008.
- [214] Qishi Liu, Yufan Jiang, Ke Jin, Jianqiang Qin, Jingui Xu, Wenting Li, Ji Xiong, Jinfeng Liu, Zuo Xiao, Kuan Sun, Shangfeng Yang, Xiaotao Zhang, and Liming Ding. 18% Efficiency organic solar cells. *Science Bulletin*, 65(4):272–275, feb 2020.
- [215] Yong Cui, Huifeng Yao, Jianqi Zhang, Kaihu Xian, Tao Zhang, Ling Hong, Yuming Wang, Ye Xu, Kangqiao Ma, Cunbin An, Chang He, Zhixiang Wei, Feng Gao, and Jianhui Hou. Single-Junction Organic Photovoltaic Cells with Approaching 18% Efficiency. *Advanced Materials*, 32(19):1908205, may 2020.

- [216] Feng Liu, Liang Zhou, Wenrui Liu, Zichun Zhou, Qihui Yue, Wenyu Zheng, Ri Sun, Wuyue Liu, Shengjie Xu, Haijun Fan, Liheng Feng, Yuanping Yi, Wenkai Zhang, and Xiaozhang Zhu. Organic Solar Cells with 18% Efficiency Enabled by an Alloy Acceptor: A Two-in-One Strategy. *Advanced Materials*, 33(27):2100830, jul 2021.
- [217] Ming Zhang, Lei Zhu, Guanqing Zhou, Tianyu Hao, Chaoqun Qiu, Zhe Zhao, Qin Hu, Bryon W. Larson, Haiming Zhu, Zaifei Ma, Zheng Tang, Wei Feng, Yongming Zhang, Thomas P. Russell, and Feng Liu. Single-layered organic photovoltaics with double cascading charge transport pathways: 18% efficiencies. *Nature Communications*, 12(1):1–10, jan 2021.
- [218] Seungjin Lee, Dahyun Jeong, Changkyun Kim, Changyeon Lee, Hyunbum Kang, Han Young Woo, and Bumjoon J. Kim. Eco-Friendly Polymer Solar Cells: Advances in Green-Solvent Processing and Material Design. *ACS Nano*, 2020.
- [219] Shaoqing Zhang, Long Ye, Hao Zhang, and Jianhui Hou. Green-solvent-processable organic solar cells. *Materials Today*, 19(9):533–543, nov 2016.
- [220] Zongwen Ma, Biao Zhao, Yongshuai Gong, Jianping Deng, and Zhan’ao Tan. Green-solvent-processable strategies for achieving large-scale manufacture of organic photovoltaics. *Journal of Materials Chemistry A*, 7(40):22826–22847, oct 2019.
- [221] Richard K. Henderson, Concepción Jiménez-González, David J. C. Constable, Sarah R. Alston, Graham G. A. Inglis, Gail Fisher, James Sherwood, Steve P. Binks, and Alan D. Curzons. Expanding GSK’s solvent selection guide – embedding sustainability into solvent selection starting at medicinal chemistry. *Green Chemistry*, 13(4):854–862, apr 2011.
- [222] M. D. Reuber. Carcinogenicity of chloroform. *Environmental Health Perspectives*, 31:171–182, 1979.
- [223] Chlorobenzene | Toxicological Profile | ATSDR.
- [224] Dichlorobenzenes | Toxicological Profile | ATSDR.
- [225] Methylene Chloride | Toxicological Profile | ATSDR.
- [226] Chloroform | Toxicological Profile | ATSDR.
- [227] EPA. TSCA Work Plan Chemical Risk Assessment N-Methylpyrrolidone (NMP) | US EPA.
- [228] National Research Council (US) Committee on Acute Exposure Guideline and on Toxicology. Carbon Disulfide Acute Exposure Guideline Levels. 2009.
- [229] Zhonghua Ma, Hanqiu Jiang, and Jiawei Wang. Clinical analysis of severe visual loss caused by inhalational methanol poisoning in a chronic process with acute onset: a retrospective clinical analysis. *BMC Ophthalmology*, 19(1):1–7, jun 2019.
- [230] Merck | united kingdom.
- [231] Lab equipment and lab supplies | fisher scientific.

- [232] Xuekun Fang, Sunyoung Park, Takuya Saito, Rachel Tunnicliffe, Anita L. Ganesan, Matthew Rigby, Shanlan Li, Yoko Yokouchi, Paul J. Fraser, Christina M. Harth, Paul B. Krummel, Jens Mühle, Simon O’Doherty, Peter K. Salameh, Peter G. Simmonds, Ray F. Weiss, Dickon Young, Mark F. Lunt, Alistair J. Manning, Alicia Gressent, and Ronald G. Prinn. Rapid increase in ozone-depleting chloroform emissions from China. *Nature Geoscience* 2018 12:2, 12(2):89–93, dec 2018.
- [233] Susann Tegtmeier. Anthropogenic chlorine under watch. *Nature Geoscience* 2018, 12(2):84–86, dec 2018.
- [234] Denis Prat, Andy Wells, John Hayler, Helen Sneddon, C. Robert McElroy, Sarah Abou-Shehada, and Peter J. Dunn. CHEM21 selection guide of classical- and less classical-solvents. *Green Chemistry*, 18(1):288–296, dec 2015.
- [235] Fergal P. Byrne, Saimeng Jin, Giulia Paggiola, Tabitha H. M. Petchey, James H. Clark, Thomas J. Farmer, Andrew J. Hunt, C. Robert McElroy, and James Sherwood. Tools and techniques for solvent selection: green solvent selection guides. *Sustainable Chemical Processes*, 4(1):1–24, may 2016.
- [236] Caitlin McDowell and Guillermo C. Bazan. Organic solar cells processed from green solvents. *Current Opinion in Green and Sustainable Chemistry*, 5:49–54, jun 2017.
- [237] Yunping Huang and Christine K. Luscombe. Towards Green Synthesis and Processing of Organic Solar Cells. *The Chemical Record*, 19(6):1039–1049, jun 2019.
- [238] Tack Ho Lee, Song Yi Park, Bright Walker, Seo Jin Ko, Jungwoo Heo, Han Young Woo, Hyosung Choi, and Jin Young Kim. A universal processing additive for high-performance polymer solar cells. *RSC Advances*, 7(13):7476–7482, jan 2017.
- [239] J. Griffin, A. J. Pearson, N. W. Scarratt, T. Wang, A. D.F. Dunbar, H. Yi, A. Iraqi, A. R. Buckley, and D. G. Lidzey. Organic photovoltaic devices with enhanced efficiency processed from non-halogenated binary solvent blends. *Organic Electronics*, 21:216–222, jun 2015.
- [240] Natalie P. Holmes, Holly Munday, Matthew G. Barr, Lars Thomsen, Matthew A. Marcus, A. L. David Kilcoyne, Adam Fahy, Jan Van Stam, Paul C. Dastoor, and Ellen Moons. Unravelling donor–acceptor film morphology formation for environmentally-friendly OPV ink formulations. *Green Chemistry*, 21(18):5090–5103, sep 2019.
- [241] Tanya Kumari, Sungwoo Jung, Yongjoon Cho, Hwang Pill Kim, Jae Won Lee, Jiyeon Oh, Jungho Lee, Sang Myeon Lee, Mingyu Jeong, Jeong Min Baik, Wook Jo, and Changduk Yang. A built-in electric field induced by ferroelectrics increases halogen-free organic solar cell efficiency in various device types. *Nano Energy*, 68:104327, feb 2020.
- [242] Yaocheng Jin, Zhiming Chen, Sheng Dong, Nannan Zheng, Lei Ying, Xiaofang Jiang, Feng Liu, Fei Huang, and Yong Cao. A Novel Naphtho[1,2-c:5,6-c’]Bis([1,2,5]Thiadiazole)-Based Narrow-Bandgap π -Conjugated Polymer with Power Conversion Efficiency Over 10%. *Advanced Materials*, 28(44):9811–9818, nov 2016.

- [243] Jiao Zhao, Suling Zhao, Zheng Xu, Dandan Song, Bo Qiao, Di Huang, Youqin Zhu, Yang Li, Zicha Li, and Zilun Qin. Highly Efficient and Operational Stability Polymer Solar Cells Employing Nonhalogenated Solvents and Additives. *ACS Applied Materials & Interfaces*, 10(28):24075–24081, jul 2018.
- [244] Shafket Rasool, Quoc Viet Hoang, Doan Van Vu, Thi Thu Trang Bui, Seon-Mi Jin, Thuy Thi Ho, Chang Eun Song, Hang Ken Lee, Sang Kyu Lee, Jong-Cheol Lee, Sang-Jin Moon, Eunji Lee, and Won Suk Shin. High-efficiency non-halogenated solvent processable polymer/PCBM solar cells via fluorination-enabled optimized nanoscale morphology. *Journal of Materials Chemistry A*, 7(43):24992–25002, nov 2019.
- [245] Szu Han Chen, Chung-Hung H. Liao, Chih-Yu Y. Chang, Kuan-Min M. Huang, Jen-Yueh Y. Chen, Chao-Hsuan H. Chen, Hsin Fei Meng, Hsiao Wen Zan, Sheng Fu Horng, Yen Chung Lin, and Min Hsin Yeh. Large-area blade-coated organic solar cells processed from halogen-free solvent. *Organic Electronics*, 75:105376, dec 2019.
- [246] Jingbo Zhao, Yunke Li, Guofang Yang, Kui Jiang, Haoran Lin, Harald Ade, Wei Ma, and He Yan. Efficient organic solar cells processed from hydrocarbon solvents. *Nature Energy*, 1(2):1–7, jan 2016.
- [247] Matthias A. Ruderer, Shuai Guo, Robert Meier, Hsin Yin Chiang, Volker Körstgens, Johannes Wiedersich, Jan Perlich, Stephan V. Roth, and Peter Müller-Buschbaum. Solvent-induced morphology in polymer-based systems for organic photovoltaics. *Advanced Functional Materials*, 21(17):3382–3391, sep 2011.
- [248] Weijia Wang, Shuai Guo, Eva M. Herzig, Kuhu Sarkar, Markus Schindler, David Magerl, Martine Philipp, Jan Perlich, and Peter Müller-Buschbaum. Investigation of morphological degradation of P3HT:PCBM bulk heterojunction films exposed to long-term host solvent vapor. *Journal of Materials Chemistry A*, 4(10):3743–3753, mar 2016.
- [249] Jiahui Wan, Xiaopeng Xu, Guangjun Zhang, Ying Li, Kui Feng, and Qiang Peng. Highly efficient halogen-free solvent processed small-molecule organic solar cells enabled by material design and device engineering. *Energy & Environmental Science*, 10(8):1739–1745, aug 2017.
- [250] Sheng Dong, Tao Jia, Kai Zhang, Jianhua Jing, and Fei Huang. Single-Component Non-halogen Solvent-Processed High-Performance Organic Solar Cell Module with Efficiency over 14%. *Joule*, 4(9):2004–2016, sep 2020.
- [251] Ling Hong, Huifeng Yao, Ziang Wu, Yong Cui, Tao Zhang, Ye Xu, Runnan Yu, Qing Liao, Bawei Gao, Kaihu Xian, Han Young Woo, Ziyi Ge, and Jianhui Hou. Eco-Compatible Solvent-Processed Organic Photovoltaic Cells with Over 16% Efficiency. *Advanced Materials*, 31(39):1903441, sep 2019.
- [252] Haiyang Chen, Rui Zhang, Xiaobin Chen, Guang Zeng, Libor Kobera, Sabina Abbrecht, Ben Zhang, Weijie Chen, Guiying Xu, Jiyeon Oh, So-Huei Kang, Shanshan

- Chen, Changduk Yang, Jiri Brus, Jianhui Hou, Feng Gao, Yaowen Li, and Yongfang Li. A guest-assisted molecular-organization approach for >17% efficiency organic solar cells using environmentally friendly solvents. *Nature Energy*, pages 1–9, nov 2021.
- [253] Xiaopeng Xu, Liyang Yu, He Yan, Ruipeng Li, and Qiang Peng. Highly efficient non-fullerene organic solar cells enabled by a delayed processing method using a non-halogenated solvent. *Energy & Environmental Science*, 13(11):4381–4388, nov 2020.
- [254] Rui Sun, Tao Wang, Zhenghui Luo, Zhicheng Hu, Fei Huang, Chuluo Yang, and Jie Min. Achieving Eco-Compatible Organic Solar Cells with Efficiency >16.5% Based on an Iridium Complex-Incorporated Polymer Donor. *Solar RRL*, 4(7):2000156, jul 2020.
- [255] Hao Wu, Haijun Fan, Shengjie Xu, Long Ye, Yuan Guo, Yuanping Yi, Harald Ade, and Xiaozhang Zhu. Isomery-Dependent Miscibility Enables High-Performance All-Small-Molecule Solar Cells. *Small*, 15(1):1804271, jan 2019.
- [256] Zhong Zheng, Omar M. Awartani, Bhoj Gautam, Delong Liu, Yunpeng Qin, Wanning Li, Alexander Bataller, Kenan Gundogdu, Harald Ade, and Jianhui Hou. Efficient Charge Transfer and Fine-Tuned Energy Level Alignment in a THF-Processed Fullerene-Free Organic Solar Cell with 11.3% Efficiency. *Advanced Materials*, 29(5):1604241, feb 2017.
- [257] Yunpeng Qin, Long Ye, Shaoqing Zhang, Jie Zhu, Bei Yang, Harald Ade, and Jianhui Hou. A polymer design strategy toward green solvent processed efficient non-fullerene polymer solar cells. *Journal of Materials Chemistry A*, 6(10):4324–4330, mar 2018.
- [258] Yong Cui, Huifeng Yao, Ling Hong, Tao Zhang, Ye Xu, Kaihu Xian, Bowei Gao, Jinzhao Qin, Jianqi Zhang, Zhixiang Wei, and Jianhui Hou. Achieving Over 15% Efficiency in Organic Photovoltaic Cells via Copolymer Design. *Advanced Materials*, 31(14):1808356, apr 2019.
- [259] Delong Liu, Bei Yang, Bomee Jang, Bowei Xu, Shaoqing Zhang, Chang He, Han Young Woo, and Jianhui Hou. Molecular design of a wide-band-gap conjugated polymer for efficient fullerene-free polymer solar cells. *Energy & Environmental Science*, 10(2):546–551, feb 2017.
- [260] Chentong Liao, Ming Zhang, Xiaopeng Xu, Feng Liu, Ying Li, and Qiang Peng. Green solvent-processed efficient non-fullerene organic solar cells enabled by low-bandgap copolymer donors with EDOT side chains. *Journal of Materials Chemistry A*, 7(2):716–726, jan 2019.
- [261] Lei Zhu, Wenkai Zhong, Chaoqun Qiu, Bosai Lyu, Zichun Zhou, Ming Zhang, Jingnan Song, Jinqiu Xu, Jing Wang, Jazib Ali, Wei Feng, Zhiwen Shi, Xiaodan Gu, Lei Ying, Yongming Zhang, and Feng Liu. Aggregation-Induced Multilength Scaled

- Morphology Enabling 11.76% Efficiency in All-Polymer Solar Cells Using Printing Fabrication. *Advanced Materials*, 31(41):1902899, oct 2019.
- [262] Long Ye, Yuan Xiong, Zheng Chen, Qianqian Zhang, Zhuping Fei, Reece Henry, Martin Heeney, Brendan T. O'Connor, Wei You, and Harald Ade. Sequential Deposition of Organic Films with Eco-Compatible Solvents Improves Performance and Enables Over 12%-Efficiency Nonfullerene Solar Cells. *Advanced Materials*, 31(17):1808153, apr 2019.
- [263] Jianguo Mei and Zhenan Bao. Side Chain Engineering in Solution-Processable Conjugated Polymers. *Chemistry of Materials*, 26(1):604–615, jan 2013.
- [264] Chen Xie, Thomas Heumüller, Wolfgang Gruber, Xiaofeng Tang, Andrej Classen, Isabel Schuldes, Matthew Bidwell, Andreas Späth, Rainer H. Fink, Tobias Unruh, Iain McCulloch, Ning Li, and Christoph J. Brabec. Overcoming efficiency and stability limits in water-processing nanoparticulate organic photovoltaics by minimizing microstructure defects. *Nature Communications*, 9(1):1–11, dec 2018.
- [265] Changkyun Kim, Hyunbum Kang, Nayoun Choi, Seungjin Lee, Youngkwon Kim, Jinwoo Kim, Ziang Wu, Han Young Woo, and Bumjoon J. Kim. C70-based aqueous-soluble fullerene for the water composition-tolerant performance of eco-friendly polymer solar cells. *Journal of Materials Chemistry C*, 8(43):15224–15233, nov 2020.
- [266] Liyang Yu, Deping Qian, Sara Marina, Ferry A. A. Nugroho, Anirudh Sharma, Sandra Hultmark, Anna I. Hofmann, Renee Kroon, Johannes Benduhn, Detlef-M. Smilgies, Koen Vandewal, Mats R. Andersson, Christoph Langhammer, Jaime Martín, Feng Gao, and Christian Müller. Diffusion-Limited Crystallization: A Rationale for the Thermal Stability of Non-Fullerene Solar Cells. *ACS Applied Materials & Interfaces*, 2019.
- [267] Laura Ciammaruchi, Osnat Zapata-Arteaga, Edgar Gutiérrez-Fernández, Jaime Martín, and Mariano Campoy-Quiles. Structure dependent photostability of ITIC and ITIC-4F. *Materials Advances*, 1(8):2846–2861, nov 2020.
- [268] Juraj Sibik, Korbinian Löbmann, Thomas Rades, and J. Axel Zeitler. Predicting Crystallization of Amorphous Drugs with Terahertz Spectroscopy. *Molecular Pharmaceutics*, 12(8):3062–3068, aug 2015.
- [269] Eric Ofosu Kissi, Holger Grohganz, Korbinian Löbmann, Michael T. Ruggiero, J. Axel Zeitler, and Thomas Rades. Glass-Transition Temperature of the β -Relaxation as the Major Predictive Parameter for Recrystallization of Neat Amorphous Drugs. *Journal of Physical Chemistry B*, 122(10):2803–2808, mar 2018.
- [270] K. Grzybowska, M. Paluch, A. Grzybowski, Z. Wojnarowska, L. Hawelek, K. Kolodziejczyk, and K. L. Ngai. Molecular Dynamics and Physical Stability of Amorphous Anti-Inflammatory Drug: Celecoxib. *Journal of Physical Chemistry B*, 114(40):12792–12801, oct 2010.

- [271] Lin Hu, Yun Liu, Lin Mao, Sixing Xiong, Lulu Sun, Nan Zhao, Fei Qin, Youyu Jiang, and Yinhua Zhou. Chemical reaction between an ITIC electron acceptor and an amine-containing interfacial layer in non-fullerene solar cells. *Journal of Materials Chemistry A*, 6(5):2273–2278, jan 2018.
- [272] Jin Hong Kim, Tim Schembri, David Bialas, Matthias Stolte, and Frank Würthner. Slip-Stacked J-Aggregate Materials for Organic Solar Cells and Photodetectors. *Advanced Materials*, page 2104678, 2021.
- [273] Qiuju Liang, Jie Han, Chunpeng Song, Xinhong Yu, Detlef-M. Smilgies, Kui Zhao, Jiangang Liu, and Yanchun Han. Reducing the confinement of PBDB-T to ITIC to improve the crystallinity of PBDB-T/ITIC blends. *Journal of Materials Chemistry A*, 6(32):15610–15620, aug 2018.
- [274] Qilin Zhang, Xin Yuan, Yifeng Feng, Bryon W. Larson, Gregory M. Su, Yin Maung Maung, Nopporn Rujisamphan, Youyong Li, Jianyu Yuan, and Wanli Ma. Understanding the Interplay of Transport-Morphology-Performance in PBDB-T-Based Polymer Solar Cells. *Solar RRL*, 4(4):1900524, apr 2020.
- [275] Zhuping Fei, Flurin D. Eisner, Xuechen Jiao, Mohammed Azzouzi, Jason A. Röhr, Yang Han, Munazza Shahid, Anthony S. R. Chesman, Christopher D. Easton, Christopher R. McNeill, Thomas D. Anthopoulos, Jenny Nelson, and Martin Heeney. An Alkylated Indacenodithieno[3,2-b]thiophene-Based Nonfullerene Acceptor with High Crystallinity Exhibiting Single Junction Solar Cell Efficiencies Greater than 13% with Low Voltage Losses. *Advanced Materials*, 30(8):1705209, feb 2018.
- [276] Jiaying Wu, Jinho Lee, Yi Chun Chin, Huifeng Yao, Hyojung Cha, Joel Luke, Jianhui Hou, Ji Seon Kim, and James R. Durrant. Exceptionally low charge trapping enables highly efficient organic bulk heterojunction solar cells. *Energy & Environmental Science*, 13:2422–2430, 8 2020.
- [277] Qicong Li, Yang Sun, Xiaodi Xue, Shizhong Yue, Kong Liu, Muhammad Azam, Cheng Yang, Zhijie Wang, Furui Tan, and Yonghai Chen. Insights into Charge Separation and Transport in Ternary Polymer Solar Cells. *ACS Applied Materials and Interfaces*, 11(3):3299–3307, jan 2019.
- [278] James W. Kingsley, Pier Paolo Marchisio, Hunan Yi, Ahmed Iraqi, Christy J. Kinane, Sean Langridge, Richard L. Thompson, Ashley J. Cadby, Andrew J. Pearson, David G. Lidzey, Richard A.L. Jones, and Andrew J. Parnell. Molecular weight dependent vertical composition profiles of PCDTBT:PC71BM blends for organic photovoltaics. *Scientific Reports*, 4(1):1–7, jun 2014.
- [279] Yiwen Wang, Weixia Lan, Ning Li, Zhaojue Lan, Zhen Li, Jingnan Jia, and Furong Zhu. Stability of Nonfullerene Organic Solar Cells: from Built-in Potential and Interfacial Passivation Perspectives. *Advanced Energy Materials*, 9(19):1900157, may 2019.

- [280] Jun Yuan, Tianyi Huang, Pei Cheng, Yingping Zou, Huotian Zhang, Jonathan Lee Yang, Sheng Yung Chang, Zhenzhen Zhang, Wenchao Huang, Rui Wang, Dong Meng, Feng Gao, and Yang Yang. Enabling low voltage losses and high photocurrent in fullerene-free organic photovoltaics. *Nature Communications*, 10:1–8, 2 2019.
- [281] D. Baran, T. Kirchartz, S. Wheeler, S. Dimitrov, M. Abdelsamie, J. Gorman, R. S. Ashraf, S. Holliday, A. Wadsworth, N. Gasparini, P. Kaienburg, H. Yan, A. Amassian, C. J. Brabec, J. R. Durrant, and I. McCulloch. Reduced voltage losses yield 10% efficient fullerene free organic solar cells with >1 v open circuit voltages. *Energy & Environmental Science*, 9:3783–3793, 11 2016.
- [282] Jakob Hofinger, Christoph Putz, Felix Mayr, Katarina Gugujonovic, Dominik Wientend, and Markus C. Scharber. Understanding the low voltage losses in high-performance non-fullerene acceptor-based organic solar cells. *Materials Advances*, 2:4291–4302, 7 2021.
- [283] J. Peet, J. Y. Kim, N. E. Coates, W. L. Ma, D. Moses, A. J. Heeger, and G. C. Bazan. Efficiency enhancement in low-bandgap polymer solar cells by processing with alkane dithiols. *Nature Materials* 2007 6:7, 6(7):497–500, may 2007.
- [284] Xia Guo, Chaohua Cui, Maojie Zhang, Lijun Huo, Ye Huang, Jianhui Hou, and Yongfang Li. High efficiency polymer solar cells based on poly(3-hexylthiophene)/indene-C 70 bisadduct with solvent additive. *Energy & Environmental Science*, 5(7):7943–7949, jun 2012.
- [285] Corey V. Hoven, Xuan Dung Dang, Robert C. Coffin, Jeff Peet, Thuc Quyen Nguyen, and Guillermo C. Bazan. Improved Performance of Polymer Bulk Heterojunction Solar Cells Through the Reduction of Phase Separation via Solvent Additives. *Advanced Materials*, 22(8):E63–E66, feb 2010.
- [286] Yong Cui, Huifeng Yao, Jianqi Zhang, Tao Zhang, Yuming Wang, Ling Hong, Kaihu Xian, Bowei Xu, Shaoqing Zhang, Jing Peng, Zhixiang Wei, Feng Gao, and Jianhui Hou. Over 16% efficiency organic photovoltaic cells enabled by a chlorinated acceptor with increased open-circuit voltages. *Nature Communications* 2019 10:1, 10(1):1–8, jun 2019.
- [287] Rakesh C. Mahadevapuram, John A. Carr, Yuqing Chen, Sayantan Bose, Kanwar S. Nalwa, Jacob W. Petrich, and Sumit Chaudhary. Low-boiling-point solvent additives can also enable morphological control in polymer solar cells. *Synthetic Metals*, 185-186:115–119, dec 2013.
- [288] Xin Song, Nicola Gasparini, and Derya Baran. The Influence of Solvent Additive on Polymer Solar Cells Employing Fullerene and Non-Fullerene Acceptors. *Advanced Electronic Materials*, 4(10), oct 2018.
- [289] Joo Hyun Kim, Abay Gadisa, Charley Schaefer, Huifeng Yao, Bhoj R. Gautam, Nrup Balar, Masoud Ghasemi, Iordania Constantinou, Franky So, Brendan T. O’Connor,

- Kenan Gundogdu, Jianhui Hou, and Harald Ade. Strong polymer molecular weight-dependent material interactions: impact on the formation of the polymer/fullerene bulk heterojunction morphology. *Journal of Materials Chemistry A*, 5:13176–13188, 6 2017.
- [290] José Darío Perea, Stefan Langner, Michael Salvador, Benjamin Sanchez-Lengeling, Ning Li, Chaohong Zhang, Gabor Jarvas, Janos Kontos, Andras Dallos, Alán Aspuru-Guzik, and Christoph J. Brabec. Introducing a new potential figure of merit for evaluating microstructure stability in photovoltaic polymer-fullerene blends. *Journal of Physical Chemistry C*, 121:18153–18161, 8 2017.
- [291] Sandra Kouijzer, Jasper J. Michels, Mauricio Van Den Berg, Veronique S. Gevaerts, Mathieu Turbiez, Martijn M. Wienk, and René A.J. Janssen. Predicting morphologies of solution processed polymer:fullerene blends. *Journal of the American Chemical Society*, 135:12057–12067, 8 2013.
- [292] Min Kim, Jaewon Lee, Sae Byeok Jo, Dong Hun Sin, Hyomin Ko, Hansol Lee, Seung Goo Lee, and Kilwon Cho. Critical factors governing vertical phase separation in polymer-*pcbm* blend films for organic solar cells. *Journal of Materials Chemistry A*, 4:15522–15535, 10 2016.
- [293] Brian A Collins, Zhe Li, John R Tumbleston, Eliot Gann, Christopher R McNeill, Harald Ade, B A Collins, J R Tumbleston, E Gann, H Ade, Z Li, and C R McNeill. Absolute Measurement of Domain Composition and Nanoscale Size Distribution Explains Performance in PTB7:PC71BM Solar Cells. *Advanced Energy Materials*, 3(1):65–74, jan 2013.
- [294] Yongye Liang, Zheng Xu, Jiangbin Xia, Szu-Ting Tsai, Yue Wu, Gang Li, Claire Ray, Luping Yu, [L P Yu, Y Y Liang, J B Xia, C Ray, G Li, Z Xu, S.-T Tsai, and Y Wu. For the Bright Future—Bulk Heterojunction Polymer Solar Cells with Power Conversion Efficiency of 7.4%. *Advanced Materials*, 22(20):E135–E138, may 2010.
- [295] Kerstin S. Wienhold, Volker Körstgens, Sebastian Grott, Xinyu Jiang, Matthias Schwartzkopf, Stephan V. Roth, and Peter Müller-Buschbaum. Effect of Solvent Additives on the Morphology and Device Performance of Printed Nonfullerene Acceptor Based Organic Solar Cells. *ACS Applied Materials and Interfaces*, 2019.
- [296] Andrew J. Pearson, Paul E. Hopkinson, Elsa Couderc, Konrad Domanski, Mojtaba Abdi-Jalebi, and Neil C. Greenham. Critical light instability in CB/DIO processed PBDTTT-EFT:PC71BM organic photovoltaic devices. *Organic Electronics*, 30:225–236, mar 2016.
- [297] Bertrand J. Tremolet De Villers, Kathryn A. O’Hara, David P. Ostrowski, Perry H. Biddle, Sean E. Shaheen, Michael L. Chabinyc, Dana C. Olson, and Nikos Kopidakis. Removal of Residual Diiodooctane Improves Photostability of High-Performance Organic Solar Cell Polymers. *Chemistry of Materials*, 28(3):876–884, feb 2016.

- [298] Wen Wang, Fei Qin, Xiaoyu Zhu, Yang Liu, Xueshi Jiang, Lulu Sun, Cong Xie, and Yinhua Zhou. Exploring the Chemical Interaction between Diiodooctane and PEDOT-PSS Electrode for Metal Electrode-Free Nonfullerene Organic Solar Cells. *ACS Applied Materials and Interfaces*, 12(3):3800–3805, jan 2020.
- [299] Long Ye, Yan Jing, Xia Guo, Hao Sun, Shaoqing Zhang, Maojie Zhang, Lijun Huo, and Jianhui Hou. Remove the Residual Additives toward Enhanced Efficiency with Higher Reproducibility in Polymer Solar Cells. *Journal of Physical Chemistry C*, 117(29):14920–14928, jul 2013.
- [300] Wenchao Huang, Eliot Gann, Zai Quan Xu, Lars Thomsen, Yi Bing Cheng, and Christopher R. McNeill. A facile approach to alleviate photochemical degradation in high efficiency polymer solar cells. *Journal of Materials Chemistry A*, 3(31):16313–16319, jul 2015.
- [301] Aurélien Tournebize, Agnès Rivaton, Heiko Peisert, and Thomas Chassé. The crucial role of confined residual additives on the photostability of P3HT:PCBM active layers. *Journal of Physical Chemistry C*, 119(17):9142–9148, apr 2015.
- [302] Matthias A. Ruderer and Peter Müller-Buschbaum. Solvent effects in polymer based organic photovoltaics. *Polymers for Energy Storage and Conversion*, pages 137–161, 5 2013.
- [303] Chao Wang, Eliot Gann, Anthony S.R. Chesman, and Christopher R. McNeill. Residual solvent additive enables the nanostructuring of ptb7-th:pc71bm solar cells via soft lithography. *AIP Advances*, 9:065024, 6 2019.
- [304] Pan Yin, Tao Zheng, Yue Wu, Gangjian Liu, Zhi Guo Zhang, Chaohua Cui, Yongfang Li, and Ping Shen. Achieving efficient thick active layer and large area ternary polymer solar cells by incorporating a new fused heptacyclic non-fullerene acceptor. *Journal of Materials Chemistry A*, 6:20313–20326, 10 2018.
- [305] J. C. Wang, X. C. Ren, S. Q. Shi, C. W. Leung, and Paddy K.L. Chan. Charge accumulation induced S-shape J–V curves in bilayer heterojunction organic solar cells. *Organic Electronics*, 12(6):880–885, jun 2011.
- [306] Wolfgang Tress, Karl Leo, and Moritz Riede. Influence of Hole-Transport Layers and Donor Materials on Open-Circuit Voltage and Shape of I–V Curves of Organic Solar Cells. *Advanced Functional Materials*, 21(11):2140–2149, jun 2011.
- [307] B. Y. Finck and B. J. Schwartz. Understanding the origin of the S-curve in conjugated polymer/fullerene photovoltaics from drift-diffusion simulations. *Applied Physics Letters*, 103(5):053306, aug 2013.
- [308] Thomas J. Aldrich, Micaela Matta, Weigang Zhu, Steven M. Swick, Charlotte L. Stern, George C. Schatz, Antonio Facchetti, Ferdinand S. Melkonyan, and Tobin J. Marks. Fluorination Effects on Indacenodithienothiophene Acceptor Packing and Electronic Structure, End-Group Redistribution, and Solar Cell Photovoltaic Response. *Journal of the American Chemical Society*, 2019.

- [309] Eric Verploegen, Chad E. Miller, Kristin Schmidt, Zhenan Bao, and Michael F. Toney. Manipulating the morphology of P3HT-PCBM bulk heterojunction blends with solvent vapor annealing. *Chemistry of Materials*, 24(20):3923–3931, oct 2012.
- [310] Abul F. Huq, Ali Ammar, Abdullah M. Al-Enizi, and Alamgir Karim. In-situ orientation and crystal growth kinetics of P3HT in drop cast P3HT:PCBM films. *Polymer*, 113:200–213, mar 2017.
- [311] Xinxin Xia, Tsz-Ki Lau, Xuyun Guo, Yuhao Li, Minchao Qin, Kuan Liu, Zeng Chen, Xiaozhi Zhan, Yiqun Xiao, Pok Fung Chan, Heng Liu, Luhang Xu, Guilong Cai, Na Li, Haiming Zhu, Gang Li, Ye Zhu, Tao Zhu, Xiaowei Zhan, Xun-Li Wang, and Xinhui Lu. Uncovering the out-of-plane nanomorphology of organic photovoltaic bulk heterojunction by GTSAXS. *Nature Communications 2021 12:1*, 12(1):1–10, oct 2021.
- [312] Washat Ware, Tia Wright, Yimin Mao, Shubo Han, Jessa Guffie, Evgeny O. Danilov, Jeromy Rech, Wei You, Zhiping Luo, and Bhoj Gautam. Aggregation controlled charge generation in fullerene based bulk heterojunction polymer solar cells: Effect of additive. *Polymers*, 13(1):1–11, jan 2021.
- [313] Yu Gu, Cheng Wang, and Thomas P. Russell. Multi-Length-Scale Morphologies in PCPDTBT/PCBM Bulk-Heterojunction Solar Cells. *Advanced Energy Materials*, 2(6):683–690, jun 2012.
- [314] Jing Guo, Yao Wu, Rui Sun, Wei Wang, Jie Guo, Qiang Wu, Xiaofeng Tang, Chenkai Sun, Zhenghui Luo, Kai Chang, Zhuohan Zhang, Jun Yuan, Tengfei Li, Weihua Tang, Erjun Zhou, Zuo Xiao, Liming Ding, Yingping Zou, Xiaowei Zhan, Chuluo Yang, Zhen Li, Christoph J. Brabec, Yongfang Li, and Jie Min. Suppressing photo-oxidation of non-fullerene acceptors and their blends in organic solar cells by exploring material design and employing friendly stabilizers. *Journal of Materials Chemistry A*, 7(43):25088–25101, nov 2019.
- [315] William R. Mateker, Thomas Heumueller, Rongrong Cheacharoen, I. T. Sachs-Quintana, Michael D. McGehee, Julien Warnan, Pierre M. Beaujuge, Xiaofeng Liu, and Guillermo C. Bazan. Molecular Packing and Arrangement Govern the Photo-Oxidative Stability of Organic Photovoltaic Materials. *Chemistry of Materials*, 27(18):6345–6353, sep 2015.
- [316] Aurélie Dupuis, Pascal Wong-Wah-Chung, Agns Rivaton, and Jean Luc Gardette. Influence of the microstructure on the photooxidative degradation of poly(3-hexylthiophene). *Polymer Degradation and Stability*, 97(3):366–374, mar 2012.
- [317] Shogo Yamane, Yasumasa Suzuki, Tetsuhiko Miyadera, Tomoyuki Koganezawa, Koji Arai, Yuki Akiyama, Masayuki Chikamatsu, Yuji Yoshida, Hiroyuki Suda, and Junji Mizukado. Relationship between photostability and nanostructures in DTS(FBTTh2)2:fullerene bulk-heterojunction films. *Solar Energy Materials and Solar Cells*, 151:96–101, jul 2016.

- [318] Hyo Sang Lee, Hyeng Gun Song, Hyeseung Jung, Myung Hwa Kim, Changsoon Cho, Jung Yong Lee, Sungnam Park, Hae Jung Son, Hui Jun Yun, Soon Ki Kwon, Yun Hi Kim, and Bongsoo Kim. Effects of Backbone Planarity and Tightly Packed Alkyl Chains in the Donor-Acceptor Polymers for High Photostability. *Macromolecules*, 49(20):7844–7856, oct 2016.
- [319] Nutifafa Y. Doumon, Mikhail V. Dryzhov, Félix V. Houard, Vincent M. Le Corre, Azadeh Rahimi Chatri, Panagiotis Christodoulis, and L. Jan Anton Koster. Photostability of Fullerene and Non-Fullerene Polymer Solar Cells: The Role of the Acceptor. *ACS Applied Materials and Interfaces*, 11(8):8310–8318, feb 2019.
- [320] Jinlong Cai, Hui Wang, Xue Zhang, Wei Li, Donghui Li, Yuchao Mao, Baocai Du, Mengxue Chen, Yuan Zhuang, Dan Liu, Hua Li Qin, Yan Zhao, Joel A. Smith, Rachel C. Kilbride, Andrew J. Parnell, Richard A.L. Jones, David G. Lidzey, and Tao Wang. Fluorinated solid additives enable high efficiency non-fullerene organic solar cells. *Journal of Materials Chemistry A*, 8(8):4230–4238, feb 2020.
- [321] Yuanpeng Xie, Xiaotian Hu, Jingping Yin, Lin Zhang, Xiangchuan Meng, Guodong Xu, Qingyun Ai, Weihua Zhou, and Yiwang Chen. Butanedithiol Solvent Additive Extracting Fullerenes from Donor Phase To Improve Performance and Photostability in Polymer Solar Cells. *ACS Applied Materials and Interfaces*, 9(11):9918–9925, mar 2017.
- [322] Seongyu Lee, Jaemin Kong, and Kwanghee Lee. Air-Stable Organic Solar Cells Using an Iodine-Free Solvent Additive. *Advanced Energy Materials*, 6(21):1600970, nov 2016.
- [323] Hongtao Liu, Zhong’an Li, and Dongbing Zhao. Rhodanine-based nonfullerene acceptors for organic solar cells. *Science China Materials*, 62:1574–1596, 7 2019.
- [324] Hyojung Cha, Jiaying Wu, Andrew Wadsworth, Jade Nagitta, Saurav Limbu, Sebastian Pont, Zhe Li, Justin Searle, Mark F. Wyatt, Derya Baran, Ji Seon Kim, Iain McCulloch, and James R. Durrant. An Efficient, “Burn in” Free Organic Solar Cell Employing a Nonfullerene Electron Acceptor. *Advanced Materials*, 29(33):1701156, sep 2017.
- [325] Xueping Yi, Carr Hoi Yi Ho, Bhoj Gautam, Lei Lei, Ashraful Haider Chowdhury, Behzad Bahrami, Qiquan Qiao, and Franky So. Effects of polymer crystallinity on non-fullerene acceptor based organic solar cell photostability. *Journal of Materials Chemistry C*, 8(45):16092–16099, nov 2020.
- [326] Derya Baran, Nicola Gasparini, Andrew Wadsworth, Ching Hong Tan, Nimer Wehbe, Xin Song, Zeinab Hamid, Weimin Zhang, Marios Neophytou, Thomas Kirchartz, Christoph J. Brabec, James R. Durrant, and Iain McCulloch. Robust nonfullerene solar cells approaching unity external quantum efficiency enabled by suppression of geminate recombination. *Nature Communications 2018 9:1*, 9(1):1–9, may 2018.

- [327] Samuel E. Root, Mohammad A. Alkhadra, Daniel Rodriguez, Adam D. Printz, and Darren J. Lipomi. Measuring the Glass Transition Temperature of Conjugated Polymer Films with Ultraviolet–Visible Spectroscopy. *Chemistry of Materials*, 29(7):2646–2654, apr 2017.
- [328] Hugo Bronstein, Dong Seok Leem, Richard Hamilton, Paul Woebkenberg, Simon King, Weimin Zhang, Raja Shahid Ashraf, Martin Heeney, Thomas D. Anthopoulos, John De Mello, and Iain McCulloch. Indacenodithiophene-co-benzothiadiazole copolymers for high performance solar cells or transistors via alkyl chain optimization. *Macromolecules*, 44:6649–6652, 9 2011.
- [329] Helen Bristow, Karl J. Thorley, Andrew J.P. White, Andrew Wadsworth, Maxime Babics, Zeinab Hamid, Weimin Zhang, Alexandra F. Paterson, Jan Kosco, Julianna Panidi, Thomas D. Anthopoulos, and Iain McCulloch. Impact of nonfullerene acceptor side chain variation on transistor mobility. *Advanced Electronic Materials*, 5:1900344, 10 2019.
- [330] Qiuju Liang, Xuechen Jiao, Ye Yan, Zhiyuan Xie, Guanghao Lu, Jiangang Liu, Yanchun Han, Q Liang, Y Yan, Z Xie, J Liu, Y Han, X Jiao, and G Lu. Separating Crystallization Process of P3HT and O-IDTBR to Construct Highly Crystalline Interpenetrating Network with Optimized Vertical Phase Separation. *Advanced Functional Materials*, 29(47):1807591, nov 2019.
- [331] Sebastian Pont, Fabrizia Foglia, Anthony M Higgins, James R Durrant, João T Cabral, S Pont, J R Durrant, J T Cabral, F Foglia, and A M Higgins. Stability of polymer:pcbm thin films under competitive illumination and thermal stress. *Advanced Functional Materials*, 28:1802520, 10 2018.
- [332] Davide Bartesaghi, Gang Ye, Ryan C Chiechi, L Jan Anton Koster, D Bartesaghi, L J A Koster, G Ye, and R C Chiechi. Compatibility of ptb7 and [70]pcbm as a key factor for the stability of ptb7:[70]pcbm solar cells. *Advanced Energy Materials*, 6:1502338, 7 2016.
- [333] Lucas Frédéric, Alaric Desmarchelier, Ludovic Favereau, and Grégory Pieters. Designs and Applications of Circularly Polarized Thermally Activated Delayed Fluorescence Molecules. *Advanced Functional Materials*, 31(20):2010281, may 2021.
- [334] Da-Wei Zhang, Meng Li, and Chuan-Feng Chen. Recent advances in circularly polarized electroluminescence based on organic light-emitting diodes. *Chemical Society Reviews*, 49(5):1331–1343, 2020.
- [335] Matthias Schulz, Jennifer Zablocki, Oliya S. Abdullaeva, Stefanie Brück, Frank Balzer, Arne Lützen, Oriol Arteaga, and Manuela Schiek. Giant intrinsic circular dichroism of prolinol-derived squaraine thin films. *Nature Communications*, 9(1):2413, dec 2018.
- [336] Matthias Schulz, Frank Balzer, Dorothea Scheunemann, Oriol Arteaga, Arne Lützen, Stefan C. J. Meskers, and Manuela Schiek. Chiral Excitonic Organic Photodiodes

- for Direct Detection of Circular Polarized Light. *Advanced Functional Materials*, 29(16):1900684, apr 2019.
- [337] Lewis E. MacKenzie and Robert Pal. Circularly polarized lanthanide luminescence for advanced security inks. *Nature Reviews Chemistry*, 5(2):109–124, feb 2021.
- [338] Colum Breen, Robert Pal, Mark R.J. Elsegood, Simon J. Teat, Felipe Iza, Kristian Wende, Benjamin R. Buckley, and Stephen J. Butler. Time-resolved luminescence detection of peroxyxynitrite using a reactivity-based lanthanide probe. *Chemical Science*, 11(12):3164–3170, mar 2020.
- [339] Yun Shen, Chuan-feng Chen, Diels À Alder Reactions, Friedel À Crafts-type Reactions, and Metal-catalyzed Cyclizations. Helicenes: Synthesis and Applications. *Chemical Reviews*, 112(3):1463–1535, 2012.
- [340] Matthias Kettner, Volodymyr V. Maslyuk, Daniel Nürenberg, Johannes Seibel, Rafael Gutierrez, Gianaurelio Cuniberti, Karl Heinz Ernst, and Helmut Zacharias. Chirality-Dependent Electron Spin Filtering by Molecular Monolayers of Helicenes. *Journal of Physical Chemistry Letters*, 9(8):2025–2030, apr 2018.
- [341] Ying Yang, Rosenildo Correa da Costa, Matthew J Fuchter, and Alasdair J Campbell. Circularly polarized light detection by a chiral organic semiconductor transistor. *Nature Photonics*, 7(8):634–638, jul 2013.
- [342] Vankayala Kiran, Shinto P. Mathew, Sidney R. Cohen, Irene Hernández Delgado, Jérôme Lacour, and Ron Naaman. Helicenes - A New Class of Organic Spin Filter. *Advanced Materials*, 28(10):1957–1962, mar 2016.
- [343] Meike Stöhr, Serpil Boz, Michael Schär, Manh-Thuong Nguyen, Carlo A. Pignedoli, Daniele Passerone, W. Bernd Schweizer, Carlo Thilgen, Thomas A. Jung, and François Diederich. Self-Assembly and Two-Dimensional Spontaneous Resolution of Cyano-Functionalized [7]Helicenes on Cu(111). *Angewandte Chemie International Edition*, 50(42):9982–9986, oct 2011.
- [344] Marc Gingras, Guy Félix, and Romain Peresutti. One hundred years of helicene chemistry. Part 2: Stereoselective syntheses and chiral separations of carbohelicenes. *Chemical Society Reviews*, 42(3):1007–1050, jan 2013.
- [345] Ying Yang, Beth Rice, Xingyuan Shi, Jochen R. Brandt, Rosenildo Correa Da Costa, Gordon J. Hedley, Detlef M. Smilgies, Jarvist M. Frost, Ifor D.W. Samuel, Alberto Otero-De-La-Roza, Erin R. Johnson, Kim E. Jelfs, Jenny Nelson, Alasdair J. Campbell, and Matthew J. Fuchter. Emergent Properties of an Organic Semiconductor Driven by its Molecular Chirality. *ACS Nano*, 11(8):8329–8338, 2017.
- [346] Chidambar Kulkarni, Amit Kumar Mondal, Tapan Kumar Das, Gal Grinbom, Francesco Tassinari, Mathijs F. J. Mabesoone, E. W. Meijer, and Ron Naaman. Highly Efficient and Tunable Filtering of Electrons’ Spin by Supramolecular Chirality of Nanofiber-Based Materials. *Advanced Materials*, 32(7):1904965, feb 2020.

- [347] R. Naaman and David H. Waldeck. Chiral-Induced Spin Selectivity Effect. *Journal of Physical Chemistry Letters*, 3(16):2178–2187, aug 2012.
- [348] Paul Valerian Möllers, Selma Ulku, Dilhara Jayarathna, Francesco Tassinari, Daniel Nürenberg, Ron Naaman, Catalina Achim, and Helmut Zacharias. Spin-selective electron transmission through self-assembled monolayers of double-stranded peptide nucleic acid. *Chirality*, 33(2):93–102, feb 2021.
- [349] S. H. Chen, D. Katsis, A. W. Schmid, J. C. Mastrangelo, T. Tsutsui, and T. N. Blanton. Circularly polarized light generated by photoexcitation of luminophores in glassy liquid-crystal films. *Nature*, 397(6719):506–508, feb 1999.
- [350] Sonia Maniappan, Ashok Badrinarayan Jadhav, and Jatish Kumar. Template Assisted Generation of Chiral Luminescence in Organic Fluorophores. *Frontiers in Chemistry*, 0:968, jan 2021.
- [351] Kyungmin Baek, Dong Myung Lee, Yu Jin Lee, Hyunchul Choi, Jeongdae Seo, Inbyeong Kang, Chang Jae Yu, and Jae Hoon Kim. Simultaneous emission of orthogonal handedness in circular polarization from a single luminophore. *Light: Science and Applications*, 8(1):2047–7538, dec 2019.
- [352] Jessica Wade, James N. Hilfiker, Jochen R. Brandt, Letizia Liirò-Peluso, Li Wan, Xingyuan Shi, Francesco Salerno, Seán T.J. Ryan, Stefan Schöche, Oriol Arteaga, Tamás Jávorfí, Giuliano Siligardi, Cheng Wang, David B. Amabilino, Peter H. Beton, Alasdair J. Campbell, and Matthew J. Fuchter. Natural optical activity as the origin of the large chiroptical properties in π -conjugated polymer thin films. *Nature Communications*, 11(1), dec 2020.
- [353] Daniele Di Nuzzo, Chidambar Kulkarni, Baodan Zhao, Eilam Smolinsky, Francesco Tassinari, Stefan C.J. Meskers, Ron Naaman, E. W. Meijer, and Richard H. Friend. High Circular Polarization of Electroluminescence Achieved via Self-Assembly of a Light-Emitting Chiral Conjugated Polymer into Multidomain Cholesteric Films. *ACS Nano*, 11(12):12713–12722, 2017.
- [354] Karl-Heinz Ernst. Molecular chirality at surfaces. *physica status solidi (b)*, 249(11):2057–2088, nov 2012.
- [355] Karl-Heinz Ernst. Stereochemical Recognition of Helicenes on Metal Surfaces. *Accounts of Chemical Research*, 49(6):1182–1190, jun 2016.
- [356] Roman Fasel, Manfred Parschau, and Karl Heinz Ernst. Amplification of chirality in two-dimensional enantiomorphous lattices. *Nature*, 439(7075):449–452, jan 2006.
- [357] Johannes Seibel, Manfred Parschau, and Karl-Heinz Ernst. Double layer crystallization of heptahelicene on noble metal surfaces. *Chirality*, 32(7):975–980, jul 2020.
- [358] S. Heutz, R. Cloots, and T. S. Jones. Structural templating effects in molecular heterostructures grown by organic molecular-beam deposition. *Applied Physics Letters*, 77(24):3938–3940, dec 2000.

- [359] Dong Kuk Kim, Daphné Lubert-Perquel, and Sandrine Heutz. Comparison of organic and inorganic layers for structural templating of pentacene thin films. *Materials Horizons*, 7(1):289–298, jan 2020.
- [360] P. Sullivan, T. S. Jones, A. J. Ferguson, and S. Heutz. Structural templating as a route to improved photovoltaic performance in copper phthalocyanine/fullerene (C₆₀) heterojunctions. *Applied Physics Letters*, 91(23):233114, 2007.
- [361] Panagiotis G. Karamertzanis and Constantinos C. Pantelides. Ab initio crystal structure prediction—I. Rigid molecules. *Journal of Computational Chemistry*, 26(3):304–324, feb 2005.
- [362] P. G. Karamertzanis† and C. C. Pantelides. Ab initio crystal structure prediction. II. Flexible molecules. *Molecular Physics*, 105(2-3):273–291, jan 2007.
- [363] Sarah L. Price, Maurice Leslie, Gareth W. A. Welch, Matthew Habgood, Louise S. Price, Panagiotis G. Karamertzanis, and Graeme M. Day. Modelling organic crystal structures using distributed multipole and polarizability-based model intermolecular potentials. *Physical Chemistry Chemical Physics*, 12(30):8478–8490, jul 2010.
- [364] Ad Becke. Density-functional exchange-energy approximation with correct asymptotic behavior. *Physical review. A*, 38(6):3098–3100, sep 1988.
- [365] P. E. Blöchl. Projector augmented-wave method. *Physical Review B*, 50(24):17953, dec 1994.
- [366] Claudia Wachsmann, Edwin Weber, Mátyás Czugler, and Wilhelm Seichter. New Functional Hexahelicenes - Synthesis, Chiroptical Properties, X-ray Crystal Structures, and Comparative Data Bank Analysis of Hexahelicenes. *European Journal of Organic Chemistry*, 2003(15):2863–2876, aug 2003.
- [367] Tetsuya Ogawa, Kiyoshi Kuwamoto, Seiji Isoda, Takashi Kobayashi, and Norbert Karl. 3,4:9,10-Perylenetetracarboxylic dianhydride (PTCDA) by electron crystallography. *Acta crystallographica. Section B, Structural science*, 55(Pt 1):123–130, feb 1999.
- [368] Joon Hak Oh, Ya Sen Sun, Rüdiger Schmidt, Michael F. Toney, Dennis Nordlund, Martin Könemann, Frank Würthner, and Zhenan Bao. Interplay between energetic and kinetic factors on the ambient stability of n-channel organic transistors based on perylene diimide derivatives. *Chemistry of Materials*, 21(22):5508–5518, nov 2009.
- [369] Philipp Furche, Reinhart Ahlrichs, Claudia Wachsmann, Edwin Weber, Adam Sobanski, Fritz Vögtle, and Stefan Grimme. Circular dichroism of helicenes investigated by time-dependent density functional theory. *Journal of the American Chemical Society*, 122(8):1717–1724, mar 2000.
- [370] A. J. Ramadan, I. Hancox, S. Huband, C. C. Parkins, S. A.F. Bon, M. Walker, S. Fearn, C. F. McConville, T. S. Jones, and L. A. Rochford. Selecting Phthalocyanine Polymorphs Using Local Chemical Termination Variations in Copper Iodide. *J. Phys. Chem. C*, 120(8):4448 – 4452, 2016.

Neutron Scattering Data Modelling

This Appendix contains additional information and full fit parameters relating to the neutron reflectivity (NR) and small angle neutron scattering (SANS) measurements in Chapter 5 and Chapter 6.

A.1 Chapter 5: Small Angle Neutron Scattering

Blend System	DIO (Vol%)	Scale (10^{-4})	B (cm^{-1})	α	χ^2/N_{pts}
PBDB-T : d52-ITIC	0	2.68 ± 0.36	1.98 ± 0.08	3.54 ± 0.04	1.28
	0.5	1.92 ± 0.34	2.75 ± 0.08	3.55 ± 0.05	1.52
	3	2.12 ± 0.43	5.10 ± 0.09	3.48 ± 0.06	0.83
PBDB-T : PC ₇₁ BM	0	20.64 ± 3.43	5.12 ± 0.10	2.83 ± 0.05	0.92
	0.5	16.02 ± 1.85	6.78 ± 0.10	3.03 ± 0.03	2.15
	1	8.15 ± 0.10	7.07 ± 0.09	3.22 ± 0.04	1.74
	3	9.50 ± 0.12	7.12 ± 0.10	3.18 ± 0.04	1.83

Table A.1: Table of SANS power law fit parameters for PBDB-T : d52-ITIC and PBDB-T : PC₇₁BM blend films processed from 0-3 Vol% DIO.

Blend System	DIO (Vol%)	Scale (10^{-3})	B (cm^{-1})	ξ nm	χ^2/N_{pts}
PBDB-T : d52-ITIC	0	5.75 ± 0.03	1.37 ± 0.07	5.05 ± 0.02	31.22
	0.5	3.88 ± 0.01	3.27 ± 0.06	8.01 ± 0.32	57.70
	3	3.48 ± 0.01	5.50 ± 0.06	7.92 ± 0.34	5.78
PBDB-T : PC ₇₁ BM	0	3.05 ± 0.01	6.65 ± 0.06	7.68 ± 0.04	26.01
	0.5	6.15 ± 0.04	6.81 ± 0.07	4.06 ± 0.02	14.8
	1	5.65 ± 0.03	7.02 ± 0.07	4.56 ± 0.02	8.44
	3	5.30 ± 0.02	7.77 ± 0.07	6.03 ± 0.02	3.71

Table A.2: Table of SANS DAB model fit parameters for PBDB-T : d52-ITIC and PBDB-T : PC₇₁BM blend films processed from 0-3 Vol% DIO.

A.2 Chapter 5: Neutron Reflectivity

A.2.1 Neutron Reflectivity of Pure Material Reference Films

NR data and fit parameters of pure films are presented below. All layers were modelled as a three-slab-layer system of silicon, silicon oxide (SiO_2) and reference film using the fixed parameters shown in (Figure A.1). Instrument resolution was fixed at 2%.

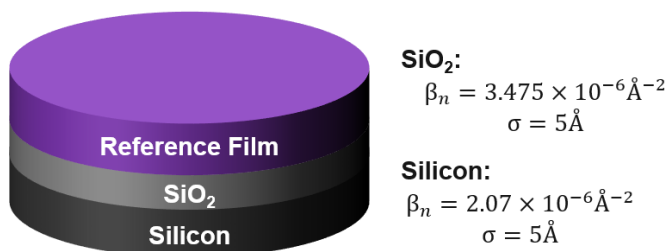


Figure A.1: An illustration of the three-slab-layer system and corresponding fixed parameters used to model NR of the pure material reference films.

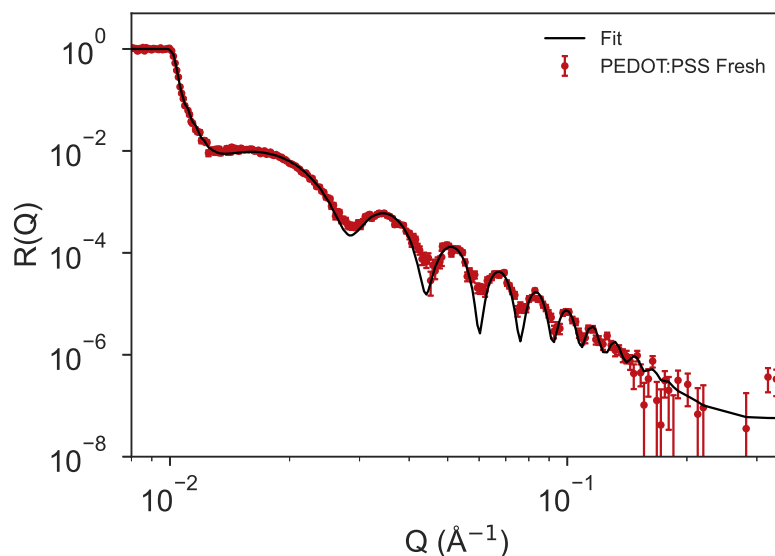


Figure A.2: NR curve of a pure PEDOT:PSS thin film on silicon

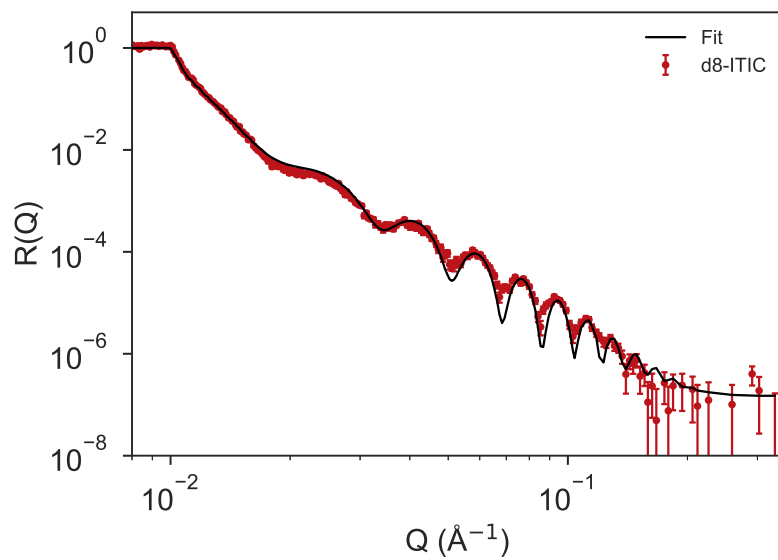


Figure A.3: NR curve of a pure d8-ITIC thin film on silicon

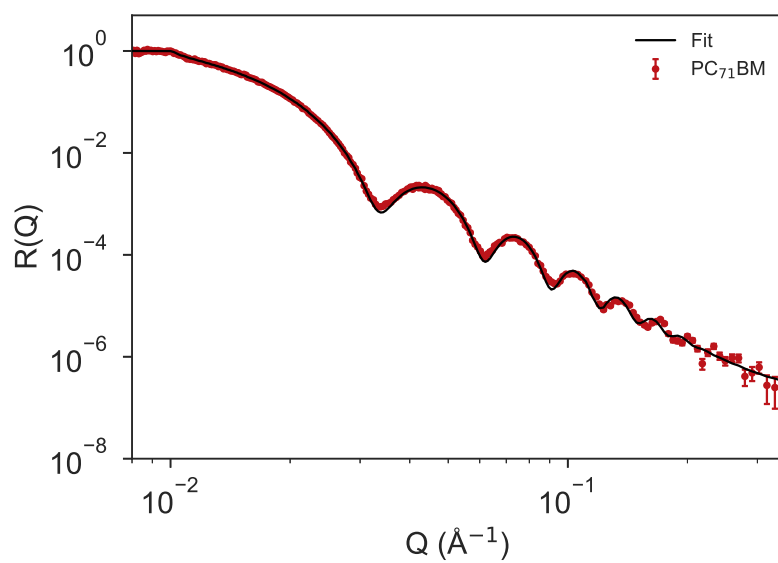


Figure A.4: NR curve of a pure PC₇₁BM thin film on silicon

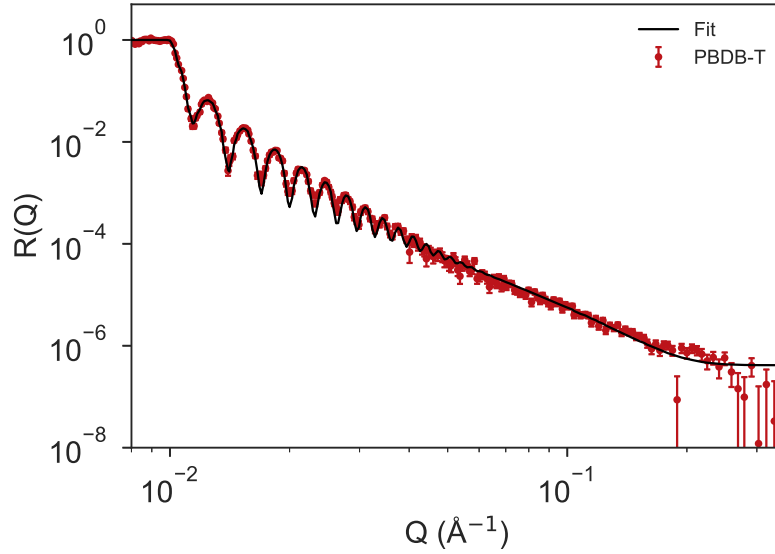


Figure A.5: NR curve of a pure PBDB-T thin film on silicon

Pure Material	I_0	B ($\times 10^{-7}$)	SiO_2	Film			χ^2/N_{pts}
			L (Å)	L (Å)	σ (Å)	β_n ($\times 10^{-6} \text{Å}^{-2}$)	
PEDOT:PSS	0.833	0.10	10	385	11	1.68	2.41
d8-ITIC	0.854	3.04	12.5	344	13	2.15	5.81
PC₇₁BM	0.958	0.45	20	201	5	4.67	3.68
PBDB-T	0.923	1.79	11	1886	29	1.15	2.38

Table A.3: Table of NR fit parameters of the pure reference film data shown in Figure A.2 - Figure A.5

A.2.2 Neutron Reflectivity Modelling of Blend Films

NR data and fit parameters of blend films are presented below. All layers were modelled as a four-slab-layer system of Si/SiO₂/PEDOT:PSS/Blend/Air using the fixed parameters shown in (Figure A.6). Instrument resolution was fixed at 2%. For PBDB-T : PC₇₁BM samples, the blend film was modelled in three different ways as: a single uniform layer, a layer with an acceptor-rich region buried at the PEDOT:PSS interface and a layer with an acceptor-rich surface. For NR curves, data has been offset by two decades for clarity. In the SLD profiles, a film depth of 0Å corresponds to the silicon/sample interface. All films were annealed at 160°C for 10 minutes.

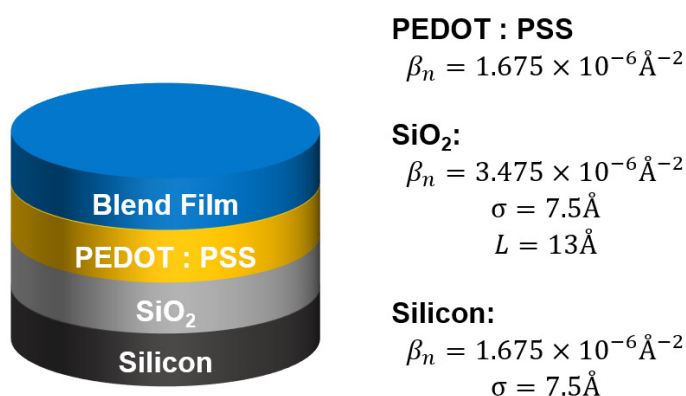


Figure A.6: An illustration of the four-slab-layer system and corresponding fixed parameters used to model NR of the blend films.

PBDB-T : PC₇₁BM 0 Vol% DIO

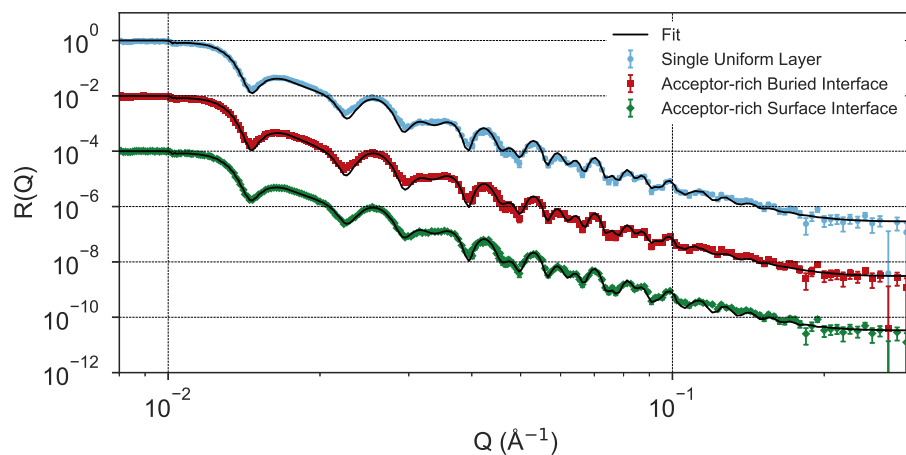


Figure A.7: NR of a PBDB-T : PC₇₁BM thin film processed with 0 Vol% DIO.

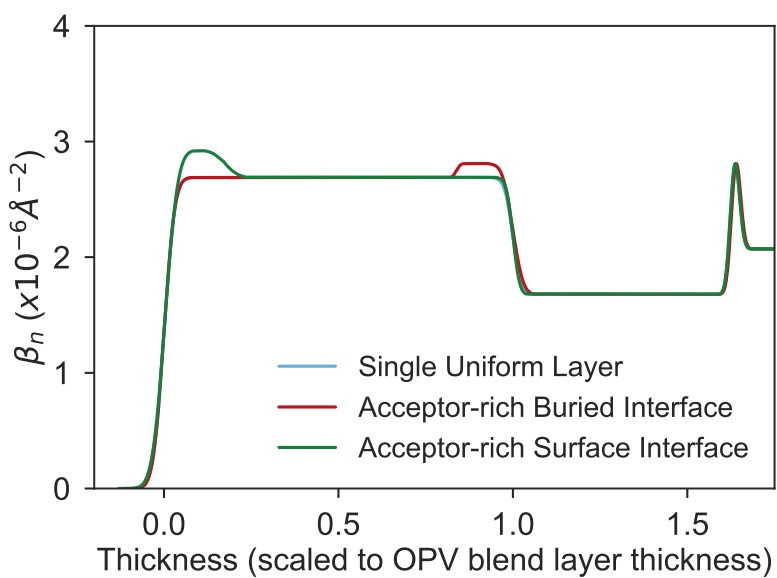


Figure A.8: SLD profiles corresponding to the NR data shown in Figure A.7 of a PBDB-T : PC₇₁BM thin film processed with 0 Vol% DIO.

Model	I_0	B ($\times 10^{-7}$)	PEDOT:PSS		Bulk Layer			Interface			χ^2/N_{pts}
			L (\AA)	σ (\AA)	L (\AA)	σ (\AA)	β_n ($\times 10^{-6} \text{\AA}^{-2}$)	L (\AA)	σ (\AA)	β_n ($\times 10^{-6} \text{\AA}^{-2}$)	
Uniform Layer	1.040	3.01	424	13	676	16	2.69	–	–	–	7.44
Buried Interface	1.019	3.13	425	15	566	16	2.69	109	5	4.92	6.37
Surface Interface	0.977	3.27	424	10	559	20	2.69	117	19	2.93	2.28

Table A.4: Table of NR fit parameters for a PBDB-T : PC₇₁BM thin film processed with 0 Vol% DIO corresponding the data shown in Figure A.7 and Figure A.8.

PBDB-T : PC₇₁BM 0.5 Vol% DIO

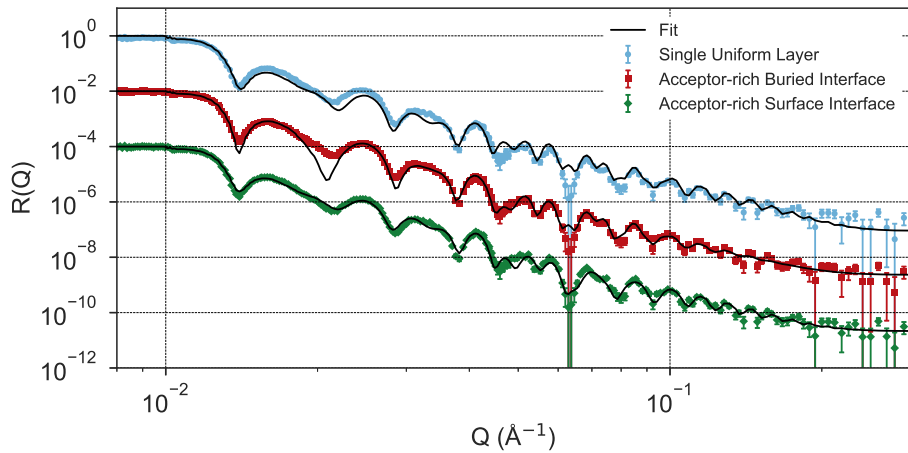


Figure A.9: NR of a PBDB-T : PC₇₁BM thin film processed with 0.5 Vol% DIO.

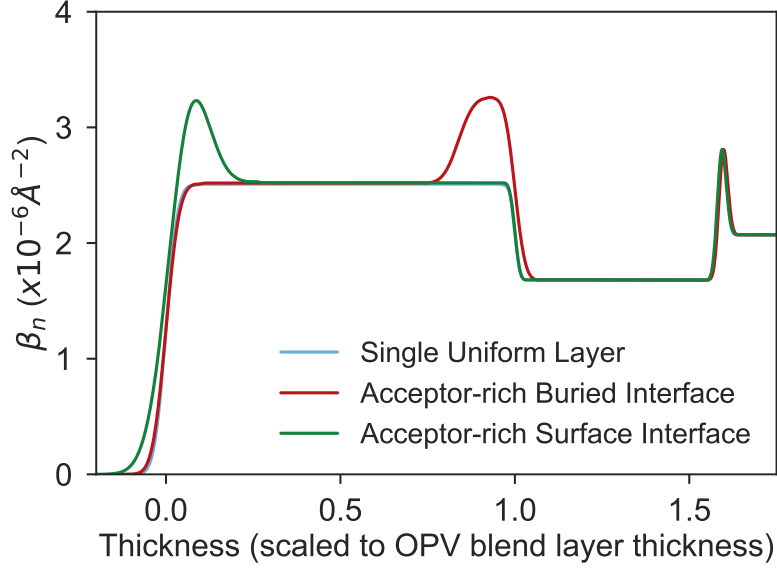


Figure A.10: SLD profiles corresponding to the NR data shown in Figure A.9 of a PBDB-T : PC₇₁BM thin film processed with 0.5 Vol% DIO.

Model	I_0	B ($\times 10^{-7}$)	PEDOT:PSS		Bulk Layer			Interface			χ^2/N_{pts}
			L (\AA)	σ (\AA)	L (\AA)	σ (\AA)	β_n ($\times 10^{-6} \text{\AA}^{-2}$)	L (\AA)	σ (\AA)	β_n ($\times 10^{-6} \text{\AA}^{-2}$)	
Uniform Layer	1.15	1.03	416	8	712	19	2.51	–	–	–	19.56
Buried Interface	0.977	2.27	418	16	597	21	2.52	115	24	3.26	17.50
Surface Interface	0.985	2.12	416	8	642	35	2.52	55	40	4.68	9.60

Table A.5: Table of NR fit parameters for a PBDB-T : PC₇₁BM thin film processed with 0.5 Vol% DIO corresponding the data shown in Figure A.9 and Figure A.10.

PBDB-T : PC₇₁BM 1 Vol% DIO

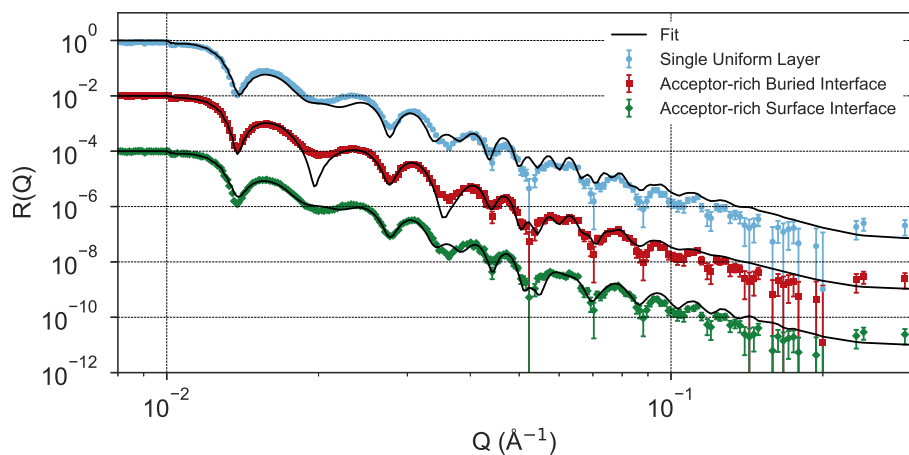


Figure A.11: NR of a PBDB-T : PC₇₁BM thin film processed with 1 Vol% DIO.

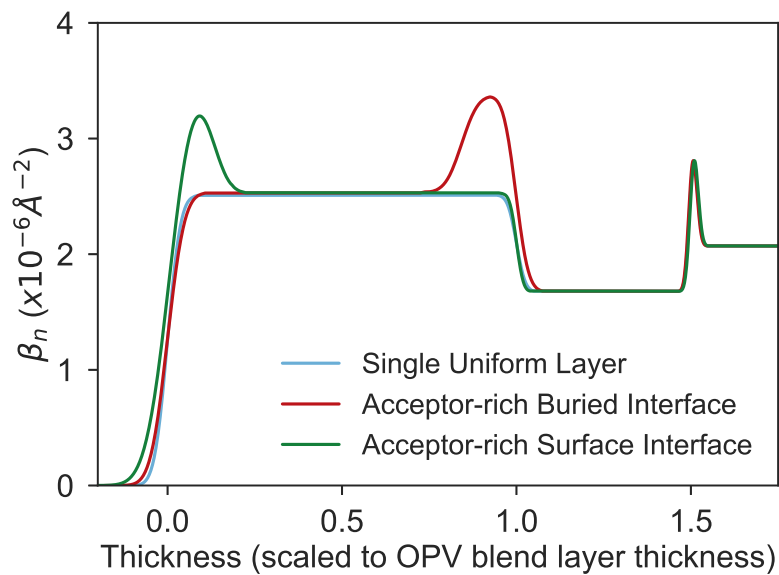


Figure A.12: SLD profiles corresponding to the NR data shown in Figure A.11 of a PBDB-T : PC₇₁BM thin film processed with 1 Vol% DIO.

Model	I_0	B ($\times 10^{-7}$)	PEDOT:PSS		Bulk Layer			Interface			χ^2/N_{pts}
			L (\AA)	σ (\AA)	L (\AA)	σ (\AA)	β_n ($\times 10^{-6} \text{\AA}^{-2}$)	L (\AA)	σ (\AA)	β_n ($\times 10^{-6} \text{\AA}^{-2}$)	
Uniform Layer	1.138	0.81	376	15	754	22	2.51	–	–	–	39.38
Buried Interface	0.944	1.00	375	21	635	29	2.53	117	28	3.38	16.68
Surface Interface	0.987	1.00	376	11	656	29	2.53	92	40	3.57	12.36

Table A.6: Table of NR fit parameters for a PBDB-T: PC₇₁BM thin film processed with 1 Vol% DIO corresponding the data shown in Figure A.11 and Figure A.12.

PBDB-T : PC₇₁BM 3 Vol% DIO

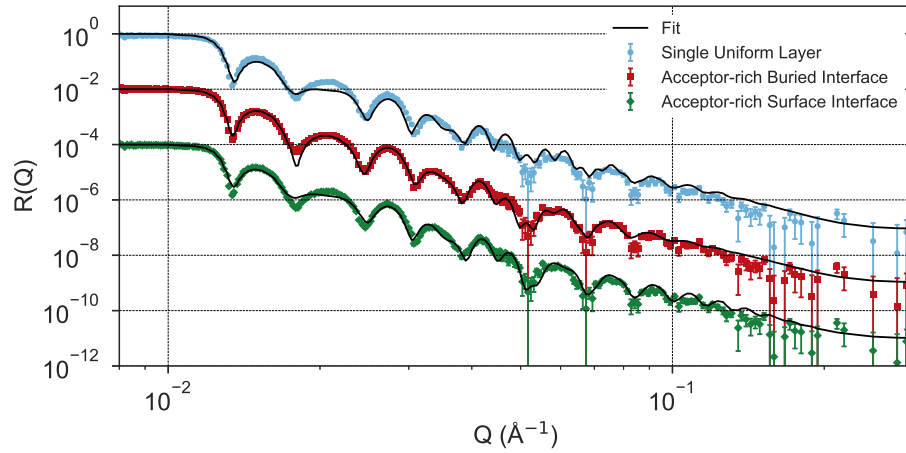


Figure A.13: NR of a PBDB-T : PC₇₁BM thin film processed with 3 Vol% DIO.

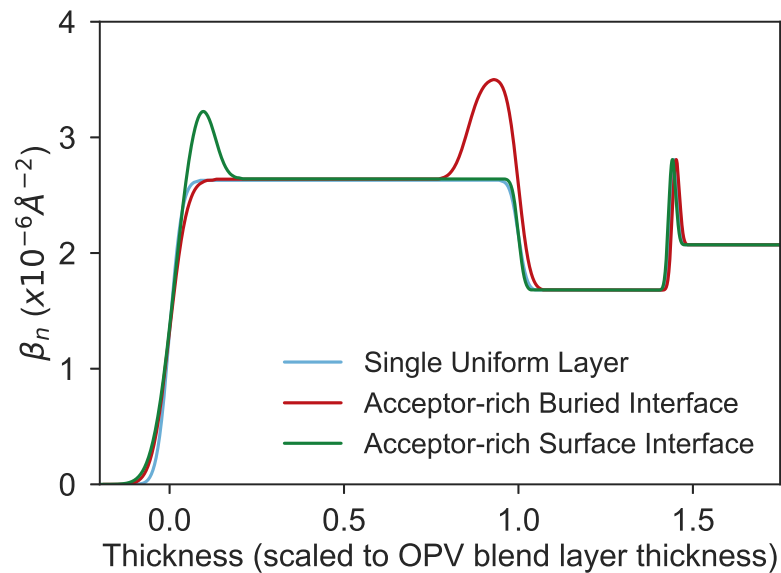


Figure A.14: SLD profiles corresponding to the NR data shown in Figure A.13 of a PBDB-T : PC₇₁BM thin film processed with 3 Vol% DIO.

Model	I_0	B ($\times 10^{-7}$)	PEDOT:PSS		Bulk Layer			Interface			χ^2/N_{pts}
			L (\AA)	σ (\AA)	L (\AA)	σ (\AA)	β_n ($\times 10^{-6} \text{\AA}^{-2}$)	L (\AA)	σ (\AA)	β_n ($\times 10^{-6} \text{\AA}^{-2}$)	
Uniform Layer	1.09	1.00	386	16	884	25	2.63	–	–	–	39.20
Buried Interface	0.928	1.00	391	23	754	35	2.64	127	29	3.52	6.20
Surface Interface	0.982	1.00	386	12	778	26	2.64	99	44	3.54	19.84

Table A.7: Table of NR fit parameters for a PBDB-T : PC₇₁BM thin film processed with 3 Vol% DIO corresponding the data shown in Figure A.13 and Figure A.14.

PBDB-T : d8-ITIC 0-3 Vol% DIO

DIO (Vol%)	I_0	B ($\times 10^{-7}$)	PEDOT:PSS		Bulk Layer			Interface Layer			χ^2/N_{pts}
			L (\AA)	σ (\AA)	L (\AA)	σ (\AA)	β_n ($\times 10^{-6} \text{\AA}^{-2}$)	L (\AA)	σ (\AA)	β_n ($\times 10^{-6} \text{\AA}^{-2}$)	
0	0.902	1.00	376	15	798	79	1.62	60	19	2.15	2.87
0.5	0.917	1.00	422	11	723	62	1.62	59	11	2.15	3.60
1	0.928	1.00	378	12	692	64	1.56	86	64	2.15	2.19
3	0.525	1.00	366	5	462	70	1.22	62	12	2.15	6.26

Table A.8: Table of NR fit parameters for PBDB-T : d8-ITIC blend films processed with 0-3 Vol% DIO corresponding to the data shown in Figure 5.15a and Figure 5.16a.

A.3 Chapter 6: Small Angle Neutron Scattering

The full fit parameters for the SANS data presented in Chapter 6 are presented below. Data were modelled using a power law model and a DAB model.

Sample	Scale ($\times 10^{-4}$)	B (cm^{-1})	α	χ^2/N_{pts}
PTB7-Th : PC₇₁BM	1.24 ± 0.82	1.77 ± 0.14	3.13 ± 0.17	0.66
PTB7-Th : d-EH-IDTBR	7.74 ± 2.37	0 ± 0.19	2.91 ± 0.08	1.18
PTB7-Th : d-O-IDTBR	0.32 ± 0.14	0.49 ± 0.15	3.68 ± 0.12	0.61
PTB7-Th : d-O-IDTBCN	5.45 ± 1.26	0 ± 0.09	2.86 ± 0.06	10.34

Table A.9: SANS power law fit parameters corresponding to the data in Figure 6.17.

DAB Model

Sample	Scale ($\times 10^{-3}$)	B (cm^{-1})	ξ (nm)	χ^2/N_{pts}
PTB7-Th : PC₇₁BM	0.82 ± 0.01	1.98 ± 0.10	13.61 ± 0.26	2.73
PTB7-Th : d-EH-IDTBR	1.67 ± 0.02	0.64 ± 0.14	8.90 ± 0.12	2.84
PTB7-Th : d-O-IDTBR	2.79 ± 0.03	0.76 ± 0.12	29.67 ± 0.51	1.52
PTB7-Th : d-O-IDTBCN	0.95 ± 0.01	0.01 ± 0.06	10.95 ± 0.12	13.98

Table A.10: SANS DAB model fit parameters corresponding to the data in Figure 6.15.

A.4 Chapter 6: Neutron Reflectivity

A.4.1 Neutron Reflectivity Modelling of Pure Material Reference Films

NR data and fit parameters of pure material reference films are presented below. All layers were modelled as a three-slab-layer system of silicon, silicon oxide (SiO₂) and reference film using the fixed parameters shown in (Figure A.15). Instrument resolution was fixed at 2%.

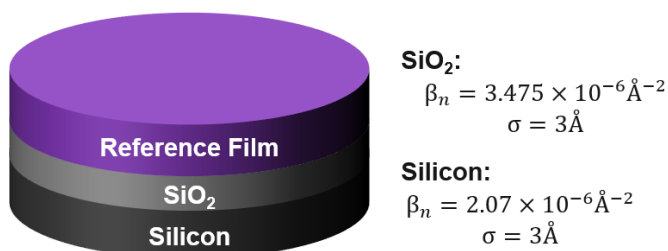


Figure A.15: An illustration of the three-slab-layer system and corresponding fixed parameters used to model NR of the pure material reference films.

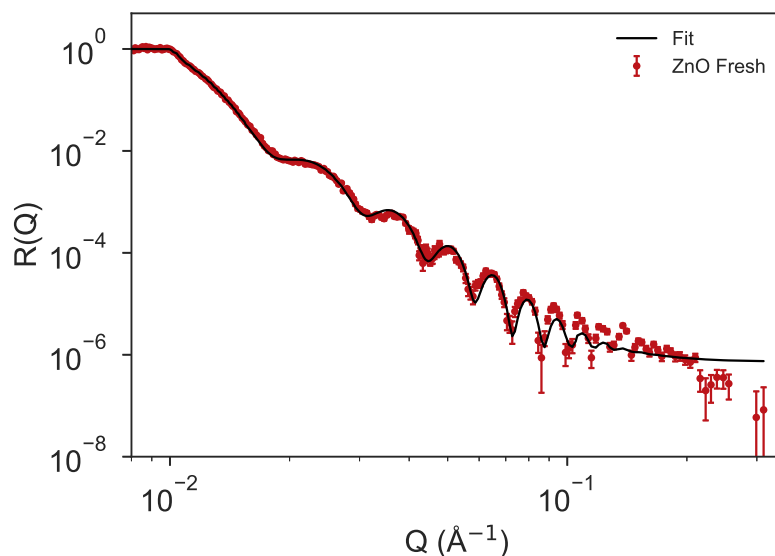


Figure A.16: NR curve of a pure ZnO thin film on silicon

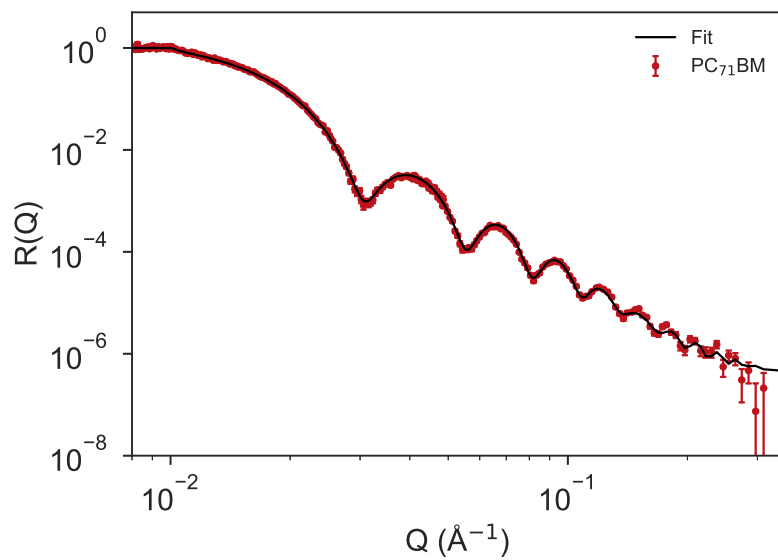


Figure A.17: NR curve of a PC₇₁BM thin film on silicon

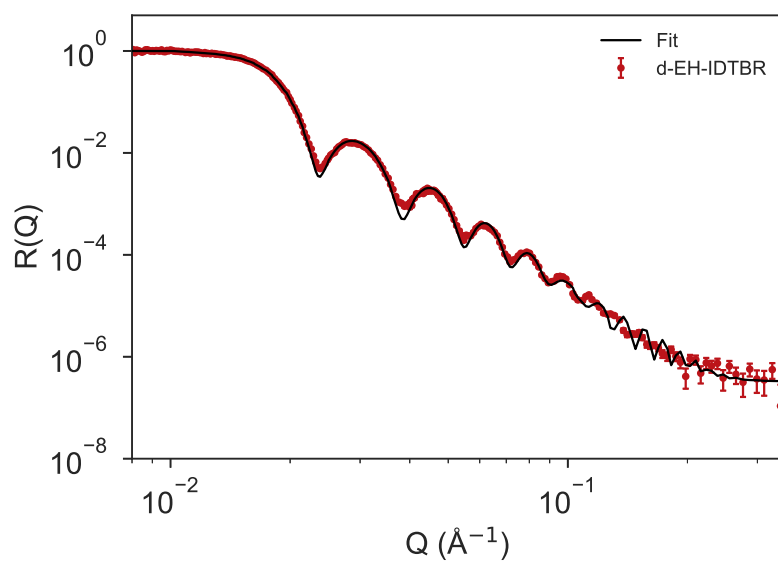


Figure A.18: NR curve of a d-EH-IDTBR thin film on silicon

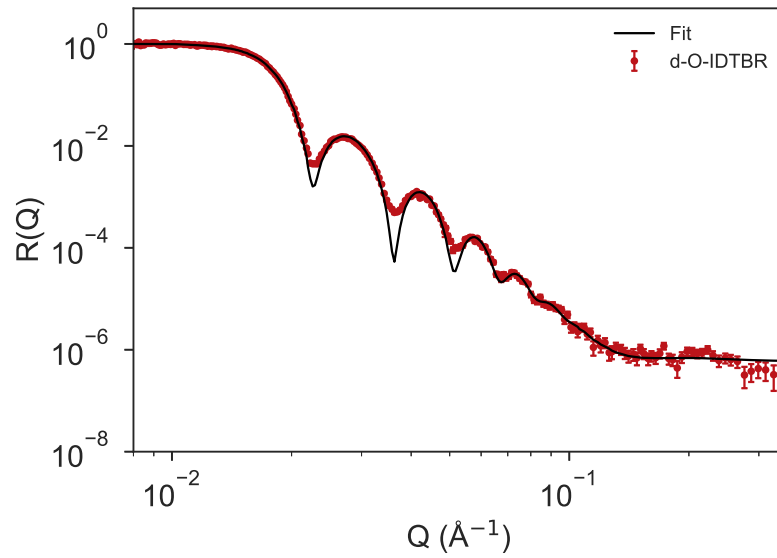


Figure A.19: NR curve of a d-O-IDTBR thin film on silicon

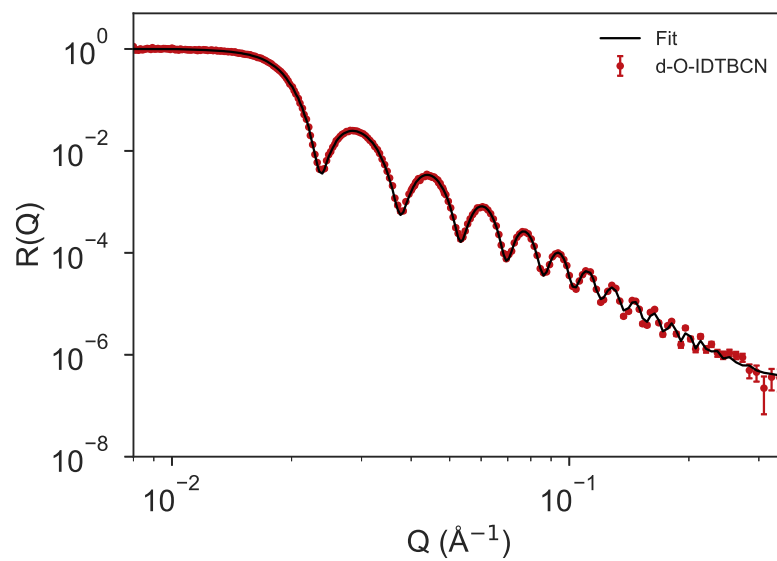


Figure A.20: NR curve of a d-O-IDTBCN thin film on silicon

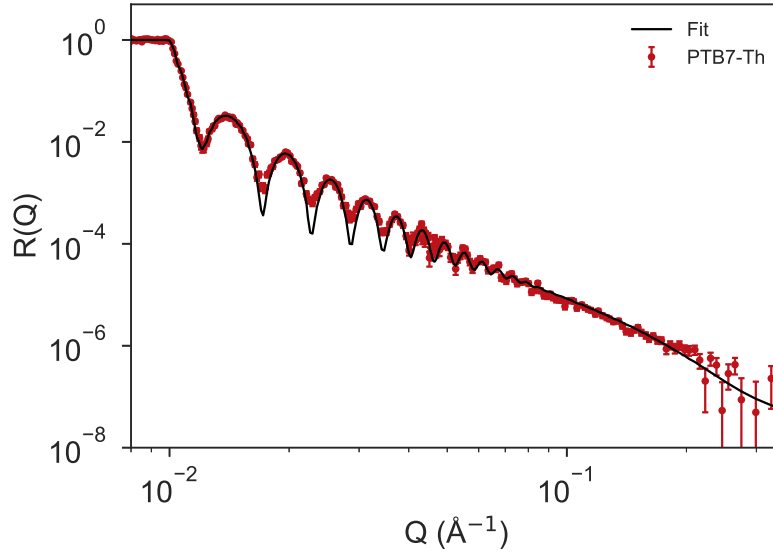


Figure A.21: NR curve of a PTB7-Th thin film on silicon

Pure Material	I_0	B ($\times 10^{-7}$)	SiO ₂	Film			χ^2/N_{pts}
			L (Å)	L (Å)	σ (Å)	β_n ($\times 10^{-6} \text{Å}^{-2}$)	
ZnO	0.953	7.07	10	415	18	2.51	4.37
PC ₇₁ BM	0.937	4.04	19	226	4	4.65	1.64
d-EH-IDTBR	0.950	2.78	29	347	8	5.03	8.61
d-O-IDTBR	0.944	5.64	20	377	31	4.91	8.36
d-O-IDTBCN	0.972	3.02	20	366	4	5.53	1.79
PTB7-Th	0.952	0.36	14	1043	25	1.14	3.30

Table A.11: Table of NR fit parameters corresponding to the data shown in Figure A.16 - Figure A.21.

A.4.2 Neutron Reflectivity Modelling of Blend Films

NR data and fit parameters of blend films are presented below. All layers were modelled as a four-slab-layer system of silicon, silicon oxide (SiO₂), ZnO and the blend film using the fixed parameters shown in (Figure A.22). Instrument resolution was fixed at 2%.

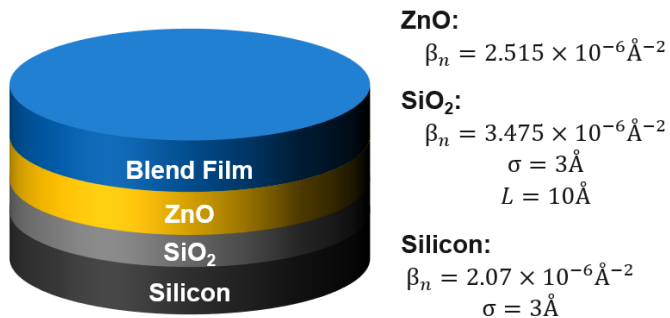


Figure A.22: An illustration of the four-slab-layer system and corresponding fixed parameters used to model neutron reflectivity of the blend films.

PTB7-Th : PC₇₁BM

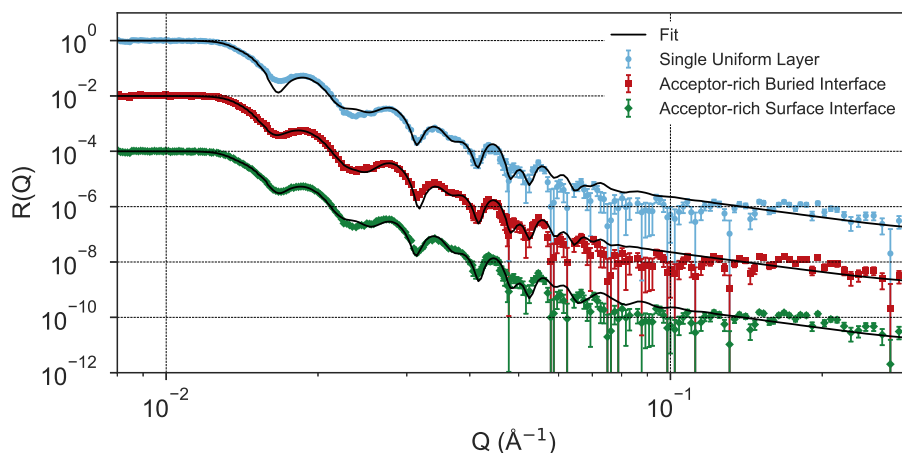


Figure A.23: NR of a PTB7-Th : PC₇₁BM thin film deposited on a ZnO coated silicon substrate and annealed at 80°C for 10 minutes. The PTB7-Th : PC₇₁BM layer has been modelled in three different ways as: a single uniform layer, a layer with an acceptor-rich region buried at the ZnO interface and a layer with an acceptor-rich surface. Data offset by two decades for clarity.

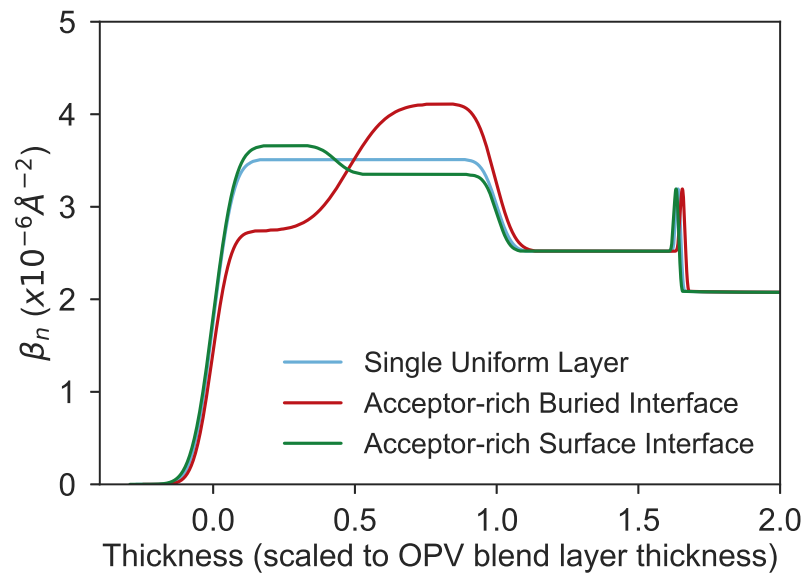


Figure A.24: SLD profiles corresponding to the NR data shown in Figure A.23 of a fresh PTB7-Th : PC₇₁BM thin film. A film depth of 0 Å corresponds to the silicon/sample interface.

Model	I_0	B ($\times 10^{-7}$)	ZnO		Bulk Layer			Interface			χ^2/N_{pts}
			L (Å)	σ (Å)	L (Å)	σ (Å)	β_n ($\times 10^{-6} \text{Å}^{-2}$)	L (Å)	σ (Å)	β_n ($\times 10^{-6} \text{Å}^{-2}$)	
Uniform Layer	0.933	1.21	417	27	658	37	3.51	–	–	–	19.56
Buried Interface	0.896	1.41	425	35	314	33	2.74	333	69	4.11	7.45
Surface Interface	0.931	1.20	412	23	374	31	3.35	284	40	3.66	7.22

Table A.12: Table of NR fit parameters for a PTB7-Th : PC₇₁BM thin film corresponding the data shown in Figure A.23 and Figure A.24.

PTB7-Th : d-EH-IDTBR

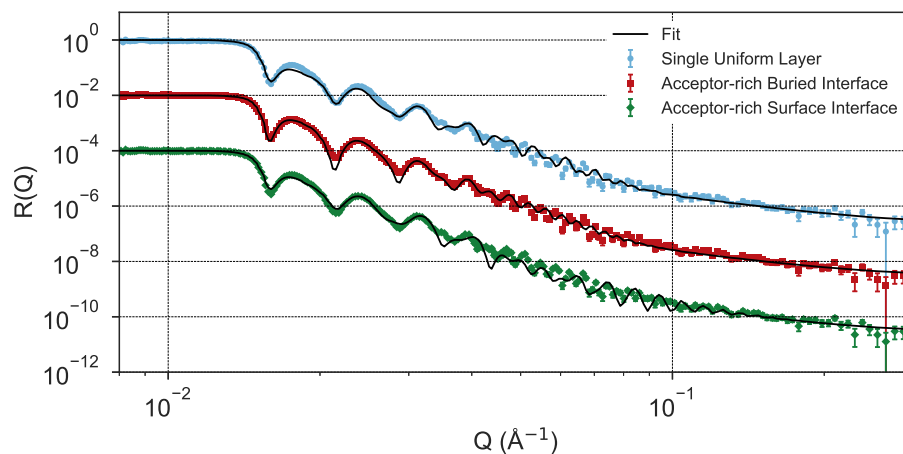


Figure A.25: NR of a PTB7-Th : d-EH-IDTBR thin film deposited on a ZnO coated silicon substrate and annealed at 80°C for 10 minutes. The PTB7-Th : d-EH-IDTBR layer has been modelled in three different ways as: a single uniform layer, a layer with an acceptor-rich region buried at the ZnO interface and a layer with an acceptor-rich surface. Data offset by two decades for clarity.

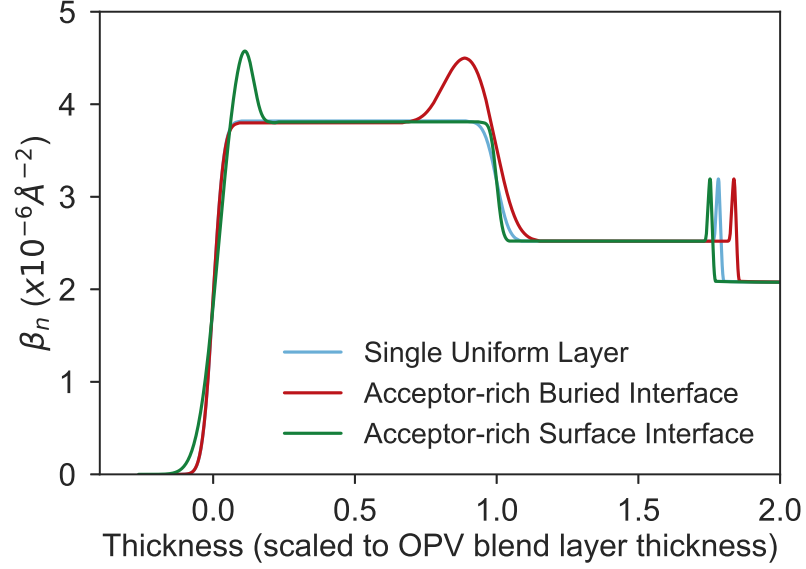


Figure A.26: corresponding SLD profiles of the NR data shown in Figure A.25. A film depth of 0 \AA corresponds to the silicon/sample interface.

Model	I_0	B ($\times 10^{-7}$)	ZnO		Bulk Layer			Interface			χ^2/N_{pts}
			L (\AA)	σ (\AA)	L (\AA)	σ (\AA)	β_n ($\times 10^{-6} \text{ \AA}^{-2}$)	L (\AA)	σ (\AA)	β_n ($\times 10^{-6} \text{ \AA}^{-2}$)	
Uniform Layer	0.998	2.74	607	27	782	23	3.82	–	–	–	34.36
Buried Interface	0.925	3.11	645	45	629	23	3.80	141	43	4.64	9.47
Surface Interface	0.946	2.88	586	13	674	18	3.81	94	46	5.00	17.16

Table A.13: Table of NR fit parameters for a PTB7-Th : d-EH-IDTBR thin film corresponding the data shown in Figure A.25 and Figure A.26.

PTB7-Th : d-O-IDTBR

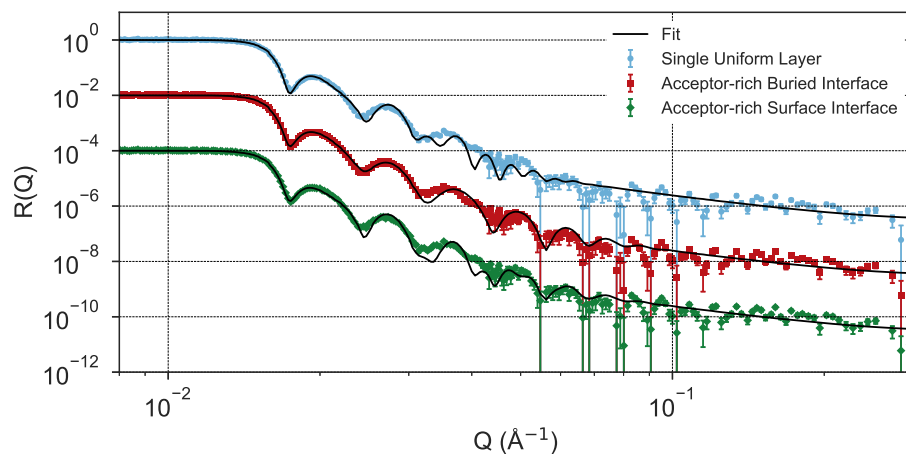


Figure A.27: NR of a PTB7-Th : d-O-IDTBR thin film deposited on a ZnO coated silicon substrate and annealed at 80°C for 10 minutes. The PTB7-Th : d-O-IDTBR layer has been modelled in three different ways as: a single uniform layer, a layer with an acceptor-rich region buried at the ZnO interface and a layer with an acceptor-rich surface. Data offset by two decades for clarity.

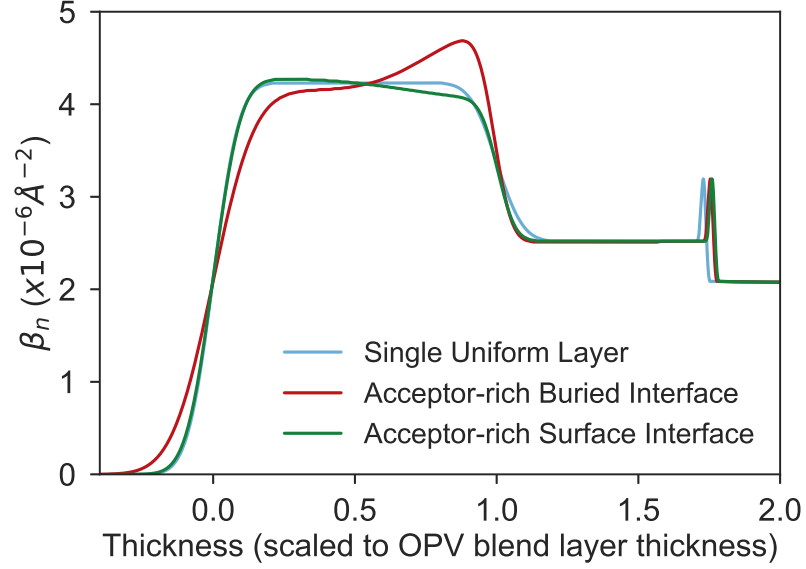


Figure A.28: corresponding SLD profiles of the NR data shown in Figure A.27. A film depth of 0 \AA corresponds to the silicon/sample interface.

Model	I_0	B ($\times 10^{-7}$)	ZnO		Bulk Layer			Interface			χ^2/N_{pts}
			L (\AA)	σ (\AA)	L (\AA)	σ (\AA)	β_n ($\times 10^{-6} \text{ \AA}^{-2}$)	L (\AA)	σ (\AA)	β_n ($\times 10^{-6} \text{ \AA}^{-2}$)	
Uniform Layer	0.928	3.07	476	48	659	47	4.23	–	–	–	7.44
Buried Interface	0.927	3.01	492	31	491	75	4.15	155	104	4.86	6.78
Surface Interface	0.932	3.04	492	31	201	150	4.02	457	50	4.26	7.90

Table A.14: Table of neutron reflectivity fit parameters for a PTB7-Th : d-O-IDTBR thin film corresponding the data shown in Figure A.27 and Figure A.28.

PTB7-Th : d-O-IDTBCN

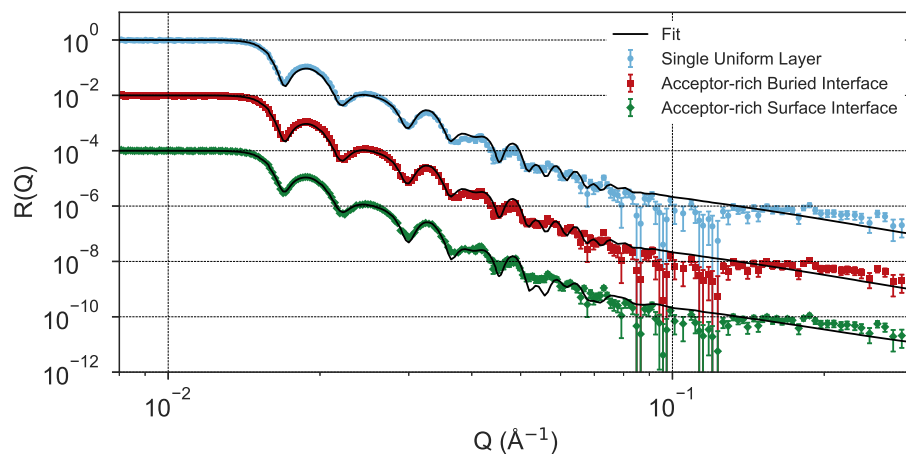


Figure A.29: NR of a PTB7-Th : d-O-IDTBCN thin film deposited on a ZnO coated silicon substrate and annealed at 80°C for 10 minutes. The PTB7-Th : d-O-IDTBCN layer has been modelled in three different ways as: a single uniform layer, a layer with an acceptor-rich region buried at the ZnO interface and a layer with an acceptor-rich surface. Data offset by two decades for clarity.

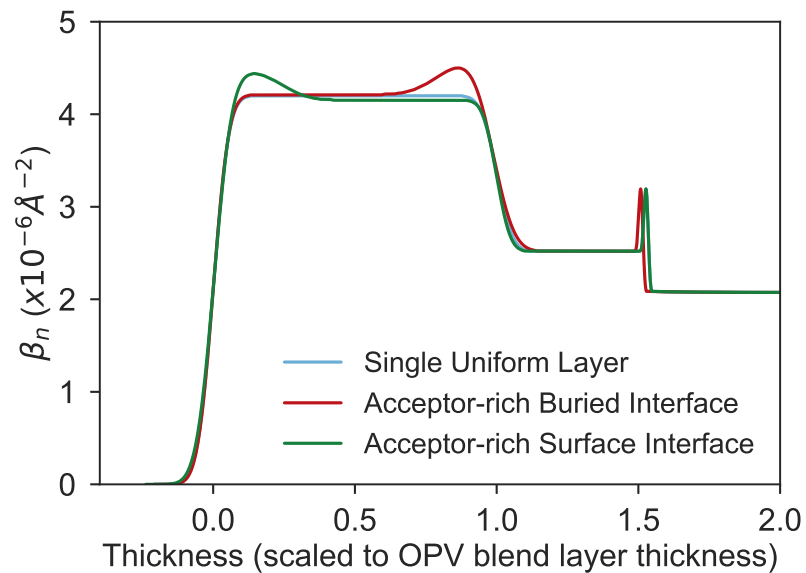


Figure A.30: corresponding SLD profiles of the NR data shown in Figure A.29. A film depth of 0 \AA corresponds to the silicon/sample interface.

Model	I_0	B ($\times 10^{-7}$)	ZnO		Bulk Layer			Interface			χ^2/N_{pts}
			L (\AA)	σ (\AA)	L (\AA)	σ (\AA)	β_n ($\times 10^{-6} \text{ \AA}^{-2}$)	L (\AA)	σ (\AA)	β_n ($\times 10^{-6} \text{ \AA}^{-2}$)	
Uniform Layer	0.997	4.80	386	32	741	32	4.20	–	–	–	13.78
Buried Interface	0.963	6.78	385	43	594	32	4.21	146	58	4.60	8.26
Surface Interface	0.971	6.85	386	28	559	54	4.15	180	37	4.47	4.35

Table A.15: Table of NR fit parameters for a PTB7-Th : d-O-IDTBCN thin film corresponding the data shown in Figure A.29 and Figure A.30.

Appendix B

UV-Vis Photostability Studies

This Appendix contains the UV-Vis absorption spectra for samples discussed in Chapter 5.

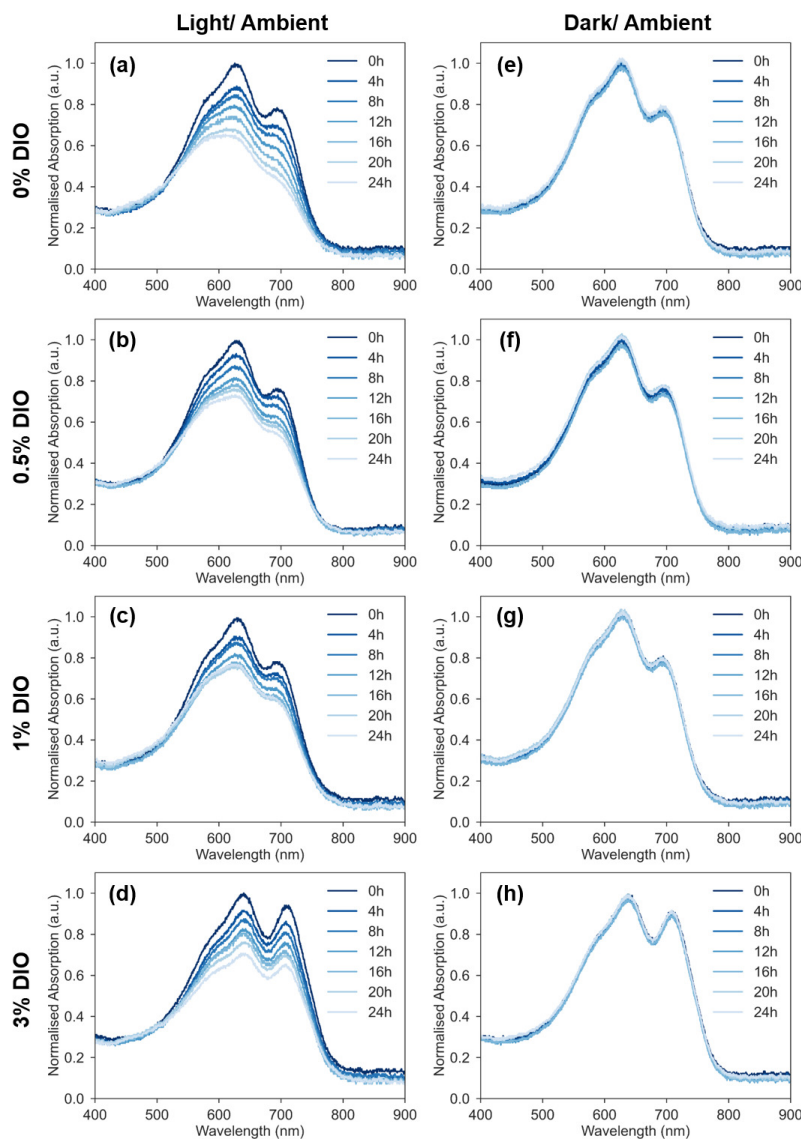


Figure B.1: Normalised UV-Vis absorption of pure PBDB-T : ITIC films processed with 0-3 Vol% DIO and aged in (a-d) light/ ambient conditions and (e-h) in the dark/ ambient conditions.

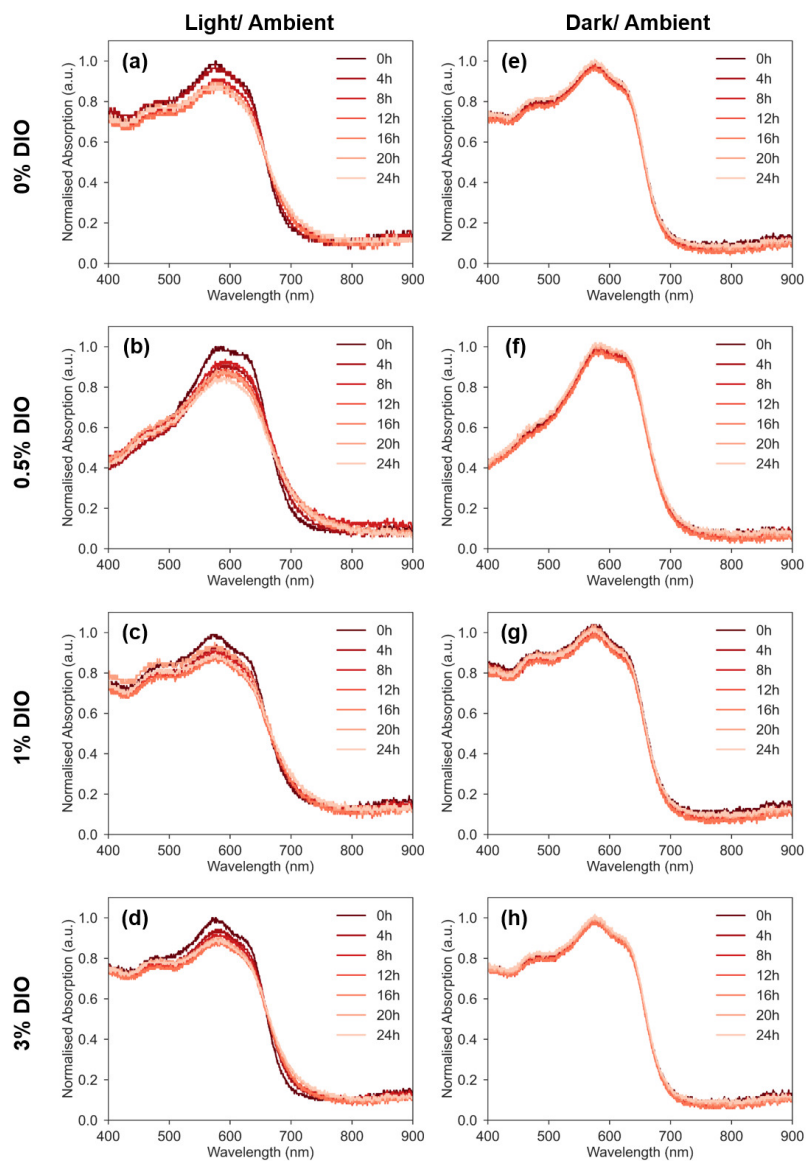


Figure B.2: Normalised UV-Vis absorption of PBDB-T : PC₇₁BM blend films processed with with 0-3 Vol% DIO and aged in (a-d) light/ ambient conditions and (e-h) in the dark/ ambient conditions. Note: PBDB-T appears to have a greater contribution than PC₇₁BM to the 0.5 Vol% DIO spectra suggesting the donor-acceptor ratio was slightly different to the expected 1:1 ratio for this particular sample.

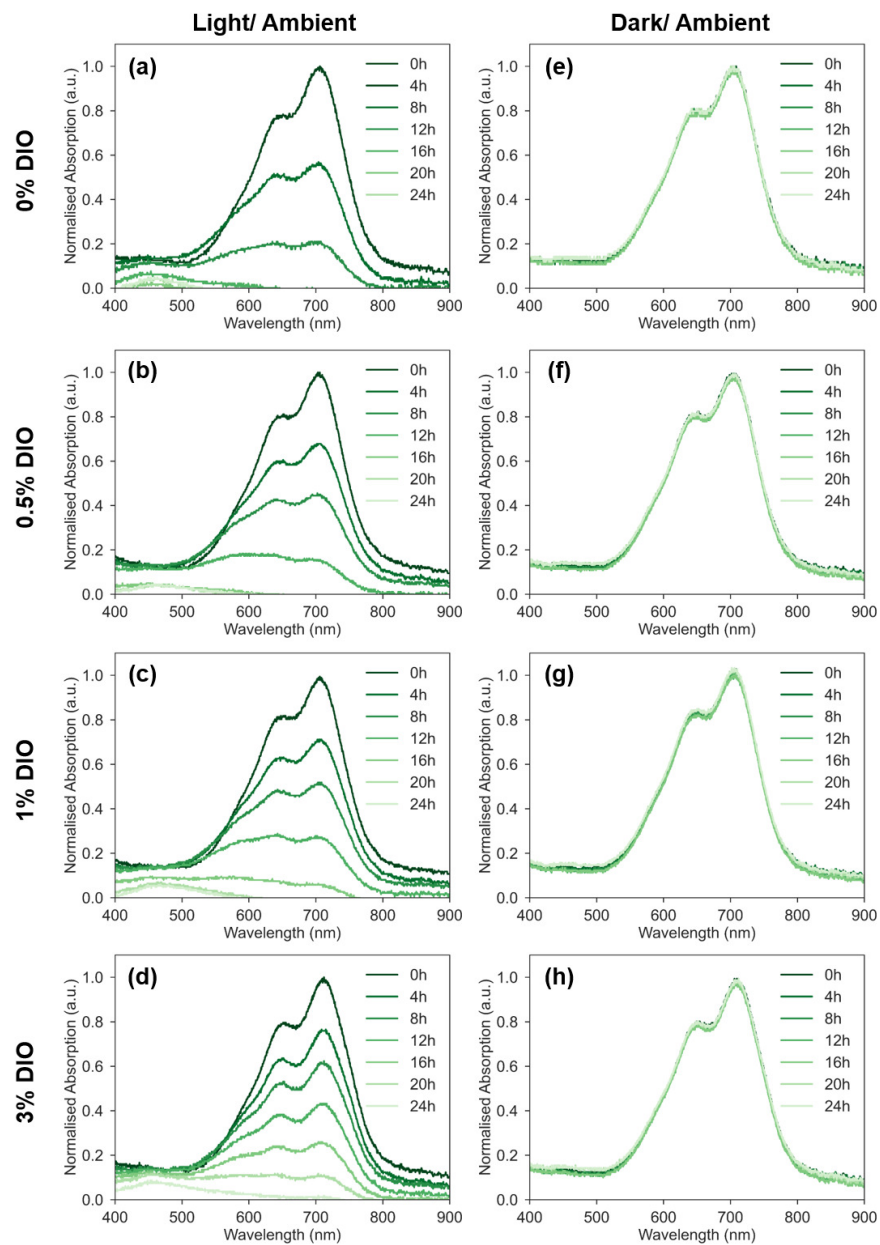


Figure B.3: Normalised UV-Vis absorption of pure ITIC films processed with 0-3 Vol% DIO and aged in (a-d) light/ ambient conditions and (e-h) in the dark/ ambient conditions.

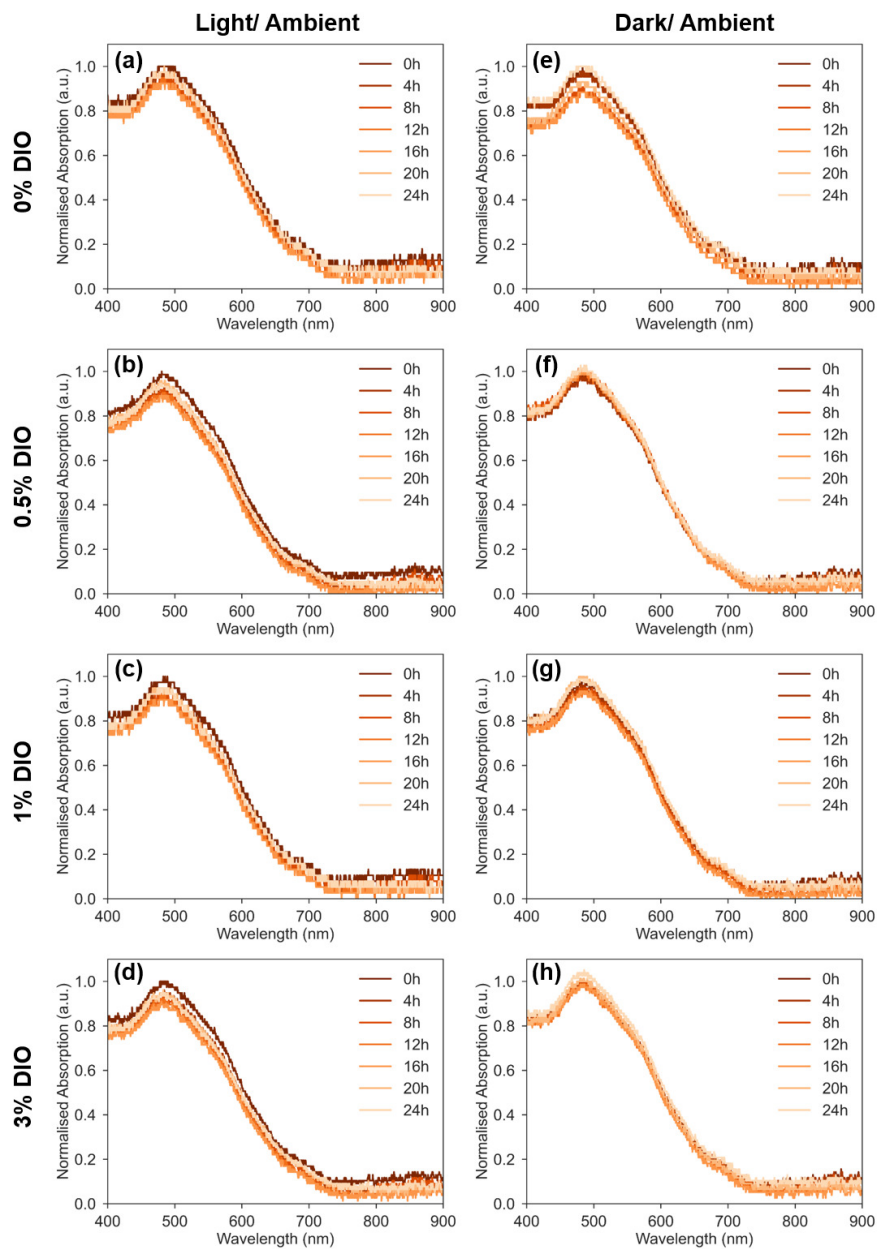


Figure B.4: Normalised UV-Vis absorption of pure PC₇₁BM films processed with 0-3 Vol% DIO and aged in (a-d) light/ ambient conditions and (e-h) in the dark/ ambient conditions.

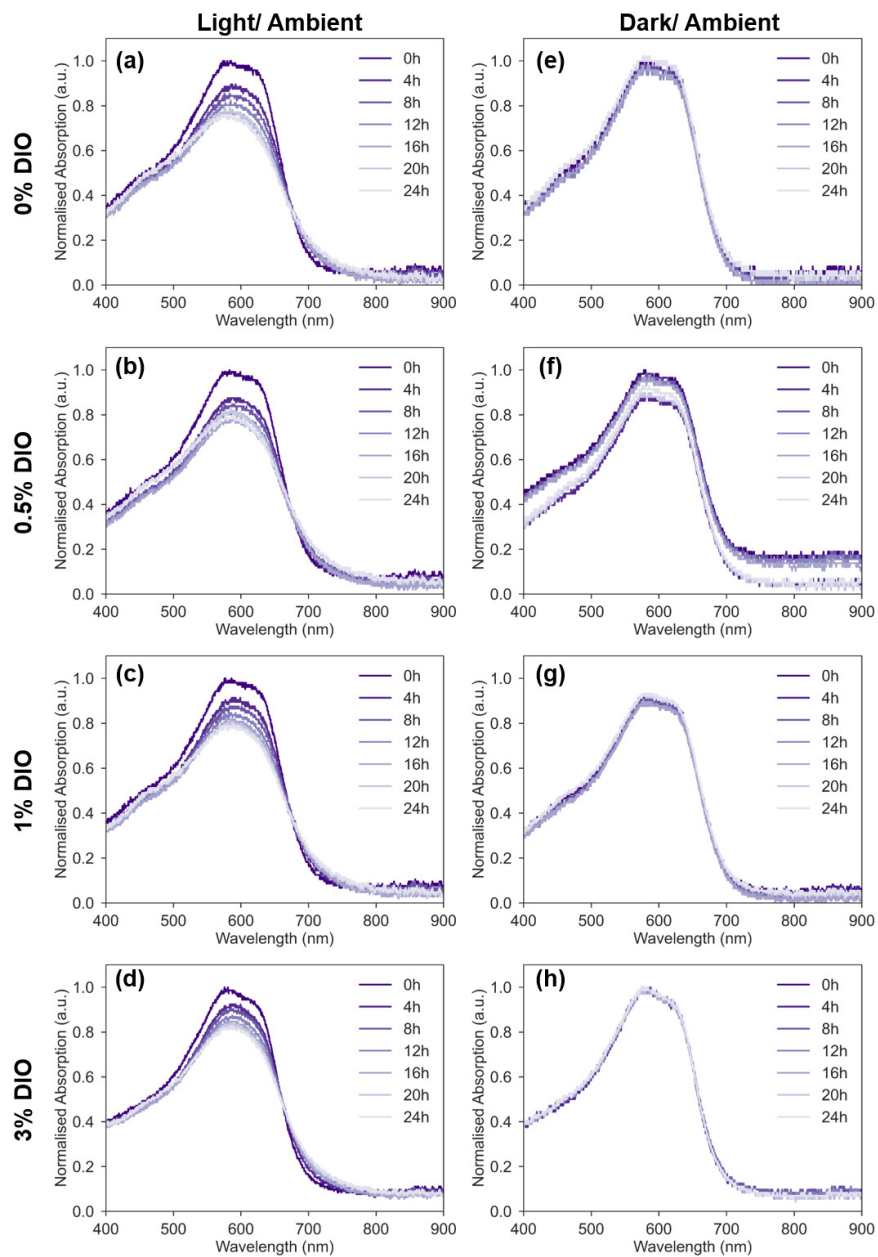


Figure B.5: Normalised UV-Vis absorption of pure PBDB-T films processed with 0-3 Vol% DIO and aged in (a-d) light/ ambient conditions and (e-h) in the dark/ ambient conditions.